Alma Mater Studiorum – Università di Bologna

DOTTORATO DI RICERCA IN

ASTROFISICA

Ciclo XXXIII

Settore Concorsuale: 02/C1 – Astronomia, Astrofisica, Fisica della Terra e dei Pianeti
Settore Scientifico Disciplinare: FIS/05 – Astronomia e Astrofisica

PAINTING DARK MATTER HALOS WITH GALAXIES IN MOCK SAMPLES FOR FUTURE SURVEYS

Presentata da: Giacomo Girelli

Coordinatore Dottorato:

Chiar.mo Prof.
Francesco R. Ferraro

Supervisore:

Dott.ssa Lucia Pozzetti

Co-Supervisore:

Dott.ssa Micol Bolzonella

Collaboratori:

Dott. Iary Davidzon
Dott. Carlo Giocoli
Prof. Federico Marulli

Esame finale anno 2021

The good thing about science is that it's true whether or not you believe in it.

Neil deGrasse Tyson

ABSTRACT

Studying galaxy formation and evolution processes is certainly non-trivial since many different physical processes are simultaneously at play and, at the same time, the cosmological context in which galaxies form an evolve needs to be taken into account. In addition, the interpretation of the various physical processes is far from being understood and countless details that contribute to the galaxies built-up and evolution are still largely unknown. The next generation of surveys, such as Euclid, are likely to shed light on many of these open questions. This will provide major improvements in our understanding of galaxy formation, cosmological parameters, and the nature of dark energy and neutrino mass. However, at the same time, the precision of models and simulations need to be improved in order to keep up with the pace of the data. In this respect, mock catalogs are extremely useful to provide forecasts, to optimise the observational strategies, to verify scientific performances and maximise the scientific exploitation of future surveys and missions.

In this thesis we present a completely empirical workflow that produces, from the outputs of a dark matter cosmological simulation, a galaxy mock catalog which is able to reproduce with accuracy a number of physical properties of galaxies such as stellar masses, star-formation rates, observed photometry, emission lines and sizes. The main goal of this thesis is to provide to the scientific community a galaxy mock catalog useful, as mentioned above, to make predictions for future surveys, to plan future observations, to understand and minimize uncertainties and to study systematics and selection effects.

The procedure we present starts from the outputs of a dark matter simulation, and consists in three steps:

1. Assignment of the stellar mass to dark matter halos. To do so, we first derived a galaxy-halo connection from $z = 0$ to $z = 8$ with a sub-halo abundance matching technique. We used the halo mass functions from two dark matter-only simulations (i.e. the DUSTGRAIN-pathfinder and Millennium I+II simulations) and observed stellar mass functions (presented in Chap. 2) on the SDSS, COSMOS and CANDELS fields that are currently the best fields with a homogeneous redshift coverage from $z = 0$ to $z = 8$ because of their statistical and photometric accuracy

in the photometric redshifts, stellar masses, and stellar mass function (SMF) determination. Then, a simple empirical model has been constructed in order to easily describe the evolution with redshift of the stellar-to-halo mass relation (SHMR, Chapter 3). We compare our results with several results from the literature and interpret the stellar-to-halo mass relation as the star-formation efficiency. Once the empirical model is defined, we populated halos with galaxies (Section 4.1) and compare it with observations.

2. Division of galaxies in star-forming and quiescent objects. This step is performed by devising a star-forming probability relation from observed stellar mass functions and applying then the relation to the simulated galaxies (Section 4.2).

3. Assignment of other physical properties. We make use of the completely empirical public code EGG (Schreiber et al., 2017) to assign a variety of physical properties, e.g. observed photometry in any desired band, star-formation rates, emission lines, sizes and SEDs (Section 4.3). In addition, we validate the distribution and evolution of several physical properties and of clustering functions and make prediction for future surveys in Chapter 5.

To conclude, (in Chapter 5), we validate the properties of our mock catalog against observed estimates. Finally, we also provide examples of the many forecasts that can be performed with the aid of our mock.

TABLE OF CONTENTS

ACRONYMS

- **AGN** : active galactic nuclei
- **AM** : abundance matching
- **B/T** : bulge/total
- **BAO** : baryonic acoustic oscillations
- **BC03** : Bruzual & Charlot (2003)
- **BH** : black hole
- **CANDELS** : cosmic assembly near-infrared deep extragalactic legacy survey
- **CDFS** : CANDELS deep field south
- **CMB** : cosmic microwave background
- **CMF** : cumulative mass function
- **CSMF** : cumulative stellar mass function
- **CHMF** : cumulative halo mass function
- **CL** : cluster
- **CLF** : conditional luminosity function
- **COSMOS** : cosmic evolution survey
- **Dec** : declination
- **DM** : dark matter
- **EM** : empirical model
- **ETG** : early-type galaxy
- **G13** : Guo et al. (2013a)
- **G19** : Girelli et al. (2019)
- **GMC** : giant molecular clouds

- **GOODS** : great observatories origins deep survey
- **GSMF** : galaxy stellar mass function
- **HOD** : halo occupation distribution
- **HUDF** : Hubble ultra-deep field
- **IMF** : initial mass function
- **H15** : Henriques et al. (2015)
- **H2O** : Hawaii-Two O
- **HMF** : halo mass function
- **IGM** : inter-galactic medium
- **ISM** : inter-stellar medium
- **IR** : infrared
- **JWST** : James Webb space telescope
- **ΛCDM** : Λ cold dark matter
- **LSST** : Vera Rubin large synoptic survey telescope
- **LTG** : late-type galaxy
- **M05** : Maraston (2005)
- **MCMC** : Monte Carlo Markov chain
- **MIPS** : multiband imaging photometer on Spitzer
- **MOONS** : multi-object optical and near-infrared spectrograph
- **NFW** : Navarro-Frenk-White
- **NICMOS** : near infrared camera and multi-object spectrometer
- **NIR** : near infrared
- **PSF** : point spread function
- **RA** : right ascension
- **SAM** : semi-analytic model
- **SDSS** : sloan digital sky survey
- **SED** : spectral energy distribution
- **SFE** : star-formation efficiency
- **SFH** : star-formation history
- **SFR** : star-formation rate
- **sSFR** : specific star-formation rate
- **SHAM** : sub-halo abundance matching
- **SHMR** : stellar-to-halo mass relation
- **SMBH** : super-massive black hole

- **SMF** : stellar mass function
- **SN** : supernova
- **SPHEREx** : spectro-photometer for the history of the universe, epoch of reionization and ices explorer
- **SPS** : stellar population synthesis
- **sSFR** : specific star-formation rate
- **TP-AGB** : thermally-pulsing asymptotic giant branch
- **UV** : ultra-violet
- **VIPERS** : VIMOS public extragalactic survey
- **VLT** : very large telescope
- **WFIRST** : wide-field infrared survey telescope
- **WL** : weak-lensing

1

INTRODUCTION

Galaxy formation and evolution is a subject of great complexity, since many different aspects are simultaneously at play. First of all, the cosmological context is fundamental since it is the base on which galaxy formation takes place. Secondly, many different physical processes involved in the process, such as gas cooling, star-formation, feedbacks and radiation, need to be taken into account simultaneously. However, the interpretation of galaxy formation and evolution is far from being understood and countless details are still unknown up to day. Among the many open questions we find the following: how do galaxies connect with dark matter? When did the first galaxies form and how did they assemble their mass though cosmic time? How does gas cool in galaxies, how do stars form, and what determines the dominant feedback processes? How can we best infer physics from available observations?

The next generation of surveys are promising tools that will provide major improvements in our understanding of galaxy formation and evolution, cosmological parameters, and the nature of dark energy and neutrino mass. At the same time, accurate models and simulations/mock catalogs are required in order to infer and interpret fundamental physics from observations. With our present knowledge, many models of galaxy formation and evolution have been developed and tested with the aid of simulation that are, however, still not able to fully reproduce observations.

This thesis aims to build galaxy mock catalogs that are fundamental not only to reveal some physical processes of galaxy formation and evolution helping in their understanding, but also to understand and minimize the systematic uncertainties and selection effects of future missions. In addition, accurate mocks are essential to make predictions about such large surveys, to test softwares that will be used to analyse the outcoming datasets, and to design future observing plans and missions. In particular, in this thesis, we develop an empirical workflow that, using our present knowlewdge (from observations and models) and starting from a cosmological dark matter simulation connects dark matter halos with galaxies physical properties.

In this Chapter, we start by describing the cosmological context and the standard cosmological model we adopted to build the mock catalogs, followed by a description of our current theoretical knowledge of the processes related to galaxy formation and evolution. Then, a brief description of the main tools used to simulate galaxies is provided. Given the many open issues in this field, one has to rely on observations, coupled with simulations, of galaxies in order to shed light on all the physical processes in play. We therefore provide a brief summary of the main statistical observed properties of galaxies. Then, the focus is placed on the future missions that are likely to greatly contribute to our understanding of galaxies. Finally, a brief summary of the structure of this thesis is presented.

1.1 Cosmological context

Modern cosmology is based on the assumption that the Universe is homogeneous and isotropic on large scales (the cosmological principle) and on Einstein's theory of General Relativity for which the structure of space-time is determined by the mass and energy content of the Universe. In an isotropic

and homogeneous Universe, which is either contracting or expanding, the general form of the metric is described by the Friedmann–Lemaître–Robertson–Walker metric:

$$ds^2 = c^2dt^2 - a^2(t)\left(\frac{dr^2}{1-kr^2} + r^2(d\theta^2 + \sin^2\theta d\phi^2)\right) \tag{1.1}$$

where $a(t)$ is the scale factor that describes the evolution of the universe, c is the speed of light in vacuum space ($= 2.997 \times 10^8$ m s^{-1}) and k is the curvature parameter, which can be either positive, zero, or negative, as schematically illustrated here:

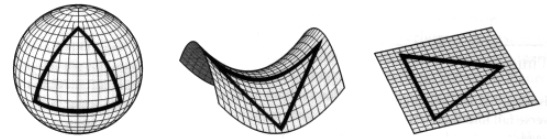

Positive Curvature Negative Curvature Flat Curvature

In general relativity the dynamic of the Universe is described by the Einstein equations, which illustrate how matter changes the space-time geometry of the Universe:

$$-\frac{8\pi G}{c^4}T^{\mu\nu} = G^{\mu\nu} + \Lambda g^{\mu\nu} \tag{1.2}$$

where $T^{\mu\nu}$ is the energy-momentum tensor (that encapsulates information about the density and flux of energy and momentum in spacetime), $G^{\mu\nu}$ is the Einstein tensor (used to describe the curvature), Λ is the so-called cosmological constant (describing the energy density of space), $g^{\mu\nu}$ is the metric tensor (that captures all the geometric and causal structure of spacetime), and G is the gravitational constant ($= 6.67 \times 10^{-11}$ m^3 kg^{-1} s^{-2}).
The Einstein equations (Eq. 1.2) can also be expressed (using the two Friedmann's equations) in the following form:

$$H^2 = \left(\frac{\dot{a}}{a}\right)^2 = \frac{8\pi G}{3}\rho - \frac{kc^2}{a^2} + \frac{\Lambda c^2}{3} \tag{1.3}$$

$$\dot{H} + H^2 = \frac{\ddot{a}}{a} = -\frac{4\pi G}{3}\left(\rho + 3\frac{p}{c^2}\right) + \frac{\Lambda c^2}{3} \tag{1.4}$$

where H is the Hubble parameter, p and ρ are the pressure and density describing the Universe (encapsulated in the energy-momentum tensor). The Hubble parameter is defined as $H = \dot{a}/a$ and measures the expansion rate of the Universe. We can also define other useful quantities that will be extensively used throughout this thesis, which are the redshift: $z = \Delta\lambda/\lambda = (1+a)^{-1}$ that describes a shift of the radiation (with a certain wavelength λ) toward longer or shorter wavelengths depending on whether the Universe is expanding or contracting. In addition, we can also define the densities of the various components of the Universe (i.e. matter, radiation, curvature and dark energy) that scale with the values at present time multiplied by their evolution with redshift and renormalized by

$E^2(z) = (H/H_0)^2$, where H_0 is the value of the Hubble constant today:

$$\Omega_m(z) = \Omega_m \frac{(1+z)^3}{E^2(z)}, \quad \Omega_r(z) = \Omega_r \frac{(1+z)^4}{E^2(z)}$$

$$\Omega_k(z) = \Omega_k \frac{(1+z)^2}{E^2(z)}, \text{ and } \quad \Omega_\Lambda(z) = \Omega_\Lambda \frac{1}{E^2(z)} .$$

All the definitions listed above have a general validity for a large variety of cosmological models that have been proposed over the years and only derive from the assumption that the cosmological principle is valid. In the following we discuss the current most popular cosmological model which has been derived directly from observations of the Universe.

1.1.1 The standard cosmological model

In 1965 Penzias and Wilson detected a signal coming from all over the sky, with spectral feature very close to a perfect black body spectrum with temperature of about 2.7 K, thus with emission peaking in the microwaves (from Wien's displacement law $\lambda_{max} \approx \frac{2.9 \cdot 10^{-3} \text{ K m}}{T}$). Through the years more refined instruments have looked at this cosmic microwave background (CMB), finding that the temperature is not uniform, but fluctuates around the mean by a fractional difference of only 10^{-5}. Therefore, through observations of the Universe in the microvawes with several missions, including the Wilkinson Microwave Anisotropy Probe (WMAP, Spergel et al. 2003) and Planck (Planck Collaboration et al., 2016) satellites, a concordance standard cosmological model has been defined. Observations have shown that the Universe started around thirteen and a half billion years ago from a much denser, hotter, and nearly homogeneous state with respect to the state we see today and has been expanding with an accelerated pace for approximately the past four billion years (see Mo, van den Bosch, & White 2010 for a very detailed book on structure formation and evolution). The whole Universe is thought to be originated from an initial singularity (the so-called Big Bang). In this standard picture, quantum fluctuations in the very early Universe were processed during a period of very rapid expansion called inflation to create the small inhomogeneities that give rise to small perturbations in the primordial density field, detected via temperature fluctuations, called anisotropies, in the cosmic microwave background, shown in Fig. 1.1. These density fluctuations are characterized by a density contrast

$$\delta(\mathbf{x}) = \frac{\rho(\mathbf{x}) - \bar{\rho}_m}{\bar{\rho}_m} \tag{1.5}$$

where $\bar{\rho}_m$ is the mean mass density of the Universe. Assuming that the primordial density fluctuations can be described as a uniform and isotropic Gaussian field, a power spectrum $P(k)$ is a complete statistical description of the initial perturbations.

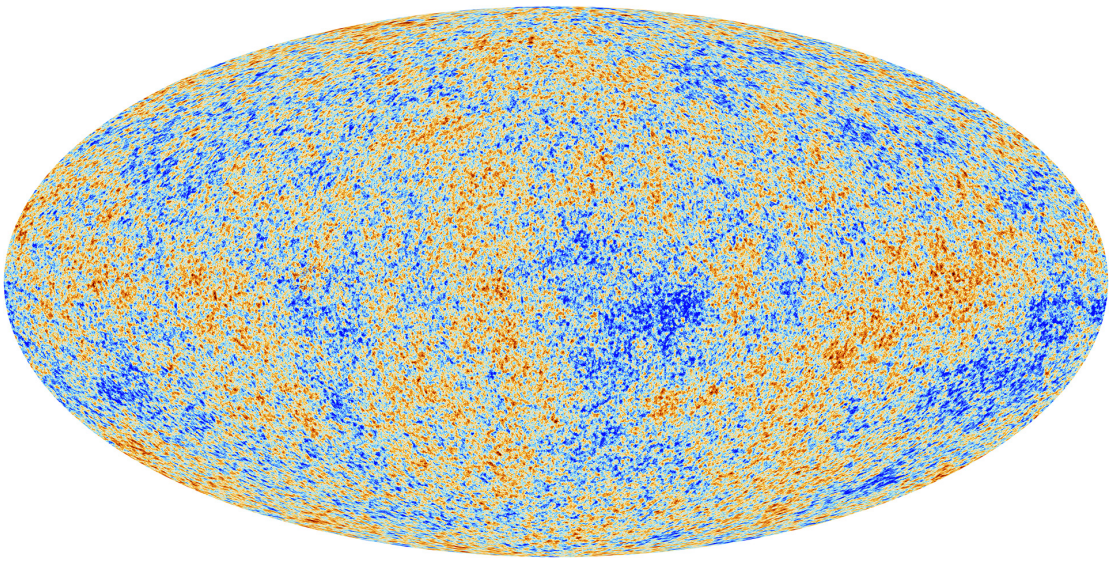

Fig. 1.1 The anisotropies of the cosmic microwave background as observed by the satellite Planck. **Credit: Planck Collaboration et al. (2016)**.

These tiny fluctuations, viewed at the time when free electrons combined with nuclei to form neutral atoms at a redshift of $z \sim 1100$, have now been studied in exquisite detail with many experiments. When combined with other observations, such as the distance-redshift relation from Type Ia SNe (e.g. Riess et al. 1998), abundances of galaxy clusters (e.g. Adami et al. 2018), constraints on the present-day expansion rate (the so called Hubble parameter H_0) from nearby Cepheid stars (e.g. Freedman et al. 2001), and galaxy clustering (e.g., baryon acoustic oscillations, Beutler et al. 2011), these measurements yield stringent constraints on the fundamental cosmological parameters (Hinshaw et al., 2013; Planck Collaboration et al., 2018). These combined observations point to a Universe that is geometrically flat, dominated by dark matter (DM) and dark energy that expands with an accelerated rate due to dark energy, that, together with dark matter, accounts for more than 95% of the energy density of the present Universe. The physical nature of both is unknown, although there are numerous theories. The most popular one, the so-called standard cosmological model, which we refer to as ΛCDM, predicts that the dark matter is cold and collisionless and makes up $\sim 25\%$ of the cosmic mass-energy density at present time, and the dark energy is in the form of a cosmological constant Λ (as expected in the most general form of Einstein's equations of general relativity), comprising $\sim 70\%$. The remaining $\sim 5\%$ is composed by baryons, i.e., normal atoms that make up stars, gas, and galaxies. In the standard cosmological model, the cosmological parameters described above take the values implied by observations of the cosmic microwave background (CMB), which are found by Planck Collaboration et al. (2016) to be

$$\begin{cases} H_0 = 67.8 \pm 0.9 \quad \text{km s}^{-1}\text{Mpc}^{-1} \\ \Omega_m = 0.315 \pm 0.013 \\ \Omega_{DM} = 0.2666 \pm 0.0022 \\ \Omega_B = 0.0494 \pm 0.0002 \\ \Omega_\Lambda = 0.685 \pm 0.012 \end{cases} \tag{1.6}$$

1.1.2 Dark matter

After the inflation, when density fluctuations have been created, the background density decreases with the expansion of the Universe itself. In the so-called hierarchical structure formation scenario, when a perturbation of the density field $\delta(\mathbf{x})$ exceeds a critical overdensity relative to the background density of the Universe, the region within that excess stops expanding and starts collapsing to form a gravitationally self-bound structure. The simplest model for collapse is a uniform sphere slightly denser than the surrounding (Bertschinger, 1985). However, in reality structures do not form spherically symmetric and the collapse process leads to a sort of virial stationary equilibrium where the total kinetic energy is related to the total gravitational potential energy:

$$\sum_{i=1}^{N} m_i \dot{\mathbf{r}}_i^2 = -\sum_{i=1}^{N} \mathbf{F}_i \cdot \mathbf{r}_i \tag{1.7}$$

where the left hand side of the equation is twice the total kinetic energy of a system, and the right hand side is the total potential energy for the system, which in the case of a uniform sphere of radius r and $M = \sum_i m_i$, if only described by the gravitational force, takes the form GM^2/r. The virial theorem (Eq. 1.7) produces a natural boundary for structures that "virialize" in an equilibrium state . Given that the birth and growth of such structures is driven mainly by gravity (as shown in Eq. (1.7)), dark matter dominates the gravitational potential. The centers of these dark matter overdensities, are the so-called halos (see e.g. Navarro et al. 1996). Once formed, halos grow through a sequence of mergers and accretion of smaller systems to form bigger and bigger halos as they move down with redshift (see Fig. 1.2 for an example of dark matter halos growth). In this picture, galaxies form at the centers of halos, and their formation is mainly driven by the cooling and condensation of gas in the center of the potential wells of the extended virialized dark matter halos (White & Rees, 1978). We will describe in more detail the physics of galaxy formation and evolution in Sect. 1.2.

1.1.3 Cosmological numerical simulations

Dark matter, therefore, builds the backbone for the formation of galaxies. The evolution of dark matter particles is described by the collisionless Boltzmann equation ($\mathrm{d}f/\mathrm{d}t = 0$) coupled to Poisson's equation ($\nabla^2\Phi = 4\pi G \int f d\mathbf{v}$). The Boltzmann equation describes the evolution of the distribution function $f = f(\mathbf{r}, \mathbf{v}, t)$ of DM (where $\mathbf{r}$ and $\mathbf{v}$ describe the position and velocity of each particle at

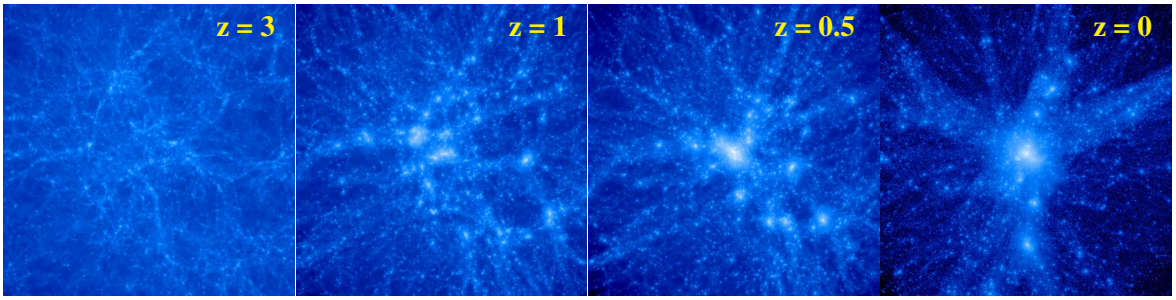

Fig. 1.2 Evolution of a dark matter density field around a cluster. **Credit: Kravtsov & Borgani (2012)**

a certain time t) under the influence of a gravitational potential Φ. This pair of equations has to be solved in an expanding background Universe dictated by the Friedmann equations, which are derived from the field equations of general relativity, as seen above. The high dimensionality of the collisionless Boltzmann equation prohibits efficient numerical solution methods based on standard techniques for partial differential equations. Therefore, over the past decades, numerical techniques have been developed to extensively study and characterize the growth of structure in a ΛCDM scenario. Cosmological simulations are typically performed with periodic boundary conditions to mimic the large-scale homogeneity and isotropy of the matter distribution of the Universe, i.e. the cosmological principle. Among the most popular numerical techniques, used to solve Boltzmann and Poisson's equations, is the N-body method. Simply put, N-body simulations integrate the differential equations defining the particle motions in gravity. In practice, the number N of particles involved, each with a certain mass m_N, is usually very large (typical simulations include many millions, the Millennium simulation included ten billion, Springel et al. 2001) and the number of particle-particle interactions that need to be computed increases on the order of N^2, and so direct integration of the differential equations can be prohibitively computationally expensive and, this is even more true when one wants to simulate large volumes of the Universe with the same particle density.

To avoid this issue, usually, numerical integration is performed over small timesteps and a number of approximation techniques have been developed (e.g. particle-mesh, Kravtsov et al. 1997; Tree particle-mesh, Hopkins 2015; Springel et al. 2005; fast-multipole, Potter et al. 2017; approximate methods, Monaco 2016). Another solution to limit computational costs is to reduce the number N of particles involved (and therefore increase the mass m_N of each individual particle), and, as a consequence, reduce the so-called resolution of the simulation (i.e. the size of the structures that can be identified), or, alternatively, one can simulate smaller volumes of the Universe maintaining the same particle density.

In addition to that, also the storage of the output data from the simulations can be prohibitively and, therefore, usually simulation data are only saved for some (pre-fixed) timesteps (i.e. the so-called snapshots).

However, producing the raw simulation data (i.e. the positions of each of the N particles as a function of time) is only the first step in the process. In order to compare simulations results to the real Universe analysis tools are needed to map the data onto real objects. Traditionally, this has been accomplished using the so-called 'halo finders' that search the dark matter density field within the simulations to find locally over-dense gravitationally bound systems, which are then tagged as dark matter haloes. A first simple method is the friends-of-friends algorithm that finds gravitationally bound particles within a certain linking length (Davis et al., 1985). Other more complex methods have been developed over the years (e.g. SUBFIND, Springel et al. 2001; ROCKSTAR, Behroozi et al. 2010). When running a halo finder algorithm, it is also fundamental to define what a halo is (see White 2001). In particular, the different definitions of the mass of a halo, and its properties, lead to differences in the analyses that follow. Concerning the halo mass definitions, among the most popular choices, there are the 'virial' mass of the halo $M_{\rm vir}$, which is the mass defined by the virial theorem (Eq. 1.7) and M_{200} which is the mass contained within R_{200} defined as the radius inside of which the mean density ρ is 200 times the critical density of the universe ρ_{crit}. However, as shown in several works (e.g. Behroozi et al. 2015, Knebe et al. 2011, Onions et al. 2012), different halo finder algorithms may obtain different halo masses by up to 10% at $z \sim 0$, and this difference increases with increasing redshift. This is still an open issue as shown in Fig. 1.3, taken from Onions et al. (2012), where the differences in cumulative number counts of subhalos among different literature halo finders is shown.

Furthermore, when a portion of the sky is observed, its three-dimensional space shape is a cone. Therefore, in order to construct mock catalogs that mimic observations, it is fundamental to build, starting from the dark matter simulation, the so-called lightcones that reproduce the geometry of observations. In short, lightcones are generally produced with the particles stored in the snapshots distributed according to their comoving distances with respect to the observer, from which the redshift was derived, and according to whether they lay within a defined aperture of the field of view, so to create a smooth redshift distribution. In addition, when moving toward higher redshifts, the volume contained within a cone becomes larger and larger, while the volume of the snapshots remains the same. Therefore, in order to push the creation of lightcones to high redshifts, several techniques have been developed to tilt the snapshots and attach them one to the other in a realistic way. Over the years several algorithms have been developed in order to create lightcones that can be used to build mock catalogs that resemble, as much as possible, the configuration of observations (e.g. MapSim , Giocoli et al. 2014 ; MoMaF , Blaizot et al. 2005; Merson et al. 2013). We show in Fig. 1.4, as an example, a schematic representation of a lightcone produced with the MapSim routine (Giocoli et al., 2014).

The gravitationally bound structures that form in these simulations, i.e. the DM halos, their mass function, their abundance, internal structure, shape, clustering, and angular momentum over cosmic time have been extensively quantified (e.g. Navarro et al. 1996, Jenkins et al. 2001, Wechsler et al. 2002, Springel et al. 2005, Giocoli et al. 2010, Despali et al. 2016 and many others). We also show in left panels of Fig. 1.6, some examples of recent N-body simulations that include the Bolshoi (Klypin et al., 2011), Millennium (Springel et al., 2001), Millennium XXL (Springel et al., 2005)

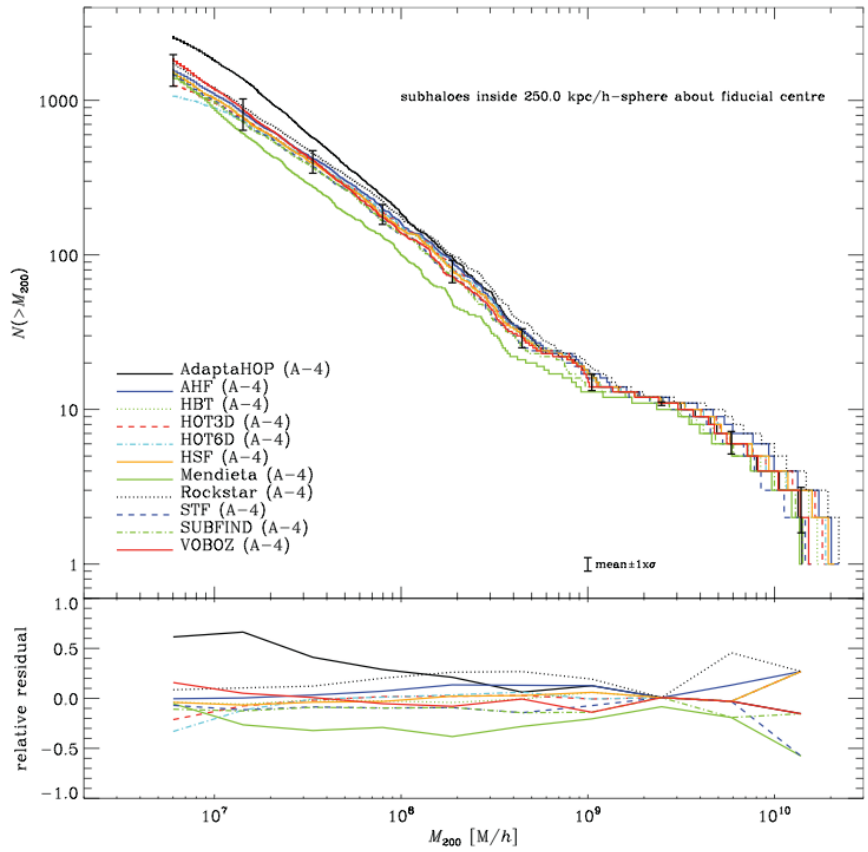

Fig. 1.3 Cumulative number counts of subhaloes above the indicated mass found (M_{200}) within a radius of 250 kpc h^{-1} from the fiducial halo centre. The bottom plot shows the relative offset from the mean of the cumulative mass curve. **Credit: Onions et al. (2012)**.

and the Aquarius (Springel et al., 2008) simulations. In addition, numerical simulations of structure formation in a ΛCDM universe predict that these dark matter halos contain a population of sub-halos. Subhalos are gravitationally bound structures that are smaller than the main halo they belong to, orbiting within the gravitational potential of their main halo. Moreover, when they enter the main halo, they are subject to various dynamical effects (e.g., Choi et al. 2007, Giocoli et al. 2014, Despali & Vegetti 2017), including dynamical friction, tidal stripping, and close encounters with other subhalos, and, therefore, they start to lose mass and may eventually be completely disrupted (these disrupted halos will then be populated by the so-called orphan galaxies, see Sect. 2.3). We show in Fig. 2.9 a schematic illustration of the fate of subhalos once they enter within their main halo. In addition, we will further discuss subhalos and their evolution in Sect. 2.3.

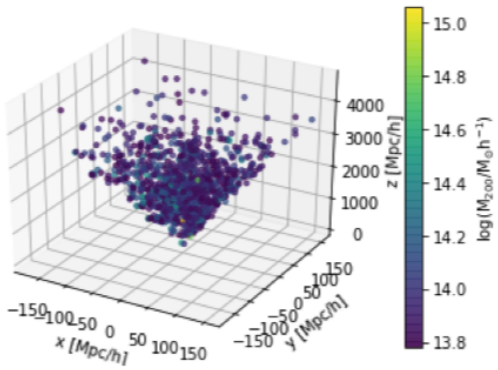

Fig. 1.4 Schematic representation of the past-light-cone constructed using the MapSim routine (Giocoli et al., 2014). The three-dimensional distribution of haloes within a lightcone with 5×5 square degrees aperture up to redshift $z = 4$ is shown. All haloes with mass larger than $M_{200} \gtrsim 6 \times 10^{13} M_{\odot}/h$, colour coded according to their mass, are displayed. **Credit: Giocoli et al. (2018)**.

1.2 Galaxy formation

As discussed in the previous section, galaxies form at the centre of dark matter halos that provide the required seeds for collapse. However, the formation and evolution of galaxies is not only regulated by gravity, as it is for dark matter, but also by a vast range of physical processes (e.g. gas cooling, star-formation, radiation fields, feedbacks) that create the galaxies we observe in the Universe. Understanding the fate of baryons that reside within the dark matter halos is fundamental since most of the information obtained from observations is carried by electromagnetic signals from this component. In the following we briefly describe the key relevant processes for the formation of a galaxy. We refer a curios reader, willing to dive deeper into these topics, to the following reviews: Dayal & Ferrara (2018), Somerville & Davé (2015), Naab & Ostriker (2017) and to the following books: Mo, van den Bosch, & White (2010) and Cimatti, Fraternali, & Nipoti (2019).

1.2.1 Gas cooling

After the decoupling between matter and radiation, baryonic matter is free to collapse and form structures within dark matter potential wells. The collapse of gas leads to the formation of a hot virialised baryonic halo at the center of the dark matter halo. At this point, the gas needs to cool down in order to collapse and form stars and structures. Cooling is a crucial ingredient in galaxy formation. Depending on temperature and density, many cooling processes can affect the gas. The function describing these processes is the cooling function: $\Lambda(T,x,Z,z)$ erg s^{-1} cm^3, where T is the temperature of the gas, x is the fraction of ionized gas, Z is the metallicity of the gas and z is the redshift. The crucial parameter is the temperature. In fact, depending on its value different processes take place: for $T_{vir} \sim 10^7\,K$ the gas is fully collisionally ionized and cools mainly through bremsstrahlung emission from free electrons. In the temperature range $10^4\,K < T_{vir} < 10^6\,K$ a number of excitation

and de-excitation mechanisms can play a role. These mechanisms include re-combinations of electron and ions, or collisional excitations. Since different atomic species have different excitation energies, the cooling rate strongly depends on the metallicity Z of the gas. At $T_{vir} < 10^4\,K$ the gas is almost completely neutral. This suppresses the cooling processes described above, and the main cooling mechanism is due to rotational and/or vibrational excitations and de-excitations of molecules. Finally, at high redshifts ($z \gtrsim 6$), an important cooling channel is due to inverse Compton scattering of the cosmic background by electrons of the hot halo. As the gas cools down, it inflows inward due both to its self-gravity and to dark matter gravity and, if the cooling is effective, this collapse is very rapid. However, collapse may increase the density and temperature of gas, increasing the cooling time and, thus, preventing collapse. It is evident then that a competition between the processes of cooling and collapse is in act and further evolution can occur only if the gas is able to effectively radiatively dissipate its internal energy. A way to characterize the relative importance of these processes is to use time scales associated to these processes. The cooling time is defined as follows:

$$t_{cool} = \frac{E_{gas}}{(dE/dt)} = \frac{3}{2}\frac{(n_e + n_H)kT}{\Lambda n_e n_H} \tag{1.8}$$

where n_H is numeric density of hydrogen atoms, n_e is numeric density of electrons, k is Boltzmann's constant and T is the temperature. This equation represents the relation between the total energy budget of the hot gaseous halo and its energy losses. The dynamical time is defined as follows:

$$t_{dyn} \propto \left(\frac{1}{G\rho}\right)^{1/2} \tag{1.9}$$

where G is the universal gravitational constant and ρ is the mass density of the gas. This time represents the typical time of collapse of a gas sphere with density ρ. We also define t_H as the age of the Universe at the considered redshift. Qualitatively speaking, if $t_{cool} < t_{dyn}$, the cooling is efficient and collapse continues efficiently on a time $t = t_{dyn}$. If $t_{dyn} < t_{cool} < t_H$ the collapse is regulated by the cooling of the gas which is typically in hydrostatic equilibrium, with a typical time dictated by cooling. If $t_{cool} > t_H$ the collapse happens on a timescale longer than the age of the Universe. For a detailed review on the subject see Ferrara (2008). Other relevant processes to take into account in the process of galaxy formation are the angular momentum of the gaseous halo, its interactions with other halos and eventual gas accretion. In fact, it is thought that, depending on the quantity of angular momentum, the gas collapses in different ways. If the gas has a large angular momentum it will produce a gaseous rotating disk, otherwise it will collapse forming a spheroidal system.

1.2.2 Star-formation

Once gas has cooled into a central, baryon dominated structure, which often resembles a rotating disk or a spheroid, the gas fragments into smaller cores that form as a result of the ongoing process of gravitational instability. Large gas agglomerates, known as Giant Molecular Clouds (GMCs), form

under the action of self-gravity. Their typical masses are, to a first approximation, set by the Jeans length which is equal to the product $\lambda_J \approx c_s t_{ff}$, where c_s is the gas sound speed in the disk, and t_{ff} the local free-fall time. If present in the early Universe, turbulent motions and magnetic fields can also contribute extra pressure to the thermal one, playing an important role in supporting the clouds against collapse. These GMCs are composed of a dense core and filaments (with densities $> 10^7$ cm^{-3}) inserted in a more diffuse gas component (with lower density: $\approx 10^2$ cm^{-3}) and are mainly composed by molecular gas (including H_2, CO and other complex molecules). How exactly these cores turn into stars is still an open question in galaxy formation with many obscure details. Qualitatively speaking, it is thought that these cores undergo gravitational collapse, becoming centrally concentrated. In the central regions of the collapsing core, the opacity becomes large enough so that the gas switches from approximately isothermal to adiabatic behaviour. Then, once the gas is hot enough to dissociate the molecular hydrogen, a second collapse occurs and a protostar is formed. However, not all the gas contained in the collapsing core is converted into stars, but only $\approx 30-50\%$ of it. We will discuss the global efficiency of a galaxy in turning its gas into stars in Sect. 3.6, where we derive some insights in galaxy formation from our results. Considering the entire GMC, the efficiency per free fall time of forming stars becomes extremely low (of the order of $\approx 1\%$). Another key ingredient to take into account is the Initial Mass Function (IMF) of the stars which is their mass distribution at birth. It is still uncertain whether the IMF resembles the function proposed by Salpeter (1955) (where the number of stars at a given mass is $N(M_s) \approx M_s^{-2.35}$), or has more complex forms like the functions proposed by Kroupa (2001) or Chabrier (2003). It is also uncertain if the IMF has a universal form or whether it depends on some parameters (e.g. the metallicity). Once star-formation has taken place, we can define a useful quantity, called star-formation rate (SFR), that describes the amount of stars produced each year by a galaxy and is usually expressed in units of solar masses $M_\odot$ per year. A variant of this quantity is the specific star-formation rate (sSFR) which is simply the SFR of a galaxy divided by its total stellar mass: $sSFR = SFR/M_*$. Finally, another convenient quantity to define is the star-formation efficiency (SFE), defined as the total fraction of baryons in a galaxy that are locked into stars. We will give a more formal definition and deepen the discussion on this interesting quantity in Sect. 3.6. For a detailed review on star-formation physics see McKee & Ostriker (2007) or see the book by Krumholz (2015).

1.2.3 Radiation fields

Radiation that comes from newly-born massive stars plays an important role in the thermal and dynamical evolution of galaxies. This is particularly true for the early stages, where the proto-galaxy is characterized by virial temperatures not greatly exceeding those resulting from photo-heating (typically $\sim 10^4$ K) by UV photons. The luminosity and the spectrum of the radiation field emitted by a star depends on its mass (m_s). In fact, massive stars tend to be more luminous and hotter: assuming that they emit as black bodies, and given the main-sequence mass dependence of the stellar radius, $R_s \propto \sqrt{m_s}$, one obtains a temperature that scales as $T_s \propto m_s^{5/8}$. This means that the spectrum of

massive stars contains a large fraction of photons with energy > 13.6 eV capable of ionizing hydrogen atoms and, for the extreme case of almost metal-free stars, the so-called Pop. III stars, also helium. This process creates ionized bubbles through which photons can freely escape from galaxies and in which star-formation is suppressed. In addition, due to this UV radiation produced by massive stars, GMC can eventually photo-evaporate and disperse, obstructing even further star-formation. Also non-ionizing UV photons (i.e. with energies < 13.6 eV) are important since they heat the surrounding gas via photoelectric effect mediated by dust grains that allow for the creation of the multiphase inter-stellar medium (ISM) structures observed in galaxies. For a full description of the radiation processes see the book by Spitzer (1978).

1.2.4 Supernovae

Massive stars play another essential role. They have short lifetimes (as the available energy from nuclear fusion $\propto m_s$): as an example, stars with $m_s \gtrsim 8\,M_\odot$ have a lifetime of $\lesssim 30$ Myr. When the star gas reservoir is finished, the core of the star collapses, igniting a powerful explosion, called supernova (SN), followed by shock waves propagating into the surrounding gas, and carving hot ($T \approx 10^6$ K) bubbles. After the explosion, a remnant, in the form of a neutron star or a black hole, is left. More than 99% of the total energy emitted by the supernova is carried by neutrinos and the remaining energy goes in the form of shock waves and radiation that leave the supernova and are injected in the surrounding medium. The SN energy injection may have a dramatic effect on the evolution of a galaxy: the production of hot gas can quench star-formation (this process in usually called "mechanical feedback"), the shocks can produce bulk motions and turbolence and heavy elements (produced in the explosion) are dispersed in the ISM, preventing efficient gas cooling and, thus, star-formation. Therefore, the role of supernovae in the global evolution of a galaxy are fundamental, even though their exact role is not completely understood (see Ostriker & McKee 1988 for a theoretical description of SN explosions and energy injection). We will discuss in the Sect. 1.2.6 the effects of SNe and their feedback to the global statistical properties of galaxies.

1.2.5 Active galactic nuclei

There are strong observational evidences that most, or perhaps all, galaxies we see today contain a super-massive black hole (SMBH) at their centre (for a review see Kormendy & Ho 2013) with masses of $\sim 0.05\%$ of the total mass of the galaxy. It is difficult to account for these large observed masses, since the progenitors must start out significantly lighter and only acquire their observed masses through accretion of the surrounding material or through mergers with other BHs. In addition, the rate of accretion is bounded by the Eddington limit, which is the maximum allowed by the balance of gravitational force versus radiative pressure. As a consequence, it is still unknown if primordial SHMH formed from a Pop III star remnant, or through the direct gravitational collapse of a gas cloud, or originated from the collapse of a cluster of stars. The majority of SMBH are quiescent or inactive, while a part of them, the so-called active galactic nuclei (AGN), are highly luminous

due to radiation from accretion, outshining their entire host galaxy (for a review see Fabian 2012). AGNs typically emit over the full wavelength range, from the radio to the X-ray, suggesting that the radiation is non-thermal. The total energy emitted by AGNs during their formation is roughly 10% of their rest mass, that makes them competitive with high mass stars with regard to the energy input into the surroundings. There are several observational signatures of feedback associated with AGNs that include high-velocity winds (which may be ejecting the cold ISM from galaxies), hot bubbles apparently generated by giant radio jets (which may be heating the hot halo gas) and mechanical compression of the surrounding gas due to the powerful outflows. Depending on which of these processes is in place (or on which is the balance between them), AGNs can both trigger new star-formation or completely suppress it, quenching a galaxy. From a theoretical point of view, the AGN feedback is modeled in two main ways: the jet (or radio) mode, and the radiative mode (sometimes called quasar mode or bright mode). In the radiative mode, mergers and rapid BH growth, followed by a quasar wind which expels gas from galaxy's center, are responsible for the quenching of a galaxy or, eventually, by compression of the gas they trigger new star-formation (Hopkins et al., 2008a,b). Concerning the jet mode, highly collimated jets of relativistic particles are the main responsibles for quenching due to the hot gas halo that is continually heated, and the supply of new cold gas is cut off (Bower et al., 2006; Croton, 2006; Kimm et al., 2009; Somerville et al., 2008). The exact impact of AGN energy injection into the galaxies, or what is the relative importance of these two main channels of AGN feedback mechanisms, is still not well understood and this is connected to our poor theoretical understanding of black holes and accretion mechanisms. It is, however, clear that, as for SNe, AGNs energy feedback can have a critical role on the formation and evolution of galaxies. In the next section we discuss the effect of AGN feedback on the population of galaxies.

1.2.6 The bigger picture and the role of feedbacks

We have detailed in the previous sections the main ingredients involved in galaxy formation and early evolution. However, galaxies are not isolated systems that evolve on their own. Cosmological simulations have shown that galaxies form at the intersection of the filaments constituting a complex network, known as the "cosmic web". Matter flows into galaxies along these filaments and feed the galaxy with new baryons (Dekel et al., 2009). The accreted intergalactic gas represents new fuel for star formation. At the same time, given its more pristine composition, intergalactic gas acts to dilute the heavy element content of the interstellar medium which is then rapidly re-enriched with heavy elements by new SN explosions associated with the stars produced with the accreted gas. Accretion is not the only way in which galaxies gain their mass. In fact, according to the hierarchical scenario, proto-galaxies are expected to undergo various mergers and interactions with other systems. Galaxy interactions and mergers may have an impact not only on star-formation, by triggering a starburst phase (a phase characterized by an intense star formation) driven by the increased density of the compressed gas, but also on galaxies morphologies and dynamics. In addition, galaxies are expected to be affected by various forms of feedback during their formation and during their lifetime. In fact,

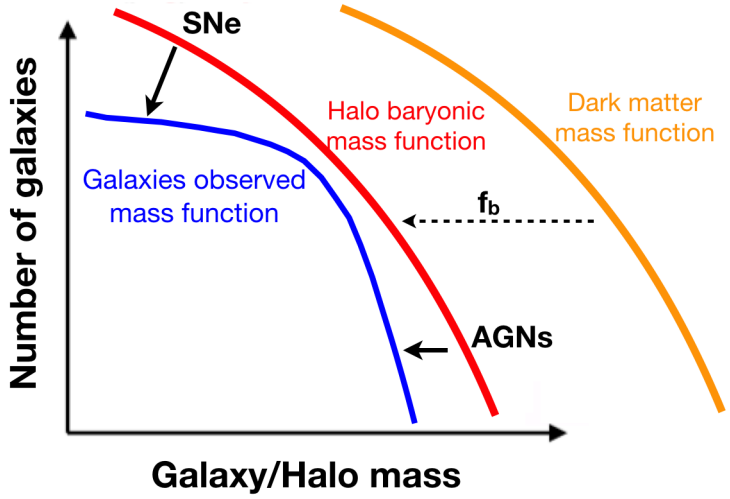

Fig. 1.5 Role of SNe and AGN feedbacks in modelling the observed stellar mass function. The halo baryonic mass function has been shifted to lower halo masses by a factor dictated by the baryon fraction f_b.

observations show that less than 10% of the global baryon budget of the Universe today is in the form of stars while the rest is mainly in the form of inter-galactic and intra-cluster medium. Instead, considering galaxies on their own, they have peak efficiencies of $\sim 20\%$ in converting baryons into stars and the rest is in the form of inter-stellar medium (e.g. Baldry et al. 2012 and see Sect. 3.6). Considering GMCs, they have, as mentioned above, an efficiency of $\approx 30-50\%$ while the rest of the gas is heated by the newly born stars and cannot collapse to form stars. However, in CDM models without some sort of feedback (or suppression of cooling and star-formation), we would expect most of the gas to have cooled and formed stars by the present day. Therefore, some form of feedback is postulated in order to reconcile our theoretical understanding of galaxy formation and evolution with observations. As mentioned above, we can identify three main sources of feedback: radiation, SNe and AGNs.

Radiation from newly-born massive stars can create hot bubbles of gas that can eventually prevent further star-formation in the region. However, massive stars only live shortly and therefore this feedback acts for a small fraction of the life of a galaxy and has a minor impact on its evolution.

More important forms of feedback are represented by SNe and AGNs. We sketch in Fig. 1.5 a comparison between the mass function of galaxies and halos which are defined as the number density of objects (i.e., halos or galaxies) per unit comoving volume in bins of (halo or stellar) mass and redshift. We will discuss in more detail in the next section the mass functions. If one expects that all the baryons contained in a halo are converted into stars, then the shapes of the halo and stellar mass functions should be identical. However, as shown, the galaxy mass function shows a less steep trend at masses below the knee (i.e. the point where the slope of the mass function changes) and a steepening at masses above it. It is therefore postulated (see e.g. Silk 1997, Silk & Mamon 2012,

Somerville & Davé 2015, Naab & Ostriker 2017) that the feedback by SNe affects the low mass part of the mass function by suppressing star-formation and, as a consequence, modifying the mass function trend. The same feedback at high stellar masses is attributed to AGNs. Throughout this thesis (and in particular in Chap. 2 and 3) we will extensively discuss the connection between dark matter halos and their associated stellar masses and we will also discuss in Sect. 3.6 the implication of such feedbacks on the SFE.

1.3 Simulations of galaxies

The vast range of scales involved in galaxy formation and evolution in a cosmological context, ranging from the sub-pc scales of star formation and its associated feedback to the super-Mpc scales associated with galaxies interactions, gave rise to a variety of techniques to simulate galaxies. Dark matter and dark energy dominate the energy budget of the Universe at $z \sim 0$, but the visible components, e.g. stars and gas, of galaxies consist of baryons. Therefore, simulating this matter component is essential to study galaxies and make predictions about the Universe, but, unfortunately, it is also the most challenging aspect of galaxy formation.

At first order, three main classes of models can be identified: the first class is composed by the models that follow the formation of individual galaxies and galaxy populations from well-defined initial conditions and all the known physics of galaxy formation is implemented in the code (e.g. hydrodynamical models). The second class models baryonic physics on top of N-body dark matter simulations through analytic models (semi-analytic models). The main goal of the simulations performed with these two classes is to tackle the open problems in galaxy formation and evolution by studying the outputs of the simulations. Common issues to this type of modelling are that some of the key processes cannot be described purely from a fundamental physics perspective (for example star-formation or AGN feedback), and, therefore, these models are forced to include some Ansatz based on empirical evidence, and, in addition, these models are usually computationally very expensive limiting the volume of the Universe one is able to simulate. The third class is composed by the models (e.g. empirical and halo-occupation distribution models) whose objective is to produce mock catalogs used to make predictions for future observations and surveys and, therefore, they are usually based on empirical evidences instead of relying on physical first principles. While performing simulations with these models is usually computationally relatively cheap (and, therefore, large volumes of the Universe can be simulated), these models strongly depend on the input observations used to calibrate the model itself and are usually less predictive than the models of the first class. Therefore, depending on the scientific goal of a specific study, one can either chose one class of models or the other.

In this Section, we briefly discuss the three main type of models adopted for simulating galaxies: hydrodynamical, semi-analytic and empirical models. Readers interested in the topic are referred to the reviews by Somerville & Davé (2015), Naab & Ostriker (2017) and Vogelsberger et al. (2020).

1.3.1 Hydrodynamical models

Hydrodynamical simulations are the most complex approach to galaxy formation. In short, one simultaneously solves the relevant equations of gravity, hydrodynamics and thermodynamics over particles or grid cells that represent dark matter, gas and stars. This is an extremely powerful, but computationally expensive, method that can track and predict the interplay between dark matter and baryons and the resulting galaxy/large scale structure properties (depending on the simulation size) once appropriate sub-grid (i.e. scales below the resolution limit) recipes for gas cooling, star formation, and feedback are implemented. Hydrodynamic simulations can be divided into two main categories: the first is the Lagrangian or smoothed particle hydrodynamics (SPH) approach in which particles carry the reference frame, and their properties (i.e. mass, temperature, metallicity) are smoothed by weighting them over all neighbours closer than a chosen separation (called the linking length). The second category comprises the Eulerian approach: these are based on a cartesian reference frame where fluid particles are discretised into cells and physical properties are calculated in the fixed cells. Given the dynamic range involved in galaxy formation, the latter method has been extended to Adaptive Mesh Refinement (AMR) techniques where cells satisfying a given criterion, for example in density or temperature, are split into sub-cells leading to a higher resolution in such regions. There are, however, some issues with these techniques (e.g. Springel 2010), such as the inability of SPH to resolve shocks and the sensitivity of AMR results to bulk velocities. This led to the development of a new class of unstructured mesh models, lying between Lagrangian and Eulerian methods, that use Voronoi tesselation to sub-divide the space around particles. This mesh continually de-forms and re-forms as particles move. Despite its obvious advantage in simultaneously tracking both dark matter and gas particles, the enormous computational effort required for hydrodynamic simulations naturally places a limit on the physical volume that can be simulated and the physical parameter space that can be explored for a given mass resolution.

We show in Fig. 1.6, a representation of some recent structure (i.e. N-body DM simulations) and galaxy hydrodynamic simulations, taken from Vogelsberger et al. (2020). In the Figure, the simulations are divided in large volume simulations providing statistical samples of galaxies, and zoom simulations resolving smaller scales in more detail. Furthermore, they are also divided in dark matter-only (N-body), and dark matter plus baryons (hydrodynamical) simulations. As already mentioned in Sect. 1.1.3, dark matter-only simulations have been extensively carried out and now converged on a wide range of predictions. The visual representation comprises several recent hydrodynamical simulations including the Illustris (Vogelsberger et al., 2014), the IllustrisTNG (Nelson et al., 2019), the EAGLE (Schaye et al., 2015), the Horizon-AGN (Dubois et al., 2014), the Magneticum (Dolag et al., 2009), the NIHAO (Wang et al., 2015) and many others. Recent hydrodynamical simulations reproduce galaxy populations whose properties, in general, agree rather well with observational data (see e.g. Schaye et al. 2015, Wang et al. 2015, Sparre et al. 2015, Nelson et al. 2018). However, many detailed predictions of these simulations are still very sensitive to the underlying implementation of

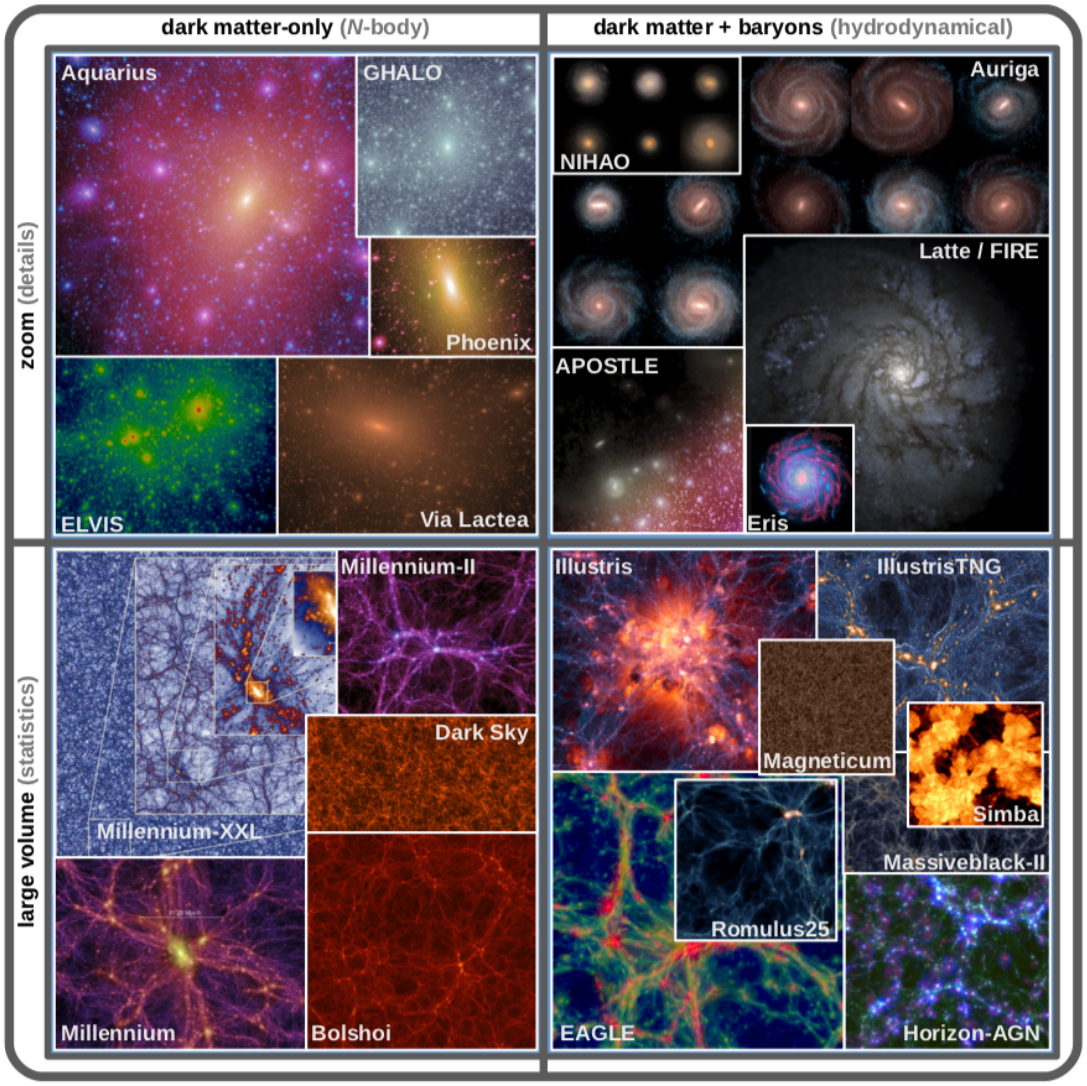

Fig. 1.6 Visual representations of some recent structure and galaxy formation simulations. In left and right panels, DM-only and DM+baryons simulations are shown, respectively. In top panels, zoom simulations are displayed that are able to resolve small scales. In bottom panels, the large volume simulations are visualized. **Credit:** Vogelsberger et al. (2020).

baryonic physics and to the Ansatz assumed for some processes still not completely understood (e.g. star-formation and AGN feedback).

1.3.2 Semi-Analytic models

Studying baryonic physics through hydrodynamical simulations is computationally expensive compared to dark matter-only N-body simulations. An alternative approach is to model baryonic physics on top of N-body dark matter simulations merger trees through analytic models. This models that combine numerical dark matter-only simulations, and analytic models for the prescription of baryonic physics, are known as semi-analytic models (SAMs). These models do not explicitly solve fundamental equations for particles, or grid cells, but rather adopt a set of simplified flow equations (that describe the physical processes discussed in Sec. 1.2) for bulk components, mapped into dark matter merger trees, and jointly track the assembly of baryons and their host dark matter halos through cosmic time (see Benson 2010 for a review). Depending on the aim, the key ingredients, like gas accretion, star formation, chemical/mechanical/radiative feedback and metal enrichment, are included with varying degrees of complexity. For example, gas and metals can be distributed following the dark matter density profile, gas can be split into cold/hot phases, outflows can preferentially carry away metal enriched gas and reionization feedback. As a result of this implementation techniques, and the lack of sub-grid resolution, these models generate average baryonic properties for a given halo. The key advantage of SAMs is their efficiency. The computational requirements of these models are enormously reduced compared with fully numerical simulations. This makes it possible to make predictions for larger volumes or simulate galaxies over a larger range of halo mass. As a consequence, it is possible to perform a wide range of calculations, using different model variations. A recent improvement consists in coupling SAMs with a Bayesian inference approach using a Markov chain Monte Carlo techniques to sample the posterior probability distribution of the multidimensional space of the model parameters (e.g. Henriques et al. 2015) in order to find the best set of model parameters that fits some input observations (i.e. cold gas mass fractions, relation between black-hole and bulge mass, ecc). Over the years several SAMs have been produced. Some examples are *DLB07* by De Lucia & Blaizot (2007), *MORGANA* by Monaco et al. (2007), *YSAM* by Lee & Yi (2013), *GALFORM-GP14* by Gonzalez-Perez et al. (2014), *GALICS 2.0* by Knebe et al. (2015), *SAGE* by Croton et al. (2016), *LGALAXIES* by Henriques et al. (2015, 2013, 2017), *SAG* by Cora et al. (2019, 2018), *ADDGALS* by DeRose et al. (2019) and many others (see the papers of the Cosmic CARNage project for a comparison between many different SAMS: Knebe et al. 2018, Asquith et al. 2018).

However, both SAMs and hydrodynamic simulations approximate physics below their respective resolution scales (galaxies for semi-analytic models; particles and/or grid elements for hydrodynamical simulations), and different reasonable approximations lead to different resulting galaxy properties (Kim et al., 2016; Lu et al., 2014).

1.3.3 Empirical models

With the advent of large galaxy surveys in the past decades, and with the perspective of future large surveys, other methods have been developed. In fact, building realistic and large mocks is fundamental for optimizing the scientific exploitation of ongoing and future large surveys, such as Euclid (Laureijs et al., 2011), Wide-Field Infrared Survey Telescope (WFIRST, Spergel et al. 2015), Multi-Object Optical and Near-infrared Spectrograph (MOONS, Cirasuolo et al. 2014), Hawaii-Two O (H2O), not only by means of understanding and minimizing the systematic uncertainties and selection effects but also to make predictions about such large surveys and to test softwares that will be used to analyse the outcoming datasets. The priors of these new methods are significantly weakened, with respect to SAMs and hydrodynamical simulations, and the physical constraints come entirely from observations. These (relatively new) methods are called empirical models, and are, little by little, growing in complexity (e.g. Birrer et al. 2014, Schreiber et al. 2017, Moster et al. 2018, Behroozi et al. 2019, Grylls et al. 2019 and this work). These methods have the advantage that they do not rely on assumptions about the many details of physical processes that drive galaxy formation. Moreover, by construction, physical properties are in agreement with observations, the parameterization of the model is flexible (given that the parametrization only depend on the input observations and can easily be changed), the computational time is drastically reduced and, as a consequence, large volumes of the Universe can be simulated. The disadvantage of this type of modelling, however, is that they are much less predictive with respect to hydrodynamic simulations or SAMs (Wechsler & Tinker, 2018) and, in addition, they strongly depend on the input observations used to calibrate the model itself.

We will extensively describe the empirical modelling technique, with an eye on the method we implemented, throughout this thesis.

1.4 Statistical properties of galaxies

It is clear from the previous Sections that a number of processes play important roles in the process of galaxy formation, however, it is still far from being understood when and how each process exactly operates and how they exactly impact on the evolution of galaxies. Given all the uncertainties at play, it is fundamental to rely on empirical methods (i.e. on observations) in order to reconstruct the statistical properties of galaxies. By doing so, we can have insights on the processes that led to the formation and evolution of galaxies. Therefore, we now turn our attention to the description of the galaxy population as a whole. In order to probe a sample of galaxies that is representative of the entire population, a large volume of the Universe needs to be considered. As a consequence, the statistical properties of the galaxy population are best addressed using large galaxy surveys, possibly with spectroscopic determination of galaxy redshifts so to reconstruct the three-dimensional space properties of the population of galaxies itself. Currently, among the the largest and/or best (in terms of redshift and mass coverage) available surveys, there are the Sloan Digital Sky Survey at $z \sim 0$ (SDSS; York et al. 2000, see Sect. 2.2.1 for a description), the Cosmic Evolution Survey at $0.2 < z < 4.0$

(COSMOS; Scoville et al. 2007, see Sect. 2.2.2) and the Cosmic Assembly Near-Infrared Deep Extragalactic Legacy Survey up to $z \sim 8$ (CANDELS; Galametz et al. 2013, see Sect. 2.2.3), which data will be extensively used in the following of this thesis.

1.4.1 Classification of galaxies

Once a significant number of galaxies has been observed, one can start to classify galaxies according to their observed properties. In the local Universe, a clear morphological dichotomy among different galaxies is found and it is also reflected in a difference in terms of the stellar population content, in colors, in star-formation rates, in stellar mass functions, in spectral features and in clustering signals (Moresco et al., 2013; Renzini, 2006). The same dichotomy among different properties is found also at high redshifts (i.e. $z > 4$) even though the clear division seen at $z \sim 0$ is less neat and the two populations overlap in some of their properties. Galaxies properties are generally calculated via fitting of their spectral-energy distribution (SED), evaluated through photometry or spectroscopy, with population synthesis models (e.g. Bruzual & Charlot 2003, Maraston 2005 and see Appendix D for a more detailed discussion on SED-fitting). However, the division into the two populations is not sharp given that among the two population several "transition" objects are found, but at first order (looking at the bulk of the galaxy population) one can classify galaxies in these two main groups. In addition, the classifications based on different properties do not perfectly overlap, since they are based on different assumptions in different analyses and, often, different definitions made by individual authors. In the following, we will give an outlook on the properties of the two populations and highlight their main features.

Upon morphological inspection, it can be found that some galaxies present spiral arms together with an elliptical-like central bulge, others have a pure elliptical or spheroidal shape and others have irregular or peculiar morphologies. This is the famous Hubble classification (Hubble, 1927), shown in Fig. 1.7, which divides galaxies into four main categories: elliptical galaxies (E0-E6 in Fig. 1.7), which present smooth and almost elliptical isophotes, spiral galaxies, which are made up by a thin disk with spiral arm structures and are sub-divided into normal (Sa-Sc) and barred spiral (SBa-SBc) according to the whether or not recognizable bar-like structure in the central part, lenticular galaxies which have an intermediate structure between spiral and elliptical (S0-SB0), and irregular galaxies (Irr), which have no recognizable morphological structure. The two main populations are divided as follows: ellipticals and lenticular galaxies together are often referred to as early-type galaxies (ETGs), while spirals and irregulars make up the class of late-type galaxies (LTGs).

This nomenclature was created because E. Hubble thought that his classification scheme was an evolutionary path of galaxies, which begin their life as an elliptical galaxies (from here the early-type nomenclature) and subsequently, due to angular momentum, would have evolved into spiral galaxies (late-type). However, it is nowadays clear that the Hubble's classification is not an evolutionary sequence, but it is still valid since it separates different types of galaxies which have born and evolved in different ways, and present different characteristics.

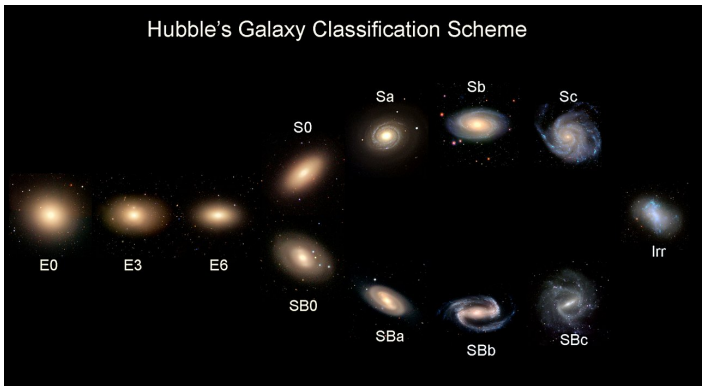

Fig. 1.7 Hubble morphological classification of galaxies. **Credit: ESO Supernova**.

Another type of classification of galaxies is based on their star formation. The so-called star-forming galaxies, have typical sSFRs of 10^{-9} yr^{-1}. There are, however, systems in which the specific star formation rates are tens times higher, but usually this activity can be kept for short timescales ($\approx 10^8$ yr). These galaxies are referred to as starburst galaxies. These short timescales are calculated with the so-called depletion time (e.g. Daddi et al. 2008, Genzel et al. 2008, Lilly et al. 2013, Tacconi et al. 2013) which is defined as the time in which a galaxy finishes its entire gas reservoir due to star-formation. The picture can be complicated when one considers mergers, gas infall, gas outflows, stellar mass changes due to star-formation, efficiency of star-formation and metallicity. When these aspects are considered, studying the depletion time in relation to other time-scales (such as the merger or the Hubble timescales) can place constrains on galaxy evolution processes (see Lilly et al. 2013 for a detailed description).

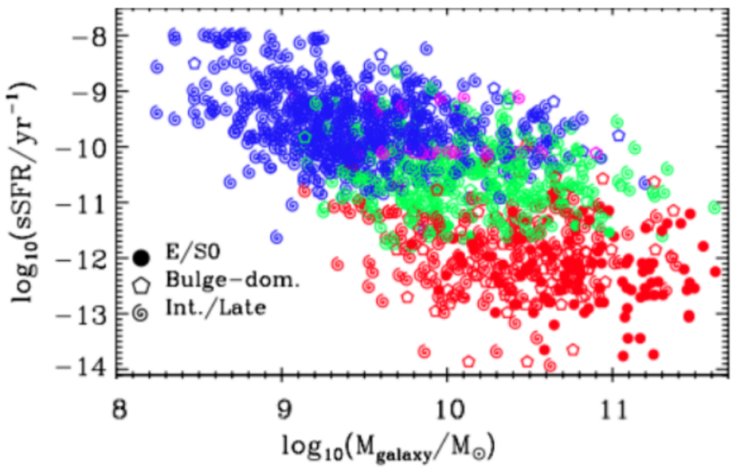

Fig. 1.8 Location of different morphological types on *sSFR* vs. galaxy stellar mass at $z \approx 0$. Different morphological types correspond to different symbols as indicated in plot. Colours correspond to different star formations: strongly star-forming objects are shown in blue, quiescent systems in red and intermediate objects with moderate star formation in green. **Credit: Cibinel et al. (2013)**.

If a system has a $\log(\text{sSFR}) \lesssim -10.5\ \text{yr}^{-1}$, it is usually referred to as a quiescent galaxy. This type of galaxies may be the final stage of a starburst galaxy which has ended intense star formation and is slowly moving towards a pure passive evolution. Usually, a special case of quiescent galaxies are the so-called passive galaxies that have a strict sSFR$= 0$ even though the nomenclature quiescent-passive is elastic and depends on the considered study, since different authors use different definitions. For example, some authors (e.g. Lilly et al. 2013) define a division based on a comparison between the inverse of the $sSFR$ and the Hubble time τ_H (i.e. the age of the Universe, if its evolution is linear, at the considered redshift). In fact, if a galaxy has $(sSFR)^{-1} \leq \tau_H$, it means that it is still significantly increasing its mass with time (and is therefore a star-forming galaxy). On the other hand, if $(sSFR)^{-1} \gg \tau_H$, the galaxy can be formally defined dead (i.e. quiescent/passive).

SFR usually reflects the morphology classification, in fact, today's ETGs generally present no active star formation, while today's LTGs do present star formation. It is shown in Fig. 1.8 how late-type spirals generally present a higher sSFR with respect to early-type objects. Figure 1.8 also reflects a tight correlation for star-forming galaxies between stellar mass and SFR which defines a main sequence that has been recognized in the local universe (e.g. Brinchmann et al. 2004) as well as at intermediate redshifts $0.5 < z < 3.0$ (e.g. Daddi et al. 2007, Rodighiero et al. 2011, Ilbert et al. 2015). The relation has the form $SFR \propto M_*^{\alpha}$, where the slope α can substantially differ from ~ 0.6 to ~ 1, and the normalization rapidly increases from $z = 0$ to $z \sim 2-2.5$ as $(1+z)^{\sim 3.5}$ then flattening all the way to the highest redshifts (see Fig. 1.9 and Rodighiero et al. 2011). Figure 1.8 also shows how the majority of massive local ($z \sim 0$) objects tend to be early-type quiescent galaxies which, then, hold the majority of the stellar mass in the local universe. This aspect will be further investigated in the next Section.

In addition, different galaxy types present different spectra with different characteristics (see Fig. 1.10) due to their different stellar population content. From quiescent to star forming galaxies, the blue continuum and emission lines become systematically stronger. For quiescent (or ETGs) galaxies, which lack hot, young stars, most of the light emerges at the longest wavelengths, where one sees absorption lines characteristic of cool K stars. In the blue, the spectrum of early-type galaxies show strong H and K absorption lines of calcium and the G band, characteristic of solar type stars. Star forming and starburst galaxies (or LTGs) emit most of their light in the blue and near ultra-violet part of the spectrum. This light is produced by hot and young stars, which also heat and ionize the interstellar medium giving rise to strong emission lines. For instance, the most bright emission lines are Hα, Hβ, [O III] and [O II] lines, which become systematically stronger going from Sa to Sc to starburst galaxies. As already mentioned, when moving towards higher redshift this rather clear separation between late-type star-forming galaxies and early-type quiescent galaxies becomes less neat. This is indeed due to increasing difficulties in observations and to different evolutionary stages of objects (i.e. there has been less time for galaxies to evolve). In fact, not only SFR and masses measurements become less reliable, but also performing a clear morphological classification (especially at high redshifts) is challenging.

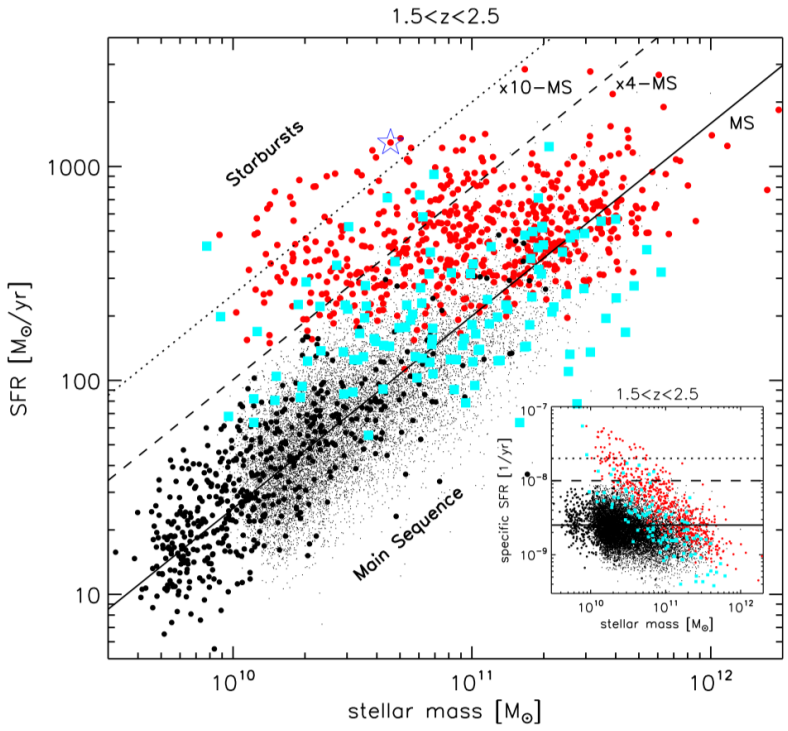

Fig. 1.9 Star formation rate vs. stellar mass relation at $1.5 < z < 2.5$. Different colors indicate different sample used. The main sequence relation at $z \sim 2$ is also shown with the black solid line. In the inset plot the same information is shown, however here the stellar mass is a function of the sSFR. **Credit: Rodighiero et al. (2011)**.

As a consequence of the different stellar content, these two broad categories of galaxies also exhibit different colors. Elliptical galaxies generally present redder colors with respect to star-forming spiral galaxies. In a color-magnitude diagram the two population segregate into the so-called blue cloud and the red-sequence (Bell et al., 2004; Faber et al., 2007). The red sequence galaxies include mostly passive galaxies with an elliptical morphology (e.g. Cassata et al. 2007), while in the blue cloud is populated by star-forming spiral galaxies. In reality, the division is not so neat since a significant fraction of dust extincted star-forming galaxies (e.g. Williams et al. 2009) can populate the red sequence and given the existence of a transition population called green valley. A way to partially break the degeneracy between dust-extincted star-forming galaxies and quiescent ones is using a rest-frame color-color classification. Among the most famous color-color classifications there are the UVJ (Williams et al., 2009) and the NUVrJ (Ilbert et al., 2010) diagrams. The latter one is shown in Fig. 1.11, where the division into star-forming and quiescent galaxies is marked by the line. Both these classifications will be used in the rest of this thesis and, in particular, in Cap. 4.

Another way to differentiate among quiescent and star-forming galaxies is to use observed color-color diagrams coupled with a SED-fitting analysis (e.g. Girelli et al. 2019, Mawatari et al. 2016). This particular method is extensively described and explored in Appendix D.

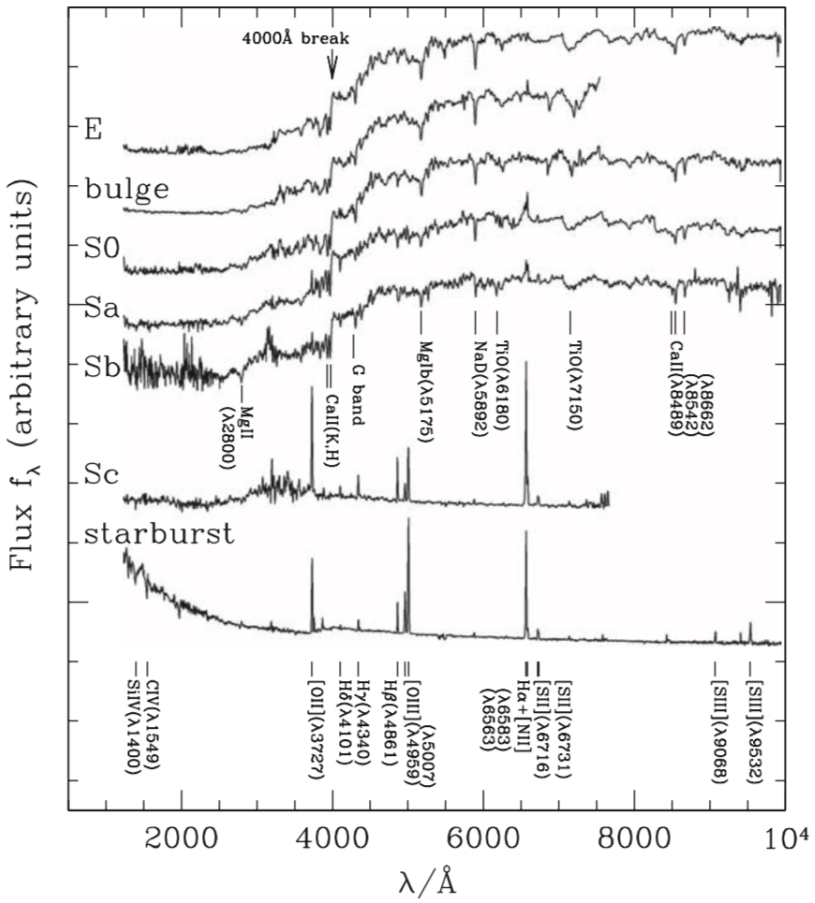

Fig. 1.10 Spectra of different types of galaxies from the ultraviolet to the near-infrared. **Credit: Mo, van den Bosch, & White (2010)**.

To sum up, we highlighted that actively star-forming spiral galaxies (LTGs), are, in general, characterized by a hot and young stellar population and, as a consequence, show blue colors. In addition, this population presents a systematically stronger blue continuum in their spectra (associated with several emission lines) with respect to quiescent (passive) elliptical galaxies (ETGs) with evolved stellar populations that display several absorption features. This latter population also presents red colors populating the so-called red sequence.

The dicothomy discussed so far is based on morphology, on the level of star formation, on stellar populations, on spectra and on colors. The division into these two main categories can also be seen in the stellar mass function, described in Sect. 1.4.3, and in the clustering signal, discussed in Sect. 1.4.4. In addition, galaxies can also be classified according to several other properties, that go beyond the scope of this thesis, like, for example, the luminosity into *bright* and *faint* objects, the surface brigthness into *high* and *low surface brightness*, their gas content into *gas-rich* and *gas-poor* and the presence of an AGN into *active* and *normal*.

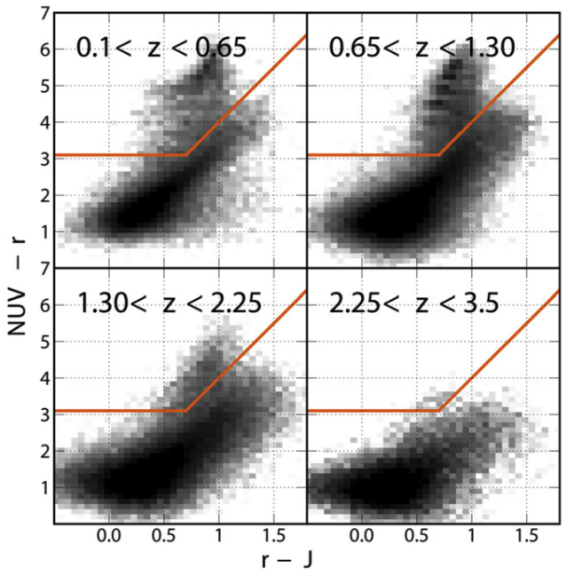

Fig. 1.11 *NUV-r/r-J* galaxy distributions in the COSMOS2015 catalog. Quiescent galaxies lie in the top-left corner.**Credit: Laigle et al. (2016)**.

1.4.2 The downsizing scenario

As extensively discussed above, in the context of a ΛCDM Universe a hierarchical formation of structures is predicted and, in this framework, early-type galaxies are considered the ideal probes to investigate the cosmic history of mass assembly. In fact, holding the majority of stellar mass in the local universe (Renzini, 2006), massive ETGs are supposed to be the end-points of the hierarchical evolution. Therefore, it is believed that these objects enclose fundamental informations about the galaxy formation and evolution processes. In this respect, several studies attempted to infer informations about these processes through local observations of ETGs at $z \sim 0$ (archeological approach) or through direct observations of their progenitors at higher redshift (see again Renzini 2006). It is nowadays clear from these observations that most massive galaxies completed their formation at higher redshifts compared to less massive systems. Moreover, massive systems appear to have formed their stellar mass more rapidly, since their stellar populations are generally older than stellar populations of less massive galaxies. This is the so-called downsizing scenario (first suggested by Cowie et al. 1996) which manifests in several ways, such as the mentioned above mass downsizing (see Fontanot et al. 2009 for a review of the many faces of the downsizing). The scenario is especially true when referred to early-type galaxies (see Fig. 1.12). There are some observational facts of this tendency (e.g. Citro et al. 2016; Fontanot et al. 2009; Thomas et al. 2010). Among them, it has been found that more massive elliptical galaxies have a higher $\left[\frac{\alpha}{Fe}\right]$ ratio. This fact can be explained by assuming that these systems had intense and short star formation histories in order to cause a prompt metal enrichment due to type II supernovae (i.e. α elements). Moreover, a fast consumption or ejection of the available gas is required. This prevents the explosion of most type Ia

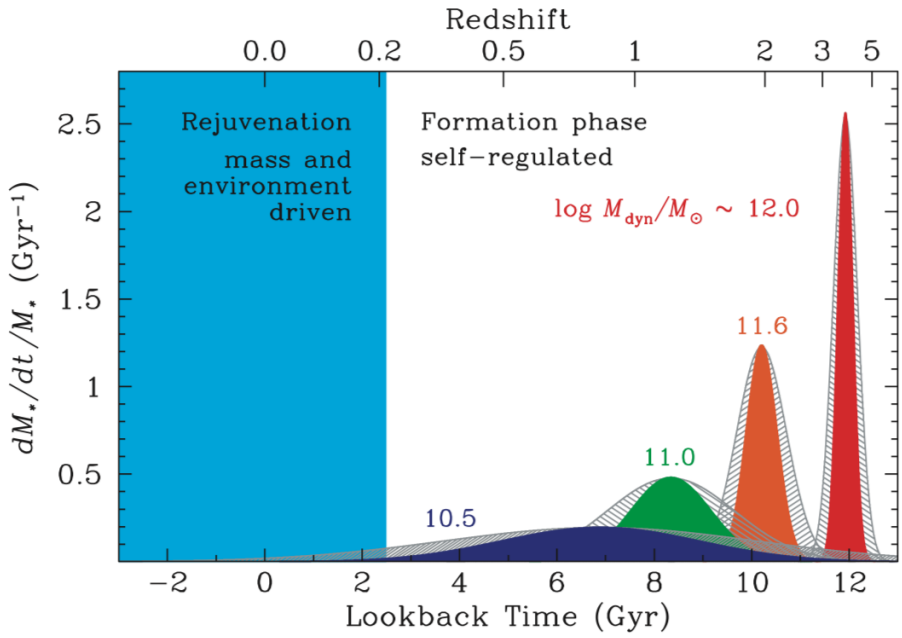

Fig. 1.12 Specific star formation rate as a function of look-back time for early-types galaxies of various masses as indicated by labels. The gray hatched curves show the range of possible variations in the formation time scales due to uncertainties in the α/Fe ratio. **Credit: Thomas et al. (2010)**.

SNe which may have contributed to Fe enrichment. The same results emerge from direct estimates of ages of stellar population of these galaxies. More massive galaxies tend to have older stellar populations. These estimates are based on colors and spectral features. In addition, the low-mass part of the SMF evolves more rapidly than the high-mass end with decreasing redshift (e.g. Ilbert et al. 2013, Pozzetti et al. 2010) suggesting that the evolution of massive galaxies takes place at earlier epochs. According to the downsizing scenario, which is then an empirical evidence from observations, massive early-type galaxies assembled the bulk of their stellar mass at higher redshift and on shorter timescales with respect to less massive ones. For instance, early type galaxies with stellar masses of $10^{10.75} M_\odot$ formed $\sim 50\%$ of their mass at $z \sim 5$ (Citro et al., 2016). At first sight, this scenario may be in conflict with the hierarchical assembly of dark matter halos where small systems form at higher redshift with respect to bigger ones. However, these two scenarios may co-exist. In fact, they refer to different phenomena: downsizing scenario refers to the formations of stellar populations while the hierarchically scenario mainly refers to dark matter halos growth. The presence of massive galaxies at high redshifts poses a fundamental problem for hierarchical models only if their number density exceeds that of correspondingly massive dark matter halos (Somerville et al., 2004). However, understanding these apparently contrasting evolutionary paths for the dark matter assembly and stellar mass assembly of galaxies is a significant challenge for current models of galaxy formation. When observations moved to higher redshift, a number of massive and evolved systems has also been found at $z > 1$. Indeed, observations have shown that a population of massive ($M_* > 10^{10} M_\odot$) galaxies

exists up to redshift $z \sim 6$ and beyond when the universe was only ~ 1 Gyr old (Yan et al. 2005, Finkelstein 2016 for a review). Furthermore, some of these galaxies show evidence of an unexpected evolved stellar population (Stefanon et al., 2013), which means that those galaxies need to have formed through an initial burst of star formation followed by quenching of star formation and a passive evolution. It is clear that baryonic physics of galaxy formation is far from being understood and involves more processes than just cooling and gas accretion at a rate dictated by gravity and by the hierarchical scenario. These evidences led to a change of the picture of galaxy formation. Recently, the supported scenario is that galaxy formation, and (early) evolution, is driven by streams of cold gas which penetrate into the galaxy, leading to an intense and rapid burst of star formation (e.g. Dekel et al. 2009, Faucher-Giguère & Kereš 2011, Goerdt et al. 2012, Mitchell et al. 2020). However, these are all theoretical predictions of galaxy formation supported by hydrodynamical simulations (see Sect. 1.3 for a description of simulations). While observations show ubiquitous outflows (see e.g. Pan et al. 2019), observations of cold accretion streams are challenging. A reason for that is the small solid angle covered by cold-flow accretion (see Faucher-Giguère & Kereš 2011, Goerdt et al. 2012) typically with an opening angle of $20^\circ - 30^\circ$ or a few percent of the sphere (~ 0.4 rad^2). Additionally, signatures of inflows can easily be masked by interstellar absorption (Rubin et al., 2012) and when selecting absorbers via metal-lines, ambiguity remains in separating a galactic scale outflow falling back onto the galaxy (i.e. a "galactic fountain") from material being accreted from the IGM for the first time. As a result, observers have mostly had to hunt for indirect signatures of cold flows, such as Lyα emissions originating from a dusty highly starbusting galaxy with large-scale superwinds (e.g. Rosdahl & Blaizot 2012) or low-metallicity line absorbers (e.g. Martin et al. 2012).

1.4.3 The mass function

When a large number of galaxies is observed, a useful tool to study the galaxy population as a whole is the galaxy stellar mass function (hereafter SMF). The SMF describes the galaxy number density as a function of stellar mass and is usually well described by a Schechter function (Schechter, 1976), which can be approximated by a power law at low masses with an exponential decline at higher masses:

$$\Phi(M)dM = \Phi_* \left(\frac{M}{M_*}\right)^{\alpha} \exp\left(-\frac{M}{M_*}\right) \frac{dM}{M_*} \tag{1.10}$$

where $\Phi(M)dM$ is the number density of galaxies with mass between M and $M + dM$, M_* is the characteristic stellar mass beyond which the function exhibits an exponential drop, α is the slope of the power law part at small masses and Φ_* corresponds to the normalization (see examples of stellar mass functions in Fig. 1.13). The study of the stellar mass function is essential to infer information about galaxy formation and evolution. In fact, it is a tracer of cosmological processes because it holds important clues about primordial density fluctuation of dark matter along with information on merging events, on phenomena which contribute to the star formation history of galaxies and on radiative processes which may contribute to the galaxy evolution. For instance, as mentioned above, at low masses the SNe feedback along with gas stripping play a role in modifying the general shape

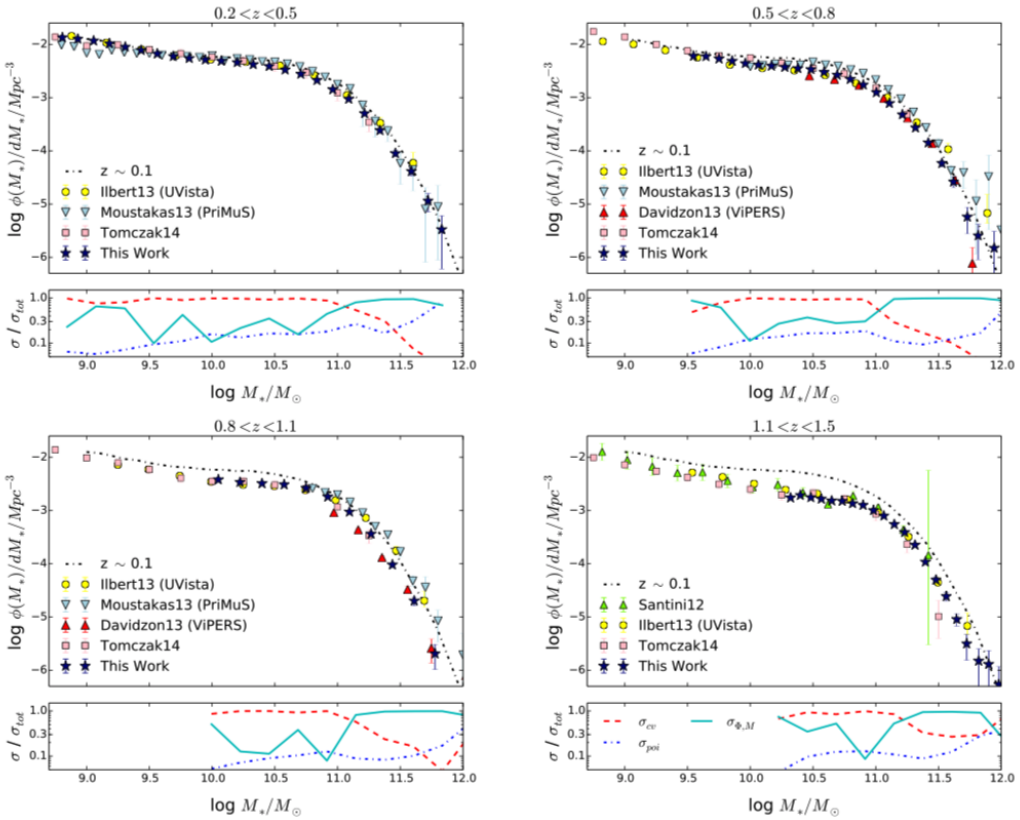

Fig. 1.13 Example of galaxy SMFs in different redshift bins with different data from various works. The bottom panels show the SMF error contributions normalised by the total SMF uncertainty (see Moutard et al. 2016a for a detailed description). **Credit: Moutard et al. (2016a).**

of the SMF. At high masses, where observations and models usually differ the most, AGN feedback modifies the shape of the function. Also when moving with redshift, normalization and slope of the function change. As already mentioned in Sect 1.4.1, through the study of the stellar mass function one can see the signature of the dichotomy of the galaxy population. It has been found that quiescent galaxies are the most massive galaxies at $z \sim 0$ and dominate the massive end of the stellar mass function up to $z \sim 1$ (Baldry et al., 2008; Ilbert et al., 2013; Pozzetti et al., 2010). Indeed, the galaxy stellar mass function represents the benchmark for galaxy formation and evolution models (e.g. Guo et al. 2011; Henriques et al. 2015) which have to reproduce observations. At the beginning of the century many studies of the galaxy population up to $z \approx 2$ have been made (e.g. Davidzon et al. 2013; Fontana et al. 2004; Pozzetti et al. 2010). Today, the SMF up to redshift 2 is sufficiently well known, and different studies are in good agreement among each other (e.g. Moutard et al. 2016a and see Fig. 1.13). Studies have then been shifted to higher redshifts. Many studies have been carried out in order to constrain the SMF at $z > 2-2.5$ (e.g. Grazian et al. 2015; Ilbert et al. 2013; Muzzin et al. 2013) and also to quantify the relative importance of the quiescent/passive population at high redshifts (e.g. Ilbert et al. 2013, Davidzon et al. 2017, Girelli et al. 2019). In addition, SMFs are important

also to understand the effects of the environment on the formation of galaxies (e.g. Davidzon et al. 2016, Bolzonella et al. 2010). Details about the SMF we use in this thesis and their characteristics are described in Sections 2.2.1, 2.2.2 and 2.2.3.

1.4.4 Large-scale structure

An important property of the galaxy population is its overall spatial distribution. Since each galaxy is associated with a large amount of mass, one might naively expect that the galaxy distribution reflects the large-scale mass distribution in the Universe. On the other hand, if the process of galaxy formation is highly stochastic, or galaxies only form in special, preferred environments, the relation between the galaxy distribution and the matter distribution may be far from straightforward. Therefore, detailed studies of the spatial distribution of galaxies in principle can convey information regarding both the overall matter distribution, which is strongly cosmology dependent, and the physics of galaxy formation. Figure 1.14 shows the distribution of the galaxies in the VIPERS survey (Guzzo et al., 2014), where the distances of the galaxies have been estimated from their spectroscopic redshifts.

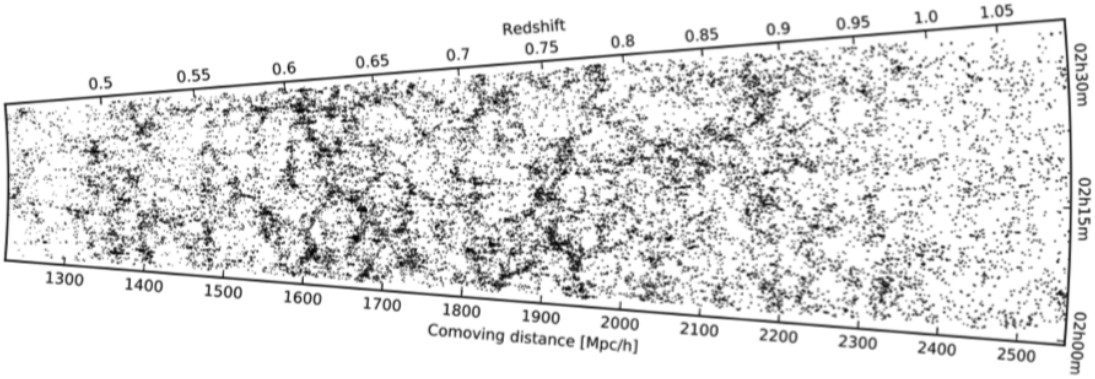

Fig. 1.14 Large-scale galaxy distribution at $0.45 < z < 1.1$ unveiled by the VIPERS. **Credit: Guzzo et al. (2014).**

Clearly the distribution of galaxies in space is not random, but shows a variety of structures. Some galaxies are located in high-density regions containing several hundreds of galaxies (which are called clusters of galaxies), or in smaller groups containing a few to tens of galaxies (called groups). The majority of all galaxies, however, are distributed in filamentary or sheet-like structures. These sheets and filaments surround large voids, which are regions that contain very few, or no, galaxies. One of the challenges in studying the spatial distribution of galaxies is to properly quantify the complexity of this cosmic web of filaments, sheets and voids. In this section and when referring, in general, to clustering, we consider the galaxy distribution as a point set in space and study the spatial correlations among these points in a statistical sense.

One of the most important statistics used to characterize the spatial distribution of galaxies is the two-point correlation function, defined as the excess number of galaxy pairs with a given separation,

r, relative to that expected for a random uniform distribution:

$$\xi(r) = \frac{DD(r)\Delta r}{RR(r)\Delta r} - 1 \tag{1.11}$$

where $DD(r)\,\Delta r$ is the number of galaxy pairs with separations in the range $r \pm \Delta r/2$, and $RR(r)\,\Delta r$ is the expected number in case of a random distribution of galaxies in space. Galaxies are said to be positively correlated on scale r if $\xi(r) > 0$, to be anticorrelated if $\xi(r) < 0$, and to be uncorrelated if $\xi(r) = 0$. Since it is relatively straightforward to measure, the two-point correlation function of

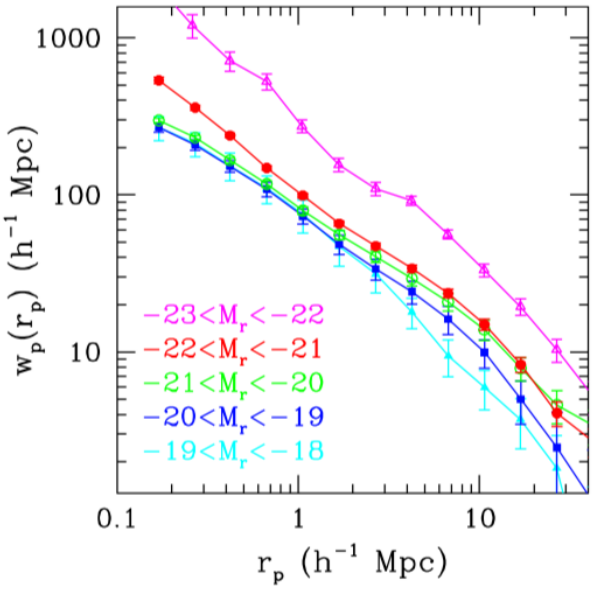

Fig. 1.15 Example of the projected correlation functions for volume-limited samples corresponding to different luminosity-bin samples. **Credit: Zehavi et al. (2011)**.

galaxies has been estimated from a variety of different samples. In many cases, redshifts are used as distances and the corresponding correlation function is called the correlation function in *redshift space*. Because of peculiar velocities, this redshift-space correlation is different from that in *real space*. If one has no information about the redshift in real space, the projected two-point correlation function can be estimated, in which galaxy pairs are defined by their separations projected onto the plane perpendicular to the line-of-sight so that it is not affected by using redshift as distance. We show in Fig. 1.15 an example of the projected correlation function evaluated on SDSS data and binned in luminosity.

Over the last few decades, a variety of local clustering studies have established an increasingly refined and quantitative characterization of the dependence of galaxy clustering on luminosity (or, equivalently, mass), morphology, color, and spectral type of galaxies (e.g. Davis et al. 1988, Guzzo et al. 1997, Zehavi et al. 2002, Madgwick et al. 2003, Zehavi et al. 2011). Luminous, or massive, galaxies generally cluster more strongly than faint galaxies, reflecting their tendency to reside in denser

environments. Galaxies with bulge-dominated morphologies, red colors, or spectral types indicating old stellar populations also exhibit stronger clustering and a preference for dense environments. In the last decade, thanks to new galaxy photometric and spectroscopic surveys, several works pushed clustering measuremens to higher redshifts (e.g. Meneux et al. 2008, de la Torre et al. 2011, Marulli et al. 2013, Durkalec et al. 2015a, Harikane et al. 2016, Harikane et al. 2018).

Gaining cosmological knowledge from galaxy clustering measurements is complicated by the existence of the galaxy bias, which is the difference between the distribution of galaxies and that of the underlying dark matter. While the clustering of dark matter from specified initial conditions can be computed reliably with cosmological N-body simulations, the detailed physics of galaxy formation (i.e. gas cooling, star formation, and the feedback effects of SNe and AGNs) is not completely understood, so galaxy bias cannot be predicted robustly from first principles. Cosmological parameter studies must adopt a parametrization for the galaxy bias. This procedure is rather straightforward at large scales, where the effects of bias are expected to be of the order of a scale-independent amplification of the matter $\xi(r)$ (Kaiser, 1987). On the other hand, for a specified cosmological model, one can constrain detailed descriptions of galaxy bias and thus gain insights into galaxy formation physics. In this thesis, we will perform several clustering measurements and present the method we adopted and the results in Sect. 5.7.

1.5 Future Missions

As we already mentioned above, the next generation of missions/surveys are promising ways to provide major improvements in our understanding of galaxy formation and evolution, cosmological parameters, and the nature of dark energy and neutrino mass. In this section we provide a brief description of the main future missions by describing their objective and giving some details about their surveys. We mainly focus on missions that are expected to cover large sky areas, for which the mocks we produce in this thesis may be useful.

Among the most important future missions, there is **Euclid** which is a space-based survey mission (Laureijs et al., 2011) from the European Space Agency (to be launched in 2022) designed to understand the origin of the Universe's accelerating expansion. It will use cosmological probes to investigate the nature of dark energy, dark matter and gravity by tracking their observational signatures on the geometry of the Universe and on the cosmic history of structure formation. In other words, the Euclid surveys will try to show how cosmic acceleration modifies the expansion history and the 3-dimensional distribution of matter in the Universe. To achieve this, Euclid will measure the shapes over a billion galaxies and accurate redshifts of tens of millions of galaxies for weak gravitational lensing and galaxy clustering studies. In fact, the mission is optimised for two independent primary cosmological probes: Weak gravitational Lensing (WL) and Baryonic Acoustic Oscillations (BAO). The Euclid wide survey will cover 15 000 deg^2 of the extragalactic sky to study the two main probes and is complemented by four deep fields totalling an area of 40 deg^2 not only for primary probes but also for the legacy science in various fields of astrophysics like galaxy formation and evolution. The

novelty of Euclid is the slitless spectroscopy in the NIR bands that aims at spectroscopically observe galaxies in the range $z \sim 1-2$ thanks to the detection of Hα emission line. Particularly relevant for galaxy formation and evolution, Euclid will produce a legacy dataset with images and photometry of more than a billion galaxies and several million spectra, out to high redshifts $z > 2$, delivering also morphologies, masses and SFRs for all these targets. In addition to that, the deep survey will be the primary target for follow-up observations using other facilities (such as, for example, CFHT, ELT). The deep data are expected to contain thousands of objects at $z > 6$ and several tens of $z > 8$. The Euclid payload consists of a 1.2 m mirror with a large field of view (~ 0.54 deg^2) complemented with a visual instruments called VIS and the near infrared instrument, called NISP that contains a slitless spectrometer (from 1.25 to 1.85 microns) and a three band photometer (Y, J, H). In addition NISP is expected to detect galaxy emitters down to fluxes of $\sim 2 \times 10^{-16}$ erg s^{-1} cm^{-2} (3.5σ) in the WIDE survey and $\sim 0.5 \times 10^{-}16$erg s^{-1} cm^{-2} in the DEEP. In addition, in order to partially overcome the fact that many observed spectra will superimpose one over the other and, therefore, be a cause of redshift measurements failures, the total wavelength coverage is split into two separate observations, using red (from 1.25 to 1.85 microns in the WIDE) and blue (from 0.92 to 1.3 microns in the DEEP) grisms. The resulting shortening of each spectrum already reduces the percentage of overlaps among spectra and reducing the redshift evaluation confusion. The wide survey is expected to reach a depth of $m_{VIS} \sim 24.5$ mag and $m_H \sim 24$ (at 10σ) while the deep survey will go 2 magnitudes deeper. It is clear that Euclid will provide an exquisite dataset, that will greatly help to place stringent constraints on some of the physical processes of galaxy formation and evolution.

A similar mission is the **Wide-Field Infrared Survey Telescope** (**WFIRST** ; Spergel et al. 2015), now named the Nancy Grace Roman Space Telescope. It is a space observatory from the NASA that will try to address the most compelling scientific problems in dark energy, exoplanets and general astrophysics using a 2.4 m telescope with a wide-field (~ 0.25 deg^2) infrared instrument (in the range $0.6-0.97$ microns) and an optical coronagraph. It is expected to make, like Euclid, precision measurements of both the growth rate of structure and the expansion history of the universe through baryon acoustic oscillations, supernovae, and weak gravitational lensing studies and will, therefore, test general relativity on the largest scales and could reveal the nature of dark energy. WFIRST will conduct a three tiered deep supernova survey, a shallow survey over 27.44 deg^2 for SNe at $z < 0.4$, a medium survey over 8.96 deg^2 for SNe at $z < 0.8$, and a deep survey over 5.04 deg^2 for SNe out to $z = 1.7$. In addition, it will measure the shapes of 380 million galaxies over 2200 deg^2 by making measurements at multiple bands (from 0.76 to 2.0 microns) while also taking spectra (in the range $0.6-0.97$ microns). The survey is expected to reach a depth of $m_H \sim 24.5$.

The **Spectro-Photometer for the History of the Universe, Epoch of Reionization and Ices Explorer** (**SPHEREx** ; Doré et al. 2014) mission is a proposed all-sky spectroscopic survey satellite designed to probe the origin and destiny of our Universe, explore whether planets around other stars could harbor life and explore the origin and evolution of galaxies. It will survey the entire sky in optical as well as near-infrared light (in the range $0.75 < \lambda < 4.8$ microns) and will study the three-

dimensional large-scale distribution of matter by measuring galaxy redshifts over a large cosmological volume at low redshifts, complementing high-redshift surveys optimized to constrain dark energy.

Another fundamental upcoming survey is **Hawaii-Two O** (**H2O**). The main objective of the survey is to provide constraints on the evolution of massive ($M/M_{\odot} > 10^{10.5}$) galaxies at $3 < z < 7$, estimate the properties of their dark matter haloes through clustering measurements, and find the first objects of the Universe responsible for the reionization of the Universe during this key epoch of galaxy evolution. The survey will carry out a 20 deg^2 deep Subaru Hyper-SuprimeCam (HSC) imaging and Keck DEIMOS + MOSFIRE near-IR spectroscopic survey of the two primary Euclid Deep Calibration Fields. The survey is expected to reach a depth of $m_g \sim 27.5$. The survey will also greatly benefit from, and will contribute to, the Euclid and WFIRST surveys, since they will survey the same sky areas.

Along with the described future surveys, there are other facilities currently under construction that will greatly help in studying galaxy formation and evolution over the entire history of the Universe, from the Milky Way, through the redshift desert and up to the epoch of reionisation at $z > 8-9$. Among the many we find the **Vera C. Rubin Observatory** (Legacy Survey of Space and Time - **LSST** ; LSST Science Collaboration et al. 2009) and the **Multi-Object Optical and Near-infrared Spectrograph** (**MOONS**, Cirasuolo et al. 2014).

The **Rubin Observatory** is a new kind of telescope currently under construction in Chile, designed to rapidly survey the night-time sky (with a 6.7 m diameter primary mirror and a 10 deg^2 field of view). The **Rubin Observatory** has been designed to achieve multiple goals in four main science themes: taking an inventory of the solar system, mapping the Milky Way, exploring the transient optical sky, and probing dark energy and dark matter. The telescope is expected to reach a depth of $m_r \sim 27.5$.

MOONS is a new conceptual design for a Multi-Object Optical and Near-infrared Spectrograph for the 8.2 m Very Large Telescope (VLT), selected by ESO. The baseline design consists of ~ 1000 fibers deployable over a field of view of ~ 500 arcmin^2, the largest patrol field offered at the VLT. The total wavelength coverage is $0.64-1.8$ microns. The instrument is expected to provide the observational power necessary to study galaxy formation and evolution over the entire history of the Universe, from our Milky Way, up to $z = 8-9$. At the same time, the high spectral resolution mode will allow astronomers to study chemical abundances of stars in our Galaxy, in particular in the highly obscured regions of the Bulge. The programmed MOONS extragalactic survey (called MOONRISE) will be an SDSS-like survey at $z \sim 1$ aiming at studying the ISM and the stellar populations of galaxies. By observing specific selected fields, MOONS will cover the same spectral range of the Euclid space observations and will, therefore, provide higher resolution spectra of galaxies complementing Euclid's observations.

1.6 This work

Next generation missions and surveys will try to address some of the open questions in galaxy formation and evolution. In order to allow an optimal scientific exploitation of them it is essential to use realistic and reliable galaxy mock catalogs. They are fundamental to make predictions about such surveys and for minimizing their systematic uncertainties and selection effects.

The main aim of this thesis is the building of galaxy mock catalogs that reproduce with accuracy observed properties of galaxies over the widest possible mass and redshift range, and, at the same time, the large scale structure of the Universe. This is done by starting from the dark matter halos that output from a N-body simulations on which we paint galaxies. Given the many obscure details of the physics of galaxy formation and evolution, we develop a fully empirical procedure solely calibrated with state-of-the-art observations. The final mocks can be used to make predictions for future surveys and also to gain some knowledge on the physics of galaxy formation and evolution. As an example the final mock catalogue will also be used for Euclid or MOONS surveys to define the optimal algorithms for clusters detection, the predictions for star-forming or early type galaxy studies, and the feasibility to exploit distribution functions as a function of galaxy properties and environment.
This thesis is organised as follows:

- In Chap. 2 the method we adopted to link dark matter halos and galaxies is described. In particular, all the tools and ingredients utilized to construct the galaxy-halo link, like the matching technique, the stellar and halo mass functions are described.
- We present the results of the galaxy-halo connection in Chap. 3. We also compare our results with a variety of other literature results and models and interpret our results by means of processes related to galaxy formation and evolution. In addition, we evaluate a simple empirical model to link stellar masses to dark matter halos.
- In Chap. 4 we describe the whole procedure we developed to create the empirical mock catalogs starting from the outputs of an N-body DM-only simulation by means of adding many physical properties of galaxies (e.g. stellar mass, sfr, photometry, emission lines).
- We validate our mock catalogs in Chap. 5. More in detail, we compare our mocks with observed datasets and make some predictions about future surveys.
- Finally in Chap. 6, we recap the main results obtained in this thesis and discuss future perspectives.

Throughout the whole thesis we adopt a standard ΛCDM cosmology with cosmological parameters set to be consistent with the Planck 2015 constraints Planck Collaboration et al. (2016) and described in Eq. 1.6, unless differently specified. In addition, all halo masses reported in this thesis (unless

differently specified) are expressed in units of $h_{67} = H_0 / (67\,\mathrm{km\,s^{-1}\,Mpc^{-1}})$ and, more precisely, in units of $M_h\, h_{67}^{-1}$. All magnitudes are expressed in the AB system and log is base 10 logarithm.

2

THE CONNECTION BETWEEN GALAXIES AND THEIR DARK MATTER HALOS

To build an empirical mock catalog, the first step consists in determining the connection between dark matter halos and galaxies. This initial step is crucial since it connects a DM-only simulation (i.e. a cosmological model) to observed galaxies in the real Universe. This connection not only provides a key test for galaxy formation models (e.g. the star formation efficiency), but it also plays an essential role in constraining cosmological models using galaxy surveys and in the building of a mock catalog of galaxies. In particular, in this Chapter, we present a brief overview of the techniques to infer the galaxy-halo connection with an eye on the method adopted in this thesis, which is the (sub)halo abundance matching. We will also describe the ingredients needed to build the connection between galaxies and their dark matter halos, which are the observed stellar mass functions and halo mass functions. Part of the analysis conducted in this Chapter and in Chapter 3 is presented in a paper we recently published: Girelli, Pozzetti, Bolzonella, Giocoli, Marulli, & Baldi (2020).

2.1 Approaches to model the galaxy-halo connection

Two broad categories of models of the galaxy-halo connection can be identified: empirical models, which use data to constrain a specific set of parameters describing the connection at a given epoch or as a function of time, and physical models, which either directly simulate or parameterize in each halo the physics of galaxy formation such as gas cooling, star formation, and feedback. A schematic summary of these approaches, from the review by Wechsler & Tinker (2018), is given in Figure 2.1, which gives an example of the galaxy and dark matter distributions for one such model, and outlines the key elements of various approaches. This image, that describes models ranging from hydrodynamic simulations to halo occupation distribution (HOD) models, is just a scheme, in reality these modelling approaches are more of a continuum. Moving from left to right, i.e. from hydrodynamic simulations to HODs, less physics is assumed and more data are used to constrain the connection. In addition, moving to the left, approaches tend to be computationally significantly more expensive and therefore it becomes more difficult to model large portions of the Universe.

In between the fully empirical and fully physical approaches, there are many different techniques to link the properties of galaxies to those of their halos. These methods derive the halo properties from the properties of its galaxy population using galaxy kinematics (Erickson et al., 1987; Li et al., 2012; More et al., 2009a,b, 2011), gravitational lensing (Coupon et al., 2015; Mandelbaum et al., 2005; Velander et al., 2014), or X-ray studies (Kravtsov et al., 2018; Lin et al., 2003, 2004), for instance. The fully physical approach consists in modelling galaxy formation in either large numerical simulations that include both gas and dark matter with some assumptions on sub-grid processes (i.e. physical processes that occur on scales smaller than the resolution of the simulation itself) and also some input observations, the so-called hydrodynamical simulations (Springel & Hernquist 2003, or the Illustris simulation Nelson et al. 2015; Sijacki et al. 2015 or the Eagle simulation McAlpine et al. 2016) or semianalytic models (SAMs) of galaxy formation (e.g., Croton et al. 2016; De Lucia & Blaizot 2007; Gonzalez-Perez et al. 2014; Henriques et al. 2015; Kauffmann et al. 1993). However, many of the physical processes involved in galaxy formation (such as star formation and feedback)

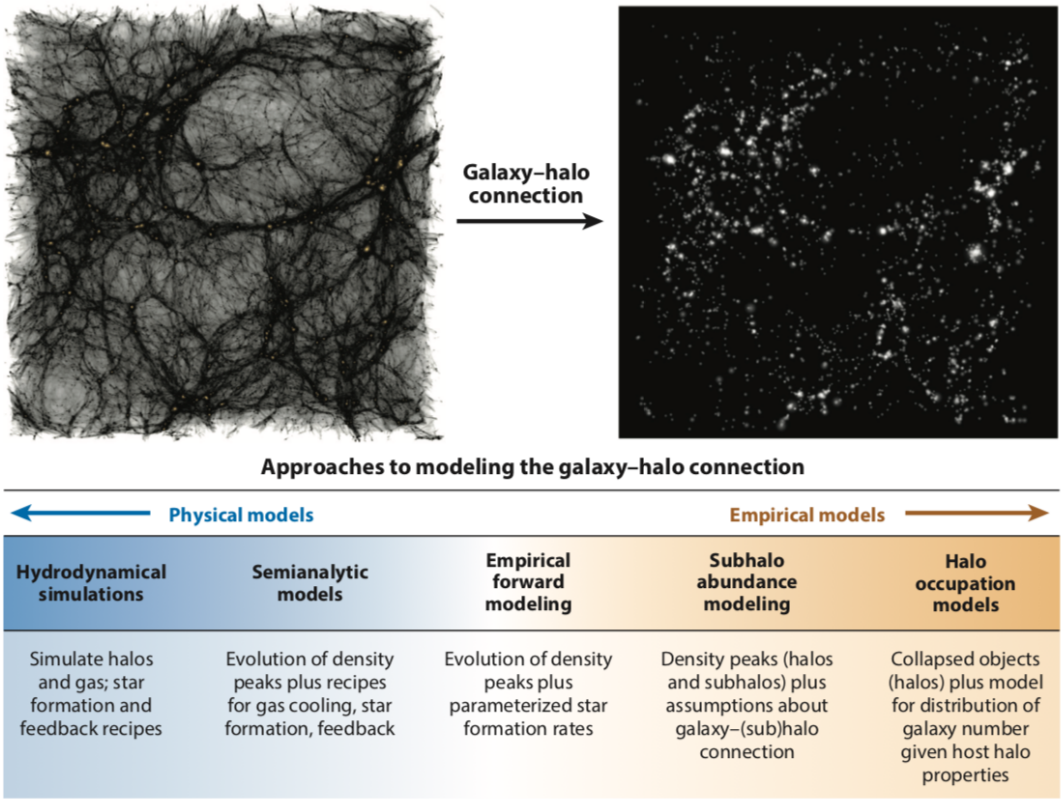

Fig. 2.1 Modelling approaches to the galaxy-halo connection. Top panel shows the dark matter distribution in a cosmological simulation (Left), compared to the galaxy distribution using an abundance matching model, tuned to match galaxy clustering properties of an observed sample (Right). The bottom grid shows the key assumptions of various models for the galaxy-halo connection. The models are listed from left to right ranging from more physical to more empirical models. **Credit: Wechsler & Tinker 2018**

are still not well understood, and in many cases, simulations are not able to reproduce the observed quantities with high accuracy (Cecchi et al. 2019, Steinhardt et al. 2016, or see Naab & Ostriker 2017; Somerville & Davé 2015 for two reviews) over large volumes.

On the other hand, given the difficulties of physical models to fully reproduce observed galaxies, with the advent of large galaxy surveys in the past decades, other completely empirical methods have been developed linking galaxies to halos by means of a statistical approach. One example is the halo occupation distribution (HOD) formalism, which specifies the probability distribution for a halo of mass M to harbor N galaxies with certain intrinsic properties, such as their clustering properties, their luminosity, their colors, or their types (e.g., Carretero et al. 2015; de la Torre & Peacock 2013; Yang et al. 2012; Zheng et al. 2007). More complex formulations of this type of modeling, such as the conditional luminosity function (CLF) formalism (e.g., van den Bosch et al. 2003; Yan et al. 2005; Yang et al. 2012), have extended the HOD approach. Because reliable galaxy clustering measurements

are not available at high redshift, the HOD and CLF approaches have typically been used only at low redshift.

In order to avoid this problem, galaxies and dark matter halos can be linked assuming that a galaxy property (i.e., the stellar mass, or the galaxy luminosity) monotonically relates to a halo property (i.e., the halo mass, the circular velocity of halos), and therefore the relation between dark matter halos or subhalos and galaxy properties can be found by performing a one-to-one association from their distributions. This approach is called (sub)halo abundance matching, hereafter SHAM, or simply AM (e.g., Behroozi et al. 2010, 2013; Guo et al. 2010; Moster et al. 2013; Reddick et al. 2013; Rodríguez-Puebla et al. 2017). The only observational input of this method is the stellar mass function (SMF) or luminosity function. This approach also predicts the clustering statistics remarkably well (see Moster et al. 2013, 2010 as examples), down to scales that depend on the resolution of the adopted simulation (an additional modeling of subhalos is required on scales smaller than the resolution). A more technical discussion of this approach is described in the following subsection. The evolution of the SHAM technique is the empirical modeling (EM, e.g., Behroozi et al. 2019; Grylls et al. 2019; Moster et al. 2018; Schreiber et al. 2017), in which dark matter halos from an N-body simulation (with merger trees, that are needed to reconstruct the halo growth history and link their evolution with galaxies star-formation history) are linked to several observed galaxy properties (such as stellar mass, star-formation rate, and quenched galaxy fractions).

2.1.1 The subhalo abundance matching technique

As mentioned above, the SHAM technique relies on the assumption that the halo mass monotonically relates to a galaxy property, that is, the stellar mass or the luminosity in a certain band. In the mock presented in this thesis, we adopted this technique to link dark matter halos to galaxies by means of the observed stellar mass functions, i.e. the number densities of galaxies in a given mass range (see Sect. 1.4.3). This SHAM approach assumes that every main (sub-) halo contains exactly one central (satellite) galaxy and that each halo is populated with a galaxy. In other words, a deterministic one-to-one relation between halo and stellar mass is assumed. To uniquely associate one halo to one galaxy, the cumulative version of the halo mass function $n(M_h)$ and of the galaxy SMF $\Phi(M_*)$ needs to be constructed. The latter was built by simply summing the number of objects (expressed as number counts, or mass functions) with stellar masses greater than the considered one, M_i:

$$n(>M_i) = \int_{M_i}^{\infty} \Phi(M')dM' \tag{2.1}$$

where Φ is the stellar mass function defined in Eq. 1.10. In Fig. 2.2 we show an example of cumulative (both stellar and halo) mass functions. On the left, cumulative stellar mass functions are shown along with their errors. These have been built following the equation above and cumulating the mass functions by Baldry et al. (2008) (see Sects. 2.2.1 for further details). On the right, the cumulative halo mass function built from theoretical parametrization by Despali et al. (2016) is shown.
From the direct comparison of the cumulative stellar and halo mass functions, one can derive the ratio

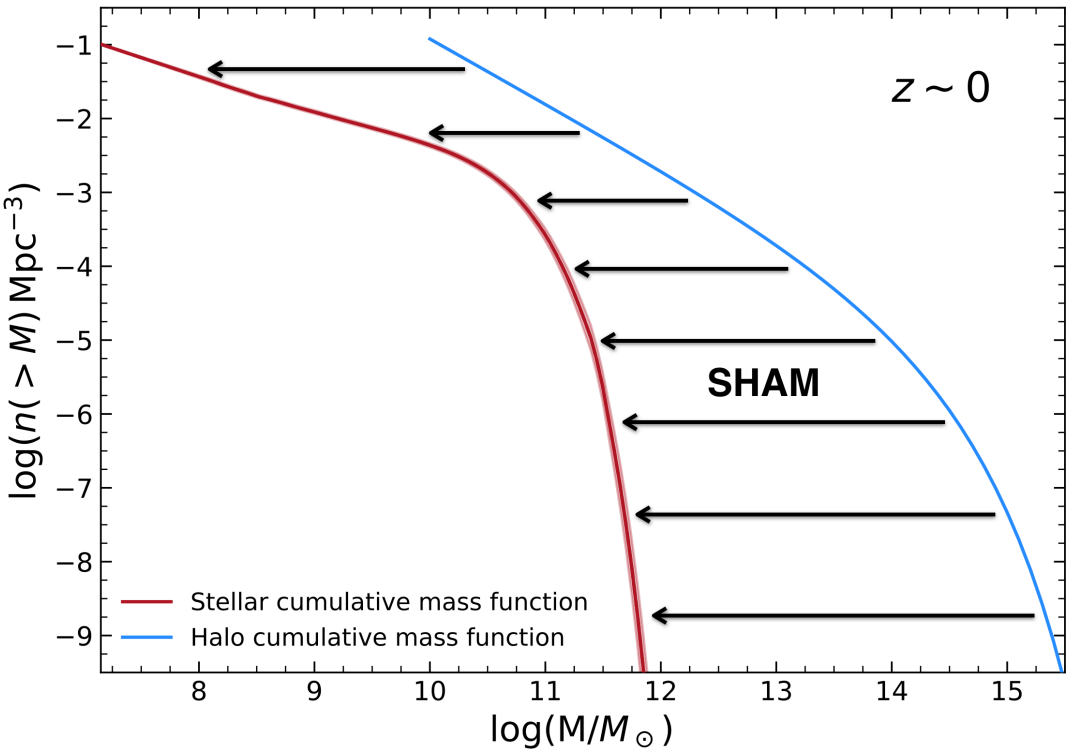

Fig. 2.2 An example of stellar cumulative mass functions (left) and halo cumulative mass functions (right) at $z \sim 0$. On the left, the line with shaded area represent the SMF by Baldry et al. (2008) (at $0.0 < z < 0.2$) with 1σ uncertainty (best fit to $1/V_{\mathrm{max}}$ points, the best fit has been cumulated as described in Eq. 2.1. On the right, the solid line shows the cumulative halo mass function (CHMF) evaluated with the theoretical parametrization by Despali et al. (2016). In addition, with arrows, we sketch the SHAM procedure to link halo masses to stellar masses.

between M_* and M_h at each fixed number density and repeat this operation in all redshift bins. In Fig. 2.2 we show with arrows this procedure.

2.1.2 Observational and relative scatter

To derive a SHMR which does not depend on the quality of the observed dataset that is used to derive the SMF, we used the intrinsic SMFs. Indeed, the intrinsic SMFs were deconvolved for all the errors associated with the stellar mass calculation, as described in Sect. 2.2. However, when realistic mock catalogs are built, an error in stellar mass at fixed halo mass needs to be applied to reproduce the observational effects in the estimate of the stellar mass from observed photometry. In other words, to perform a comparison with the observed rather than with the intrinsic SMFs (i.e. the SMFs deconvolved by the Eddington bias, see the next section for a detailed discussion), a scatter needs to be applied. Usually this scatter is calculated by randomly extracting values from a log-normal distribution with variance σ_{obs}, where σ_{obs} depends on the observations one wants to compare with.

In the following of this thesis, when referring to this type of scatter, we will adopt the nomenclature *observational scatter*.

In addition to that, one expects that in nature, two halos of the same mass may harbor galaxies with different stellar masses because they can have different merger histories, spin parameters, and concentrations and therefore one does not expect a one-to-one relation between halos and galaxies but instead a relation with some scatter. This can be taken into account by introducing an additional *relative scatter* (σ_R) to the intrinsic SHMR relation evaluated in the simple one-to-one comparison of the cumulative mass functions.

In the literature, several approaches have been followed: in general, the scatter is drawn from a log-normal distribution with a variance that can be constant at all halo masses and redshifts (e.g., $\sigma_R = 0.15$ dex for Moster et al. 2013, 2010), or can be considered as an additional free parameter and its value is fitted in the model, such as Behroozi et al. (2010, 2013) and Legrand et al. (2019) that keep it constant with halo mass but not with redshift. As an example, Legrand et al. (2019) found values that range from 0.14 dex at $z \sim 0.35$ to 0.46 dex at $z \sim 5$. Using X-ray observations on clusters, Erfanianfar et al. (2019) found a mean scatter of 0.21 and 0.25 dex for the stellar mass of the brightest cluster galaxies in a given halo mass at low ($0.1 < z < 0.3$) and high ($0.3 < z < 0.65$) redshifts, respectively. In addition, recent results from hydrodynamic simulations (e.g., Eagle, see Schaye et al. 2015) have shown that this scatter depends on halo masses (Matthee et al., 2017), ranging from 0.25 at $M_h = 10^{11}\,M_\odot$ to 0.12 dex at $M_h = 10^{13}\,M_\odot$. Matthee et al. (2017) also found a weak trend for halo masses above $M_h = 10^{12}\,M_\odot$. Recent works, such as Moster et al. (2018), self-consistently introduced scatter in the SHMR by taking the full formation history of halos into account. They found a scatter that depends both on halo masses and redshifts.

We evaluated the SHMR both in the presence of this *relative* scatter in stellar mass at fixed halo mass and in its absence. In particular, we follow the approach detailed in Moster et al. (2010). First, we evaluate the model SMF which is then convolved with this scatter to reproduce the observed intrinsic SMF. We then derive the SHMR through the direct comparison of the model SMF and the HMFs. We fix the standard deviation (σ_R) of the log-normal distribution to 0.2 dex at all halo masses and redshifts (as done in Moster et al. 2013, 2010). Similar values have been presented in several works mentioned above. However, given the current uncertainties of the value of this scatter and its unknown dependence on redshift and mass, we present our results both for the case calculated without the scatter and with the addition of it. Qualitative results are, however, preserved when this *relative* scatter is included, while the differences quantitatively depend on the exact value of the scatter that is introduced.

2.1.3 Parameterizing the SHMR

In order to parameterize the SHMR that we derived in a given redshift bin, we adopt the simple double power-law function proposed by Moster et al. (2010),

$$\frac{M_*}{M_h}(z) = 2A(z)\left[\left(\frac{M_h}{M_A(z)}\right)^{-\beta(z)} + \left(\frac{M_h}{M_A(z)}\right)^{\gamma(z)}\right]^{-1}, \tag{2.2}$$

where A is the normalization of the SHMR at the characteristic halo mass M_A, while β and γ describe the slopes of the relation at low- and high-mass ends, respectively (Fig. 2.3). The double power law shape derives from the feedback-modified shape of the SMFs (see Sect. 1.2.6). If no feedback mechanisms were in place, the SHMR would have a constant value with M_h, but, since SNe and AGNs feedbacks suppress star-formation at low and high stellar masses, the SHMR shape is modified, showing a decrease at masses above and below the peak (that approximately coincides with the knee of the SMF). In order to build an empirical model, we also need to parametrize the redshift dependence the the SHMR. We will explore this aspect in detail in Sect. 3.2.

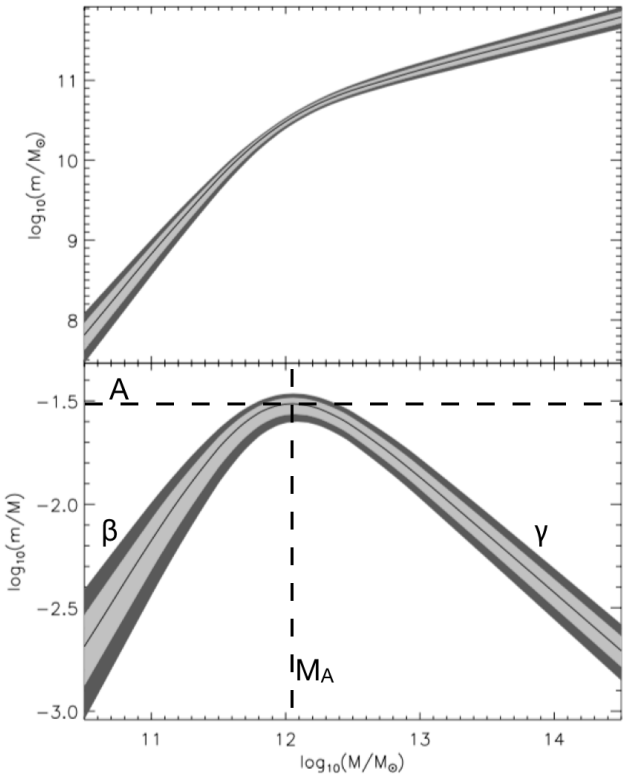

Fig. 2.3 Derived relation between stellar mass and halo mass in Moster et al. (2010). The light shaded area shows the 1σ confidence region while the dark and light shaded areas together show the 2σ region. The upper panel shows the relation between the stellar mass and the halo mass, while the lower panel shows the relation between the ratio of stellar over halo mass and the halo mass. **Credit: Moster et al. (2010)**

2.2 Observed stellar mass functions

As explained in the previous sections, in order to build a SHMR, we need observed SMFs. In this Section, we describe the SMFs used to calibrate the SHMR. The SMF of galaxies (see Sect. 1.4.3 for a detailed description) has been extensively studied over the past years out to $z \sim 4-7$ (e.g., Davidzon et al. 2017; Fontana et al. 2006; Grazian et al. 2015; Ilbert et al. 2013; Muzzin et al. 2013; Pozzetti et al. 2007, 2010; Song et al. 2016; Stark et al. 2009). Traditionally, the SMF is modeled with a Schechter function (Schechter, 1976), but it has been found that a double Schechter function provides a better fit to observations (e.g., Baldry et al. 2008; Pozzetti et al. 2010, see also Sect. 1.4.3). For all the SMFs we used in this work that we describe in the following sections, we rescaled the data points to our cosmology (i.e., to Planck15 values) and to a Chabrier IMF.

2.2.1 Data at $z \sim 0$

At $z \sim 0$ we use the SMF derived by Baldry et al. (2008). This measurement have been obtained for galaxies in the New York University Value-Added Galaxy Catalog (NYU-VAGC) low-z sample of galaxies (Blanton et al., 2005) derived from the Sloan Digital Sky Survey (SDSS). The data cover cosmological redshifts from 0.0033 to 0.05, where the redshifts were corrected for peculiar velocities using a local Hubble-flow model (Willick et al., 1997). The Data Release 4 (DR4) version of the NYU-VAGC low-z sample includes data for 49 968 galaxies.

Baldry et al. (2008) determined the stellar masses by fitting Petrosian *ugriz* magnitudes of each galaxy to the observed frame using the NYU-VAGC magnitudes and PEGASE stellar population synthesis (SPS) models (Fioc & Rocca-Volmerange, 1997) and a variety of different extinction laws (from a Small Magellanic Cloud screen law to a $\lambda^{-0.7}$ power law). The authors also showed that their results obtained with PEGASE models or BC03 models (Bruzual & Charlot, 2003) are consistent with each other. When no stellar mass was available for a galaxy, the stellar mass was determined using a color-M/L relation calibrated to the particular set of stellar masses. Moreover, these data were matched to stellar masses estimated by Kauffmann et al. (2003), Gallazzi et al. (2005), and Panter et al. (2007). Finally, Baldry et al. (2008) averaged between the different stellar mass estimates by applying a weight depending on the normalized number density as a function of redshift for all four mass estimates, and by recomputing the SMF of the sample. They obtained an accurate SMF for $z \sim 0$ galaxies shown in Fig. 2.4.

Bernardi et al. (2013) discouraged the use of Petrosian magnitudes to derive masses and luminosities in SDSS, advocating possible problems in the resulting mass-to-light ratios; this could affect the massive end of the SMFs, which might be underestimated. The expected effect, however, only concerns the brightest objects at very low redshift. The flux loss on datasets at higher redshifts has not yet been established.

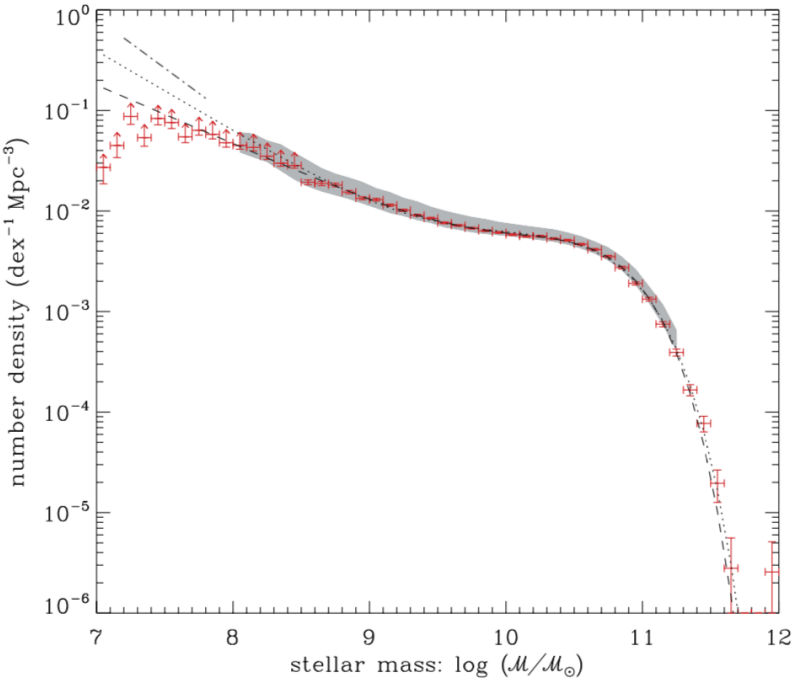

Fig. 2.4 Baldry et al. (2008) stellar mass functions. SMF extending down to $10^7 M_\odot$ determined from the NYU-VAGC. The points represent the non-parametric SMF with Poisson error bars. The dashed line represents a double-Schechter function. The dotted line shows the same type of function with a faint-end slope of $\alpha_2 = -1.8$. The dash-dotted line represents a power-law slope of -2.0. The shaded region shows the range in the GSMF accounting for the different stellar mass measurements. **Credit: Baldry et al. (2008)**

2.2.2 Data at $0.2 < z < 4$

For data at $0.2 < z < 4$, we use the SMFs calculated by Ilbert et al. (2013), which were estimated in the COSMOS field (Scoville et al., 2007) using one of the best dataset available in terms of depth of multiwavelength data ($I_{\rm AB} \sim 26.5$), covered area (~ 2 deg^2) and number of bands available (more than 35 bands). Ilbert et al. (2013) selected the sample using near-infrared data from the UltraVISTA DR1 data release (McCracken et al., 2012). The sample was built by restricting the analysis to objects with $K_s < 24$ and to sources in regions with good image quality, totaling an area of 1.52 deg^2. The photometric redshifts and stellar masses were derived with high precision by fitting the spectral energy distribution (SED) with the code *LePhare* (Arnouts et al., 2002; Ilbert et al., 2006) and Bruzual and Charlot SPS models (Bruzual & Charlot, 2003). To compute photometric redshifts, a variety of extinction laws were considered (Calzetti et al. 2000; Prevot et al. 1984 and a modified version of the Calzetti law that includes a bump at 2175 Å), while in the computation of stellar masses they only considered the Calzetti et al. (2000) extinction law. Galaxies with masses as low as $M \sim 10^{10} M_\odot$ are detected up to $z = 4$. A minimum mass $M_{\rm limit}$ was derived as the 90% completeness limit and was used as the lower boundary in the evaluation of the SMF.

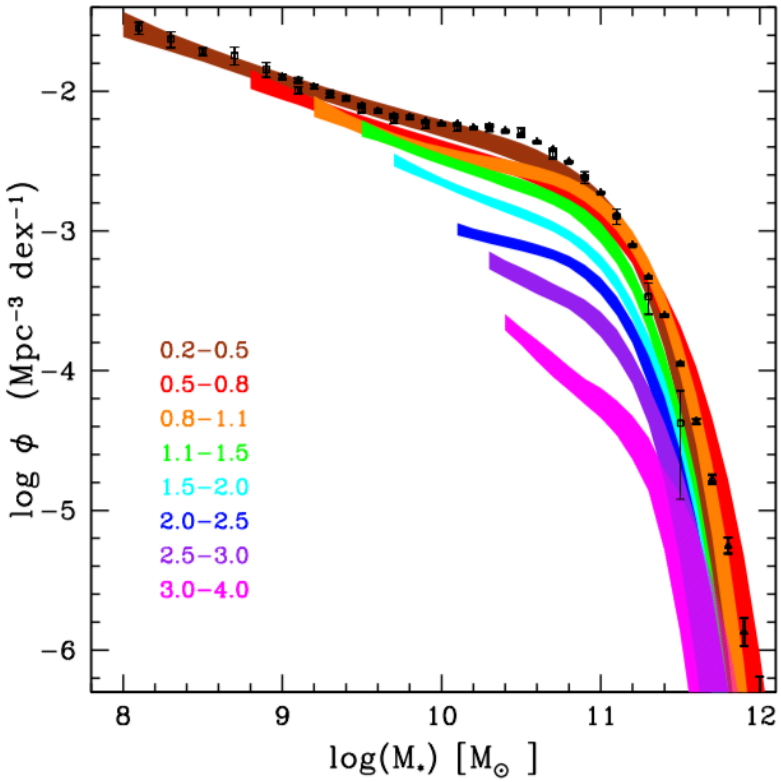

Fig. 2.5 Ilbert et al. (2013) galaxy stellar mass functions up to $z = 4$ for the full sample. Each colour corresponds to different redshift bins of variable width. Fits are shown in the mass range covered by our dataset. The filled areas correspond to the 68% confidence level regions, after accounting for Poissonian errors, cosmic variance, and the uncertainties due to the template fitting procedure. The open triangles and squares correspond to the local estimates by Moustakas et al. (2013) and Baldry et al. (2012), respectively. **Credit: Ilbert et al. (2013)**

Ilbert et al. (2013) estimated the SMF in eight redshift bins from $z = 0.2$ to $z = 4.0$ using different methods to determine the possible biases. In Fig. 2.5 the derived SMFs are shown for all redshift bins. In this work we considered their best-fit Schechter function on the binned $1/V_{\rm max}$ (Schmidt, 1968) points and relative uncertainties, computed by adding the errors due to galaxy cosmic variance in quadrature to the template-fitting procedure and the Poissonian errors.

To derive an SHMR that is as general as possible and does not depend on the quality of the observed dataset that is used to derive the SMF, we used the intrinsic SMF, derived by Ilbert et al. (2013), which was corrected for the bias due to the uncertainties in the stellar mass estimate. Because the galaxy density exponentially decreases toward massive galaxies, errors in the stellar mass scatter more galaxies toward the massive end than in the opposite direction (Eddington, 1913). This biases the estimate of the high-mass end (Caputi et al., 2011; Kitzbichler & White, 2007). The detailed procedure for correcting for this bias is described in Ilbert et al. (2013), and permits determining the intrinsic SMF: the stellar mass uncertainties are well characterized by the product of a Lorentzian

distribution $L(x) = \frac{\tau}{2\pi} \frac{1}{(\tau/2)^2+x^2}$ with $\tau = 0.04(1+z)$ and a Gaussian distribution G with $\sigma = 0.5$. The observed SMF is the convolution of the intrinsic SMF, parameterized with a double Schechter function ϕ, and the stellar mass uncertainties: $\phi_{\rm convolved} = \phi\,(L \times G)$. By estimating $\phi_{\rm convolved}$ that fits the $1/V_{\rm max}$ datapoints, it is therefore possible to determine the intrinsic ϕ.

For $z \sim 0$ data (described in Sect. 2.2.1), we use the best-fit Schechter function from the Baldry et al. (2008) data without the deconvolution to determine the intrinsic ϕ: this effect would act in the opposite direction of the flux underestimation suggested by Bernardi et al. (2013). Because of the lack of a precise estimate of the two effects, we consider face value data.

2.2.3 Data at $3.5 < z < 7.5$

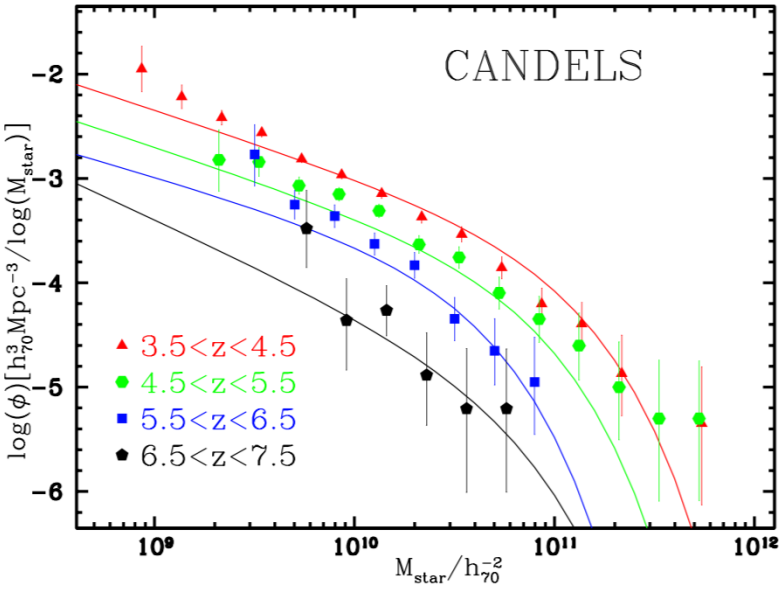

Fig. 2.6 Grazian et al. (2015) stellar mass functions. SMFs from $z = 4$ to $z = 7$ in the CANDELS UDS and GOODS-South fields. The error bars take into account the Poissonian statistics, the cosmic variance and the uncertainties derived through Monte Carlo simulations. The solid continuous curves show the Schechter function derived through a best-fit approach which corrects the observed data points for the Eddington bias. **Credit: Grazian et al. (2015)**

For data at $3.5 < z < 7.5$, we used Grazian et al. (2015) SMFs, which were estimated in the CANDELS fields. They combined wide and deep HST Spitzer and VLT observations in the CANDELS UDS (Galametz et al., 2013), GOODS-South (Guo et al., 2013b), and HUDF (Beckwith et al., 2006; Bouwens et al., 2010) fields to study the evolution of the SMF in four redshift bins between $3.5 < z < 7.5$. The HST data cover 369 arcmin^2 down to a magnitude limit of $H_{160} = 26.7$ and 27.5 for the UDS and GOODS-South field, respectively. In addition to the imaging data already adopted by Galametz et al. (2013) and Guo et al. (2013b), they included the deep K-band images obtained from the VLT Hawk-I survey HUGS (Fontana et al., 2014), reaching $K = 26.5$ at 5σ over

the GOODS-South and HUDF fields and the deep IRAC images from the SEDS survey (Ashby et al., 2013). Finally, also the deep *B*-band imaging from VIMOS at VLT has been added. The high-quality photometry from the near-UV to 8 μm has been used to derive accurate estimates of photometric redshifts and stellar masses. For the photometric redshifts the technique explored in Dahlen et al. (2013) has been adopted, which combines different photometric redshift solutions with a Bayesian technique to provide probability distribution functions in redshift, taking into account the biases and the scatter of each individual solution. These have been calibrated with more than 150 spectroscopic redshifts in the range $3.5 < z < 7.5$, resulting in an overall precision of $\sigma_z/(1+z) \sim 0.037$. With this database the SMFs reach masses as low as $M_* \sim 10^9 M_\odot$ at $z = 4$ and $\sim 6 \times 10^9 M_\odot$ at $z = 7$. Following a standard approach, Grazian et al. (2015) have used the BC03 spectral synthesis code to predict galaxy colors for a wide range of galaxy properties, including different star formation histories, ages, metallicities and dust content, and derived galaxy stellar mass from the best-fitting spectral template at the photometric redshift.

They find that their results are quite stable against different choices of the adopted SFH and also including cosmic variance, contribution of AGN and nebular lines and continuum. Also Grazian et al. (2015) provide an estimate of the SMF corrected for the Eddington bias. In Fig. 2.6 datapoints are shown along with the best-fit Schecter functions corrected for the Eddington bias in the four redshift bins.

2.2.4 Building cumulative stellar mass functions

As described in the previous sections, we used several observed estimates of the stellar mass functions to evaluate the connection between dark matter halos and galaxies. In order to do so, as detailed in Sect. 2.1.1, we built the cumulative stellar mass function by simply applying Eq. 2.1 to the analytic Schechter fit (with a continuous and uniform coverage in mass) for each redshift bin. We show all the cumulative stellar mass function we built in Fig. 2.7. These estimates will be used to evaluate the stellar-to-halo mass relation. We remind here that all SMFs (with the exception of the redshift bin $0.0 < z < 0.2$) have been corrected for the Eddington bias and therefore represent the *intrinsic* cumulative stellar mass functions.

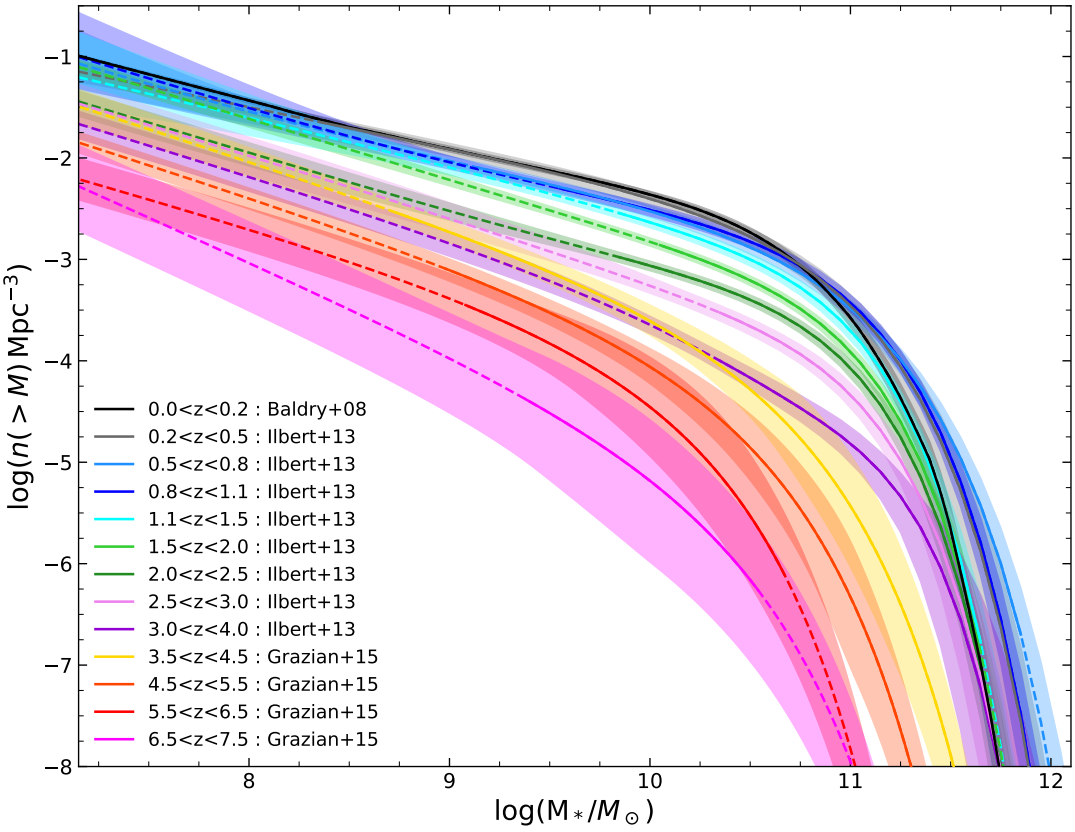

Fig. 2.7 The CSMFs used in the (sub-) halo abundance matching in different redshift bins. Solid and dashed lines with shaded area represent the SMF with 1σ uncertainty (best fit to $1/V_{\rm max}$ points; with the exception of the redshift bin $0.0 < z < 0.2$, the best fits have been corrected for the Eddington bias) cumulated as described in Sect. 2.1.1. Solid lines represent the SMF in the mass range where galaxies have been observed while dashed lines show the extrapolation.

2.3 Halo mass functions

In this section we describe the halo mass functions (HMFs) we built starting from two N-body dark matter simulations. Simulations are limited by the computational power and time, and therefore they are optimized either to maximize the area, partially sacrificing resolution, or to maximize the resolution, i.e. pushing the simulation down to low halo masses, over smaller sky areas. In our case, we used two different N-body simulation: the DUSTGRAIN-pathfinder simulation (Giocoli et al., 2018) with lightcones over $\sim$72 deg^2 down to $\log(M_h/M_\odot) \sim 12.5$ and the Millennium I+II simulation (Springel et al., 2005) whose lightcones have been built over 3.14 deg^2 but its halo masses go down to $\log(M_h/M_\odot) \sim 10.2$. In the following sections, the characteristics of the two simulation will be fully described along with the ingredients used to build the cumulative halo mass functions.

2.3.1 DUSTGRAIN-pathfinder

The first population of dark matter halos we used was drawn from a cosmological N-body collisionless simulation run with the code MG-GADGET (Puchwein et al., 2013; Springel et al., 2005, 2001) within the DUSTGRAIN-*pathfinder* simulation set presented in Giocoli et al. (2018). Standard cosmological parameters were set to be consistent with the Planck 2015 cosmic microwave background (CMB) based cosmological constraints (Planck Collaboration et al., 2016) mentioned above. The simulation was performed in a periodic cosmological box of $750\,\mathrm{Mpc}\,h^{-1}$ per side, and contained 768^3 particles with a particle mass of $m_{\mathrm{CDM}} = 8.1 \times 10^{10}\,M_{\odot}\,h^{-1}$.

Halo catalogs

The collapsed CDM structures were identified in each comoving snapshot by means of a friends-of-friends algorithm (FoF, Davis et al. 1985) applied to the CDM particles with linking length $\lambda = 0.16 \times d$, where d is the mean interparticle separation, retaining only structures with more than 32 particles, which correspond approximately to $\sim 10^{12.4}\,M_{\odot}\,h^{-1}$. In addition to these FoF catalogs, the SUBFIND algorithm (Springel et al., 2001) was used to identify gravitationally bound structures and to associate standard quantities, such as the radius R_{200}, inside of which the mean density ρ is 200 times the critical density of the universe ρ_{crit} (White, 2001), and the mass M_{200} contained within R_{200}, of the main diffuse substructure of each FoF group.

The comoving boxes have a size of $750\,\mathrm{Mpc}\,h^{-1}$ on a side and range from $z = 0$ to $z = 99$ for a total of 33 stored snapshots. More in detail, the boxes we considered are located at redshifts $z = 0.0$, 0.1, 0.2, 0.3, 0.4, 0.5, 0.6, 0.7, 0.8, 0.9, 1.0, 1.2, 1.4, 1.6, 1.8, 2.0, 2.25, 2.5, 3.0, 3.5, and 4.0. The lightcones were built using the MapSim routine (Giocoli et al., 2014) as described in Giocoli et al. (2018), with the particles stored in the snapshots from $z = 0$ to $z = 4$. Particles from different snapshots were distributed according to their comoving distances with respect to the observer, from which the redshift was derived, and according to whether they lay within a defined aperture of the field of view. Giocoli et al. (2018) created 256 different lightcone realizations, each with an area of $72.18\,\mathrm{deg}^2$, by randomizing the various comoving cosmological boxes.

We selected only halos with masses $M_{200} \geq M_{\mathrm{min,halo}} = 10^{12.5}\,M_{\odot}$ for the comoving boxes and the lightcones because of the mass resolution of the simulation. In this way, we ensured that our catalogs are complete, as we show in Fig. 2.8, which presents the halo mass distribution.

We also made use of subhalos: main (or central) halos contain a population of subhalos, which are the remnants of accreted halos (see Fig. 2.9 for a schematic illustration). Because of the resolution of the DUSTGRAIN-*pathfinder* simulation, subhalos are one order of magnitude less abundant than main halos, as we also show in Fig. 2.8. We further note that central halos with subhalos are on average more massive than central halos without subhalos at $z < 1$, whose contribution is almost negligible at masses above $M_h \sim 10^{14}\,M_{\odot}$. We investigate the characteristics and relative importance of subhalos in the next sub-section.

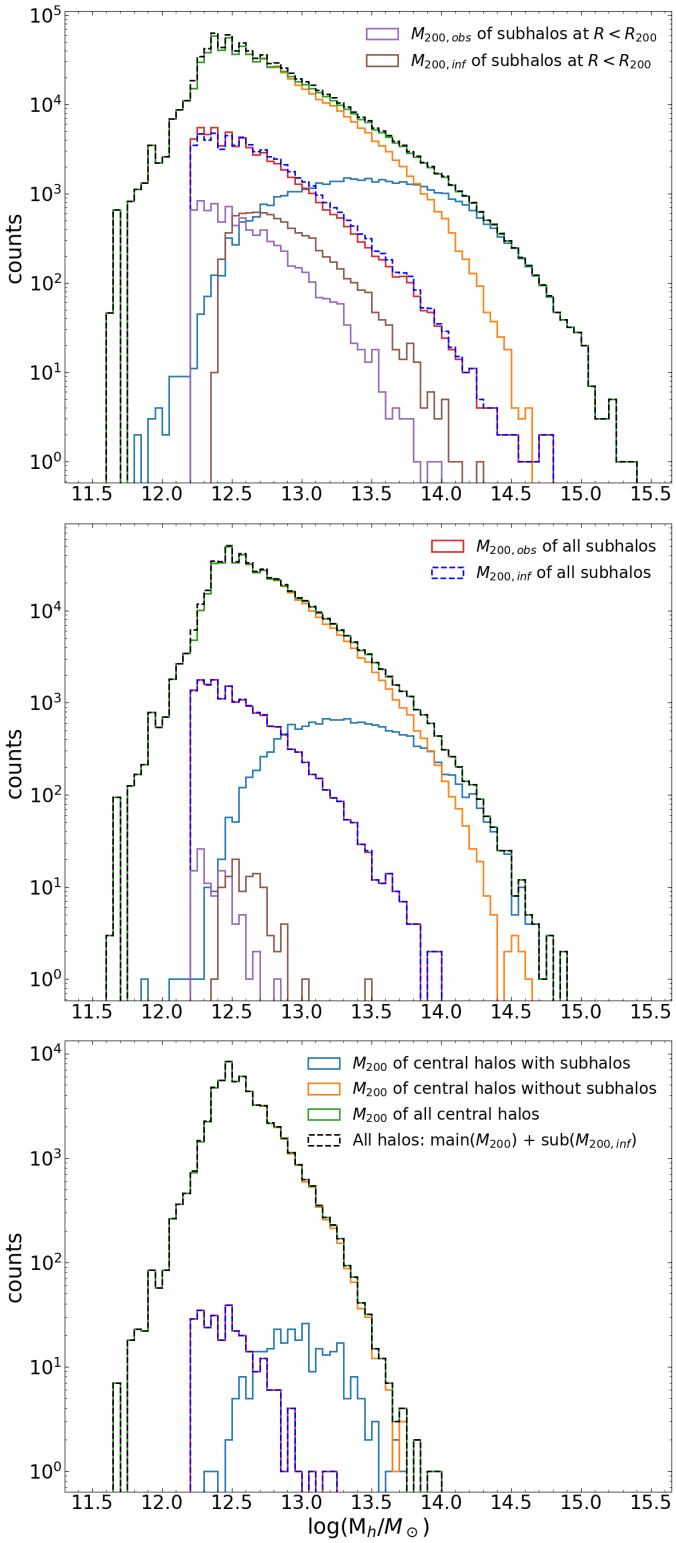

Fig. 2.8 Histograms of halo masses for three comoving boxes located at $z = 0$ (top panel), $z = 1$ (central panel), and $z = 3$ (bottom panel). In all panels, we show the distribution of observed mass (violet) and infall mass (brown) of subhalos that have entered R_{200} of their main halo (i.e., are located at $R < R_{200,\mathrm{main\,halo}}$). We also show the distribution of observed (red) and infall (blue) masses of all subhalos and the mass distribution of main (or central) halos with subhalos (light blue), the distribution of main halos without subhalos (orange), the total distribution of all main halos (green), and the distribution of all halos (black; i.e., both main and subhalos) considering the infall mass for subhalos.

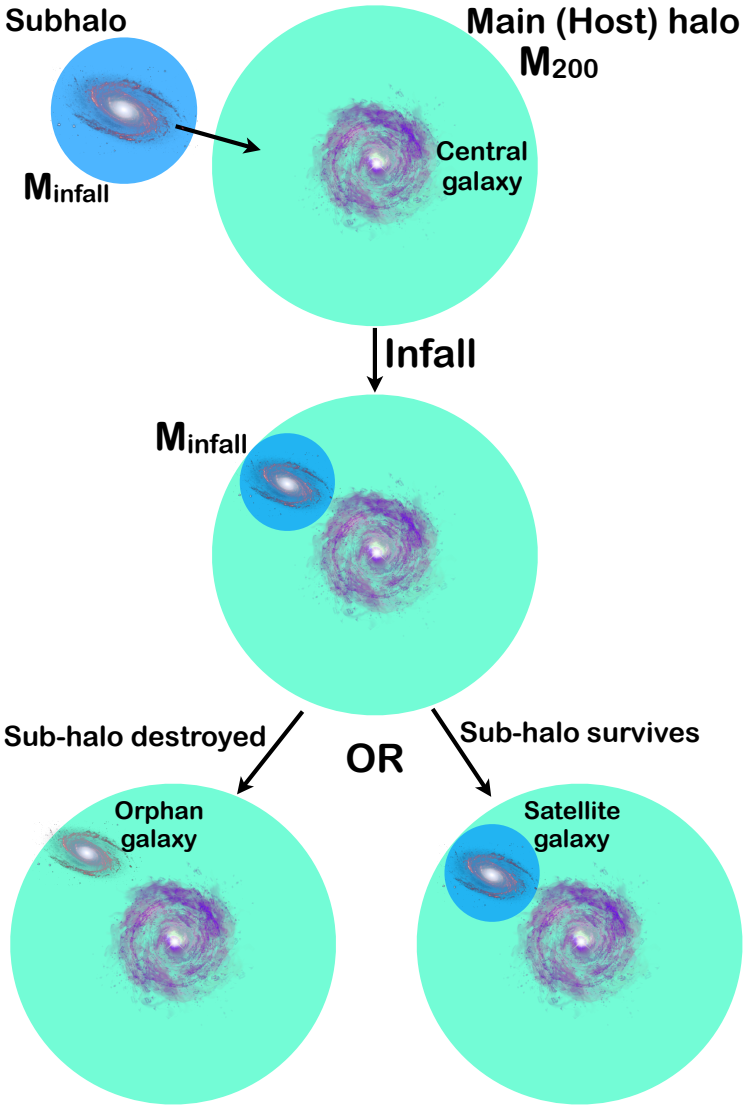

Fig. 2.9 Schematic illustration of a halo/subhalo interaction.

Subhalos and infall mass

Subhalos are gravitationally bound structures that are smaller than the main halo they belong to, orbiting within the gravitational potential of their main halo. Moreover, when they enter $R_{200,\mathrm{main\,halo}}$, they start to lose mass through various dynamical effects, including dynamical friction, tidal stripping, and close encounters with other subhalos, and they may eventually be completely disrupted (e.g., Choi et al. 2007). We show in Fig. 2.9 a schematic illustration of the fate of subhalos once they enter the main halo. Stars are centrally concentrated and more tightly bound than the dark matter, and the stellar mass of a galaxy that is accreted by a larger system is therefore expected to change only slightly, even though most of the dark matter has been stripped off (Conroy et al., 2006; Nagai & Kravtsov, 2005). Therefore, the subhalo mass at the time of observation is not the best tracer for the potential well that shaped the galaxy properties. A better tracer is the subhalo mass at the time it was accreted to the host halo (hereafter, the "infall mass"). This was first proposed by Conroy et al. (2006) and was used in several works (e.g., Behroozi et al. 2010; Moster et al. 2013, 2010; Reddick et al. 2013). We followed Gao et al. (2004) to parameterize the retained mass fraction of each subhalo as a function of its distance from the host halo center r in units of the radius R_{200} of its host halo,

$$\frac{M_{\mathrm{obs}}}{M_{\mathrm{inf}}} = 0.65 \left(\frac{r}{R_{200}}\right)^{2/3}, \tag{2.3}$$

where M_{inf} is the infall mass, M_{obs} is the mass of the subhalo at the moment of observation (i.e., after losing mass through interactions). We also evaluated the infall redshift by calculating the accretion time t_m by inverting the relation presented in Giocoli et al. (2008),

$$M_{\mathrm{inf}}(t) = M_{\mathrm{obs}} \exp\left[\frac{t - t_m}{\tau(z)}\right], \tag{2.4}$$

where $\tau(z)$ describes the redshift dependence of the mass-loss rate. van den Bosch et al. (2005) proposed the following equation for $\tau(z)$:

$$\tau(z) = \tau_0 \left[\frac{\Delta_V(z)}{\Delta_0}\right]^{-1/2} \left[\frac{H(z)}{H_0}\right]^{-1}, \tag{2.5}$$

with $H(z)$ the Hubble constant at redshift z, $\tau_0 = 2.0\,\mathrm{Gyr}$, and $\Delta_V = \rho/\rho_{\mathrm{crit}}$ (Bryan & Norman, 1998).

We followed this approach because the merger trees of the simulation were not stored, and therefore the infall mass cannot be calculated directly from the snapshots or lightcones. However, as shown in Gao et al. (2004), Eq. 2.3 has been calibrated for subhalos with masses higher than $6 \times 10^{10} h^{-1} M_{\odot}$ in a ΛCDM cosmology, and therefore it is suitable for the regime of subhalo masses in our simulation.

In the remainder of this work, we use the infall mass of the subhalos because, as we described above, it is a better tracer of the gravitational potential well at the moment of galaxy formation. It is therefore expected to provide a tighter link to the stellar mass than the mass at the time of observation.

In Fig. 2.8 we show the histograms representing the mass distribution of subhalos that have lost mass (i.e., those located at $r < R_{200}$ at the time of observation) for three comoving boxes both at the time of observation and at the infall time. For subhalos at $r < R_{200}$ the median mass loss at all redshifts is $\delta log(M_h) = 0.25\,\mathrm{dex}$, with a maximum mass loss of $\delta log(M_h)_{\mathrm{max}} = 1.26\,\mathrm{dex}$ (this only occurs in a few cases). Fig. 2.8 shows, however, that because of the mass resolution of the simulation we adopted, the total contribution of subhalos to the density of the total population of halos is almost negligible.

It might be argued that galaxies can also lose or acquire stellar mass through gravitational interaction between different galaxies in different halos (or subhalos), or through simple star formation activity from the time of the infall to the time of observation. The median time elapsed between the infall of the subhalo into the main halo and the observation time is $\delta(t) = 0.6\,\mathrm{Gyr}$. The stellar mass loss through gravitational interactions can be modeled through simulations of galaxy formation and evolution. As an example, Kimm et al. (2011) adopted a semianalytic approach and tried to model the mass loss of satellite galaxies at the moment they enter into their main halos: the authors found that the majority of baryonic mass loss is in the form of hot and cold gas that is present in the disk or halo of the galaxy. The stellar mass loss is not trivial to model, and quantitative values were not provided. On the other hand, galaxies continue to form stars with a rate that depends on their gas reservoirs, stellar initial mass function (IMF), and several other parameters. Using the Illustris hydrodynamic simulation, Niemiec et al. (2019) found that subhalos can lose a large portion of their dark matter at accretion, but continue to form stars, which increases the stellar mass up to $\sim 6\%$ after 1 Gyr from the accretion event. Considering the median timescale of 0.6 Gyr, the uncertainties in treating the processes of stellar mass loss and gain, and the numerous variables at play, we decided to take the stellar mass changes after the infall into the main halos not into account. In the following, unless specified otherwise, the halo mass M_h represents

$$M_h = \begin{cases} M_{200}, \text{ for main halos} \\ M_{\mathrm{inf}}, \text{ for subhalos} \end{cases} . \tag{2.6}$$

2.3.2 Millennium I+II

The second population of dark matter halos we used was drawn from two different cosmological N-body simulations, i.e. the Millennium (Springel et al., 2005) and Millennium II (Boylan-Kolchin et al., 2009) which have been combined in the so-called Millennium I+II simulation. In the construction of the combined catalog, using the technique detailed in Angulo & White (2010) and Angulo & Hilbert (2015), cosmological parameters were set to be consistent with the Planck 2015 cosmic microwave background (CMB) based cosmological constraints (Planck Collaboration et al., 2016), even though the two individual simulations were run with slightly different cosmological parameters. The Millennium simulation was performed in a periodic cosmological box of 500 Mpc h^{-1} per side, and contained 216^3 particles with a particle mass of $m_{\mathrm{CDM}} = 8.61 \times 10^8\, M_\odot\, h^{-1}$, with $h = H_0\,/(100\,\mathrm{km\,s^{-1}\,Mpc^{-1}})$. The Millennium II simulation was run in a periodic cosmological box of

100 Mpc h^{-1} with 432^3 particles with a mass of $m_{\rm CDM} = 6.89 \times 10^6\, M_\odot\, h^{-1}$. Both simulations were run from $z = 127$ to $z = 0$ with a modified version of the GADGET code(Springel et al., 2001).

Halo catalogs

The collapsed CDM structures were identified on-the-fly during the simulation by a friends-of-friends algorithm (FoF, Davis et al. 1985) with linking length $\lambda = 0.2$, retaining only structures with more than 20 particles, which correspond approximately to $\sim 10^{10.23}\, M_\odot\, h^{-1}$ for the Millennium simulation and to $\sim 10^8\, M_\odot\, h^{-1}$ for the Millennium II simulation. On top of these FoF catalogs, the SUBFIND algorithm (Springel et al., 2001) was run to identify gravitationally bound structures and to associate standard quantities, as done in the DUSTGRAIN-*pathfinder* simulations. The comoving boxes of the Millennium I+II simulation have a size of 500 Mpc h^{-1} on a side and range from $z = 0$ to $z = 127$ for a total of 58 stored snapshots and a total of 43 snapshots from $z = 8$ to $z = 0$. The lightcones were built by Henriques et al. (2012), using the Mock Map Facility (MoMaF) developed by Blaizot et al. (2005) with the particles stored in the snapshots of the Millennium I simulation. A similar technique to the one used for the DUSTGRAIN-*pathfinder* simulation has been used to contruct the lightcones. A total of 24 different lightcone realizations, each with an area of 3.14 deg^2 were created, by randomizing the various comoving cosmological boxes.

We downloaded the snapshots and lightcones from the VIRGO - Millennium Database[1]. In Fig. 2.12 we show the halo mass function for all the 24 lightcones along with the Despali et al. (2016) theoretical parametrization and the so-called "global HMF" which represents the mean value of the halo mass function of the 24 lightcones in each mass bin. As it can be seen the halo catalogs are complete down to $\log(M_h/M_\odot) \sim 10.4$. We therefore selected only halos from $z = 0$ to $z = 8$ with masses $M_{200} \geq M_{\rm min,halo} = 10^{10.2}\, M_\odot\, {\rm h}^{-1}$ for the comoving boxes and the lightcones in order to ensure that our catalogs are complete in halo masses. We remind here that the lightcones, produced by Henriques et al. (2012), include only halos from the Millennium I simulation, while comoving boxes combine results from the Millennium I and Millennium II simulations. In the following of this thesis we will use the nomenclature "Millennium I+II" when generally referring to Millennium results.

Subhalos and infall mass

As already discussed above the best tracer for the potential well that shaped the galaxy properties is the subhalo mass at the time it was accreted to the host halo, i.e. the “infall mass”. In the Millennium I+II database, halos are classified with a flag called ‘type’ which brings information about the relative position of the halos. In particular, a halo can be at the center of the FOF group (type=0 also called "central"), at center of the subhalo that is not at the center of its FOF group (type=1 also called "satellite"), or is a satellite that has lost its subhalo, or simply has lost enough mass to fall below the resolution limit of the simulation (type=2 also called "orphans"). In this classification, type=0 objects are main halos which contain several subhalos (type=1) and orphans (type=2), which have lost

[1] http://gavo.mpa-garching.mpg.de/MyMillennium/

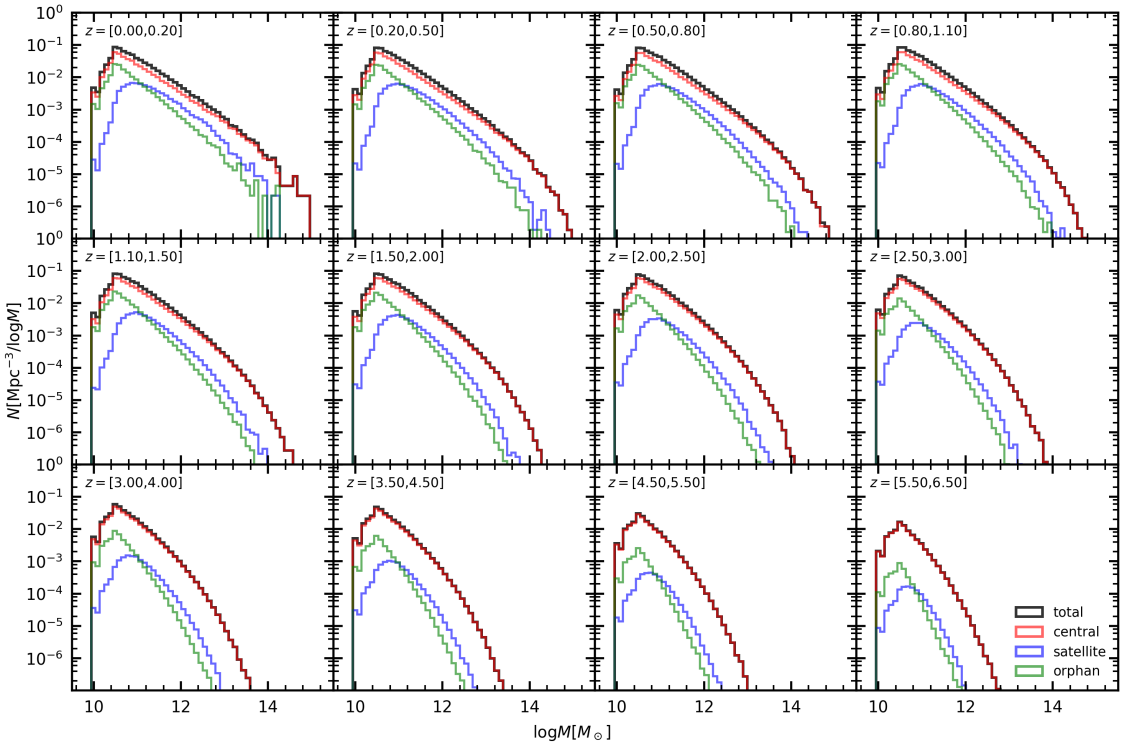

Fig. 2.10 Histogram of halo masses of the Millennium I+II simulation in several redshift bins (highlighted in panels). In black we show the distribution of masses of all halos. In red the mass distribution of central galaxies is shown (type=0), while in blue and red we show the distributions of infall masses for satellite (type=1) and orphans (type=2), respectively.

part, or all, of their mass since their infall into the main halo. Type=2 objects, the so-called orphan galaxies, need to be taken into account in order to construct a complete sample for the population of subhalos/satellite galaxies. We show in Fig. 2.9 a schematic illustration of the evolution of subhalos once they enter the main halo. We show in Fig. 2.10 the mass distribution of the three type of halos in redshift bins, along with the distribution of all halos. As it is clear from Fig. 2.10, it is fundamental to consider satellite and orphan objects in order to construct a complete sample of halos. We also note that for $\log(M_h/M_\odot) \gtrsim 11\,\mathrm{h}^{-1}$ the satellite population dominates over the orphan one, while this trend is reversed for masses $\log(M_h/M_\odot) \lesssim 11\,\mathrm{h}^{-1}$. We highlight here that the Millenniun I+II lightcones were specifically produced for the Henriques et al. (2015) SAM. In the creation of the lightcones, in order to take into account orphan galaxies, a dynamical friction time is set to take track of the DM sub halos disruption and the consequent merging of the galaxy into the central one. In the lightcones, the position of orphan galaxies is registered until such galaxies merge onto the central one. In this sense, the lightcones we use are able to keep track of orphan galaxies up to the time they merge into the central one, even though they are not completely independent from the Henriques et al. (2015) SAM halo modeling. The database already provides infall masses for all subhalos of type 1 and 2, and therefore by considering the infall mass we also take into account orphan galaxies. As above, in

the following, unless specified otherwise, the halo mass M_h represents

$$M_h = \begin{cases} M_{200}, \text{ for main halos (type 0)} \\ M_{\rm inf}, \text{ for subhalos (type 1 \& 2)} \end{cases} . \tag{2.7}$$

2.3.3 Building the cumulative halo mass functions

In order to build the cumulative halo mass functions, as detailed in Sect. 2.1.1, we simply apply Eq. 2.1 to the number counts of halos for each redshift bin. Further, to extend the SHMR not only at any redshift, but also in the widest possible mass range, we compared the halo mass functions (HMFs) of the simulation to theoretical parameterizations.

DUSTGRAIN-*pathfinder* simulation

In Fig. 2.11 we show a comparison of the cumulative halo mass functions (CHMF) of the ΛCDM DUSTGRAIN-*pathfinder* simulation with those reported by Despali et al. (2016), who measured the HMF using a suite of six N-body cosmological simulations with different volumes and resolutions (see Despali et al. 2016 for details). We computed the Despali et al. (2016) CHMFs for halos whose mass is defined as $200\,\rho_{crit}$ in order to match the halo mass definition of the simulation we used. In particular, we show the CHMF computed from lightcones without taking the infall mass for the subhalos into account, and the one using the infall mass. Using the lightcones, we were able to precisely select the redshift intervals in which we calculated the CHMF. The comoving boxes, instead, are located at fixed redshifts. To calculate the CHMF, we therefore considered all the boxes located in the same redshift bin. We also evaluated the halo CHMF for boxes with or without the infall mass for the subhalos. We estimate the relative difference of the CHMF of the simulation with respect to the Despali et al. (2016) mass function in the bottom panels of Fig. 2.11, showing that the differences between the CHMFs of the simulation (on comoving boxes and light cones) and the theoretical CHMFs are minimal: the maximum difference is only a few percent of the value of the Despali et al. (2016). Fig. 2.11 also clearly shows that even if the median difference between the infall mass and observed mass is 0.25 dex, the halo mass function does not change signficantly, regardless of the infall mass for subhalos. When we consider the mass of subhalos at the infall or the mass at observation, the differences in mass functions are lower than 1%. This is reasonable because only a few subhalos have already entered R_{200}, and have therefore lost mass. This is because the simulation is limited to very massive halos ($\log(M_h/M_\odot) \geq 12.5$). Their total influence on the HMF at high halo masses and on the derived SHMR is therefore very limited because the fraction of subhalos with respect to main halos is small ($\sim 10\%$ at $\log(M_h/M_\odot) = 12.5$ and $z = 0$, consistent with the results by Rodríguez-Puebla et al. 2017 and Despali & Vegetti 2017). This is also visible in the histograms of Fig. 2.8, which clearly show that the effect of subhalos is negligible compared to the total halo distribution, regardless of the infall mass.

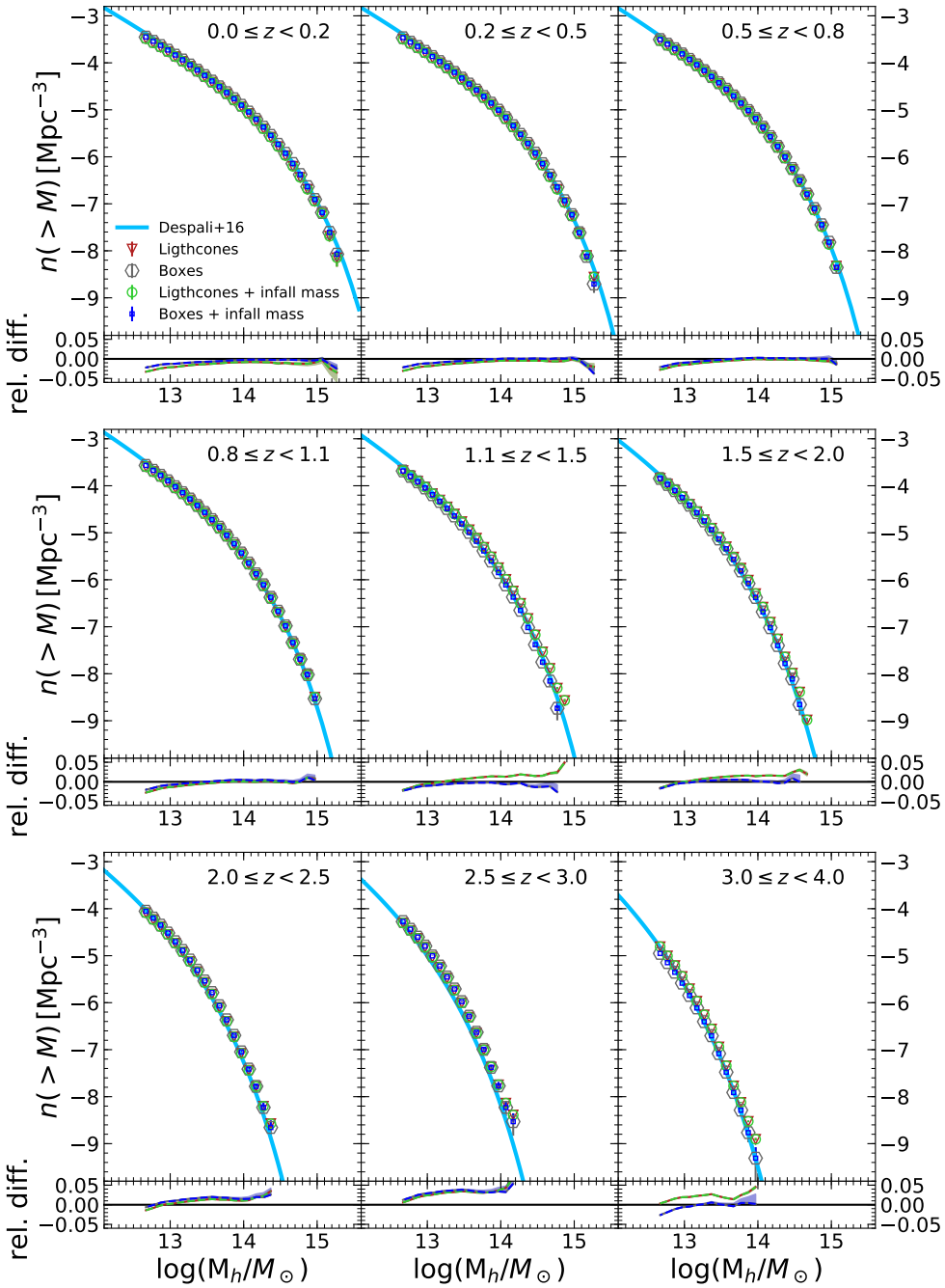

Fig. 2.11 Cumulative halo mass functions in nine different redshift bins. The cyan line represents the Despali et al. (2016) halo mass function calculated at the center of the redshift bin. The colored points represent the halo mass function of the ΛCDM DUSTGRAIN-*pathfinder* simulation: red triangles are the halo CMF evaluated on the ligthcones without taking the infall mass for the subhalos into account, green circles make use of the infall mass, gray hexagons represent the halo CMF using comoving boxes without using the infall mass for the subhalos, and blue squares are derived from simulation boxes taking the infall mass into account. The bottom panels represent the relative difference of the CMF of the simulation with respect to the Despali et al. (2016) mass function.

In order to derive the SHMR relation on a wider mass range than allowed by the HMFs of ΛCDM DUSTGRAIN-*pathfinder* simulations, we adopted the Despali et al. (2016) HMF: in this way, we were able to compute the SHMR from the lowest observed stellar masses ($M_* \sim 10^8\,M_\odot$, $M_h \sim 10^{10.5}\,M_\odot$) to the highest ($M_* \sim 10^{12}\,M_\odot$, $M_h \sim 10^{15}\,M_\odot$) from $z = 0$ to $z = 4$ (i.e. in the range of the lightcones). We want to highlight that the Despali et al. (2016) has been calibrated on main halos only, and, therefore, when the contribution of subhalos becomes important (i.e. $\log(M_h/M_\odot) =\lesssim 12$), it cannot be a good representation of the (sub)HMF anymore. Finally, we stress that in order to build a realistic mock catalog of galaxies, however, the derived SHMR relation needs to be applied to the infall mass of subhalos to derive the corresponding stellar mass.

Millennium I+II simulation

In this case, given the relatively small area of each individual lightcone of the Millennium I+II simulation (i.e. 3.14 deg^2), the number of massive galaxies is limited, especially at low redshifts where the volume is small. In order to enlarge the statistics of massive galaxies and construct a reliable HMF, we simply sum up the counts of all the 24 lightcones in each mass bins and divide by the volume multiplied by 24. In this way, we constructed a "global" HMF that reaches high halo masses and can be used to build the SHMR. The global HMF is shown with open black points in Fig. 2.12.

In the previous subsection, we showed that the halo mass function reported by Despali et al. (2016) is a reasonable approximation for the halo mass functions of the DUSTGRAIN-*pathfinder* simulation given the limited mass range of the simulation. In fact, for masses above $\log(M_h/M_\odot) = 12.5$, i.e. the mass limit of the DUSTGRAIN-*pathfinder* simulation, the contribution by subhalos to the total numer of halos is very limited. However, by pushing the limit of halo masses to lower values, as done in Millennium I+II simulation, the Despali et al. (2016) is not a reasonable approximation anymore. This can be seen in Fig. 2.12 where we show with a blue dashed line the Despali et al. (2016) halo mass function calculated at the mean redshift of each bin. In fact, for masses $\log(M_h/M_\odot) \lesssim 13$ and $z \lesssim 3$, the Despali et al. (2016) HMF starts to show differences with respect to the HMF of the Millennium I+II simulation, reaching differences of a factor of ~ 2 at $\log(M_h/M_\odot) = 11$ at $0.0 < z < 0.2$. For higher masses, or redshifts, the Despali et al. (2016) and the Millennium I+II HMFs are again in good agreement. This is reasonable given that the Despali et al. (2016) HMF is calibrated on main halos only, and therefore, when the contribution of subhalos is limited (i.e. at high halo masses or high redshifts), it provides a good approximation of the halo+subhalo mass function.

To sum up, for the DUSTGRAIN-*pathfinder* simulation, given that it is limited in halo masses (i.e. $\log(M_h/M_\odot) \gtrsim 12.5$, which corresponds to $M_* \sim 10^{11}\,M_\odot$, as it will be seen in Chapter 3, to evaluate the SHMR we use the Despali et al. (2016) halo mass function theoretical parametrization in order to push the relation down to lower halo masses neglecting, however, the contribution of sub-halos (i.e. $M_h \sim 10^{10.5}\,M_\odot$ corresponding to $M_* \sim 10^8\,M_\odot$ which is the observed limit of the SMFs presented in Sect. 2.2) from $z = 0$ to $z = 4$. For the Millennium I+II simulation, we use the global HMF

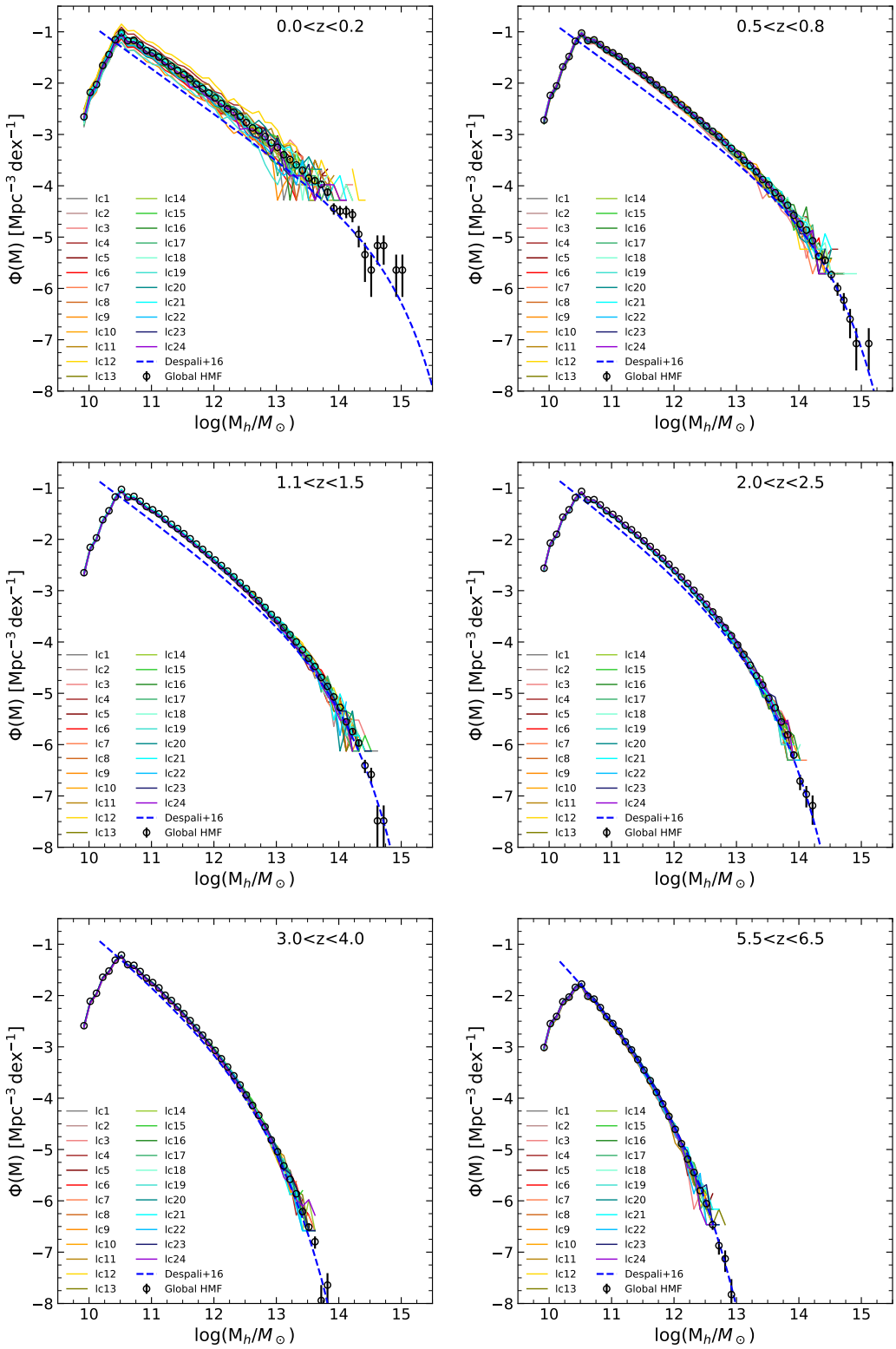

Fig. 2.12 Halo mass function of the Millennium I+II simulation at $0.0 < z < 0.2$ (top left), $0.5 < z < 0.8$ (top right), $1.1 < z < 1.5$ (center left), $2.0 < z < 2.5$ (center right), $3.0 < z < 4.0$ (bottom left) and $5.5 < z < 6.5$ (bottom right). In all panels we also show with a dashed blue line the Despali et al. (2016) HMF calculated at the mean redshift of each bin. In addition, with black open points, we show the so-called "global HMF" which represents the mean value of the halo mass function of the 24 lightcones in each mass bin. The error we show is a standard Poisson error evaluated on the summed counts of the 24 lightcones in each mass bin.

evaluated on all 24 lightcones with which we are able to reach lower halo masses ($M_h \sim 10^{11}\,M_\odot$, i.e. $M_* \sim 10^{7.5}\,M_\odot$) from $z = 0$ to $z = 8$.

3

RESULTS ON THE STELLAR-TO-HALO MASS RELATION

Given the procedure described in the previous Chapter, here we derive the relationship that connects the stellar mass of a galaxy to the mass of its dark matter halo, present our results for the DUSTGRAIN-*pathfinder* and Millennium I+II simulations and compare their results in the common mass range. In addition, we define a simple empirical model which allows us to assign stellar masses to a given halo knowing its halo mass and redshift. We also discuss the impact of scatter on the results and extensively compare with literature results and semi-analytic models of galaxy formation and evolution. Finally, we study the evolution of the stellar-to-halo mass relation (SHMR) from $z \sim 8$ to $z \sim 0$.

For all the fits performed in this chapter, we use the software package *emcee*, which is a purely python implementation of the Monte Carlo Markov chain (MCMC) method (Foreman-Mackey et al., 2013). This algorithm allows sampling the posterior distribution for the free parameters. We always used 200 walkers (each performing 2000 steps) with a different starting point each randomly selected from a Gaussian distribution around the original starting prior (chosen from the results presented in Moster et al. 2010). The first half of the steps were discarded as a burn-in phase. The convergence of the fits has always been assessed through the Gelman-Rubin diagnostic (Gelman & Rubin, 1992). This test compares the variance within one chain of the MCMC with the variance between chains. The two variances are combined in a weighted sum to obtain an estimate of the variance of a parameter. The square root of the ratio of this estimated variance within the chain variance is called the potential scale reduction $\hat{R}$, and for a well-converged chain it should approach 1. Values higher than 1.1 indicate that the chains have not yet fully converged (Gelman & Rubin, 1992). The best-fit values, the 1σ and 2σ uncertainties, are always computed using the 50th, 16th, 84th, 2nd and 98th percentiles of the posterior distributions of the free parameters of the fit.

3.1 The relation between stellar and halo masses

In this Section, we present the results that emerge from the application of the (sub)halo abundance matching technique, as detailed in Sec. 2.1.1, to the observed stellar mass functions, presented in Sect. 2.2 and shown in Fig. 2.7, and the halo mass functions described in Sect. 2.3, to evaluate the SHMR. To estimate the errors in the relation, we repeat the same operation on the upper and lower 1σ errors of the cumulative SMFs shown in Fig. 2.7 with shaded areas.

3.1.1 Results on DUSTGRAIN-*pathfinder* simulation

As previously explained, given the good agreement above the limiting mass $\log(M_h/M_\odot) = 12.5$, we adopted the Despali et al. (2016) HMF to describe the HMF of the DUSTGRAIN-*pathfinder* simulation: in this way, we can extrapolate the estimate of the SHMR to lower halo masses with respect to the ones allowed by the simulation from $z = 0$ to $z = 4$ (i.e. in the range of the lightcones). However, we stress that the extrapolation is valid only for main halos, given that the Despali et al. (2016) HMF has been calibrated on main halos only.

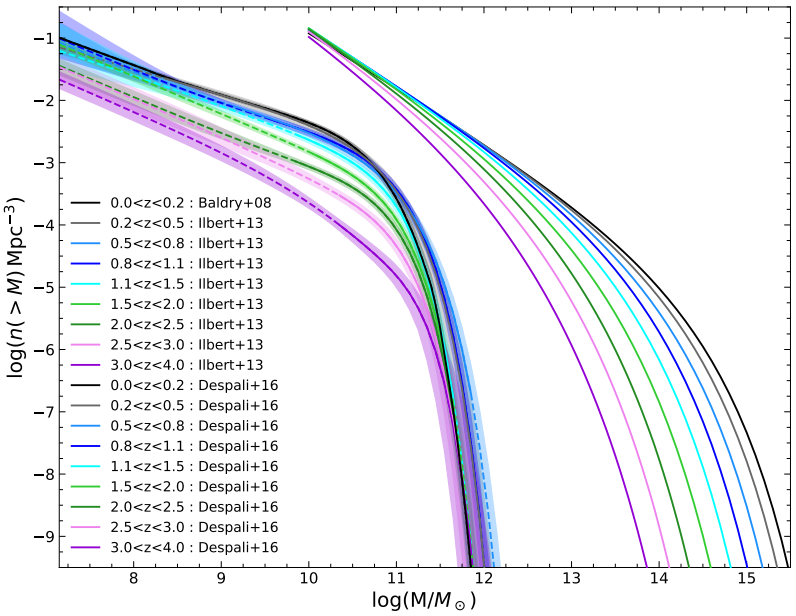

Fig. 3.1 Halo and stellar cumulative mass functions for the DUSTGRAIN-*pathfinder* simulation in all redshift bins from $z = 0$ to $z = 4$. Halo mass functions are shown in the right part of the plot and are represented by the Despali et al. (2016) HMF. On the left, cumulative stellar mass functions are shown along with their 1σ uncertainties (shown with shaded areas). Solid lines indicate the observed range of galaxies, while dashed lines represent the extrapolation using the best-fit Schechter function.

To evaluate the SHMR, we applied the SHAM approach (described in Sect. 2.1.1) to the cumulative (both stellar and halo) mass functions to each redshift bin up to $z = 4$, shown in Fig. 3.1. Figure 3.2 shows, in the top panel, our results (without relative scatter) for the Despali et al. (2016) HMF in the $\log(M_h/M_\odot)$-redshift-$\log(M_*/M_\odot)$ plane, color-coded for $\log(M_*/M_h)$ where the bell-shaped SHMR is evident. In the bottom panel we also show a projection on a two-dimensional plane where on a $\log(M_h/M_\odot)$-redshift plane, the colored layer shows $\log(M_*/M_\odot)$. It is already evident from this figure the opposite behaviours with redshift at fixed halo mass of the corresponding stellar mass, as we quantify later.

For each of the nine redshift bins, we performed a fit using Eq. 2.2 and always find a value of the Gellmann-Rubin diagnostic $\hat{R}$ ranging from 1.01 to 1.06, indicating that the fits have converged. The best-fit parameters are listed in Table 3.1. Figure 3.3 shows our results in a $\log(M_*/M_h) - \log(M_h/M_\odot)$ plane in the different redshift bins used by Baldry et al. (2008) and Ilbert et al. (2013) to compute the SMF. In the Figure, we show the points that were computed using the halo CMF of lightcones of the DUSTGRAIN-*pathfinder* simulation, which take the subhalo infall masses into account, and the best fit of the relation evaluated using the Despali et al. (2016) CMF that was fit with Eq. 2.2, and its 1σ uncertainties. We remind here that we adopted the mean CHMF of all the 256 lightcones of the simulation. This figure shows that the small differences between the halo CMFs of Despali et al. (2016) and those from the lightcones (using the infall masses for subhalos) translate

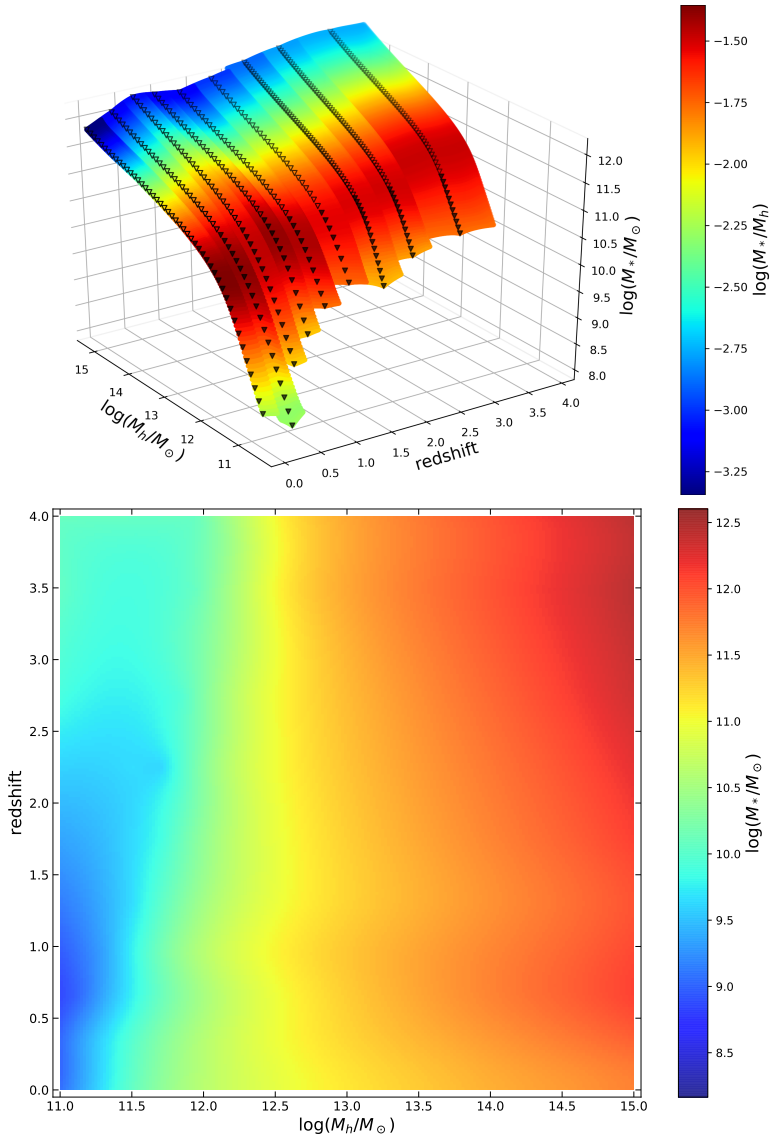

Fig. 3.2 The SHMR derived using the Despali et al. (2016) HMF. In top panel, the $\log(M_h/M_\odot)$-redshift-$\log(M_*/M_\odot)$ plane is shown, color-coded by $\log(M_*/M_h)$. Points represent the observed relation derived from the CMFs. Open points show the halo mass range of the DUSTGRAIN-*pathfinder* simulation (i.e., $\log(M_h/M_\odot) \geq 12.5$), and open and solid points indicate the halo mass range we used to derive the SHMR with the Despali et al. (2016) HMF. In bottom panel, the $\log(M_h/M_\odot)$-redshift plane is shown, color-coded by $\log(M_*/M_\odot)$. The colored layers are a linear interpolation between observed data points.

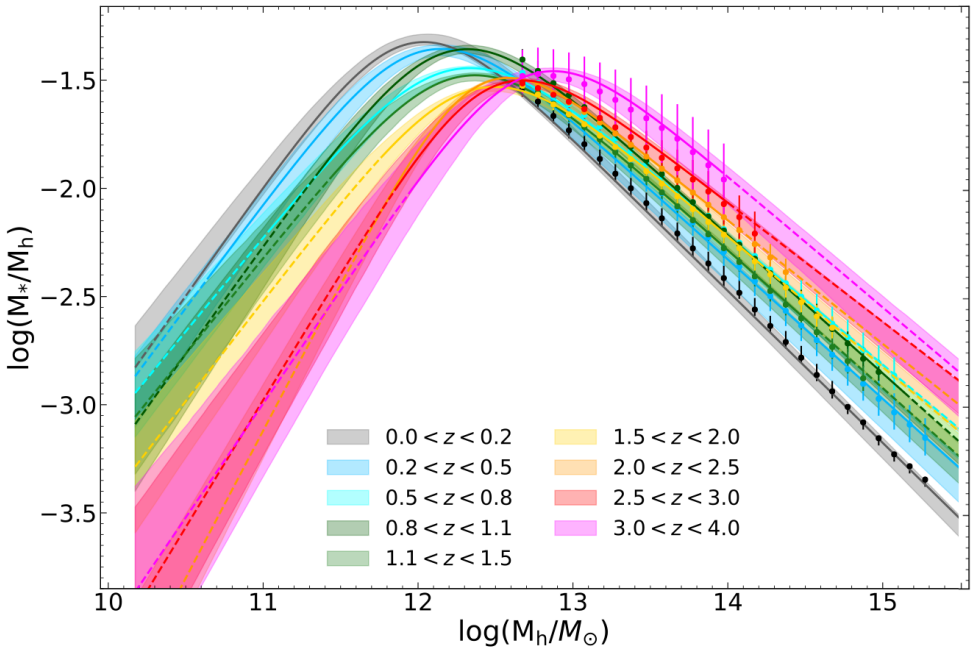

Fig. 3.3 The SHMR for the Despali et al. (2016) case (representing the DUSTGRAIN-*pathfinder* simulation) derived in the $\log(M_*/M_h) - \log(M_h/M_\odot)$ plane. Points with error bars represent the observed relation obtained from the CMFs of the lightcones (i.e., they represent the halo mass range of the ΛCDM DUSTGRAIN-*pathfinder* simulation), and the lines and corresponding shaded area represent the relation derived using the Despali et al. (2016) mass function and the 1σ error bar. The solid line identifies the observed mass range of galaxies, and the dashed line represents the extrapolation using the best-fit Schechter function.

into negligible differences in the SHMR. We are therefore confident that for the mass regime of the simulation (i.e., for $\log(M_h/M_*) \geq 12.5$), the same relation holds both for the simulation and for the theoretical halo mass function. In addition, from this plot it is evident that at fixed halo mass, the corresponding stellar mass increases with redshift (up to $z \sim 4$) at halo masses above the peak of the SHMR ($\log(M_h/M_\odot)_{peak} \sim 12.0$ at $z \sim 0$) and viceversa for masses below the SHMR peak.

As shown in Fig. 3.3, starting from low halo masses, the SHMR in the various redshift bins monotonically increases (with slope β) as a function of halo mass and reaches a peak at M_A, after which the relation decreases monotonically (with slope γ) at higher halo masses. The redshift evolution of the SHMR shows that above the characteristic halo mass M_A, the SHMR increases with increasing redshift, while this trend is reversed at lower masses. In Appendix A.1 we show the best-fits to the data derived from the direct comparison of the CMFs for all redshift bins with their corresponding contour plot that shows all the one and two dimensional projections of the posterior probability distributions of the free parameters of the fit.

Table 3.1 Best-fit parameters of the SHMR for the Despali et al. (2016) case (representing the DUSTGRAIN-*pathfinder* simulation) in Eq. 2.2 and their 68% confidence interval.

Δz	A	M_A	β	γ
$0.00 \leq z < 0.20$	$0.0465^{+0.0015}_{-0.0015}$	$11.77^{+0.03}_{-0.03}$	$1.00^{+0.05}_{-0.05}$	$0.702^{+0.006}_{-0.006}$
$0.20 \leq z < 0.50$	$0.0431^{+0.0025}_{-0.0025}$	$11.86^{+0.08}_{-0.07}$	$0.97^{+0.11}_{-0.09}$	$0.644^{+0.020}_{-0.019}$
$0.50 \leq z < 0.80$	$0.0353^{+0.0015}_{-0.0014}$	$12.05^{+0.07}_{-0.07}$	$0.88^{+0.11}_{-0.10}$	$0.599^{+0.021}_{-0.019}$
$0.80 \leq z < 1.10$	$0.0429^{+0.0018}_{-0.0017}$	$12.03^{+0.06}_{-0.05}$	$0.99^{+0.15}_{-0.13}$	$0.638^{+0.014}_{-0.014}$
$1.10 \leq z < 1.50$	$0.0328^{+0.0013}_{-0.0013}$	$12.10^{+0.06}_{-0.06}$	$0.89^{+0.15}_{-0.13}$	$0.638^{+0.018}_{-0.016}$
$1.50 \leq z < 2.00$	$0.0287^{+0.0008}_{-0.0007}$	$12.20^{+0.06}_{-0.05}$	$0.93^{+0.16}_{-0.14}$	$0.604^{+0.018}_{-0.017}$
$2.00 \leq z < 2.50$	$0.0297^{+0.0006}_{-0.0006}$	$12.21^{+0.03}_{-0.03}$	$1.36^{+0.14}_{-0.13}$	$0.571^{+0.013}_{-0.012}$
$2.50 \leq z < 3.00$	$0.0294^{+0.0010}_{-0.0009}$	$12.31^{+0.07}_{-0.06}$	$1.18^{+0.22}_{-0.19}$	$0.551^{+0.028}_{-0.025}$
$3.00 \leq z < 4.00$	$0.0335^{+0.0021}_{-0.0020}$	$12.55^{+0.12}_{-0.10}$	$1.05^{+0.22}_{-0.18}$	$0.605^{+0.063}_{-0.052}$

3.1.2 Results on Millennium I+II simulation

As explained in Sect. 2.3.3, given that we have 24 lightcones available, we used the global HMF of the Millennium I+II simulation to build the SHMR in order to enlarge the statistics at high halo masses. As for the DUSTGRAIN-*pathfinder* case, we applied the SHAM technique (described in Sect. 2.1.1) to the cumulative mass functions, shown in Fig. 3.4, to each redshift bin up to $z = 8$. We remind here that we adopted the "global HMF" evaluated by adding up all the HMF calculated on the all available lightcones of the simulation. We note here that, while the massive part of CHMF strongly evolves with cosmic time (redshift) due to the hierarchical growth of the haloes, the SMFs have a milder evolution in particular in its massive end. As we comment later these different behaviours lead to the evolution of the SHMR with cosmic time.

Figure 3.5 shows in the top panel our results (without *relative* scatter) in a $\log(M_h/M_\odot)$-redshift-$\log(M_*/M_\odot)$ plane, color-coded, via linear interpolation through results of the fits, for $\log(M_*/M_h)$ where the bell-shaped SHMR is evident from $z \sim 0$ to $z \sim 8$. In the bottom panel we also show a projection on the two-dimensional plane $\log(M_h/M_\odot)$-redshift, where the colored layer shows $\log(M_*/M_\odot)$. Once again, for each of the thirteen redshift bins, defined by the observed SMFs, we performed a fit using Eq. 2.2. We always find a value of the Gellmann-Rubin diagnostic $\hat{R}$ ranging from 1.03 to 1.09, indicating that the fits have converged well. The best-fit parameters are listed in Table 3.2.

Figure 3.6 shows our results in a $\log(M_*/M_h) - \log(M_h/M_\odot)$ in six different redshift bins. It is evident from the figure that the low halo mass power law seems to be broken for $M_h < M_{upturn}$, where the SHMR shows an upturn. The mass of the upturn roughly corresponds to $M_{upturn} \sim 10^{11} M_\odot$ at all redshift (that roughly corresponds to $M_* \sim 10^{8.5} M_\odot$), even if its precise value depends on the redshift bin which is considered (e.g. $M_{\rm upturn} \sim 10^{11} M_\odot$ for $0.8 < z < 1.1$ and $M_{upturn} \sim 10^{11.2} M_\odot$ for $2.0 < z < 2.5$). In fact, this upturn is a signature of the upturn which is seen in the SMFs below $M_* \sim 10^{8.5} M_\odot$ (see Baldry et al. 2008 as an example). Some authors (e.g. Behroozi et al. 2013) find the same upturn and use it as an argument against fitting a double power law to the observed SHMR. However, given the large errorbars at these masses (that are evident in Fig. 3.6), we feel confident that the double power law we adopted for the fit is a good approximation even in the presence of this upturn in the input SMFs.

Figure 3.7 shows our results (without *relative* scatter) for the Millennium I+II simulation, in a $\log(M_*/M_h) - \log(M_h/M_\odot)$ plane at $z < 4$ in the top panel (i.e. in the different redshift bins used by Baldry et al. 2008 and Ilbert et al. 2013 to compute the SMF) and at $z > 4$ in the bottom one (i.e. the redshift bins used by Grazian et al. 2015 to calculate the SMFs). We show the best fit of the relation using Eq. 2.2, along with the corresponding 1σ uncertainties. In this case, given that the Millennium I+II simulation goes down to low halo masses (i.e. $\log(M_h/M_\odot) \sim 10.2\,{\rm h}^{-1}$) we've been able to evaluate the SHMR from $\log(M_h/M_\odot) \sim 10.37$ to $\log(M_h/M_\odot) \sim 15$ without any theoretical parametrization. We also report in Appendix A.3 the best-fit plots along with their corresponding posterior distributions for all redshift bins.

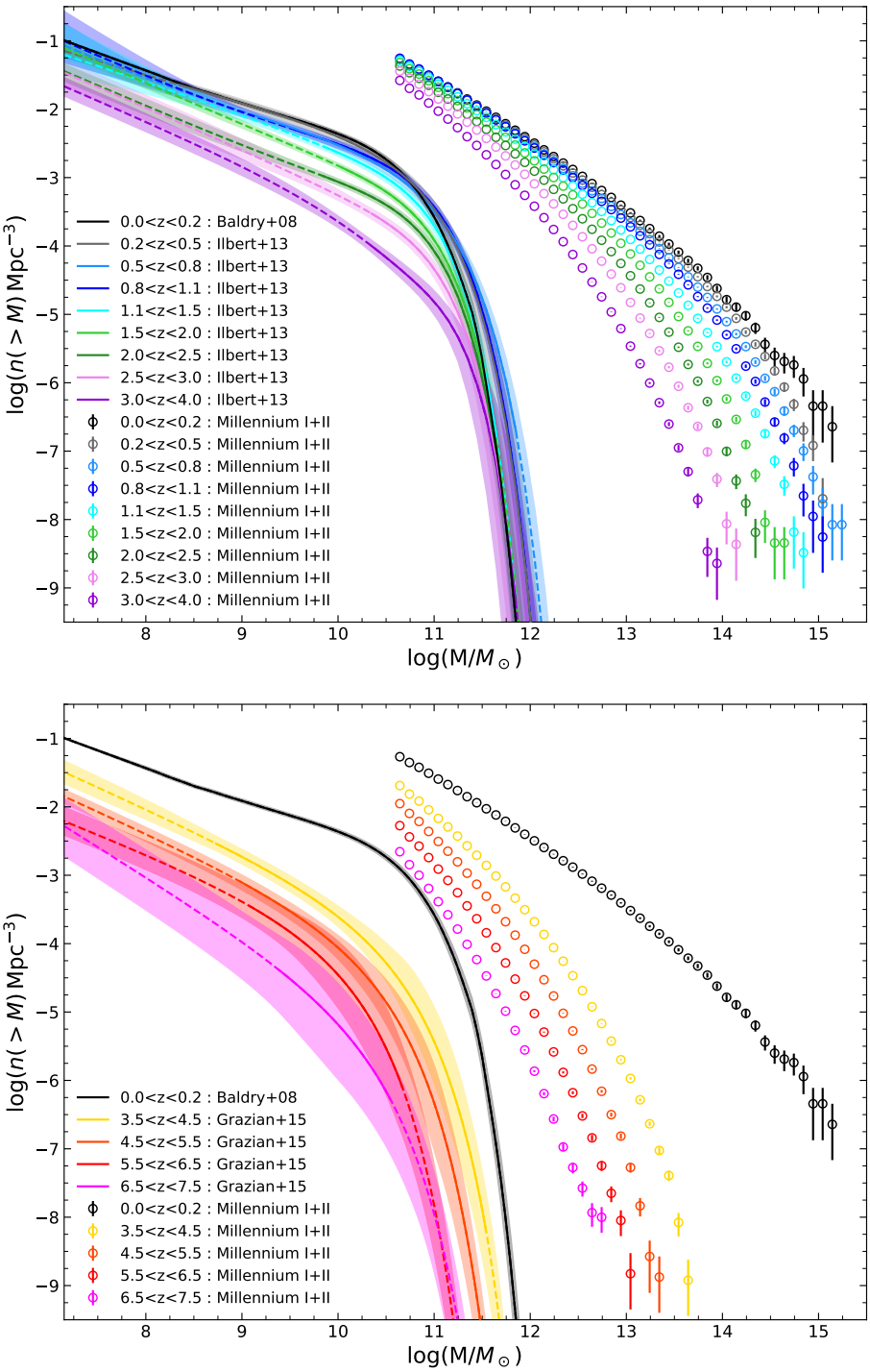

Fig. 3.4 Halo and stellar cumulative mass functions for the Millennium I+II simulation in all redshift bins from $z = 0$ to $z = 4$ in top panel and from $z = 4$ to $z = 8$ in bottom panel. For both panels, halo mass functions are shown in the right part of the plot and represent the global HMF (as calculated in Sect. 2.3.2 and limited to $\log(M_h/M_\odot) > 10.37$, i.e. the completeness limit of the simulation). On the left, we show the cumulative stellar mass functions along with their 1σ uncertainties (shown with shaded areas). Solid lines indicate the observed range of galaxies, while dashed lines represent the extrapolation using the best-fit Schechter function.

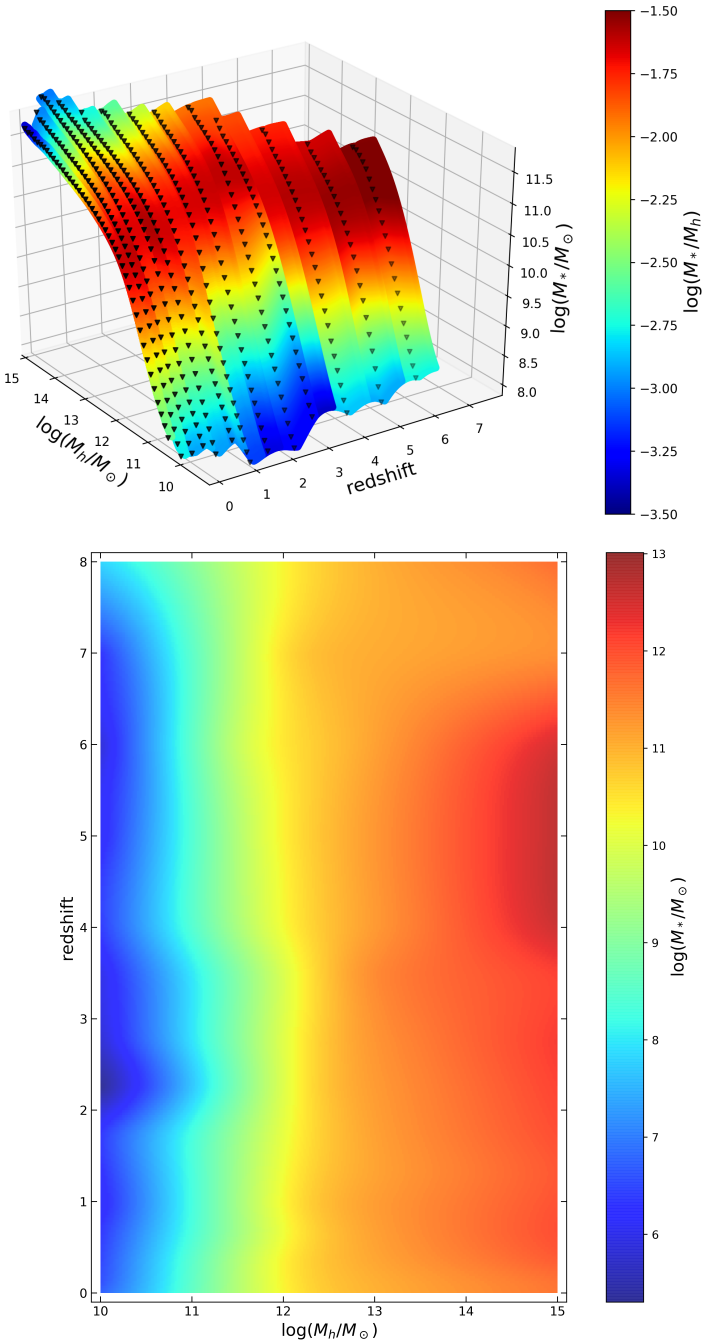

Fig. 3.5 The SHMR derived using the global HMF of the Millennium I+II simulation. In the top panel, the $\log(M_h/M_\odot)$-redshift-$\log(M_*/M_\odot)$ plane is shown, color-coded by $\log(M_*/M_h)$. Points represent the observed relation derived from the CMFs. In the bottom panel, the $\log(M_h/M_\odot)$-redshift plane is shown, color-coded by $\log(M_*/M_\odot)$. The colored layers are a linear interpolation between observed data points and are shown to ease a visual inspection. Therefore, in some cases (e.g. halos of $M_h = 10^{15} M_\odot$ at $z > 5$) the colored layers may not be representative of the true distribution of halos and galaxies, and are reliable only in the range of observed datapoints, shown with points.

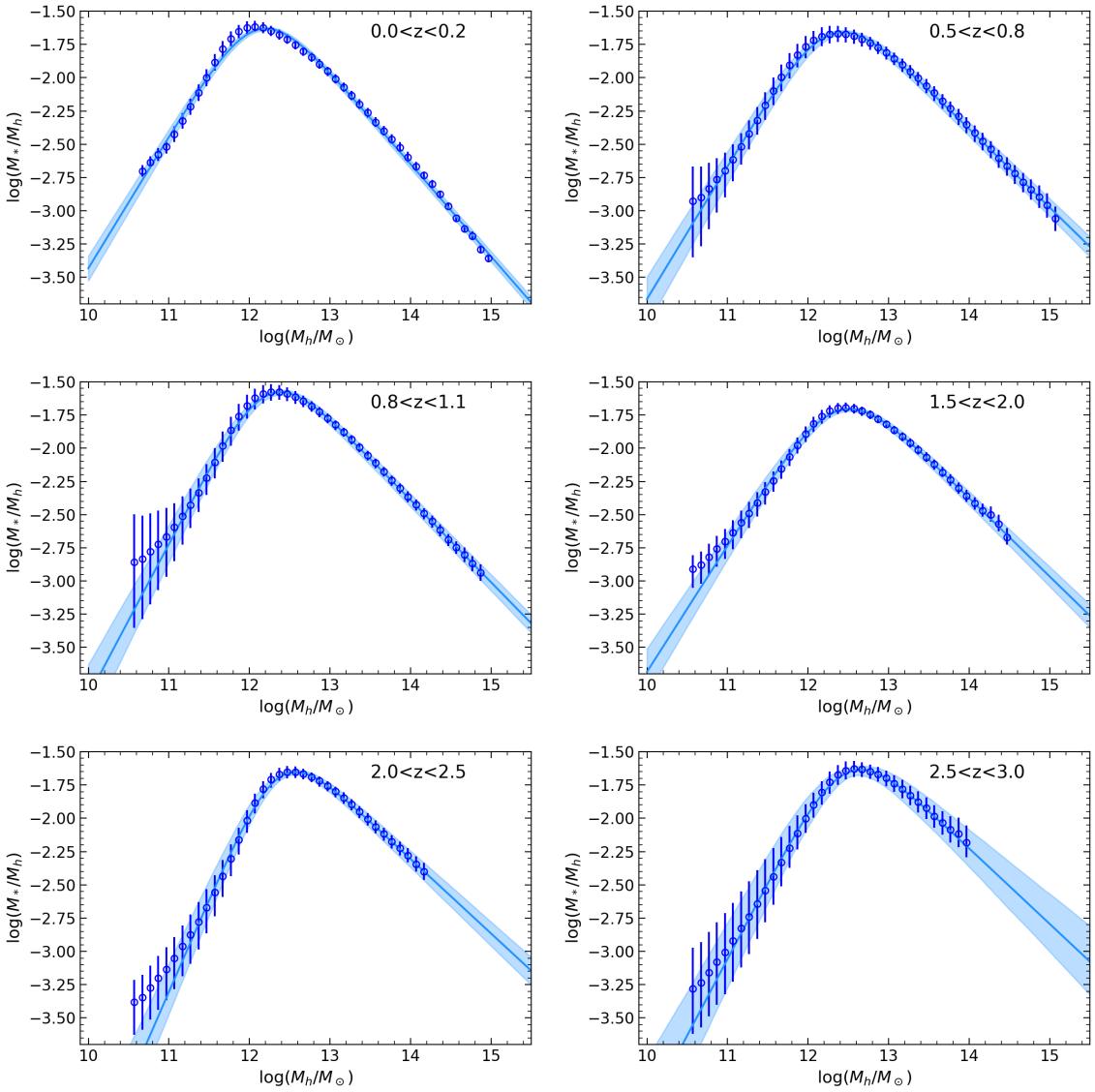

Fig. 3.6 SHMR derived on the Millennium I+II simulation in six different redshift bins: $0.2 < z < 0.5$ (top left), $0.5 < z < 0.8$ (top right), $0.8 < z < 1.1$ (center left), $1.5 < z < 2.0$ (center right), $2.0 < z < 2.5$ (bottom left) and $2.5 < z < 3.0$ (bottom right). In all panels we show blue points the SHMR evaluated on the Millennium I+II simulation, with their relative best-fit model shown with solid lines and shaded areas (representing the 1σ errors of the fit).

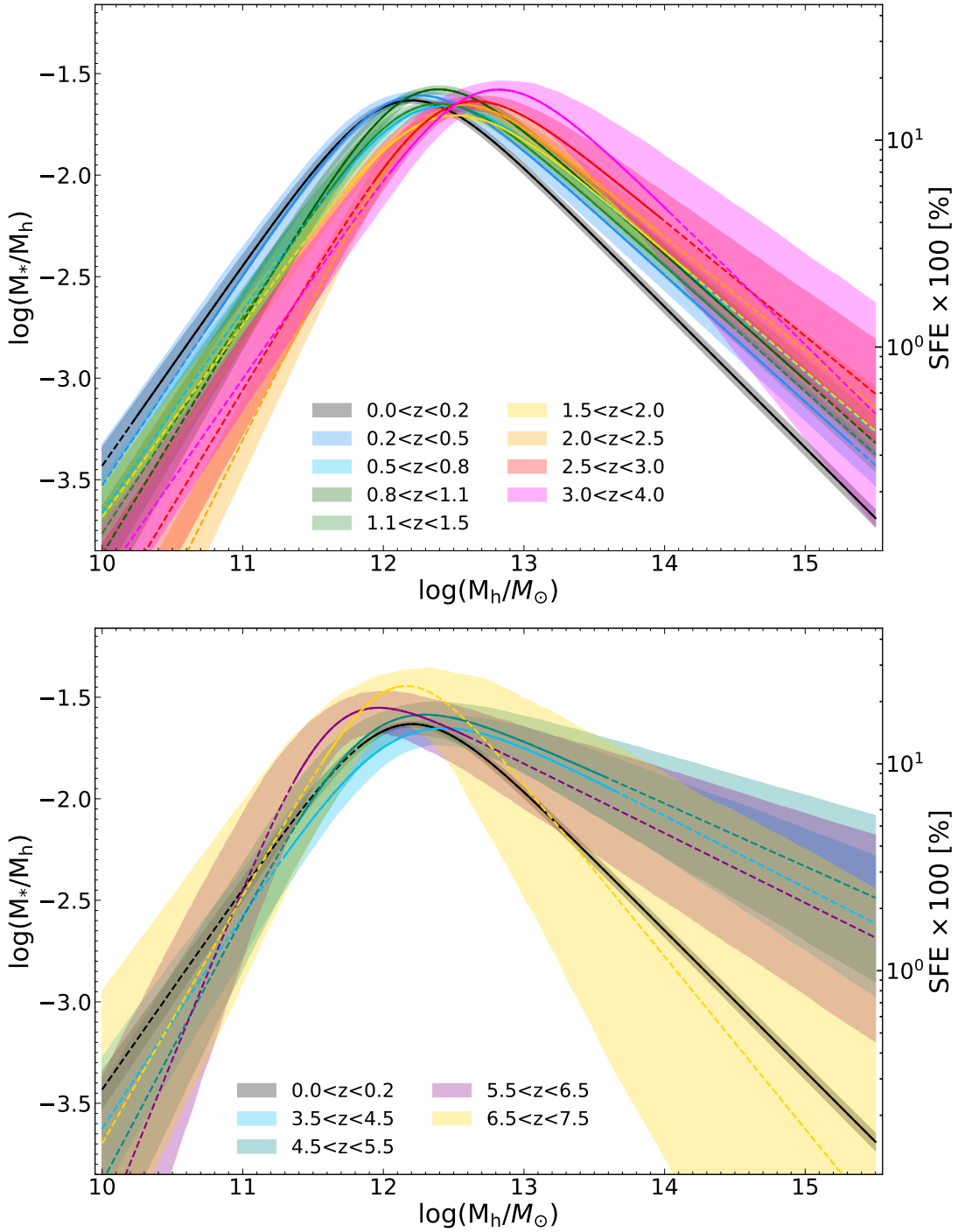

Fig. 3.7 The SHMR for the Millennium I+II case derived in the $\log(M_*/M_h) - \log(M_h/M_\odot)$ plane. Results are divided in two panels according to their redshift range and input SMFs. In top panel we show results for Baldry et al. (2008) and Ilbert et al. (2013) SMFs going from $z = 0$ to $z = 4$. In bottom panel we show results using the Grazian et al. (2015) SMFs from $z = 3.5$ to $z = 7.5$. The solid line identifies the observed mass range of galaxies, and the dashed line represents the extrapolation using the best-fit Schechter function. The right-hand side y-axis is labeled with the SFE expressed in percentage (defined as $M_*/M_h\, f_b^{-1}$).

Table 3.2 Best-fit parameters of the SHMR for the Millennium I+II case in Eq. 2.2 and their 68% confidence interval.

Δz	A	M_A	β	γ
$0.00 \leq z < 0.20$	$0.0275^{+0.0008}_{-0.0008}$	$12.08^{+0.03}_{-0.03}$	$0.97^{+0.04}_{-0.04}$	$0.669^{+0.009}_{-0.009}$
$0.20 \leq z < 0.50$	$0.0286^{+0.0015}_{-0.0016}$	$12.09^{+0.08}_{-0.07}$	$1.03^{+0.09}_{-0.08}$	$0.600^{+0.024}_{-0.022}$
$0.50 \leq z < 0.80$	$0.0251^{+0.0009}_{-0.0010}$	$12.26^{+0.07}_{-0.06}$	$0.98^{+0.09}_{-0.08}$	$0.565^{+0.021}_{-0.020}$
$0.80 \leq z < 1.10$	$0.0299^{+0.0012}_{-0.0013}$	$12.21^{+0.05}_{-0.05}$	$1.13^{+0.12}_{-0.10}$	$0.597^{+0.016}_{-0.016}$
$1.10 \leq z < 1.50$	$0.0257^{+0.0009}_{-0.0009}$	$12.23^{+0.05}_{-0.05}$	$1.04^{+0.11}_{-0.09}$	$0.599^{+0.021}_{-0.021}$
$1.50 \leq z < 2.00$	$0.0227^{+0.0006}_{-0.0007}$	$12.37^{+0.05}_{-0.05}$	$0.92^{+0.07}_{-0.06}$	$0.574^{+0.026}_{-0.024}$
$2.00 \leq z < 2.50$	$0.0240^{+0.0009}_{-0.0009}$	$12.36^{+0.05}_{-0.05}$	$1.37^{+0.14}_{-0.11}$	$0.544^{+0.035}_{-0.033}$
$2.50 \leq z < 3.00$	$0.0260^{+0.0016}_{-0.0017}$	$12.48^{+0.10}_{-0.10}$	$1.11^{+0.16}_{-0.11}$	$0.557^{+0.085}_{-0.076}$
$3.00 \leq z < 4.00$	$0.0308^{+0.0034}_{-0.0040}$	$12.72^{+0.11}_{-0.14}$	$0.96^{+0.09}_{-0.06}$	$0.666^{+0.213}_{-0.195}$
$3.50 \leq z < 4.50$	$0.0230^{+0.0030}_{-0.0035}$	$12.06^{+0.13}_{-0.18}$	$1.03^{+0.18}_{-0.11}$	$0.334^{+0.096}_{-0.100}$
$4.50 \leq z < 5.50$	$0.0253^{+0.0036}_{-0.0042}$	$11.89^{+0.12}_{-0.15}$	$1.28^{+0.23}_{-0.14}$	$0.304^{+0.106}_{-0.102}$
$5.50 \leq z < 6.50$	$0.0265^{+0.0053}_{-0.0056}$	$11.59^{+0.13}_{-0.14}$	$1.74^{+0.58}_{-0.30}$	$0.333^{+0.131}_{-0.128}$
$6.50 \leq z < 7.50$	$0.0424^{+0.0096}_{-0.0114}$	$12.08^{+0.14}_{-0.22}$	$1.17^{+0.39}_{-0.22}$	$0.877^{+0.452}_{-0.469}$

As for the DUSTGRAIN-*pathfinder*+Despali results, also for the Millennium I+II the SHMR is well described by a double power law function with different slopes at low and high mass and a peak at M_A. However, as shown in Fig. 3.7, results at $z < 4$ and at $z > 4$ show opposite trends with redshift while maintaining the same trends with halo masses. This result is due to the differential evolution of the SMF which slows down at late cosmic times (i.e. $z < 4$) in particular for its massive end, while the HMF shows a more continuous evolution. In fact, as for the results on the Despali et al. (2016) case, at $z < 4$ above the characteristic halo mass (denoted M_A), the SHMR increases with increasing redshift, and the trend reverses at lower masses. At $z > 4$, for masses above M_A, the SHMR decreases with increasing redshift while it increases for masses below M_A. We will discuss this "inverting" trend in further detail in Sect. 3.6.

3.1.3 The effect of relative scatter

Up until now we presented and discussed the results when no scatter is applied to the SHMR evaluation. In this section, as discussed in Sect. 2.1.2, we also introduce a *relative* scatter, in order to take into account the different merging histories, spin parameters and concentrations of halos at fixed halo mass. In Fig. 3.8 we show a comparison of the SHMR derived with and without the relative scatter (σ_R) for the DUSTGRAIN-*pathfinder* and Millennium I+II simulations. The points show that the scatter mainly affects the massive end of the SHMR (because it mostly affects the massive-end slope of the SMF) but also more weakly affects the low-mass end. At high halo masses (i.e., $\log(M_h/M_\odot) \gtrsim 13$), the SHMR without scatter predicts higher stellar masses at fixed halo mass. At low halo masses (i.e., $\log(M_h/M_\odot) \lesssim 12$), the tendency is reversed. This effect is due to the fact that we derive the model SMF, deconvolving the observed one and conserving the integrated number densities. For this reason the resulting model SMF, needed to derive the SHMR with relative scatter, has a lower massive

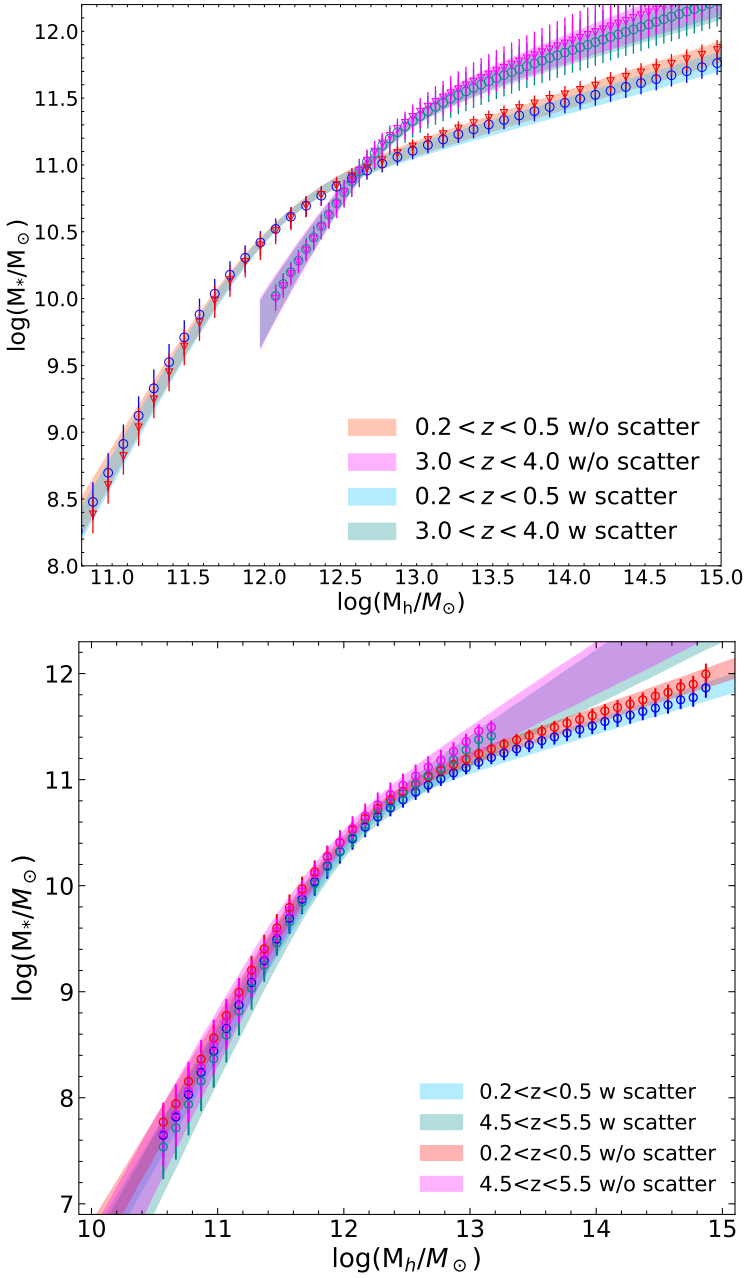

Fig. 3.8 Comparison of the SHMR evaluated with or without the relative scatter ($\sigma_R = 0.2$ dex) in two different redshift bins. In the top panel we show the results for the DUSTGRAIN-*pathfinder* simulation while on the bottom results for the Millennium I+II. For both panels we show the points that represent the direct comparison of the CMFs and the 1σ confidence region of the best-fit using Eq.2.2 with shaded regions.

Table 3.3 Best-fit parameters of the SHMR for the Despali et al. (2016) case with relative scatter with $\sigma_R = 0.2$ dex (representing the DUSTGRAIN-*pathfinder* simulation) in Eq. 2.2 and their 68% confidence interval.

Δz	A	M_A	β	γ
$0.00 \leq z < 0.20$	$0.0494^{+0.0018}_{-0.0019}$	$11.81^{+0.03}_{-0.03}$	$0.94^{+0.04}_{-0.04}$	$0.726^{+0.006}_{-0.006}$
$0.20 \leq z < 0.50$	$0.0429^{+0.0026}_{-0.0026}$	$11.87^{+0.06}_{-0.06}$	$0.99^{+0.08}_{-0.07}$	$0.669^{+0.016}_{-0.015}$
$0.50 \leq z < 0.80$	$0.0348^{+0.0016}_{-0.0015}$	$12.07^{+0.06}_{-0.06}$	$0.86^{+0.09}_{-0.08}$	$0.622^{+0.017}_{-0.015}$
$0.80 \leq z < 1.10$	$0.0429^{+0.0019}_{-0.0018}$	$12.03^{+0.04}_{-0.04}$	$1.04^{+0.11}_{-0.09}$	$0.657^{+0.011}_{-0.011}$
$1.10 \leq z < 1.50$	$0.0325^{+0.0013}_{-0.0013}$	$12.11^{+0.05}_{-0.05}$	$0.87^{+0.13}_{-0.11}$	$0.659^{+0.014}_{-0.013}$
$1.50 \leq z < 2.00$	$0.0285^{+0.0008}_{-0.0007}$	$12.21^{+0.04}_{-0.04}$	$0.94^{+0.12}_{-0.10}$	$0.624^{+0.014}_{-0.013}$
$2.00 \leq z < 2.50$	$0.0297^{+0.0006}_{-0.0006}$	$12.23^{+0.03}_{-0.02}$	$1.31^{+0.12}_{-0.10}$	$0.604^{+0.010}_{-0.009}$
$2.50 \leq z < 3.00$	$0.0294^{+0.0009}_{-0.0009}$	$12.33^{+0.06}_{-0.05}$	$1.13^{+0.19}_{-0.16}$	$0.583^{+0.023}_{-0.020}$
$3.00 \leq z < 4.00$	$0.0330^{+0.0018}_{-0.0018}$	$12.55^{+0.10}_{-0.09}$	$1.05^{+0.21}_{-0.17}$	$0.626^{+0.045}_{-0.038}$

Table 3.4 Best-fit parameters of the SHMR for the Millennium I+II case with relative scatter ($\sigma_R = 0.2$ dex) in Eq. 2.2 and their 68% confidence interval.

Δz	A	M_A	β	γ
$0.00 \leq z < 0.20$	$0.0229^{+0.0007}_{-0.0006}$	$12.11^{+0.03}_{-0.03}$	$0.99^{+0.04}_{-0.04}$	$0.694^{+0.009}_{-0.009}$
$0.20 \leq z < 0.50$	$0.0239^{+0.0012}_{-0.0013}$	$12.12^{+0.08}_{-0.07}$	$1.03^{+0.09}_{-0.08}$	$0.625^{+0.024}_{-0.022}$
$0.50 \leq z < 0.80$	$0.0211^{+0.0008}_{-0.0008}$	$12.28^{+0.06}_{-0.06}$	$1.00^{+0.08}_{-0.07}$	$0.590^{+0.021}_{-0.019}$
$0.80 \leq z < 1.10$	$0.0252^{+0.0010}_{-0.0011}$	$12.23^{+0.05}_{-0.05}$	$1.14^{+0.11}_{-0.10}$	$0.620^{+0.017}_{-0.016}$
$1.10 \leq z < 1.50$	$0.0216^{+0.0007}_{-0.0008}$	$12.25^{+0.05}_{-0.05}$	$1.06^{+0.10}_{-0.08}$	$0.619^{+0.022}_{-0.021}$
$1.50 \leq z < 2.00$	$0.0191^{+0.0005}_{-0.0005}$	$12.38^{+0.05}_{-0.05}$	$0.95^{+0.07}_{-0.06}$	$0.591^{+0.024}_{-0.023}$
$2.00 \leq z < 2.50$	$0.0202^{+0.0007}_{-0.0007}$	$12.37^{+0.05}_{-0.05}$	$1.39^{+0.14}_{-0.11}$	$0.560^{+0.034}_{-0.032}$
$2.50 \leq z < 3.00$	$0.0218^{+0.0013}_{-0.0014}$	$12.47^{+0.10}_{-0.09}$	$1.14^{+0.16}_{-0.12}$	$0.567^{+0.085}_{-0.076}$
$3.00 \leq z < 4.00$	$0.0259^{+0.0028}_{-0.0032}$	$12.71^{+0.10}_{-0.13}$	$0.99^{+0.09}_{-0.06}$	$0.679^{+0.203}_{-0.189}$
$3.50 \leq z < 4.50$	$0.0195^{+0.0024}_{-0.0029}$	$12.09^{+0.12}_{-0.16}$	$1.05^{+0.16}_{-0.10}$	$0.354^{+0.096}_{-0.099}$
$4.50 \leq z < 5.50$	$0.0211^{+0.0031}_{-0.0037}$	$11.91^{+0.12}_{-0.15}$	$1.31^{+0.24}_{-0.15}$	$0.310^{+0.111}_{-0.111}$
$5.50 \leq z < 6.50$	$0.0220^{+0.0043}_{-0.0047}$	$11.62^{+0.13}_{-0.15}$	$1.70^{+0.52}_{-0.28}$	$0.343^{+0.130}_{-0.132}$
$6.50 \leq z < 7.50$	$0.0353^{+0.0079}_{-0.0095}$	$12.08^{+0.15}_{-0.22}$	$1.22^{+0.42}_{-0.23}$	$0.849^{+0.466}_{-0.441}$

end and higher low-end. As in the case without scatter, we performed a fit using Eq.2.2 and list the results in Table 3.3 for the DUSTGRAIN-*pathfinder* simulation and Table 3.4 for the Millennium I+II simulation. We report in Appendix A.2 and A.4 the best-fit plots along with their corresponding posterior distributions. In Fig. 3.8 we also show the 1σ confidence regions. The introduction of a relative scatter mainly affects the parameter γ, which controls the massive end slope but also influences all other parameters because they are all correlated. We note that the effect of the scatter is always on the order of a few percent of the SHMR, even if its effect is systematic and depends on the exact value of the scatter introduced. Qualitative results are, therefore, preserved when the *relative* scatter is included, while differences quantitatively depends on the standard deviation adopted to draw the *relative* scatter.

As already said, the aim of this thesis is to build mock catalogs for future surveys which reproduce the observed Universe. Since we expect that in nature two halos of the same mass may host galaxies with different stellar masses, in the following of this work, all the results will be presented for the case with *relative* scatter with $\sigma_R = 0.2$ dex without explicitly mention it.

3.1.4 Comparison of DUSTGRAIN-*pathfinder* and Millennium I+II SHMR

Figure 3.9 shows the results for both our cases (i.e. the Despali et al. (2016) and Millennium I+II) in several redshift bins, where the differences between the SHMR evaluated using the Despali et al. (2016) HMF and the global HMF from the Millennium I+II simulation are evident. The Despali et al. (2016) and Millennium I+II cases are in agreement for $\log(M_h/M_\odot) \gtrsim 12.5$, meaning that the Despali et al. (2016) HMF is a good approximation only for halo masses $\log(M_h/M_\odot) \gtrsim 12.5$, while for lower halo masses it isn't anymore. This is reasonable given that the Despali et al. (2016) HMF has been calibrated on main halos only, and, therefore, when the contribution of subhalos becomes important, it cannot be a good representation of the (sub)HMF anymore. Many studies have explored the total influence of subhalos on the HMF (e.g. Despali & Vegetti 2017, Rodríguez-Puebla et al. 2017) and found that at high halo masses the fraction of subhalos with respect to main halos is small. Their contribution to the total number of halos reaches $\sim 10\%$ at $\log(M_h/M_\odot) = 12.5$ and $z = 0$, decreasing with increasing halo mass or redshift, which is consistent to what we find for both our cases (see histograms in Figs. 2.8 and 2.10). This is also evident in Fig. 2.12 where we show the Despali et al. (2016) HMF along with the global HMF of the Millennium I+II simulation, and, it is evident that the two HMFs start to differ significantly starting from $\log(M_h/M_\odot) \sim 12.5$ where the contribution of subhalos steepens the HMF. Therefore, it is reasonable that the SHMR for our two cases are fully consistent down to halo masses $\log(M_h/M_\odot) = 12.5$, while they start to differ below this treshold.

In the following of this chapter we will present the results for the Millennium I+II simulation only (with some exceptions that will be explicitly explained), keeping in mind that at high halo masses (i.e. $\log(M_h/M_\odot) \gtrsim 12.5$) the same results apply to the DUSTGRAIN simulation as well.

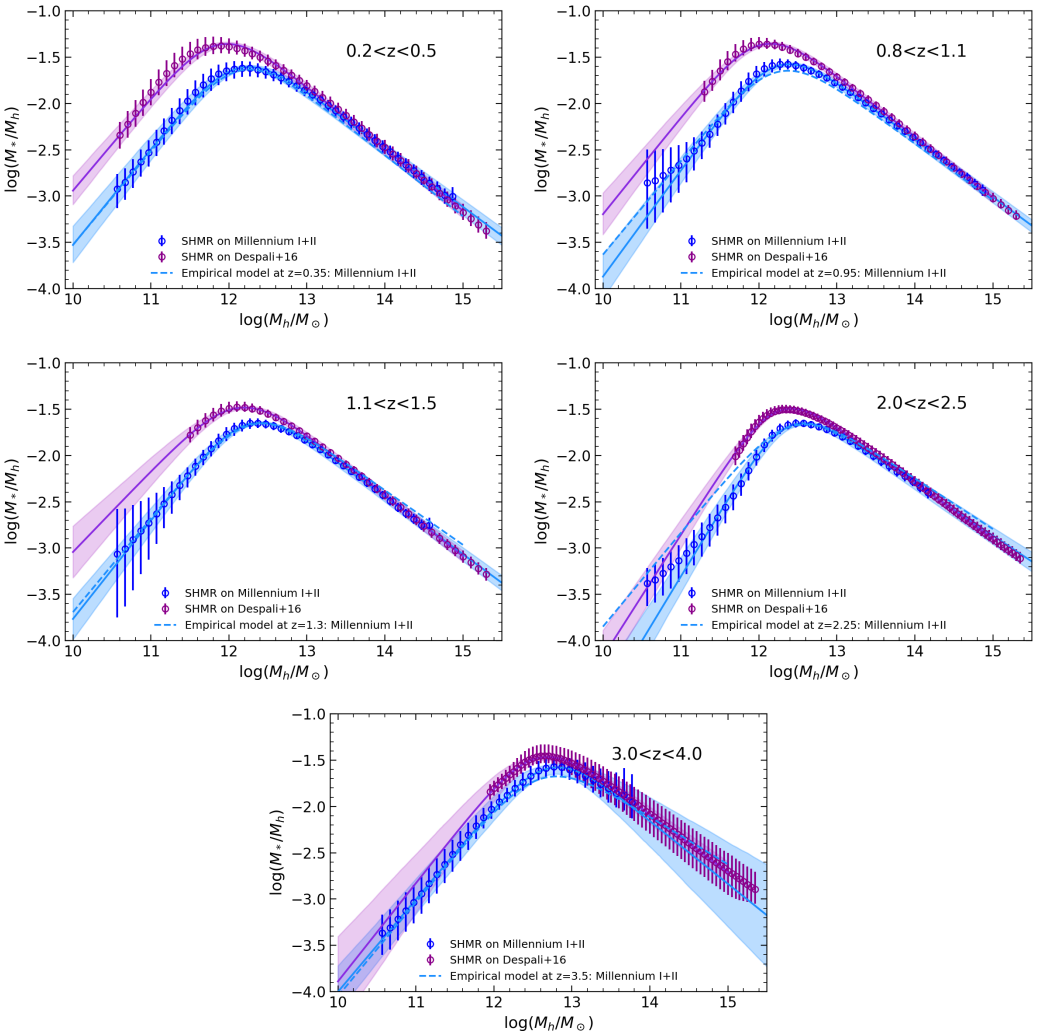

Fig. 3.9 SHMR derived on the Despali et al. (2016) HMF (representing the DUSTGRAIN-*pathfinder* simulation) and Millennium I+II simulation with empirical models in six different redshift bins: $0.2 < z < 0.5$ (top left), $0.8 < z < 1.1$ (top right), $1.1 < z < 1.5$ (center left), $2.0 < z < 2.5$ (center right)and $3.0 < z < 4.0$ (bottom). In all panels we show with violet and blue points the SHMR evaluated on the DUSTGRAIN-*pathfinder* and Millennium I+II simulations, respectively, with their relative best-fit model shown with solid lines and shaded areas (representing the 1σ errors of the fit). In addition, with blue dashed lines we show the empirical best-fit model evaluated at the intermediate redshift of the bin.

3.2 Building the empirical model

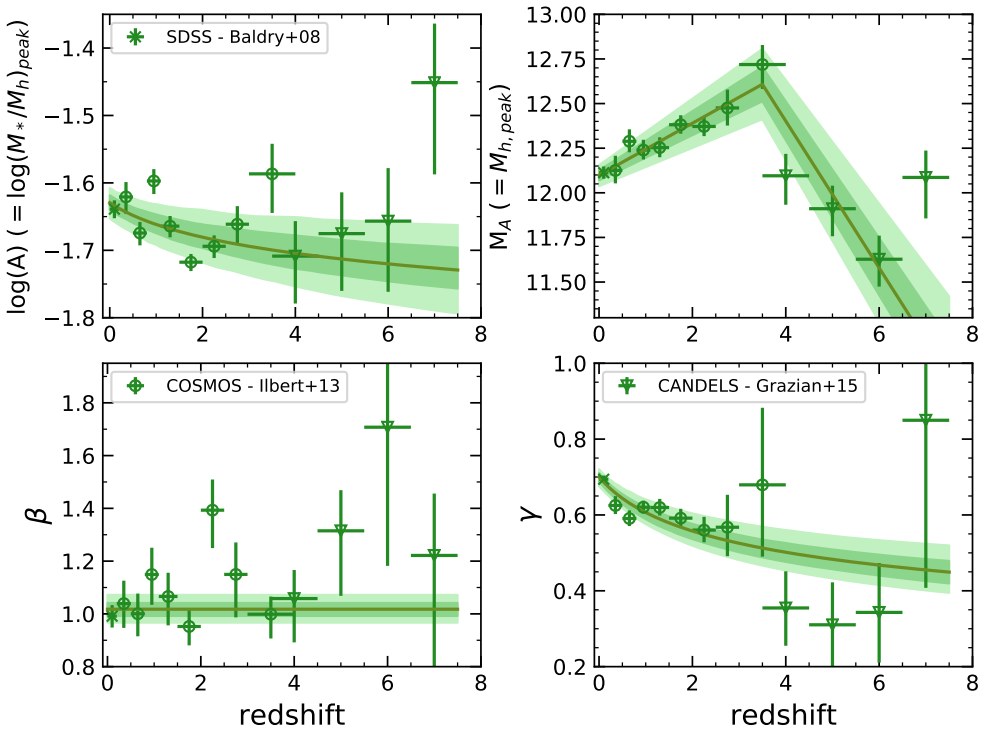

Fig. 3.10 Evolution of the parameters M_A, A, γ, and β shown with stars, circles and triangles for the Baldry et al. (2008), Ilbert et al. (2013) and Grazian et al. (2015) data, respectively. We also show the empirical best-fit models and the 1σ uncertainties (shown with solid lines and shaded areas, respectively) in green.

In this section, we define a redshift dependence of the SHMR parameterization in order to construct an empirical model that describes its evolution with cosmic time. Studying the evolution of the SHMR helps to place constraints on the processes involved in galaxy formation and evolution. Furthermore, with this information, we can define an empirical model that can be used to populate the N-body simulation lightcones (or boxes) with galaxies at different redshifts using the appropriate redshift-dependent SHMR. In Fig. 3.10 we show the evolution of the parameters of the fit M_A, A, γ, and β in the different redshift bins for the Millennium I+II case with *relative* scatter (also listed in Table 3.4). We chose the following redshift dependences for the parameters of Eq. 2.2 and perform a fit in order to evaluate the empirical model:

$$\log M_A(z) = \begin{cases} (\log M_A)_{z=0} + z\cdot\mu_1 = B_1 + z\cdot\mu_1 & \text{if } z \leq 3.5 \\ (\log M_A)_{z=3.5} - z\cdot\mu_2 = B_2 - z\cdot\mu_2 & \text{if } z > 3.5 \end{cases}, \tag{3.1}$$

$$A(z) = \left(\frac{M_*}{M_h}\right)_{z=0} \cdot (1+z)^{\nu} = C\cdot(1+z)^{\nu}, \tag{3.2}$$

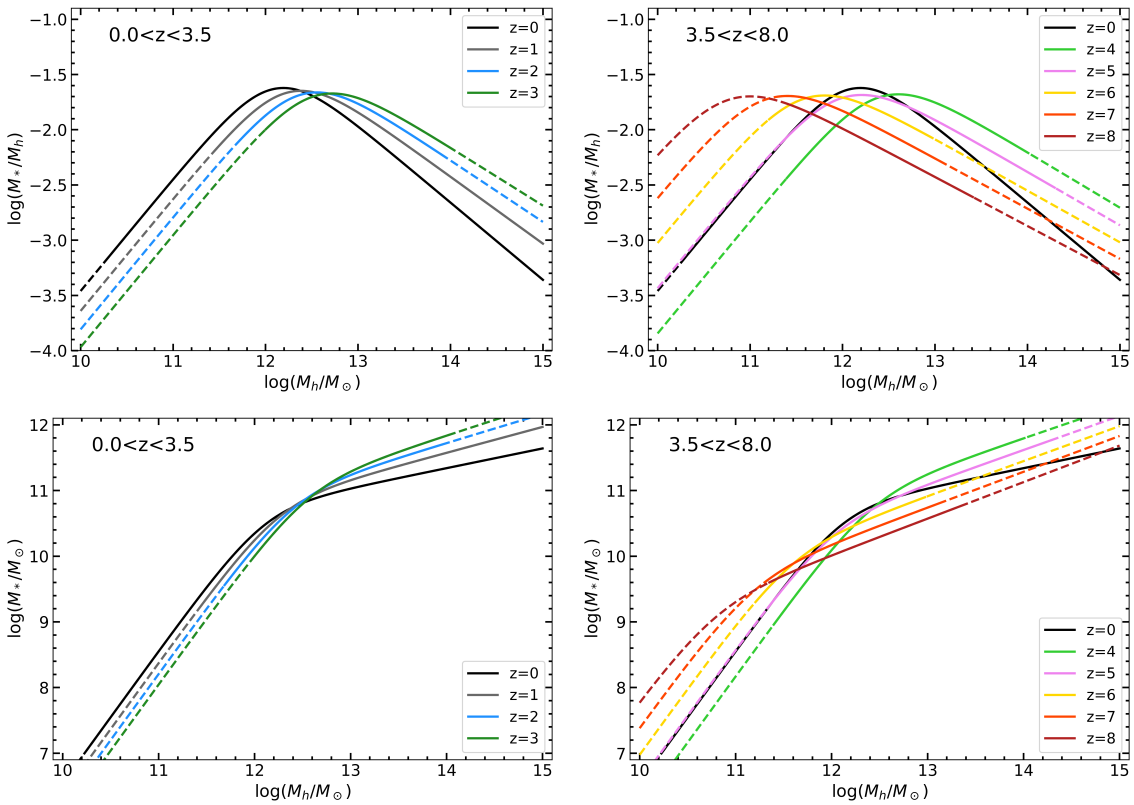

Fig. 3.11 The empirical model derived from the Millennium I+II case shown in the $\log(M_*/M_h) - \log(M_h/M_\odot)$ plane (top panels) and in the $\log(M_*/M_\odot) - \log(M_h/M_\odot)$ plane (bottom panels) at different redshifts. In left panels we show results of the empirical model up to $z = 3.5$ (i.e. up to the changing slope for M_A) at some fixed redshifts. In the right panels we show the empirical model at $z > 3.5$ at some redshifts.

$$\gamma(z) = \gamma_0 \cdot (1+z)^\eta = D \cdot (1+z)^\eta \,, \tag{3.3}$$

$$\beta(z) = F \,. \tag{3.4}$$

We report in Table 3.5 the best-fit parameters and their 1σ errors and show the best-fit results (along with their 1 and 2σ errors) in Fig. 3.10. The last redshift bin (i.e. $6.5 < z < 7.5$) has not been considered for the fit of the empirical model because, as shown in Fig. A.40, the points derived from the direct comparison of the CMFs barely reach M_A, and, therefore, the estimate of γ (and partially those of M_A, A) is not reliable for this redshift bin (as also evident from their large error bars in Fig. 3.10).

We note that above the characteristic halo mass M_A, the SHMR slope (γ) shows a decreasing trend with increasing redshift. Conversely, for masses below M_A, we find a constant trend of the SHMR slope (β). For the normalization $A = (M_*/M_h)_{\rm peak}$, we find a decreasing trend with increasing redshift

Table 3.5 Best-fit parameters of the SHMR evolution evaluated on the Millennium I+II simulation with relative scatter ($\sigma_R = 0.2$ dex) in Eqs. 3.1, 3.2, 3.3, and 3.4, and their 68% confidence interval.

	B_1	μ_1	B_2	μ_2	C	ν	D	η	F
Best fit	12.09	0.15	12.61	-0.42	0.02	-0.11	0.70	-0.21	1.01
$1\sigma^+$	0.03	0.02	0.06	0.03	0.01	0.03	0.01	0.02	0.02
$1\sigma^-$	0.03	0.02	0.06	0.03	0.01	0.03	0.01	0.03	0.02

from $z = 0$ to $z = 8$. We also find that M_A, which is the mass where the SHMR peaks ($M_A = M_{h,\mathrm{peak}}$), increases with increasing redshift up to $z = 4$. Starting from $z \sim 3.5 - 4$ we find a decreasing trend of M_A with increasing redshift. This can be due to the large uncertainties in the SHMR evaluation at these redshifts, as discussed in the previous section. We fixed at $z = 3.5$ the transition of M_A from an increasing to a decreasing trend with redshift and therefore the value and uncertainties of the parameter B_2 directly derive from the fit of the $z < 4$ datapoints. We report in Appendix B, the posterior distributions of the fit of the empirical model.

In addition, Fig. 3.10 shows that the empirical models predict an evolution of the parameters with redshift that smoothes out all features characteristic of the field on which the input SMFs have been evaluated, such as the well-known overdensity in the COSMOS field located at $z \sim 0.7$ (e.g., McCracken et al. 2015). This overdensity shifts the high-mass end of the SMF to higher stellar masses and therefore shifts the parameter M_A of the best fit to higher values (and, consequently, γ to lower values).

We show in Fig. 3.11 the empirical model, that links the halo mass to the ratio between stellar mass and halo mass (top panels) and to the stellar mass (bottom panles) at various redshifts. In addition, in Fig. 3.9, we show the empirical model in different redshift bins (calculated at the mean redshift of each bin) along with the points of the direct comparison of the CMFs and their fit. It is evident from Fig. 3.9 that the empirical model predicts remarkably well the observed SHMR, and should, in principle, reproduce equally well the input observed SMFs when applied to dark matter simulations. We will explore this aspect later on in this thesis.

3.3 Comparison with literature

In Fig. 3.12 we show a comparison of our best-fit SHMR for the Millennium I+II simulation with several literature results at $z \sim 0$, a comparison at $z \sim 1$ and $z \sim 3$ is shown in Fig. 3.13 and a comparison at $z \sim 5$ and $z \sim 7$ is shown in Fig. 3.14. Up to $z \sim 3$, we also show, as a reference, our results on the DUSTGRAIN-*pathfinder*+Despali et al. (2016) case, even though, as we already discussed above, the SHMR evaluated in this case is reliable only at $\log(M_h/M_\odot) \gtrsim 12.5$, but only for main halos above this limit. We want to highlight here that we adopted the estimates derived from COSMOS for the SMF, which is the largest field observed so far with a continuous and homogeneous coverage in redshift from $z = 0.2$ to $z = 4$. This field also has one of the best statistical accuracies in photometric redshifts, stellar masses, and SMFs determination for such a wide redshift range.

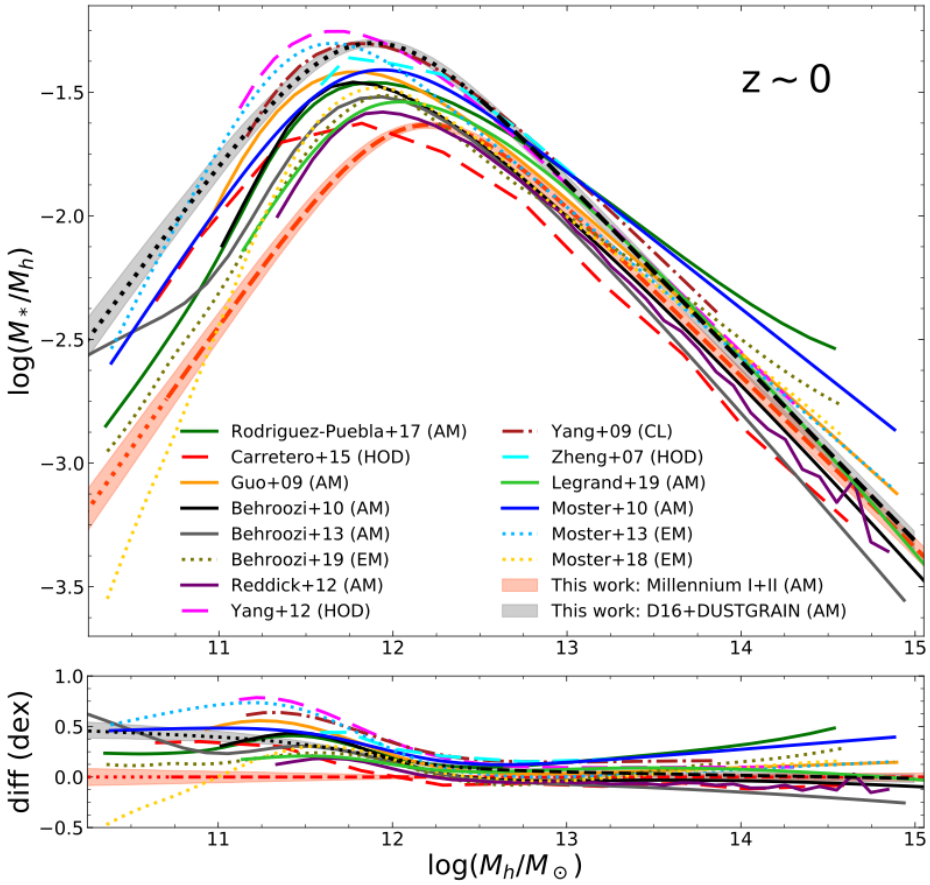

Fig. 3.12 SHMR derived on the Millennium I+II simulation compared to literature at $z \sim 0$. We show the Millennium I+II results in orange dashed lines (with shaded areas representing the 1σ errors) and their extrapolation to higher/lower masses, with the best-fit, with an orange dotted line. For completeness, also results on the DUSTGRAIN-*pathfinder* simulation are shown in dashed black line and its extrapolation using the Despali et al. (2016) HMF in dotted black line. The comparison includes results from abundance matching (AM; Behroozi et al. 2010, 2013; Legrand et al. 2019; Moster et al. 2010; Rodríguez-Puebla et al. 2017, empirical modeling (EM; Behroozi et al. 2019; Moster et al. 2018, 2010), halo occupation distributions (HOD; Carretero et al. 2015; Yang et al. 2012; Zheng et al. 2007) and clusters selected from SDSS spectroscopic data (CL;Yang et al. 2009). In the bottom panel we show the logarithmic difference between our results and the other literature works centred on the Millennium I+II results. The shaded areas represents our 1σ errors.

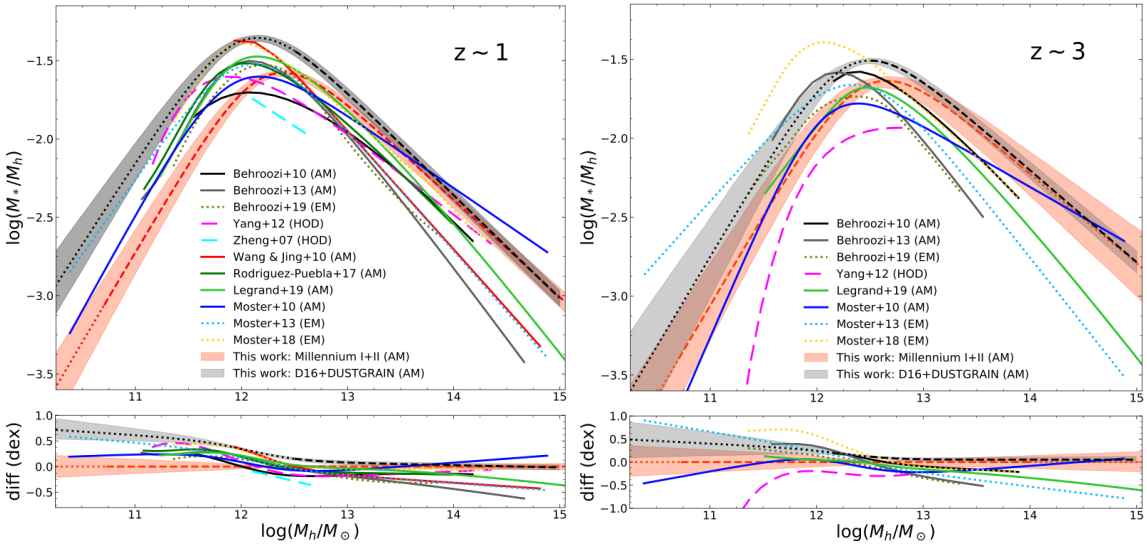

Fig. 3.13 SHMR derived on Millennium I+II simulation compared to literature at $z \sim 1$ (left) and $z \sim 3$ (right). We show the Millennium I+II results in orange dashed lines (with shaded areas representing the 1σ errors) and their extrapolation to higher/lower masses, with the best-fit, with an orange dotted line. For completeness, also results on the DUSTGRAIN-*pathfinder* simulation are shown in dashed black line and its extrapolation using the Despali et al. (2016) HMF in dotted black line. Other symbols are the same as Fig. 3.12.

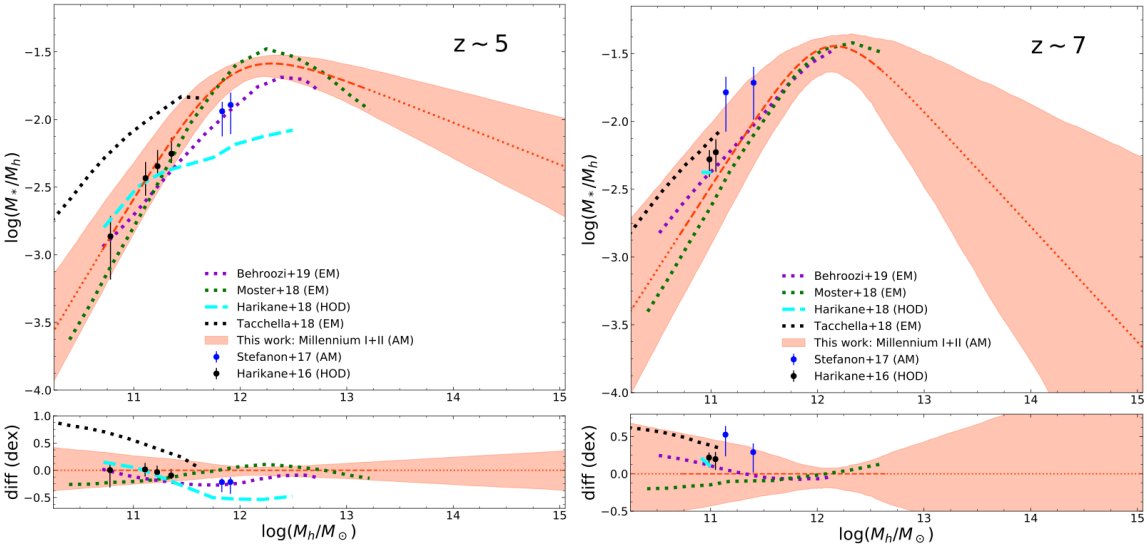

Fig. 3.14 SHMR derived on Millennium I+II simulation compared to literature at $z \sim 5$ (left) and $z \sim 7$ (right). We show the Millennium I+II results in orange dashed lines (with shaded areas representing the 1σ errors) and their extrapolation to higher/lower masses, with the best-fit, with an orange dotted line. We also show with dotted lines results from EM (Behroozi et al. 2019; Moster et al. 2018; Tacchella et al. 2018), with dashed lines results from HODs (Harikane et al., 2018) and with points various results from AM and HODs (Harikane et al., 2016; Stefanon et al., 2017).

Our results are shown along with their corresponding 1σ errors of the fit at the redshifts indicated in the plots. More precisely, for $z \sim 0$ we used results in the bin $0.0 < z < 0.2$, for $z \sim 1$ and $z \sim 3$ we show the results in the bins $0.8 < z < 1.1$ and $2.5 < z < 3.0$, respectively, and, for $z \sim 5$ and $z \sim 7$ we plot the best-fits in the redshift bins $4.5 < z < 5.5$ and $6.5 < z < 7.5$, respectively.

Performing a comparison with other works is not always straightforward because different papers used different dark matter simulations (or theoretical parametrizations of the HMF) and have often made different assumptions on the cosmological model, on the definition of halo mass, on the measurement of stellar mass or on the *relative* scatter adopted[1]. Corrections for differences in the underlying cosmology have been applied by Behroozi et al. (2010) using the process detailed in their Appendix A. The assumptions used to derive stellar masses have not been adjusted instead because such adjustments can be complex and difficult to apply using simple conversions. We only converted the IMF of all stellar masses into that of the Chabrier (2003) and Bruzual & Charlot (2003) stellar population synthesis model. Additionally, we converted all quoted halo masses to M_{200} masses, as defined in Sections 2.3.1 and 2.3.2, by assuming a Navarro et al. (1997) profile (NFW) and by calculating the correction between our halo mass definition and the mass definitions used in other works. For the sake of clarity, we do not show errors of other literature works in the figures, but they can be found in Behroozi et al. (2010), and, depending on the study and its assumptions, they are of the same order of our errors (e.g. Moster et al. 2013, 2010) or larger (up to a factor of ~ 2.5, especially for those taking into account many free parameters, e.g. Behroozi et al. 2010, 2013). We present a detailed description of all literature results we show, and how they compare to our results in Appendix C.

In general, we find a large spread among all literature studies that increases with increasing redshift. Most of the cited works show some differences with respect to our results at all redshifts. We point out here that, given that it is much harder to directly measure the SHMR at $z > 0$, at progressively higher redshifts, published results become less and less numerous.

At $z = 0$ our results agree (within 0.3 dex with two cases reaching differences of 0.5 dex) with most of the literature, within the dispersion, at high halo masses (i.e. $\log(M_h/M_\odot) \gtrsim 13$), while differences can become larger than 0.7 dex (a factor ~ 5) at low and intermediate halo masses ($\log(M_h/M_\odot) < 12.5$). We also note that at $\log(M_h/M_\odot) < 12.5$ our results are among the lowest ones in M_*/M_h scale.

At redshifts $z \sim 1$ and $z \sim 3$, the dispersion between different works increases, even though at intermediate halo masses (i.e. $\log(M_h/M_\odot) \sim 12.5$) the dispersion between different results is small ($\lesssim 0.2$ dex). In the other mass ranges, differences are almost always, but with some exceptions, higher than 0.3 dex in most of the halo mass range. At $z = 3$ most of the works do not agree with each other, even up to ~ 1 dex.

[1]Most of the other literature data were kindly provided by Peter Behroozi and are also shown in several other papers (e.g., Behroozi et al. 2019, 2010, 2013). We also made extensive use of the semiautomated tool *WebPlotDigitalizer* to extract datapoints from literature plots.

At redshifts $z \sim 5$ and $z \sim 7$, the errors of our relation become large and therefore it is difficult to perform a detailed comparison. In general, it seems that all literature results at these redshifts agree well one between the other and especially with our results (within the errors), with the exception of the Tacchella et al. (2018) EM that shows differences with our results as large as ~ 1 dex at low halo masses at $z \sim 5$. This large difference cannot be ascribed to the different *relative* scatter introduced in the SHMR, since Tacchella et al. (2018) used a similar scatter to the one used in this work (see Appendix C).

We also point out that our results on the DUSTGRAIN-*pathfinder*+Despali et al. (2016) case are, in general, among the highest (in $\log(M_*/M_h)$ scale) in the literature. This is reasonable since, as we mentioned many times above, the Despali et al. (2016) HMF is calibrated on main halos only, resulting in a less steep HMF that reflects in a higher SHMR normalization with respect to a simulation where all halos and subhalos are considered. We also note that, at $z \sim 0$, the results by Yang et al. (2009), calibrated on cluster and groups of the SDSS survey, are in agreement with our Despali et al. (2016) results down to $\log(M_h/M_\odot) \sim 11$. This is again reasonable, if we naively assume that main halos correspond to galaxy clusters (and groups) central galaxies and, therefore, when performing an abundance matching we assign all stellar mass of a cluster to the central galaxy, and, consequently, the SHMR we evaluate holds for clusters (and groups) central galaxies.

It is evident that there are still discrepancies between different works in literature, and this is particularly true at higher redshifts. Part of these differences are due to the different methods and modelling that were used and can not be quantified. A part can also be ascribed to the SMFs (or luminosity functions) that were adopted to derive the relation. In addition, with dark matter simulations, the most critical issues remain subhalo finding algorithms. The fact that different works adopt different dark matter simulations, that have different resolutions, inevitably leads to differences in the halo, and subhalo, masses that algorithms can detect. As shown in several works (e.g. Behroozi et al. 2015; Knebe et al. 2011; Onions et al. 2012), different halo finder algorithms may obtain halo masses that are different by up to 10% at $z \sim 0$, and this difference increases with increasing redshift.

Furthermore, as also discussed in Sect. 2.1.2, different works adopt different prescriptions for the *relative* scatter that is introduced in the relation. This inevitably leads to differences (even if small, as seen in Sect. 3.1.3) in the SHMR evaluation.

Finally, another open issue is the effect of baryons on the calculus of the SHMR (e.g. see Nadler et al. 2017). In fact, a recent results on the Illustris simulation (Chua et al., 2017) found that baryonic physics can impact the subhalos infall masses leading to a suppression of low mass subhalos ($\log(M_h/M_\odot) \lesssim 10$) and making the HMF more shallow as a function of subhalo mass. However, in this work we focus on halos and subhalos with $\log(M_h/M_\odot) > 10.2$ and therefore, we can ignore these effects for our study. Other works (e.g. Abadi et al. 2010) have studied the effect of baryons on the halo potential wells finding that low mass galaxies make the potentials less triaxial. However, these results are limited to low mass halos ($\log(M_h/M_\odot) \lesssim 12$) and it is difficult to precisely determine the impact on the galaxies themselves, and therefore, we ignore this possible effect.

3.4 Comparison with semi-analytic models

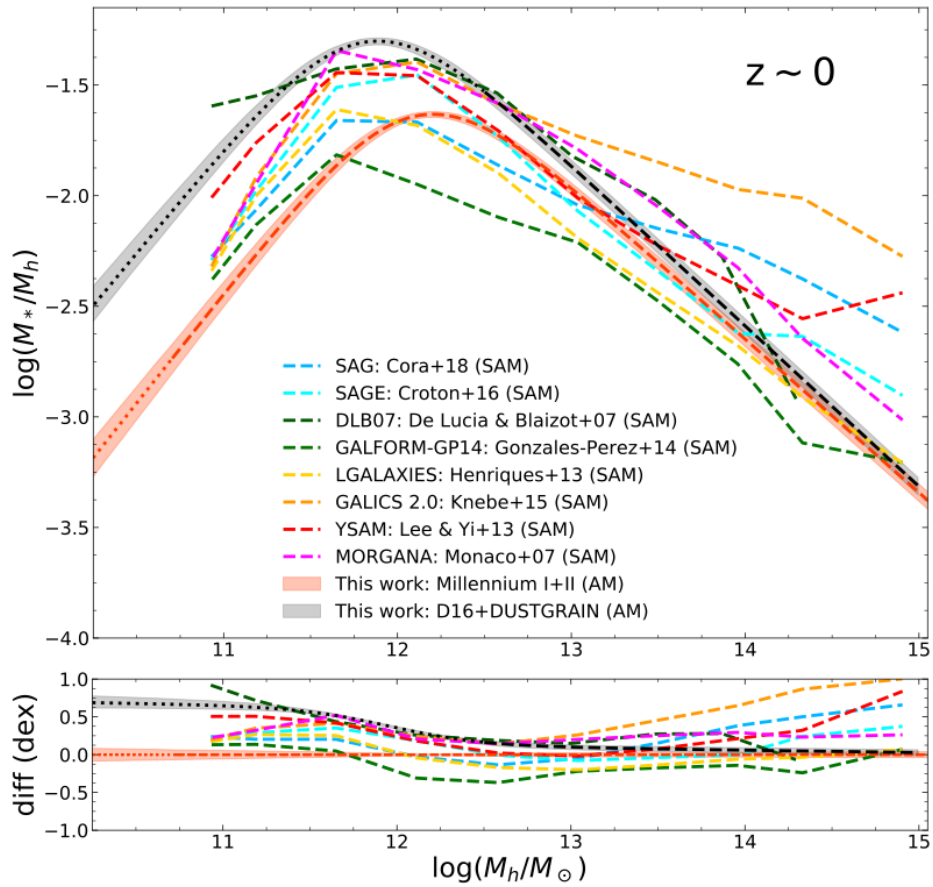

Fig. 3.15 SHMR derived on Millennium I+II simulation compared to SAMs of the COSMIC CARNage project at $z \sim 0$. We show our results in dashed orange lines, its 1σ errors with orange shaded areas and their extrapolation to higher/lower masses, with the best-fit, with an orange dotted line. For completeness, also results on the DUSTGRAIN-*pathfinder* simulation are shown in dashed black line and its extrapolation using the Despali et al. (2016) HMF in dotted black line.

In Fig. 3.15 we compare our best-fit result at $z \sim 0$ to the results of eight SAMs of galaxy formation and evolution. These SAMs were run on the same underlying CDM simulation (cosmological box of comoving width $125\,h^{-1}$ Mpc) and the same merger trees within the Cosmic CARNage project (Asquith et al., 2018; Knebe et al., 2018). The SAMs are *SAG* by Cora et al. (2019, 2018), *SAGE* by Croton et al. (2016), *DLB07* by De Lucia & Blaizot (2007), *GALFORM-GP14* by Gonzalez-Perez et al. (2014), *LGALAXIES* by Henriques et al. (2015, 2013, 2017), *GALICS 2.0* by Knebe et al. (2015), *YSAM* by Lee & Yi (2013), and *MORGANA* by Monaco et al. (2007). The galaxy formation models used in the project are described in Knebe et al. (2018, 2015), where all of them are summarized in a concise and unified manner, along with their main features and differences. However, it is worth mentioning that all models have been calibrated with SMFs at $z = 0$ (Baldry et al., 2012, 2008; Li

& White, 2009), SMFs at $z = 2$ (Domínguez Sánchez et al., 2011; Ilbert et al., 2013; Muzzin et al., 2013; Tomczak et al., 2014), star formation rate function at $z = 0.15$ by Gruppioni et al. (2015), cold gas mass fraction at $z = 0$ evaluated by Boselli et al. (2014), and the relation of black hole to bulge mass (Kormendy & Ho, 2013; McConnell & Ma, 2013). In order to further align the various galaxy formation models, they have all assumed a Chabrier IMF, a metallicity yield of 0.02, and a recycled fraction of 0.43. Moreover, a *Planck* cosmology was used, and the halo mass was defined as M_{200}, as in this work. In addition, the stellar masses are convolved with a $0.08(1+z)$ dex scatter to account for at least part of the observational errors in measuring stellar masses. Results from the Cosmic CARNage simulations therefore do not require any rescaling of the properties in order to allow a comparison with our results. All the considered semi-analytic galaxy formation models populate the dark matter halos with galaxies whose properties depend on the details of the formation history of the halo in which they are placed. Subsequent galaxy evolution then shapes the galaxy SMF and therefore the SHMR. Figure 3.15 shows that the scatter at $z \sim 0$ is already large between the SHMR of different SAMs, and this is particularly evident in the position of the peak of the relation. We investigate this in more detail in the following section. From the comparison, we find that none of the eight models reproduces the observed SHMR we propose at $z = 0$ at every mass. The large differences between our result and the SAMs (which at maximum is up to a factor of ~ 10 in (M_*/M_h) at $\log(M_h/M_\odot) = 15.0$ when our results are compared to *GALICS 2.0*) reflect the intrinsic difficulty of treating the physical processes related to galaxy formation and evolution.

3.5 Evolution of the SHMR

In Fig. 3.16 we show the evolution of the SHMR as a function of redshift at several fixed halo masses (from $\log(M_h/M_\odot) = 10$ to $\log(M_h/M_\odot) = 15$) according to the empirical model we evaluated in Sect. 3.2. We note that for halo masses $\log(M_{h\odot}) < 12.5$ the SHMR decreases a a function of redshift from $z = 0$ up to $z = 3.5$ where it switches trend. For masses $\log(M_{h\odot}) > 12.5$ the trend is reversed: the SHMR decreases as a function of redshift from $z = 0$ to $z = 3.5$ where it starts to increase with decreasing cosmic time. It is also evident at $\log(M_h/M_\odot) = 11.5$, 12 and 12.5 that the relation at $z \sim 4$ starts to bend so to invert completely its trend at $\log(M_h/M_\odot) > 13$.

In Fig. 3.17 we show the evolution of the SHMR as a function of redshift at two fixed halo masses: one located at masses below the peak ($\log(M_h/M_\odot) = 11.0$), and the other above it ($\log(M_h/M_\odot) = 13.0$) and compare to literature results. Figure 3.11 has clearly shown that the redshift evolution has completely opposite trends at these two masses, similarly to other AM, HOD, EM, and CL literature results. We have described before the opposite trends of the SHMR at $z < 4$ and $z > 4$. At $\log(M_h/M_\odot) = 11.0$, our SHMR shows a strong evolution (more than ~ 0.5 dex) of its value with a decreasing trend from $z = 0$ to $z \sim 3.5$. Assuming a simple hierarchical structure formation scenario, we would expect that M_*/M_h remains constant with redshift. However, baryons do not share the bottom-up evolution of dark matter halos, as proven by several results (e.g., Cowie et al. 1996; Fontanot et al. 2009; Thomas et al. 2010). The most massive galaxies (mainly early-type galaxies

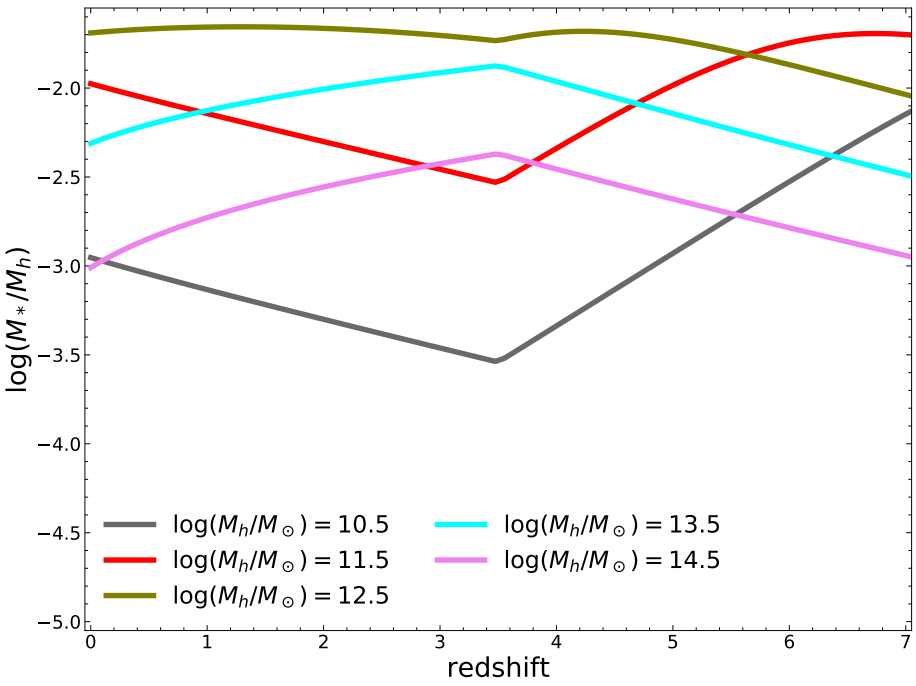

Fig. 3.16 Evolution of the SHMR at several halo masses according to our empirical model.

hosted in galaxy groups and clusters) are dominated by old stellar populations, and appear to have formed their stellar mass relatively quickly at the beginning of their life, while faint field galaxies (usually late-type galaxies) appear to have continued to actively form stars over the last billion years, and their stellar population is dominated by young stars. This is the so-called downsizing scenario (see Sect. 1.4.2).

Considering SAMs and EM, the value of the SHMR appears not to evolve as much as we find. Moreover, different SAMs disagree on whether the SHMR value decreases, as in our work (e.g. *SAG*, *DLB07*, and *LGALAXIES*), or remains approximately constant (e.g., *YSAM* and *GALFORM-GP14*). This indicates that the downsizing effect is not well reproduced by the evolution of M_*/M_h in all analyzed SAMs. This might be due to the well-known overcooling problem (e.g., Benson et al. 2003): galaxies are modeled to form as gas cools inside of dark matter halos (White & Rees, 1978). However, the mass function of dark matter halos rises steeply at low masses (Reed et al., 2007). Because cooling is very efficient in these low-mass halos, the galaxy mass and/or luminosity function are expected to show a similar slope at the low-mass or low-luminosity end. The observed slopes are instead much shallower (as a consequence of the downsizing effect), and therefore some form of feedback is postulated to mitigate this discrepancy, typically from supernovae and AGN. However, these feedback mechanisms are still not fully understood and their modeling is accordingly uncertain. We also note that the model *MORGANA* is the only SAM that shows an increasing trend with increasing redshift. This may be due to the resolution of the simulation and/or an excessive overcooling that probably is due to the treatment of the feedback mechanisms. For our results, we find that the value of M_*/M_h

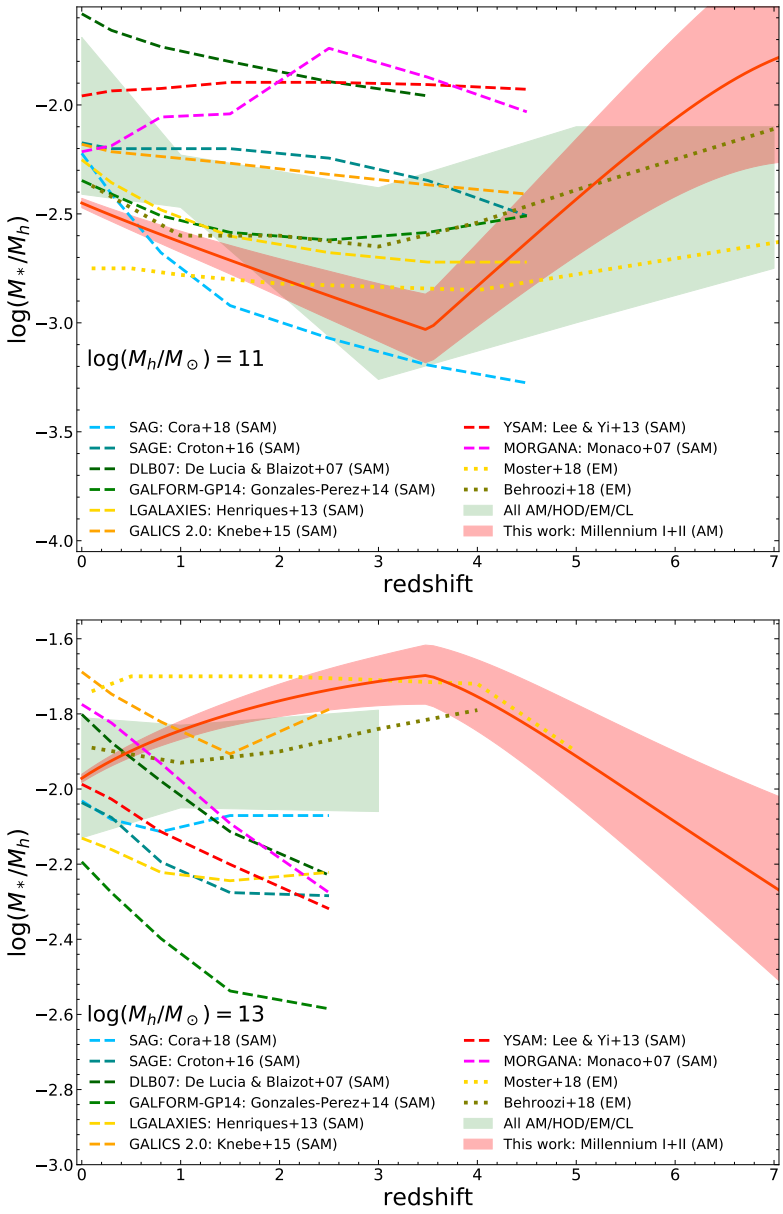

Fig. 3.17 Evolution of the SHMR at fixed halo masses of $\log(M_h/M_\odot) = 11.0$ (top) and $\log(M_h/M_\odot) = 13.0$ (bottom). Our results derive from the model described in Sect. 3.2 are shown red dashed lines. The corresponding shaded area represent 1σ uncertainties for our model. Other dashed colored lines represent the eight SAMs of the Cosmic CARNage project. The evolution in the two panels is shown from $z = 0$ to $z = 5$ because data at higher redshifts for these halo masses are lacking in the Cosmic CARNage simulations as well as in other literature results. Green shaded regions show the range covered by all the AM, HOD, EM, and CL results, as presented in Figs. 3.12 and 3.13 and described in Sect. 3.3 (without the results of this work) with the exception of the models by Behroozi et al. (2019) and Moster et al. (2018) since their results reach high redshifts and a meaningful comparison can be performed. Their results are shown in dotted lines. We note that not all the works in literature extend their results down to $\log(M_h/M_\odot) = 11$ or up to $\log(M_h/M_\odot) = 13$, and we therefore show only those whose results reach these masses.

does not decrease for all redshifts, but instead it decreases up to $z \sim 3.5$ and then it switches trend and starts increasing. As discussed in Sect. 3.6, this trend is common to other recent results (e.g. Behroozi et al. 2019) and may be due to the little time (i.e. ~ 0.6 Gyr) that elapses between $z \sim 5$ and $z \sim 3.5$ and/or to still not completely understood processes of galaxy formation and evolution at such high redshifts. We will discuss this aspect in further detail in Sect. 3.6.

At $\log(M_h/M_\odot) = 13.0$, we find an increasing value of the SHMR with increasing redshift (up to $z \sim 3.5$), in accordance with other similar AM, HOD, EM, and CL literature results, and its evolution becomes even stronger at higher halo masses (shown in Fig. 3.11). All SAMs instead show an opposite decreasing trend (with the exception of *SAG* and *LGALAXIES,* which show an approximately flat trend). We show their evolution only up to $z = 2.5$ because SAMs lack data at higher redshifts at this halo mass as a consequence of the relatively small volume of the simulation, which does not contain such rare massive halos at $z > 2.5$. These different trends may be an indication that some physical processes are not yet accurately modeled in SAMs, such as feedback mechanisms that may affect the build-up of stellar mass in galaxies. However, the box size of the underlying cosmological simulation for dark matter ($125\,\mathrm{Mpc}\,h^{-1}$ on a side) is too small to carry out a definitive comparison between SAMs and other results such as ours. Once again, concerning our results, we find that the increasing trend with redshift reverses at $z \sim 3.5$. This may be again due to some unknown physics in the early Universe or to uncertainties in the SMFs we adopted to calibrate our model.

Evolution of the SHMR peak

In Fig. 3.18 we show the redshift evolution of the peak halo mass $M_{h,\mathrm{peak}}$ and of the corresponding $(M_*/M_h)_{\mathrm{peak}}$ value. We show our results from the best fit of the observed SHMR shown in Fig. 3.9, whose uncertainties are mainly due to errors in the SMFs (i.e., photometric redshift errors, stellar mass errors, cosmic variance, and Poissonian errors) along with the best-fit empirical models, defined in Sect. 3.2. We also show several results from the literature (described in Sect. 3.3) and SAMs (presented in Sect. 3.4). We do not show the errors of other works for clarity. The errors are comparable to the errors we show for our results.

Fig. 3.18 shows that we observe an approximately flat trend of the evolution of the $(M_*/M_h)_{\mathrm{peak}}$ value (with only a slight decrease by a factor of ~ 1.2 from $z = 0$ to $z = 2$) although the uncertainties at high redshift are quite large. At $0.8 < z < 1.1$, our data show an anomalous increase that is due to the SMFs we adopted. In fact, the SMF in this redshift bin show a shift toward higher stellar masses with respect to the general evolution of the other redshift bins (see Fig. 2.7). This may be due to an overdensity of massive galaxies in the COSMOS field or to uncertainties in the SED-fitting procedure at these redshifts.

We find in general that even though the general trend of the evolution of the SHMR peak is different in the literature, most of the works find that the value of $(M_*/M_h)_{\mathrm{peak}}$ decreases with increasing redshift (e.g., Moster et al. 2013, 2010; Yang et al. 2012) and only few works find that it remains approximately constant (e.g., Behroozi et al. 2013; Moster et al. 2018). Moreover, there

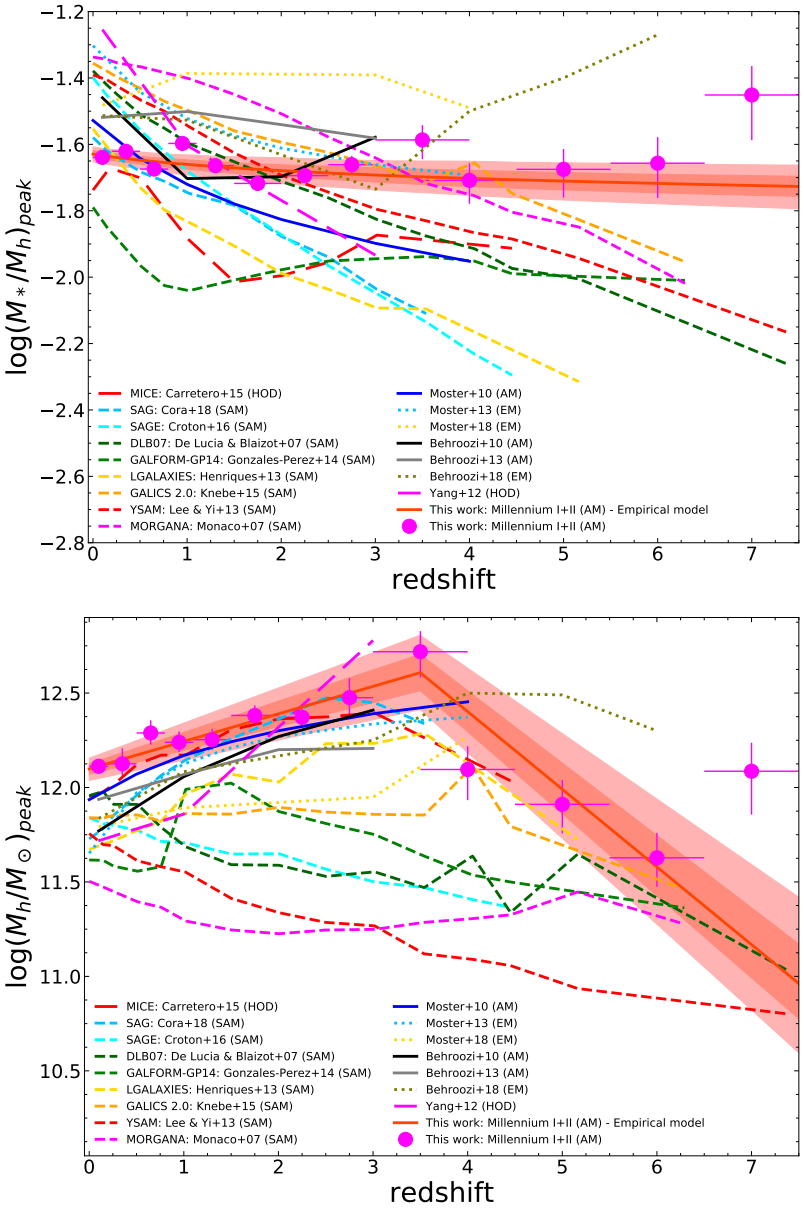

Fig. 3.18 Evolution of the SHMR at the peak (top) and the halo mass at the peak (bottom) compared with previous literature works and results of SAMs of galaxy formation and evolution. For both panels, magenta open points and error bars represent the fit of our measured SHMR while dashed orange line (and its corresponding shaded area) represent our best-fit empirical model (and its corresponding 1 and 2σ errors). Other symbols are the same as Fig. 3.12.

is still a large scatter between literature results (up to a factor of ~ 4 in M_*/M_h), which leaves this an open question. Concerning the SAMs, we observe a general trend with the $(M_*/M_h)_{\rm peak}$ value decreasing with increasing redshift for all but *GALFORM-GP14*, which presents a minimum a $z \sim 0.9$ and remains flat thereafter.

In Fig. 3.18 we also show the evolution of the $M_{h,\rm peak}$. We find an increasing value of $M_{h,\rm peak}$ with increasing redshift up to $z \sim 4$ and then a decreasing trend. We showed in Fig. 3.18 (bottom panel) that some literature works (e.g., Behroozi et al. 2010, 2013; Moster et al. 2013, 2010; Yang et al. 2012) have reported the same trend with redshift, while others (e.g., Carretero et al. 2015) and SAMs do not show the same trend. In general, SAMs show lower values; some of them (*SAGE*, *GALFORM*, *YSAM*, and *DLB07*) show a decreasing trend with increasing redshift, with the exception, at least marginally, of *SAG* and *LGALAXIES*, which yield a rising $M_{h,\rm peak}$ value up to redshift $z \sim 3$. However, the scatter between different studies is large in this case as well (up to a factor of ~ 3 in M_h, and it increases with redshift). This implies that much work remains to be done in order to precisely determine the SHMR at all redshifts and understand the physical processes that give rise to it. In the next section we discuss the implications of such results on galaxy formation and evolution processes.

3.6 Star-formation efficiency

In this Section we will discuss our results, presented in previous Sections and interpret them in relation to the processes related to galaxy formation and evolution and, in particular, through the star-formation efficiency (SFE).

We show in in Fig. 3.7 the redshift evolution of the SHMR shown that can also be interpreted as an evolution of the SFE. In the literature there are many different definitions of the SFE (e.g. Leroy et al. 2008 defines the SFE as the star formation rate surface density per unit neutral gas surface density along a line of sight). In our work, we define the SFE as the fraction of baryons locked in stars: $f_* = (M_*/M_h) f_b^{-1}$, where f_b is the cosmological baryon fraction (i.e., 0.153 for our Planck cosmology). If we assume a constant value of f_b with redshift, then the value of (M_*/M_h) corresponds to the SFE. In fact, as also described in Sect. 1.2 of this thesis, in the current picture of galaxy formation, gravitational potential wells of dark matter halos, which become bigger with the halo mass growth, provide the seeds for baryonic gas collapse that forms a hot virialised baryonic halo at the centre of the dark matter halo itself. Then the gas starts to cool down at a rate that depends on its temperature and density, and it inflows inward the gravitational potential wells. If the equilibrium between cooling, heating by collapse and angular momentum is reached, the gas starts to fragment into small cores and star formation takes place (see Dayal & Ferrara 2018 for a recent and extensive review). It is therefore evident that studying the SHMR, and in particular its interpretation as the SFE, gives us an insight on the processes involved in galaxy formation that regulate the abundance of baryonic gas which is converted into stars.

In Fig. 3.7 we show the SFE as a function of the halo mass as calculated from the SHMR. In addition, in Fig. 3.19, we show the SFE as calculated from the empirical model as a function of M_*.

We find that the SFE is always lower than 20% showing always a peak at intermediate halo/stellar masses (i.e. at $M_A = M_{h,\mathrm{peak}}$) and decreasing both at lower and higher halo/stellar masses. For example for $M_* > 10^{11.5} M_\odot$ the SFE has very low values ($< 1\%$) at $z = 0$, then it reaches its maximum at $z = 3$ ($\sim 10\%$), meaning that massive galaxies were much more efficient in producing stars at higher redshifts and then, moving down with redshift, while their gas reservoir reduces the star-formation drops accordingly.

The bell shape of the SHMR (and, therefore, of the SFE) can be interpreted by means of the various feedbacks that are in play in galaxy formation and evolution. Given the galaxy formation scenario described above, one would expect that the halo and stellar mass functions exhibit a similar slope, since galaxies form within halos themselves. The observed slopes of SMFs are instead much shallower than those of the HMFs, and therefore some form of feedback is postulated to mitigate this discrepancy, typically from supernovae and AGN (see Sect. 1.2.6). For masses below the peak (i.e. $\log(M_{h,\mathrm{peak}}) \sim 12.1$ at $z \sim 0$ that corresponds to $\log(M_*/M_\odot) \sim 10.6$) it is thought that the stellar feedback, in the form of SN feedback, plays an essential role in shaping galaxy masses and properties. At higher halo masses instead, the AGN feedback is invoked to shape the SMFs as we observe them (Moster et al., 2010; Yang et al., 2012). In particular, both these feedbacks suppress star-formation at low and high halo masses, leading to a decrease in the SFE, while for intermediate halo masses (i.e. at $M_A = M_{h,\mathrm{peak}}$) these feedbacks are much less important.

At $z < 4$ (i.e. top panels of Figs. 3.7 and 3.19), we find that the SFE increases for increasing redshifts at masses higher than the peak of the SHMR. This trend is reversed for masses below this limit. This means that massive galaxies (i.e., for halo masses higher than the SHMR peak) formed stars with a higher efficiency at higher redshifts. In contrast, low-mass galaxies (i.e., for halo masses lower than the SHMR peak) formed with higher efficiency at lower redshifts. This is another view of the so-called downsizing effect (the term was coined by Cowie et al. 1996 to describe this behavior, see Sect. 1.4.2): the gas in the smaller halos has a longer cooling time with respect to larger halos and therefore, in small halos, the star-formation is delayed.

At $z > 4$ (i.e. bottom panels of Figs. 3.7 and 3.19), the redshift evolution of the SFE shows an opposite trend to what is found at $z < 4$ i.e. above the characteristic halo mass M_A, the SHMR increases for decreasing redshift, and the trend is reversed at lower masses. At these redshifts we rely on observed mass functions evaluated by Grazian et al. (2015). Conducting observations at these redshifts is a challenging task and it is evident by looking at the errors of the SMFs at $z > 4$ in Fig. 2.7. Usually $z > 4$ observations are limited to small sky areas which are, therefore, affected by high cosmic variance and the observed mass range of galaxies at these redshifts (shown with solid lines in bottom panels of Figs. 3.7 and 3.19) is limited. Also the population of dark matter halos undergoes a much less pronounced evolution from $z = 8$ to $z = 4$ with respect to the evolution from $z = 4$ to $z = 0$, as shown in Fig. 2.12. In addition, the uncertainties in stellar mass estimates at $z > 4$ remains large (as shown in Fig. 6 of Moster et al. 2018) and therefore drawing definitive conclusions at these redshifts is not trivial. However, we want to highlight that the studies by Moster et al. (2018) and Behroozi

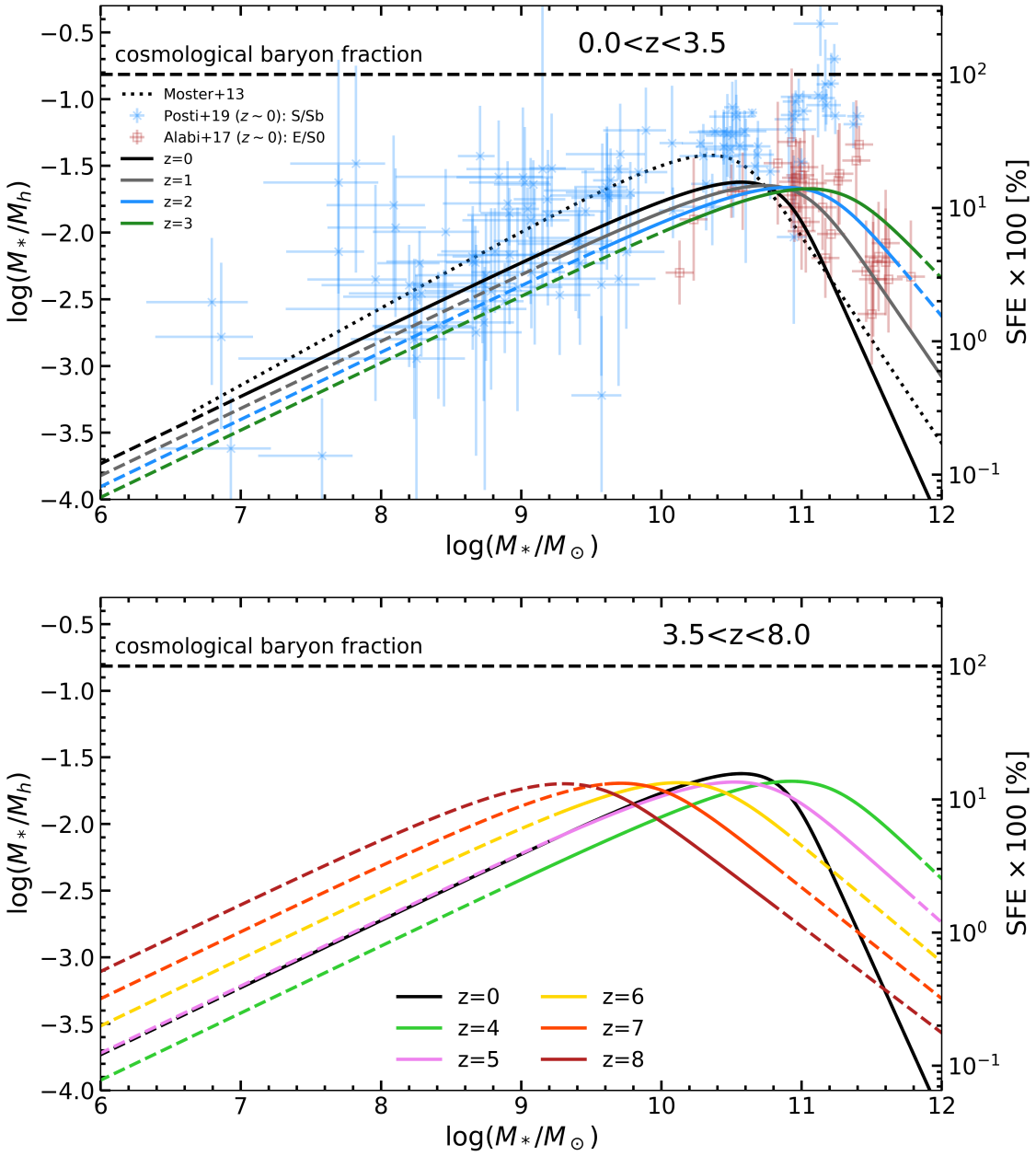

Fig. 3.19 Evolution of the SHMR in a $\log(M_*/M_\odot) - \log(M_*/M_h)$ plane at $0 < z < 4$ (top panel) and $4 < z < 8$ (bottom panel). Solid and dashed lines show the SHMR predicted by the empirical model (presented in Sect. 3.2). The solid line identifies the observed mass range of galaxies, and the dashed line represents the extrapolation using the empirical model. Literature results for spiral galaxies (at $z \sim 0$) by Posti et al. (2019) are shown with blue points while results on local elliptical and lenticular galaxies by Alabi et al. (2017) are shown with red points. As a reference, the results by Moster et al. (2013) at $z = 0$ is shown with a black dotted line. The right-hand side y-axis is labeled with the SFE expressed in percentage (defined as $M_*/M_h\, f_b^{-1}$). The top black thick dashed line shows the cosmological baryon fraction ($f_b = 0.153$) that correspond to a SFE$= 100\%$.

et al. (2019) also found, in accordance with our results, a SHMR (SFE) evolution with redshift that reverses at $z \sim 4$.

The clear evolution of the SHMR that is in place from $z = 4$ to $z = 0$, is a signature of almost 12 Gyr of co-evolution of galaxies and dark matter halos where several feedbacks and interactions occur. Defining an analogous evolution from $z = 8$ to $z = 4$ is not a trivial task due to large errors that affect observations at these redshifts.

Many recent studies have tried to put tighter constraints on the evolution of the SHMR (and, therefore, on the evolution of the SFE) at $z > 4$, however, there is not consensus on whether the evolution is even in place or not. The Harikane et al. (2018) SFE model, derived through clustering measurements coupled with an HOD modeling over ~ 100 deg^2, predicts a non evolving SHMR with redshift. This result is in accordance with the predictions of the empirical model of Tacchella et al. (2018) that assigns a star-formation rate (SFR) to a dark matter halo based on the growth rate of the halo and, consequently, derives its SFE. In addition, the Harikane et al. (2018) and Tacchella et al. (2018) models are in agreement with the results obtained by Stefanon et al. (2017) via abundance matching on deep IRAC observations. On the contrary, other studies (e.g. Moster et al. 2018, Behroozi et al. 2019 and this work) find an evolving SFE with redshift. Both the Moster et al. 2018 and Behroozi et al. (2019) empirical models determine individual galaxy star formation rates from their host halos potential well depths, assembly histories, and redshifts, similarly to what is done in Tacchella et al. (2018) model. Then, for each halo, the galaxy stellar mass is derived from the star formation histories along the halo assembly and merger history. Even if the various models have similar approaches they still find results that do not agree on whether the SFE is evolving with redshift at $z > 4$ or not. In addition, by looking at Fig. 3.17, it is clear that even SAMs do not agree among themselves on whether there is an evolution in the SHMR (i.e. in the SFE) with redshift, and, if present, what is the direction of such evolution. However, due to the limited volume on which the considered SAMs have been run, there are no data available at $z > 4$. The disagreement between different SAMs once again highlights the difficulty in treating all the feedback processes that are in play in galaxy formation and evolution that shape the SHMR, letting us conclude that a lot of effort (both theoretical and observational) still needs to be done in order to adress the relative importance of the AGN and SN feedbacks and how they affect the galaxy population properties.

Many other recent studies have also tried to put constraints on the SFE at $z > 8$. These studies are, however, usually limited to very small samples of galaxies, given the difficulty of observing galaxies at these redshifts. Also in this case, there is not agreement on whether the SFE evolves at $z > 8$ (i.e. Marrone et al. 2018, Oesch et al. 2016, Bowler et al. 2020) or remains approximately constant with redshift (e.g. Oesch et al. 2018, Stefanon et al. 2020, Harikane et al. 2018).

Considering all the uncertainties in play at $z > 4$, and the disagreements between different literature results, we cannot put tighter constraints on the SFE and its evolution nor draw definitive conclusions on the trends we find at $z > 4$.

As mentioned above, we can also interpret the value of $(M_*/M_h)_{\rm peak}$ as the peak of SFE. It indicates that galaxies with these characteristic masses are in general the most efficient at turning

baryons (gas) into stars during their lifetime. We find that the peak of the SFE ranges from ~ 0.16 to $\sim 0.14 \pm 0.02$ (going from $z = 0$ to $z = 6$), which means that $\sim 15 - 20\%$ of all available gas has been turned (and remain locked) into stars; the peak efficiency lies at $z \sim 0$ (with the exception of the bin $0.8 < z < 1.1$, due to an overdensity of massive galaxies in the COSMOS field or to uncertainties in the SED-fitting procedure at these redshifts, as mentioned in Sect. 3.5). A high fraction of gas that is processed in stars returns to the ISM at the end of stellar evolution (up to $30 - 50\%$ depending on the age, star formation history, and IMF, e.g., up to 48% for a Chabrier IMF, Bruzual & Charlot 2003). When we also account for the return fraction R in calculating the SFE (including all the gas involved in the star formation), the values we find would therefore be $(1 - R)^{-1}$ times higher (up to ~ 1.9 for a Chabrier IMF corresponding to a SFE$\sim 30\%$).

The overall low star-formation efficiencies at all halo masses suggest that most of the baryons are in the form of interstellar and intergalactic diffuse gas. A recent study by Posti et al. (2019), whose results are shown in Fig. 3.19, found that the SFE for local spiral galaxies is a monotonically increasing function of M_* with no sign of a decline at high masses and that massive spirals (i.e., $M_* \gtrsim 10^{11} M_\odot$) have $f_* \sim 0.3 - 1$. This indicates that these systems have turned nearly all the baryons associated with their halos into stars and that, in these systems, the AGN feedback does not play an essential role in shutting down star-formation. However, this result has been derived only on local massive spirals by analysing their rotation curves (and, therefore, these objects may not be representative of the whole spiral/blue population). By looking at the results on local elliptical and lenticular galaxies by Alabi et al. (2017) in Fig. 3.19, we find that these systems show in general a lower SFE with respect to local spirals that decreases with increasing M_*. In these galaxies the AGN feedback it thought to play an essential role in shutting down star-formation and, as a consequence, the SFE is reduced too. In general, when comparing with Posti et al. (2019) and Alabi et al. (2017) results, our model predicts a lower SFE at all masses (especially at high M_* when compared to Alabi et al. 2017). This can be due to the *relative* scatter we implemented in Sect. 3.1.3. If we assume that $\sigma_R < 0.2$ dex, than the model would predict higher stellar masses at fixed halo masses (see Fig. 3.8) bringing our results more in agreement with Posti et al. (2019) and Alabi et al. (2017) results. As already discussed in Sect. 2.1.2 and 3.1.3, there is not consensum in the literature on the precise value of the *relative* scatter in the SHMR and, the differences among different models quantitatively depend also on the exact value of the scatter that is introduced. Several works have suggested that the shape of the SHMR depends on the galaxy type (e.g., Conroy et al. 2007; Mandelbaum et al. 2006; Rodríguez-Puebla et al. 2015), with red and passive early-type galaxies residing in most massive halos with respect to blue late-type galaxies. However, it is not straightforward to precisely determine from a simulation which halos host late- or early-type galaxies because the halo masses of these two classes of objects overlap at approximately the peak of the SHMR.

In Fig. 3.18 we also show the evolution of the $M_{h,\mathrm{peak}}$ that approximately coincides with the knee of the SMF, with an offset depending on the slopes of the HMF and SMF. As mentioned above, star formation is most effective and least influenced by either stellar or AGN feedback for these halo masses (Moster et al., 2010; Yang et al., 2012). We can therefore infer that the trend we find up to

$z \sim 4$ may be a signature of the downsizing effect. In other words, we find that the halo mass for which star formation is most efficient monotonically decreases with cosmic time. Massive galaxies were therefore formed at earlier times than less massive objects, even if $(M_*/M_h)_{\rm peak}$ slightly increases with cosmic time. This considerations hold up to $z \sim 4$. Above this threshold we cannot draw any secure conclusion due to many unknown processes that shape galaxies and to uncertainties in the SMFs.

Effects of the evolution of the baryon fraction

It has been argued by several authors (Andreon, 2010; Eckert et al., 2016; Giodini et al., 2009; Gonzalez et al., 2013) that the baryon fraction is not constant with (halo) mass. The studies have focused mostly on local ($z \sim 0$) galaxy groups and clusters (i.e., for total masses of $\log(M_{500}/M_\odot) \gtrsim 13$), where the total content of matter inside R_{500} can be measured through X-ray studies. The general trend reported in these studies is that the baryon fraction increases with increasing mass and approximately reaches the universal baryon fraction at the highest measured masses ($\log(M_{500}/M_\odot) \sim 15$). As an example, Gonzalez et al. (2013) found a decrease in baryon fraction by a factor ~ 1.5 from $\log(M_{500}/M_\odot) \sim 15$ to ~ 14. If we qualitatively assume that the baryon fraction decreases with decreasing halo mass throughout the entire range of halo masses we considered (from $\log(M_h/M_\odot) \sim 10.5$ to 15), the SFE trend should change. In particular, if this scenario is in place, the SFE at $z < 4$ will still increase with redshift at masses higher than the peak of the SHMR, while below the peak, the decreasing trend we find may be less steep. In order to explore whether the baryon fraction evolves with redshift, we can rely on hydrodynamic simulations, such as Davé (2009) and Davé et al. (2010). These authors ran set of simulations with a modified version (Oppenheimer & Davé, 2008) of the N-body+hydrodynamic code GADGET-2 (Springel et al., 2005). Several physical processes were considered, such as star formation, radiative cooling, metal-line cooling, supernovae, kinetic outflows, and stellar winds. Davé and collaborators found an approximately constant baryon fraction with halo mass at high redshifts (i.e., $z \sim 3$). At low redshift ($z \sim 0$), they found the same trend in mass as was reported in the studies mentioned above, that is, the baryon fraction increases with increasing halo masses and approximately reaches the universal baryon fraction at the highest halo masses ($\log(M_h/M_\odot) \sim 15$). The main result the authors find is that the baryon fraction decreases with increasing cosmic time at fixed halo masses (as an example, at $\log(M_h/M_\odot) = 12$, they find that the baryon fraction decreases by a factor ~ 1.4 from $z = 3$ to $z = 0$). This is particularly true at low halo masses (i.e., $\log(M_h/M_\odot) \lesssim 12$). If the baryon fraction also depends on redshift, this would lead to a modification of the values of SFE we find and would enhance the evolution from high to low redshifts at masses below the SHMR peak.

To summarize, when we consider a constant baryon fraction with cosmic time and halo mass, we find that, with increasing redshift (up to $z \sim 4$) the SFE increases at masses higher than the peak of the SHMR. This trend is reversed for masses below this limit. For $z > 4$ the evolution with redshift shows an opposite trend but we cannot draw definitive conclusions on its meaning, while the trend

with halo mass is preserved. When we instead consider an evolution of the baryon fraction with halo mass, cosmic time, or a combination of both, as predicted by some hydrodynamic simulations, the trends we find (with cosmic time and halo masses) are not affected at $z < 4$, even though the precise values of the SFE might change.

4

BUILDING THE MOCK CATALOGS

In this Chapter, we describe in detail the full procedure to construct the empirical mock catalog. The method we implemented starts from the output of an N-body dark matter simulation: we adopted the lightcones of the DUSTGRAIN-*pathfinder* (Giocoli et al., 2018) and Millennium I+II (Springel et al., 2005) simulations. The information we used from the DM simulations is the following:

- halo mass: expressed as $M_{200,crit}$ for main halos and M_{infall} for sub-halos and orphans or, alternatively, if the infall mass is not provided (i.e. for the DUSTGRAIN simulation), the distance from the main halo (as explained in Sections 2.3.1 and 2.3.2);
- redshift of each halo and subhalo;
- *RA* and *Dec*, since we are also interested in clustering studies, as we will discuss in detail in the next Chapter.

For the Millennium I+II simulation we used all the 24 available lightcones, from $z = 0$ to $z = 8$ with halo masses $M_{200} > 1.7 \times 10^{10} M_{\odot}$, where each lightcone covers an area of 3.14 deg^2. For the DUSTGRAIN-*pathfinder* we used 256 lightcones, from $z = 0$ to $z = 4$ with halo masses $M_{200} > 3.16 \times 10^{12} M_{\odot}$, each with an area of 72.18 deg^2.

Once we have these informations, we can apply our method that we sketch below, but extensively describe and discuss in the following Sections:

1. Assigning stellar masses to DM halos: this has been done using the empirical model proposed in Sect. 3.2, described by Equations 2.2, 3.1, 3.2, 3.3 and 3.4, whose best-fit parameters are listed in Table 3.5. When assigning the stellar mass also the *relative* scatter needs to be applied (see Sect.4.1). The model has the advantage that it employs a simple functional form to assign the stellar mass to dark matter halos.

2. Dividing into star-forming and quiescent objects: we divide galaxies into these two classes using the relative ratio of the SMFs for the blue and the red population (the classification in red/blue is done via color selections, see Sect. 4.2 for details). In particular, we used the stellar mass function by Peng et al. (2010) for SDSS $z \sim 0$ data and SMFs by Ilbert et al. (2013) for $0.2 < z < 4.0$ galaxies (see Sect. 4.2).

3. Galaxy physical properties: with the informations retrieved with the previous two steps, we run the public code EGG (Empirical Galaxy Generator) by Schreiber et al. (2017). The code takes in input informations about the stellar mass, redshift and a star-forming/quiescent classification in order to evaluate other physical properties through empirical recipies calibrated mainly on the CANDELS fields. With this step we have informations about the star formation rate, the photometry, the sizes, the dust extinction and the emission lines for our mock catalog (see Sect. 4.3).

In addition, we sketch in Fig. 4.1 the flow-chart followed for the creation of the mock catalog. In the following Sections we describe and test each step of our method and present our first results for the mock catalogs we produced.

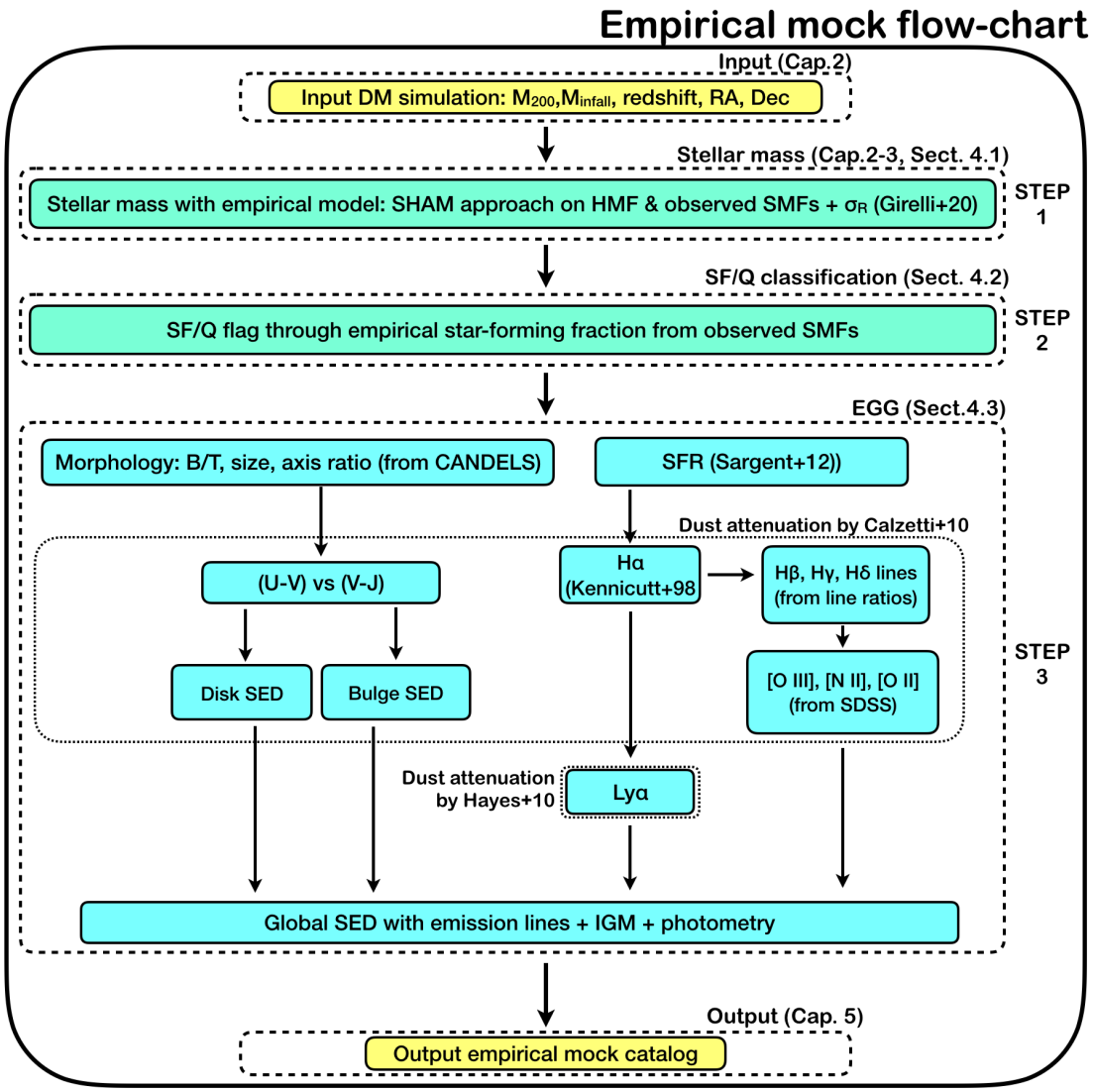

Fig. 4.1 Flow chart of the empirical mock catalog.

4.1 Step 1: assigning the stellar masses

We assign the stellar mass to dark matter halos by using the model proposed in Sect. 3.2 using its simple functional form (Equations 2.2, 3.1, 3.2, 3.3, and 3.4). Given its simplicity, this step is computationally very cheap and can be run relatively quick on all available lightcones of the two DM simulations we use. When evaluating the stellar mass, we also need to account for the *relative* scatter, as described in Sec. 2.1.2. To this aim, we first assigned the stellar mass according to the empirical model (whose parameters are listed in Table 3.5) and then we scattered the assigned stellar masses using a log-normal distribution with standard deviation $\sigma_R = 0.2$ dex. The effect of the introduction of the *relative* scatter can be clearly seen in left panels of Fig. 4.2, where we the points show the dispersion of the stellar masses due to the *relative* scatter. In the Figure we have also divided into red

and blue galaxies, but we will discuss this division in the next section. In this Figure, we compare with Henriques et al. (2015) SAM and also divide its galaxies into red and blue according to the authors original classification (i.e. based on a modified $NUVrJ$ diagram). We find that our results agree well for low-mass low-z galaxies (i.e. for masses below the peak at $0 < z < 1$) but differ substantially at other masses and redshifts (this was already evident in Fig. 3.15). Another relevant difference is in the amount of scatter. Apparently, the Henriques et al. (2015) SAM shows a much larger scatter in stellar mass at fixed halo mass at all redshifts and halo masses. This may be due to the scatter in the mergers and SFHs of galaxies at a fixed halo mass that lead to differences in the resulting stellar masses.

In addition, it is interesting to see in Fig. 4.3 the distribution of stellar masses divided by the halo types of the Millennium I+II simulation. Moreover, in Fig. 4.4, we show the distribution of stellar masses for the three halo types (i.e. central, satellite, orphan) divided into mass bins of the main halos they reside in. It is evident that central halos host (for any halo mass bins) the more massive galaxies (as one would expect by observing clusters of galaxies), while satellite halos host intermediate mass galaxies together with orphans that become dominant at low masses. We also note that for the smallest main halos, almost only the central galaxy is present and, therefore, the contribution of satellite and orphan galaxies is negligible down to low stellar masses (e.g. for main halos with $11 < \log(M_h/M_\odot) < 12$ at $0.2 < z < 0.5$ the contribution by satellite and orphan galaxies can be ignored down to $\log(M_*/M_\odot) \sim 8.5$). Therefore, as it was also evident in Fig. 2.10, up to a certain mass (i.e. $M_* \sim 10^{8.5} M_\odot$ at $z \sim 0$), orphan galaxies are important in order to construct a complete sample of galaxies, while their contribution become less important at higher masses (at $\log(M_*/M_\odot) \sim 10$ and $z \sim 0.35$ they contribute to less than 10% of the total number of halos).

After the stellar mass was assigned to simulated DM halos of the lightcones of the DUSTGRAIN-*pathfinder* and Millennium I+II simulations, we calculated the SMFs in several redshift bins (defined by the input observations we used, i.e. Baldry et al. 2008; Grazian et al. 2015; Ilbert et al. 2013). We calculated the SMFs on all available lightcones and the resulting SMF we present in the following is the mean value of the mass function of all the lightcones in each mass bin.

We show our resulting SMFs and their evolution with redshift for the Millennium I+II and DUSTGRAIN-*pathfinder* simulations in Figs. 4.5 and 4.6, respectively. For both simulations, we limited the SMFs calculations to stellar masses for which our mocks are complete in stellar mass, i.e. stellar masses $M_* \gtrsim 10^{11} M_\odot$ for the DUSTGRAIN-*pathfinder* and $M_* \gtrsim 10^{7} M_\odot$ for the Millennium I+II evaluated with the empirical model on the completeness limit of the DM halos (the precise values depend on the considered redshift, given that the empirical model evolves with redshift, and can be clearly seen in Fig. 4.5).

In Figs. 4.7, 4.8 and 4.9 we show the resulting SMFs for both our simulations in thirteen different redshift bins (from $z = 0$ to $z = 7.5$) along with the SMFs on which the SHMR is calibrated (i.e. Baldry et al. 2008, Ilbert et al. 2013 and Grazian et al. 2015) adding many other literature results by Pozzetti et al. (2010), Davidzon et al. (2013), Tomczak et al. (2014), Davidzon et al. (2017), Mortlock et al. (2011), Santini et al. (2012), Song et al. (2016) and Stefanon et al. (2015). In addition, we also show results by two SAMs by Henriques et al. (2015) and Fontanot et al. (2017).

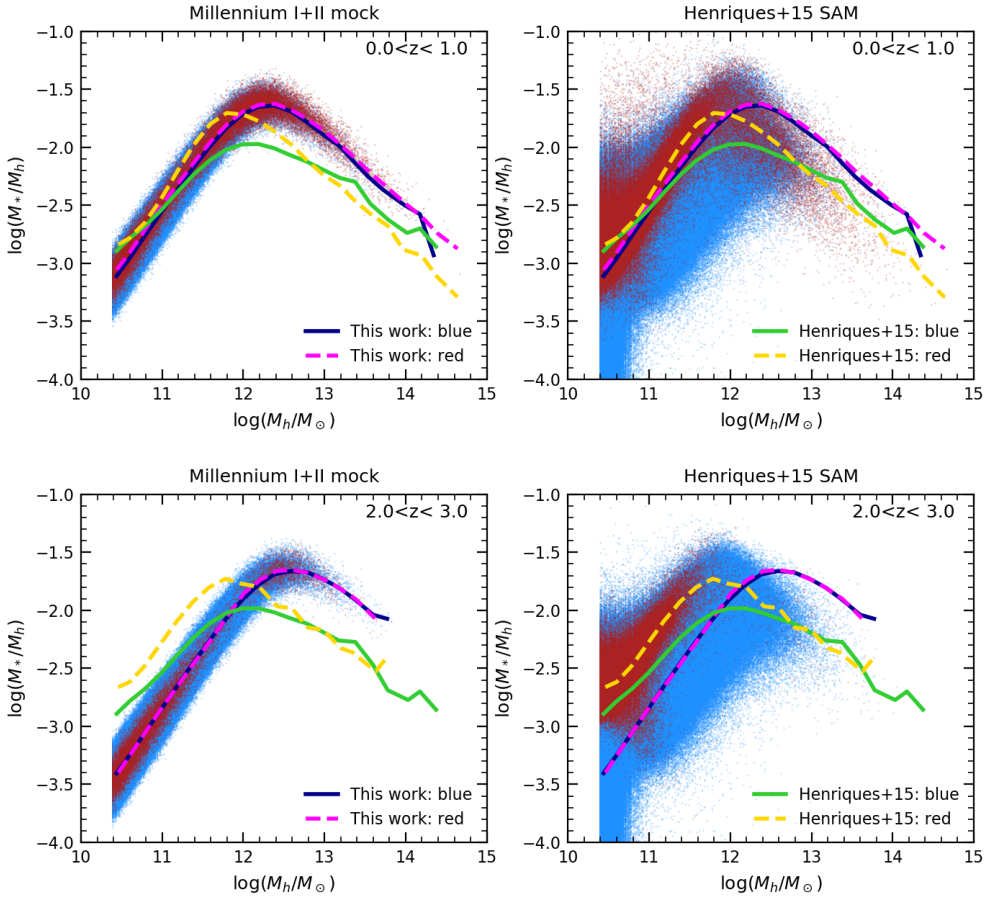

Fig. 4.2 SHMR shown in a $\log(M_h/M_\odot) - \log(M_*/M_h)$ plane for the Millennium I+II results and Henriques et al. 2015 SAM, both evaluated on lightcone 23. In the left panels we show with points the results on the Millennium I+II simulation, divided into red and blue galaxies with the technique detailed in Sect. 4.2. In right panels the points represent Henriques et al. (2015) results divided into red and blue galaxies with the authors prescription (based on a modified NUVrJ diagram). In top panels we show the redshift bin $0.0 < z < 1.0$ and in bottom panels the bin $2.0 < z < 3.0$. In all panels, we show with lines the SHMR median values (calculated in bins of M_h) for our mock and Henriques et al. (2015) SAM. Solid lines are for SF galaxies, dashed lines for Q galaxies.

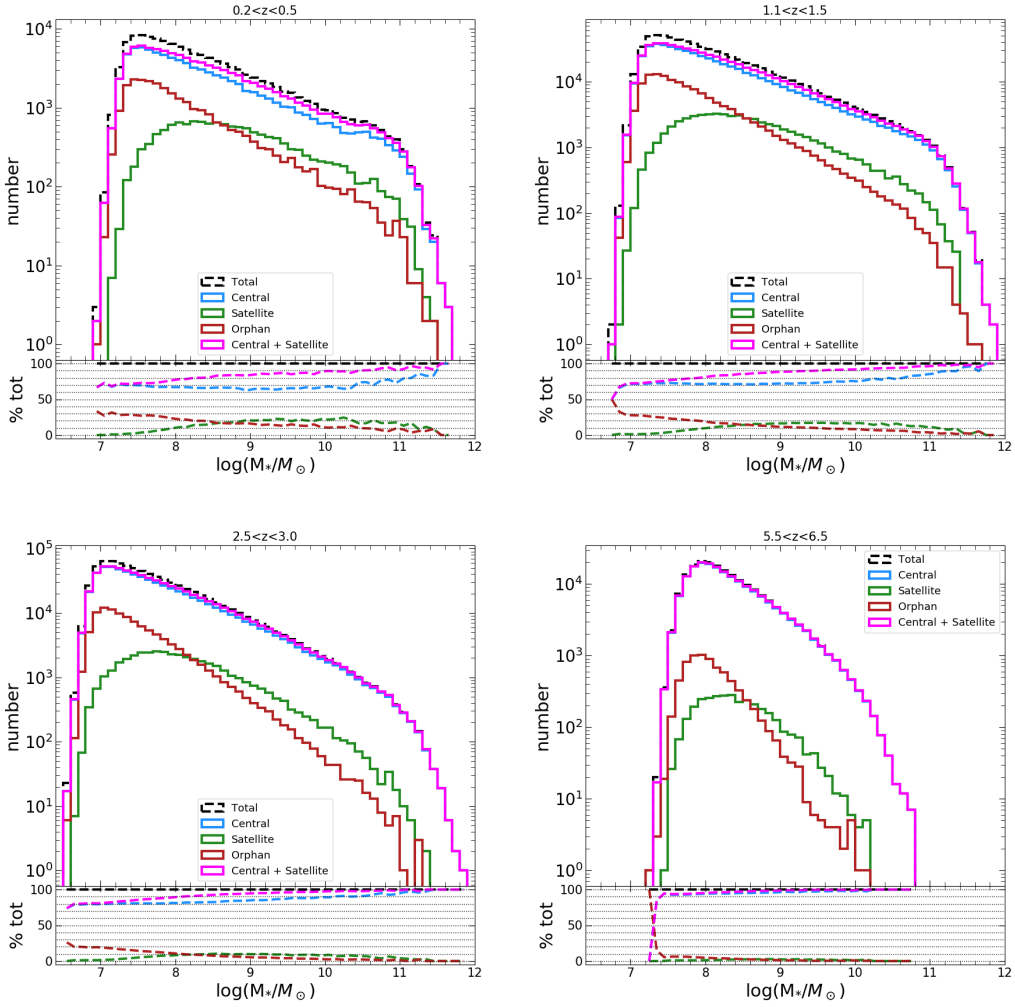

Fig. 4.3 Distribution of stellar masses of the various type of halos of the Millennium I+II simulation in four redshift bins for the lightcone 23. In particular, the distribution of all halos is shown in black dashed line. With blue, green and red lines the contribution of the central, satellite and orphan halos is shown, respectively. Finally with a magenta line the contribution by central and satellite galaxies together is shown. In bottom panels the contribution (in percentage) of each component to the total is shown.

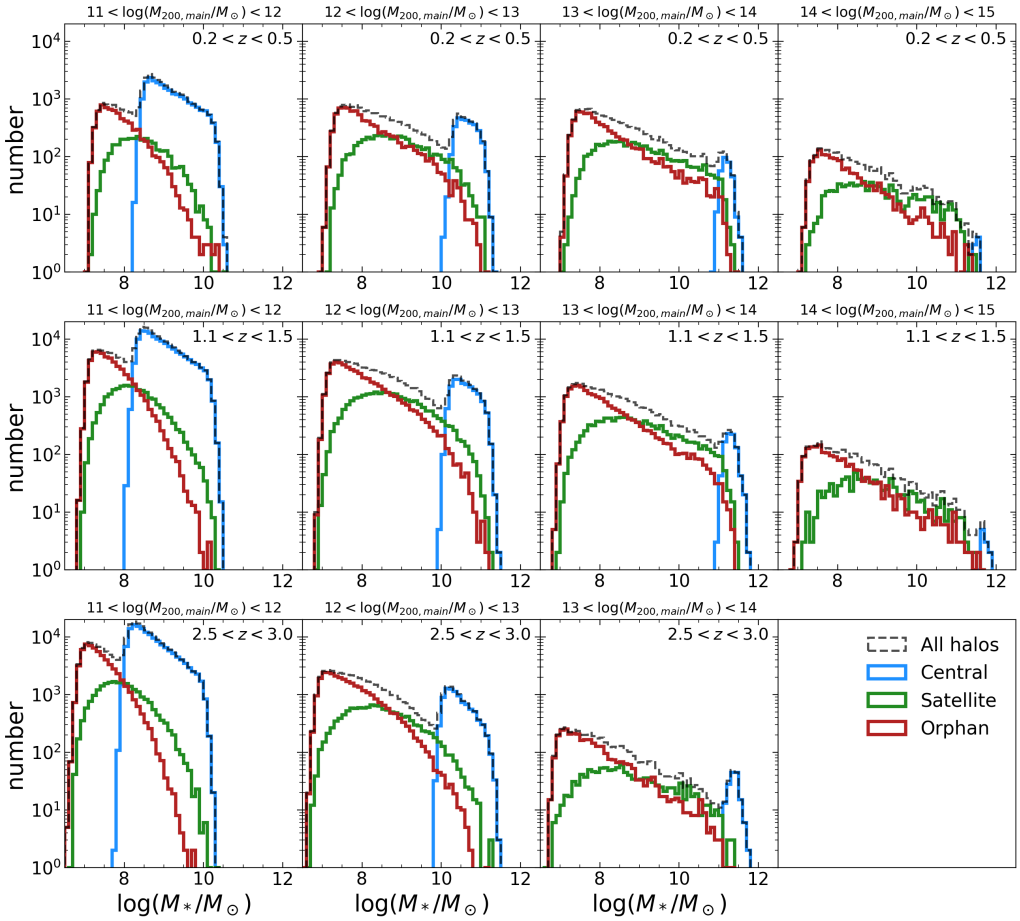

Fig. 4.4 Distribution of stellar masses of the various type of halos of the Millennium I+II simulation in three redshift bins for the lightcone 23 divided into mass bins of the main fof group halos reside in. In particular, the distribution of all halos is shown in black dashed line. With blue, green and red lines the contribution of the central, satellite and orphan halos is shown, respectively. In Top, Middle and bottom lines we show the distributions at $0.2 < z < 0.5$, $1.1 < z < 1.5$ and $2.5 < z < 3.0$, respectively. From left to right columns, four mass bins of the main fof halo are shown.

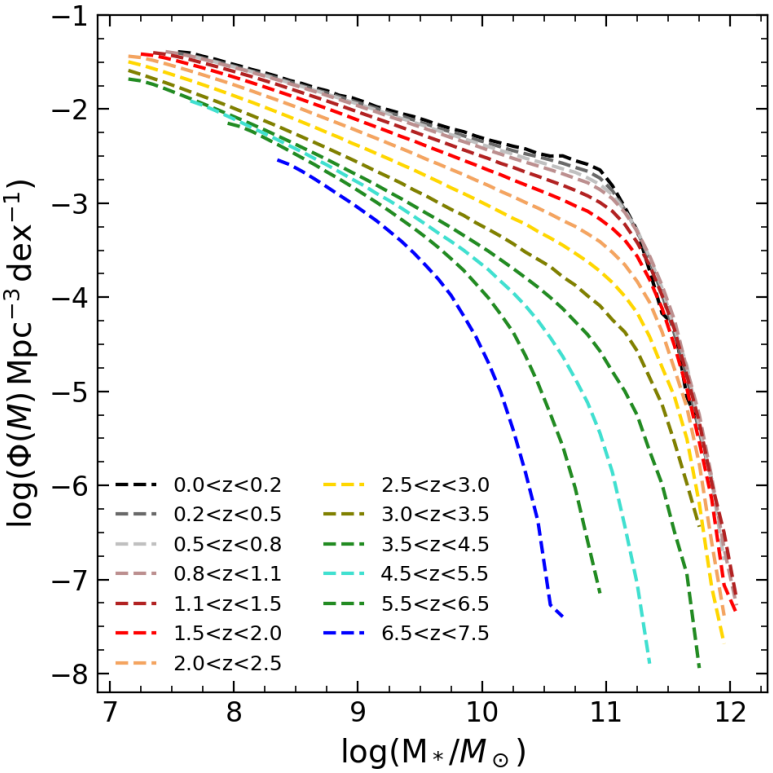

Fig. 4.5 Evolution of the stellar mass functions for the Millennium I+II simulation from $z = 0$ to $z = 7.5$.

We report here the main features of the data we compare with. For instance, the Tomczak et al. (2014) SMFs were estimated from the ZFOURGE survey (Straatman et al., 2016), which includes three pointings in CDFS (Giacconi et al., 2002), COSMOS, and UDS (Lawrence et al., 2007) fields. The total area used to evaluate SMFs by Tomczak et al. (2014) is $\sim 0.09\,\mathrm{deg}^2$ from $z = 0.2$ to $z = 3.0$. Davidzon et al. 2017 SMFs were evaluated in the COSMOS field following Ilbert et al. (2013), but with a different data release (Laigle et al., 2016). Moreover, Davidzon et al. (2017) restricted their analysis to a smaller area than Ilbert et al. (2013) (i.e., the ultra-deep stripes covered by ULTRA-Vista with an area of $0.62\,\mathrm{deg}^2$) but with deeper observations ($K_s = 24.7$ compared to $K_s = 24$ of Ilbert et al. 2013), which in turn can increase the cosmic variance in Davidzon et al. (2017). This and the different SED-fitting procedure lead to the differences between the two works that are visible in Figs. 4.7, 4.8 and 4.9 (especially in the redshift bin $0.8 \leq z < 1.1$). The Pozzetti et al. (2010) SMFs were derived on the COSMOS field as well, but with the zCOSMOS spectroscopic survey data (Lilly et al., 2007), which cover $\sim 1.4\,\mathrm{deg}^2$ up to $z \sim 1$. In this case, redshifts were estimated from spectroscopy, and stellar masses were derived by SED-fitting of the multiband photometry. The SMFs by Davidzon et al. (2013) were evaluated using the spectroscopic VIMOS Public Extragalactic Redshift Survey (VIPERS) (Guzzo et al., 2014; Scodeggio et al., 2018) covering $\sim 10\,\mathrm{deg}^2$ from $z \sim 0.5$ to $z \sim 1.1$.

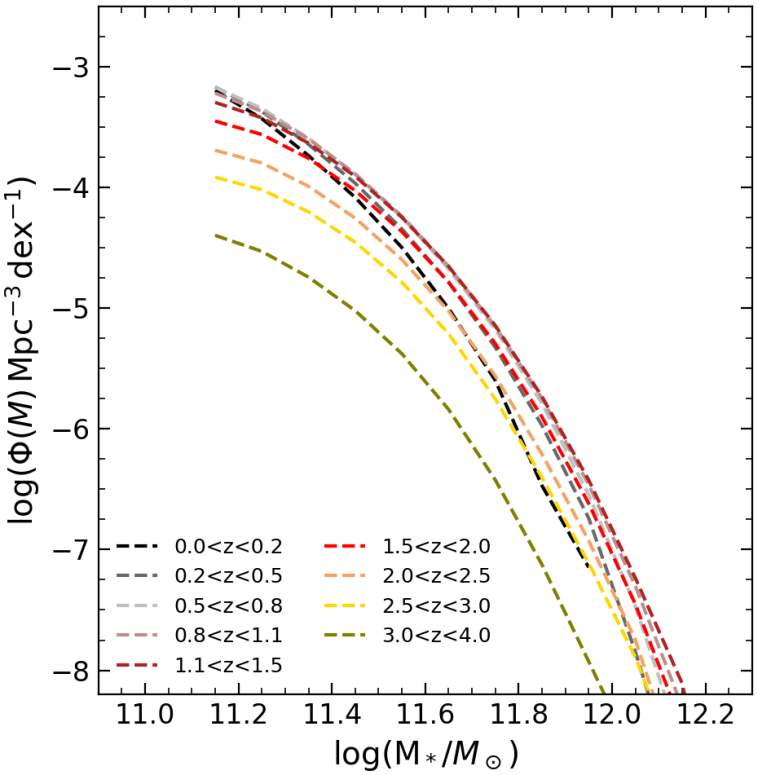

Fig. 4.6 Evolution of the stellar mass functions for the DUSTGRAIN-*pathfinder* simulation from $z = 0$ to $z = 4$.

The SMFs by Mortlock et al. (2011) was derived in the Great Observatories Origins Deep Survey (GOODS) with the Near Infrared Camera and Multi-Object Spectrometer (NICMOS) (Conselice et al., 2011) on board the Hubble Space Telescope ($H_{160} = 26.8$ over ~ 43.7 arcmin^2). The Santini et al. (2012) SMFs, is a study in the GOODS-S field on a relatively small but deep field ($K_s = 25.5$, over ~ 33 arcmin^2). Song et al. (2016) evaluated the SMFs from $z = 4$ to $z = 8$ from a rest-frame ultraviolet (UV) selected sample of galaxies, found via photometric redshifts over an area of ~ 280 arcmin^2 in the Cosmic Assembly Near-infrared Deep Extragalactic Legacy Survey (CANDELS)/Great Observatories Origins Deep Survey (GOODS) fields and the Hubble Ultra Deep Field. Finally, Stefanon et al. (2015) evaluated the SMFs for massive galaxies ($\log(M_*/M_\odot) > 11$) at $4 < z < 7$ using a Spitzer IRAC catalog of objects, obtained by complementing the K_s-band selected UltraVISTA catalog with objects detected in IRAC only in the COSMOS/UltraVISTA field (covering ~ 1.6 deg^2). When available (i.e., Davidzon et al. 2017; Grazian et al. 2015; Ilbert et al. 2013) we also show the best-fit intrinsic Schechter function along with the $1/V_{\rm max}$ estimates, and in the other cases (i.e., Davidzon et al. 2013; Mortlock et al. 2011; Pozzetti et al. 2010; Santini et al. 2012; Song et al. 2016; Stefanon et al. 2015; Tomczak et al. 2014) we show only the $1/V_{\rm max}$ estimates. In addition, where needed (e.g. Grazian et al. 2015), we converted the observational estimates to a Chabrier IMF (Chabrier, 2003). For the

results of the SAM by Henriques et al. (2015), since it was run on the Millennium I+II simulation, we directly downloaded the lightcone from the VIRGO - Millennium Database[1] and derived the SMFs in the same way we calculated ours. The data of the Fontanot et al. (2017) SAM have been kindly provided by the author himself.

By looking at Figs. 4.7, 4.8 and 4.9, we note that the results on the DUSTGRAIN-*pathfinder* and Millennium I+II simulations are consistent to each other. This result is expected since both simulations are run with a standard ΛCDM cosmological framework, and therefore their results are consistent in their common mass range (i.e. $\log(M_h/M_\odot) > 12.5$, as also explained in Sect. 2.3.3). We note, however, that, even though the DUSTGRAIN-*pathfinder* is limited to $M_* \gtrsim 10^{11}\,M_\odot$ galaxies, it reaches, at all redshifts, higher stellar masses than those by the Millennium I+II. This is reasonable if we consider that each lightcone of the DUSTGRAIN-*pathfinder* simulation covers an area ~ 23 times larger that the one covered by one lightcone of the Millennium I+II and, in addition, the number of lightcones of the simulations is very different (256 for the DUSTGRAIN-*pathfinder* and 24 for the Millennium I+II). Therefore, the DUSTGRAIN-*pathfinder* simulation covers a much larger volume compared to the Millennium I+II and, as a consequence, it is able to catch more massive halos that host very massive galaxies. We also remind here that the SMFs we evaluated on the DUSTGRAIN-*pathfinder* simulation are limited to $z < 4$.

We note that, as discussed in Sect. 3.2, the parameters of the empirical model (adopted to assign the stellar mass) depend on redshift, as described by Eqs. 3.1, 3.2, 3.3, and 3.4 and, therefore, the model may not perfectly reproduce the observed SMFs we used to calibrate the SHMR at every redshift because these SMFs are evaluated on specific fields (i.e. SDSS, COSMOS and CANDELS), which have their specific features. The results for the DUSTGRAIN-*pathfinder* and the Millennium I+II simulations agree very well with the observations with which we calibrated the relation (i.e. Baldry et al. 2008; Grazian et al. 2015; Ilbert et al. 2013) at all masses and redshifts (see Figs. 4.7, 4.8 and 4.9). We remind here that we used the best-fit Schechter functions (corrected for the Eddington bias) to calibrate the model and therefore our results does not necessarily show the same trend as the $1/V_{\rm max}$ datapoints which are not corrected for the Eddington bias. This is visible in Fig. 4.9 (middle left panel), where our SMF reproduce very well the Grazian et al. (2015) best-fit but seems to under-predict the number of massive galaxies if we look at datapoints.

When we compare with other observations, our results are in good agreement with the literature observed SMFs at all redshifts. We find, however, some differences with Santini et al. (2012) results between $z = 2$ and $z = 3$ especially at low masses, where Santini et al. (2012) results predict higher number densities with respect to our model and other observations. In addition, when comparing with Stefanon et al. (2015) results at $z > 5$, we find that our model predicts much smaller stellar masses. This can be due to the specific technique implemented in the literature works to calculate stellar masses. We can clearly see from Figs. 4.7, 4.8 and 4.9 that up to $z \sim 1$ our results agree well with both SAMs at masses $M_* \lesssim 10^{11}\,M_\odot$, but at higher masses it seems that the Henriques et al. (2015) SAM

[1] http://gavo.mpa-garching.mpg.de/MyMillennium/

is lower than our estimates while the Fontanot et al. (2017) is higher than them. At $z \gtrsim 1$, in some redshift bins (e.g. $1.1 < z < 1.5$, $1.5 < z < 2.0$, $3.5 < z < 4.5$, $4.5 < z < 5.5$) our results agree well with Fontanot et al. (2017) SAM, while in others (e.g. $2.0 < z < 2.5$, $2.5 < z < 3.0$, $5.5 < z < 6.5$) they show different shapes and normalizations. In addition, it is a general result (at all redshifts) that the Henriques et al. (2015) SAM tends to under-predict the observed number of massive galaxies (Cecchi et al., 2019; Girelli et al., 2019). Current SAMs still struggle to reproduce observed stellar mass functions with accuracy and this is particularly true when referring to the massive end, where the AGN feedback plays an essential role in shaping the SMF. This points out a well known issue in our current understanding of galaxy formation and evolution which is the contribution of feedbacks, and in particular the feedback by AGNs, in the various stages of structure formation (see Naab & Ostriker 2017; Somerville & Davé 2015 for two reviews) but, at the same time, also the stellar masses estimates from observations may be biased by the presence of AGNs in the sample.

To sum up, the good overall agreement, between our results and several literature results, indicates a realistic assignment of galaxy masses into halos. We also showed that current SAMs are in disagreement one between the other and, in some cases, also disagree with our results. This indicates that several physical mechanisms of galaxy formation and evolution are still not completely understood. We point out here that our results depend on the SMFs we used to calibrate the relation, and if the calibrating SMFs change, the SHMR changes accordingly. Nonetheless, SDSS, COSMOS and CANDELS are currently the best fields with a homogeneous redshift coverage from $z = 0$ to $z = 8$ because of their statistical and photometric accuracy in the photometric redshifts, stellar masses, and SMF determination.

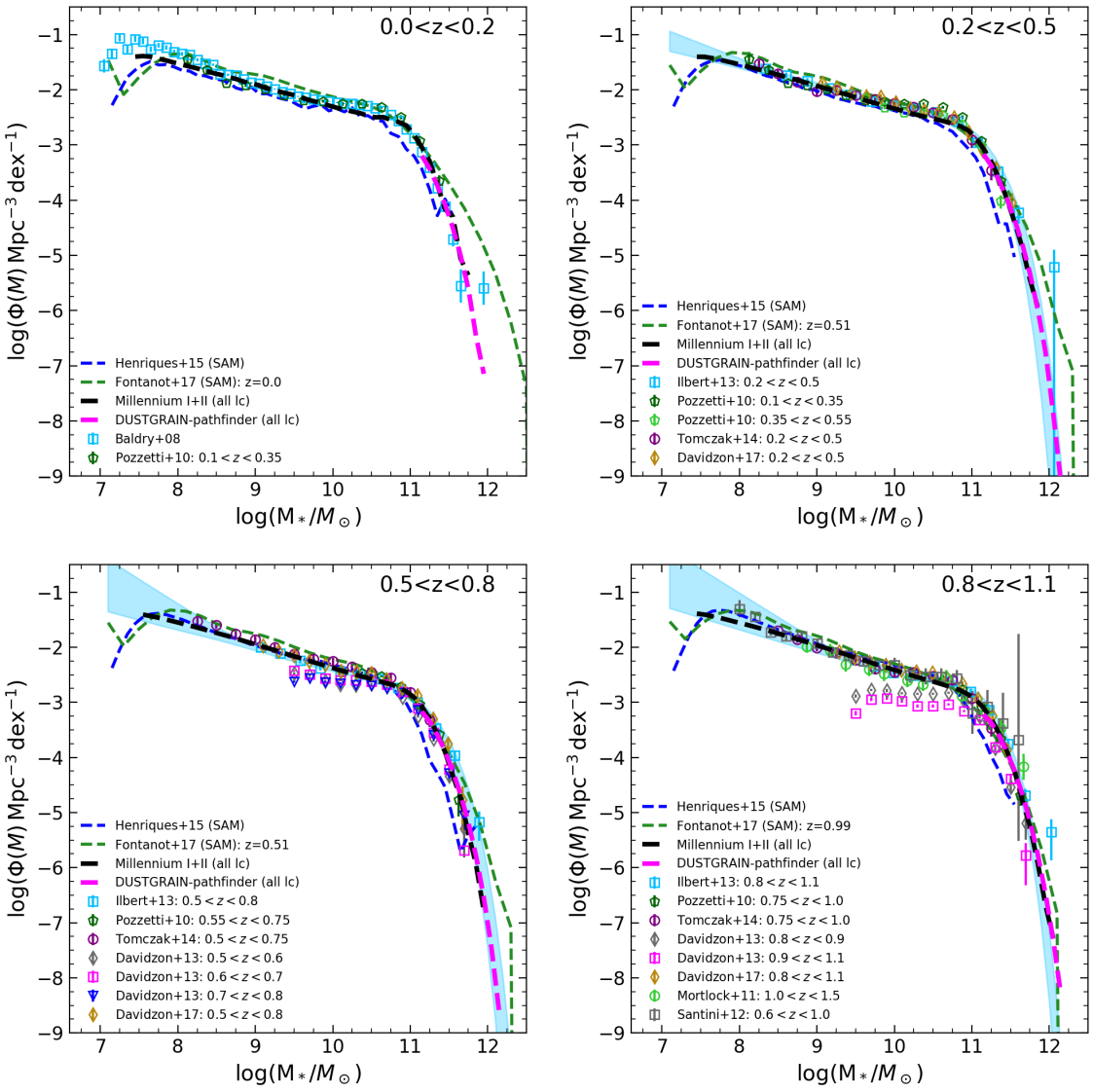

Fig. 4.7 Stellar mass function evaluated on the Millennium I+II and DUSTGRAIN-*pathfinder* simulations shown with thick dashed black and magenta lines, respectively, from $z = 0$ to $z \sim 1$. For both simulations, we evaluated the SMFs on all available lightcones and averaged between their results. We also show with colored dashed lines results from semi-analytic models of galaxy formation and evolution (Fontanot et al., 2017; Henriques et al., 2015) and with open points results from several literature results (Baldry et al., 2008; Davidzon et al., 2013, 2017; Ilbert et al., 2013; Mortlock et al., 2011; Pozzetti et al., 2010; Santini et al., 2012; Tomczak et al., 2014).

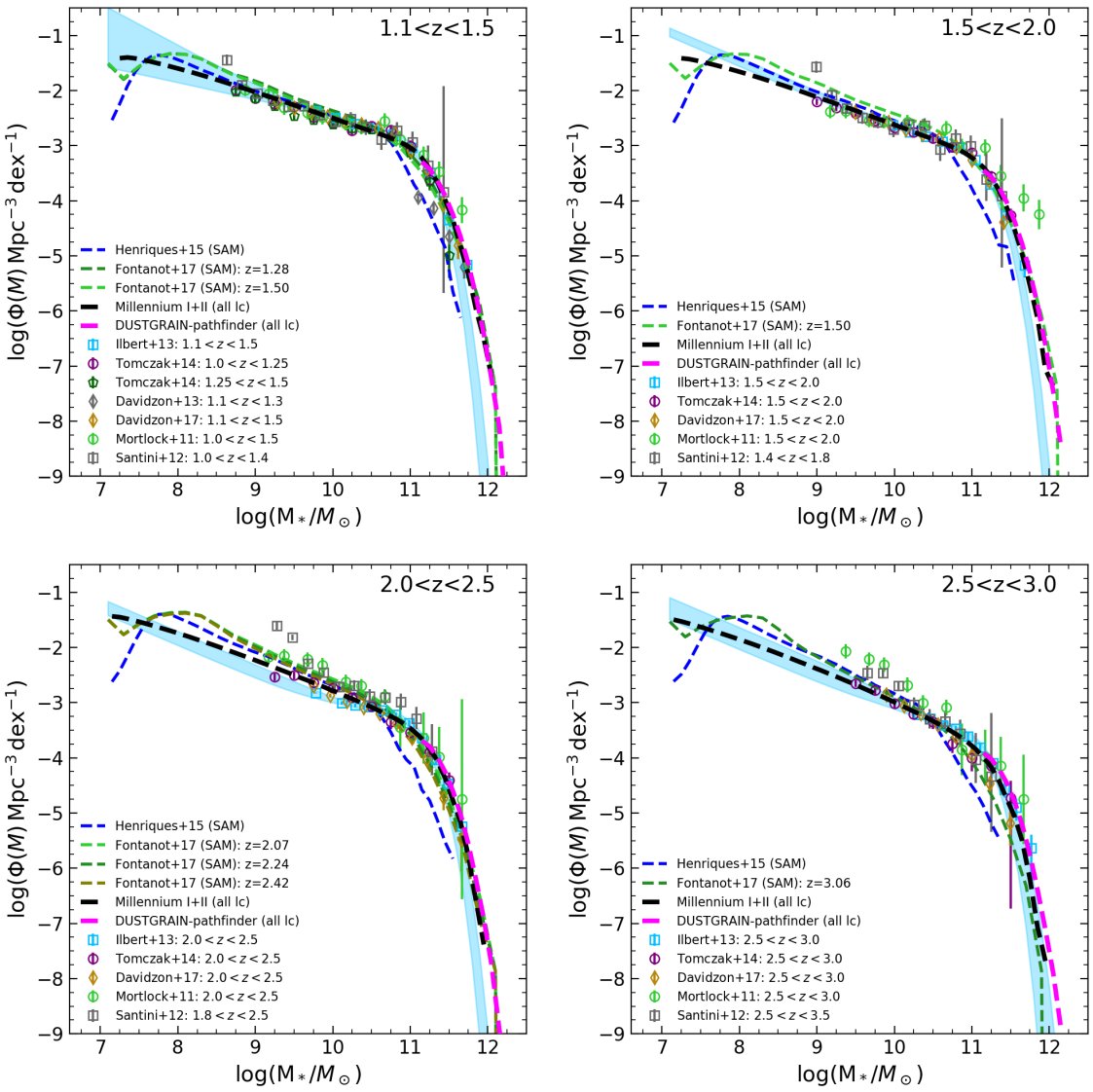

Fig. 4.8 Stellar mass function evaluated on the Millennium I+II and DUSTGRAIN-*pathfinder* simulations shown with dashed black and magenta lines, respectively, from $z \sim 1$ to $z \sim 3$. Lines and symbols as in Fig. 4.7.

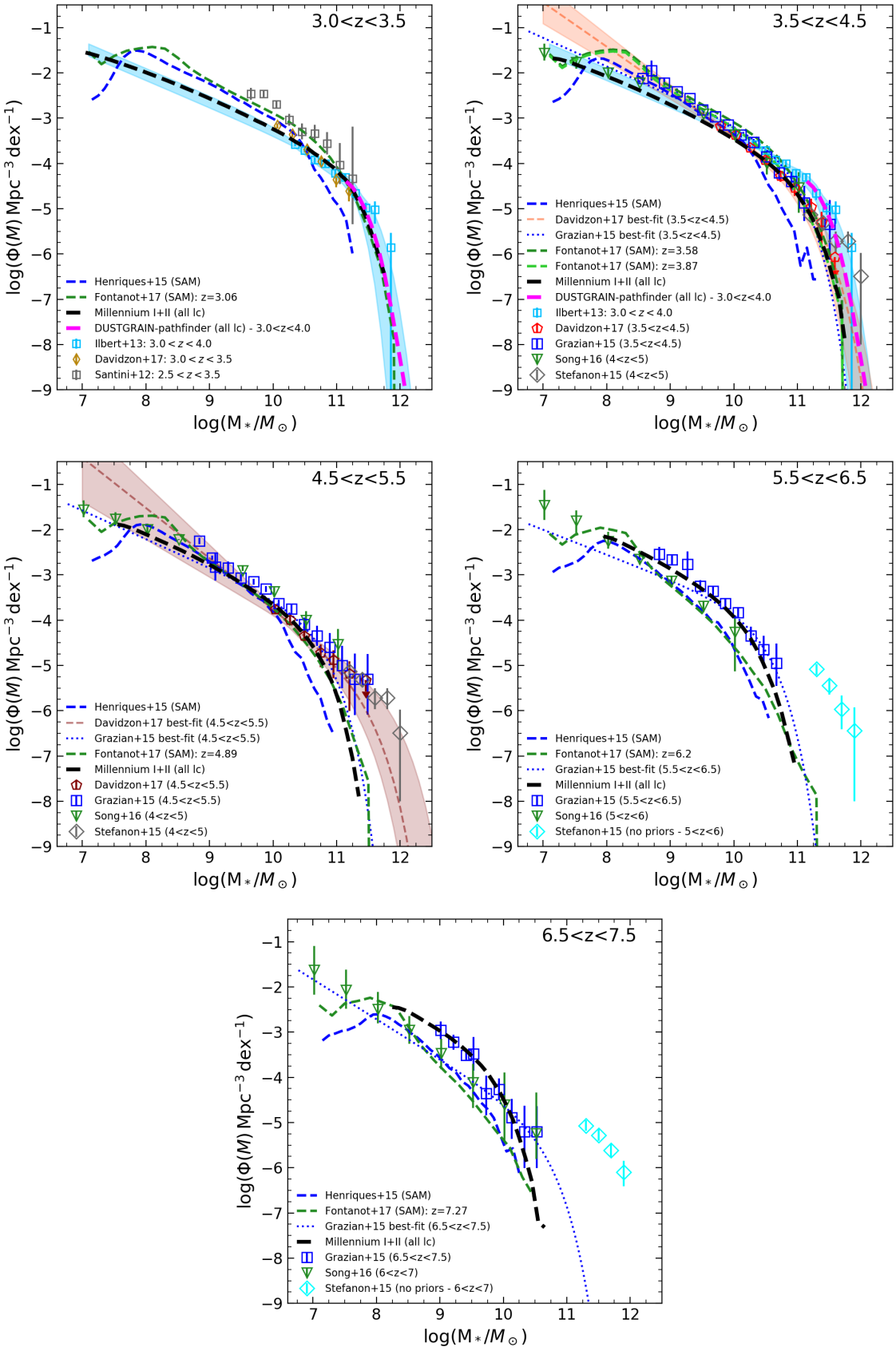

Fig. 4.9 Stellar mass function evaluated on the Millennium I+II and DUSTGRAIN-*pathfinder* simulations shown with dashed black and magenta lines, respectively, from $z \sim 3$ to $z \sim 7.5$. Lines and symbols as in Fig. 4.7 with the addition of literature observed stellar mass functions by Grazian et al. (2015); Song et al. (2016); Stefanon et al. (2015).

4.2 Step 2: dividing into star-forming and quiescent objects

In order to divide the simulated galaxies into the two populations, we first have to estimate the probability of a galaxy with a given M_* and redshift to be either star-forming or quiescent. To this aim, we use observed estimates of the SMFs for the blue and the red population. In particular, for consistency with the data adopted to calibrate the empirical model for stellar masses, we used the stellar mass function divided for red and blue population by Peng et al. (2010) (at $z \sim 0$ on the SDSS survey) and Ilbert et al. (2013) (at $z > 0$ on the COSMOS field).

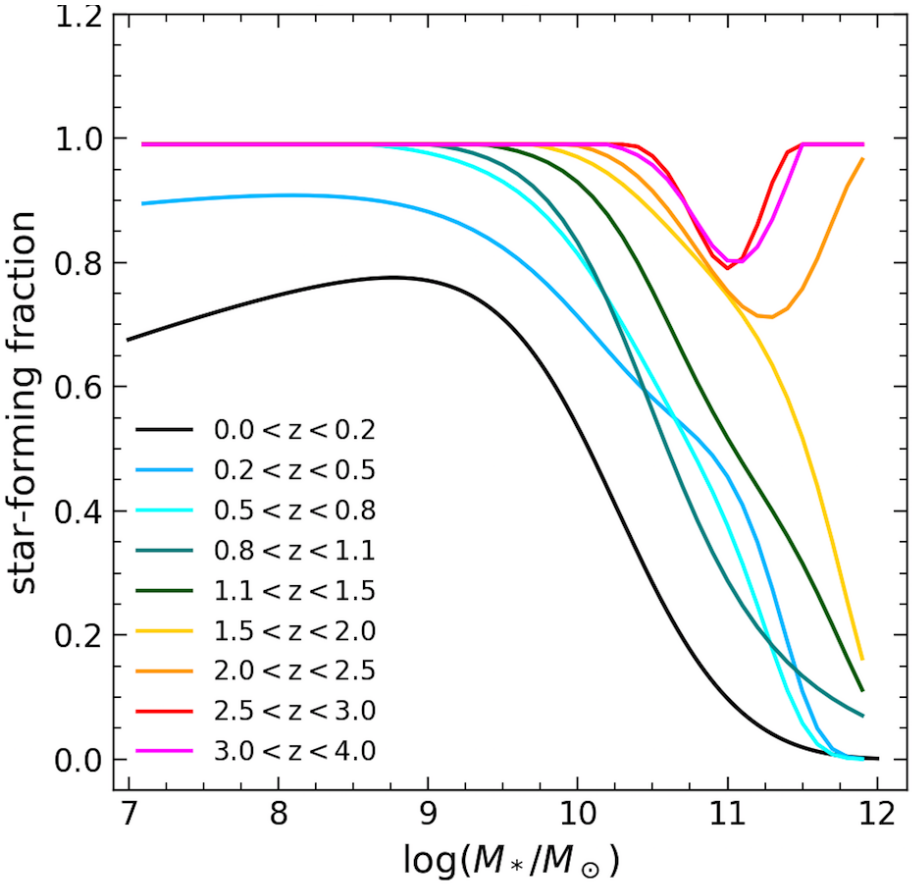

Fig. 4.10 Star-forming empirical fraction of galaxies as evaluated using the best-fit Schechter functions by Peng et al. (2010) and Ilbert et al. (2013) in different redshift bins from $z = 0$ to $z = 4$.

At $z \sim 0$ we used the SMFs evaluated by Peng et al. (2010) obtained for galaxies observed from the SDSS DR7 (Abazajian et al., 2009) using the standard $1/V_{\rm max}$ approach along with Bruzual & Charlot (2003) SPS models and a Chabrier (2003) IMF. The population of galaxies has been divided into red passive (or quiescent) and blue star-forming using the rest-frame $(U-B)$ color with a cut that slightly changes with redshift and stellar mass. For the blue galaxies they used a single Schechter function to fit the datapoints, while for the red galaxies a double (two-component) Schechter function is used. At

$0.2 < z < 4.0$ we used the SMF by Ilbert et al. (2013) which we have described in Sect. 2.2.2. Ilbert and collaborators divided the red passive (or quiescent) from the blue star-forming galaxies using the observed frame colour selection $(NUV - r)$ - $(r - J)$ (Ilbert et al., 2010; Williams et al., 2009). For the blue galaxies they have used a double Schechter function to fit the datapoints at all redshifts, while for the red galaxies a double Schechter function is used only in the redshift bin $0.2 < z < 0.5$ switching then to a single Schechter function at the other redshifts.

In order to evaluate the star-forming fraction as a function of redshift and stellar mass, we simply calculated the relative ratio between the total and blue population using the best-fit Schechter functions for the two populations from $\log(M_*/M_\odot) = 7$ to $\log(M_*/M_\odot) = 12$ in different redshift bins from $z = 0$ to $z = 4$. In Fig. 4.10 we show the stellar mass as a function of the star-forming fraction in different redshift bins. We can clearly see that the star-forming fraction increases with decreasing stellar mass and increasing redshifts. We also note that at some redshifts, for example at $0.2 < z < 0.5$, the star-forming fraction does not show a smooth trend with stellar mass but, instead, presents some variations in the steepness of the curve. Also at high redshifts (i.e. $z > 2$) the star-forming fraction decreases with increasing stellar mass up to a certain mass where the trend reverses. These trends are due to the ratio of the two Schecther functions (where both the functions for the star-forming and the total population are double Schechters). At $z \gtrsim 4$ SMFs divided by type are not available, and therefore we cannot evaluate a star-forming probability at $z > 4$. In fact, it is still debated the contribution of quiescent galaxies to the overall population at $z > 4$. Many recent studies (see, for example, Girelli et al. 2019, Merlin et al. 2018, Merlin et al. 2019b, Valentino et al. 2020) have tried to put tighter constraints to this elusive population, however, it is not clear yet what is their contribution to the global population of galaxies. In addition, different studies adopt different criteria/classifications to identify quiescent galaxies (e.g. based on the specific star-formation rate, on their rest-frame colors, on observed colors, ecc.) adding this up to the global uncertainties that characterize this population. Since the global contribution of quiescent galaxies at high redshift is not clear, we do not allow the star-forming fraction to exceed 99% up to $z = 6$ at any mass and naively fix this limit as the maximum value allowed for the star-forming fraction, granting, therefore, for some quiescent galaxies up to $z \sim 6$. At $z > 6$ we let the star-forming fraction approach 100% because no quiescent candidates have been identified at these redshifts and given also that at $z = 6$ the Universe is only ~ 0.6 Gyr old which is not enough to create such evolved systems. In order to assign to each galaxy of our mock (which are, at this point, charachterized by a stellar mass, redshift, positions and all halo properties) a star-forming/quiescent flag, we did not perform a fit on the star-forming fractions with some functional form (like other works have done, e.g. Béthermin et al. 2017), but, instead, we first calculate a star-forming probability for each galaxy, by interpolating among our results and extrapolating at $z > 4$ (shown in Fig. 4.10) between the star-forming fraction, the stellar mass and the redshift. Then, by randomly extracting a probability from a uniform distribution, we assigned a star-forming or quiescent flag to each mock galaxy.

We show in Fig. 4.11, as an example, the star-forming fraction of the mock galaxies in the lightcone 23 of the Millennium I+II simulation in different redshift bins. Along with the results on

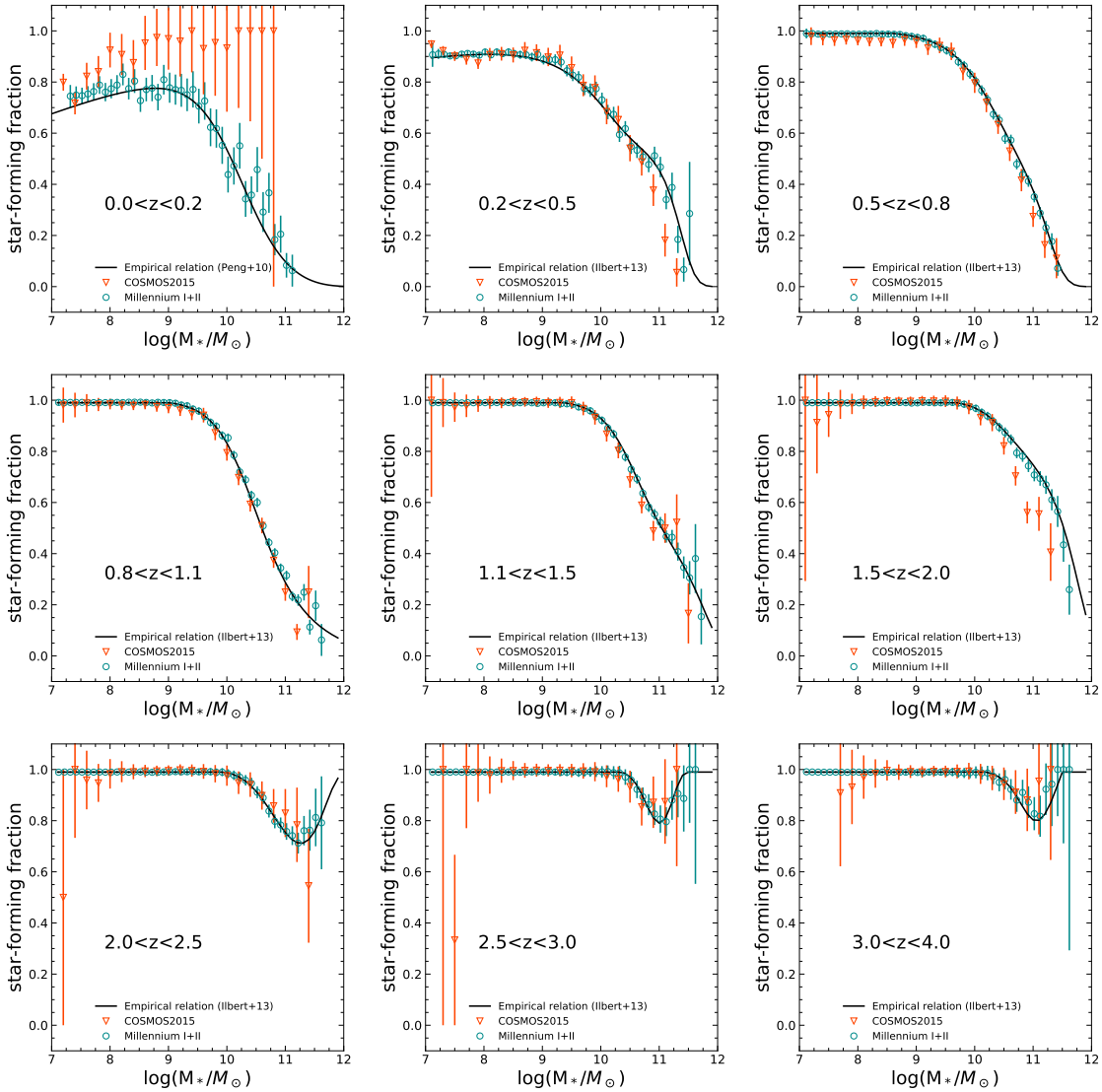

Fig. 4.11 Star-forming fraction of mock galaxies for the lightcone 1 of the Millennium I+II simulation. We show our results with open dark-cyan circles. Errorbars represent the Poissonian errors in each mass bin.We show the empirical relation we evaluated on Peng et al. (2010) and Ilbert et al. (2013) SMFs with a solid black line. We also show with open orange triangles the star-forming fraction evaluated on the COSMOS2015 catalog (Laigle et al., 2016).

the lightcone, we also show the star-forming empirical fraction (already shown in Fig. 4.10) and the results on the COSMOS2015 (Laigle et al., 2016) catalog[2]. In the catalog, the quiescent/star-forming have been identified using their locations in the rest-frame color-color plane $(NUV-r)$-$(r-J)$ (Ilbert et al., 2013, 2010; Williams et al., 2009). We note that in the redshift bin $0.0 < z < 0.2$ both our mock galaxies and the COSMOS2015 catalog have large errorbars. This is due to to the small volumes covered by both datasets at these redshifts (since they cover quite small sky areas: 3.14 deg^2 for the mock and 1.38 deg^2 for the observed catalog) that translates into few objects located in each mass bin. In other redshift bins, we find good agreement between our mock and the observed catalog at all redshifts. In addition, the same inverting trends at high redshift and stellar masses is found both in the mock and in observation, letting us conclude that the Schechter best-fit functions, used to divide into the two populations, are a good representation of observed data. In addition, in Fig. 4.2 we show how different galaxy types populate halos of different masses and compare with Henriques et al. (2015) results. For example, we can see that at low redshift (i.e. $0 < z < 1$) at high halo masses ($M_h \gtrsim 10^{12} M_\odot$) that correspond to high stellar masses ($M_h \gtrsim 10^{10.5} M_\odot$), quiescent galaxies are more numerous than star-forming ones (as it was also evident in the SMFs in Fig. 4.12). In addition, we remind that, by construction, in our model SF and Q galaxies share the same SHMR shape. Interestingly, the Henriques et al. (2015) SAM shows a mixed population of galaxies at high halo/stellar masses letting us deduce that the SHMR shape may be different for SF and Q galaxies. When comparing our results to Henriques et al. (2015) SAM, we find similar results at low redshift, while at high-z our model predicts more massive SF/Q galaxies at halo masses above the peak and less massive galaxies for galaxies below the peak. This is most probably due to the specific method implemented in this work and in the SAM to assign the stellar mass ans devise the SF/Q division. In fact, Henriques et al. (2015) used a modified version of the $NUVrJ$ diagram in order to reconcile the number of massive quiescent galaxies with observations. This difference may explain the differences we find between our mock and Henriques et al. (2015) results.

Once we assigned the star-forming/quiescent flag to our mock catalogs, we are able to evaluate the SMFs divided by type and compare to observations in order to test our division. We show in Figs. 4.12, 4.13 and 4.14 our resulting SMFs divided by type for both our simulations, compared to several observations. We show data on which we calibrated the mocks, i.e. Peng et al. (2010) and Ilbert et al. (2013) and also other literature data by Davidzon et al. (2017) and Girelli et al. (2019). As already mentioned above, Davidzon et al. 2017 SMFs were evaluated in the COSMOS field with the data release of 2016 (COSMOS2015, Laigle et al. 2016) and divided into red and blue components using the location of galaxies in the $(NUV-r)$-$(r-J)$ color diagram. We also report datapoints of a recent study we conducted using the COSMOS2015 catalog (Girelli et al., 2019). The aim of this work was to select and identify massive ($\log(M_*/M_\odot) \geq 10.6$) and quiescent candidates at the

[2]We selected COSMOS2015 data from the region with the best quality photometry by applying the following flags: FLAG_PETER=1, which defines good optical areas, that is, masking regions where bright stars may contaminate the photometry of nearby objects, while FLAG_COSMOS=1 and FLAG_HJMCC=0 define the area in COSMOS field covered by UltraVISTA.

highest redshifts (i.e. $z > 2.5$) through two novel observed color-color selections coupled with a SED-fitting analysis. We identified several quiescent candidates based on a cut in observed colors and in the specific star-formation rate (sSFR), which is a different criteria adopted by the other works we compare with. We report the full Girelli et al. (2019) study (hereafter G19) in Appendix D.

By looking at Figs. 4.12, 4.13 and 4.14 we find that, in general, our results are in good agreement with observed estimates of the SMFs divided by type, for both our simulations. We are in fairly good agreement with data from G19 in all redshift bins, considering that G19 study has been conducted in a very conservative way and, therefore, its results represent a lower limit to the number of massive and quiescent galaxies at those redshifts and also considering that this work and G19 adopt a different classification of for red/quiescent objects (based on the sSFR for G19 and on SMFs by type in this work).

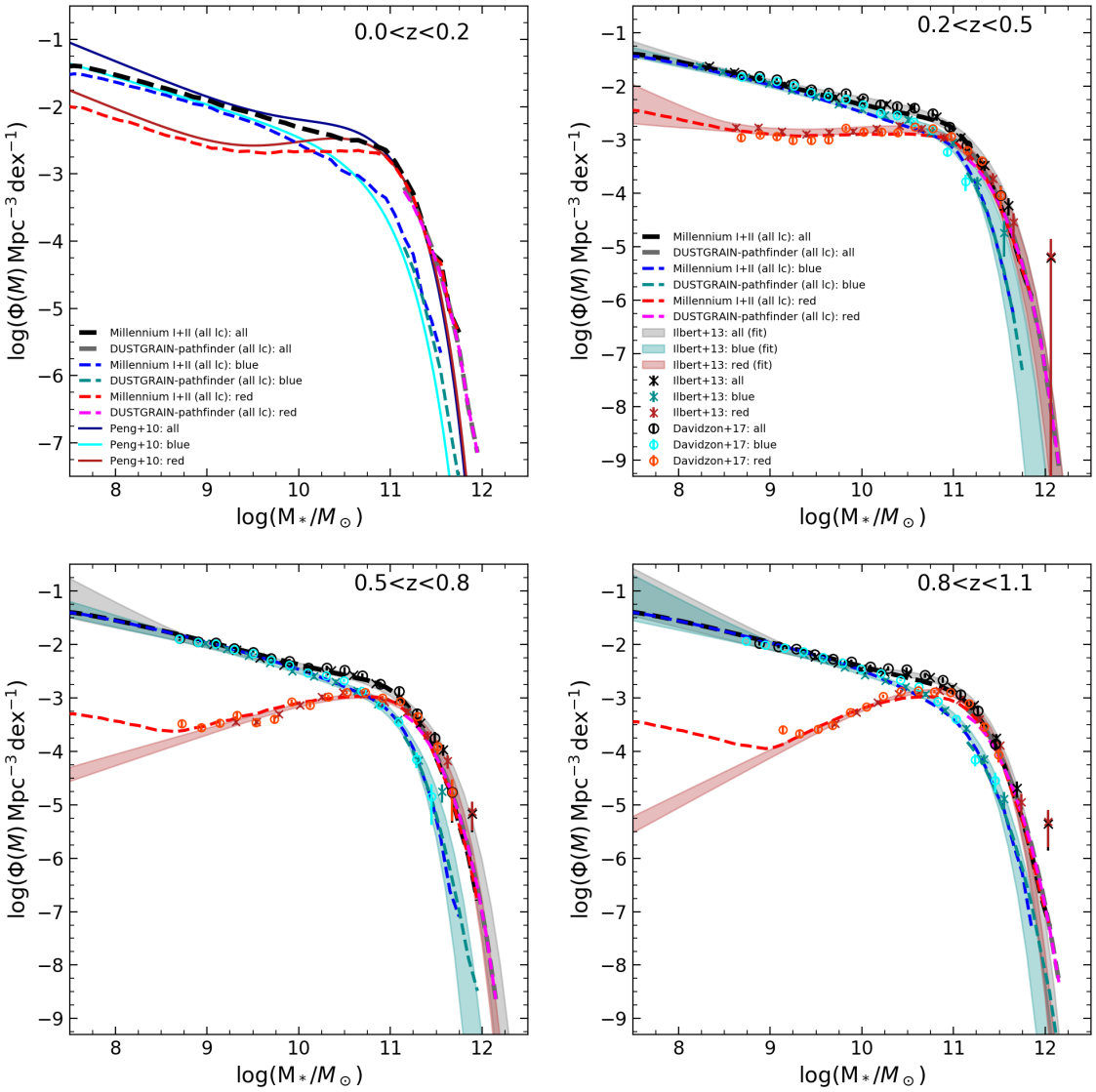

Fig. 4.12 Stellar mass function evaluated on the Millennium I+II and DUSTGRAIN-*pathfinder* simulations, divided by type. We show with dashed black, blue and orange the results on the Millennium I+II simulation for the total, star-forming and quiescent galaxies, respectively, from $z = 0$ to $z \sim 1$. With dashed grey, dark-cyan and magenta lines, the results on the DUSTGRAIN-*pathfinder* simulation are shown for the global, star-forming and quiescent population, respectively. For both simulations, we evaluated the SMFs on all available lightcones and averaged between their results. We also show with colored solid lines (and shaded areas) the best-fit results of the literature results we used to calibrate the star-forming/quiescent galaxy division (i.e. Peng et al. 2010 and Ilbert et al. 2013) for the global, star-forming and quiescent population. In addition, with crosses and open points we show the $1/V_{max}$ results for the works by Ilbert et al. (2013) and Davidzon et al. (2017), respectively, for the three populations of galaxies.

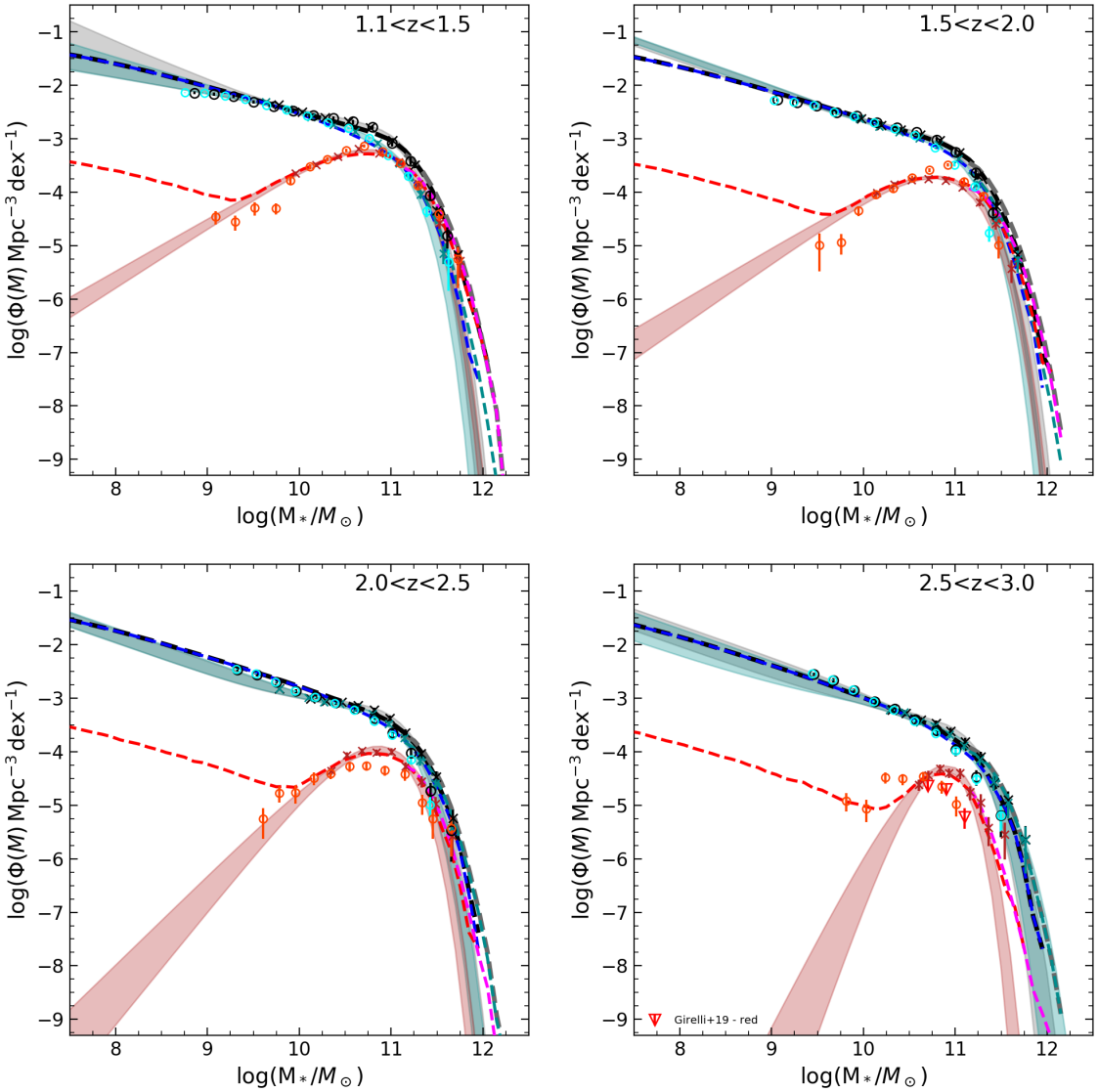

Fig. 4.13 Stellar mass function evaluated on the Millennium I+II and DUSTGRAIN-*pathfinder* simulations, divided by type from $z \sim 1$ to $z \sim 3$. Lines and symbols as in Fig. 4.12 with the addition of literature observed stellar mass functions by Girelli et al. (2019).

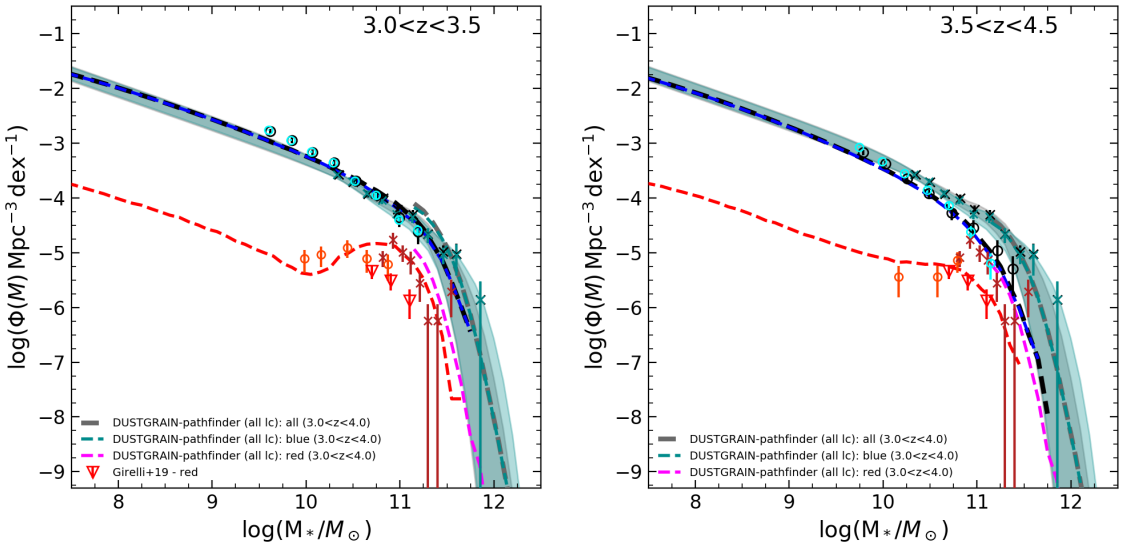

Fig. 4.14 Stellar mass function evaluated on the Millennium I+II and DUSTGRAIN-*pathfinder* simulations, divided by type from $z \sim 3$ to $z \sim 4.5$. Lines and symbols as in Fig. 4.13.

4.3 Step 3: run EGG

As a third step, with informations about the stellar mass, redshift and star-forming/quiescent flag, we can assign other physical properties to galaxies by running the public code EGG (Empirical Galaxy Generator) by Schreiber et al. (2017, 2018).

The EGG code is a C++ code that has been designed to generate large mock galaxy catalogs for deep fields from the UV to the submillimeter. The procedure implemented in EGG is purely empirical and has been calibrated to produce realistic observable properties, with an emphasis on reproducing accurate flux distributions across the electromagnetic spectrum. The calibration of EGG was performed on the deep CANDELS fields (Grogin et al., 2011; Koekemoer et al., 2011), where rich photometry is available for galaxies as faint as $R \sim 27$ (at 5σ depth).

In the EGG model, each galaxy is represented as a two-component system composed of a disk and a bulge, and to each component is attributed a different SED based on recipes (see Schreiber et al. 2017 for a detailed description) that are tied to three main galaxy properties: its total stellar mass, its redshift, and its type (star-forming or quiescent). The code may generate ex-novo on its own these three main properties (by randomly extracting from CANDELS distribution functions) or can take them from the user. We use the latter configuration, feeding the code with our mock catalogs in order to maintain the halo information from the DM simulations. In addition, as inputs to the code, we also provide the filter transmission curves of the bands for which we are interested in calculating the photometry. We chose several bands of different instruments and telescopes ranging from the UV to the infrared listed in Table 4.1.

We sketch in Fig. 4.1 the workflow followed by EGG (and more in general by the whole mock catalog we produce) and describe its steps in the following. Once, for each galaxy, its total stellar mass, its redshift, and its type are set, a probabilistic model is used to randomly assign to each galaxy its morphological parameters. More in detail, the code considers that each galaxy is made by a bulge (with Sersic index $n = 4$) and a disk (with $n = 1$). The fraction of the stellar mass that goes into one or the other component is defined by the bulge-to-total ratio (B/T), which is estimated with the results by Lang et al. (2014) who measured the average B/T ratio in the CANDELS fields, using the following relations:

$$\log(B/T)_{SF} = -0.7 + 0.27 \times (\log(M_*/M_\odot) - 10), \text{ for SF galaxies;} \tag{4.1}$$

$$\log(B/T)_{Q} = -0.3 + 0.1 \times (\log(M_*/M_\odot) - 10), \text{ for Q galaxies.} \tag{4.2}$$

Then a log-normal scatter of 0.2 dex is added in order to simulate the width of the distribution reported in Lang et al. (2014). Other morphological parameters (such as the axis ratio and half-light radius) are calibrated using van der Wel et al. (2012) and assigned to both the bulge and the disk of each galaxy.

At the same time, given the redshift and the stellar mass, the code assigns a star-formation rate (SFR) to each galaxy by following the Two Star Formation Mode model (Sargent et al., 2012), recalibrated with the results of Schreiber et al. (2015). This model relies on the existence of the

Table 4.1 List of filters used in this work to generate photometry through EGG.

Telescope/Instrument	Filter	$\lambda_{\rm eff}$ (Å)	$\Delta\lambda$ (Å)
Galex	FUV	1545.8	233
Galex	NUV	2313.9	748
CFHT-MegaPrime	u	3823.3	670
CFHT-WIRCAM	J	12538.1	1560
CFHT-WIRCAM	H	16311.4	3000
CFHT-WIRCAM	$K_{\rm s}$	21590.4	3120
LSST	u	3670.7	623
LSST	g	4826.8	1425
LSST	r	6223.2	1358
LSST	i	7545.9	1245
LSST	z	8690.9	1021
LSST	y	9710.2	853
Subaru-SC	B	4458.3	946
Subaru-SC	V	5477.8	955
Subaru-SC	r	6288.7	1382
Subaru-SC	i^{+}	7683.9	1497
Subaru-SC	z^{++}	9105.7	1370
Subaru-SC	$NB711$	7119.9	72.5
Subaru-SC	$NB816$	8149.4	119.5
Subaru-HSC	g	4776.9	1245
Subaru-HSC	r	6288.5	1360
Subaru-HSC	i	7683.7	1475
Subaru-HSC	z	8906.1	760
Subaru-HSC	y	9791.4	820
Ultra-VISTA	Y	10214.2	970
Ultra-VISTA	J	12534.6	1720
Ultra-VISTA	H	16453.4	2900
Ultra-VISTA	$K_{\rm s}$	21539.9	3090
HST-WFC3	$F435W$	4222.5	1030
HST-WFC3	$F775W$	5354.4	1180
HST-WFC3	$F850LP$	9194.4	1530
HST-WFC3	$F098M$	9879.6	1650
HST-WFC3	$F105W$	10577.2	2870
HST-WFC3	$F125W$	12500.9	2960
HST-WFC3	$F160W$	15419.0	2800
Blanco Telescope-DECAM	g	4841.8	1290
Blanco Telescope-DECAM	r	6438.5	1470
Blanco Telescope-DECAM	i	7820.9	1470
Blanco Telescope-DECAM	z	9172.3	1470
Euclid	VIS	7156.4	3640
Euclid	Y	10861.6	2660
Euclid	J	13686.6	4040
Euclid	H	17726.6	5020
Spitzer-IRAC	[3.6μm]	35634.3	7460
Spitzer-IRAC	[4.5μm]	45110.1	10110
Spitzer-IRAC	[5.8μm]	57593.4	14140
Spitzer-IRAC	[8.0μm]	79594.9	28760
Spitzer-MIPS	[24μm]	238497.0	52320

$SFR - M_*$ sequence and assigns to galaxies a SFR based on its redshift, mass and type, following these relations:

$$\begin{aligned}\log(SFR_{SF}) = \log(M_*/M_\odot) - 9.67 + 1.82\log(1+z) \\ - 0.38\, max[0.0, \log(M_*/M_\odot) - 9.59 - 2.22\log(1+z)] \text{ for SF galaxies;}\end{aligned} \tag{4.3}$$

$$\log(SFR_Q) = min[\log(SFR_{SF}), 0.5(\log(M_*/M_\odot) - 11) + (\log(1+z) - 0.6)] \text{ for Q galaxies.} \tag{4.4}$$

In addition, a dispersion of 0.3 dex for SF galaxies and 0.4 dex for Q galaxies is implemented . Moreover, the 3.3% of galaxies are randomly selected and put in a "starburst" mode where their SFR in enhanced by 0.72 dex (i.e. a factor of ~ 5.2, following Schreiber et al. 2015 and Rodighiero et al. 2011).

Then, the model generates a pair of $(U-V)$ and $(V-J)$ rest-frame colors for the bulge and disk components separately. These colors are then used to pick a SED from a lookup table. Once a rest-frame SED is attributed to a galaxy bulge and disk, the model redshifts the SED to the observed frame and then applies absorption from the intergalactic medium (using the prescription by Inoue et al. 2014). The SEDs in the lookup table were produced by averaging the SEDs of observed galaxies with similar colors. The SEDs of observed galaxies were chosen as the best-fit SEDs produced by a SED-fitting code (FAST; Kriek et al. 2009) and using the photometric redshifts produced with EAzY (Brammer et al., 2008) that used model SEDs by Bruzual & Charlot (2003) SPS and Calzetti et al. (2000) dust law on $z \sim 1$ galaxies from the COSMOS survey (Scoville et al., 2007). Even though the resulting lookup table only contains 250 unique SEDs in the optical, the fact that each galaxy has a different SED for its bulge and disk, and a different bulge-to-total ratio, ensures that the chances of having two galaxies in the mock catalog with the exact same SED are small. This is even more true since emission lines fluxes are also randomly drawn from the disk component (emission lines from the bulge component are considered negligible). The emission lines included in the code, in our range of interest, are (from long to short wavelength) Hα, [N II], [O III], Hβ, Hγ, Hδ, [O II] and Lyα. The first line assigned by the code is Hα for which the luminosity is set using the Kennicutt (1998) conversion factor and the star-formation rate (SFR) generated by EGG, with a random scatter of 0.15 dex to account for the fact that the EGG SFR is a 100 Myr average while Hα is tracing shorter timescales. The rest of the Balmer series is then generated using line ratios of case-B recombination. For [O III] and [N II], Schreiber and collaborators have calibrated new empirical relations using Baldwin et al. (1981) diagram (BPT diagram) as observed in the SDSS DR7 catalogs (Brinchmann et al., 2004) to link these lines to the Hα and Hβ fluxes. To evaluate such empirical relations, first the gas-phase metallicity is defined as $Z = \log(O/H) - \log(O/H)_\odot$ and has been estimated from the stellar masses and SFRs using the empirical Fundamental Metallicity Relation by Mannucci et al.

(2010):

$$12+\log(O/H) = 8.9+0.37\left[\log\left(\frac{M_*}{M_\odot}\right)-10\right]-0.14\log(SFR)-0.19\left[\log\left(\frac{M_*}{M_\odot}\right)-10\right]^2 \\ -0.12\left[\log\left(\frac{M_*}{M_\odot}\right)-10\right]\log(SFR)-0.054\left[\log(SFR)\right]^2. \tag{4.5}$$

Then, other line ratios are defined: $R_{\beta 3}=\log([OIII]/H\beta)$, $R_{\alpha 2}=\log([NII]/H\alpha)$, $R_+=R_{\beta 3}+R_{\alpha 2}$ and $R_-=R_{\beta 3}-R_{\alpha 2}$ and such relations are fitted to the quantities in SDSS:

$$\langle R_-\rangle = -0.08498-1.06Z+5.673Z^2+3.383Z^3 \tag{4.6}$$

$$\sigma[R_-] = 0.2666-0.2179Z+0.4402Z^2+1.457Z^3 \tag{4.7}$$

$$\langle R_+\rangle = -0.6416-0.5353R_- -0.2532R_-^2+0.0118R_-^3 \tag{4.8}$$

$$\sigma[R_+] = 0.12-0.064R_- +0.0423R_-^2-0.00507R_-^3 \tag{4.9}$$

However, such relations are only valid for SDSS-like galaxies (i.e. $z\sim 0$) and, therefore, in the code a correction for high redshift galaxies is applied. In particular, to take into account the redshift evolution in the $[NII]/H\alpha$ ratio (Shapley et al., 2015), an offset is added (calculated from a linear interpolation between 0 and 0.3 dex from $z=1$ to $z=2.3$, respectively) for galaxies with $\log(M_*/M_\odot)<10.5$.

Also [O II] has been calculated from the SDSS data using the ratio [O II]/Hβ. In particular, the quantity $R_{\beta 2}$ is defined as $R_{\beta 2}=\log([OII]/H\beta)$, and the following relations are fitted on SDSS data, after correcting for dust reddening using the Balmer decrement and the Calzetti et al. (2000) curve:

$$\langle R_{\beta 2}\rangle = 0.4967+0.3529R_{\beta 3}-0.46R_{\beta 3}^2-0.2208R_{\beta 3}^3 \tag{4.10}$$

$$\sigma[R_{\beta 2}] = 0.07-0.02R_{\beta 2}+0.0524R_{\beta 3}^2+0.0262R_{\beta 3}^3 \tag{4.11}$$

Finally for Lyα, following Sobral et al. (2018) the line luminosity is set to be 8.7 times the one of Hα and is attenuated with a random escape fraction tied to the galaxy's dust attenuation using the prescription of Hayes et al. (2010).

For all other lines, the attenuation by dust was generated using the Calzetti et al. (2010) dust screen prescription, using the attenuation of the continuum multiplied by a factor $A(z)$=1.7, 1.3, and 1.0 at $z=0$, 1, and 2, respectively (Pannella et al., 2015), plus a random scatter of 0.1 dex, and, more precisely, following this relation: $A_{V,lines}=0.5\times A(z)\left[0.95\times\log(SFR/SFR_{UV})+A_{V,disk}\right]$, where $A(z)$ is the extra factor mentioned above, SFR_{UV} is the star-formation rate in the UV and $A_{V,disk}$ is the dust extinction for the disk component of the galaxy. This result is very similar to the one found in Saito et al. (2020). In addition, all lines are assumed to have a velocity dispersion of $\log(\sigma_v/\mathrm{km\,s^{-1}})=0.12\log(M_*/10^{10}M_\odot)+1.78$ with a random scatter of 0.3 dex (following the results by Stott et al. 2016).

The code, however, has some limitations for obtaining a realistic representation of the Universe. In particular the galaxy SEDs generated by EGG do not include reddening from the Milky Way and the produced catalogs are missing foreground stars and active-galactic nuclei (AGNs, or quasars). This work is focused on galaxies and on creating a galaxy mock catalog with intrinsic properties of galaxies. However, in real catalogs stars and AGNs are present and can potentially be a source of contamination at any redshift. In addition, for observations, the Milky way extinction is present and also, depending on the instrument used and the observing conditions, a certain noise in photometry is usually present. These issues are not addressed in this work but can be source of biases and, therefore, when using the final mocks of this work one needs to take this caveat into consideration.

To sum up, the purely empirical EGG code has been calibrated on the SDSS, COSMOS and CANDELS fields for different physical properties. It takes in input informations about the stellar mass, redshift and a star-forming/quiescent classification in order to evaluate physical properties through empirical recipes such as the star formation rate, the photometry, the sizes, the dust extinction and the emission lines. We run the code EGG on both our mocks (the DUSTGRAIN-*pathfinder* and Millennium I+II) with the bands listed in Table 4.1. To conclude, following the scheme in Fig. 4.1, we have built a mock catalog assigning galaxies properties the halos of the lightcones from the Millennium I+II and DUSTGRAIN DM simulations.

In the next Chapter we will proceed to test some physical properties that have been evaluated with the code EGG and make some forecasts for future surveys and galaxy formation and evolution studies.

5

VALIDATION OF THE MOCKS AND FORECASTS

Given the workflow described in Chapter 4, we are able to produce a completely empirical mock catalog starting from just a few information from a DM N-body simulation. To assess the performance and possible limitations of our method, in this Chapter, we compare mock galaxy properties, distributions, and relations to observations that were not used to calibrate our methodology.

For this purpose we use a single lightcone for each DM simulation adopted in this work (i.e. DUSTGRAIN and Millennium I+II) and run the entire workflow.

For the Millennium I+II we chose lightcone 23, given that its halo mass function resembles the "global HMF" defined in Sect. 2.3.2. The lightcone ranges from $z = 0$ to $z = 8$ with halo masses $M_{200} > 1.7 \times 10^{10} M_{\odot}$, over an area of 3.14 deg^2.

For the DUSTGRAIN-*pathfinder* we chose the lightcone 1 (for the same reason described above) that goes from $z = 0$ to $z = 4$ with halo masses $M_{200} > 3.16 \times 10^{12} M_{\odot}$ with an area of 72.18 deg^2. As mentioned several times in this work (see e.g. Chap. 4), this simulation is limited to very massive objects and is complete for stellar masses $\log(M_*/M_{\odot}) \gtrsim 11$, and, therefore, it is not always possible to perform meaningful comparisons with observations that have different mass limits or very limited in area.

In the following sections, first we briefly highlight why the galaxy mock catalogs we present are useful, then we compare the mock galaxies from these realizations to the redshift evolution of observed quantities including star-formation rates and star-formation rate densities, emission lines, observed photometry, rest-frame colors and clustering signal at different redshifts. Finally, we also provide some examples of the forecasts that can be performed with the use of the mocks presented in this thesis.

5.1 Why are these catalogs useful?

Many different mock catalogs (like the well know Flagship mock catalogs[1]) will be used to provide forecasts, to optimise the scientific strategies and maximise the scientific exploitation of the Euclid mission and other future surveys and missions. In particular, such mock catalogs can be used not only to test and optimise the data selection, reduction and analysis pipelines but also to study systematics and selection effects. Therefore, a mock catalog needs to be realistic or in other words it needs to reproduce the observed universe.

The main probes of future missions like Euclid are cosmological open questions. Therefore, currently available mocks mostly concentrate on reproducing the main cosmology probes of future missions, like the 3D spatial distribution of galaxies, lensing and DM properties. However, given the large sky areas that these missions will cover, they will also bring an enormous impact in the fields of galaxy formation and evolution. In this context, the catalogs we present in this thesis represent a step forward for the creation of mocks that are useful for galaxy formation and evolution studies. In fact, apart from several physical properties (e.g. stellar mass, SFR, dust extinction), photometry (in any desired band) and emission lines, with the aid of EGG also the spectra with emission lines can be

[1] https://www.euclid-ec.org/?page$_id = 4133$

extracted in our mock catalogs. Moreover, EGG combined with the software SkyMaker (Bertin, 2009) is also able to produce galaxy images in any desired band (given that the PSF of a given instrument in the desired band is known). In addition, EGG is able to produce SEDs that can extend up to the wavelength of the input SED catalog. Therefore, with the workflow developed in this thesis it is straightforward to build mock catalogs with SED that extend from the radio to the X-rays bands by changing the input SED catalog. With all these information, several useful insights for galaxy evolution studies can be extracted such as the galaxy-halo connection, the evolution of the SFE and SFR with cosmic time, clusters and environment properties. Moreover, our catalogs can also be used to gain cosmology insights from, for example, lensing studies (with the position, halo mass and extension of the mock galaxies). In addition, our method has a "simulation independent" approach meaning that it only needs information about the DM halo masses, their redshift and position and, therefore, is completely independent from the cosmological model build underneath the DM halos. Therefore, using this method one can easily construct new mock catalogs and also perform alternative cosmology studies, for example, using the DUSTGRAIN simulation set that modelled alternative gravity solutions to the general relativity. Moreover, given the elasticity of the method we propose, it is rather straightforward and fast to produce ex-novo new catalogs once a new DM simulation is available on e.g. larger sky areas and/or volumes. However, as mentioned in the previous chapter, the mocks produced with the workflow described in this thesis do not contain any information about the characteristics of the instrument that will be used or the galaxy survey details. It is therefore essential that, when using our mock for predictions on observations, an error due to the instrument systematics errors needs to be applied. Moreover, as already mentioned, also an error in the photometry and, consequently, in the physical properties still needs to be applied.

5.2 Photometry and colors

In Figures 5.1, 5.2, 5.3 and 5.6 we compare the number counts of our mocks to several observations in the u-CFHT, i-Subaru, H-UltraVISTA and $[3.6]\mu m$ IRAC bands (see Table 4.1 for details on the filters). In particular we show the number counts normalized by the area and the binning of each plotted dataset. In addition, in Fig. 5.4, we show the number counts in the H band divided into galaxy types and in Fig. 5.5 we also show the $M_* - m_H$ plane in several redshift bins.

The procedure implemented in EGG to extract photometry and colors starts by splitting each input galaxy (characterized by a stellar mass, a redshift and a type) into its bulge and disk components and then assigns to each component $(U-V)_{rf}$ and $(V-J)_{rf}$ colors. From these colors, a SED is assigned from EGG's library to the bulge and disk of each galaxy and then the two SEDs are combined with each other and with emission lines to create the final SED. With the final SED, photometry can be easily calculated in any desired band.

In all Figures we compare with the COSMOS2015 catalog (Laigle et al., 2016)[2]. For all bands we show data from the 3″ aperture corrected for the photometric and systematic offsets and galactic extinction in order to compute the total magnitudes. In addition, when using the stellar mass of the catalog we use the median stellar mass $M_{*,med}$ of the posterior distribution function. In order to perform a fair comparison with DUSTGRAIN results we also plot COSMOS2015 results selected to have stellar masses $\log(M_{*,med}/M_{\odot}) \geq 11$.

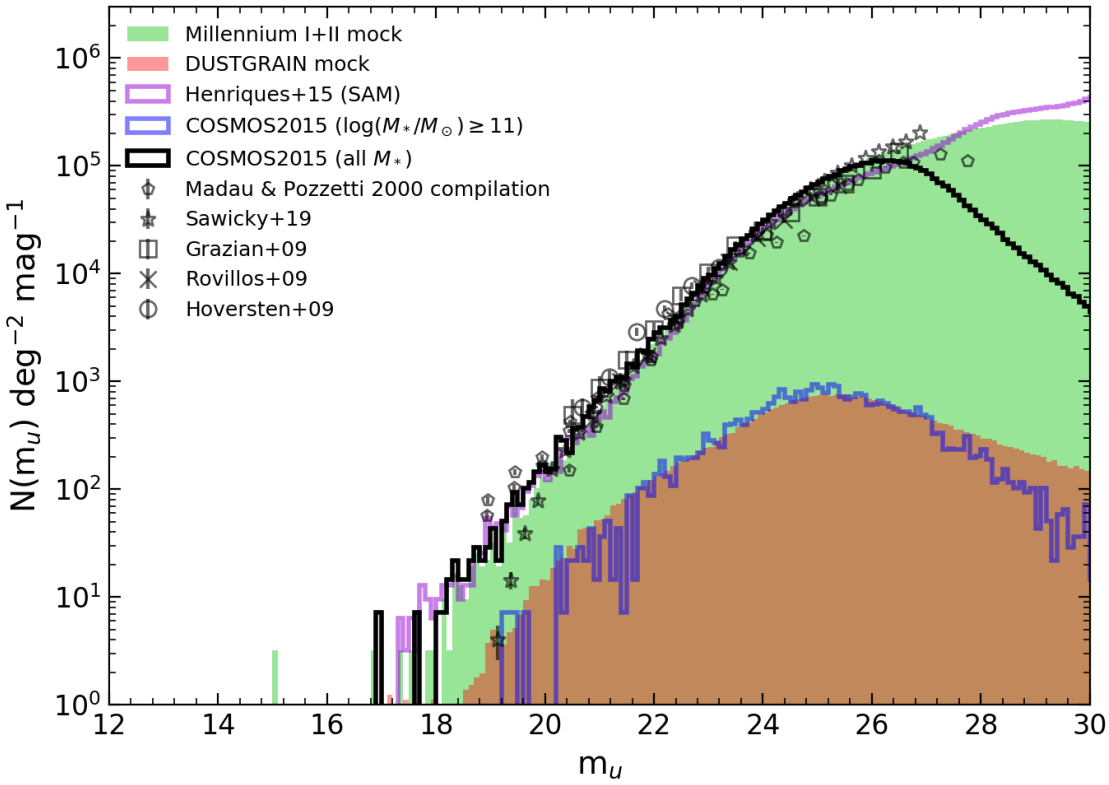

Fig. 5.1 Number counts in the u band of the CFHT telescope (see Table 4.1 for details) normalized by the area and the binning used to count objects. Results for the Millennium I+II and DUSTGRAIN mocks are shown with green and red filled histograms, respectively. Results by Henriques et al. (2015) SAM are shown with a violet filled histogram, while results on COSMOS2015 (with and without a stellar mass cut at $\log(M_{*,med}/M_{\odot}) \geq 11$ to compare with DUSTGRAIN results) are shown with black and blue open histograms. Literature results include the compilation by Madau & Pozzetti (2000) and individual results by Grazian et al. (2009), Rovilos et al. (2009), Hoversten et al. (2009) and Sawicki et al. (2019).

[2]We selected the data of the catalog from the region with the best quality photometry by applying the following flags: FLAG_PETER=1, which defines good optical areas, that is, masking regions where bright stars may contaminate the photometry of nearby objects, while FLAG_COSMOS=1 and FLAG_HJMCC=0 define the area in COSMOS field covered by UltraVISTA. Moreover, only "galaxy type" objects are selected (i.e. TYPE=0). The resulting total area of the catalog is 1.38 deg^2.

In addition, we also show in all Figures the results of the SAM by Henriques et al. (2015) downloaded from the VIRGO - Millennium Database[3].

We also collected, for each band, several observational results from different studies, mentioned in the various captions.

In the optical band u, shown in Fig. 5.1, both our mock catalogs are in excellent agreement with observations over a wide magnitude range. It is evident that our Millennium I+II mock, compared to data from literature, is complete at least up to $m_u \sim 27$. Indeed, above our minimum halo mass (i.e. $M_h > 10^{10.37} M_\odot$) the number counts in the u band show a maximum at $m_u \sim 29$ above which the mock is probably incomplete. In addition, the Millennium I+II mock shows good agreement with COSMOS2015 data down to $m_u \sim 18$ and up to $m_u \sim 27$ with Sawicki et al. (2019). The Henriques et al. (2015) SAM is in rather good agreement with the Millennium I+II mock catalog up to $m_u \sim 25$ where it starts to differ from our results.

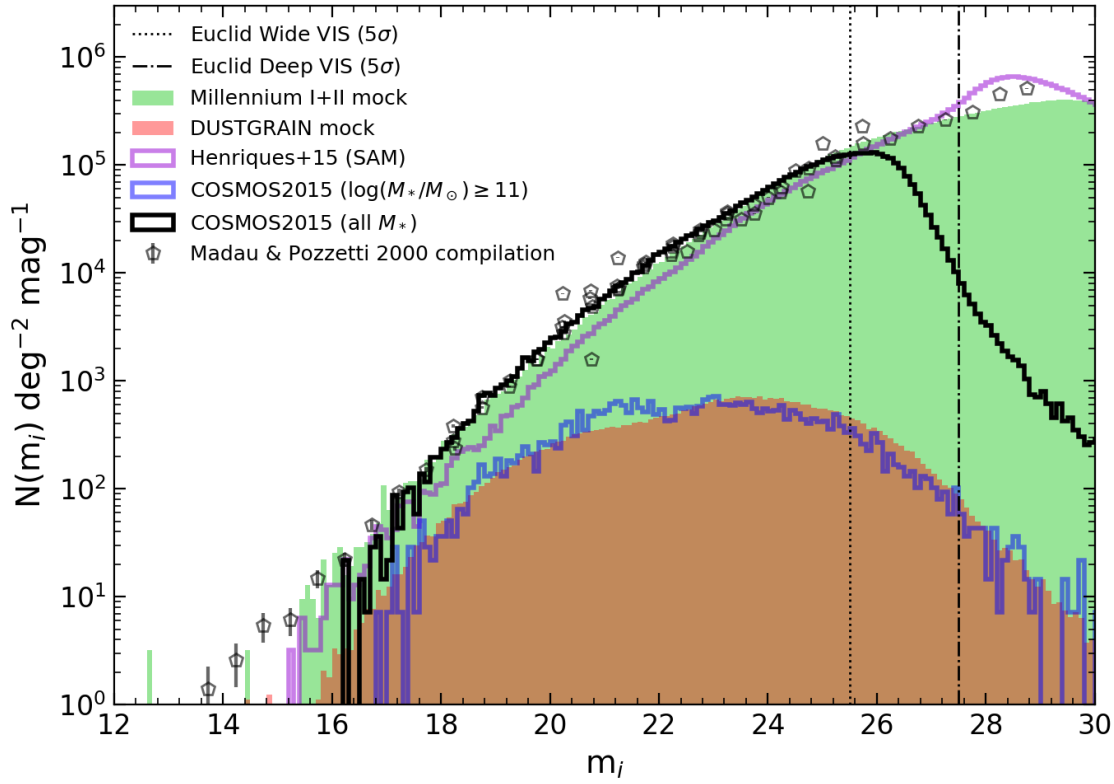

Fig. 5.2 Number counts in the i band of the Subaru Telescope (see Table 4.1 for details) normalized by the area and the binning used to count objects. Lines and points as in Fig. 5.1. We also show two vertical lines that represent the expected limiting magnitudes of the Euclid *VIS* band (see Table 4.1 for details) at 5σ. The dotted and dashed-dotted lines represent the limits for the Wide and Deep surveys, respectively.

[3] http://gavo.mpa-garching.mpg.de/MyMillennium/

Also the i band counts, shown in Fig. 5.2, are in good agreement with COSMOS2015 data down to $m_i \sim 17$ and with Madau & Pozzetti (2000) results from $m_i \sim 15$ to $m_i \sim 27.5$ and are, therefore, complete at least up to $m_i \sim 27.5$. Above our minimum halo mass (i.e. $M_h > 10^{10.37} M_\odot$) the number counts in the i band show a maximum at $m_i \sim 29.5$ above which the mock is probably incomplete. It appears that the Millennium I+II mock does not predict galaxies with magnitudes brighter than $m_i \sim 15$ (probably due to the limited area of the lightcone), while the Madau & Pozzetti (2000) datapoints show that galaxies with $14 < m_i < 15$ exist. In this band, the Henriques et al. (2015) SAM results predict lower counts with respect our results up to $m_i \sim 26$ where the trends are reversed. These differences are certainly ascribable to the different modelling techniques adopted even though exactly identifying the process that produces these low number counts in the SAM is not a trivial task and goes beyond the scope of this work. By inspecting the Euclid VIS limits (shown with vertical lines), which is a very broad-filter in Euclid encompassing the wavelengths of r, i, and z filters, it is evident that current observed catalogs (i.e. COSMOS2015) are not complete down to the Deep Survey limits, while our mocks are.

Moving towards the NIR, the number counts in the H band, shown in Fig. 5.3, appear to be in excellent agreement with observed data from the lowest ($m_H \sim 14.5$) to the highest ($m_H \sim 28$) magnitudes, and, therefore, complete at least up to $m_H \sim 28$ with $m_H \sim 28.5$ corresponding to the maximum of the H band number counts above which the mock is probably incomplete. As described for the i band, the Henriques et al. (2015) SAM shows an underprediction of the number counts with respect to our Millennium I+II mock with an overprediction at $m_H \gtrsim 26$. Also in this Figure, it is evident that our mocks are complete for the magnitude limits predicted for the Euclid survey.

In Fig. 5.4, we also show the number counts in the H band divided by galaxy type. Both the COSMOS2015 and the Henriques et al. (2015) SAM data have been divided into the two populations using the NUVrJ diagram (Ilbert et al., 2010). We divided our mock catalogs into the two populations using both the procedure described in Sect. 4.2 (a-priori division), which relies on the ratio between the best-fit Schechter functions by Peng et al. (2010) and Ilbert et al. (2013), and the $NUVrJ$ diagram (a-posteriori division). The resulting histograms appeared to be fully consistent one between the other and, therefore, for consistency with our workflow we show the results using our a-priori division. By looking at the number counts for the quiescent/passive population (right panel of Fig. 5.4) we note that at the distribution of our mocks and the results from the COSMOS2015 catalog appear different. In particular, it seems that the Millennium I+II mock predicts higher number counts at $m_H \lesssim 17$ and lower counts at $m_h \gtrsim 20-21$ with respect to COSMOS2015. Therefore the Millennium I+II mock catalog has a lower density of passive galaxies in the range $19 \lesssim m_H \lesssim 24.7$ (i.e. the 3σ limit of the COSMOS2015 catalog) with respect to the COSMOS2015 catalog. The DUSTGRAIN mock, on the contrary, appears to predict higher number counts of quiescent galaxies between $m_H \sim 21$ and $m_H \sim 24.7$ with respect to COSMOS2015 even though this could be explained by simply considering the different areas covered. In fact, the DUSTGRAIN mock, given its large area (72.18 deg^2) is able to catch a larger number of massive and passive galaxies. In Fig. 5.5 we also show the $M_* - m_H$ plane in several redshift bins. In this case, it emerges that the Millennium I+II and COSMOS2015 results

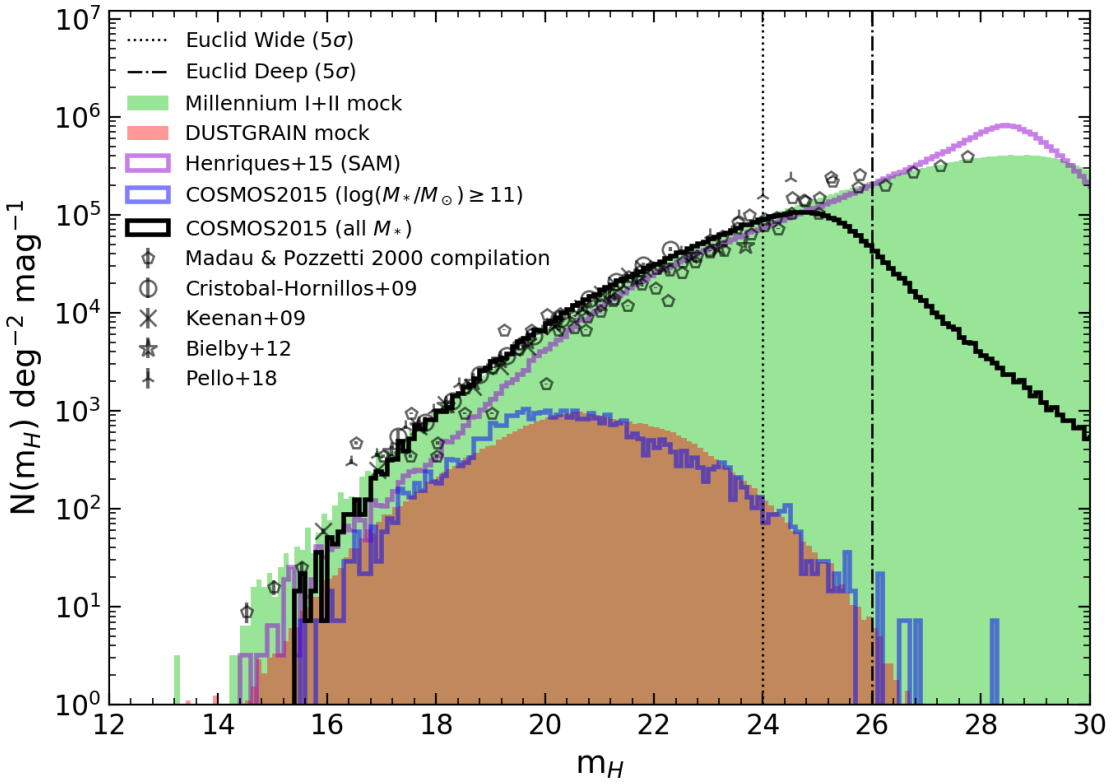

Fig. 5.3 Number counts in the H band of the UltraVISTA telescope (see Table 4.1 for details) normalized by the area and the binning used to count objects. Lines and points as in Fig. 5.1. Literature results comprise those by Madau & Pozzetti (2000), Cristóbal-Hornillos et al. (2009), Keenan et al. (2009), Bielby et al. (2012) and Pelló et al. (2018). We also show two vertical lines that represent the expected limiting magnitudes of the Euclid H band (see Table 4.1 for details) at 5σ. The dotted and dashed-dotted lines represent the limits for the Wide and Deep surveys, respectively.

are in good agreement even though our mock predicts narrower contours. This is due to the fact that in our mocks photometric errors are still not implemented and would act in the direction of broadening the contours. In addition, in this Figure the different mass limits of the COSMOS2015 catalog and our mocks are evident.

Finally, in Fig. 5.6, we show the number counts in the $[3.6]\mu$m IRAC band. The Millennium I+II mock is in good agreement with COSMOS2015 data down to $m_{[3.6]} \sim 18$ and up to the 3σ COSMOS2015 magnitude limit ($m_{[3.6]} = 25.5$). The Henriques et al. (2015) SAM once again undepredicts (with respect to our mock) the number counts for $m_{[3.6]} \lesssim 22$ and overpredicts our counts for $m_{[3.6]} \gtrsim 27$. By looking at other observations, i.e. Ashby et al. (2015) and the SPLASH-SXDF catalog (Mehta et al., 2018), our mock is in good agreement up to the faintest limit ($m_{[3.6]} \sim 26$), while an increase in the number counts is evident at $m_{[3.6]} < 18$. This increase is likely due to the contribution of stars that, at these magnitudes, become increasingly important as one moves down with magnitudes. In the COSMOS2015 catalog, stars have been removed through a χ^2 comparison of

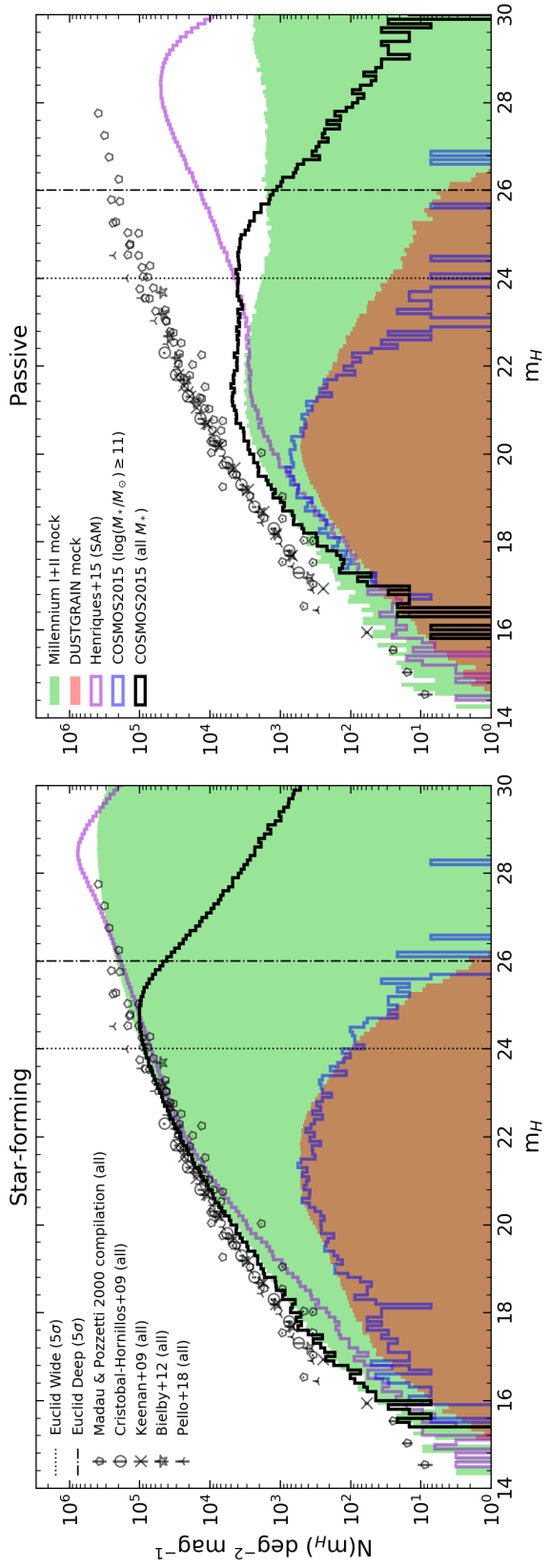

Fig. 5.4 Number counts in the *H* band of the UltraVISTA telescope (see Table 4.1 for details) normalized by the area and the binning used to count objects and divided into star-forming (left panel) and quiescent (right panel) objects. For the Millennium I+II and DUSTGRAIN mocks galaxies have been divided into the two populations using the procedure described in Sect. 4.2. For the COSMOS2015 and Henriques et al. (2015) SAM galaxies have been divided into the two populations using the *NUVrJ* diagram. Lines and points as in Fig. 5.1. Gray literature points represent the total population of galaxies and are shown as a reference.

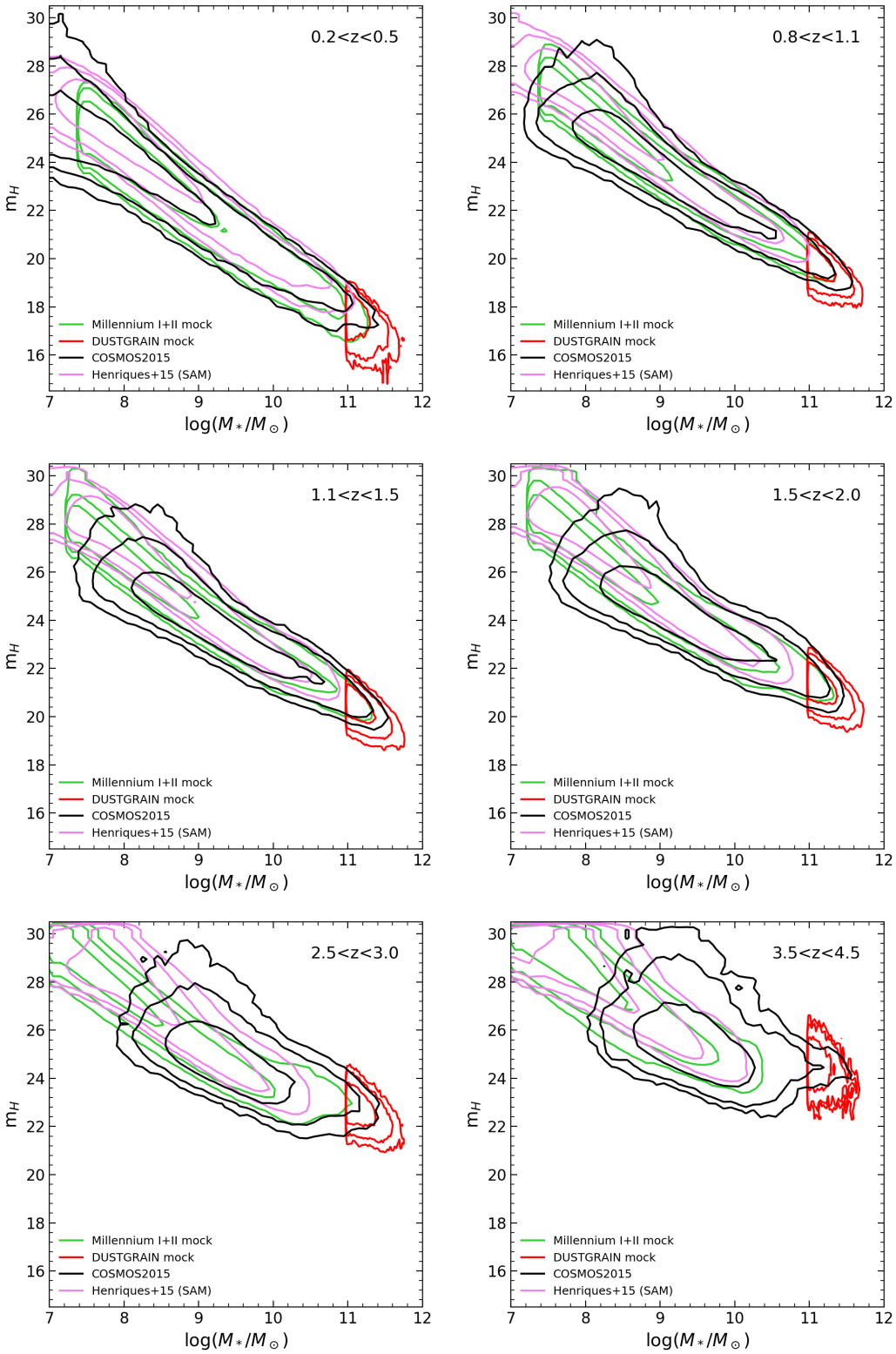

Fig. 5.5 M_* - m_H plane in six different redshift bins. The results for the DUSTGRAIN and Millennium I+II mocks are shown with red and green contours, respectively. Results from Henriques et al. (2015) SAM are shown with violet contours and results on the COSMOS2015 catalog with black contours. For all the results shown, the contours encompass 65, 95 and 99% of the objects.

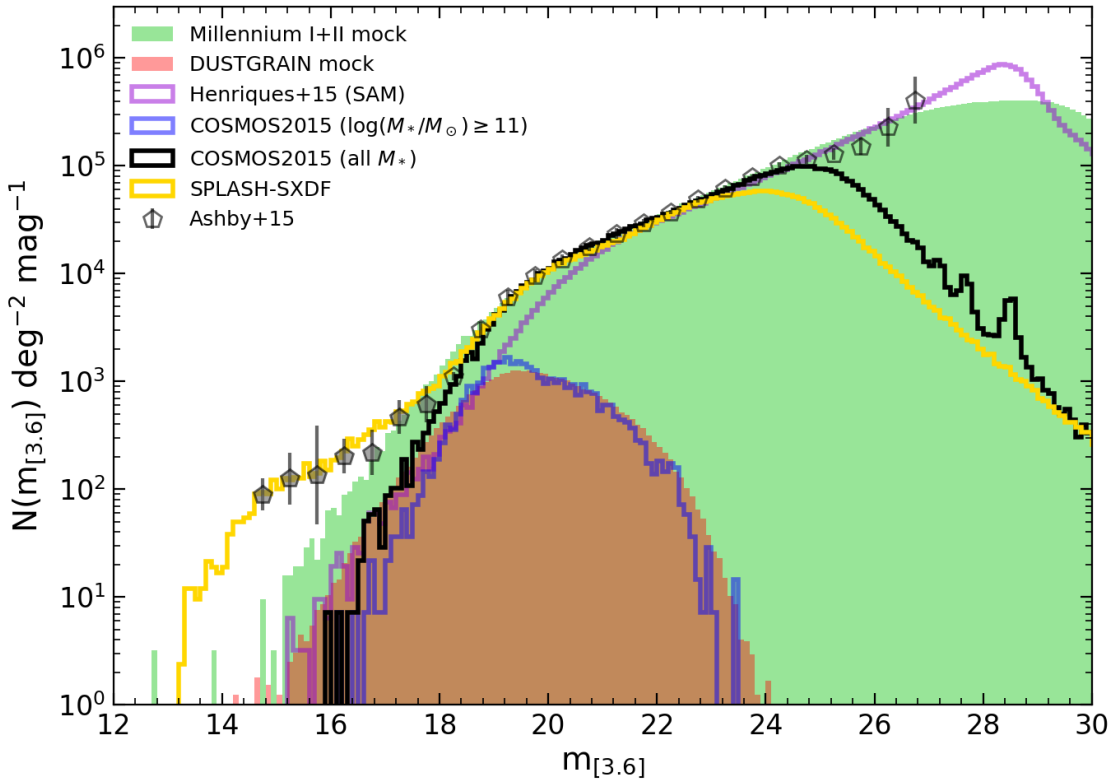

Fig. 5.6 Number counts in the $[3.6]\mu$m IRAC band (see Table 4.1 for details) normalized by the area and the binning used to count objects. Lines and points as in Fig. 5.1. In addition, we also show number counts of the SPLASH-SXDF catalog (Mehta et al., 2018). At $m_{[3.6]} < 18$ the contribution of stars becomes important even though their exact contribution cannot be assessed with accuracy. Literature results include those by Ashby et al. (2015) shown with pentagons. Where points are filled indicate the range where contamination of stars becomes dominant.

stars and galaxies templates, while for Ashby et al. (2015) and the SPLASH-SXDF catalog stars have not been removed. In our mocks, stars are not added and therefore at $m_{[3.6]} < 18$ it is not trivial to perform a reliable comparison of number counts in this band. Finally, we find that above our minimum halo mass (i.e. $M_h > 10^{10.37} M_\odot$) the number counts in the $[3.6]\mu$m IRAC band show a maximum at $m_{[3.6]} \sim 29$ above which the mock is probably incomplete.

To sum up, we find an overall good agreement in the number counts of observed photometry from the optical to the IR bands over a large magnitude range for the total population of galaxies. The overall good agreement between our mocks and observations suggests that the SED assignment, based on stellar mass and galaxy type, performed in EGG is well calibrated and reproduces good a large variety of observational results over a large magnitude range. However, a deeper investigation is needed in order to characterize the differences that emerge when number counts divided by galaxy type are considered.

Rest-frame colors

In order to address the differences in number counts when galaxy types are considered, we investigate in this section how the mock catalogs populate the rest-frame $NUVrJ$ diagram (Ilbert et al., 2010; Williams et al., 2009) and how the results compare with COSMOS2015 data. It is also fundamental to study the $NUVrJ$ diagram in order to asses the performances of the code EGG and, eventually, identify its limitations and re-calibrate the code.

We show in Figures 5.7, 5.8 and 5.9 the $NUVrJ$ diagram from $z = 0$ to $z = 4$ (divided into several redshift bins) for the Millennium I+II mock catalog and COSMOS2015 catalog. For both catalogs we selected only objects with $m_H < 25$ and $\log(M_*/M_\odot) \geq 9.5$ in order to ensure a fair comparison and that both catalogs are complete at these masses. In Figs. 5.10 and 5.11 we show the $NUVrJ$ diagram from $z = 0$ to $z = 4$ for the DUSTGRAIN mock and COSMOS2015 catalogs, selected with $\log(M_*/M_\odot) \geq 11$.

In the plots we also highlight the fraction of objects that populate each region of the diagram: quiescent galaxies populate the region marked with A (where $(NUV-r)_{rf} > 3(r-J)_{rf}$ and $(NUV-r)_{rf} > 3.1$). We then select a "transition" region (0.5 mag broad), marked with B where we expect to have objects that may transition from a star-forming to a quiescent phase. Finally, in the region marked with C we expect to find star-forming galaxies. In left panels of the figures, we show the results of the Millennium I+II mock that are colored according to our SF/Q division (see Sect. 4.2). It is evident that, for example, objects classified as quiescent by our method mostly populate region A, even though some of them also populate the other two regions. An analog result is found for star-forming objects that mostly populate region B and C but also lay in region A. By comparing the fraction of SF/Q galaxies in the mock (labeled as $f_{Q,mock}$ in left panels) and the fraction of objects in regions $(B+C)$ and A for COSMOS2015, we find fully consistent results. This was already evident in Figs. 4.12, 4.13 and 4.14, where we have shown that the mocks SMFs divided by type are consistent with observations. However, when comparing the fraction of objects in regions A, B or C for the mock and the COSMOS2015, some differences emerge that are less than $\sim 5\%$ at all redshifts for the Millennium I+II mock and increase to maximum differences of $\sim 20\%$ for the DUSTGRAIN mock. These differences are due to the fact that EGG calibrates the SED assignment on on the UVJ diagram instead of the $NUVrJ$ and this leads to some differences in the final outputs rest-frame colors. In addition, for the DUSTGRAIN mock, we find that its star-forming population occupies a much larger color region than COSMOS2015. These large differences can be ascribed to the very different areas covered. In fact, the DUSTGRAIN mock is able to catch a much larger number of massive galaxies at all redshifts with respect to COSMOS2015. This SED assignment calibration then, could lead also to some differences in the observed photometry when considering the two galaxy populations (as we have shown in Fig. 5.4), even though the global properties are very well reproduced.

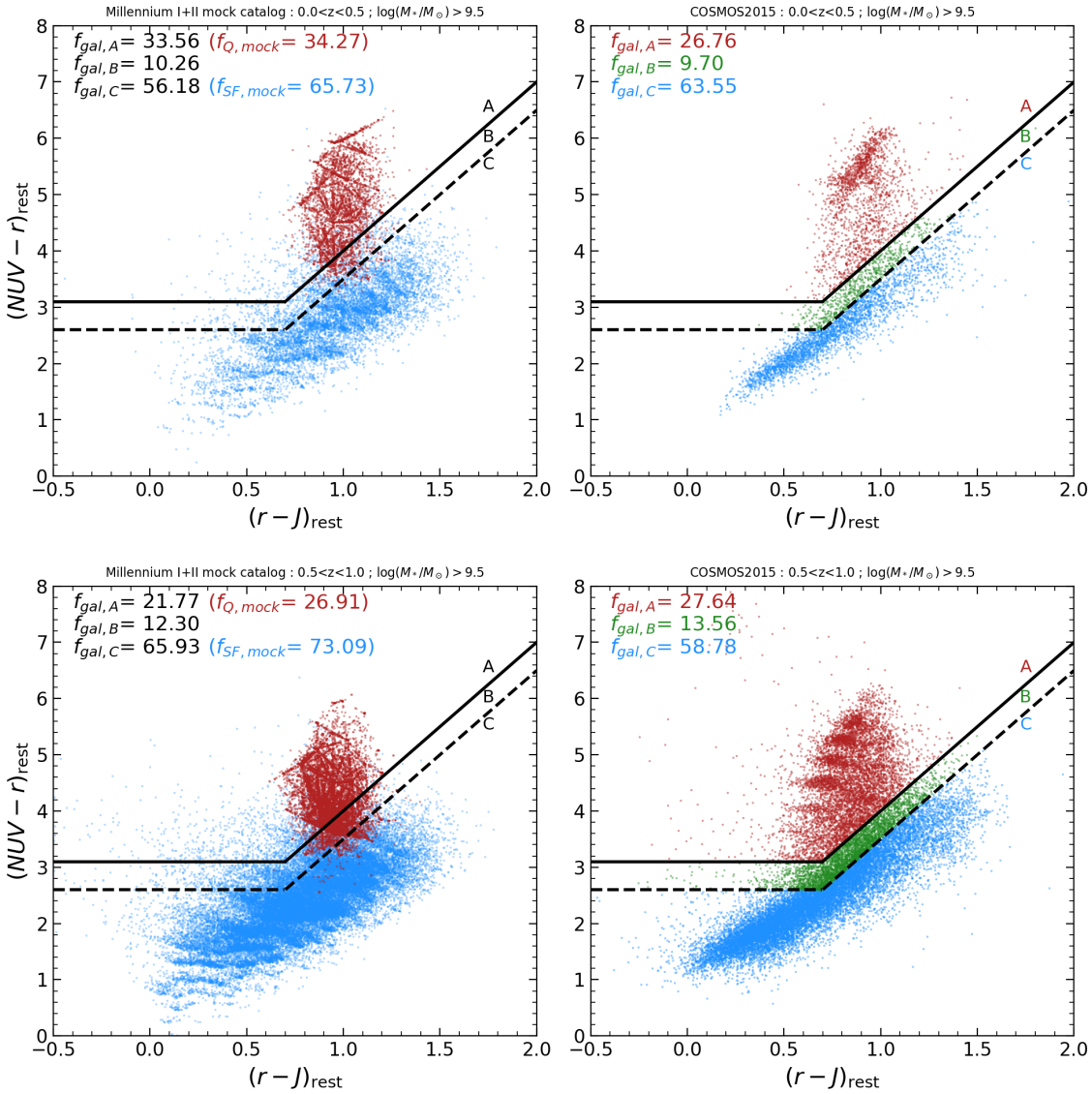

Fig. 5.7 *NUVrJ* diagram in two redshift bins (highlighted in plots) from $z = 0$ to $z = 1$ for the Millennium I+II mock catalog (left panel) and COSMOS2015 catalog (right panel). Both objects in the mock catalog and COSMOS2015 catalog have been selected with a stellar mass cut: $\log(M_*/M_\odot) \geq 9.5$. In both panels the plane is divided into three regions, labeled A, B and C, and the percentage of objects in each region is indicated in top left corners. For the panel on the left, objects are colored according to the SF/Q division implemented in the mock, devised in Sect. 4.2. In addition, the percentage of objects classified as SF or Q are indicated in parenthesis. For the right panel, objects are colored based on which region (A, B or C) they populate.

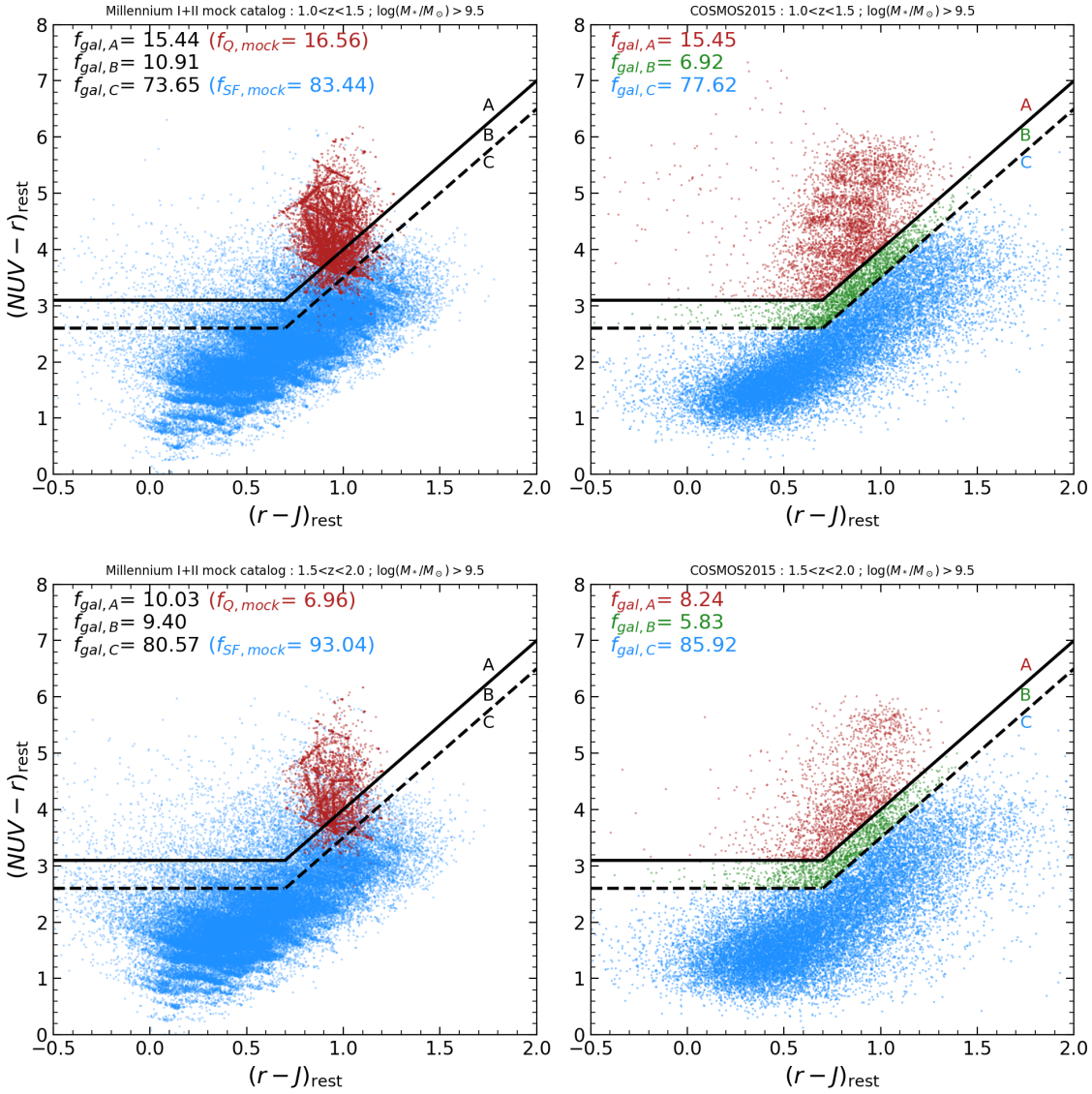

Fig. 5.8 *NUVrJ* diagram in two redshift bins (highlighted in plots) from $z = 1$ to $z = 2$ for the Millennium I+II mock catalog (left panel) and COSMOS2015 catalog (right panel). Labels, symbols and regions as in Fig. 5.7.

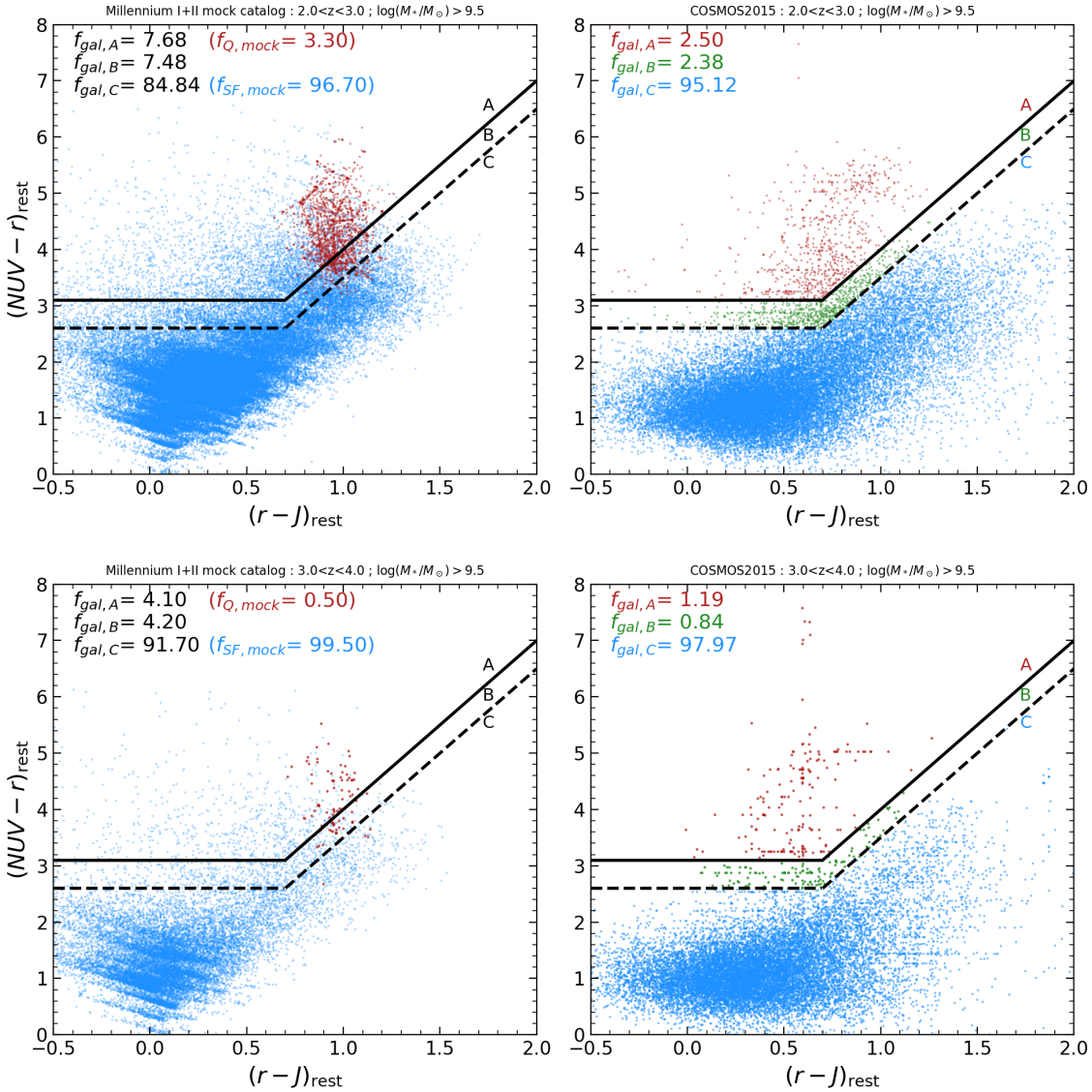

Fig. 5.9 *NUVrJ* diagram in two redshift bins (highlighted in plots) from $z = 2$ to $z = 4$ for the Millennium I+II mock catalog (left panel) and COSMOS2015 catalog (right panel). Labels, symbols and regions as in Fig. 5.7.

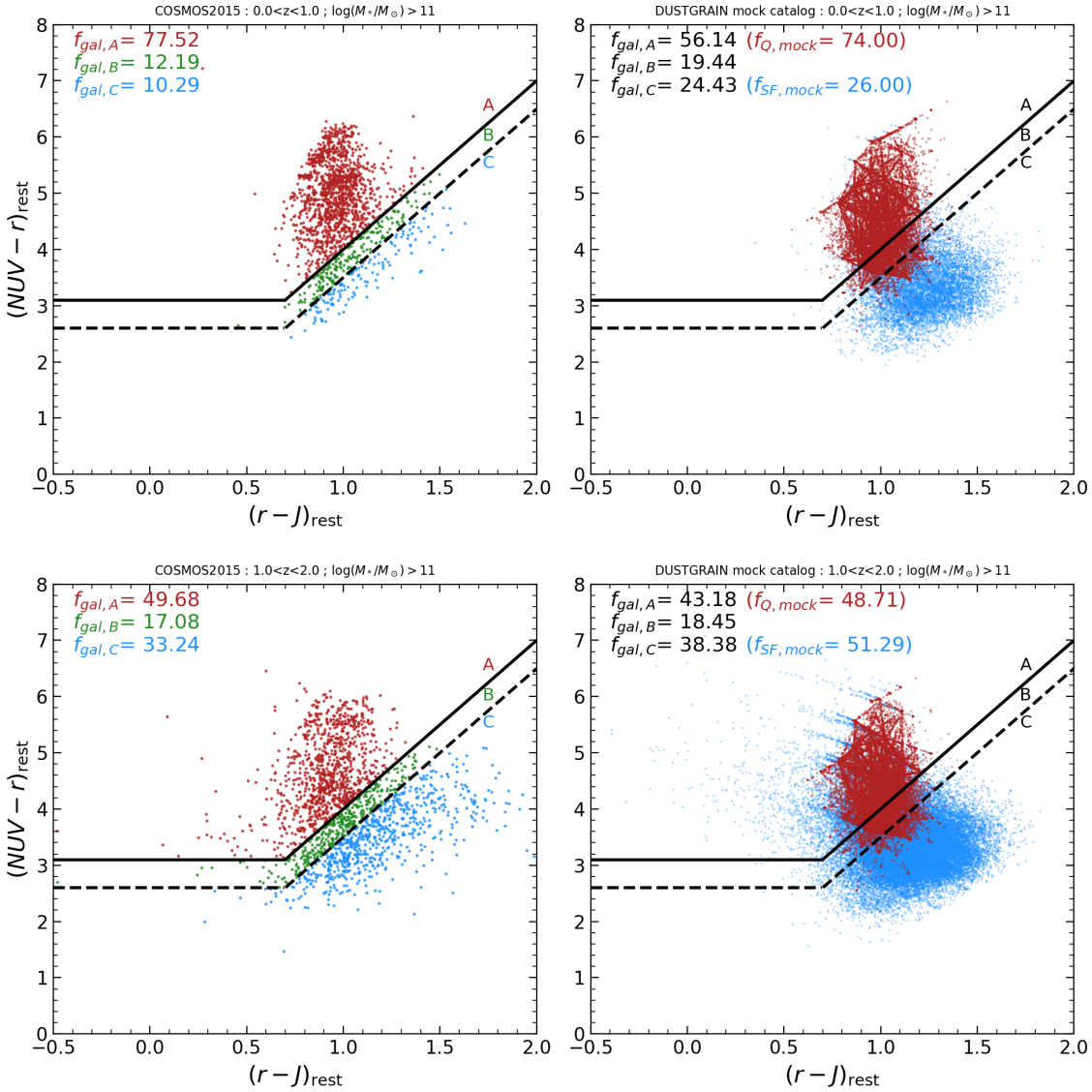

Fig. 5.10 *NUVrJ* diagram in two redshift bins (highlighted in plots) from $z = 0$ to $z = 2$ for the DUSTGRAIN mock catalog (right panel) and COSMOS2015 catalog (left panel). Both objects in the mock catalog and COSMOS2015 catalog have been selected with a stellar mass cut: $\log(M_*/M_\odot) \geq 11$, given that DUSTGRAIN mock is complete only down to those stellar masses. Labels, symbols and regions as in Fig. 5.7.

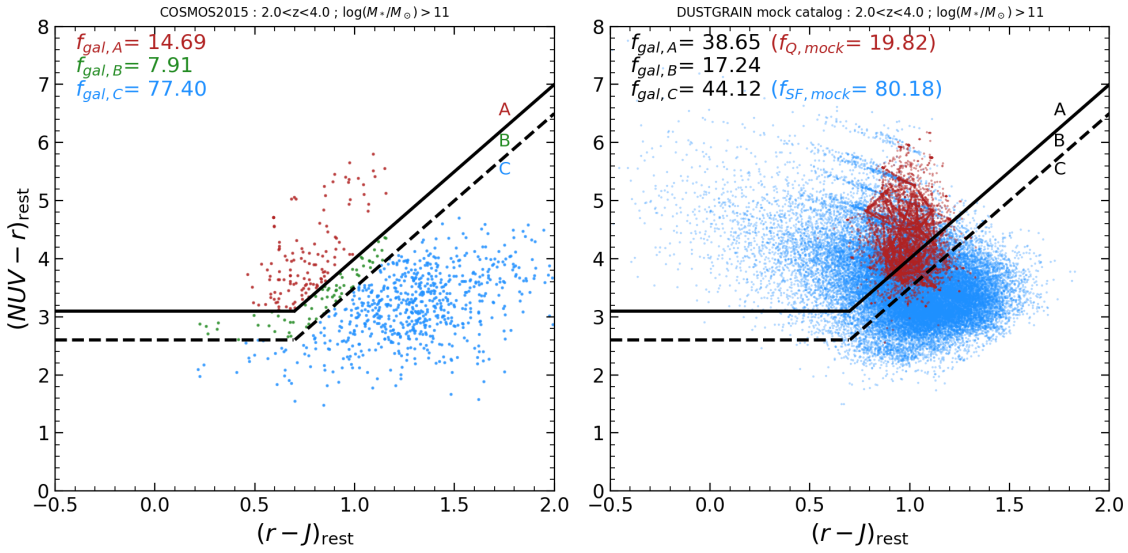

Fig. 5.11 *NUVrJ* diagram in two redshift bins (highlighted in plots) from $z = 2$ to $z = 4$ for the DUSTGRAIN mock catalog (left panel) and COSMOS2015 catalog (right panel). Labels, symbols and regions as in Fig. 5.7.

5.3 SFR

Determining the galaxy stellar mass function and the star formation rate distributions is among the foremost goals of extragalactic surveys targeting (and linking) nearby (e.g., Bell et al. 2003, Baldry et al. 2010, Bothwell et al. 2011, Baldry et al. 2012) and distant galaxies (e.g., Ilbert et al. 2010, Rodighiero et al. 2010, Ilbert et al. 2013, Muzzin et al. 2013, Davidzon et al. 2017). Therefore, an important physical property of galaxies, that needs to be reproduced with accuracy by a mock catalog, is the SFR. Star-forming galaxies at both high and low redshifts obey a tight relation: the so-called "galaxy main sequence" (e.g. Elbaz et al. 2007, Pannella et al. 2009, Speagle et al. 2014). SF galaxies on the main sequence are complemented by a component of starburst galaxies (a few percent of the total population; e.g., Rodighiero et al. 2011) with highly increased SFRs.

As described in Sect. 4.3, the code EGG assigns a SFR to each galaxy using the Two Star Formation Mode model by Sargent et al. (2012) (recalibrated by Schreiber et al. 2015), relying on the existence of the $SFR - M_*$ sequence and assigning a SFR based on Equations 4.3 and 4.4 adding a dispersion and a fraction of starburst galaxies.

In Figures 5.12 and 5.13 we show the $SFR - M_*$ plane in several redshift bins from $z = 0$ to $z = 6.5$ where we compare our results with several literature results. We show in every redshift bin (with the exception of the redshift bin $0.0 < z < 0.2$) results of the COSMOS2015 catalog, whose objects have been selected as described in the previous section and divided into SF/Q according to the NUVrJ diagram. We also show in various redshift bin the best-fit modes by Speagle et al. (2014) and Pearson et al. (2018). In addition, several other literature observations are shown (and cited in captions).

In general, we find that our results agree well with several observations at masses $\log(M_*/M_\odot) \gtrsim 9$ and a main sequence is clearly visible. Below this threshold it seems that the model implemented in EGG underpredicts the SFR from either observations and theoretical predictions, even though, as visible in COSMOS2015 results, it is difficult to draw definitive conclusions given the large spread in observations at these masses.

In order to have a more general view, we show in Fig. 5.14, the star-formation rate density (SFRD) from $z = 0$ to $z = 8$ calculated on the Millennium I+II mock compared with several literature results. Given the deep limit of our mock in M_h we are complete also in stellar mass and SFR down to very low values (down to $M_* \sim 10^{7.4} M_\odot$ at $z \sim 0$). For this reason, for our mock, we simply sum up the SFR of galaxies, in bins of redshift, and divide by the volume of each redshift bin. For the calculation on the Millennium I+II we chose the same redshift bins used in SMFs (see e.g. Fig. 4.5). We do not show the results for the DUSTGRAIN mock given its incompleteness in stellar masses.

We collected several results from observations in UV/optical bands (i.e. Driver et al. 2018, Bouwens et al. 2015), in IR bands (i.e. Dunlop et al. 2017, Loiacono et al. 2020, Gruppioni et al. 2020, Khusanova et al. 2020, Rowan-Robinson et al. 2016, Sánchez et al. 2019), in radio bands (Novak et al. 2017), from observations of gamma-ray bursts (Kistler et al. 2009). We also show results on the COSMOS2015 catalog and from Henriques et al. (2015) SAM on which we calculated the

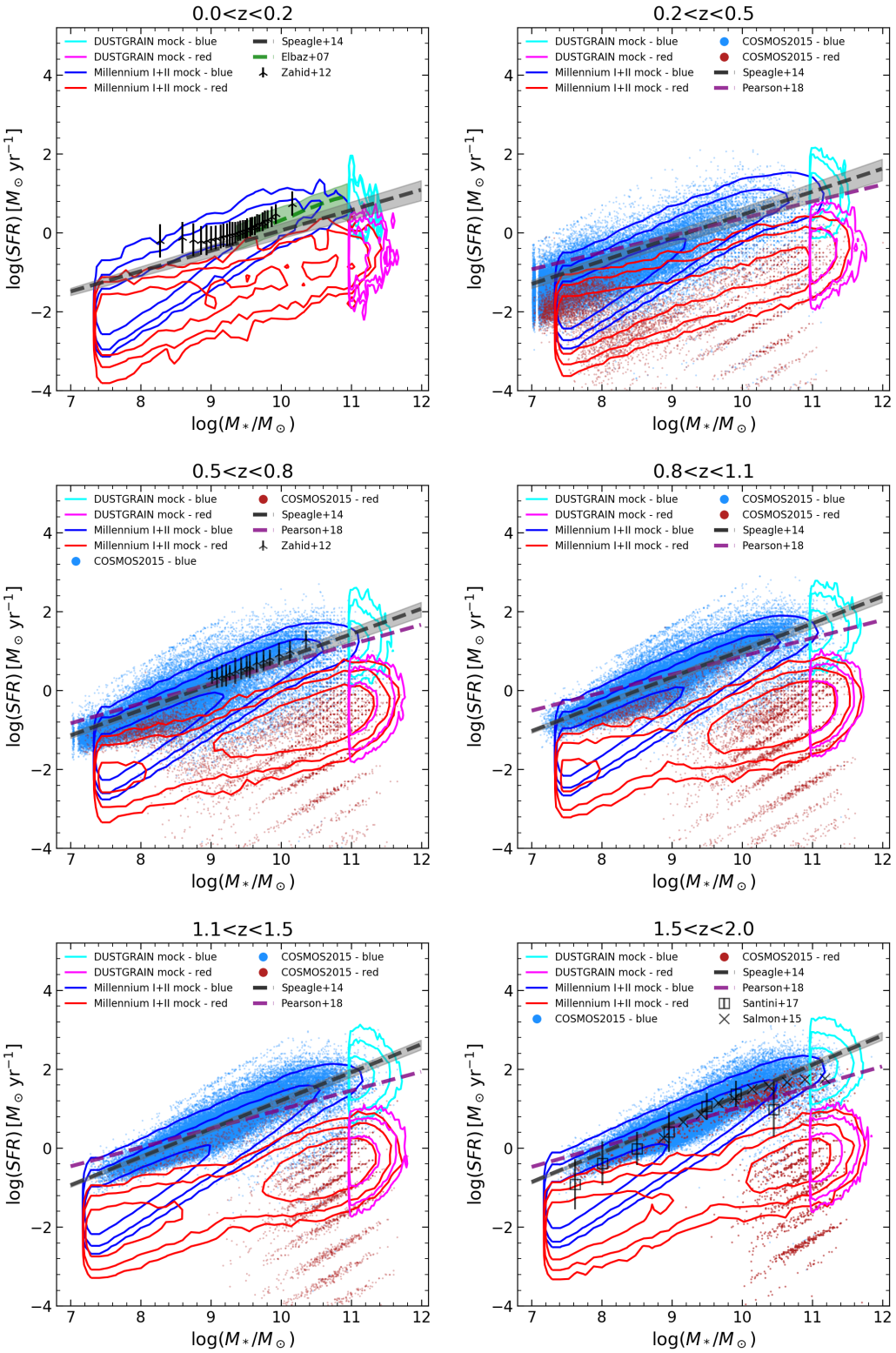

Fig. 5.12 M_* - SFR plane in six different redshift bins from $z = 0$ to $z = 2$. The results for the DUSTGRAIN and Millennium I+II mocks are divided by type (star-forming or quiescent) according to the division described in Sect. 4.2 and are shown with colored contours that encompass 65, 95 and 99% of the objects. The COSMOS2015 catalog is shown in red and blue points. Several literature results, that include those by Speagle et al. (2014), Elbaz et al. (2007), Zahid et al. (2012), Pearson et al. (2018), Santini et al. (2017) and Salmon et al. (2015), are shown with lines and symbols.

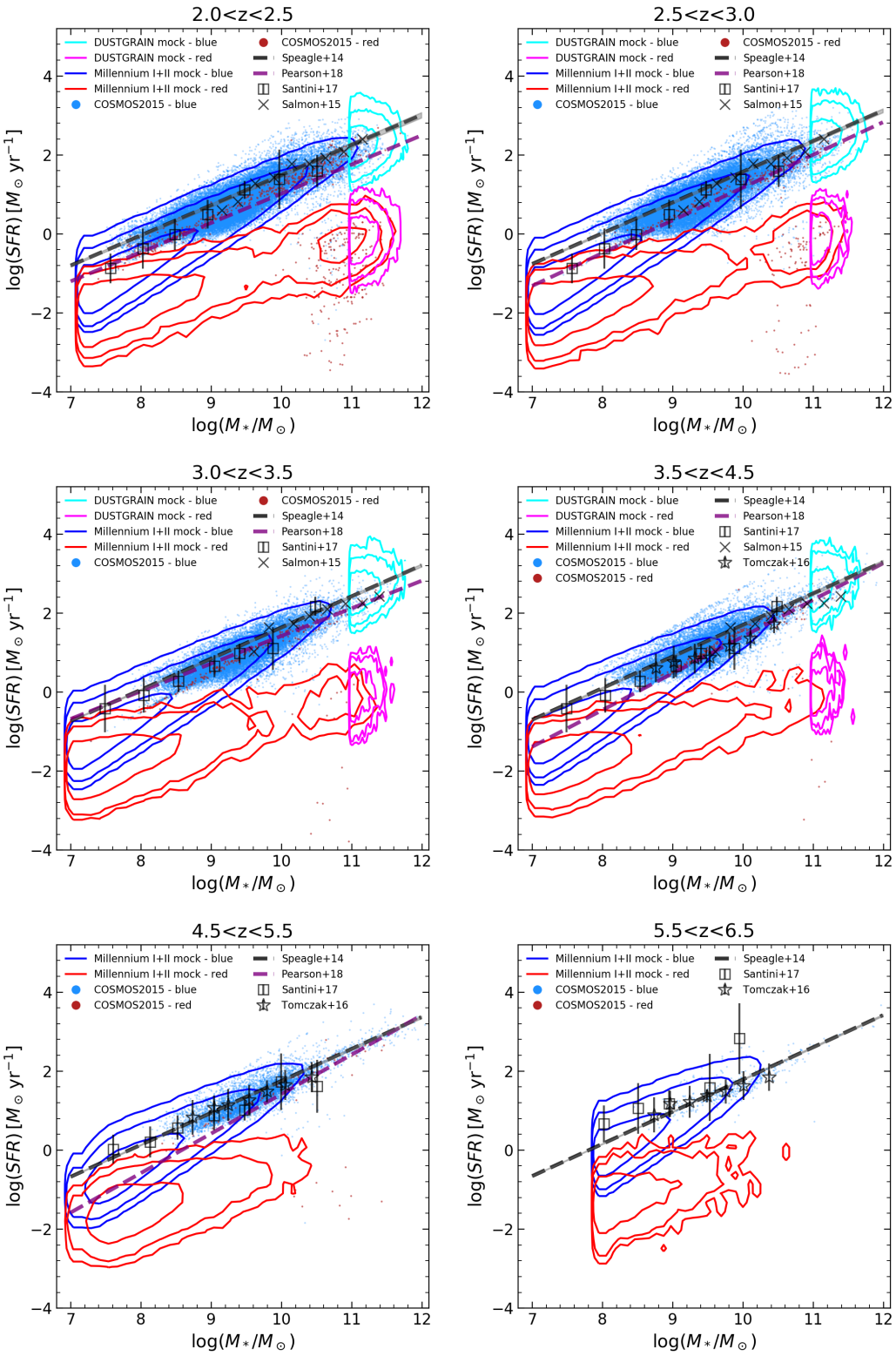

Fig. 5.13 M_* - SFR plane in six different redshift bins from $z = 2$ to $z \sim 7$. Lines and symbols as in Fig. 5.12. Additional literature results include those by Tomczak et al. (2016).

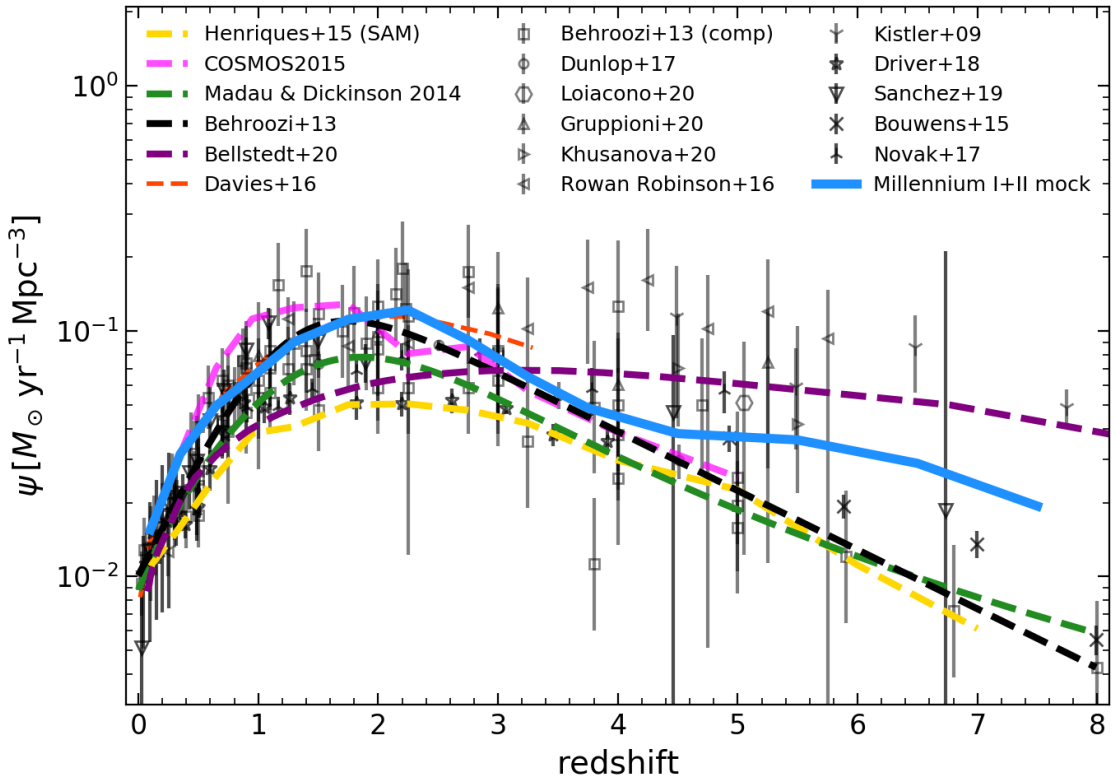

Fig. 5.14 Star-formation rate density from $z = 0$ to $z = 8$. Results for the Millennium I+II simulation are shown with a solid blue line. Results for the DUSTGRAIN simulation are not shown due to their incompleteness in stellar masses. The COSMOS2015 catalog is shown with dashed magenta line. Results from Henriques et al. (2015) SAM are shown with a yellow dashed line. Several literature results (Madau & Dickinson 2014, Behroozi et al. 2013, Bellstedt et al. 2020, Davies et al. 2016, Dunlop et al. 2017, Loiacono et al. 2020, Gruppioni et al. 2020, Khusanova et al. 2020, Rowan-Robinson et al. 2016, Kistler et al. 2009, Driver et al. 2018, Sánchez et al. 2019, Bouwens et al. 2015, Novak et al. 2017) are shown with lines and open gray symbols.

SFRD in the same way we did for our mock. In addition, we also display several models from the literature. More in detail, we show Madau & Dickinson (2014) results that fit a variety of different observations (see their paper for details). Then, we show the Behroozi et al. (2013) model that has been built starting from several observations within an empirical framework taking into account DM halos growth histories, stellar masses and SFR. Finally, Bellstedt et al. (2020) and Davies et al. (2016) results have both been obtained with a reconstruction of the star formation history of nearby galaxies in the GAMA survey (Driver et al., 2011) by analysing the fossil record of the stellar populations (with a similar method of the one presented in Heavens et al. 2004).

We find, in general, a good agreement with literature observed data given their large dispersion (from a factor of 2 at $z < 1$ up to 1.5 orders of magnitudes at $z \sim 6$). At $z > 4$ the Millennium I+II mock may seem to overshoot the SFRD of some observations (i.e. Bouwens et al. 2015) and best-fit

models (i.e. Behroozi et al. 2013 and Madau & Dickinson 2014), even though it is in agreement with IR estimates (e.g. Sánchez et al. 2019, Loiacono et al. 2020) and underpredicts other recent results (i.e.Bellstedt et al. 2020).

5.4 Emission lines

Among the most important properties that our mocks need to reproduce, in order to make predictions for future surveys, there are the emission lines. As already mentioned in Sect. 1.5, Euclid will survey the sky with slitless spectroscopy (from 1.25 to 1.85μm) aiming to observe $z \sim 1-2$ galaxies thanks to the Hα emission line. Also other future missions, such as WFIRST and MOONS, will survey similar spectral ranges and, therefore, it is crucial, for a mock catalog, to reproduce with accuracy emission lines.

We briefly remind here, as also extensively described in Sect. 4.3, the procedure implemented in EGG to assign emission lines. The code first assigns Hα using the Kennicutt (1998) relation and the SFR previously assigned. Secondly, the rest of the Balmer series is then generated using line ratios of case-B recombination. Then [NII], [OIII] and [OII] are assigned given the metallicity assigned using the empirical Fundamental Metallicity Relation (Mannucci et al., 2010) and SDSS observations (plus some offsets at high redshifts). Finally, Lyα is calculated following Sobral et al. (2018) results and the line luminosity is set to be 8.7 times the one of Hα.

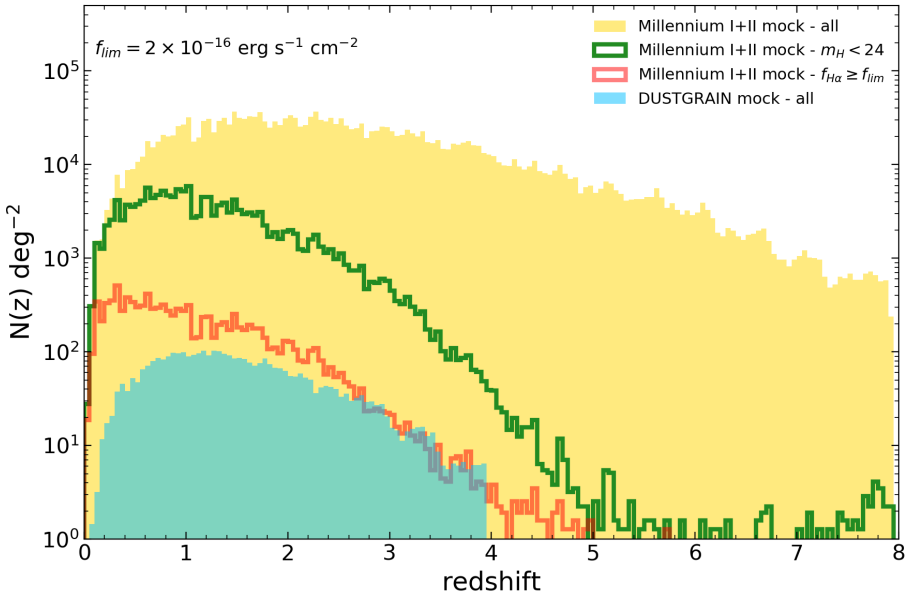

Fig. 5.15 Redshift distribution of mock galaxies with different H band and Hα fluxes limits. The results for the Millennium I+II and DUSTGRAIN simulations are shown with a yellow and cyan histograms, respectively. Green and yellow open histograms represent the Millennium I+II mock with cuts in the Euclid H band and in the Hα line flux as indicated in plot.

We chose Euclid as our reference future survey, and we will will validate some specific predictions for the survey. We show in Fig. 5.15 the redshift distribution of the galaxies in our mocks. In particular, we show the distribution of all galaxies, the distribution of Hα emitters with an Hα flux above the expected spectroscopic flux limit with NISP for the Wide Survey ($f_{H\alpha} \geq 2.0 \times 10^{-16}$erg/s/cm^2) and also the distribution of galaxies with $m_H < 24$ which is the 5σ limit selection for Euclid in the Wide Survey. We note that our mock is deeper than Euclid limits and therefore suitable for Euclid forecasts. As expected, the Hα limits will select only a small fraction (less than 10%) of galaxies selected by the photometric limit ($m_H < 24$).

In the following sections we show some redshift distributions of emission lines, along with several line ratios and compare our results with literature ones.

Hα

As mentioned above, the line Hα is fundamental to make predictions for Euclid.

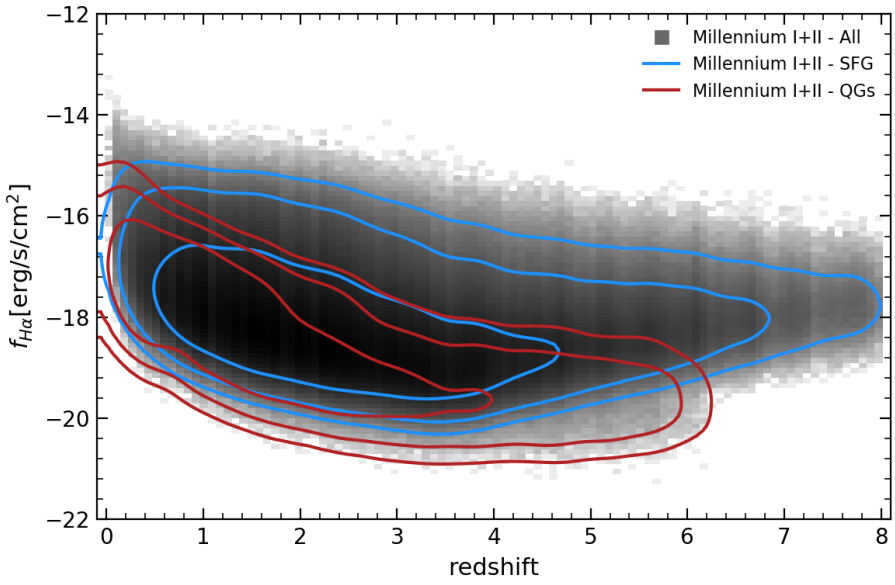

Fig. 5.16 Hα flux versus redshift for the Millennium I+II mock divided into galaxy types. In grey the 2-D histogram the distribution for all galaxies in the mock is shown. Contours, colored in blue and red, encompass the 68, 95 and 99% of the objects for the star-forming and quiescent populations, respectively.

We show in Fig. 5.16 the Hα flux as a function of redshift for the galaxies in the Millennium I+II mock. Since we didn't impose any observational limit in our mock, Hα fluxes in the plot can assume very low values, even fainter than $10^{-17}/10^{-18}$ erg s^{-1}cm^2. We show the total population as well as the star-forming and quiescent ones. As expected, star-forming galaxies show, in general, a higher Hα flux with respect to quiescent ones, even though, at low stellar masses, the division between star-forming and quiescent galaxies is less neat due to similar SFR-mass relations at low

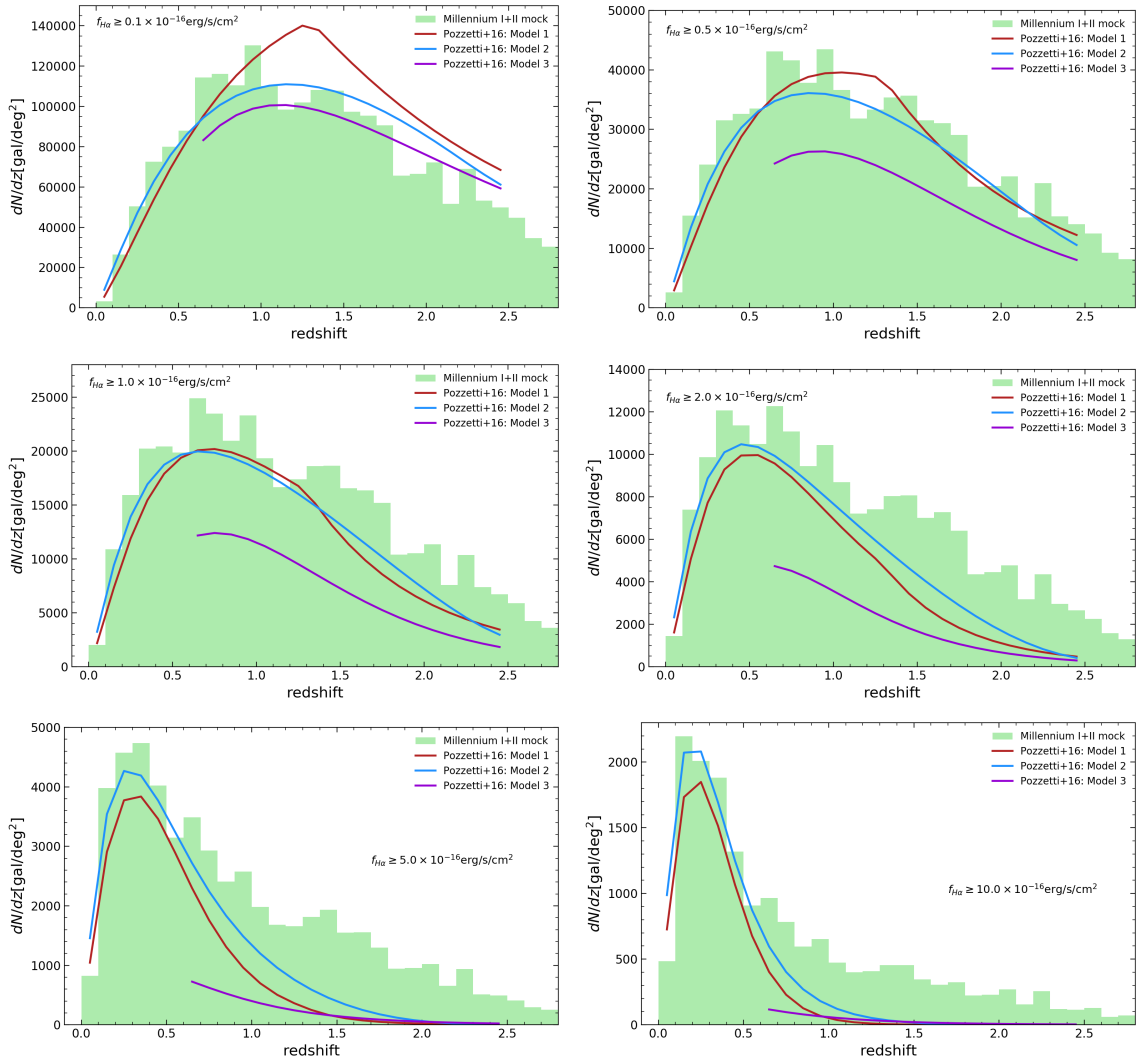

Fig. 5.17 Redshift distribution of Hα emitters with different minimum line fluxes. The results for the Millennium I+II simulation are shown with a green histogram. The empirical models by Pozzetti et al. (2016) are shown with colored solid lines.

masses (see Figs. 5.12 and 5.13). As already mentioned in Sect. 4.3, the code EGG divides each input galaxy into its bulge and disk components (and this holds also for quiescent galaxies) and assigns to each of these components certain properties and the Hα line is assigned only to the disk component. In addition, as described in Sect. 4.2, we always allow for at least 1% of quiescent galaxies at all masses and redshifts. Therefore, in some cases, when considering both of these effects combined, we may find some low-mass quiescent galaxies that show a non-null Hα emission down to fluxes of $10^{-20}\,\mathrm{erg\,s^{-1}cm^2}$.

In this Section we investigate the Hα assignment and compare with state-of-the-art literature empirical models. In particular, we compare with Pozzetti et al. (2016) empirical models. These models have been built by fitting observed luminosity functions from Hα surveys. Three different models have been built with different fitting methodologies, functional forms for the luminosity function, subsets of the empirical input data, and treatment of systematic errors (see Pozzetti et al. 2016 for details). In Fig. 5.17 we show the redshift distribution of Hα emitters with several different

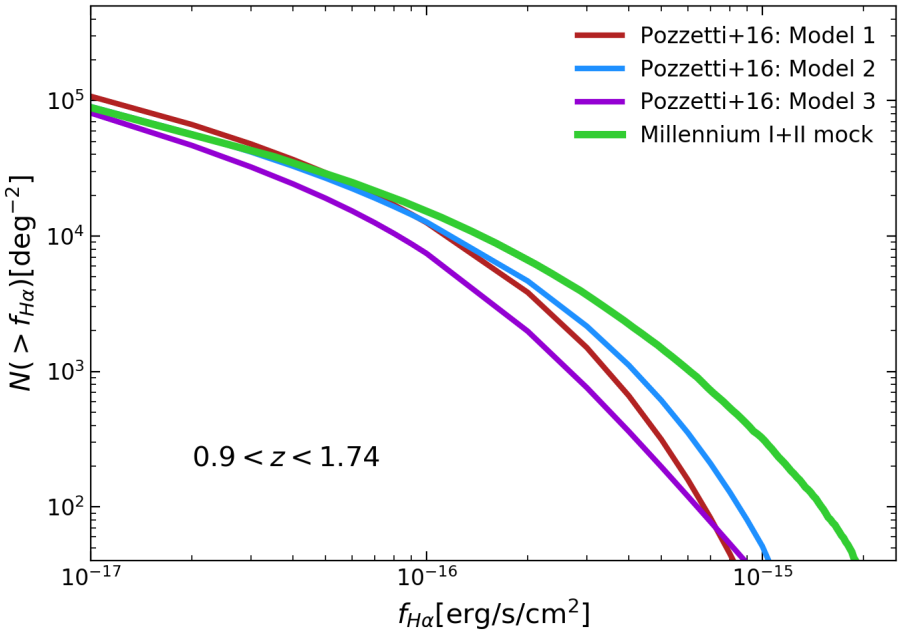

Fig. 5.18 Cumulative distribution of Hα emitters as a function of Hα flux in the Euclid redshift range. The results for the Millennium I+II simulation are shown with a green line. The empirical models by Pozzetti et al. (2016) are shown with red, blue and purple solid lines.

flux limits for the Millennium I+II mock and compare with Pozzetti et al. (2016) models. We do not show DUSTGRAIN results given their incompleteness in stellar masses. As evident in the different panels, our mock is in agreement with Pozzetti et al. (2016) models for faint flux limits (up to $f_{H\alpha} \sim 1.0 \times 10^{-16}\mathrm{erg/s/cm^2}$) while for brighter flux limits the mock seems to overestimate the number counts at $z \gtrsim 1$. Differences are up to a factor of $\sim 2.6, 1.8, 4.7$ at $z \sim 1.5$ for $f_{H\alpha} \geq$

2.0×10^{-16}erg/s/cm^2 for Pozzetti et al. (2016) Model 1, 2 and 3, respectively, that grow to a factor of $\sim 4.5, 2.5, 6$ at $z \sim 2.0$.

We also show in Fig. 5.18 the cumulative number counts of Hα emitters as a function of Hα flux in the redshift range where Euclid will observe Hα emitters (i.e. $0.9 < z < 1.74$, see Sect. 1.5). Also in this plot, it emerges that, for $f_{H\alpha} \gtrsim 1.0 \times 10^{-16}$erg/s/cm^2 our mock overpredicts the number of Hα emitters with respect to Pozzetti et al. (2016) models.

This overestimation may be due to several reasons. Firstly, as mentioned above, the differences in the number counts can be caused by the recipe implemented in EGG for the lines dust attenuation. In fact, it seems that the code tends to under-attenuate the Hα fluxes predicting too many bright Hα emitters with respect to Pozzetti et al. (2016) models.

BPT diagram and other line ratios

A useful tool to evaluate the reliability of the emission line assignment is the location in the Baldwin, Phillips, & Terlevich (1981) diagram, often called BPT diagram. Baldwin, Phillips, & Terlevich (1981) demonstrated that it is possible to distinguish type 2 AGNs from normal star-forming galaxies by considering the intensity ratios of two pairs of relatively strong emission lines, and this technique was refined by Veilleux & Osterbrock (1987). It has become standard practice to classify objects according to their position on the BPT diagram (see e.g. Kewley et al. 2001, Kauffmann et al. 2003, Brinchmann et al. 2004, Kewley et al. 2013, Juneau et al. 2014a, Zhang et al. 2020) that compares the ratio [OIII]/Hβ versus the ratio [NII]/Hα. The exact demarcation between star-forming galaxies and AGN is subject to considerable uncertainty and therefore we chose as our fiducial demarcation the Kauffmann et al. (2003) division, defined as: $\log([\mathrm{OIII}]/\mathrm{H}\beta) = 0.61 \,/\, \{\log([\mathrm{NII}]/\mathrm{H}\alpha) - 0.05\} + 1.3$, that has been evaluated on SDSS galaxies. In addition, we also consider the maximum limit allowed for starburst galaxies (SB) as calculated by Kewley et al. (2001) that defines a division at $\log([\mathrm{OIII}]/\mathrm{H}\beta) = 0.61 \,/\, \{\log([\mathrm{NII}]/\mathrm{H}\alpha) - 0.47\} + 1.19$. Kewley and collaborators used a combination of photoionization and stellar population synthesis models to place a theoretical upper limit on the location of star-forming models in the BPT diagrams. Their models allow for a wide range

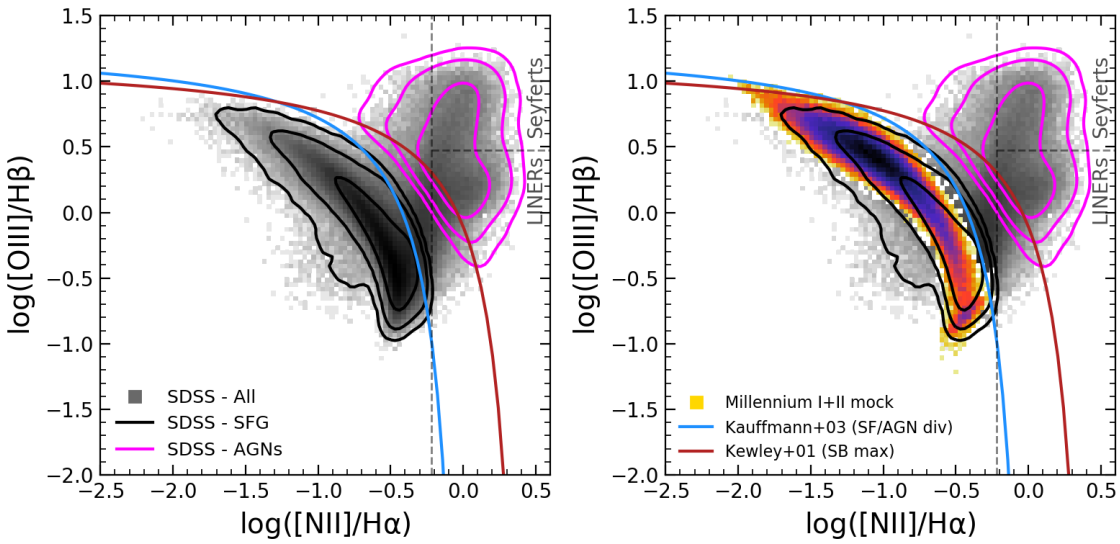

Fig. 5.19 BPT diagram where we plot the ratio [OIII]/Hβ versus the ratio [NII]/Hα for all SDSS DR8 objects (left) and for our Millennium I+II mock (right) overplotted on SDSS results. We also show contours for SDSS star-forming galaxies and AGNs (shown in black and magenta, respectively) that encompass 68, 95 and 99% of the objects of such classification. The solid light-blue line represents the Kauffmann et al. (2003) division between SF galaxies and SGNs, while the solid red line represents the Kewley et al. (2001) maximum starburst limit. With grey dashed lines the divisions for the LINER and Seyfert galaxies, as defined in the text, are displayed.

in metallicity, ionization parameter and dust depletion, and also make allowances for the effects of

shock excitation by supernovae. The Kewley et al. (2001) division for the maximum SB demarcation represents a very conservative limit. Galaxies with emission-line ratios that place them above the Kewley et al. (2001) line cannot be explained by any possible combination of parameters in a star-forming model and can be classified as AGNs. Objects falling between the Kauffmann et al. (2003) and Kewley et al. (2001) lines can be either AGNs or starburst galaxies and need to be treated carefully. In our mocks, AGNs have not been implemented and, therefore, objects falling between the two lines should be considered as starburst galaxies. Another division one can make is among Seyfert galaxies, often defined to have [OIII]/H$\beta > 3$ and [NII]/H$\alpha > 0.6$, and LINERs that have [OIII]/H$\beta < 3$ and [NII]/H$\alpha > 0.6$.

We show in Fig. 5.19 how our mock catalog populates the BPT diagram and how it compares with SDSS datapoints. In particular, we downloaded SDSS DR8 data from the survey database[4] (York et al. 2000, Abazajian et al. 2009). The emission line measurements are based on the methods of Kauffmann et al. (2003), Brinchmann et al. (2004) and Tremonti et al. (2004) by first performing a SED-fitting with high resolution Bruzual & Charlot (2003) models and then, once the stellar continuum and any remaining residual has been removed, the nebular emission lines are fitted simultaneously as Gaussians (see cited paper for details). For all plots that follow we chose a minimum S/N$=5$ for every emission line and exclude spectroscopically confirmed stars. SDSS galaxies selected in this way range from $z = 0$ to $z = 0.4$ and have stellar masses in the range $7 < \log(M_*/M_\odot) < 12$ and magnitude $r < 17.77$. For our mock catalog, when comparing to SDSS data, we selected all star-forming galaxies (see Sect. 4.2 for details on the SF/Q division) in the range $0 < z < 0.4$ with stellar masses $7 < \log(M_*/M_\odot) < 12$. Also in this case, due to incompleteness in stellar masses, we do not show DUSTGRAIN mock results. As visible from the Figure we find a good agreement between our mocks and SDSS results, even though their bulk of the population is located in different parts of the diagram. This is due to the fact that we have not applied any magnitude limit to our mock. In fact, the SDSS redshift distribution is peaked at low ($z \sim 0$) redshifts, while our mocks N(z) is skewed towards larger values, but we decided not to perform an exact matching because our lightcone at these redshifts cover a small volume.

Also by checking the stellar mass distributions, we find that SDSS galaxies peak at $\log(M_*/M_\odot) \sim 10$ while our mock peaks at $\log(M_*/M_\odot) \sim 7.5$. A quantitative comparison should take into account also the magnitude limit of the sample and its spectroscopic limit. We decided not to build a redshift and mass matched sample because our lightcone at these redshifts cover a small volume and the matching would leave us with a sample too small to perform a meaningful comparison.

We show in Figs. 5.20, 5.21, 5.22 several other line ratios. In particular, Fig. 5.20 shows the [OII]/[OIII] versus [NII]/Hα diagram, Fig. 5.21 displays the [OIII]/Hβ versus Hα/Hβ diagram and Fig. 5.22 represents the [OIII]/Hβ versus [NII]/[OII] diagram. As for the BPT diagram we find good agreement among our results and star-forming SDSS galaxies with a shift of the bulk of the populations due to the different mass and redshift distributions. In Fig. 5.23, we show the so-called Mass-excitation

[4] http://www.sdss3.org/dr8/spectro/spectro_access.php

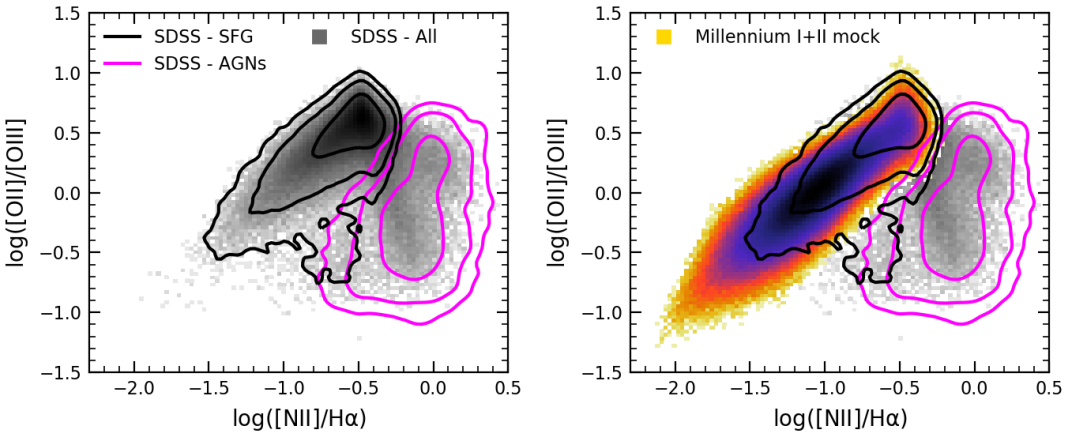

Fig. 5.20 [OII]/[OIII] versus [NII]/Hα diagram for the SDSS DR8 datapoints (left) and for our Millennium I+II mock (right) overplotted on SDSS results. Contours and histograms as in Fig. 5.19.

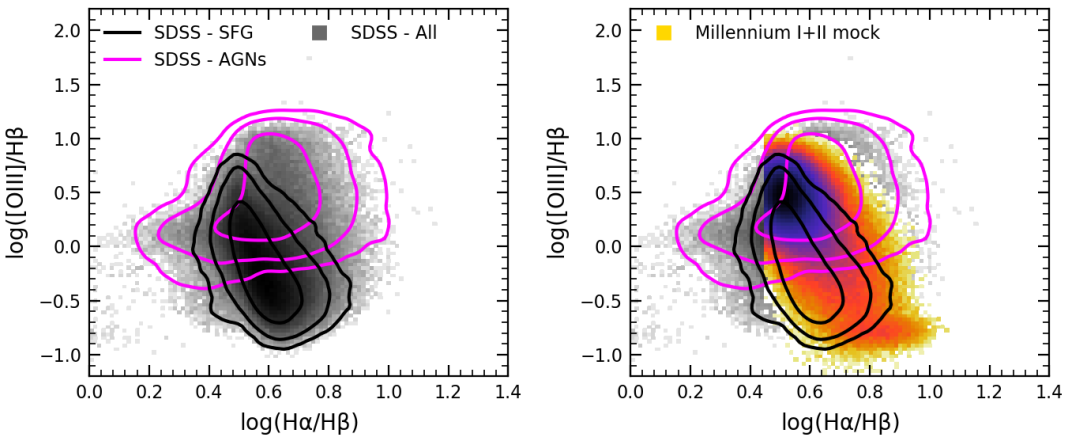

Fig. 5.21 [OIII]/Hβ versus Hα/Hβ diagram for the SDSS DR8 datapoints (left) and for our Millennium I+II mock (right) overplotted on SDSS results. Contours and histograms as in Fig. 5.19.

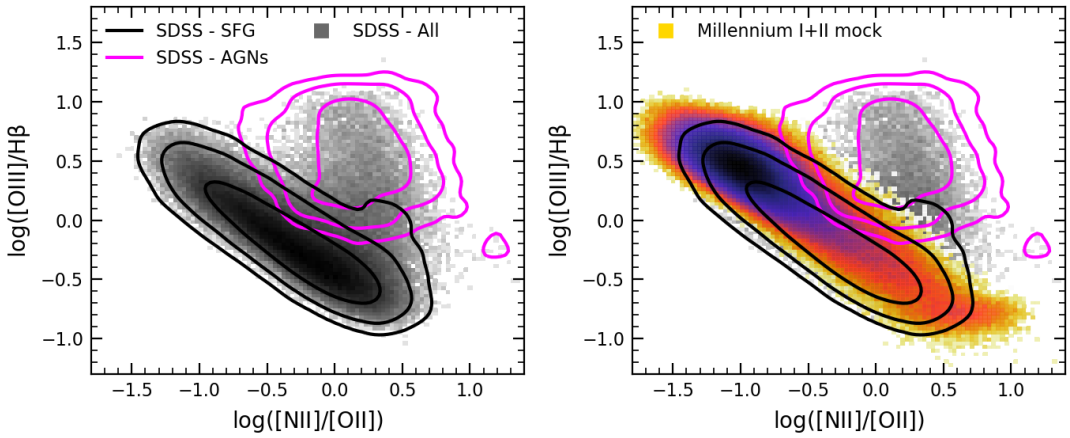

Fig. 5.22 [OIII]/Hβ versus [NII]/[OII] diagram for the SDSS DR8 datapoints (left) and for our Millennium I+II mock (right) overplotted on SDSS results. Contours and histograms as in Fig. 5.19.

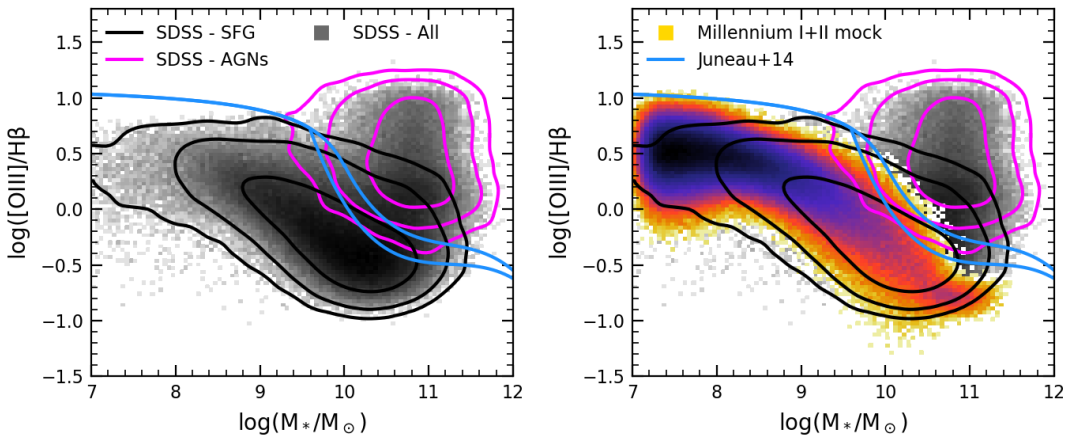

Fig. 5.23 Mass-excitation diagram (MEx): [OIII]/Hβ versus $\log(M_*/M_\odot)$ for the SDSS DR8 datapoints (left) and for our Millennium I+II mock (right) overplotted on SDSS results. We show with a solid light-blue line the Juneau et al. (2014b) demarcation that divides the space in three areas characterizing AGNs, transition and SF galaxies. Contours and histograms as in Fig. 5.19.

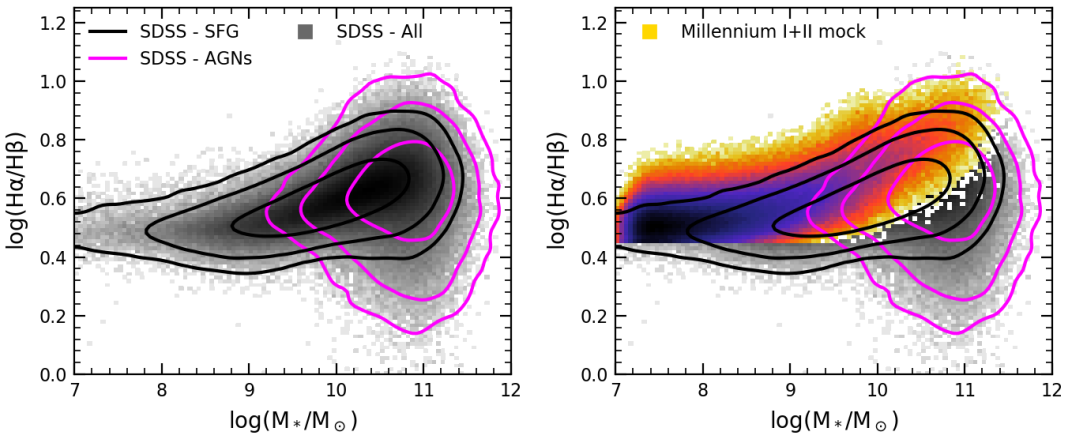

Fig. 5.24 Hα/Hβ versus $\log(M_*/M_\odot)$ for the SDSS DR8 datapoints (left) and for our Millennium I+II mock (right) overplotted on SDSS results. Contours and histograms as in Fig. 5.19.

diagram (MEx) first proposed by Juneau et al. (2011) and revisited in Juneau et al. (2014b). This diagram is designed to distinguish between AGNs and SFG in the absence of spectroscopy which includes Hα. This happens, for example, at high-z if near-IR spectroscopy is not available. It relies on the ratio [OIII]/Hβ against the stellar mass. Juneau et al. (2014b) define, using SDSS DR7, three different regions in the [OIII]/Hβ-stellar mass plane that should be populated by AGNs, transition objects and SFGs. We show such demarcations in Fig. 5.23. Also in this case, we find good agreement with star-forming SDSS data and Juneau et al. (2014b) division. It is particularly evident the different stellar mass distribution between our mocks and SDSS data. Finally, in Fig. 5.24 we show the Hα/Hβ ratio versus the stellar mass. Also in this case, by comparing the bulk distributions of SDSS and Millennium I+II mock, the different mass distributions are evident. Also in this case, the locus of observed galaxies is well represented by our mock catalog.

Moving toward higher redshifts, in Fig. 5.25, we show the BPT diagram for our mock in the redshift range $1.43 < z < 1.74$ and how it compares with the results of the near-IR Fiber Multi-Object Spectrograph (FMOS)-COSMOS survey (Kashino et al., 2019). The survey targeted 5382 galaxies over the 1.7 deg^2 COSMOS field and measured the spectroscopic redshift and flux of rest-frame optical emission lines (Hα, [N II], Hβ, [O III]). We downloaded the public available data from the survey database[5]. The catalog includes 1204 Hα detections at 3σ at $1.43 < z < 1.74$ down to the limit of 1.0×10^{-17}erg/s^{-1}cm^2 with masses from $9 \lesssim \log(M_*/M_\odot) \lesssim 11.5$. We impose a minimum S/N$=$ 1.5 for every emission line and evaluated the total fluxes with the corrections provided in the catalog. The final selected subsample comprises 173 objects. In addition, in order to divide among SFG and AGNs we use the conservative Kewley et al. (2001) division. We find that 148 galaxies may be classified as SFG while 25 are identified as AGNs. We will show this division in all following Figures. For our mock catalog, we selected star-forming galaxies in the range $1.43 < z < 1.74$ with

[5] http://member.ipmu.jp/fmos-cosmos/FC_catalogs.html

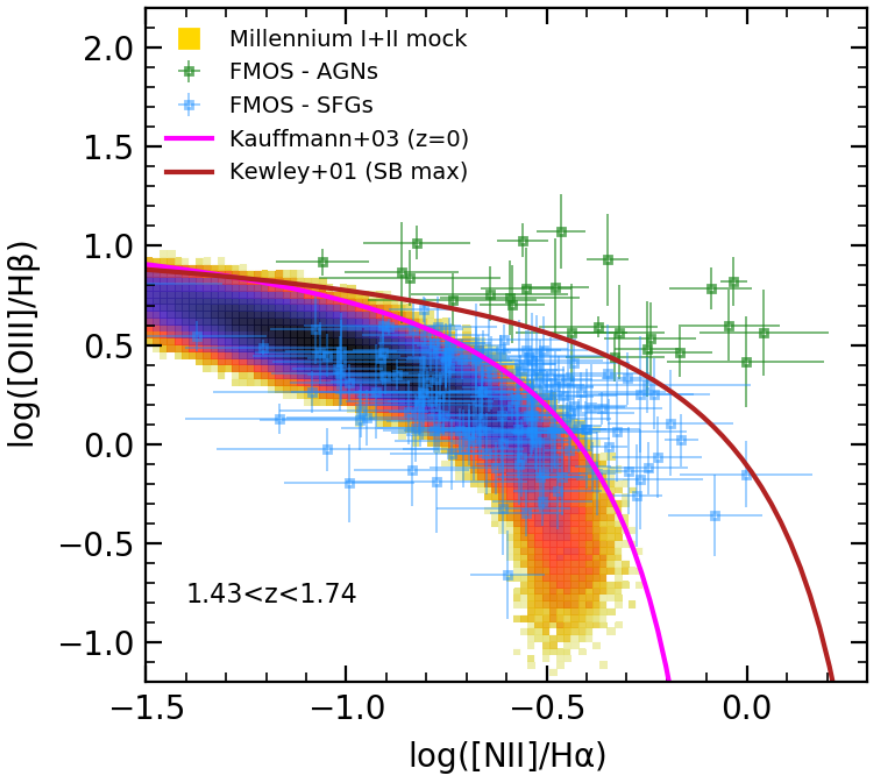

Fig. 5.25 BPT diagram at $1.43 < z < 1.74$ where we plot the ratio [OIII]/Hβ versus the ratio [NII]/Hα for FMOS objects (with open squares) and for our Millennium I+II mock (with 2-D histogram). Objects of the FMOS catalog that fall below the Kewley et al. (2001) limit are shown in light blue while the others are shown in green. The solid magenta line represents the Kauffmann et al. (2003) division between SF galaxies and SGNs, while the solid red line represents the Kewley et al. (2001) maximum starburst limit.

$9 \lesssim \log(M_*/M_\odot) \lesssim 11.5$. Due to the large uncertainties that characterize high redshift observations, it is difficult to draw secure conclusions on the comparison, however the general locus of galaxies seems to match between observations and our mock catalog.

The large dispersion among observations can also be seen in Fig. 5.26, where we show the [NII]/Hβ-M_* diagram and the MEx diagram. Also in this case, our mock galaxies populate the same diagram region as observed SFG while secure AGNs (shown in green) tend to populate higher regions of the diagram. The same conclusions also hold for the results shown in Fig. 5.27, where we show Hα/Hβ versus the stellar mass.

We can also check which regions of the various diagrams are populated by star-forming galaxies and which by quiescent ones. We show in Fig. 5.28 four different line ratios diagrams and how our mocks, divided into SF/Q galaxies, populate it. It emerges that, in general, by inspecting the innermost contour (that comprises the majority of galaxies) the bulk SF and Q galaxies populate different regions of the diagrams even though the regions overlap when considering all contours. For example by

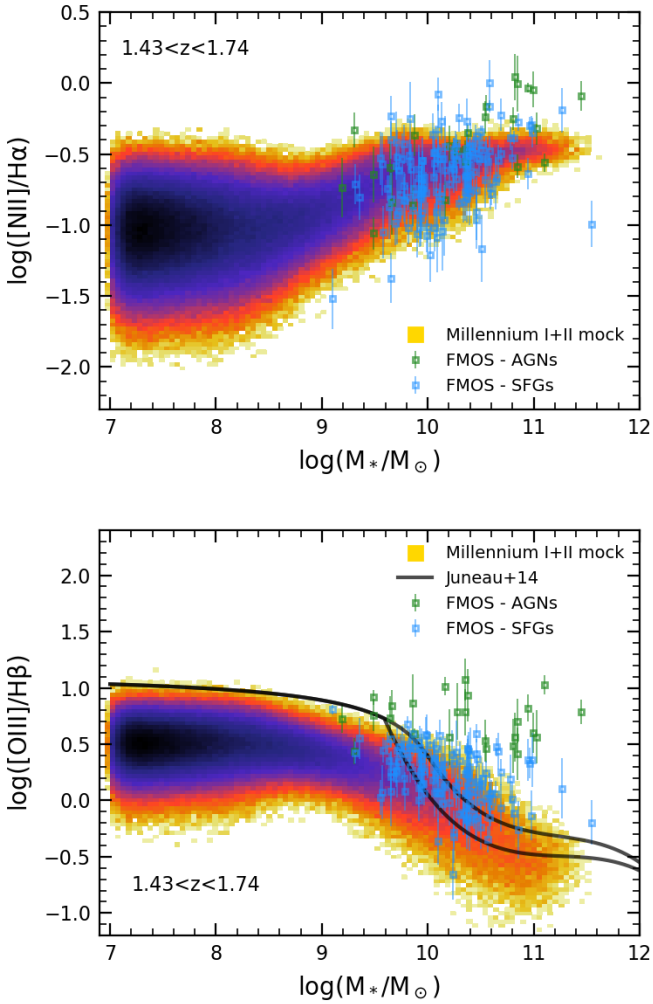

Fig. 5.26 [NII]/Hα versus $\log(M_*/M_\odot)$ (top panel) and the MEx diagram [OIII]/Hβ versus $\log(M_*/M_\odot)$ (bottom panel) at $1.43 < z < 1.74$ for FMOS objects (with open squares) and for our Millennium I+II mock (with 2-D histogram). Objects of the FMOS catalog that fall below the Kewley et al. (2001) limit in Fig. 5.25 are shown in light blue while the others are shown in green. In bottom panel, the Juneau et al. (2014b) demarcation is shown with a solid black line that divides the space in three areas characterizing AGNs, transition and SF galaxies.

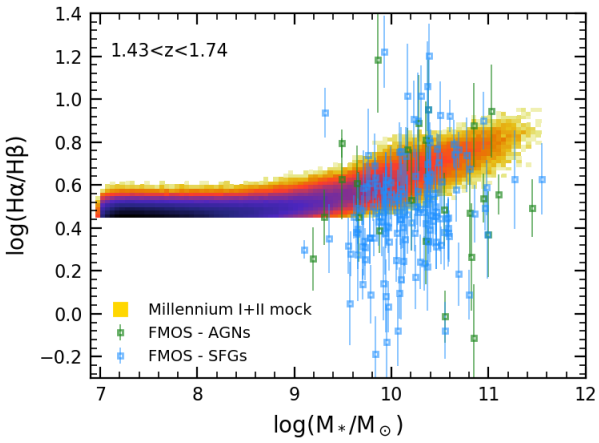

Fig. 5.27 Hα/Hβ versus $\log(M_*/M_\odot)$ for FMOS objects (shown with open squares) and for our Millennium I+II mock (shown with 2-D histogram).

looking at the BPT diagram (top left panel of Fig. 5.28) we find that quiescent galaxies tend to mostly populate a region with low [OIII]/Hβ ratio and high [NII]/Hα ratio, while the bulk of the star-forming population is placed at higher [OIII]/Hβ and lower [NII]/Hα ratios. This trend is due to the fact that on average quiescent galaxies have higher mass and metallicities (corresponding to higher [NII]/Hα values) and lower ionizing fluxes (corresponding to lower [OIII]/Hβ values). However, some overlap among the two populations is present.

We also show, in Fig. 5.29 how our mock populates the $f_{H\alpha} - m_{H,Euclid}$ plane and how each type of galaxy (i.e. SF or Q) populates the regions of this diagram. It is clearly visible, when comparing with FMOS data, that our mock is fully consistent with observed datapoints and goes down to much lower Hα fluxes and m_H magnitudes. This is extremely useful to make prediction for future deep observations in order to make forecasts about the number of objects that can be detected at any redshift with certain flux and/or magnitude limits. For example, we find that less than 0.02% of the objects have fluxes brighter than 2.0×10^{-16}erg/s^{-1}cm^2 at $0.9 < z < 1.74$ and H magnitude fainter than the Euclid limit of 24 and could, therefore, be missed by the Euclid.

To summarize, in this Section we investigated the emission line assignement performed in our mock catalogs. In particular, we inspected the Hα distributions with several line flux limits and also several line ratios and diagrams. We compared with empirical models and state-of-the-art observations. For Hα we find that our mock predicts higher number densities of Hα emitters with $f_{H\alpha} > 1.0 \times 10^{-16}$erg/s^{-1}cm^2 with respect to Pozzetti et al. (2016) empirical models. This is likely due to the line dust attenuation recipe in EGG. This aspect needs a more accurate investigation. When considering other emission lines and line ratios, in general, we find good agreement with observations at all redshifts and, in those cases, it does not emerge a significant difference with observations, as we found in Hα.

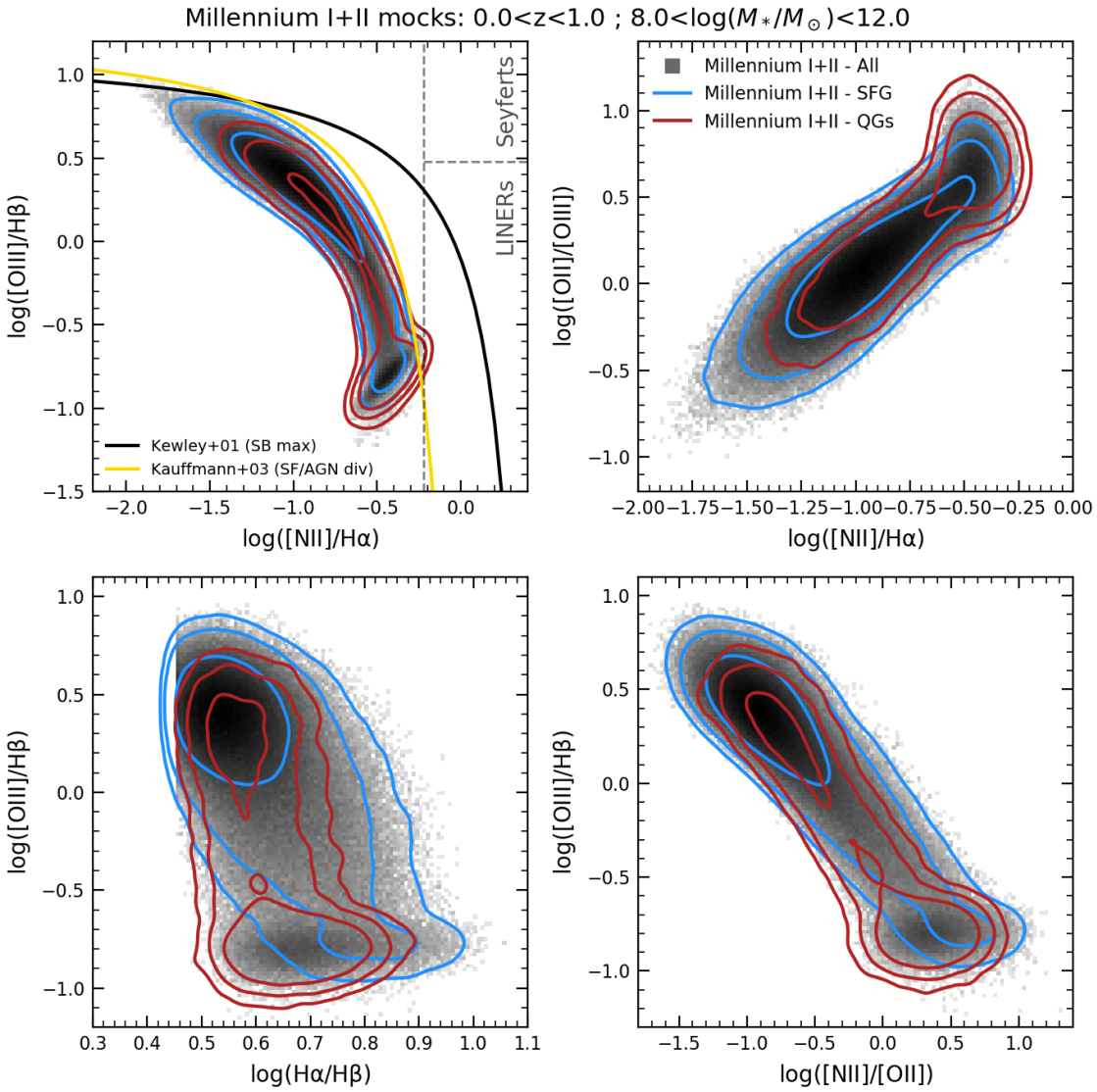

Fig. 5.28 The Millennium I+II mock catalog divided into SF/Q populations in four different diagrams: [OIII]/Hβ vs [NII]/Hα in top left panel, [OII]/[OIII] vs [NII]/Hα in top right panel, [OIII]/Hβ vs Hα/Hβ in bottom left panel and [OIII]/Hβ vs [NII]/[OII] in bottom right panel. The mock has been selected in the range $0 < z < 1$ with $8 < \log(M_*/M_\odot) < 12$. With the grey 2-D histogram the distribution of all galaxies is shown, while with blue and red contours (encompassing the 65, 95 and 99% of the objects) we show the distribution of star-forming and quiescent galaxies in the mock, respectively (divided as described in Sect. 4.2). In top left panel, we also show the Kauffmann et al. (2003) and Kewley et al. (2001) demarcations, as well as the divisions into Seyfert and LINERs galaxies.

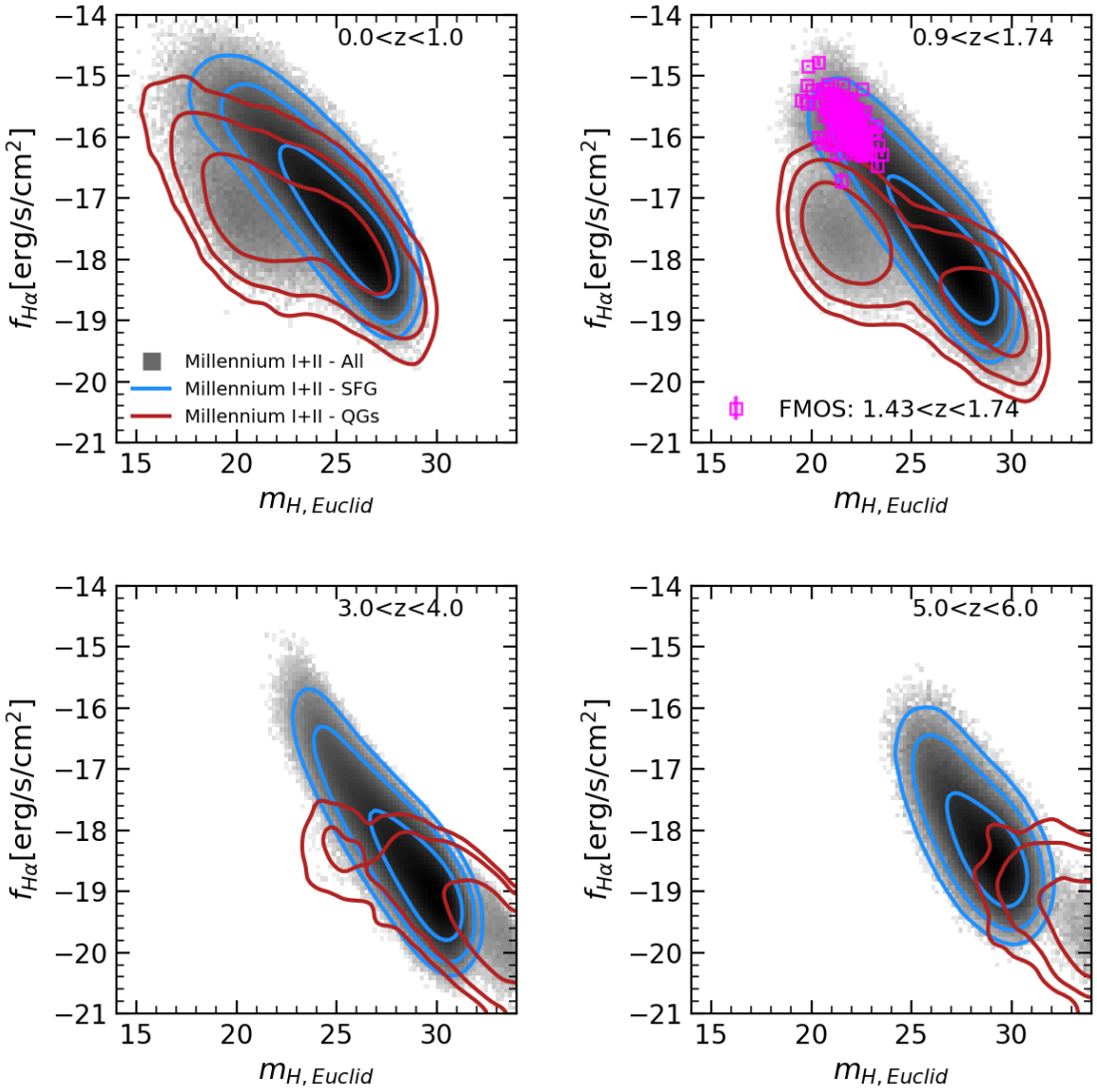

Fig. 5.29 The distribution of Millennium I+II mock galaxies in the $f_{H\alpha} - m_{H,Euclid}$ plane in some redshift bins from $z = 0$ to $z = 7$. The whole population is shown with a 2D histogram in grey, while with contours (encompassing 65%, 95% and 99% of the objects) we show the location of SF galaxies (blue) and quiescent objects (red). In the top right panel we show the Euclid redshift range, i.e. $0.9 < z < 1.74$ where also FMOS galaxies ($1.43 < z < 1.74$) are shown in magenta.

5.5 Dust

In this section we investigate the dust content of our mock galaxies to verify whether their properties reproduce observations and, in particular, whether it could be the cause of the differences we observe in Hα counts with respect to observation. Although dust emission is a complex process involving a continuum of values for the properties of the dust grains (see e.g. Savage & Mathis 1979, Mathis & Whiffen 1989, Mathis 1990, Draine 2003), a simple two- (or three-) component dust model usually describes successfully the basic characteristics of the UV-optical extinction and the FIR emission of the dust in galaxies. During the years many different attenuation laws have been proposed (see e.g. Gordon et al. 2003 for a comparison among different laws): some evaluated on starburst or local galaxies (e.g. Meurer et al. 1999, Calzetti et al. 2000, Schlafly & Finkbeiner 2011), others derived from the Large Magellanic Cloud (e.g. Fitzpatrick 1986), some on the Milky Way (e.g. Seaton 1979) and others combine al these probes (e.g. Pei 1992, Weingartner & Draine 2001).

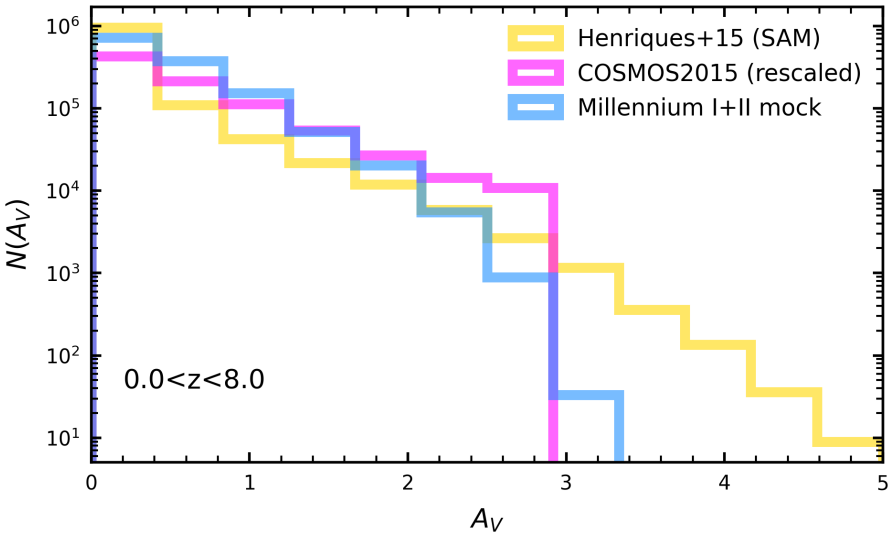

Fig. 5.30 A_V distribution for the Millennium I+II mock. We calculated the dust extinction distribution of the mock catalog from $z = 0$ to $z = 8$ (shown in blue histogram) by averaging between the A_V values for the bulge and the disk weighting with the B/T ratio. Also results of the COSMOS2015 catalog and Henriques et al. (2015) SAM are shown with magenta and yellow histograms, respectively. COSMOS2015 results have been rescaled to the same area covered by the mock catalog and Henriques et al. (2015) SAM (i.e. 3.14 deg^2).

As already explained in Sect. 4.3, the code EGG divides each galaxy into the bulge and disk components and assigns to each galaxy component a certain dust amount, based on Calzetti et al. (2000) dust screen law, already evaluated in the SEDs lookup table. In addition, also to each emission line a dust reddening is applied following Calzetti et al. (2000) law with the exception of Lyα where the dust reddening follows the prescription by Hayes et al. (2010). Therefore, in order to evaluate a single A_V value for each galaxy of our mock, we made an average between the bulge and disk extinction

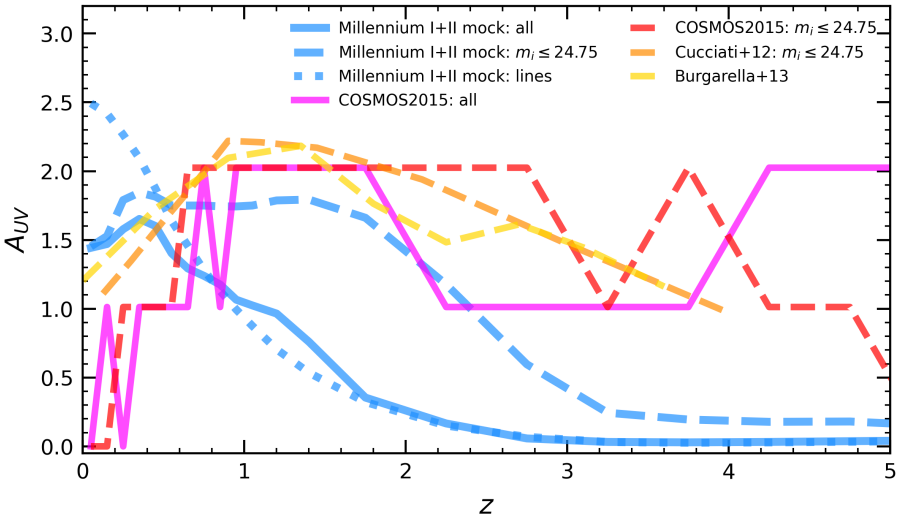

Fig. 5.31 Median A_{UV} values of the galaxies as a function of redshift for the Millennium I+II mock. We show with a solid blue line the A_{UV} for all the galaxies of the mock while dashed blue line represents the A_{UV} for the galaxies with $m_i \leq 24.75$. We also show the median A_{UV} values applied to the emission lines. We also show results of the COSMOS2015 catalog for all the galaxies and for those with$m_i \leq 24.75$ with magenta and red lines, respectively. Cucciati et al. (2012) and Burgarella et al. (2013) results are shown with orange and yellow lines, reespectively.

values, weighted by means of the bulge to total ratio (B/T). In the following plots, once again we only show Millennium I+II mock results, given the incompleteness of DUSTGRAIN mock. In Fig. 5.30, we show the A_V distribution for the Millennium I+II mock and compare it with the observed catalog COSMOS2015 and Henriques et al. (2015) SAM. The COSMOS2015 catalog provides $E(B-V)$ values and therefore, assuming a Calzetti et al. (2000) law[6], we multiplied $E(B-V)$ by $R_V = 4.05$ in order to evaluate A_V. In general, we find a good agreement with COSMOS2015 results and, on the contrary, we find some differences from Henriques et al. (2015) SAM, that predicts many objects with high extinction values.

In Fig. 5.31, we show the extinction in the UV band A_{UV} of our Millennium I+II mock catalog. To evaluate the curves, we evaluated the median values of A_V extinction in bins of redshift (with width $\Delta z = 0.1$) and then multiplied by a factor of 2.5, which is roughly the factor to go from A_V to $A_{2500\,\text{Å}}$ (that slightly depends on the extinction law). In the Figure we also show the extinction for the emission lines, translated in the UV band with the correction described above. The same correction is also applied to COSMOS2015 results. We also show the results by Cucciati et al. (2012), that have been evaluated on VVDS observations with a magnitude limit of $m_i \leq 24.75$. In order to perform a meaningful comparison, we also show the results for the Millennium I+II mock and COSMOS2015 catalog applying the same magnitude cut. In addition, we also show results by Burgarella et al. (2013)

[6]For the sake of precision, in COSMOS2015 three different extinction curves have been considered: one is the Calzetti et al. (2000) law, the second is Prevot et al. (1984) law and the other is a modified version of Calzetti et al. (2000) law including a bump at 2175Å. For simplicity, we assume that for all galaxies a classic Calzetti et al. (2000) law has been used.

that calculated extinction values in the UV with VVDS and in the far-infrared from Herschel/PEP and Herschel/HerMES data. When comparing with observations, we find, in general, that our mock galaxy catalog overpredicts extinction values at low redshift. At $z \sim 0.2$, for example, our mock shows an A_{UV} value ~ 1.25, ~ 1.1 and ~ 2.5 times larger with respect to Cucciati et al. (2012), Burgarella et al. (2013) and COSMOS2015 results, respectively. On the contrary, at higher redshifts our mock predicts lower values with respect to observations: e.g. at $z \sim 3$ our mock predicts an A_{UV} value ~ 3.75, ~ 3.75 and ~ 2.5 times smaller with respect to Cucciati et al. (2012), Burgarella et al. (2013) and COSMOS2015 results, respectively. These results confirm that the dust extinction implemented in EGG may require a recalibration of the relations implemented in the code to produce results more similar to observations.

5.6 Sizes

In this section, we validate some of the morphological parameters assigned by EGG in our mock catalog. The size distribution of the stellar bodies of galaxies provides important clues about the assembly history of galaxies and the relationship with their dark matter halos. Moreover, it has been found that the size of a galaxy correlates with its stellar mass (i.e. the mass-size relation Shen et al. 2003), and sizes at fixed mass were also globally smaller in the past (e.g. Ferguson et al. 2004, Daddi et al. 2005, Shen et al. 2003, van der Wel et al. 2014). Furthermore, some observational effects depend on galaxy size, like the spectral resolution in Euclid slitless spectroscopy and, therefore, it is crucial that a mock catalogs reproduces also the distribution of sizes of galaxies. Briefly, as already mentioned several times, in the EGG model, each galaxy is split in two components: a disk and a bulge whose contribution is evaluated with the Lang et al. (2014) results. Then, all other morphological parameters are assigned using van der Wel et al. (2012) results.

In Fig. 5.32, 5.33 and 5.34 we compare the results for our Millennium I+II mock catalog with the results obtained on the CANDELS fields by Dimauro et al. (2018). The catalog by Dimauro et al. (2018) unifies the bulge-disk decomposition of ~ 17600 galaxies in the CANDELS fields from different observations (i.e. Galametz et al. 2013 for UDS, Guo et al. 2013b for GOODS-S, Barro et al. 2017 for GOODS-N and Stefanon et al. 2017 for COSMOS) spanning a quite large redshift range (up to $z \sim 2$) complete up to $m_H \sim 23$. In the catalog, for each galaxy, a morphological probability for it to be a spheroid, a disk and an irregular galaxy is given. These probabilities are calculated with a Deep Learning technique introduced by Huertas-Company et al. (2015).

In order to perform a fair comparison with such observations, we selected the results of both our Millennium I+II mock and the observed catalog in the range $0.5 < z < 2.0$ with $m_H < 23$. In addition, for our mock, we divided our galaxies into "pure bulges" when $B/T > 0.8$ and "pure disks" when $B/T < 0.2$. When referring to all galaxies (i.e. $0.0 < B/T < 1.0$) we will use the nomenclature "2 component galaxies" (this is because EGG always assigns to each galaxy a bulge and a disk component). For the observed catalog, we define "pure bulges" those galaxies that have a probability $> 80\%$ of being a spheroid combined with a probability $< 10\%$ of being irregular. "Pure disks" are

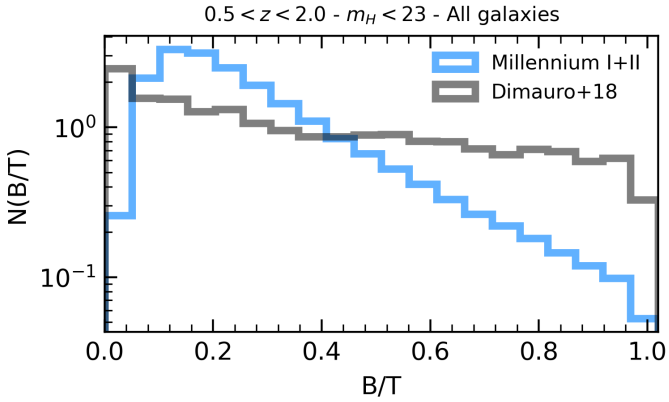

Fig. 5.32 B/T distribution of Millennium I+II mock galaxies in the range $0.5 < z < 2.0$ with $m_H < 23$ is shown in blue. Also the distribution of the Dimauro et al. (2018) catalog is shown with a solid grey line.

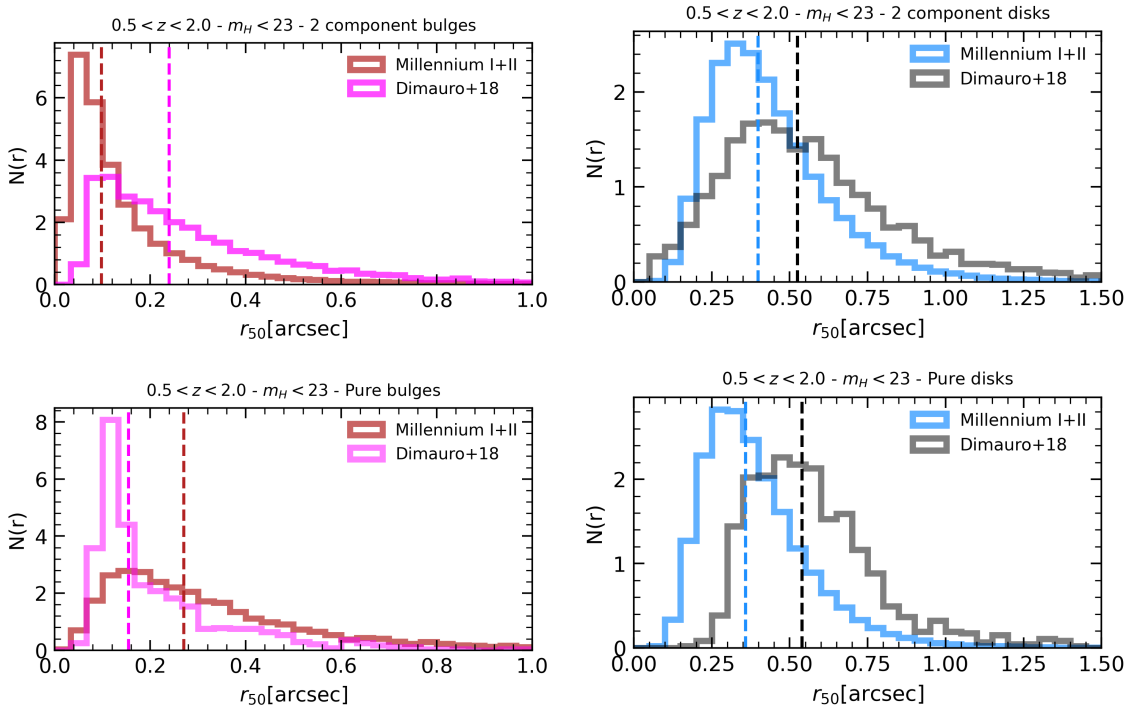

Fig. 5.33 Distributions of the half-light radius (r_{50}) in the range $0.5 < z < 2.0$ with $m_H < 23$. In top left panel, the r_{50} distribution of the bulges of the 2 component galaxies is displayed while in bottom panel the distribution of "pure bulges" is shown. In top right panel, we show the r_{50} distribution of the disks of the 2 component galaxies and in bottom right panel the distribution of "pure disks". In all panels we show the results for the Millennium I+II mock (in red in left panels and in blue in right ones) and also the results of the Dimauro et al. (2018) catalog (in magenta on the left panels and in grey in right panels). Vertical dashed lines show the median value of r_{50} for the distributions with the same color.

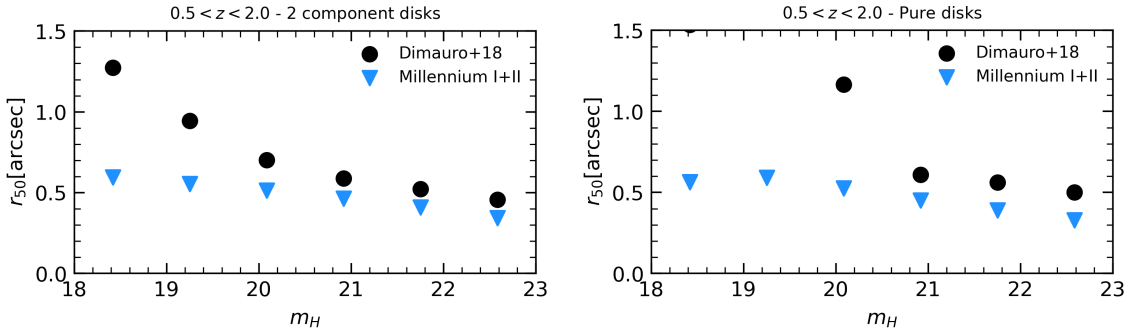

Fig. 5.34 Half-light radius (r_{50}) as a function of m_H for galaxies at $0.5 < z < 2.0$. In left panel, the r_{50} distribution of the disks of the 2 component galaxies is displayed while in right panel, we show the r_{50} distribution of "pure disks". The plotted points represent the median values in bins of redshift. In all panels we show the results for the Millennium I+II mock (blue triangles) and also the results of the Dimauro et al. (2018) catalog (in black dots).

defined in an analogous way (a probability $> 80\%$ of being disks and a probability $< 10\%$ of being irregular).

From Fig. 5.32 it emerges that observed galaxies show a flatter distribution of the B/T ratio with respect to our mock catalog. In addition, when analysing Fig. 5.33 and in particular the median r_{50} values (shown with vertical dashed lines), we can clearly notice that our mock catalog predicts, in general, smaller half-light radiuses with respect to the observed ones. There is an exception for "pure bulges" where observations show smaller half-light radiuses with respect to our mock. It looks like there is a systematic offset between our mock and the Dimauro et al. (2018) catalog. This is even more evident in Fig. 5.34, where the median values of r_{50} as a function of the magnitude in the H band is shown. In this figure we note that our mock catalog predicts much smaller disks (by more than a factor of 2 at $m_H < 19$) with respect to Dimauro et al. (2018), especially at bright magnitudes. Apparently, our mock predicts smaller sizes with respect to observed galaxies by Dimauro et al. (2018). This may be explained by the fact that in our mock every galaxy is always represented by two components, while in observations, when one of the two components is too small or faint, it can be lost. This can also explain the peaked distributions we find in Fig. 5.32 for the two component galaxies.

Further investigation is needed in order to asses whether the size prescriptions implemented in EGG may reproduce observations, or if the distributions we see in the mock depend on the specific relation adopted by the code that is clearly different than the Dimauro et al. (2018) ones. If needed, a recalibration of the code shall be performed.

5.7 Clustering

A fundamental quantity that our mock needs to reproduce, in order to be able to make predictions for future surveys, is the spatial distribution of galaxies, or, in other words, the clustering signal. As also mentioned in Sect. 1.4.4, the two-point correlation function (2PCF) is the simplest estimator for quantifying galaxy clustering, because it is related to the second moment of the galaxy distribution, i.e. its variance. In practice, it describes the excess probability $\xi(r)$ of observing a pair of galaxies at a given separation r, with respect to a random distribution (Peebles, 1980). In our mocks, since we consider lightcones where peculiar velocities and Hubble recession are incorporated, galaxies populate the redshift-space. Galaxy separations can be split into the tangential and radial components, r_p and π (Davis & Peebles, 1983). By doing this, we can estimate the projected two-point correlation function $w(r_p)$ in which galaxy pairs are defined by their separations projected onto the plane perpendicular to the line-of-sight so that the clustering evaluation is not affected when ignoring peculiar velocities. In practice, when computing $w(r_p)$, a finite upper integration limit π_{max} has to be chosen:

$$w(r_p) = 2\int_0^{\pi_{max}} \xi(r_p,\pi')d\pi' \tag{5.1}$$

The value of π_{max} needs to be high enough to include most of the clustering signal dispersed along the line of sight by peculiar motion and, at the same time, it should not be too high to avoid adding only noise, which is dominant above a certain π.

We performed the calculation of the projected two-point correlation function on both our mock catalogs (i.e. the Millennium I+II and DUSTGRAIN) in various redshift bins (from $z = 0.2$ to $z = 3.5$) with several stellar mass cuts and compared with measurments of the VIPERS survey (Marulli et al., 2013), of the zCOSMOS survey (de la Torre et al., 2011; Meneux et al., 2009) and of the VUDS survey (Durkalec et al., 2018). All the measurements were made with the *CosmoBolognaLib*[78] (Marulli et al., 2016), a set of free software C++/Python numerical libraries for cosmological calculations. The projected correlation function was measured on the lightcones, using the Landy & Szalay (1993) estimator, which has been shown to provide a nearly unbiased estimate of the 2PCF, while minimizing its variance (see, e.g., Keihänen et al., 2019),

$$\hat{\xi}(r) = \frac{N_{RR}}{N_{GG}}\frac{GG(r)}{RR(r)} - 2\frac{N_{RR}}{N_{GR}}\frac{GR(r)}{RR(r)} + 1\,, \tag{5.2}$$

where $GG(r)$, $RR(r)$, and $GR(r)$ are the binned numbers of galaxy-galaxy, random-random, and galaxy-random pairs with distance $r \pm \Delta r$, while $N_{GG} = N_C(N_G-1)/2$, $N_{RR} = N_R(N_R-1)/2$, and $N_{GR} = N_G N_R$ are the total numbers of galaxy–galaxy, random–random, and galaxy–random pairs, respectively.

[7] https://github.com/federicomarulli/CosmoBolognaLib
[8] https://gitlab.com/federicomarulli/CosmoBolognaLib

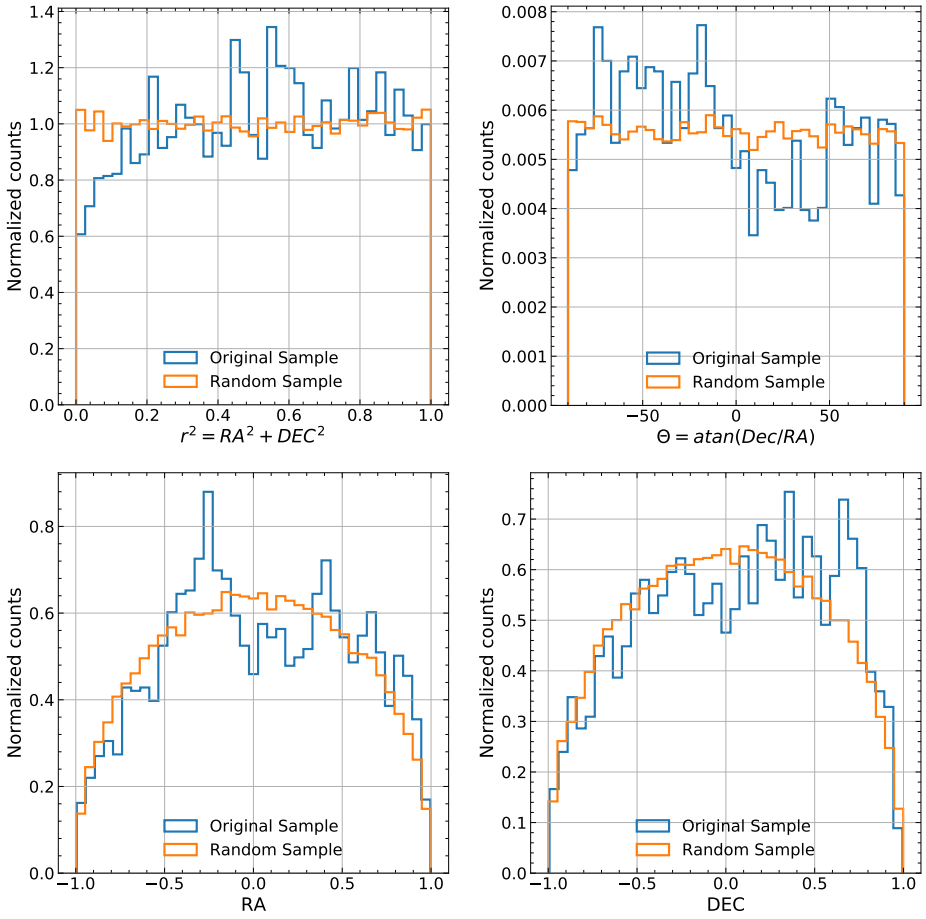

Fig. 5.35 Distributions of r^2, Θ, RA and Dec for lightcone 23 of the Millennium I+II mock at $0.5 < z < 0.7$ for galaxies with $\log(M_*/M_\odot) > 10.34$. We denote with "Original sample" the distribution as it is in the lightcone and "Random sample" the sample we randomly extracted from the "Original Sample".

To construct the random samples we first converted the right ascension (RA) and declination (Dec) of each galaxy into pseudo-polar coordinates (r^2, Θ), following these transformations: $r^2 = (\mathrm{RA}^2 + \mathrm{Dec}^2)$ and $\Theta = \arctan(\mathrm{Dec}/\mathrm{RA})$. This has been done because the RA and Dec coordinates of the lightcone are circularly distributed (see bottom panels in Fig. 5.35) and extracting a random samples from such distribution is not trivial. With these coordinate transformations we constructed flat distributions and a random sample could be easily extracted. We show in Fig. 5.35, as an example, the r^2, Θ, RA and Dec distributions in a redshift and mass bin. Once a random sample has been extracted from the r^2 and Θ distributions, we re-converted the coordinates in RA and Dec. The redshifts of the random objects are extracted from the redshift distribution of galaxies within each lightcone smoothed with a Gaussian filter since we want to maintain the general distribution in redshift and get rid of fluctuations due to substructures. We tested several values of the standard deviation σ for the Gaussian kernel and found that for values of $\sigma \geq 200$ Mpc the distributions do not retain memory

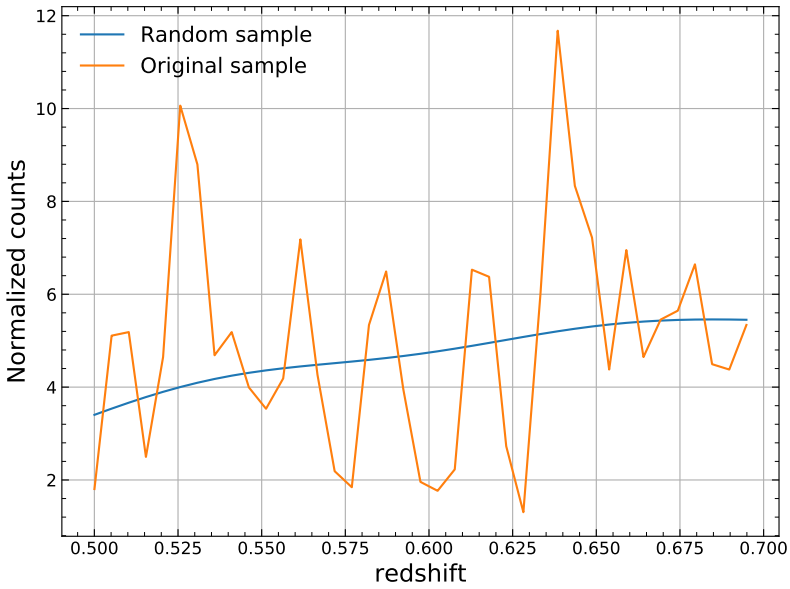

Fig. 5.36 Distributions of redshift for lightcone 23 of the Millennium I+II mock between $z = 0.5$ and $z = 0.7$ for galaxies with $\log(M_*/M_\odot) > 10.34$. We denote with "Original sample" the distribution as it is in the lightcone and "Random sample" the sample we randomly extracted from the "Original Sample" after the Gaussian filtering.

of fluctuations of the original distribution and follow the original global shape. We therefore chose 200 Mpc as the standard deviation of the Gaussian filter we adopt. We show in Fig. 5.36 the redshift distribution in a specific redshift and mass bin (the same as Fig. 5.35). In all cases, we generated the random samples to be twenty times larger than the galaxy samples with the exception of the redshift bin $2.0 < z < 3.5$, where we limited our random sample to be twelve times larger the galaxy sample, due to our computational limited resources.

We computed $\omega(r_p)$ from a minimum separation in the first dimension of $r_{p,\min} = 0.02$ Mpc to a maximum scale of $r_{p,\max} = 120$ Mpc over 15 bins that were equally separated in logarithmic scale. In order to perform a meaningful comparison with other studies, in the second direction, the computation was done up to a certain $\pi_{p,\max}$ which has been chosen depending on the observations we are comparing with (usually this limit is chosen as a compromise between robustness and the need to exclude noisy bins at large separations): $\pi_{p,\max} = 30$ Mpc when comparing to the VIPERS survey and $\pi_{p,\max} = 20$ Mpc when considering the zCOSMOS and the VUDS surveys.

The uncertainties were estimated with the bootstrap method by dividing the datasets into 12 subsamples, which were then resampled in 100 datasets with replacements, measuring $\omega(r_p)$ in each of them (Norberg et al., 2009).

We show in Figs. 5.37 and 5.38 our evaluation of the projected correlation function in several mass and redshift bins. In Fig. 5.39 the projected correlation function of our mock catalogs divided by galaxy type is displayed. Finally, in Fig. 5.40 the projected correlation function of our mock catalogs

at high redshift (i.e. $2.0 < z < 3.5$) is shown. The calculation for the DUSTGRAIN mock is limited to galaxies with $\log(M_*/M_\odot) > 11$ where it is complete. Moreover, we show its results only for scales > 1 Mpc because we found no sign of the one-halo term (i.e. for scales $\lesssim 1$ Mpc where the clustering among subhalos populating the same main halo becomes important). To determine whether the lack of the one-halo term of our mock galaxy catalogs was caused by the adopted prescriptions to model stellar masses, we repeated the analysis by measuring the projected correlation function of the full-halo catalogs, without any mass selection. We found no sign of the one-halo term in this case either. It can therefore be ascribed to the resolution of the simulation. Thus our clustering measurements for the DUSTGRAIN mock are only reliable at large scales ($\gtrsim 1$ Mpc).

In Figs. 5.37 and 5.38 our evaluation is also compared to VIPERS (over ~ 24 deg^2) and zCOSMOS (over ~ 1.7 deg^2) results binned in stellar mass. The projected correlation function of the VIPERS galaxies has been measured by Marulli et al. (2013) with a method very similar to ours. The random sample has been contructed with 30 times more objects than galaxies. The weighting scheme adopted has been described by Pezzotta et al. (2017) and de la Torre et al. (2017) and the errors were estimated with the bootstrap method in the same way as for our mock catalogs. Also the zCOSMOS estimates, measured by Meneux et al. (2009), use a very similar approach to our. The correction scheme is a simplified version of the one discussed in Pollo et al. (2005) and the errors were estimated using a bootstrap method.

By inspecting Figures 5.37 and 5.38 we find a clear dependance of the signal with stellar masses: more massive objects appear to be more clustered than less massive ones. This dependance has been well established in the past (e.g. Davis et al. 1988, Guzzo et al. 1997, Zehavi et al. 2002, Madgwick et al. 2003, Zehavi et al. 2011) and is a clear indication that stellar mass assignment in our mock catalog is accurate. In addition, we find excellent agreement with the VIPERS results at all scales and masses. When comparing with zCOSMOS estimates, it appears that our results underestimate the signal at intermediate and large scales (i.e. $\gtrsim 1$ Mpc). However, it has been discovered that in the COSMOS field an overabundance of rich structures is present. In particular at $z \sim 0.73$ a large filamentary structure, called the COSMOS Wall, was found (Iovino et al., 2016) and is responsible for an enhancement of the clustering signal on scales above $1-2$ Mpc (Meneux et al. 2009, de la Torre et al. 2010). Therefore, the differences between our and zCOSMOS estimates are imputable to the overabundance of structures in zCOSMOS at the considered redshifts.

In Fig. 5.39, we show the projected correlation function of our mock catalogs divided by galaxy type at $0.6 < z < 1.0$ and compare with the estimates by de la Torre et al. (2011) on zCOSMOS data over ~ 1.7 deg^2. We selected only galaxies with $\log(M_*/M_\odot) > 10.6$ which is the mass completeness limit in zCOSMOS and divided into red and blue galaxies using the procedure described in Sect. 4.2. De la Torre and collaborators performed a similar analysis to the one done in Meneux et al. (2009) but improved some details by adding, for example, a correction to take into account for the overabundance of structures in zCOSMOS and a correction for the non-uniform sampling inside each pointing (see details in de la Torre et al. 2011). Moreover, the division into red and blue population, was based on morphologies of galaxies and, in particular, on the concentration, asymmetry and the Gini coefficient

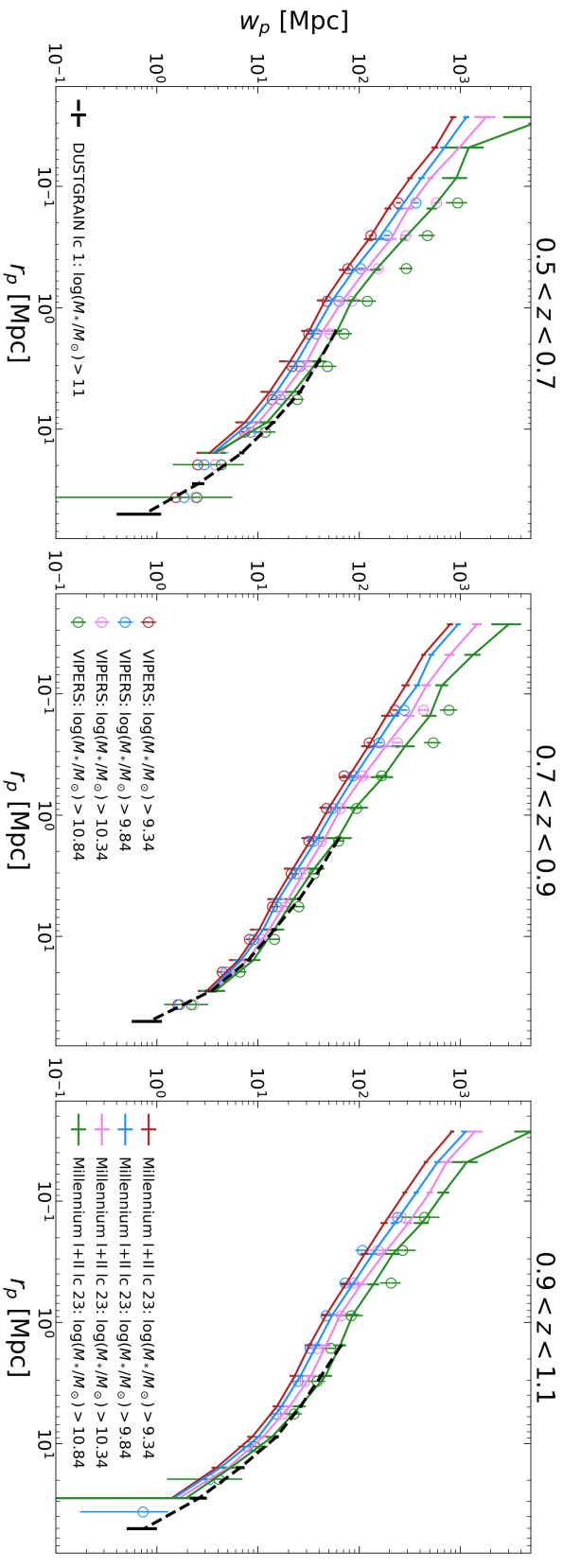

Fig. 5.37 Projected 2pt correlation function in three different redshift bins (from $z = 0.5$ to $z = 1.1$) each in different mass bins, as indicated in inset labels. Results for both the Millennium I+II (for lightcone 23) and DUSTGRAIN (for lightcone 1) simulations are shown with lines. Open points represent results on the VIPERS survey (Marulli et al., 2013) in the same mass and redshift intervals.

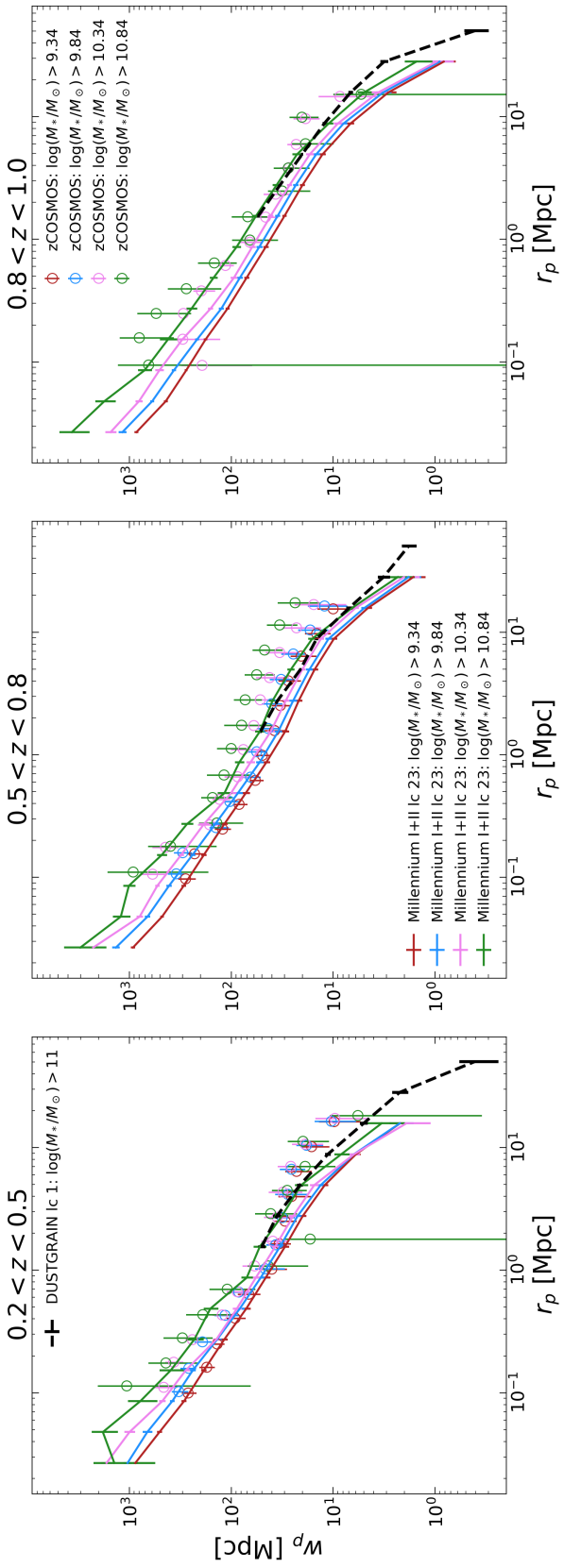

Fig. 5.38 Projected 2pt correlation function in three different redshift bins (from $z = 0.2$ to $z = 1.0$) each in different mass bins, as indicated in inserted labels. Results for both the Millennium I+II (for lightcone 23) and DUSTGRAIN (for lightcone 1) simulation are shown with lines. Open points represent results on the zCOSMOS survey (Meneux et al., 2009) in the same mass and redshift intervals.

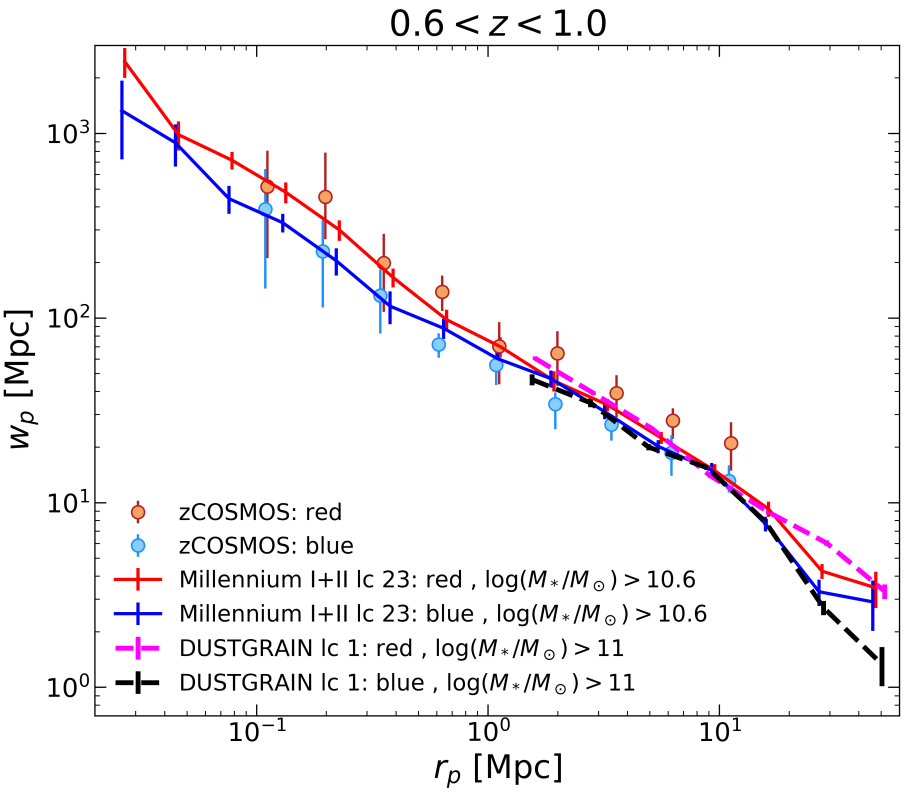

Fig. 5.39 Projected 2pt correlation function at $0.6 < z < 1.0$ divided into red and blue galaxies. Results for both the Millennium I+II (for lightcone 23) and DUSTGRAIN (for lightcone 1) simulation are shown with lines. Points represent results on the zCOSMOS survey (de la Torre et al., 2011) in the same mass and redshift interval.

(e.g. Abraham et al. 1996, Lotz et al. 2004). Even though the division into red and blue galaxies is different between our mock and de la Torre et al. (2011), we expect that at these redshifts the two classifications mostly overlap (see e.g. Moresco et al. 2013). We find that red galaxies are more clustered that blue ones. This is an effect of the well-known color/morphology/dynamical segregation in clusters of galaxies (e.g. Dressler 1980) in which red galaxies populate the inner parts of a cluster while less massive blue galaxies are more scattered around the centre. This is an indication that the SF/Q division adopted for our mock catalogs can be considered, in first approximation, correct. Also in this case, there is good agreement with results on zCOSMOS at all scales.

In Fig. 5.40, the projected correlation function of our mock catalogs divided in three stellar mass bins at $2.0 < z < 3.5$ is shown and compared with the estimates by Durkalec et al. (2018) on the VUDS survey over ~ 0.92 deg^2. Durkalec and collaborators used the correction scheme developed in Durkalec et al. (2015b) to take into account possible errors introduced by the target selection, or the possible underestimation of the correlation function related to the small fraction of incorrect redshifts present in their sample. Also in this case a bootstap method has been used to calculate the errors. In this case, when comparing VUDS results to ours we find that our mocks predict a slightly larger signal

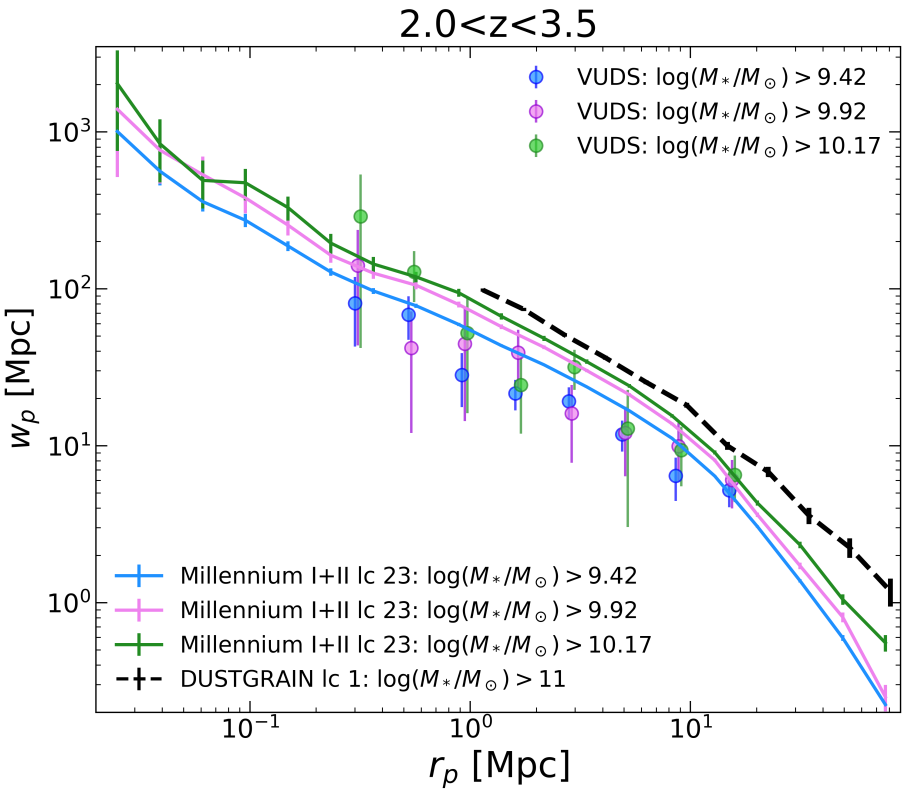

Fig. 5.40 Projected 2pt correlation function at $2.0 < z < 3.5$ in different stellar mass bins, as indicated in inserted labels. Results for both the Millennium I+II (for lightcone 23) and DUSTGRAIN (for lightcone 1) simulation are shown with lines. Points represent results on the VUDS survey (Durkalec et al., 2018) in the same mass and redshift intervals (points for the mass bins $\log(M_*/M_\odot) > 9.92$ and $\log(M_*/M_\odot) > 10.17$ have been slightly shifted to higher r_P in oder to avoid overlap among them and ease visual comparison).

at intermediate scales ($1 \lesssim r_p \lesssim 8$ Mpc) while preserving the trend with stellar masses. However, Durkalec et al. (2018) results show large error bars and it is difficult to draw definite conclusions on this comparison.

To sum up, we find that our mock catalogs predict a dependence of the clustering signal from the stellar mass and the galaxy type indicating that more massive or red galaxies are more clustered than less massive or blue galaxies. These results are in agreement with previous studies and, in addition, we find an overall good agreement with literature data to which we compare with, indicating that the stellar mass and SF/Q division in the mocks is accurate.

5.8 Forecasts for future surveys

In this section we present some example of the many forecasts that can be performed using the mock catalog we presented in this thesis. We focus on the lightcone 23 of the Millennium I+II mock only given its completeness down to low stellar masses/faint fluxes. In particular, we will provide some general forecasts that can be applied for any survey along with some forecasts specific for the Euclid Mission (see Sect. 1.5).

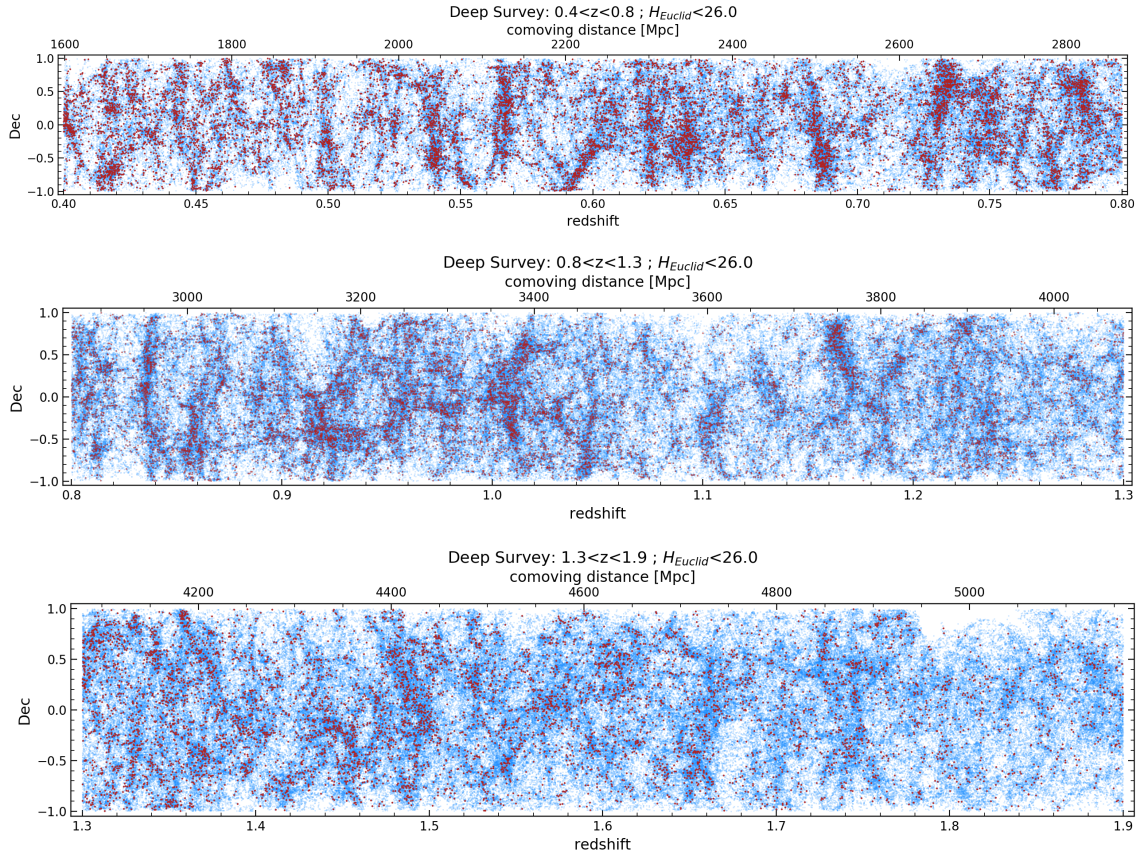

Fig. 5.41 Position of galaxies in the Millennium I+II mock (3.14 deg^2) in a redshift-Dec plane in the redshift range of the Euclid Deep Survey ($0.4 < z < 1.9$). Galaxies have been selected to selected to have $H_{Euclid} < 26$ and are shown with colors according to their type (red for Q galaxies, blue for SF galaxies). The upper x-axis is also labeled according to the comoving distance.

Large Scale Structure

We show in Figs 5.41, 5.42, 5.43 and 5.44 the distribution of the galaxies in our mock in a Dec-redshift plane in the Euclid redshift range. As already described in Sect. 1.5, Euclid will perform two surveys. The first is the Wide Survey which will cover over 15000 deg^2 reaching a depth of $H_{Euclid} \sim 24$ and will detect Hα emitters down to $f_{H\alpha} \sim 2 \times 10^{-16}\,\mathrm{erg\,s^{-1}\,cm^{-2}}$ from $z \sim 0.9$ to $z \sim 1.8$. The second

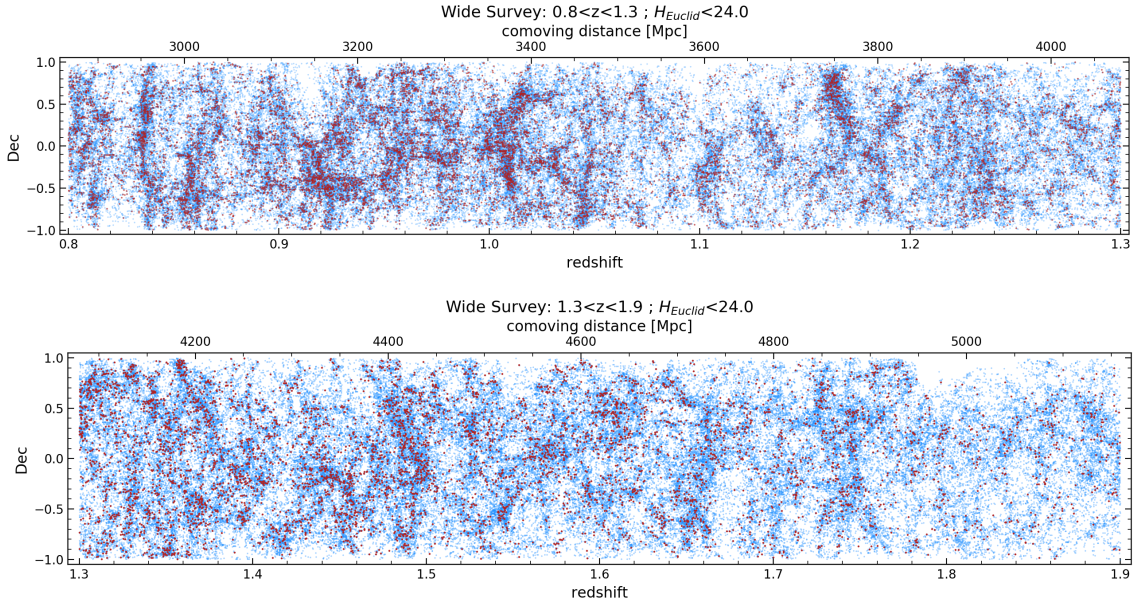

Fig. 5.42 Position of galaxies in the Millennium I+II mock (3.14 deg^2) in a redshift-Dec plane in the redshift range of the Euclid Wide Survey ($0.8 < z < 1.9$). Galaxies have been selected to have $H_{Euclid} < 24$ and are shown with colors according to their type (red for Q galaxies, blue for SF galaxies). The upper x-axis is also labeled according to the comoving distance.

is the Deep Survey, over 40 deg^2 reaching $H_{Euclid} \sim 26$ and will detect Hα emitters down to line fluxes of $\sim 0.5 \times 10^{-16}$ erg s^{-1} cm^{-2}. Thanks to the blue grism this survey will cover a more extended redshift range from $z \sim 0.4$ to $z \sim 1.8$.

We show, in Fig. 5.41, in three different panels, the galaxies in the redshift bin $0.4 < z < 1.9$ that have $H_{Euclid} < 26$ which is the magnitude limit for the Euclid Deep Survey. Moreover, also the division into red and blue galaxies is shown. As expected, red galaxies mainly populate high density regions, i.e. clumps and filaments. Blue galaxies instead populate also less dense environments. In Fig. 5.42 we show the same plots specifically for the Euclid Wide survey, i.e. from $z = 0.8$ to $z = 1.9$ with $H_{Euclid} < 24$. Also in this case we clearly notice the red galaxies segregation. In Fig. 5.43, we show the same distribution of Fig. 5.41 for the Deep Survey (i.e. $0.4 < z < 1.9$ with $H_{Euclid} < 26$) highlighting the position of Hα emitters with $f_{H\alpha} > 0.5 \times 10^{-16}$erg s^{-1} cm^{-2}. Figure 5.44, as Fig. 5.42, displays the results for the Wide survey (i.e. $0.8 < z < 1.9$ with $H_{Euclid} < 24$) with the Hα emitters selected to have $f_{H\alpha} > 2 \times 10^{-16}$erg s^{-1} cm^{-2}.

From these figures it is evident that with the empirical workflow developed in this thesis, we are able to reproduce realistic galaxy distributions, thanks also to the input DM simulation from which we extracted not only DM halos masses but also their positions.

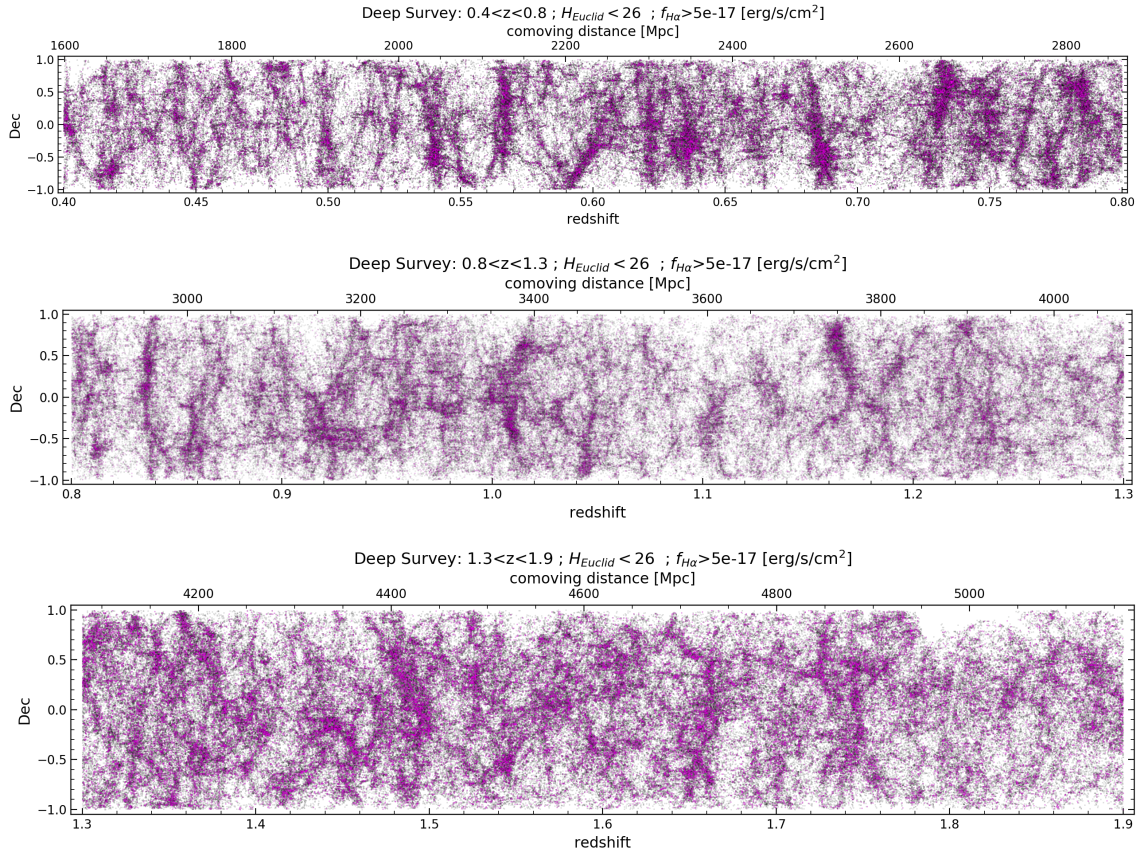

Fig. 5.43 Position of galaxies in the Millennium I+II mock (3.14 deg^2) in a redshift-Dec plane in the redshift range of the Euclid Deep Survey ($0.4 < z < 1.9$). Galaxies with $f_{H\alpha} > 0.5 \times 10^{-16}$erg/s/cm^2 are shown in magenta, while the whole population of galaxies is shown in black. The upper x-axis is also labeled according to the comoving distance.

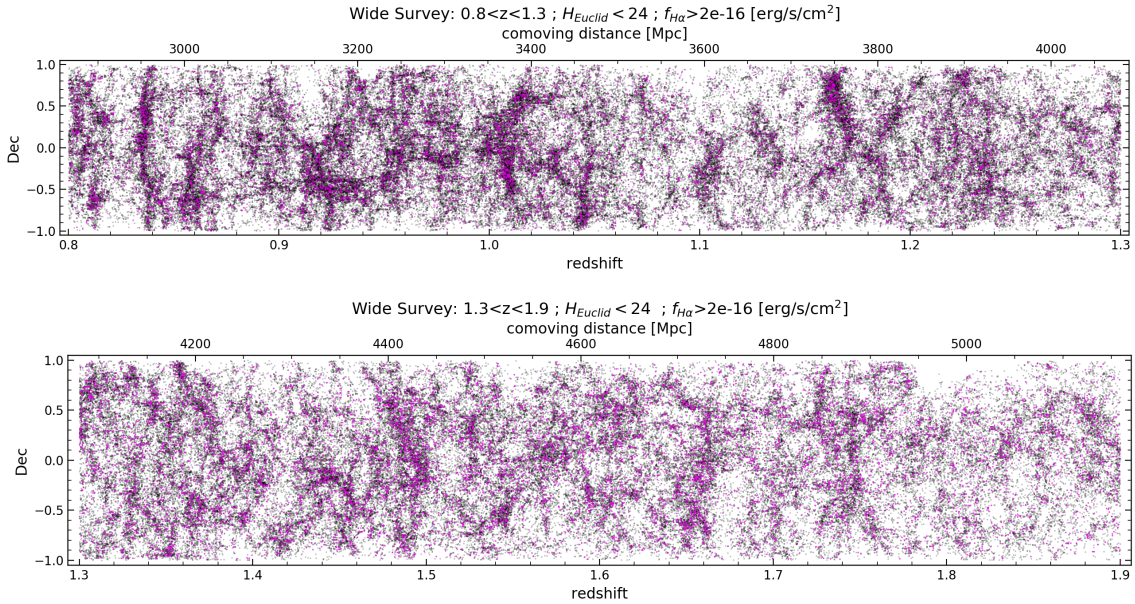

Fig. 5.44 Position of galaxies in the Millennium I+II mock (3.14 deg^2) in a redshift-Dec plane in the redshift range of the Euclid Wide Survey ($0.8 < z < 1.9$). Galaxies with $f_{H\alpha} > 2 \times 10^{-16}$erg/s/cm^2 are shown in magenta, while the whole population of galaxies is shown in black. The upper x-axis is also labeled according to the comoving distance.

Galaxy clusters

Galaxy clusters represent the third cosmological tool of the Euclid survey (Laureijs et al., 2011). Together with galaxy clustering and lensing by large scale structure, the evolution of the cluster mass function is fundamental for measuring dark energy parameters and constrain possible deviations from the general relativity. In addition, galaxy clusters are an extreme environment for galaxy evolution. In fact, in cluster environments, galaxies evolve the most in morphology and in star-formation efficiency due to the several interactions and merger that occur is such a dense environment.

The Euclid Mission is expected to observe nearly 3 million galaxies in clusters of mass above $10^{14}\,M_{\odot}$ (Sartoris et al., 2016). An issue concerns the identification of the cluster membership of galaxies due to the Euclid's photometric redshifts errors. To address this issue, a lot of effort has been put in developing cluster-finding algorithms to optimally select galaxy clusters and their members (see e.g. Euclid Collaboration et al. 2019, Maturi et al. 2019). Therefore, in order to test such softwares, realistic galaxy (and clusters) mock catalogs are essential. In this Section, we highlight the main features of the clusters present in our mock catalog to show its utility for testing such softwares and, in general, for cluster studies.

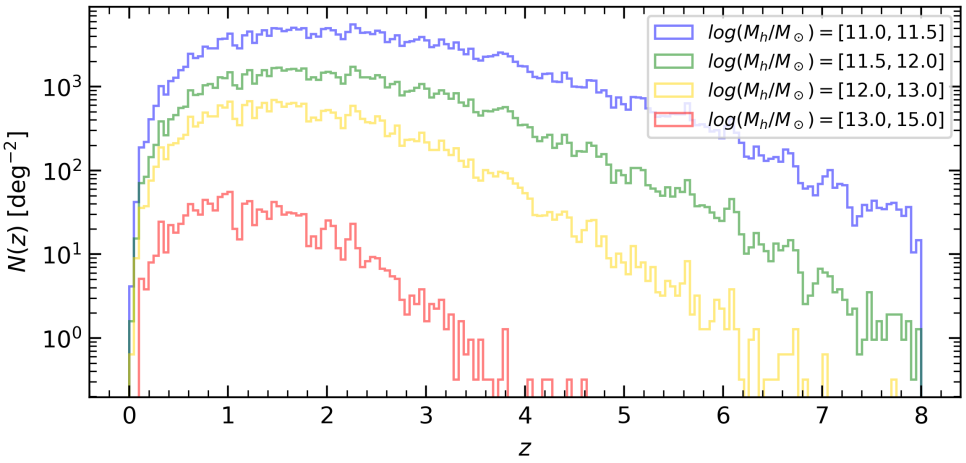

Fig. 5.45 Redshift distribution of galaxy clusters in different FOF mass bins for the Millennium I+II mock.

We show in Fig. 5.45 the redshift distribution of galaxy clusters and groups divided into several FOF mass bins. We do not impose any a-priori selection on the number of members of clusters/groups. Then, in Fig. 5.46 we focus on massive clusters with $M_{h,FOF} \geq 10^{14}\,M_{\odot}$ that are, as mentioned above, the clusters that will be identified with higher signal-to-noise from the detection algorithms (Euclid Collaboration et al., 2019). First, we show the redshift distribution of such clusters that peaks at $z \sim 0.8$. This is due to the very narrow lightcones we adopted (only 3.14 deg^2) that do not allow for many massive clusters at low redshifts. We find ~ 17 clusters per square degree in our mock catalog, meaning that in the Wide Survey $\sim 10^5$ clusters will be detected. Then we also show the total number

of observed cluster members and the ratio between the observed number and total number of cluster members as a function of redshift given photometric and spectroscopic requirements of the Euclid mission. In particular, we note that when applying the $H_{Euclid} < 24$ cut, the number of observed cluster members drops by more than 50% at $z \gtrsim 0.6$ and, when introducing the Hα minimum flux limit (i.e. $f_{H\alpha} > 2 \times 10^{-16} \mathrm{erg\,s^{-1}\,cm^{-2}}$), only $\sim 10\%$ of cluster members are observed at $z \gtrsim 0.6$. When combining the photometric and spectroscopic requirements we find no significant differences to when only the spectroscopic limit is applied. In Figs 5.47 and 5.48 we show, as examples, two galaxy clusters, located at $z \sim 0.3$ and $z \sim 1$, respectively, with $M_{h,FOF} \geq 10^{14} M_{\odot}$, in a RA-Dec plane. In these Figures we show the location of each galaxy of the cluster along with giving information about the stellar mass, the type (i.e. SF or Q) and the magnitude in the H band of each galaxy member. We also report the information on whether they are central, satellite or orphan galaxies. As expected, we clearly notice that the central galaxy is a massive quiescent galaxy with $M_* > 10^{11} M_{\odot}$ and that other quiescent galaxies are more centrally concentrated with respect to star-forming objects. We also note that more massive galaxies are, in general, more concentrated toward the cluster centre. The cluster shown in Fig. 5.48 falls in the Euclid redshift range, and, therefore, we also highlight the Hα emitters that are 18 in total (versus the 427 total members). This may indicate that also Hα emitters at $z \sim 1$ may be helpful to identify galaxy clusters at such redshifts. In addition, in Fig. 5.49, we show the red sequence for the two clusters considered. It has been found that galaxies in clusters follow well defined relations, such as the ubiquitous relation between galaxy color and magnitude (the color-magnitude relation, hereafter CMR). The CMR displays a bimodal galaxy distribution with a tight red concentration defining what is called the red sequence and more diffuse blue distribution known as the blue cloud. Notably, most of the quiescent galaxy population lies on the red sequence, while the majority of star-forming galaxies fall within the blue cloud. The existence of the red sequence indicates that star formation has been reduced, or quenched, for most quiescent galaxies that appear to be coeval and, therefore, show similar colors even up to high redshifts (i.e. $z \sim 1-2$, see e.g. Kodama & Arimoto 1997, Gladders & Yee 2000, Bell et al. 2004, Andreon et al. 2008, Mei et al. 2009). Usually, the CMR is evaluated using rest-frame colors, possibly bracketing the 4000Å break, however, given that galaxies within a cluster lie at the same redshift, also observed colors can be used. In Fig. 5.49, we show the CMR diagram with observed colors matching U-B rest-frame and clearly see that Q galaxies of our clusters follow a more or less tight relation exhibiting redder colors that SF objects. In both cases, we also note that the central galaxy, as expected, is the brightest object and shows the redder colors of the cluster. In addition, we also show a theoretical prediction made with Bruzual & Charlot (2003) SPS models of a galaxy formed at $z = 5$ with an exponentially declining star-formation history with $\tau = 0.1$ Gyr to mimic the central galaxy. In both examples shown, we find that the prediction made with SPS models are very similar to the central galaxy of our cluster. This indicates once again that the clusters in our mock catalog are realistic. Finally, in Fig. 5.50, we show the magnitude distribution in several bands of the cluster members. In the figure, we also show the value of the magnitude m_* at the clusters redshifts for the H band. This value indicates the characteristic magnitude at which the power law of the luminosity function, represented by a

Schechter function, cuts off. We evaluated this value with Bruzual & Charlot (2003) SPS models adopting an exponentially declining star-formation history (with τ ranging from 0.1 to 1 Gyr) and several redshift of formation (from $z = 5$ to $z = 3$). These values have been derived by comparing literature data to the magnitude evolution from a SPS model: it has been seen that the evolution of the magnitude at the knee of the luminosity function of clusters evolves as a galaxy with exponentially declining SFH with $\tau \sim 0.1$ Gyr and formation redshift $\gtrsim 3$ (e.g. Kodama & Bower 2003, Strazzullo et al. 2006, Andreon 2013). These values are also in agreement with observed data by de Propris et al. (1999) and Fassbender et al. 2014. In both clusters we clearly see that with Euclid we will be able to recover the luminosity function even at magnitudes below the knee, indicating once again the usefulness of our mock catalogs to make predictions for cluster studies.

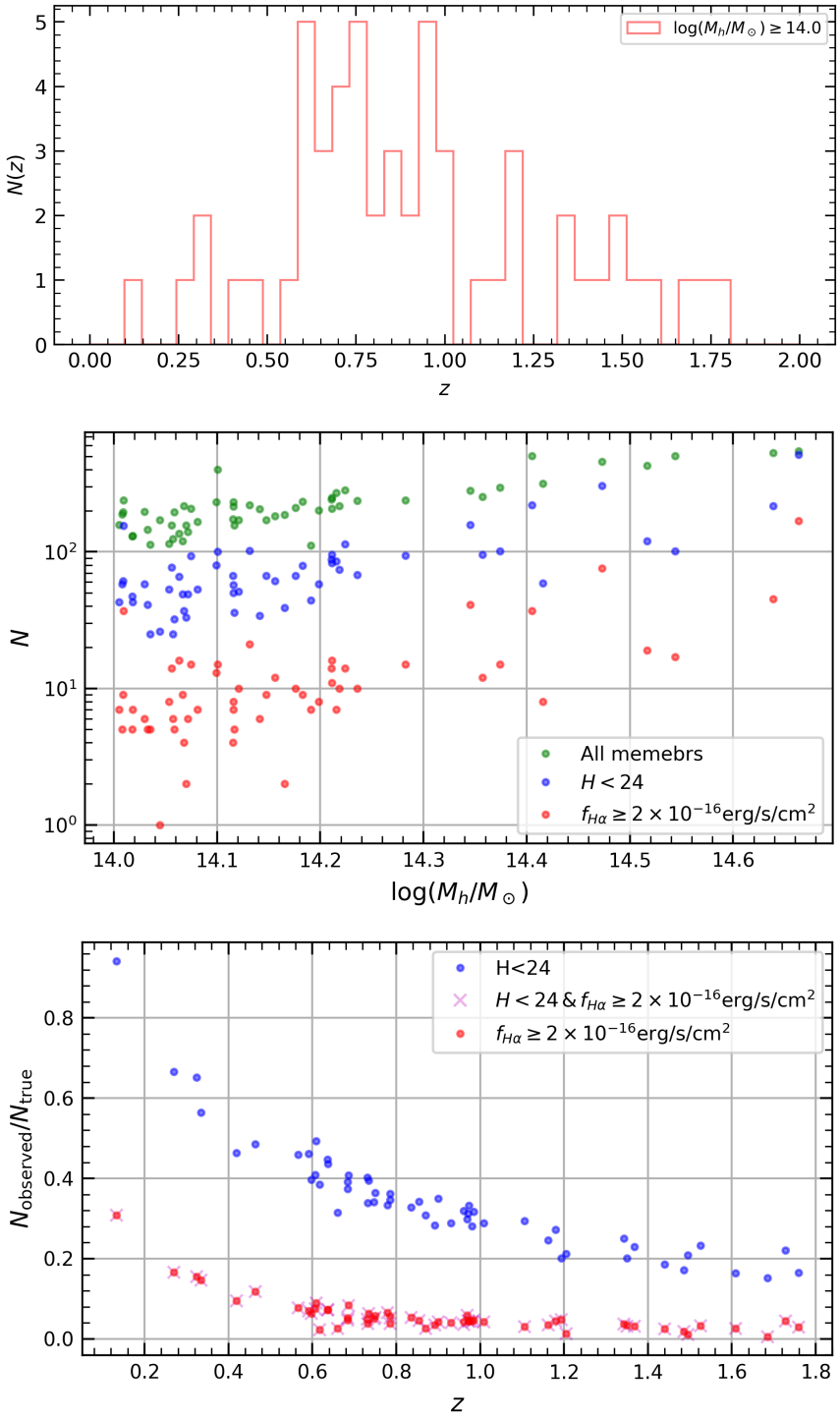

Fig. 5.46 Top: redshift distribution of most massive halos, i.e. main halos with $M_h > 10^{14} M_\odot$. Middle: total number of galaxy members in each massive halo. We show the total number of cluster members in green, the number of members with $H_{Euclid} < 24$ in blue and the number of members with $f_{H\alpha} > 2 \times 10^{-16}$erg s^{-1} cm^{-2} in red. Bottom: fraction of observed galaxies within massive (i.e. $M_h > 10^{14} M_\odot$) main halos with respect to the true total number as a function of redshift. We show the fraction of galaxies with $H_{Euclid} < 24$ in blue points, the fraction of galaxies with $f_{H\alpha} > 2 \times 10^{-16}$erg s^{-1} cm^{-2} with red points and the fraction of galaxies with $H_{Euclid} < 24$ and $f_{H\alpha} > 2 \times 10^{-16}$erg s^{-1} cm^{-2} with pink crosses.

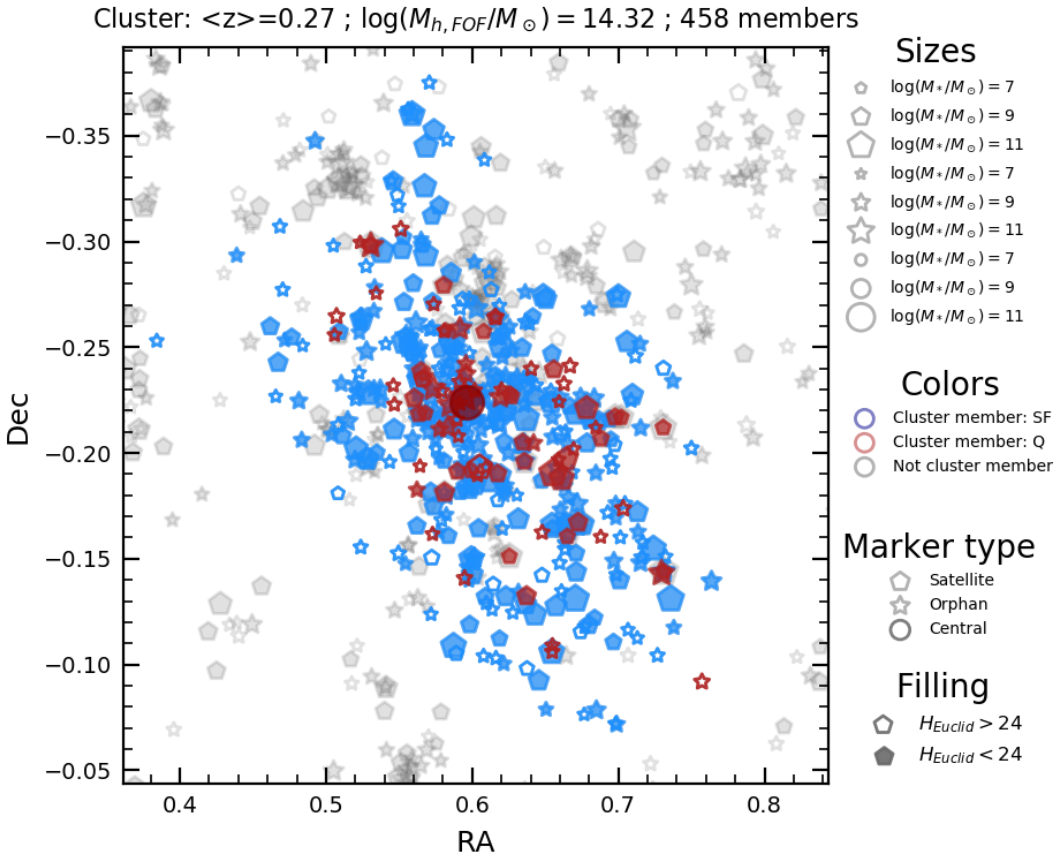

Fig. 5.47 Cluster of galaxies of the Millennium I+II mock with $ID_{FOF} = 369006543000013$. We show a cluster with 458 members with a mean redshift of 0.27 in a $Ra - Dec$ plane. Colored points represent the cluster members (SF galaxies in blue, Q galaxies in red) while grey points show all galaxies that are within the expected Euclid's photometric error: $0.05(1+z)$, i.e. galaxies in the range $0.24 < z < 0.3$ (see Euclid Collaboration et al. 2020). The size of each point represents its mass as indicated in legend on the right. Moreover, we plot with pentagons galaxies that reside in satellite halos, with stars orphan galaxies and with a circle the central galaxy of the cluster. Finally, we also show with filled and open points galaxies with $H_{Euclid} < 24$ and $H_{Euclid} > 24$, respectively, to show the number of cluster members that Euclid will be able to observe.

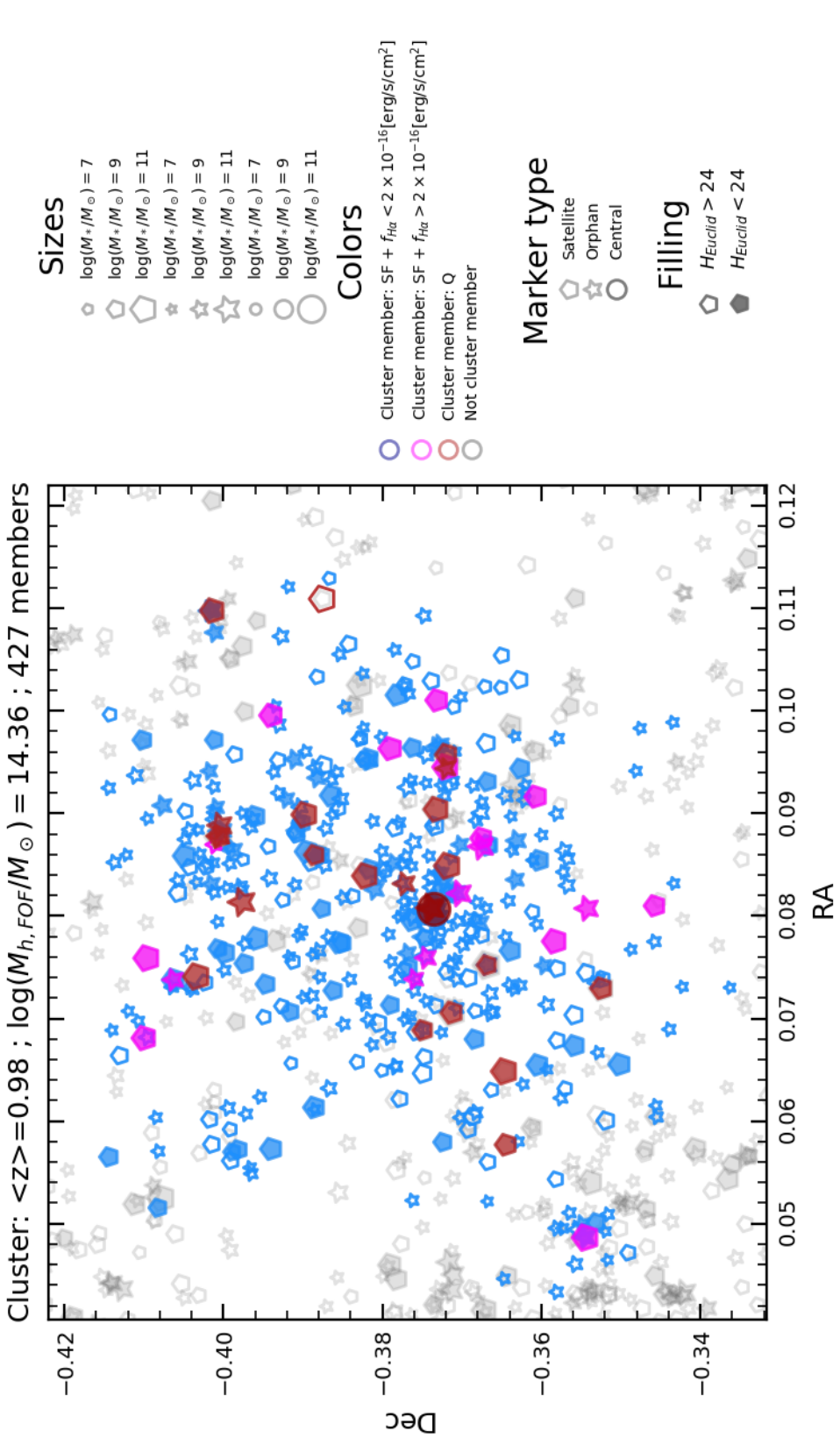

Fig. 5.48 Cluster of galaxies of the Millennium I+II mock with $ID_{FOF} = 407000569000024$. We show a cluster with 427 members with a mean redshift of 0.98 in a $Ra - Dec$ plane. Labels and symbols as in Fig. 5.47 with the addition that we show SF galaxies with $f_{H\alpha} > 2 \times 10^{-16}$[erg/s/cm^2] in magenta and galaxies with $f_{H\alpha} < 2 \times 10^{-16}$erg s^{-1} cm^{-2} in blue.

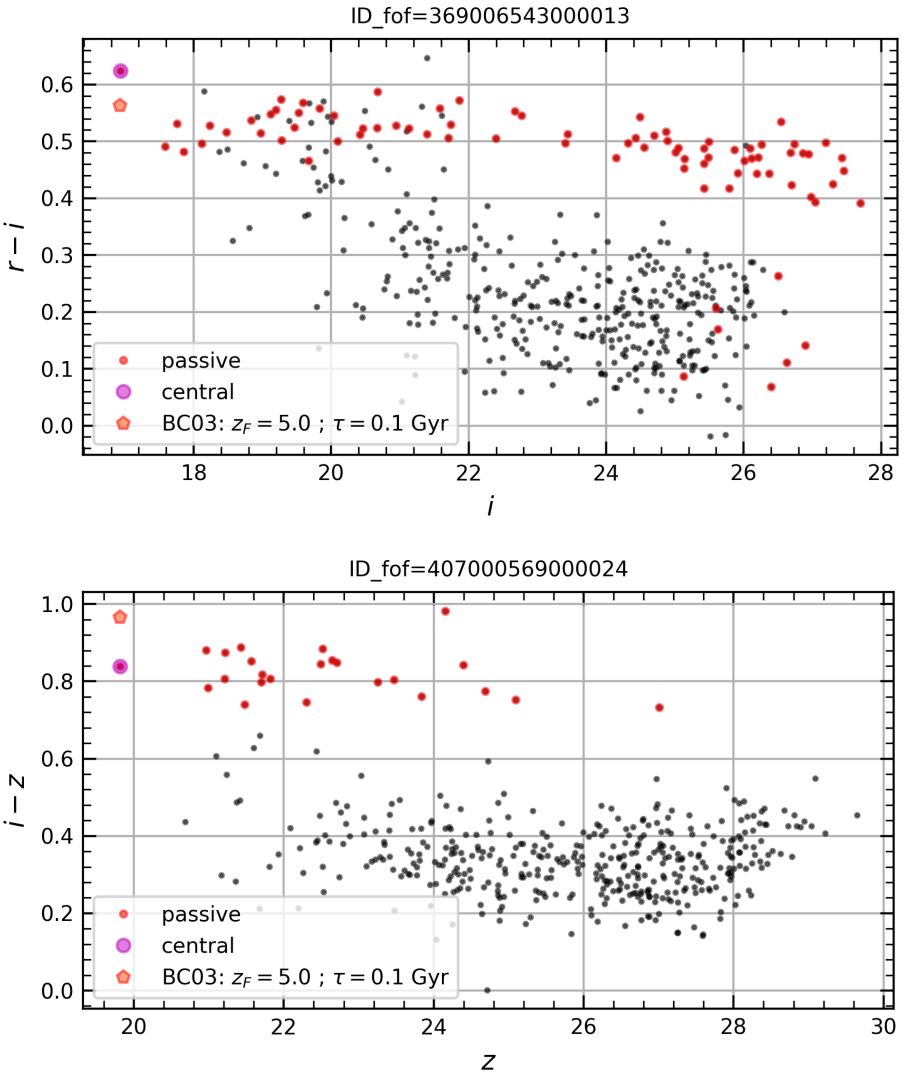

Fig. 5.49 Red sequence of the clusters with $ID_{FOF} = 369006543000013$ (top) and $ID_{FOF} = 407000569000024$ (bottom), shown in Figs 5.47 and 5.48. We show, in observed frame, the $(r-i)$ vs. i plane for the first cluster and $(i-z)$ vs. z for the second, approximately corresponding in both cases to $(U-B)_{rest}$ vs. B_{rest}. In both panels we show with red points the Q galaxies of the cluster, with black points the SF galaxies and in magenta the central galaxy. In addition, we show with a red pentagon the theoretical prediction made with Bruzual & Charlot (2003) SPS models of a galaxy formed at $z = 5$ with an exponentially declining star-formation history with $\tau = 0.1$ Gyr placed at the redshift of the cluster.

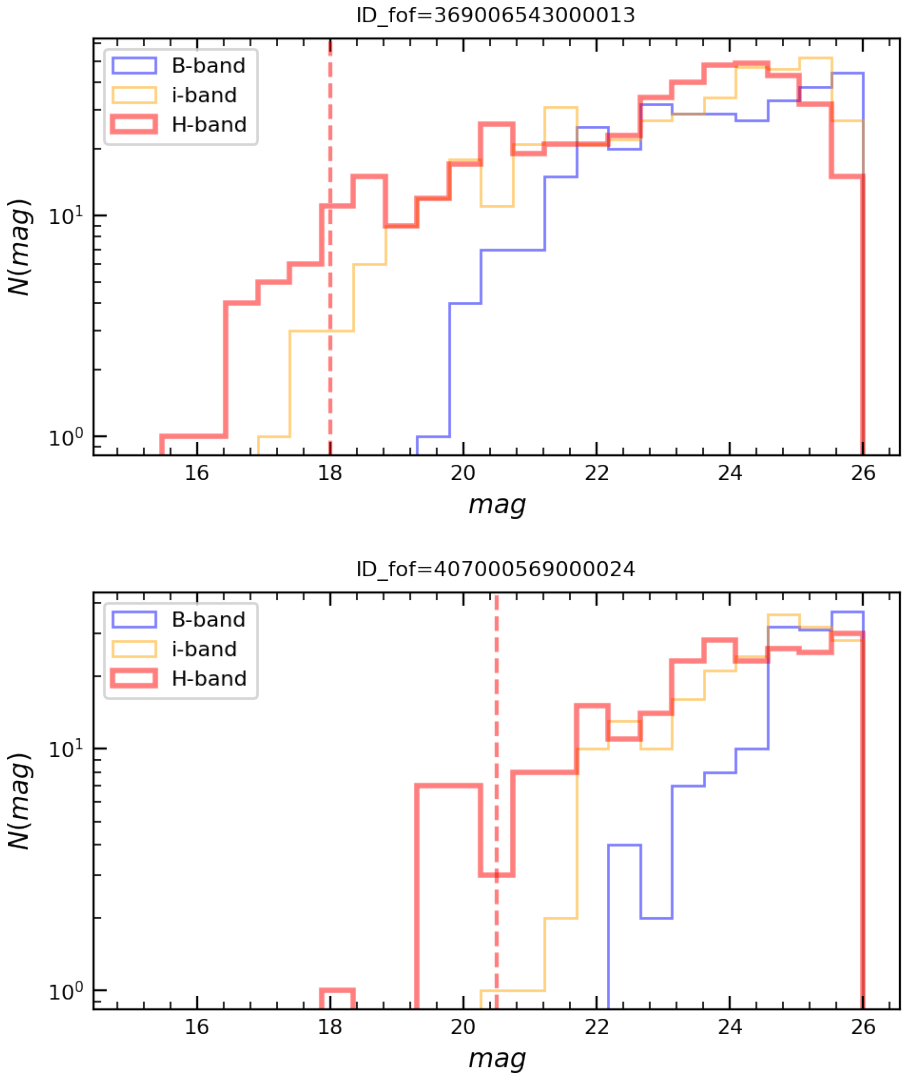

Fig. 5.50 Histogram of the magnitude distribution of the cluster members for several bands (B in blue, i in yellow, H in red). In top panel, we show the distribution for the cluster with $ID_{FOF} = 369006543000013$ and in bottom panel for the cluster with $ID_{FOF} = 407000569000024$. Vertical dashed lines represent the value of m_* at the clusters redshifts for the H band that have been evaluated through SPS models.

Sizes of Hα emitters

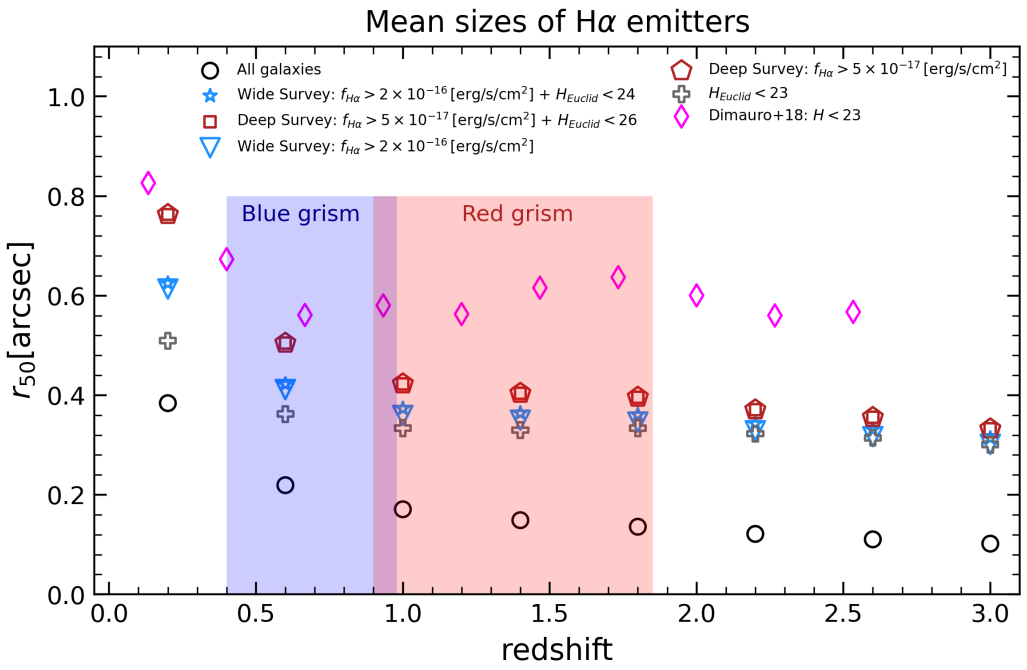

Fig. 5.51 Half-light radius (r_{50}) as a function of redshift from $z = 0$ to $z = 3$. We show the mean values in several redshift bins for all galaxies in the mock with black open points, for the galaxies selected to have $H_{Euclid} < 23$ with grey crosses and results by Dimauro et al. (2018) with magenta diamonds. In addition, we show the mean values for Hα emitters with two different line flux limits at $f_{H\alpha} > 2 \times 10^{-16}$erg s^{-1} cm^{-2} for the Wide Survey and $f_{H\alpha} > 0.5 \times 10^{-16}$erg s^{-1} cm^{-2} for the Deep Survey with blue triangles and red pentagons. Moreover, we also show the latter distributions with the additional cut in $H_{Euclid} = 24$ and $H_{Euclid} = 26$ with blue star and red squares for the Wide and Deep surveys, respectively. Finally, we also show with shaded blue and red areas the redshift ranges covered by the blue and red grisms of Euclid, respectively.

As mentioned in Sect. 1.5, Euclid aims at spectroscopically observe galaxies in the range $z \sim 1-2$ thanks to the detection of Hα emission line. In the Wide Survey, Euclid is expected to detect Hα luminosities for $\sim 4 \times 10^7$ sources going below the knee of the luminosity function out to $z \sim 1.8$ (Laureijs et al., 2011). However, when performing slitless spectrocopy, like in Euclid, the spectral resolution (i.e. the ability of a spectrograph to resolve features) is inversely proportional to the galaxy size. Therefore, the galaxy size impacts on the ability of an instrument to measure line fluxes and, as a consequence, its redshift. Therefore, as already mentioned in Sect. 5.6, it is important for a mock catalog to reproduce realistic sizes in order to make useful predictions. In this section, we briefly explore the sizes of the Hα emitters present in our mock catalog. We show in Fig. 5.51 the mean sizes of Hα emitters in several redshift bins and applying several magnitude and line fluxes limits. More in detail, we applied the selections for the Euclid Deep (i.e. $H_{Euclid} < 26$ and $f_{H\alpha} > 0.5 \times 10^{-16}$erg s^{-1} cm^{-2}) and Wide (i.e. $H_{Euclid} < 24$ and $f_{H\alpha} > 2 \times 10^{-16}$erg s^{-1} cm^{-2})

surveys. We note that, adding the magnitude cut in H_{Euclid} to the line fluxes limits does not affect much the distributions. When considering Hα emitters, their sizes are on average bigger with respect to the mean sizes of all galaxies. Finally, when comparing with observations, we find that the sizes of our mock are smaller than those predicted by Dimauro et al. (2018). A recent study by Bagley et al. (2020), using HST datasets, found a median effective radius $R_{eff} \sim 0.39''$ for galaxies at $0.9 < z < 1.6$ with $H < 24$ and $f_{H\alpha} > 2 \times 10^{-16}$erg s^{-1} cm^{-2}. This value in in agreement with the predictions of our mock. Once again, this suggests that more investigation for galaxy sizes in our mock is needed.

Galaxies redshift distributions

Finally, in this section we show the redshift distributions of galaxies divided into galaxy types and adopting several Euclid magnitude cuts. As explained in Sect. 1.5, Euclid will perform the Wide and Deep surveys that will go as deep as $H = 24$, $VIS = 24.5$ and $H = 26$, $VIS = 26.5$, respectively. In addition, Hα emitters will be detected down to fluxes of $\sim 2 \times 10^{-16}$ erg s^{-1} cm^{-2} in the Wide survey and $\sim 0.5 \times 10^{-16}$erg s^{-1} cm^{-2} in the Deep. In Fig. 5.52 and 5.53, we show the redshift distributions of the galaxies in the Millennium I+II mock divided by galaxy type with several magnitude cuts in the Euclid H and VIS bands, respectively. In addition, we also show the distributions of galaxies selected with the Hα flux limits. These figures can be extremely useful to make predictions about the number of galaxies that Euclid will be able to observe in specific redshift intervals, of a specific galaxy type, with certain magnitude limits or with some minimum line fluxes.

For example, concerning high-z studies, we find that Euclid will detect ~ 285 objects per square degree in the Wide Survey with $H_{Euclid} < 24$ at $4 < z < 7$ and this number increases to ~ 12687 objects per square degree in the Deep Survey with $H_{Euclid} < 26$ in the same redshift interval. While, in the Deep Survey, with $H_{Euclid} < 26$, Euclid will see ~ 2977 objects per square degree at $z > 7$.

Another example, is shown in Fig. 5.54 where we focus on quiescent galaxies and show the number of quiescent galaxies that can be detected with the blue grism (i.e. when the $D4000$ break enters the grism at $z > 1.453$) at several minimum H_{Euclid} limits. We also show the distributions in redshift of quiescent galaxies of our mock at several H_{Euclid} limits. We clearly see that with the Wide limits (i.e. $H_{Euclid} < 24$) no quiescent galaxies can be detected at $z \gtrsim 3.5$, while in the Deep (i.e. $H_{Euclid} < 26$), quiescent galaxies can be detected up to $z \sim 4$. In particular, in the Deep Survey ($H_{Euclid} < 26$) over 40 deg^2, Euclid Blue Grism will detect $\sim 10^5$ quiescent galaxies at $z > 1.453$.

Finally, in Fig. 5.55, we show the distribution of the Lyα line flux as a function of redshift. This line is especially important for studying high-z galaxies within the re-ionization epoch. We find that ~ 0.31 objects per square degree satisfy the $f_{Ly\alpha} > 5 \times 10^{-17}$ erg s^{-1} cm^{-2} limit at $z > 6.5$, meaning that in the Deep Survey ~ 12 Lyα emitters at $z > 6.5$ will be detected, even though at such redshifts current observed uncertainties are very large.

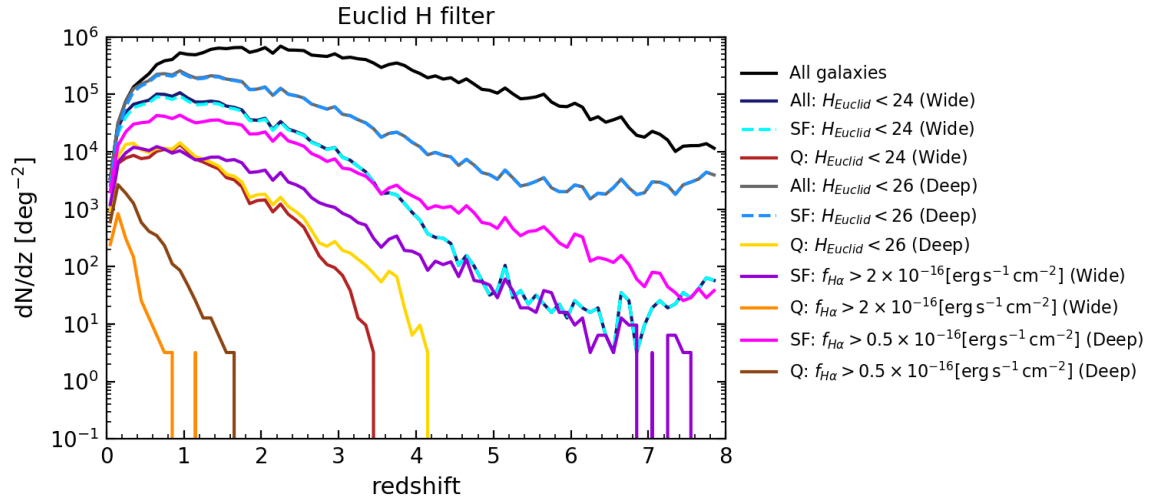

Fig. 5.52 Redshift distribution of galaxies dN/dz in the lightcone 23 of the Millennium I+II mock catalog divided by galaxy type. We also show the distributions with magnitude cuts in the Euclid H band (for the Wide and Deep Surveys) and in Hα line fluxes. We show the distribution for all the galaxies in the mock with a black solid line. Distributions for SF galaxies with $H_{Euclid} < 24$, $H_{Euclid} < 26$, $f_{H\alpha} > 2 \times 10^{-16}$erg s^{-1} cm^{-2} and $f_{H\alpha} > 0.5 \times 10^{-16}$erg s^{-1} cm^{-2} are shown with dashed cyan, dashed blue, violet and magenta lines, respectively. Distributions for Q galaxies with $H_{Euclid} < 24$, $H_{Euclid} < 26$, $f_{H\alpha} > 2 \times 10^{-16}$erg s^{-1} cm^{-2} and $f_{H\alpha} > 0.5 \times 10^{-16}$erg s^{-1} cm^{-2} are shown with dark red, yellow, orange and brown lines, respectively.

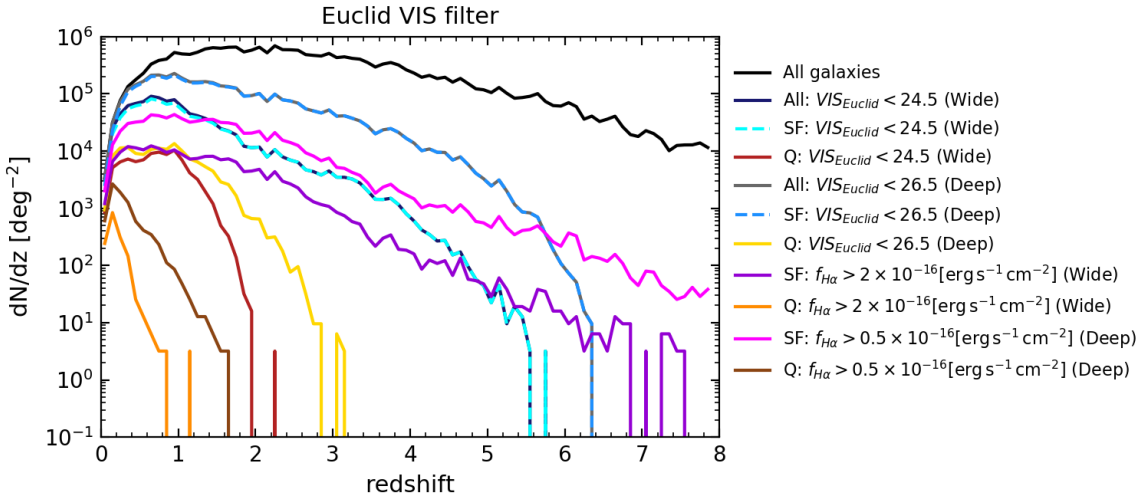

Fig. 5.53 Redshift distribution of galaxies dN/dz in the lightcone 23 of the Millennium I+II mock catalog. We also show the distributions with magnitude cuts in the Euclid VIS band (for the Wide and Deep Surveys) and in Hα line fluxes. Lines as in Fig. 5.52.

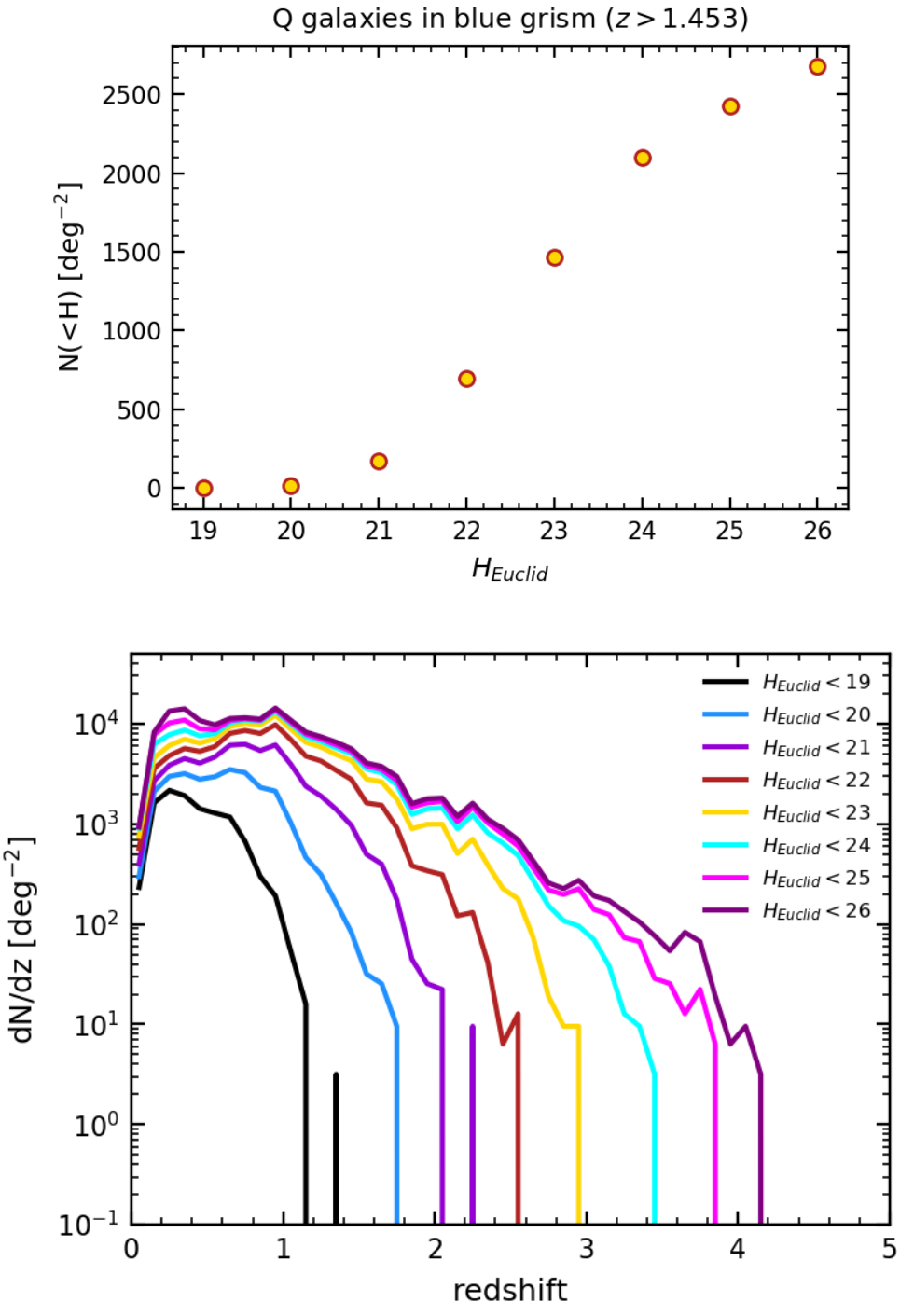

Fig. 5.54 Top: the number of quiescent galaxies (per square degree) at several maximum H_{Euclid} limits that can be detected with the blue grism (i.e. Q galaxies at $z > 1.453$). Bottom: redshift distributions of quiescent galaxies given several H_{Euclid} limits.

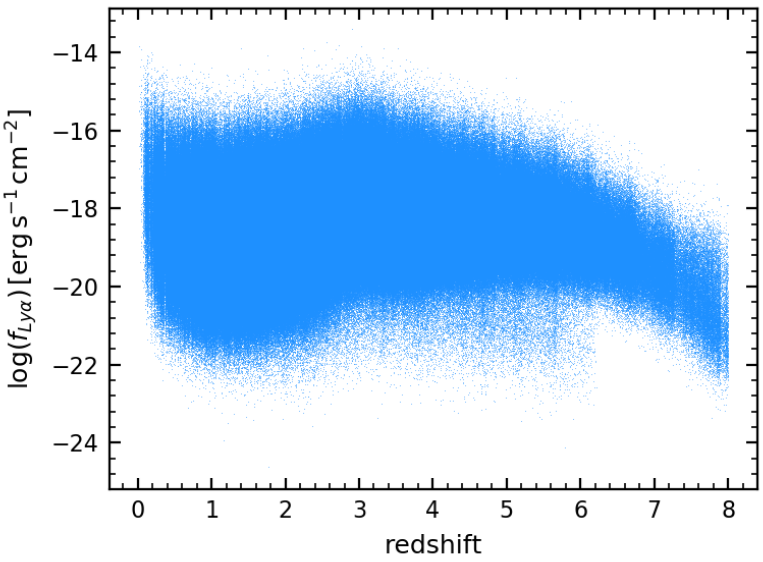

Fig. 5.55 Distribution of the Lyα fluxes as a function of redshift.

6

SUMMARY AND CONCLUSIONS

Next generation missions and surveys (e.g. Euclid, MOONS, JWST, LSST) will explore large volumes of the Universe and are promising tools that will provide major improvements in our understanding of galaxy formation and evolution, cosmological parameters, and the nature of dark energy and neutrino mass. Such future missions will produce huge datasets to be analysed. Therefore, in order to maximize their scientific exploitation, derive and minimize systematic uncertainties and, in general, take full advantage of the forthcoming datasets of future missions it is essential to use realistic and reliable galaxy mock catalogs to make predictions. Broadly speaking, realistic mocks must reproduce many observed properties, such as the number density of galaxies as a function of magnitude, mass, color, and spectral type, their redshift and spatial distribution, as well as the properties of specific classes of galaxies such as Hα emitters and the properties of the early-type galaxy population, cluster properties, cluster's members and also the properties of the underlying DM halos in which galaxies reside.

In this thesis we first derived an empirical model to link DM halos and galaxies, adopting a (sub)halo abundance matching technique. Then we presented an empirical technique that, starting from the outputs of an N-body DM simulation, is able to create a galaxy mock catalog with a large variety of observed and physical properties. The method can be roughly divided into three steps: the first step consists in assigning galaxy stellar masses to DM halos. The second step divides galaxies into star-forming and quiescent objects and, finally, the third step assigns other physical properties of galaxies using the public code EGG (Schreiber et al., 2017). Next, we tested the method on the lightcones of two different ΛCDM DM simulations (the Millennium I+II (Springel et al., 2001) and DUSTGRAIN-*pathfinder* (Giocoli et al., 2018) simulations) and compared our results to many observations for several properties.

The empirical method presented in this thesis is very flexible and therefore it can be easily applied to *any* input DM simulation with the only the following information:

- halo masses (M_{200} for main halos),
- M_{infall} for satellites and orphans, or, alternatively, the distance of the subhalo from the central halo,
- the redshift of each halo,
- the position of each halo (in order to allow for clustering measurements),
- M_{FOF} for all halos (in order to allow for clusters studies).

The method is computationally cheap since it only relies on empirical relations and constraints without the explicit implementation of the physical processes involved in galaxy formation and evolution and, therefore, very large volumes of the Universe can be simulated. These characteristics make this method particularly useful to create large galaxy mock catalogs to make predictions, to test algorithms and to minimize uncertainties for future surveys and missions.

6.1 Summary

In the following, we briefly summarize the content of this thesis and highlight the main results along with the open issues we are currently facing and the plans to overcome such problems.

6.1.1 The connection between galaxies and their dark matter halos

In Chapter 2, we described in detail the method adopted to link DM halos and galaxies. We adopted the (sub)halo abundance matching technique, that, by means of a direct comparison among the halo and stellar mass functions, can provide a stellar-to-halo mass relation (SHMR). In addition, when deriving the relation we incorporated a scatter in stellar mass at fixed halo mass (called *relative* scatter) fixed at $\sigma_R = 0.2$ dex, in order to take into account the dispersion in stellar mass at fixed halo mass, due to the effects of different merging histories, spin parameters and concentrations of halos. In order to contruct a homogenous and extended in redshift sample, we adopted state-of-the-art observed stellar mass functions of SDSS galaxies at $z \sim 0$ (Baldry et al., 2008), from the COSMOS field at $0.2 < z < 4.0$ (Ilbert et al., 2013) and from the CANDELS fields at $4 < z < 8$ (Grazian et al., 2015). We stress here that SDSS, COSMOS and CANDELS are currently the best fields with a homogeneous redshift coverage from $z = 0$ to $z = 8$ because of their statistical and photometric accuracy in the photometric redshifts, stellar masses, and SMF determination. As mentioned above, we used the lightcones of two different ΛCDM DM simulations: the Millennium I+II (Springel et al., 2001) and DUSTGRAIN-*pathfinder* (Giocoli et al., 2018) simulations. To briefly recap: for the Millennium I+II simulation we used all the 24 available lightcones, from $z = 0$ to $z = 8$ with halo masses $M_{200} > 1.7 \times 10^{10} M_{\odot}$, where each lightcone is over an area of 3.14 deg^2. For the DUSTGRAIN-*pathfinder* we used 256 lightcones, from $z = 0$ to $z = 4$ with halo masses $M_{200} > 3.16 \times 10^{12} M_{\odot}$, each with an area of 72.18 deg^2. We then analytically described the SHMR in each redshift bin perfoming a fit with a simple double power law function that only depends on four parameters: M_A (the halo mass at the trend inversion, if present), A (the ratio between the stellar and halo masses at the inversion), γ (the slope at masses above M_A) and β (the slope for masses below M_A) and evaluated their evolution with redshift, building an empirical models throughout the entire cosmic history from $z \sim 8$ to the present.

6.1.2 Results on the stellar-to-halo mass relation

In Chapter 3 we present the results for both DM simulations with and without the inclusion of the *relative* scatter. Our main results and findings can be summarized as follows:

1. The SHMR we derived in the various redshift bins monotonically increases (with slope $\beta \sim 1$) as a function of halo mass and reaches a peak at $M_A \sim 11.6 - 12.5$ (depending on redhift), after which the relation decreases monotonically (with slope $\gamma \sim 0.3 - 0.7$) at higher halo masses.

2. The SHMR at $z < 4$ and at $z > 4$ shows opposite trends with redshift while maintaining the same trends with halo masses: at $z < 4$ the SHMR increases with increasing redshift for $M_h > M_A$

and decreases for $M_h < M_A$. At $z > 4$ the trends are reversed. This is due to the differential evolution of the SMF that reflects in the SHMR itself.

3. The introduction of a relative scatter mainly affects the massive end slope (in particular, the parameter γ shows larger values when the scatter is introduced) but also marginally influences all other parameters because they are all correlated. We note that the effect of the scatter is always of the order of a few percent of the SHMR, even if its effect is systematic and depends on the exact value of the scatter introduced .

4. The SHMR can interestingly be interpreted as the star-formation efficiency (SFE, $f_* = (M_*/M_h)f_b^{-1}$), that is simply defined as the fraction of baryons locked in stars. When considering a constant baryon fraction ($f_B = 0.153$ for a Planck15 cosmology), we find that the SFE is always lower than 20% showing a peak at intermediate halo/stellar masses, i.e. at M_A that roughly corresponds to $\log(M_*/M_\odot) \sim 10.3 - 10.5$ which is the transition mass between different galaxy types (Bolzonella et al., 2010; Kauffmann et al., 2003; Pozzetti et al., 2010). Then the SFE decreases at lower and higher masses.

5. We also built a simple empirical model to describe the evolution of the SHMR with cosmic time. Defining such a model is useful, not only to study the evolution of the SHMR with time and extract some physical information, but also to easily populate any input halo with a galaxy with a certain stellar mass at any redshift. We find that M_A, which is the mass where the SHMR peaks, increases with increasing redshift up to $z = 4$ where it switches trend and decreases rapidly up to $z \sim 8$. The parameter A, which is the value of M_*/M_h at the peak, instead shows a mild decreasing trend with increasing redshift from $z \sim 0$ to $z \sim 8$. The same decreasing trend is also found for γ, while β is well fitted with a constant value even if the uncertainties of the measures of this parameter are quite large (given that it is difficult to probe the low mass part of the SHMR due to both observational limits and resolution limits of DM simulations).

6. When comparing our SHMR with literature results (both observations and SAMs) we find a large spread among all literature works that increases with increasing redshift even up to one order of magnitude at $z \gtrsim 3$. The same differences are also found when comparing the SHMR peaks we evaluate with literature results.

The SHMRs bell shape can be explained by means of the feedback mechanisms operating in galaxies where SNe suppress galaxy formation at masses below the peak and AGNs at masses above it. In addition, if galaxies followed the same hierarchical merging history of halos, we would expect that M_*/M_h remains constant with redshift, but galaxies follow a downsizing scenario, explaining our observed redshift evolution. Recent observational studies (e.g. Posti et al. 2019), using dynamic to derive galaxy halo masses, found evidences that the SHMR (and, consequently, the SFE) depends on the galaxy type, with red and passive early-type galaxies residing in most massive halos with respect to blue late-type galaxies. In particular, massive star-forming galaxies show a much larger SFE with respect to the same mass passive galaxies.

An open issue concerns the SFE and its evolution with redshift. We find that at $z < 4$ the SFE increases with increasing redshift at masses higher than M_A and decreases for lower ones. At $z > 4$ the trends are reversed, even though the errors are very large and don't let us draw any definitive conclusion on the real evolutionary trends at high-z. By comparing with literature (e.g. Stefanon et al. 2017, Harikane et al. 2018, Moster et al. 2018, Behroozi et al. 2019), we find that there is not agreement yet on whether the SFE is evolving or if it remains approximately constant at $z > 4$. This is an open issue that will be addressed in future years with deeper galaxy observations. Finally, another open problem is the exact value of the baryon fraction and on whether it evolves with redshift and/or depends on halo masses. Several observational and theoretical works (e.g. Andreon 2010, Eckert et al. 2016, Davé et al. 2010) have tried to resolve this issue, but it is still not clear if the baryon fraction depends on redshift and halo masses. However, if we consider an evolution of the baryon fraction with halo mass, cosmic time, or a combination of both (like e.g. a baryon fraction that decreases with increasing cosmic time at fixed halo masses), the overall trends of the SFE at $z < 4$ we find are not affected.

6.1.3 Building the mock catalogs

In Chapter 4 we describe in detail the empirical procedure we have followed to create our mock catalogs. As mentioned above, once we have the information about the halos (i.e. their mass M_{200} , M_{infall}, redshift and position), we produce our mock catalogs in three steps:

1. We assigned stellar masses to halos using the empirical model presented previously. We also incorporate the relative scatter (with $\sigma_m = 0.2$ dex) when calculating the stellar masses. We validated our method finding excellent agreement between our mocks and several observed estimates of the SMFs. We also find that orphan galaxies are fundamental in order to construct a complete sample of galaxies, while their contribution become less important at high masses (at $\log(M_*/M_\odot) \gtrsim 10$ and $z \sim 0.35$ they contribute to less than 10% of the total number of halos).

2. We divide the galaxies into star-forming and quiescent objects by first evaluating a star-forming fraction from $z = 0$ to $z = 4$ with the aid of observed SMFs divided by galaxy type using Peng et al. 2010 and Ilbert et al. 2013 SMFs. Then we assigned a SF/Q flag according to the probability distribution. In order to test the reliability of such classification, we then calculated the SMFs divided by type for our mock finding a good agreement between our mock and the observed estimates.

3. We assigned all other physical properties with the public code EGG (Schreiber et al., 2017, 2018). The EGG code is purely empirical and has been calibrated on the scaling relations of galaxies observed in the CANDELS fields in order to reproduce several observed properties that are assigned solely based on the stellar mass, redshift and SF/Q flag. In the code, each galaxy is split into two components: a bulge and a disk. To each of these components morphological parameters and SED are assigned from a lookup table (composed by 250 dust-extincted optical

SEDs built from stacked observations in the COSMOS field) according to the SF/Q flag based on the position of each galaxy in the UVJ rest-frame diagram. At the same time, the SFR, emission lines, galaxy sizes and global SEDs are calculated. However, the galaxy SEDs generated by EGG do not include reddening from the Milky Way and the produced catalogs are missing foreground stars and active-galactic nuclei (AGNs, or quasars). These issues are not addressed in this work but can be source of biases in scientific analyses and, therefore, when using the final mocks of this work one needs to take this caveat into consideration.

6.1.4 Validation of the mocks and forecasts

Finally, in Chapter 5 we validated properties of our mock catalog. In particular, we run the entire workflow on lightcone 23 of the Millennium I+II simulation up to $z \sim 8$ (limited to $M_h > 10^{10.2} M_\odot$ therefore $M_* \gtrsim 10^{7.2} M_\odot$ at $z \sim 0$) and on lightcone 1 of the DUSTGRAIN simulation up to $z \sim 4$ (limited to $M_h > 10^{12.5} M_\odot$ therefore $M_* \gtrsim 10^{11} M_\odot$ at $z \sim 0$) and proceed to validate such results. We tested the following properties:

1. Photometry and colors: we compare the number counts of our mocks to several observations in the u-CFHT, i-Subaru, H-UltraVISTA and $[3.6]\mu$m IRAC bands. In addition, in all cases we also show the results of the Henriques et al. (2015) SAM which has been applied to the same Millennium I+II lightcone we used. In general, we find excellent agreement with observations from the faintest to the brightest objects (up to mag$\sim 28-29$ in all bands which approximately match with the limiting magnitudes in the mock). We find, however, some differences with observed estimates when looking at number counts divided by galaxy types. To address such differences, we explore how our mocks populate the rest-frame $NUVrJ$ diagram and how it compares with results on the COSMOS2015 catalog. We found some differences among our results and COSMOS2015 catalog and these are due to the fact that EGG calibrates the SED assignment on the UVJ diagram instead of the NUVrJ. This leads to some differences in the final outputs rest-frame colors and, in general, in photometry, when considering the SF/Q populations separately.

2. SFR: we evaluate the $SFR - M_*$ plane in several redshift bins from $z = 0$ to $z = 6.5$ and compare with the literature. In general, we find that our results agree well with several observations at $\log(M_*/M_\odot) \gtrsim 9$ and the main sequence is clearly visible. Below this mass it seems that the model implemented in EGG underpredicts the SFR of literature observations and models, even though it is difficult to draw definitive conclusions given the large spread in observations at these masses. We also calculated the star-formation rate density from $z = 0$ to $z = 8$ calculated on the Millennium I+II mock compared with several literature results. Also in this case, we find a good agreement with literature results given also their large dispersion especially at $z > 4$.

3. Emission lines: we started by inspecting the Hα line. We have verified that the Hα emission is different for quiescent and star-forming galaxies. Then, we computed the redshift distribution of

Hα emitters with several different flux limits and compared with Pozzetti et al. (2016) empirical models. We also evaluated the cumulative number counts of Hα emitters as a function of Hα flux. In both cases, we find that our mock overpredicts the number of Hα emitters with respect to Pozzetti et al. (2016) models for $f_{H\alpha} \gtrsim 1.0 \times 10^{-16}$erg/s/cm^2. For example, for $f_{H\alpha} \geq 2.0 \times 10^{-16}$erg/s/cm^2 and $z \sim 1.5$ our mock overpredicts Pozzetti et al. (2016) models 1,2 and 3 by a factor of ~ 2.6, 1.8, and 4.7, respectively. This can be due to the line dust attenuation recipe implemented in EGG. Then we validated other emission lines of our mock with the aid of the BPT diagram, the MEx diagram and other line ratios and compared with SDSS data at $z \sim 0$ and FMOS data at $1.43 < z < 1.74$. In general, we find good agreement with observations at all redshifts and, in this case, a significant difference with observations does not emerge.

4. Dust: in order to investigate whether the dust assignment is realistic, we compared the A_V distribution of our mock to COSMOS2015 and Henriques et al. (2015) SAM ones. We find good agreement with COSMOS2015 results. When comparing the A_{UV} values as a function of redshift of our mock with observed estimates by Cucciati et al. (2012) and Burgarella et al. (2013), we find that our mock predicts higher extinction values than the literature at low redshift ($z \sim 0$) while at high redshift it predicts lower values. These results, as for the Hα emisssion, indicate that the dust extinction implemented in EGG might possibly be not fully realistic and could require a recalibration.

5. Sizes: we also validated some of the morphological parameters assigned by EGG by comparing with Dimauro et al. (2018) catalog. In particular, we inspected the distribution of the B/T ratio and the distributions of the half-light radiuses for the 2-component galaxies (i.e. all galaxies of the mock), for the "pure bulges" (i.e. galaxies with B/T$> 0/8$) and for the "pure disks"(i.e. galaxies with B/T< 0.2). In general, we find that our mock catalog predicts in all cases (with the exception of the "pure bulges") smaller half-light radiuses with respect to Dimauro et al. (2018). However, when comparing with Bagley et al. (2020) for Hα emitters, we find a good agreement with our results. More investigation is therefore needed in order to assess whether the morphological prescriptions implemented in EGG can be improved or whether the differences can be ascribed to the uncertainties of observations.

6. Clustering: we calculated the projected two-point correlation function for our mock catalogs. In particular, to compare to observed estimates (i.e. Marulli et al. 2013, Meneux et al. 2009 and Durkalec et al. 2018), we calculated the clustering signal in several redshift bins (from $z = 0.2$ to $z = 3.5$) and stellar mass bins (from $\log(M_*/M_\odot) \sim 9$ to $\log(M_*/M_\odot) \sim 12$). In addition, we also evaluated the 2pt correlation function per galaxy type and compared with de la Torre et al. (2011) results at $0.6 < z < 1.0$. In general, we find that our mock catalogs predict a dependence of the clustering signal from the stellar mass and the galaxy type indicating that, as expected, more massive or red galaxies are more clustered than less massive or blue

galaxies. Our results are also in good agreement with observed estimates on the total population of galaxies in zCOSMOS, VIPERS and VUDS surveys and with the population of galaxies divided by type in zCOSMOS.

7. Forecasts: finally, we also provide some examples of the many forecasts for Euclid and other surveys that can be performed using the mock catalogs of this thesis. In particular, we display the large scale structure of our mocks in a Dec-redshift plane and found that red galaxies mainly populate high density environments while blue galaxies also populate less dense environments. In addition, we explored in detail the galaxy clusters present in our mock and specifically focus on two clusters (one at $z \sim 0.3$ and one at $z \sim 1$) by showing their members positions, their color-magnitude diagram and their magnitude distributions in several bands. Moreover, we also show the size distribution of Hα emitters that can be used for end-to-end simulations for Euclid spectral resolution. To conclude, we also show the galaxies number counts of our mocks dividing galaxies by their type and with several magnitude cuts in Euclid H and VIS bands and the number counts of Lyα emitters that can be detected at $z > 6.5$.

6.2 Future perspectives

In this thesis, we have presented our empirical mock catalogs that respond to the urge of producing large and accurate galaxy mock catalogs in view of future missions. Mock catalogs are fundamental not only to maximise the scientific exploitation of such future missions but also to infer and interpret fundamental physics from observations. We developed a fully empirical workflow that starts from the outputs of an N-body DM simulation and produces a complete galaxy catalog with many properties spanning from stellar masses and SFR to observed frame photometry and emission lines and morphological parameters. This thesis represents an attempt to provide large, deep and accurate galaxy mock catalogs to the community with as many physical properties as possible. Some observations are still not reproduced with a high level of accuracy by our mock catalogs that, therefore, can be further improved. Our mocks can also be a good starting point to help solve open issues in galaxy formation and evolution. In the following, we pinpoint some of them.

1. An open problem that needs to be tackled is whether the SHMR and its shape depend on the galaxy type. In the last years few studies have found evidences in this direction, however, more work is needed to precisely determine from a simulation which halos host late- or early-type galaxies, especially around the peak of the SHMR where the halo masses of these two classes of objects overlap.

2. It is still much debated whether the SFE is evolving at $z > 4$ or if it remains approximately constant. Answering this question is important in order to understand the evolution of star formation across cosmic time and, as a consequence, the stellar mass assembly of galaxies. With our work, given the large errors in the input SMFs, and, consequently, the output SHMR,

we couldn't place tight constraints on this aspect even though we find a hint towards an evolving scenario. This aspect definitely needs a more careful analysis with different input SMFs or a different modelling (see e.g. Moster et al. 2018 or Behroozi et al. 2019).

3. Concerning the mock creation and in particular the SF/Q division, we only considered quiescent SMFs up to $z = 4$ and for higher redshifts (up to $z \sim 6$) we naively allowed for a 1% of quiescent galaxies. This aspect definitely needs an improvement by considering SMFs divided by type at higher redshifts and treating extremely high-z quiescent galaxies ($z \sim 5$) with care. However, this simplistic approach is able to correctly reproduce the statistical properties of the quiescent population up to the highest redshifts. Recently, several quiescent candidates have been identified at high-z (see e.g. Girelli et al. 2019) and, therefore, it is important for a mock catalog to realistically reproduce this population of galaxies.

4. The validation of the mock catalogs still needs to be completed by checking some properties, such as stellar and gas metallicity. In addition, other properties (e.g. dust and sizes) still need to be investigated in depth. According to the findings of our validation, the code EGG will be recalibrated for the properties that still don't match observations. For example, if the dust content will be proven to be inaccurate, we will proceed to produce a new SED library in the code or, alternatively, a simple recalibration of the line dust obscuration, in order to accurately predict the dust content of the galaxy population as a whole.

5. Given the flexibility of our method, we will run the entire workflow on different DM simulations, in order to create even larger (and deeper) mocks that can be used for predictions for larger surveys (e.g. the Euclid's Wide Survey). Moreover, the method can also be applied on simulations with alternative cosmologies like, for example, on the DUSTGRAIN simulation set.

6. Finally, several other forecasts and predictions for future surveys (e.g. Euclid, MOONS, H2O) still need to be performed along with simulating observed errors of such surveys.

A

POSTERIOR PROBABILITY DISTRIBUTIONS

In this Appendix, we report all the best-fits and the plots of all the one and two dimensional projections of the posterior probability distributions of the free parameters of the various fits done in this thesis. Each Section reports the posteriors of a specific case which will be detailed at the beginning of the Section.

A.1 DUSTGRAIN-*pathfinder* without scatter

Here we report the plots for each redshift bin of the best-fits to the data (described in Sect.3.1.1 using Eq. 2.2) derived from the direct comparison of the CMFs with their corresponding contour plot that shows all the one and two dimensional projections of the posterior probability distributions of the free parameters of the fit.

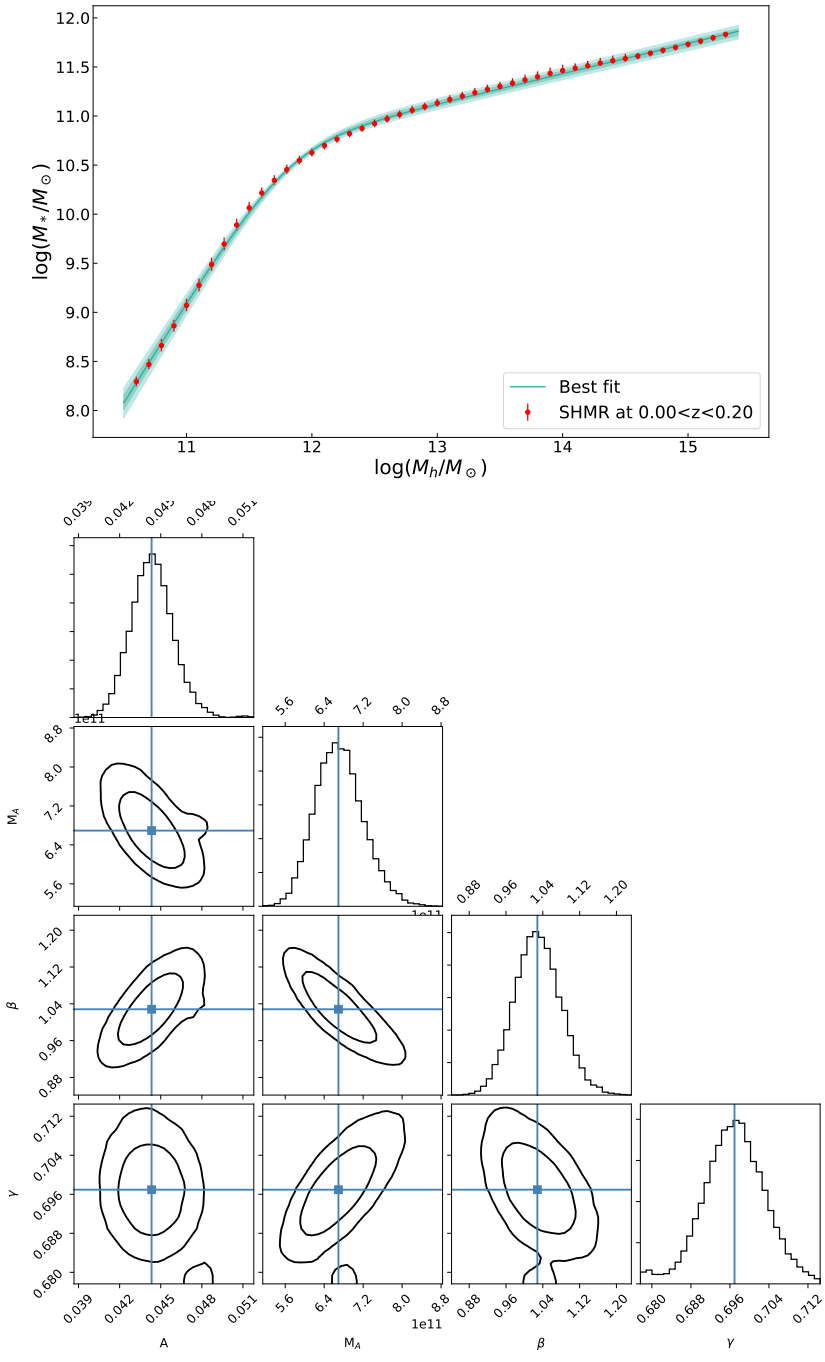

Fig. A.1 Best-fit and posterior probability distribution for the DUSTGRAIN-*pathfinder* without *relative* scatter at $0.0 < z < 0.2$. In the top panel, we show with red points the data derived from the direct comparison of the CMFs. In light-green we show the best-fit model with shaded areas representing the 1σ and 2σ errors.The bottom panel shows the contour plot that shows all the one and two dimensional projections of the posterior probability distributions of the free parameters of the fit (i.e. A, M_A, β and γ).

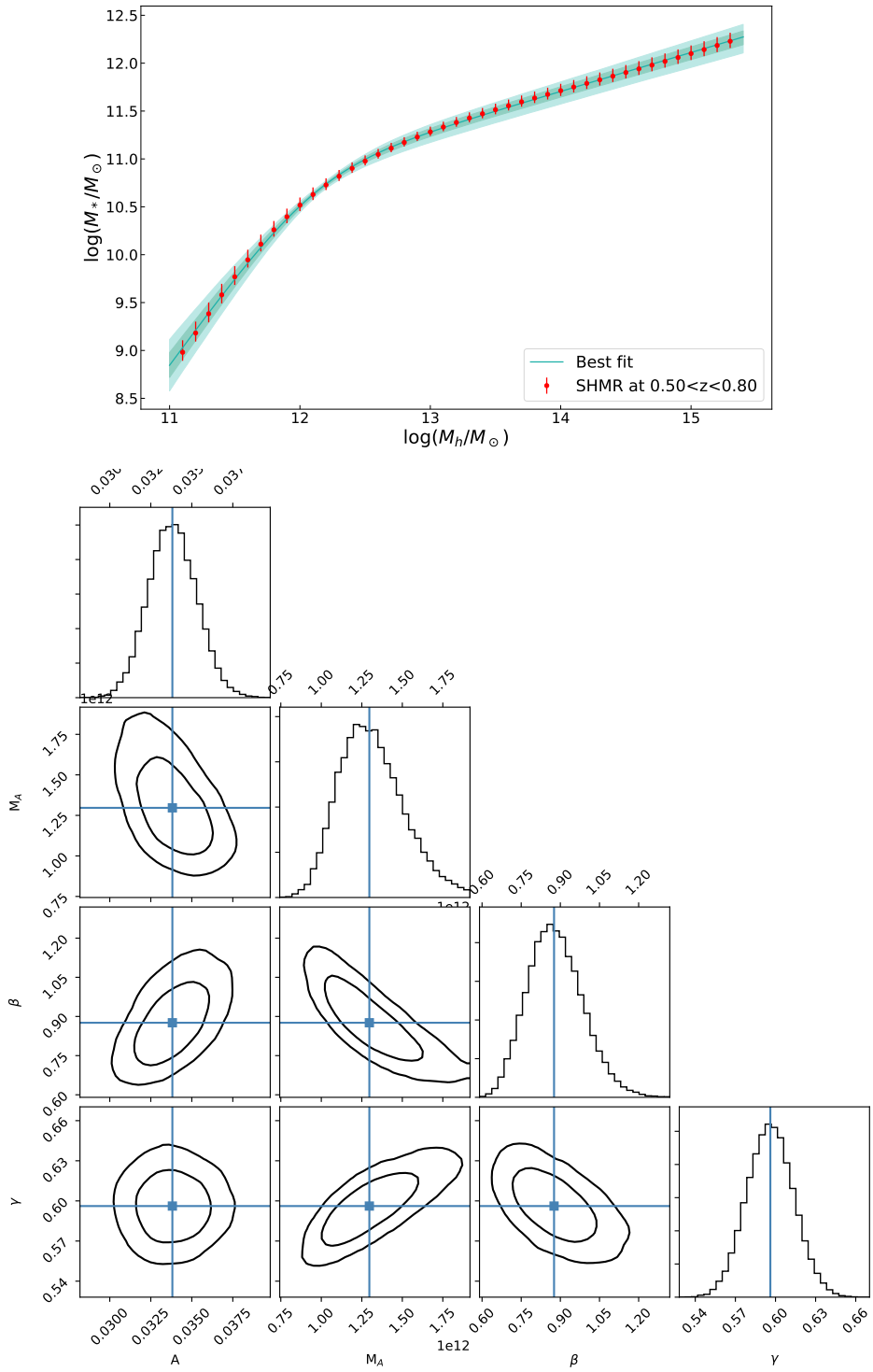

Fig. A.2 Best-fit and posterior probability distribution for the DUSTGRAIN-*pathfinder* without *relative* scatter at $0.5 < z < 0.8$. Points, lines and colors as in Fig. A.1.

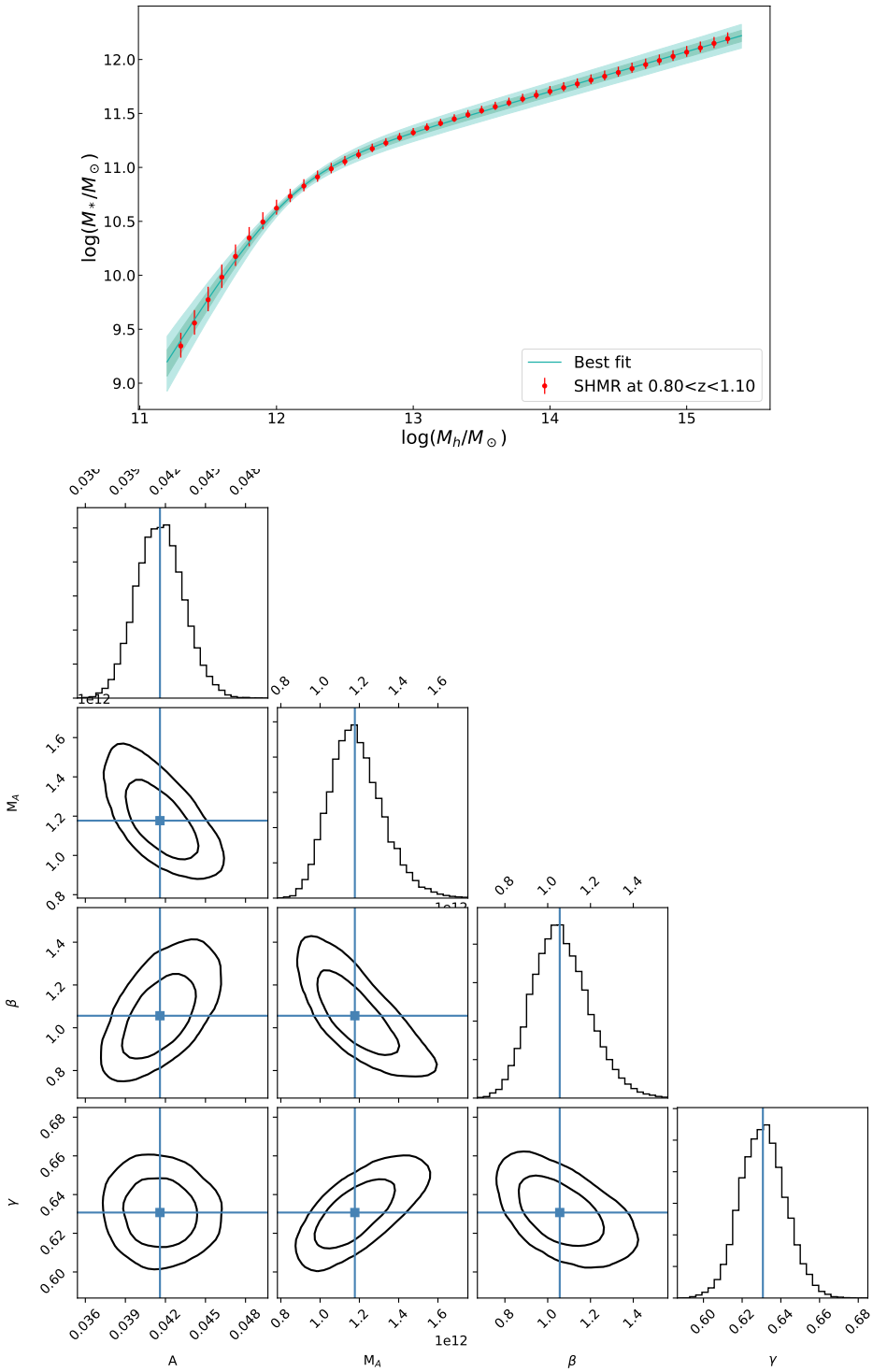

Fig. A.3 Best-fit and posterior probability distribution for the DUSTGRAIN-*pathfinder* without *relative* scatter at $0.8 < z < 1.1$. Points, lines and colors as in Fig. A.1.

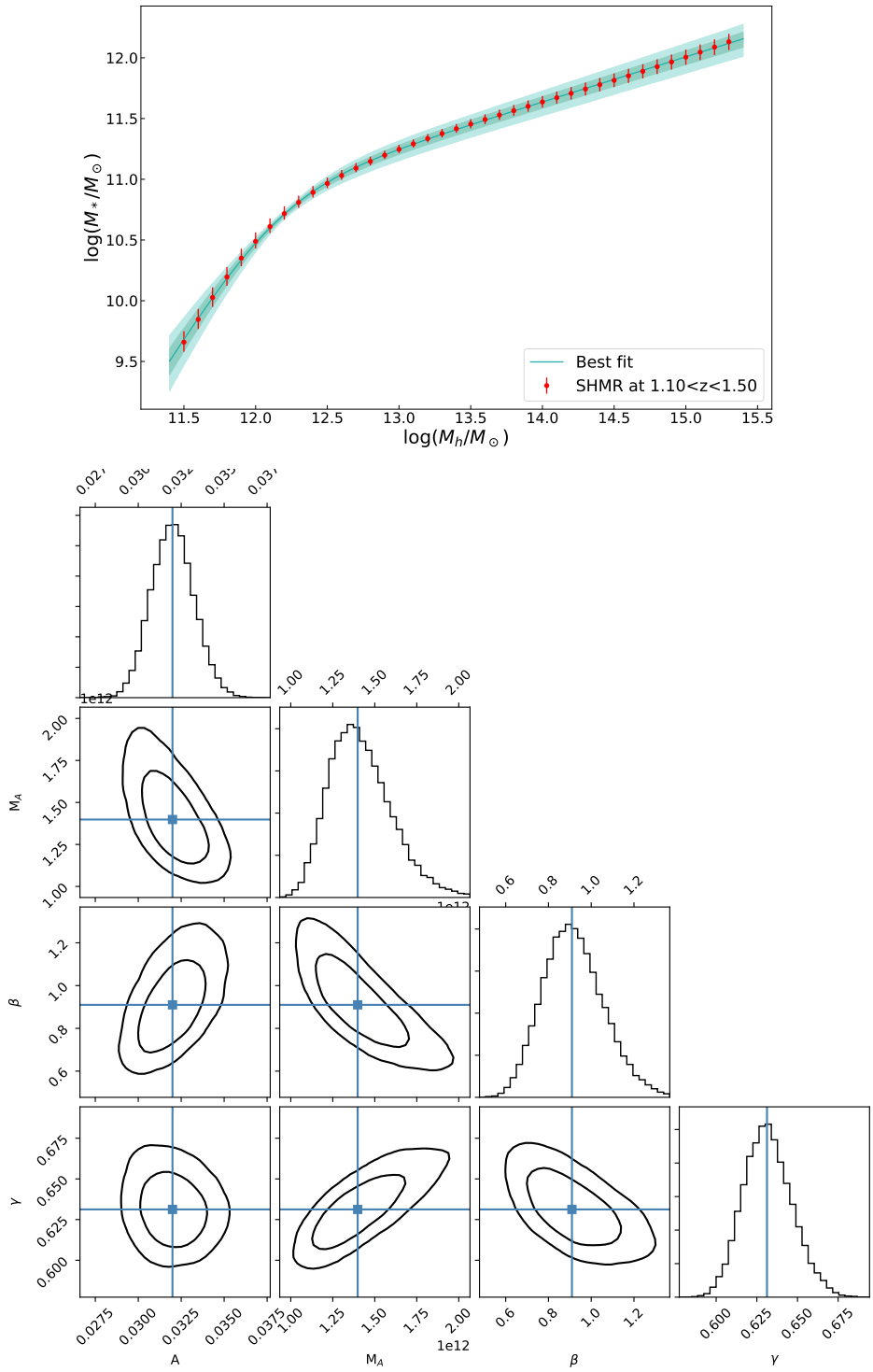

Fig. A.4 Best-fit and posterior probability distribution for the DUSTGRAIN-*pathfinder* without *relative* scatter at $1.1 < z < 1.5$. Points, lines and colors as in Fig. A.1.

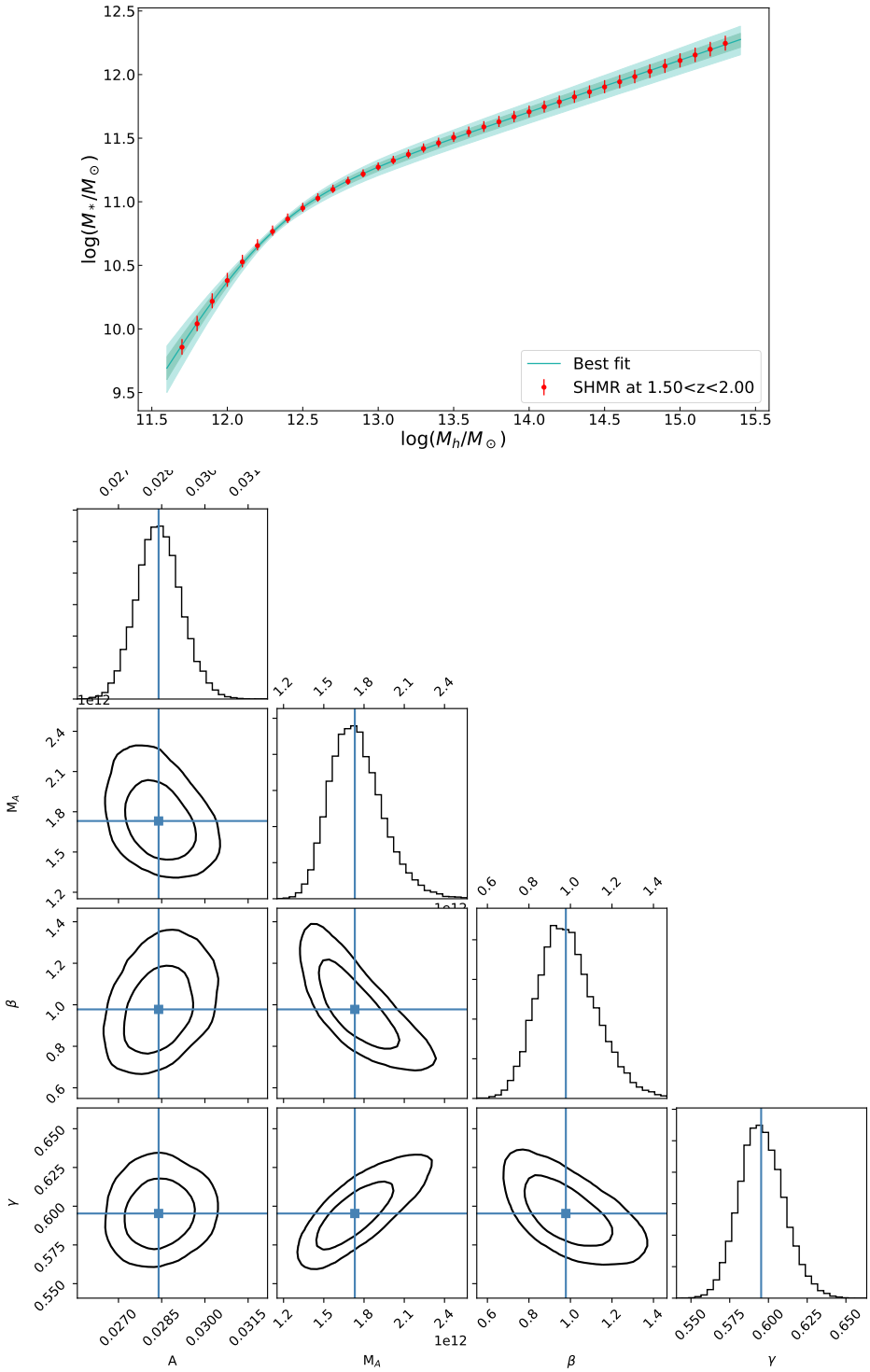

Fig. A.5 Best-fit and posterior probability distribution for the DUSTGRAIN-*pathfinder* without *relative* scatter at $1.5 < z < 2.0$. Points, lines and colors as in Fig. A.1.

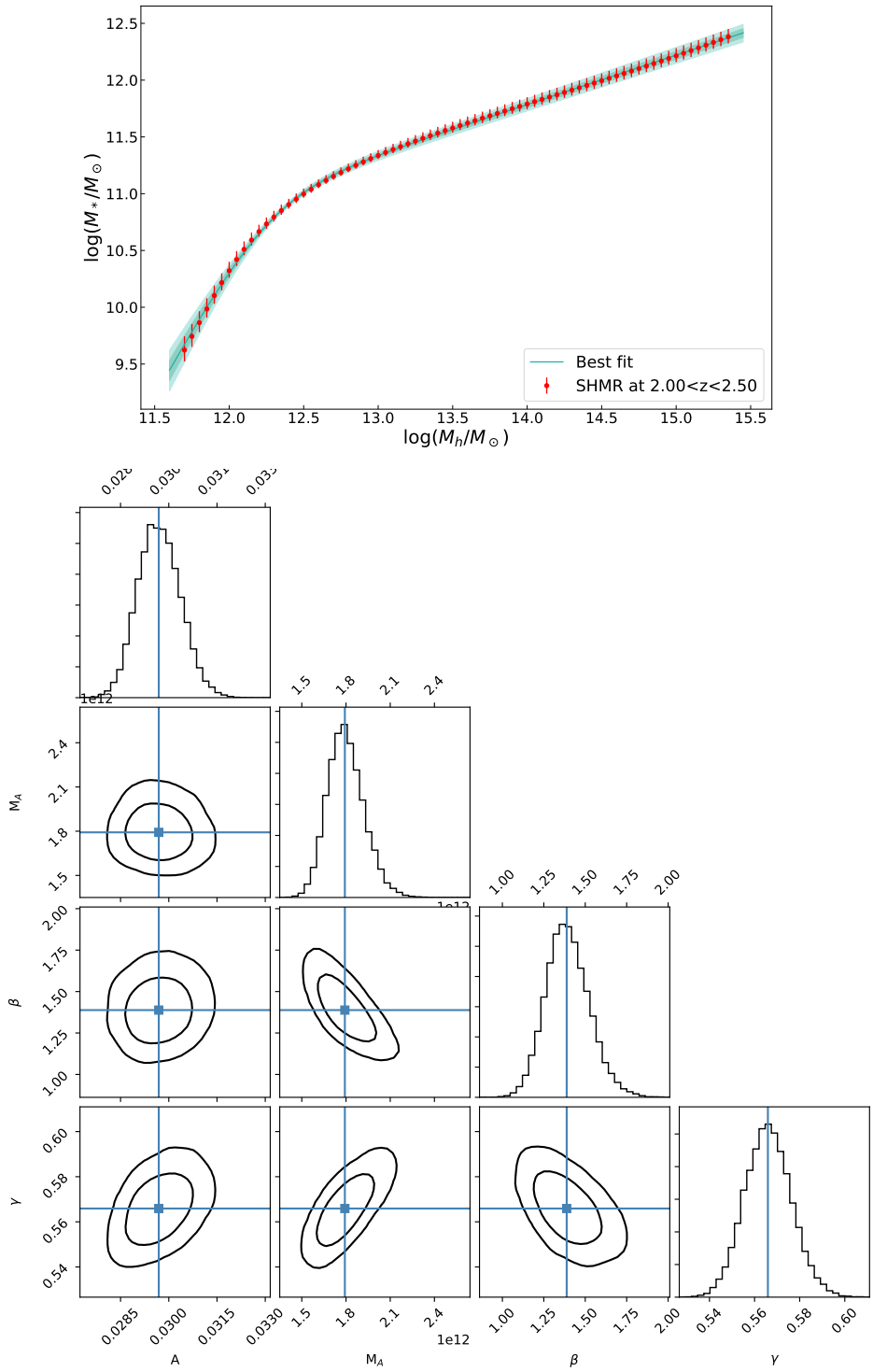

Fig. A.6 Best-fit and posterior probability distribution for the DUSTGRAIN-*pathfinder* without *relative* scatter at $2.0 < z < 2.5$. Points, lines and colors as in Fig. A.1.

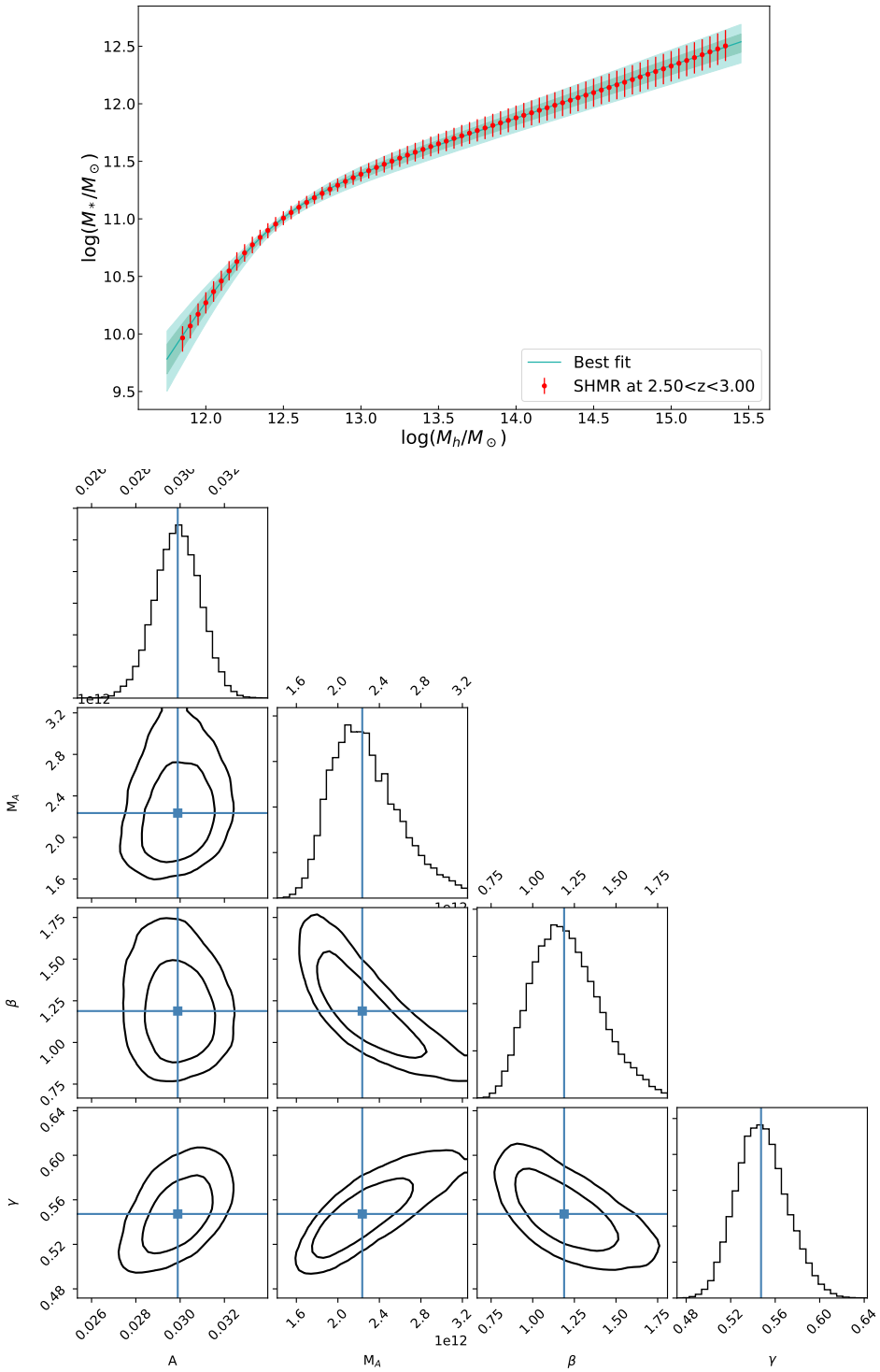

Fig. A.7 Best-fit and posterior probability distribution for the DUSTGRAIN-*pathfinder* without *relative* scatter at $2.5 < z < 3.0$. Points, lines and colors as in Fig. A.1.

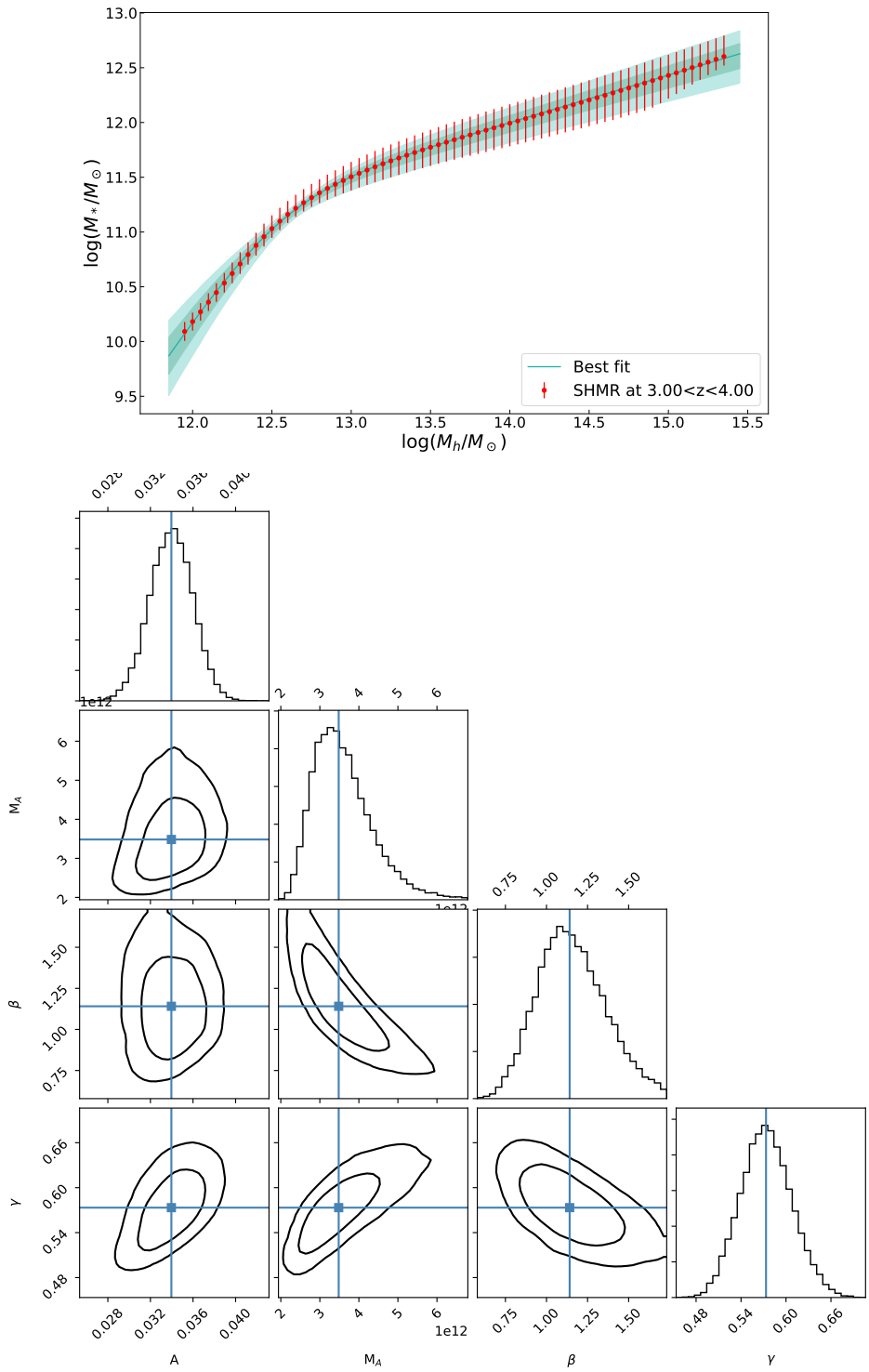

Fig. A.8 Best-fit and posterior probability distribution for the DUSTGRAIN-*pathfinder* without *relative* scatter at $3.0 < z < 4.0$. Points, lines and colors as in Fig. A.1.

A.2 DUSTGRAIN-*pathfinder* with *relative* scatter

Here we report the plots for each redshift bin of the best-fits to the data (described in Sect.3.1.1 using Eq. 2.2) derived from the direct comparison of the CMFs with their corresponding contour plot that shows all the one and two dimensional projections of the posterior probability distributions of the free parameters of the fit.

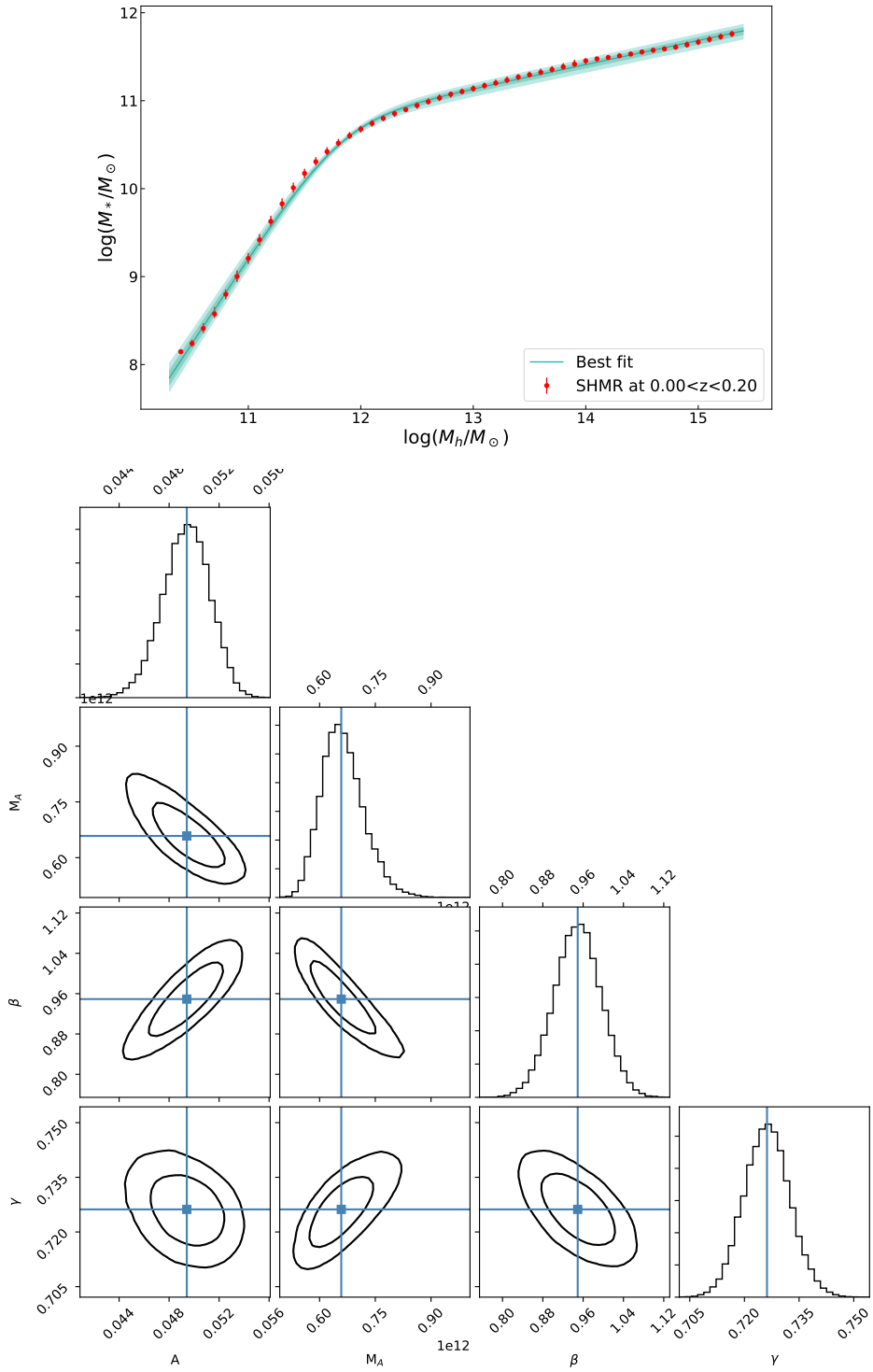

Fig. A.9 Best-fit and posterior probability distribution for the DUSTGRAIN-*pathfinder* with *relative* scatter at $0.0 < z < 0.2$. Points, lines and colors as in Fig. A.1.

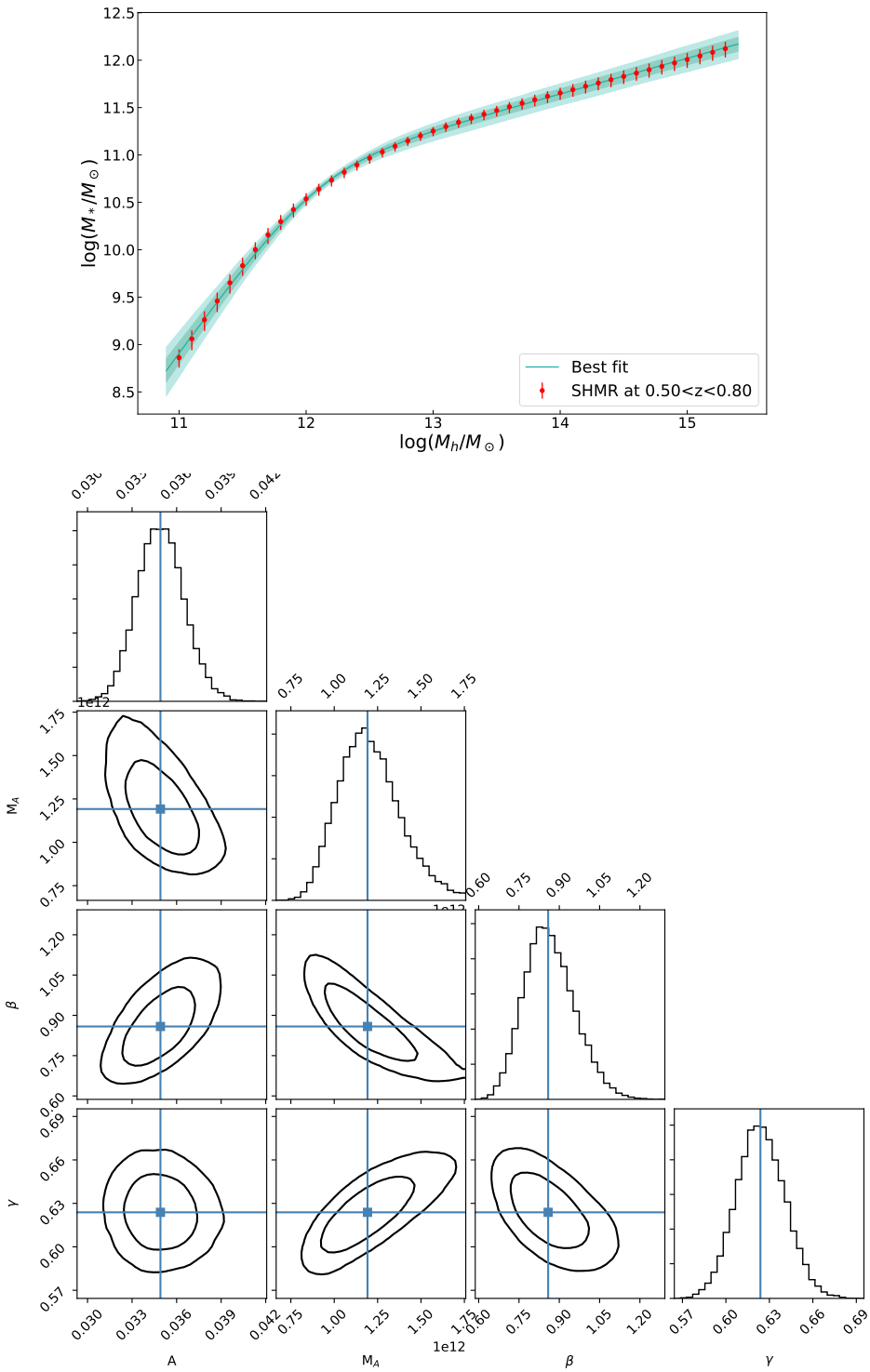

Fig. A.10 Best-fit and posterior probability distribution for the DUSTGRAIN-*pathfinder* with *relative* scatter at $0.5 < z < 0.8$. Points, lines and colors as in Fig. A.1.

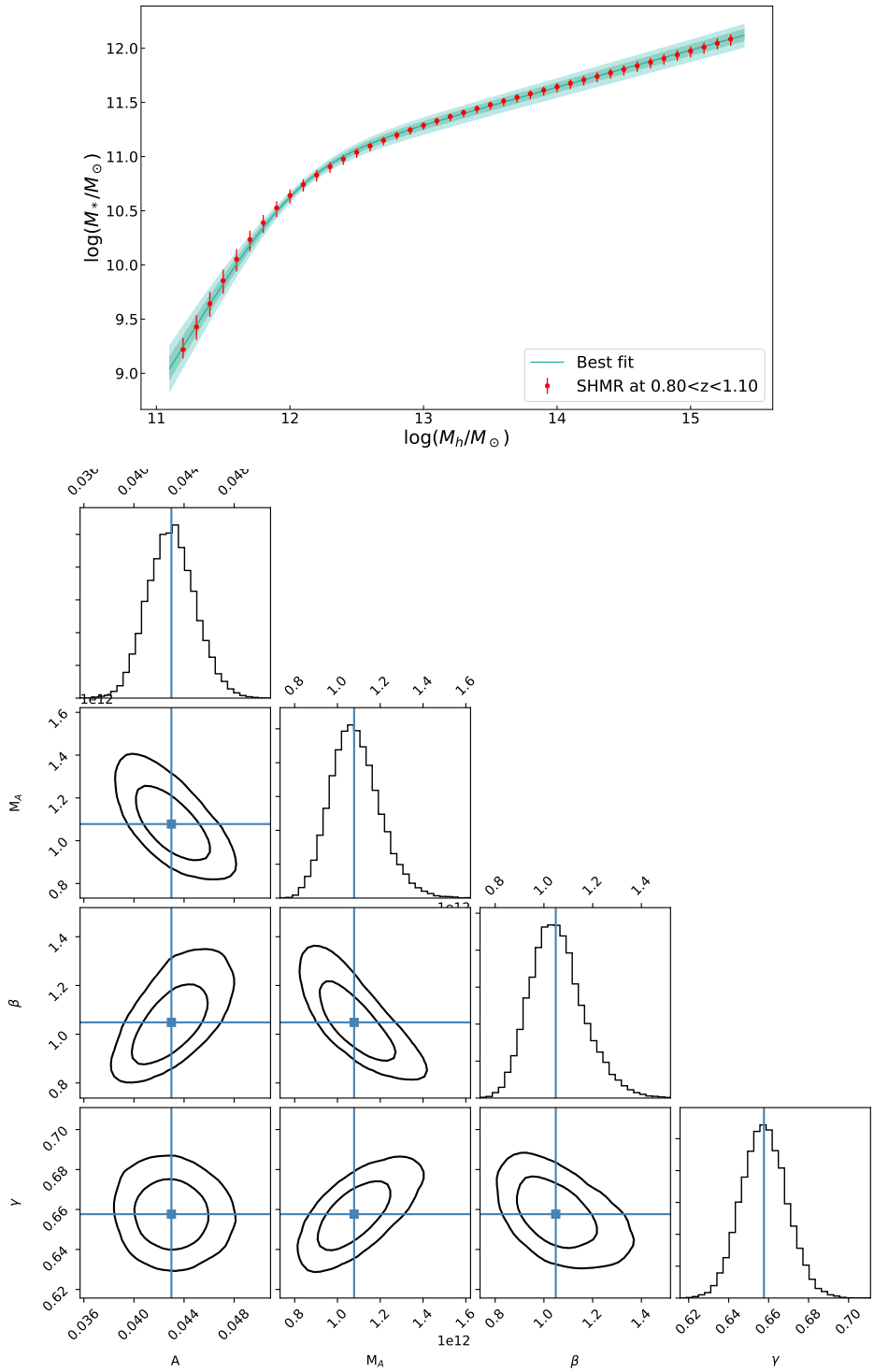

Fig. A.11 Best-fit and posterior probability distribution for the DUSTGRAIN-*pathfinder* with *relative* scatter at $0.8 < z < 1.1$. Points, lines and colors as in Fig. A.1.

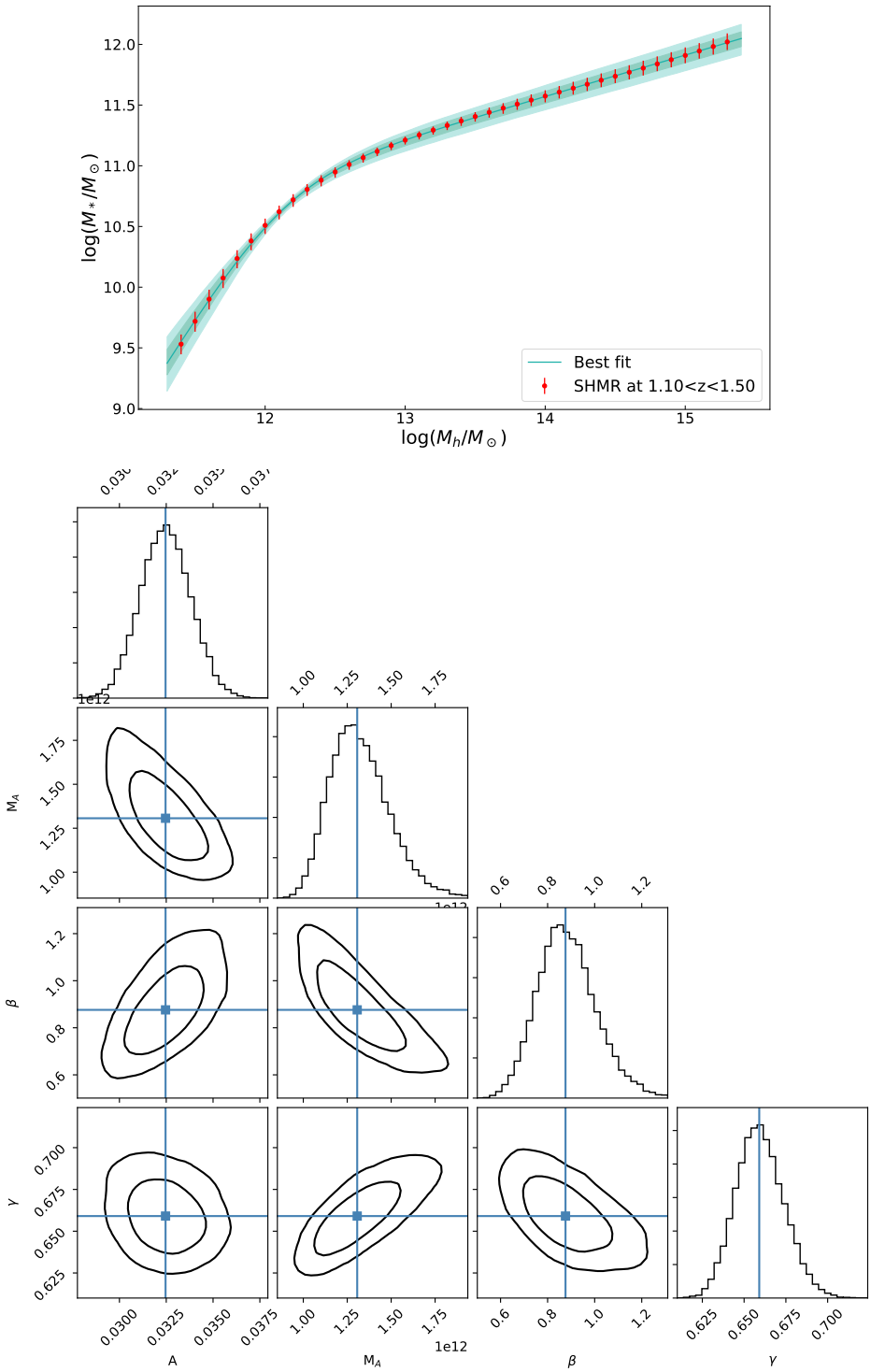

Fig. A.12 Best-fit and posterior probability distribution for the DUSTGRAIN-*pathfinder* with *relative* scatter at $1.1 < z < 1.5$. Points, lines and colors as in Fig. A.1.

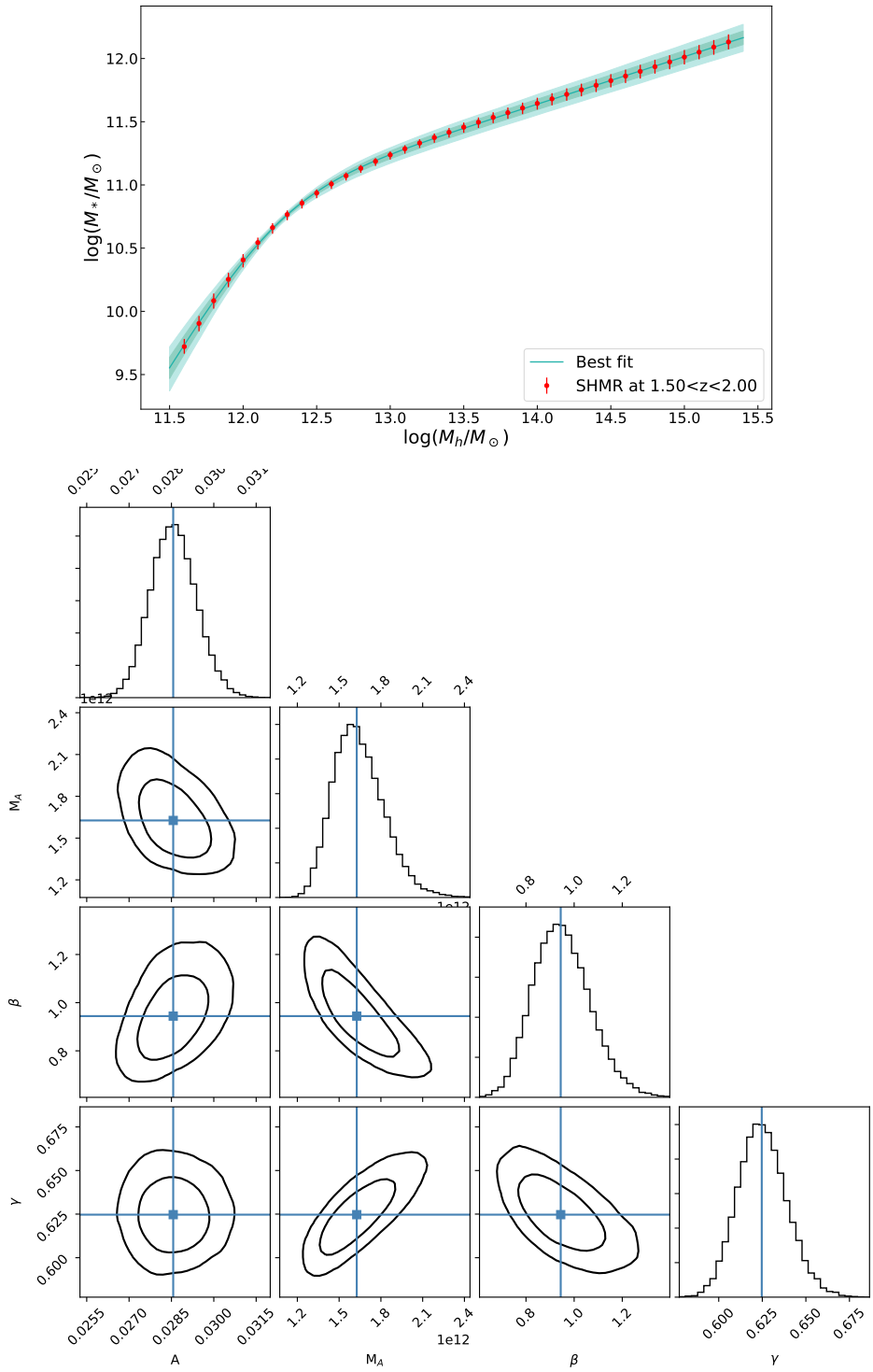

Fig. A.13 Best-fit and posterior probability distribution for the DUSTGRAIN-*pathfinder* with *relative* scatter at $1.5 < z < 2.0$. Points, lines and colors as in Fig. A.1.

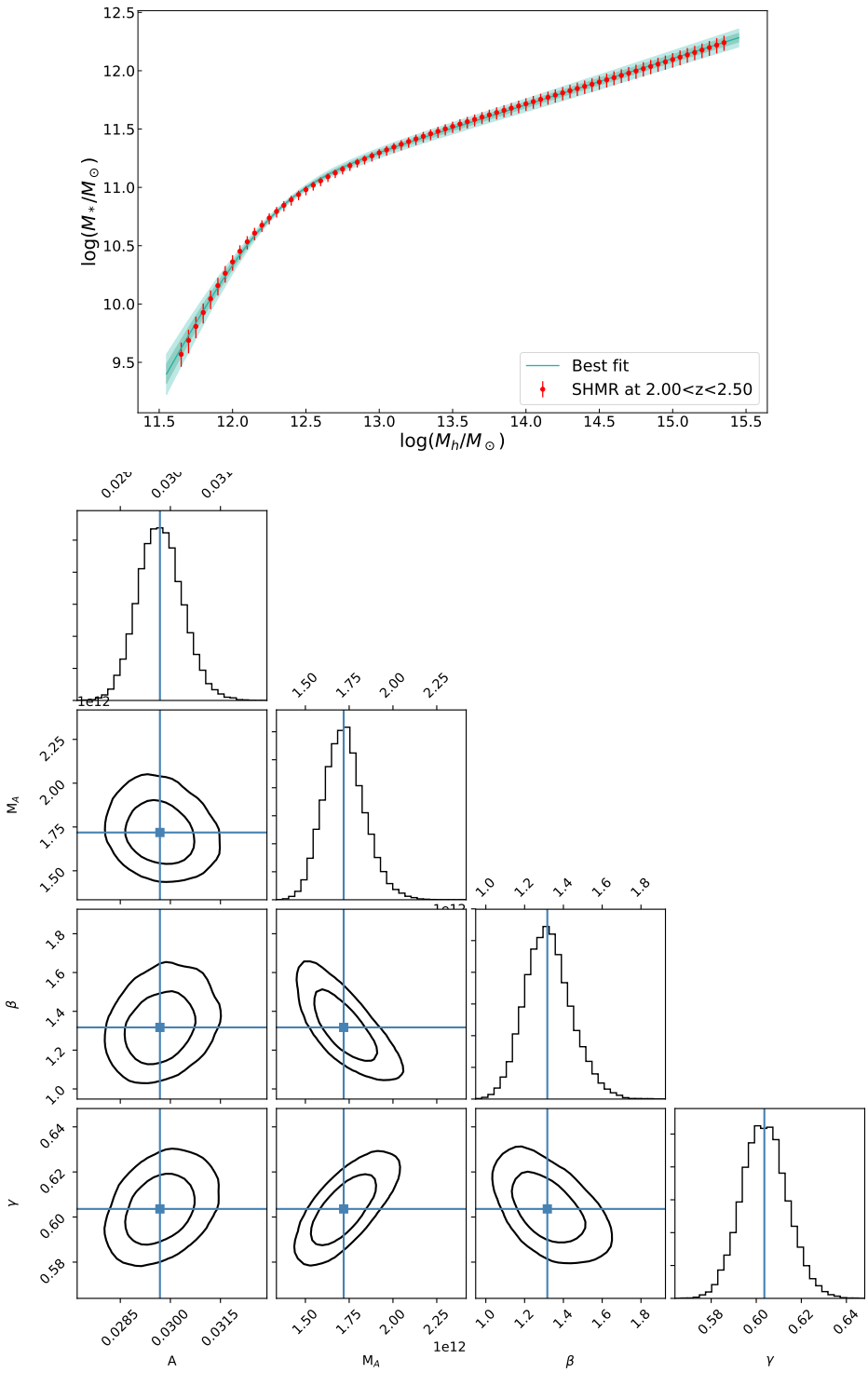

Fig. A.14 Best-fit and posterior probability distribution for the DUSTGRAIN-*pathfinder* with *relative* scatter at $2.0 < z < 2.5$. Points, lines and colors as in Fig. A.1.

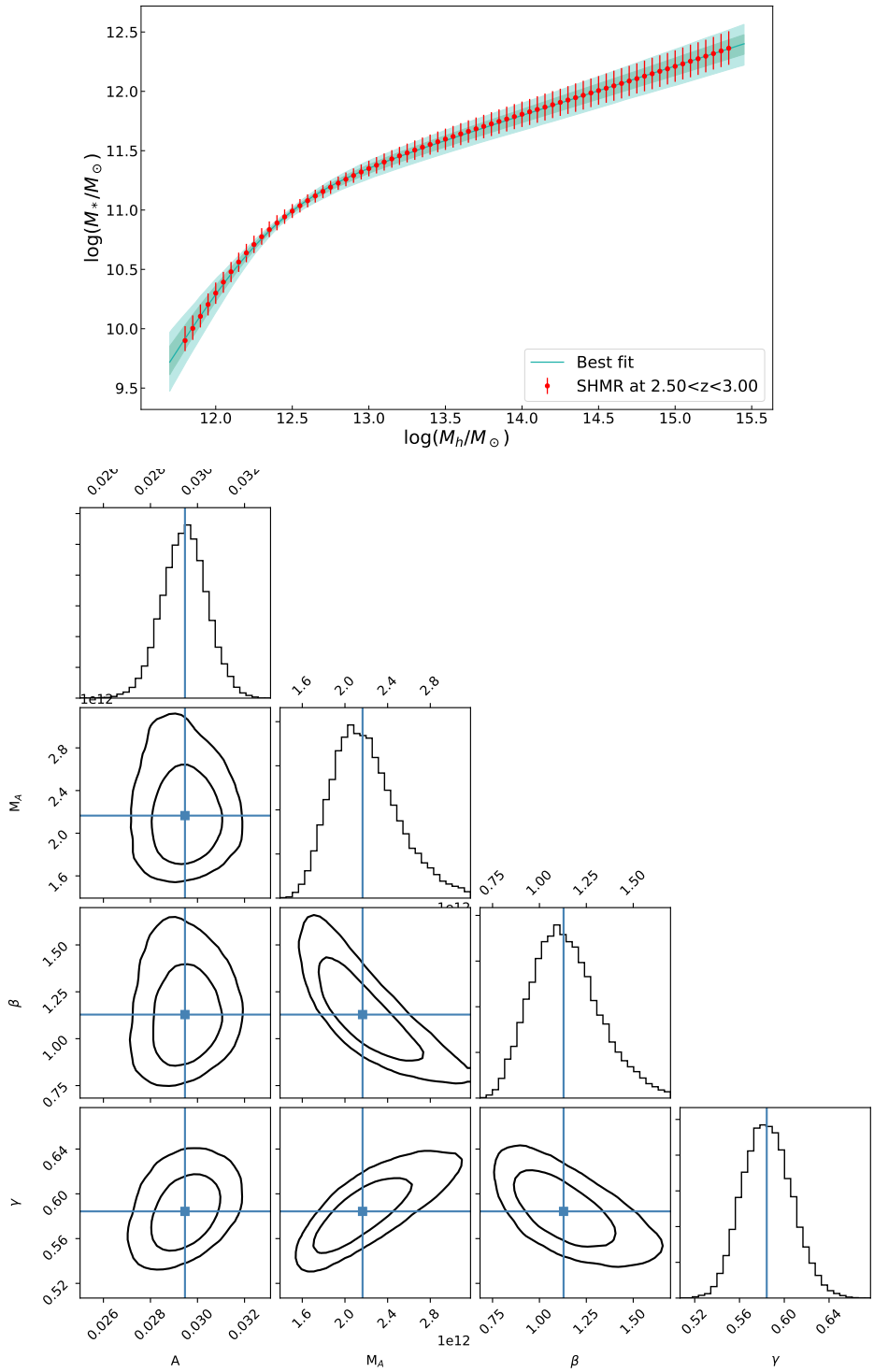

Fig. A.15 Best-fit and posterior probability distribution for the DUSTGRAIN-*pathfinder* with *relative* scatter at $2.5 < z < 3.0$. Points, lines and colors as in Fig. A.1.

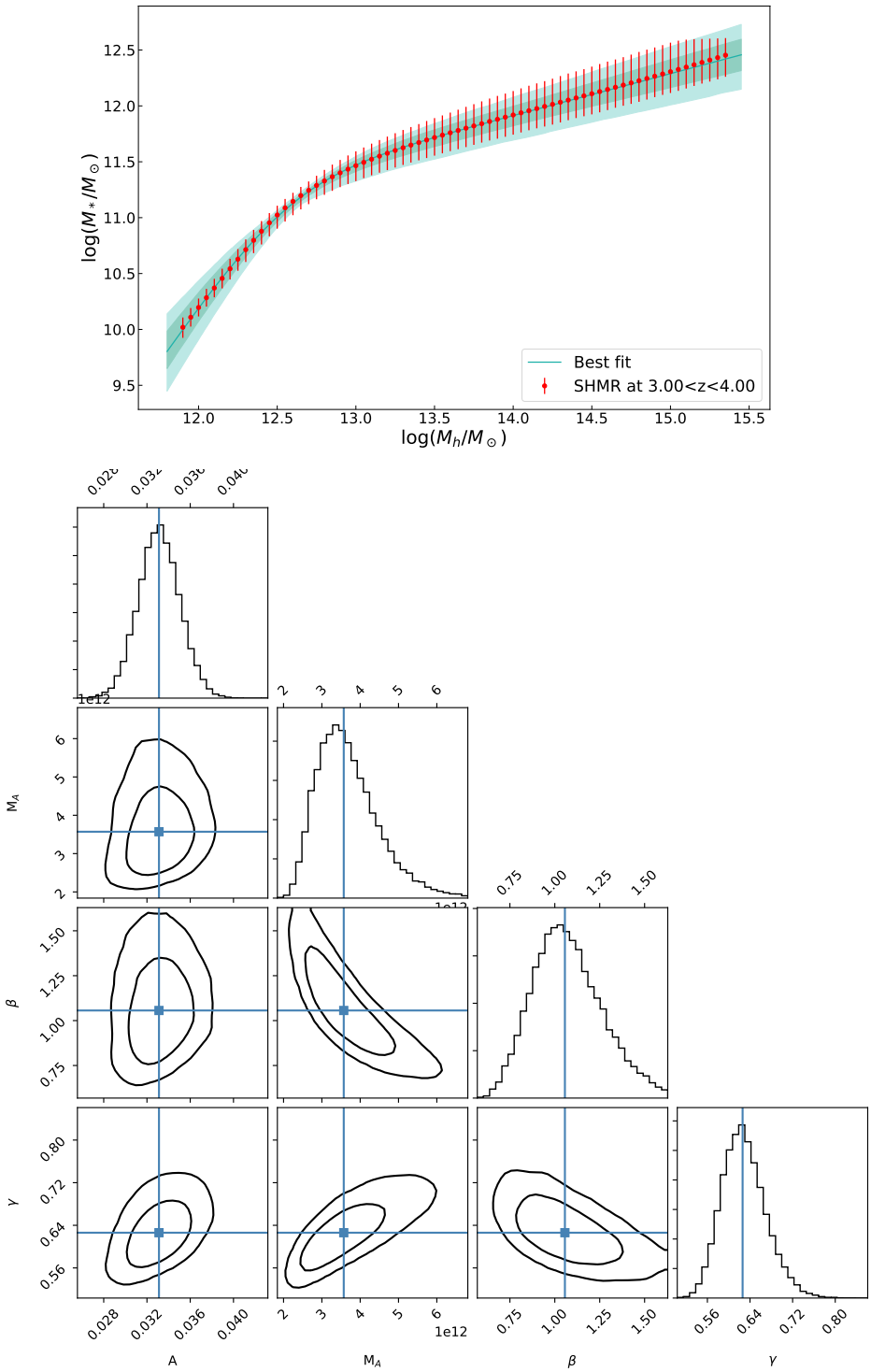

Fig. A.16 Best-fit and posterior probability distribution for the DUSTGRAIN-*pathfinder* with *relative* scatter at $3.0 < z < 4.0$. Points, lines and colors as in Fig. A.1.

A.3 Millennium I+II without scatter

Here we report the plots for each redshift bin of the best-fits to the data (described in Sect.3.1.2 using Eq. 2.2) derived from the direct comparison of the CMFs with their corresponding contour plot that shows all the one and two dimensional projections of the posterior probability distributions of the free parameters of the fit.

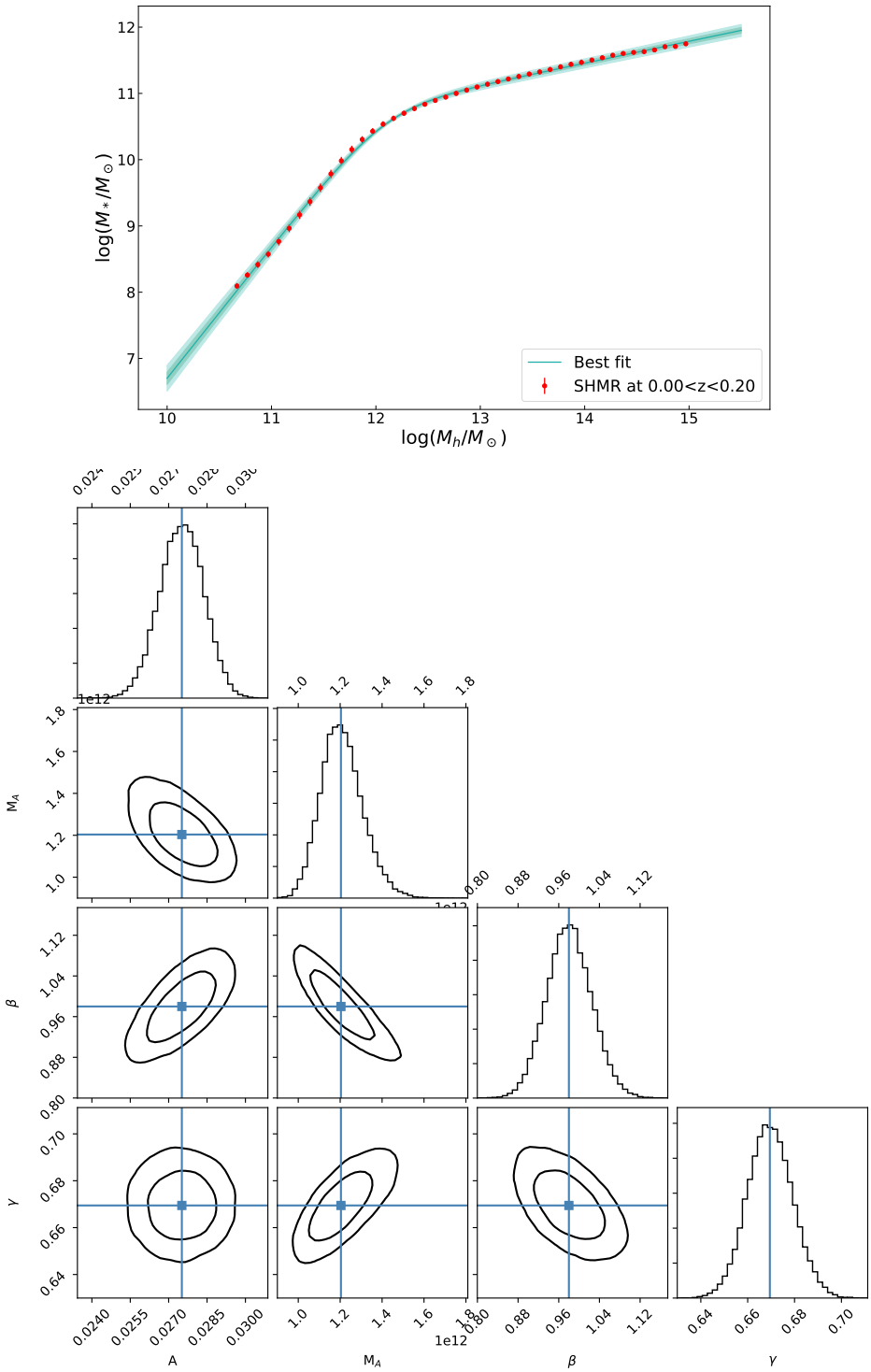

Fig. A.17 Best-fit and posterior probability distribution for the Millennium I+II without *relative* scatter at $0.0 < z < 0.2$. Points, lines and colors as in Fig. A.1.

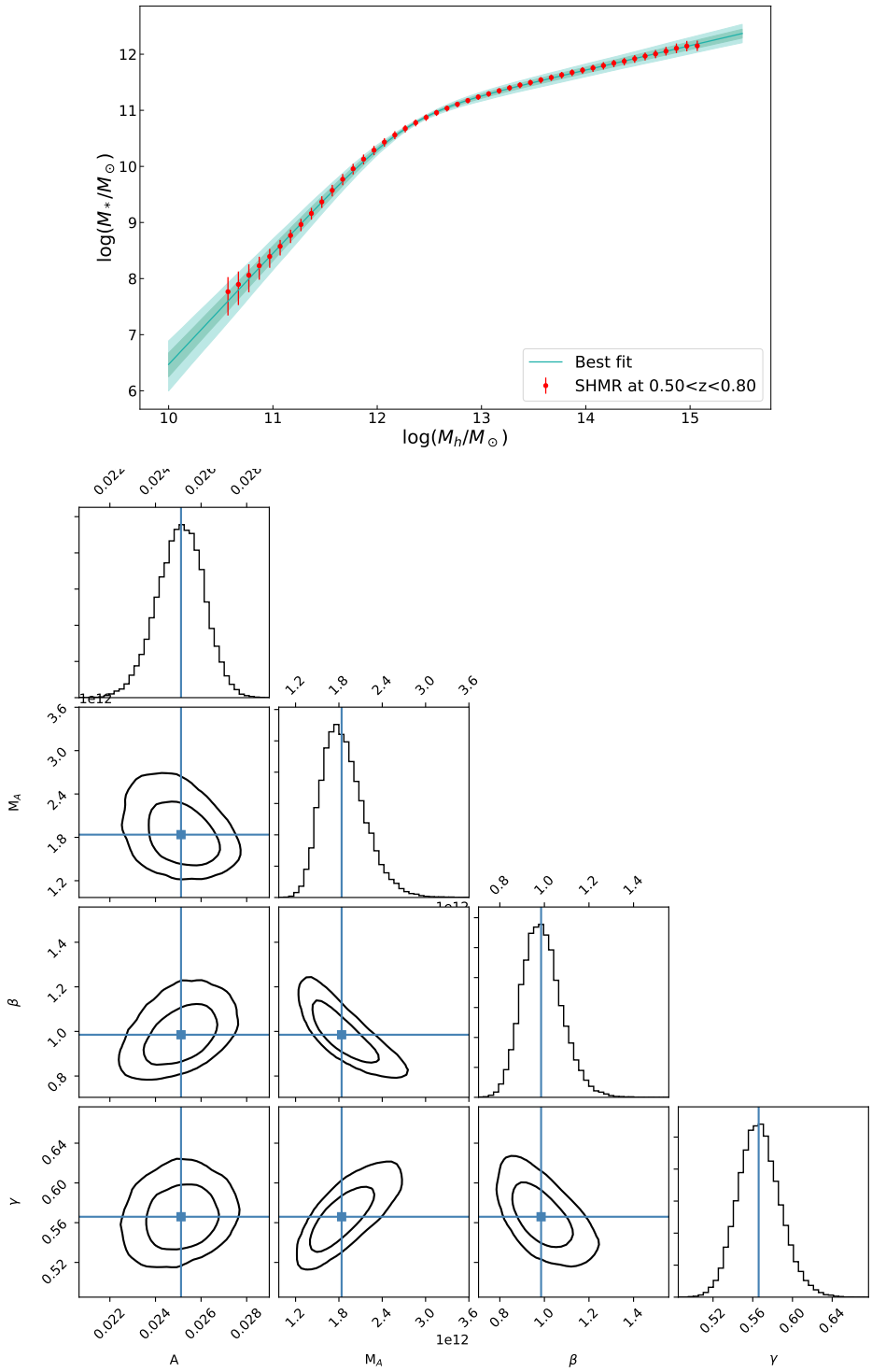

Fig. A.18 Best-fit and posterior probability distribution for the Millennium I+II without *relative* scatter at $0.5 < z < 0.8$. Points, lines and colors as in Fig. A.1.

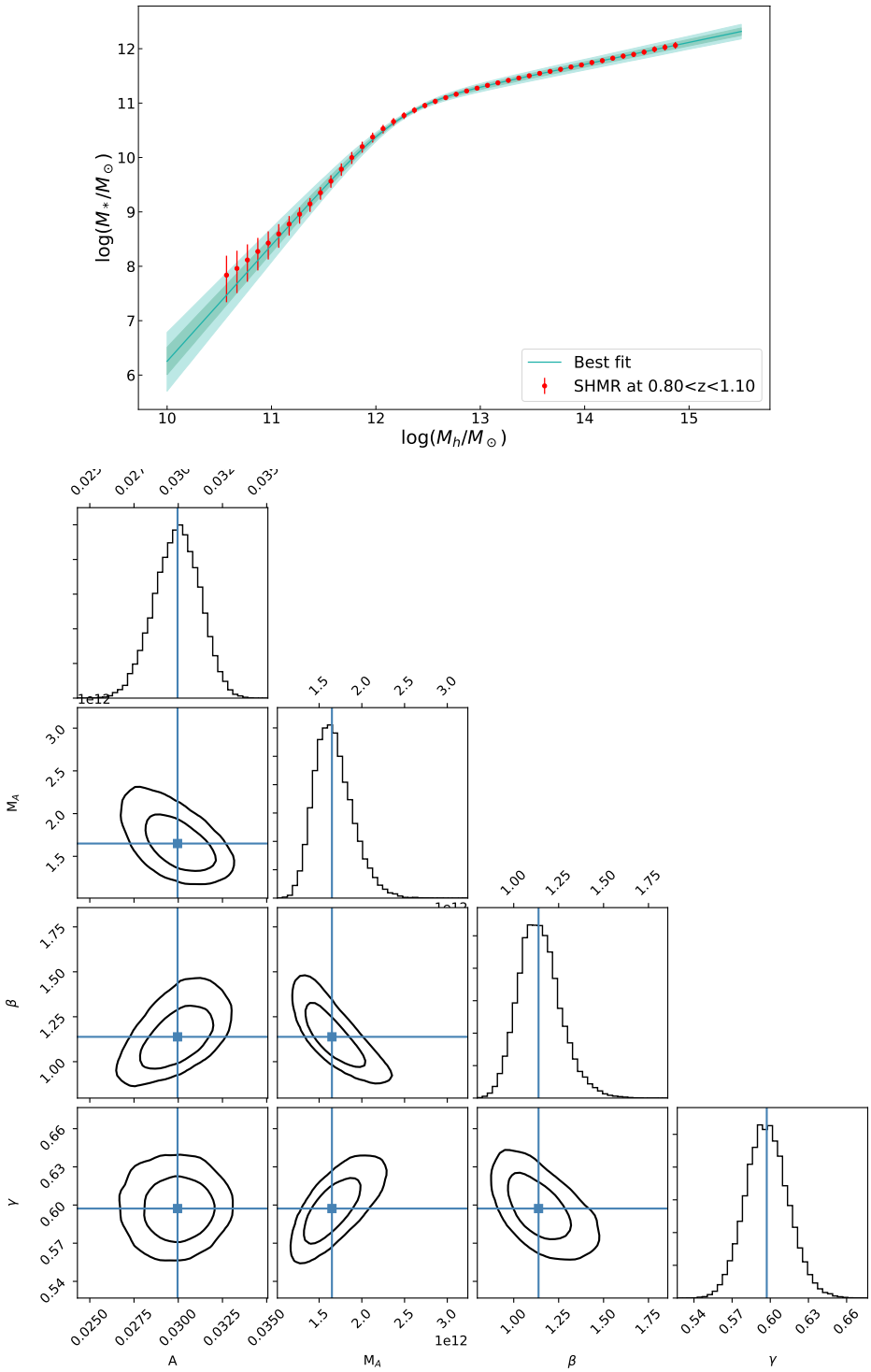

Fig. A.19 Best-fit and posterior probability distribution for the Millennium I+II with *relative* scatter at $0.8 < z < 1.1$. Points, lines and colors as in Fig. A.1.

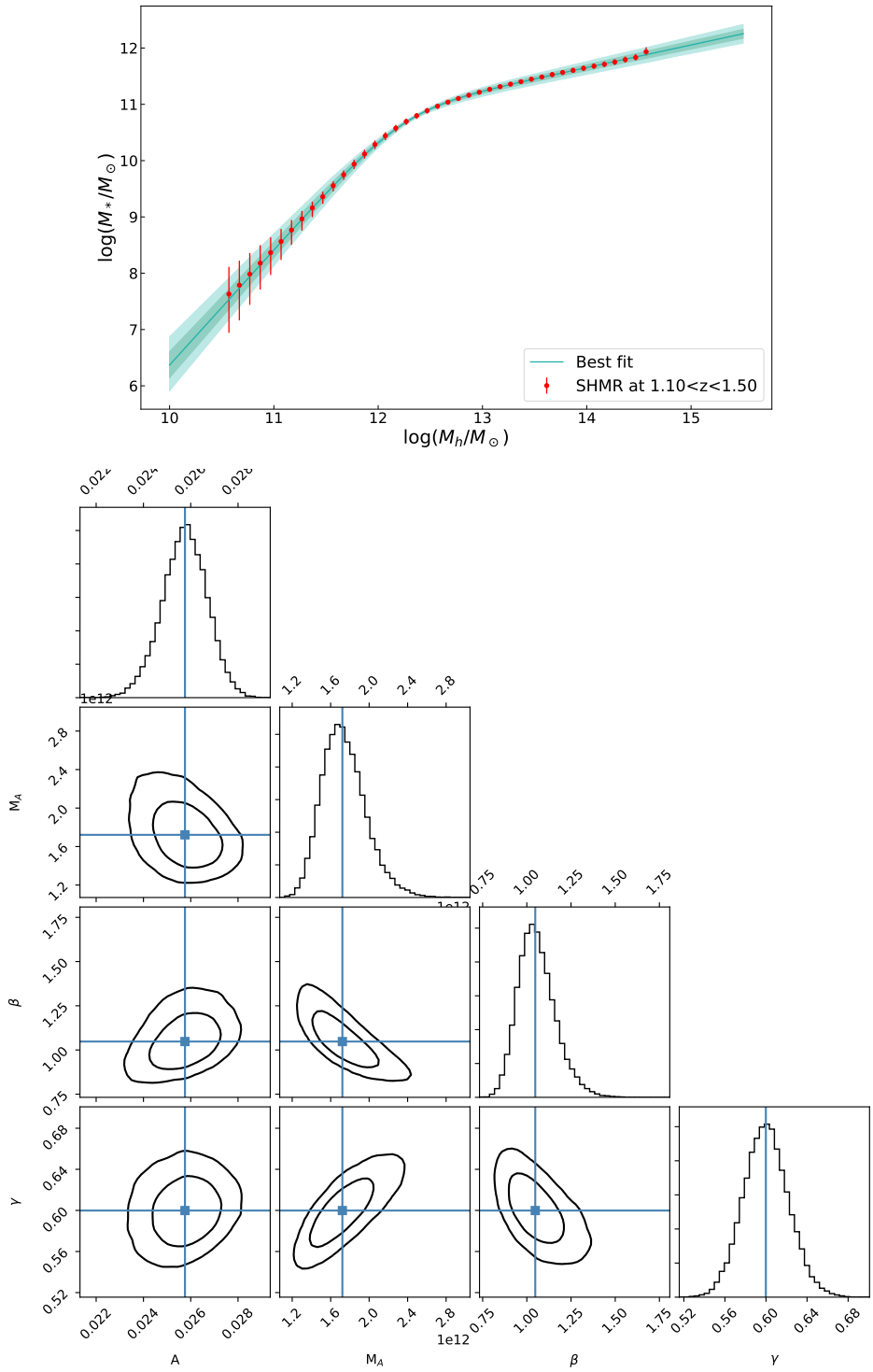

Fig. A.20 Best-fit and posterior probability distribution for the Millennium I+II without *relative* scatter at $1.1 < z < 1.5$. Points, lines and colors as in Fig. A.1.

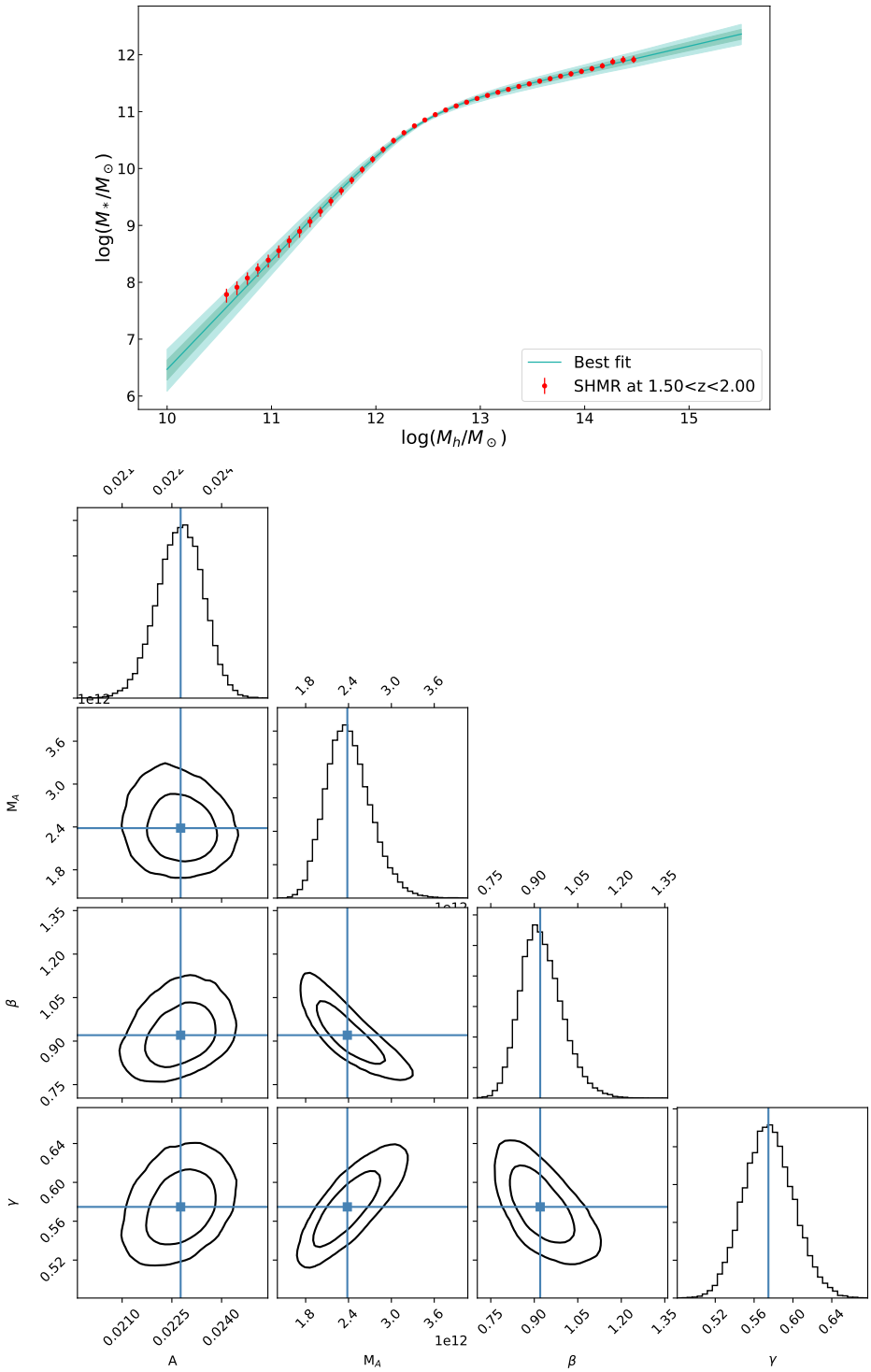

Fig. A.21 Best-fit and posterior probability distribution for the Millennium I+II without *relative* scatter at $1.5 < z < 2.0$. Points, lines and colors as in Fig. A.1.

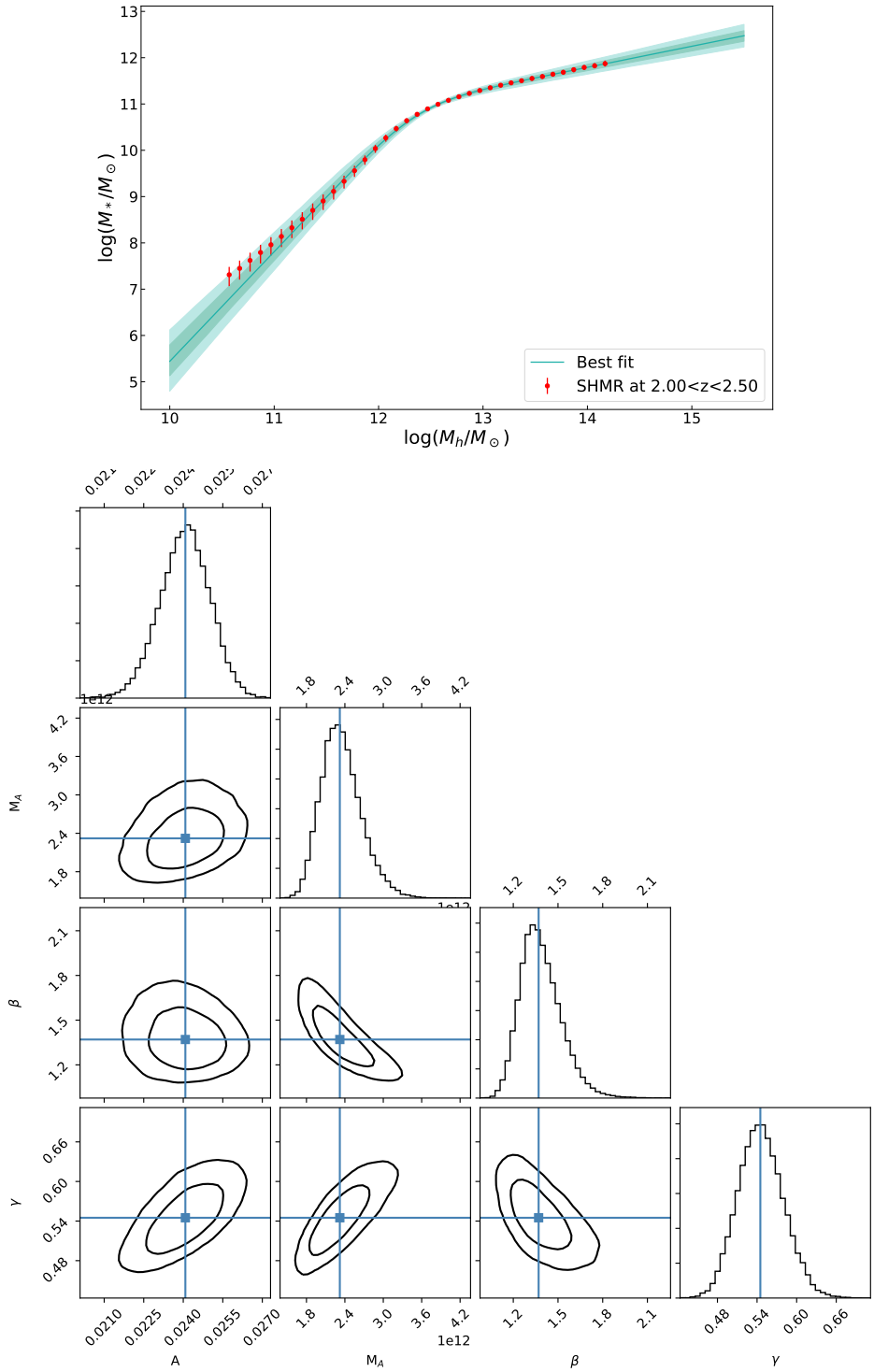

Fig. A.22 Best-fit and posterior probability distribution for the Millennium I+II with *relative* scatter at $2.0 < z < 2.5$.Points, lines and colors as in Fig. A.1.

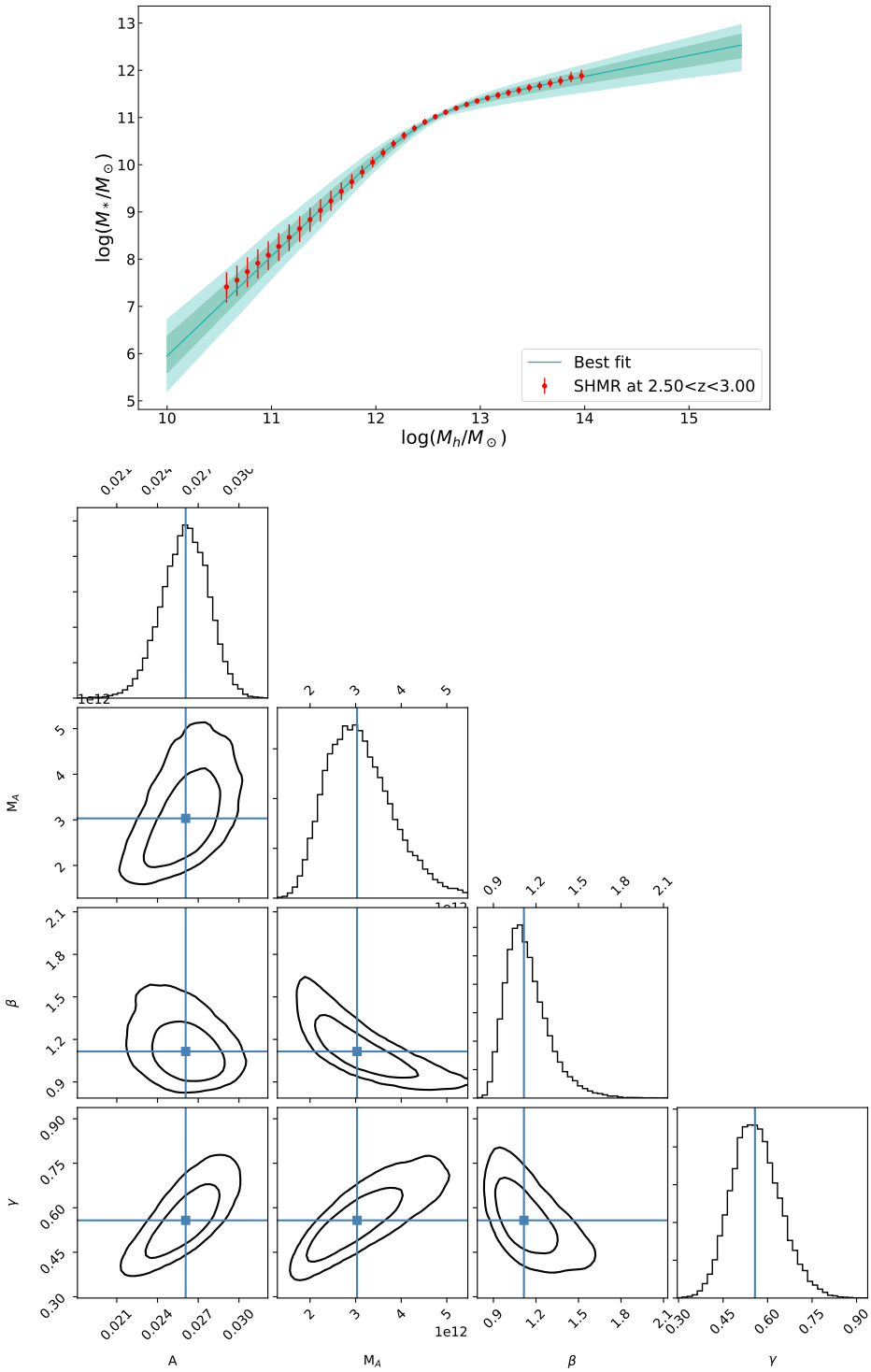

Fig. A.23 Best-fit and posterior probability distribution for the Millennium I+II without *relative* scatter at $2.5 < z < 3.0$. Points, lines and colors as in Fig. A.1.

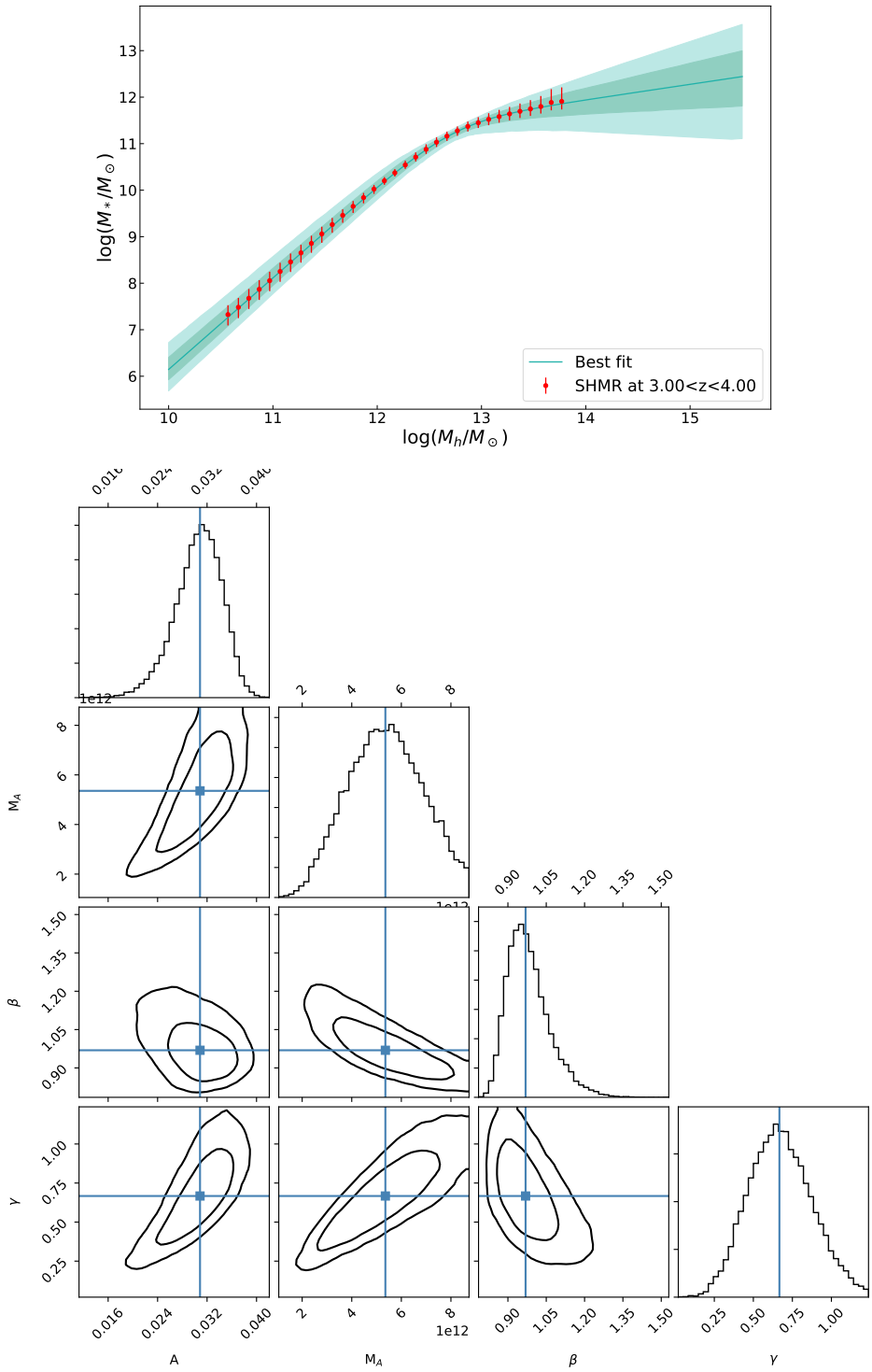

Fig. A.24 Best-fit and posterior probability distribution for the Millennium I+II without *relative* scatter at $3.0 < z < 4.0$. Points, lines and colors as in Fig. A.1.

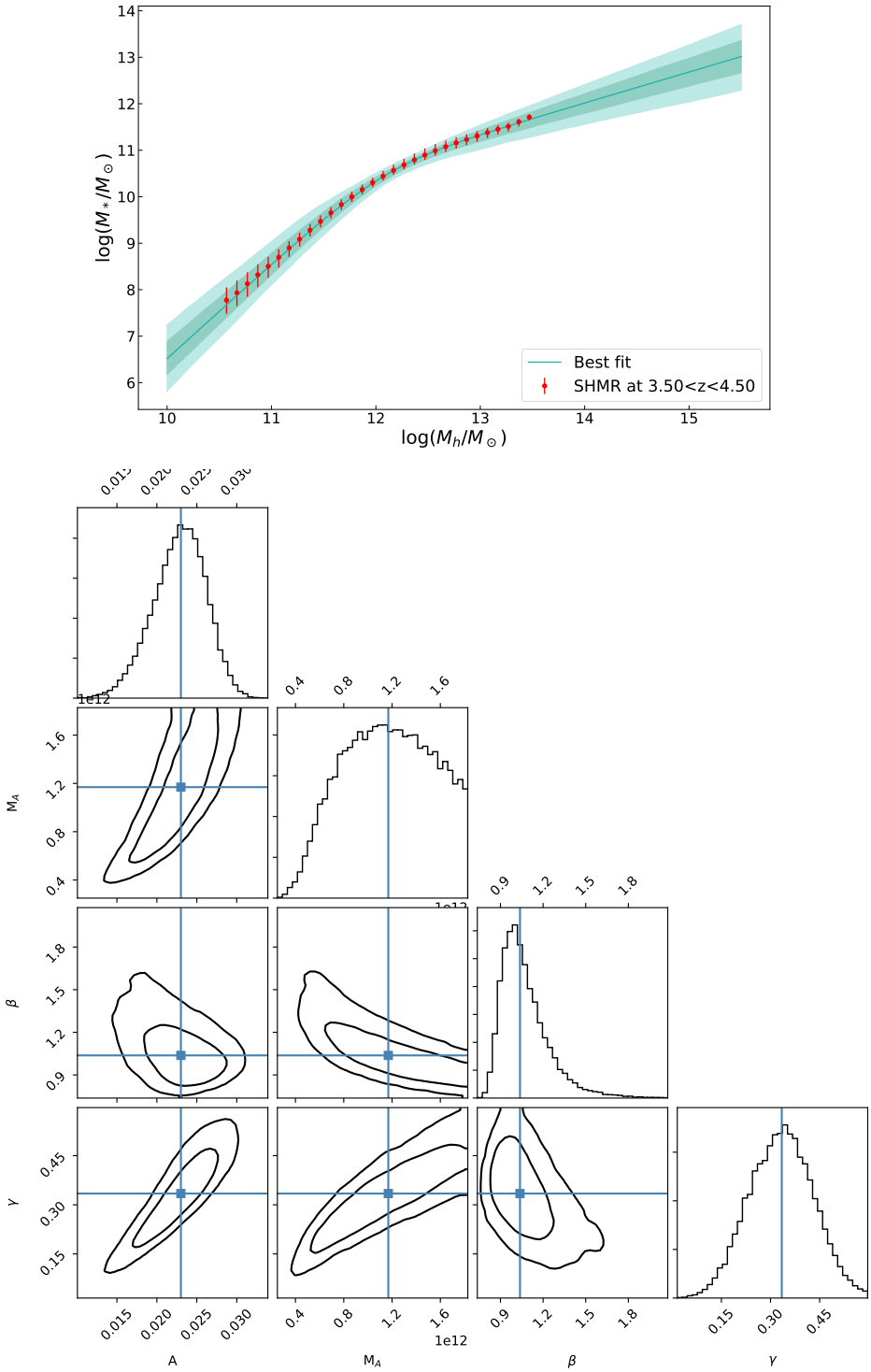

Fig. A.25 Best-fit and posterior probability distribution for the Millennium I+II without *relative* scatter at $3.5 < z < 4.5$. Points, lines and colors as in Fig. A.1.

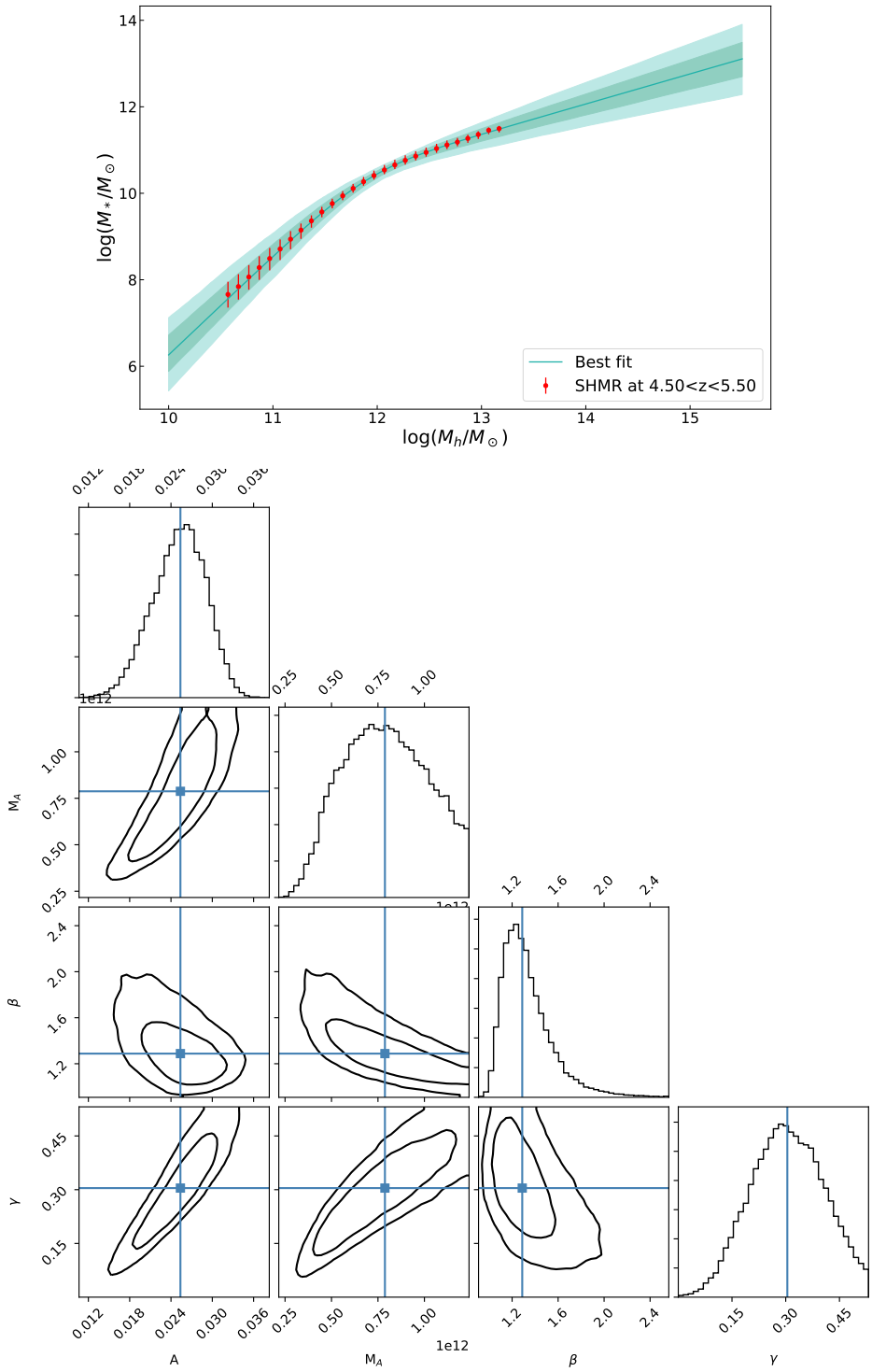

Fig. A.26 Best-fit and posterior probability distribution for the Millennium I+II without *relative* scatter at $4.5 < z < 5.5$. Points, lines and colors as in Fig. A.1.

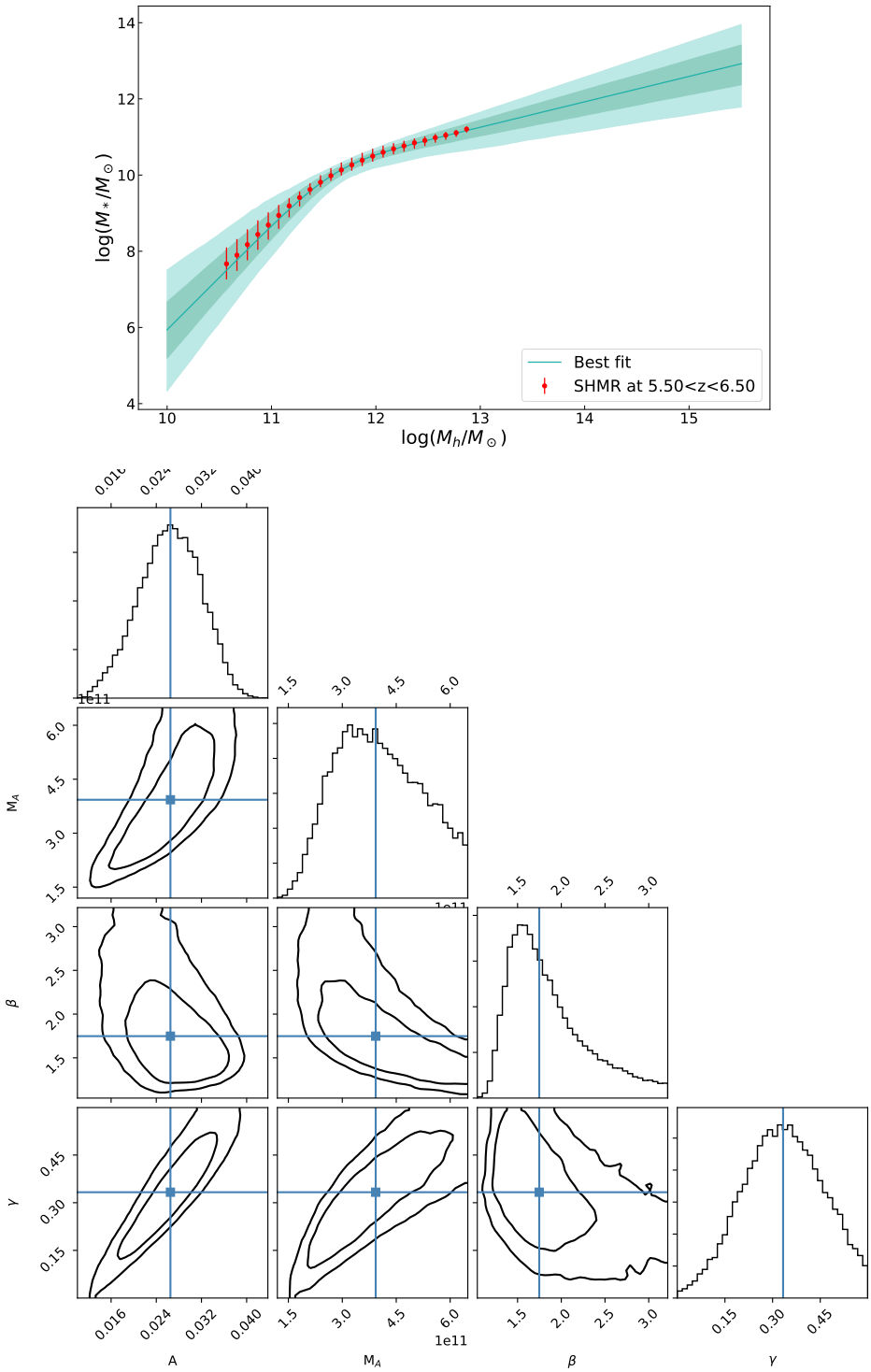

Fig. A.27 Best-fit and posterior probability distribution for the Millennium I+II without *relative* scatter at $5.5 < z < 6.5$. Points, lines and colors as in Fig. A.1.

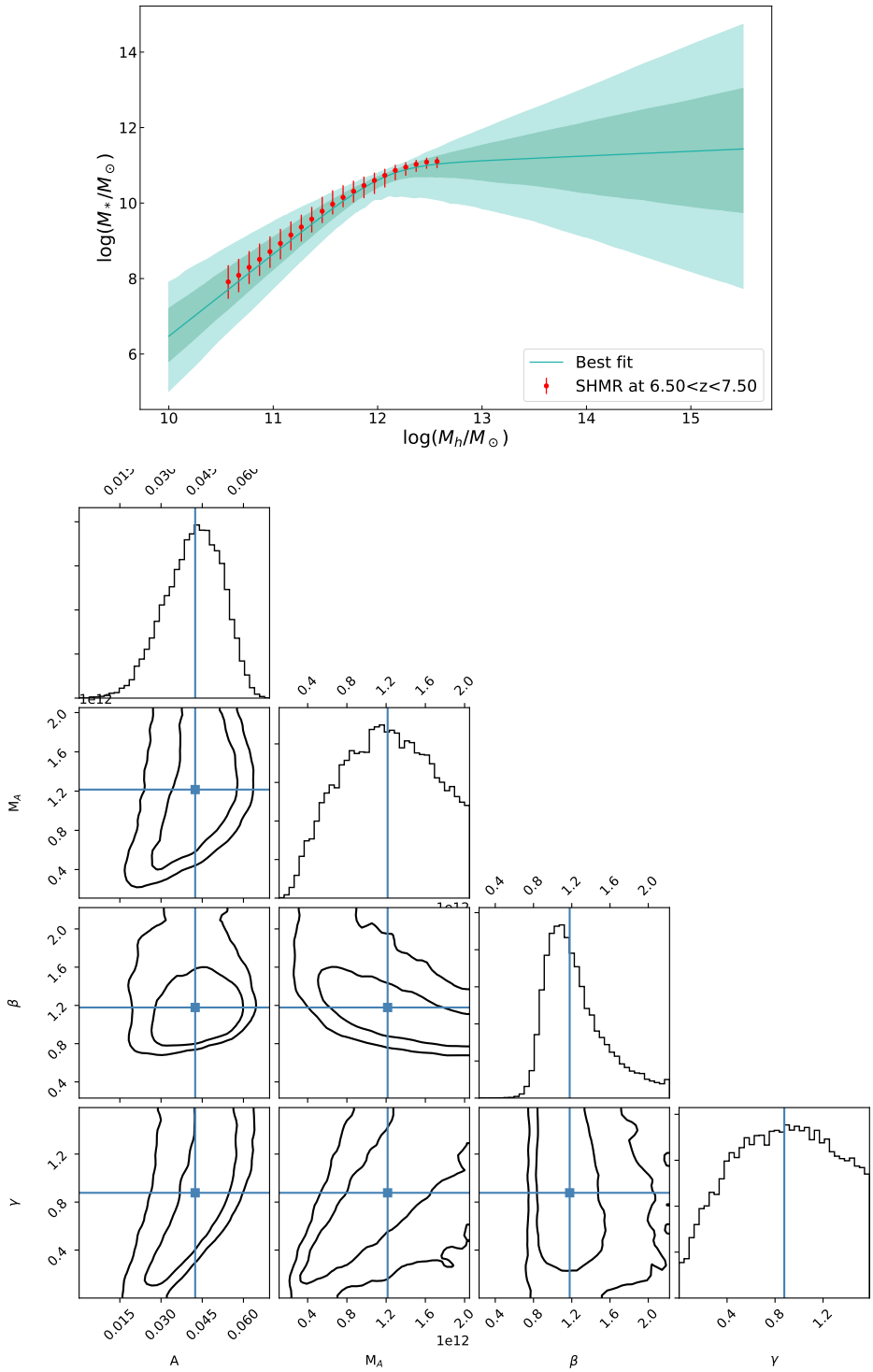

Fig. A.28 Best-fit and posterior probability distribution for the Millennium I+II without *relative* scatter at $6.5 < z < 7.5$. Points, lines and colors as in Fig. A.1.

A.4 Millennium I+II with *relative* scatter

Here we report the plots for each redshift bin of the best-fits to the data (described in Sect.3.1.2 using Eq. 2.2) derived from the direct comparison of the CMFs with their corresponding contour plot that shows all the one and two dimensional projections of the posterior probability distributions of the free parameters of the fit.

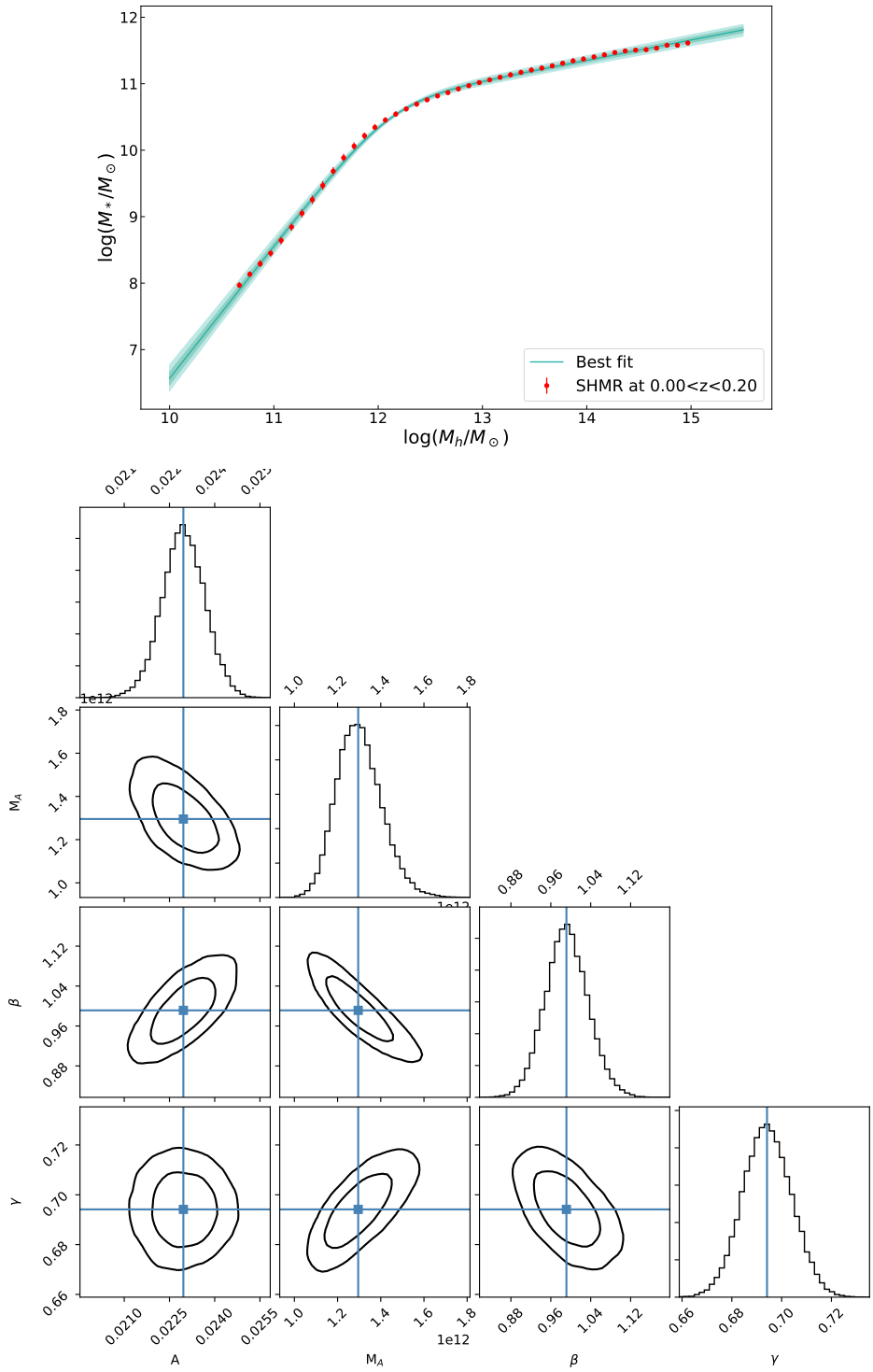

Fig. A.29 Best-fit and posterior probability distribution for the Millennium I+II with *relative* scatter at $0.0 < z < 0.2$. Points, lines and colors as in Fig. A.1.

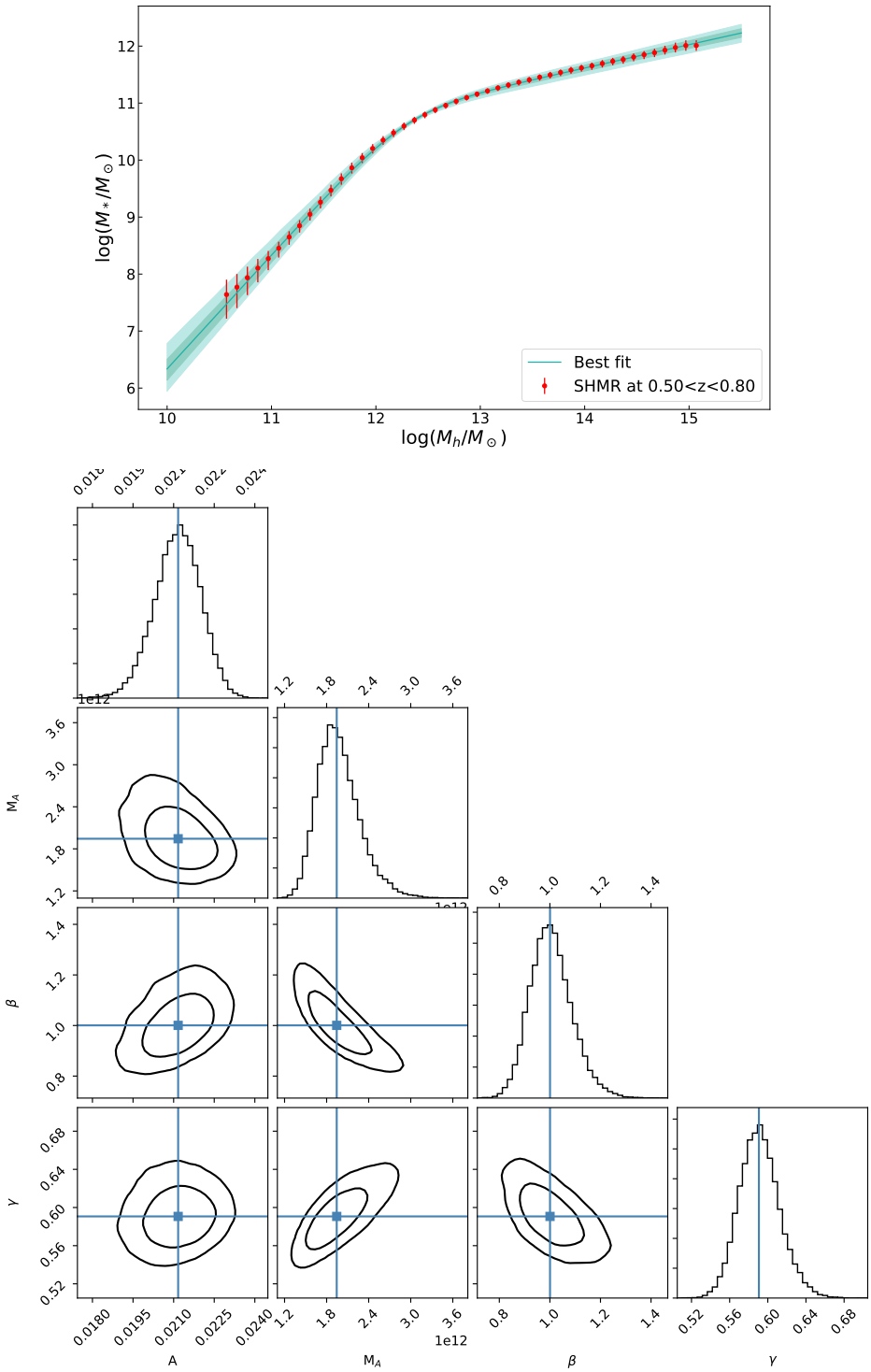

Fig. A.30 Best-fit and posterior probability distribution for the Millennium I+II with *relative* scatter at $0.5 < z < 0.8$. Points, lines and colors as in Fig. A.1.

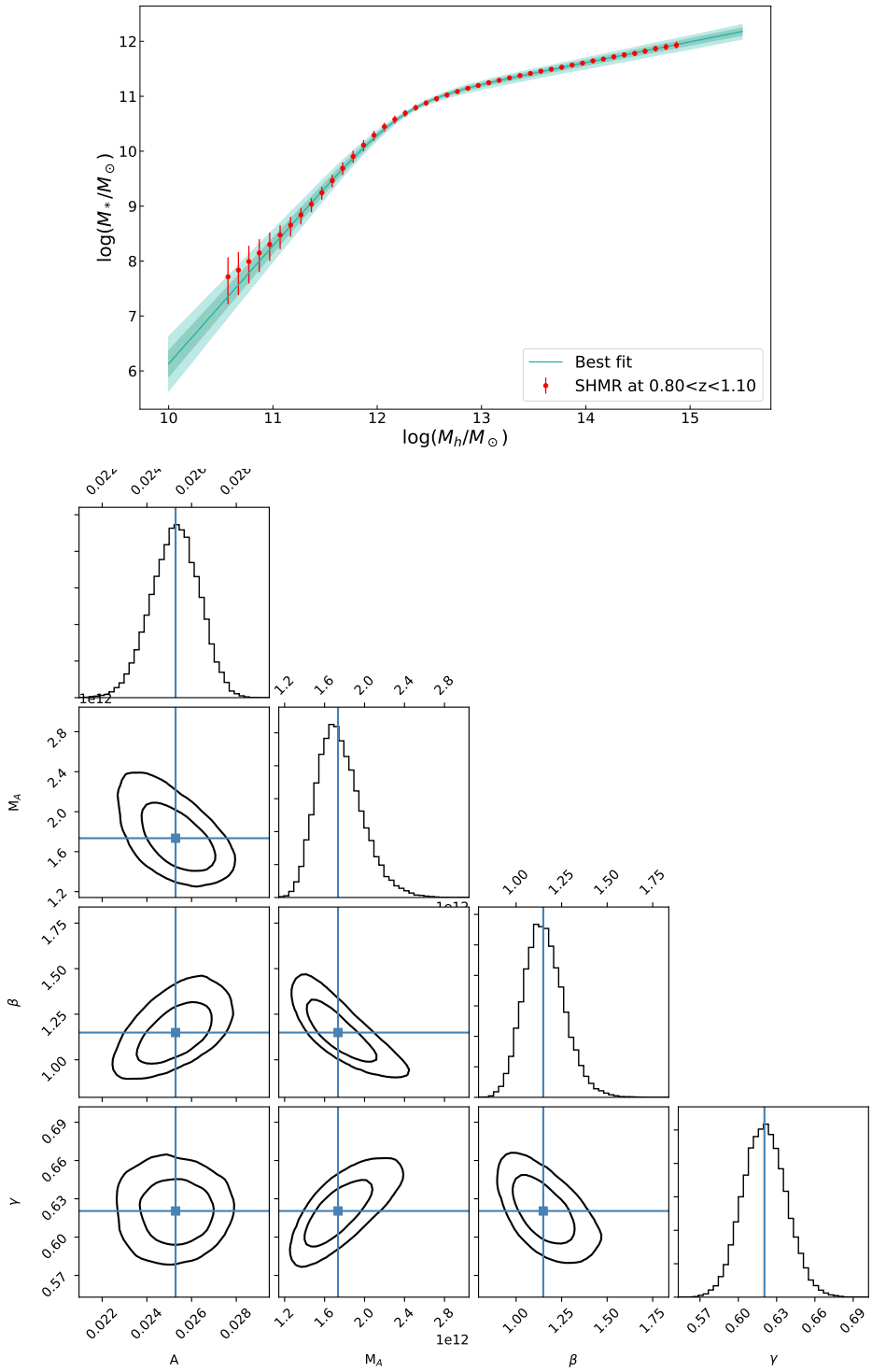

Fig. A.31 Best-fit and posterior probability distribution for the Millennium I+II with *relative* scatter at $0.8 < z < 1.1$. Points, lines and colors as in Fig. A.1.

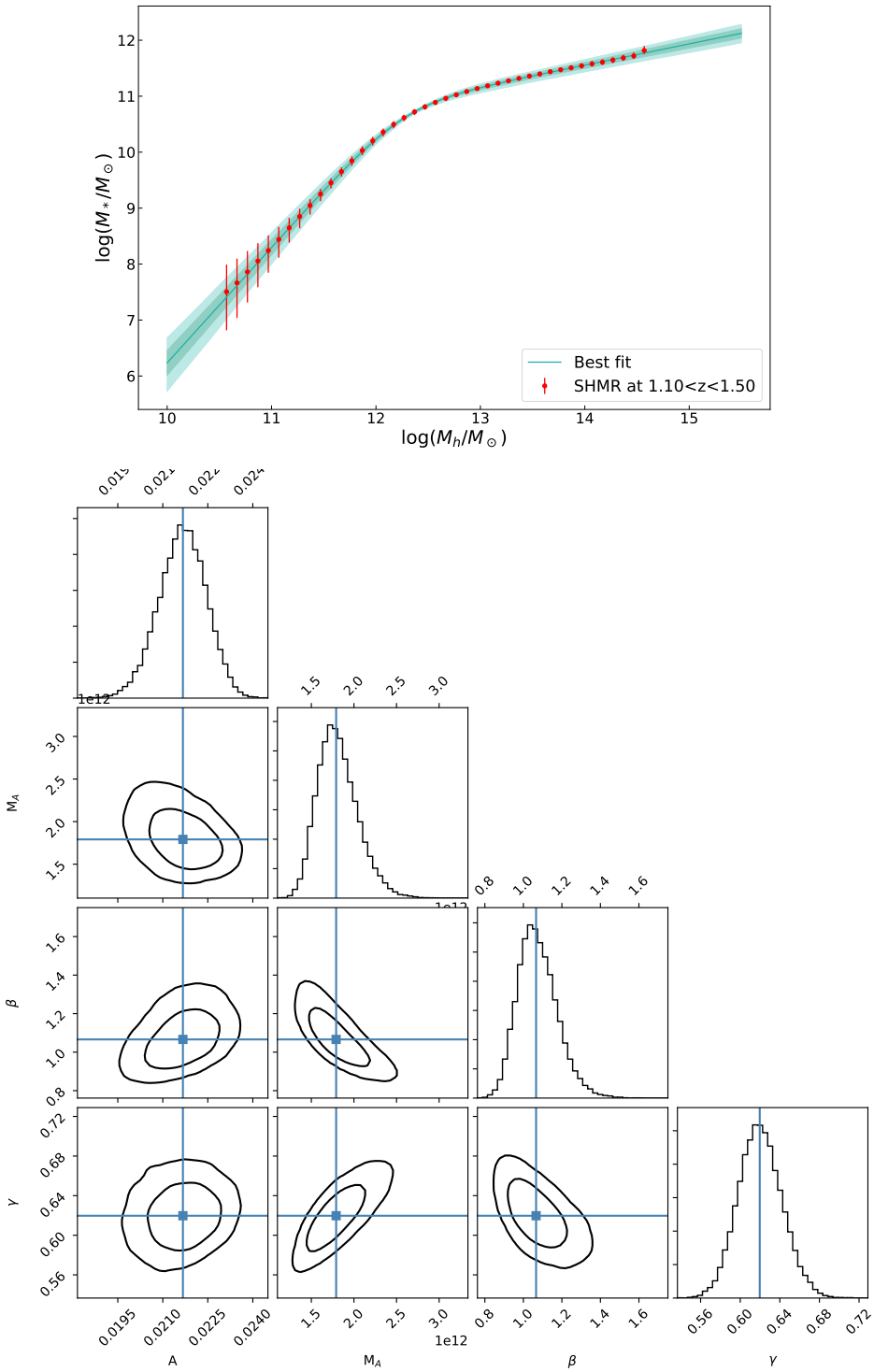

Fig. A.32 Best-fit and posterior probability distribution for the Millennium I+II with *relative* scatter at $1.1 < z < 1.5$. Points, lines and colors as in Fig. A.1.

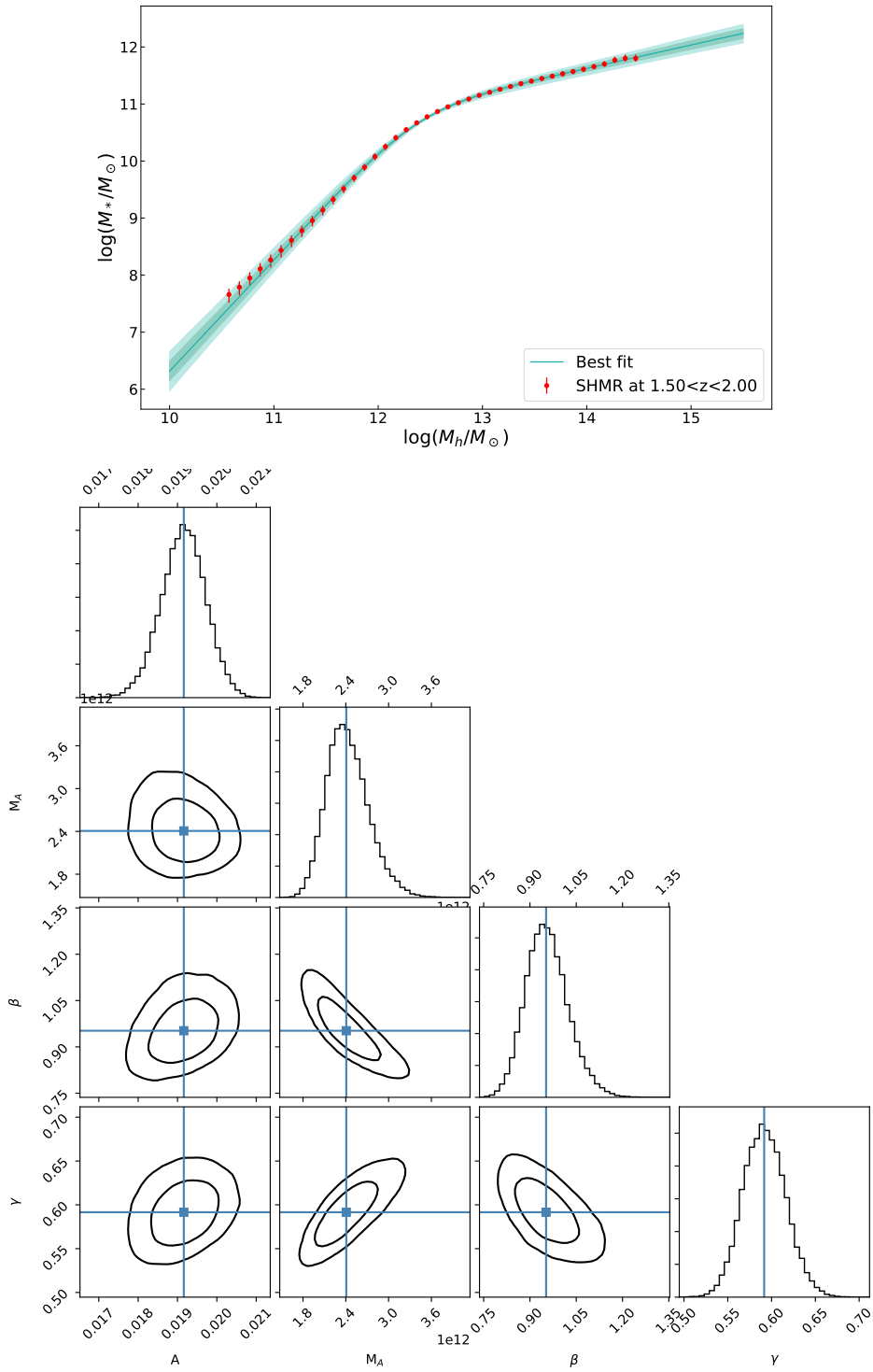

Fig. A.33 Best-fit and posterior probability distribution for the Millennium I+II with *relative* scatter at $1.5 < z < 2.0$. Points, lines and colors as in Fig. A.1.

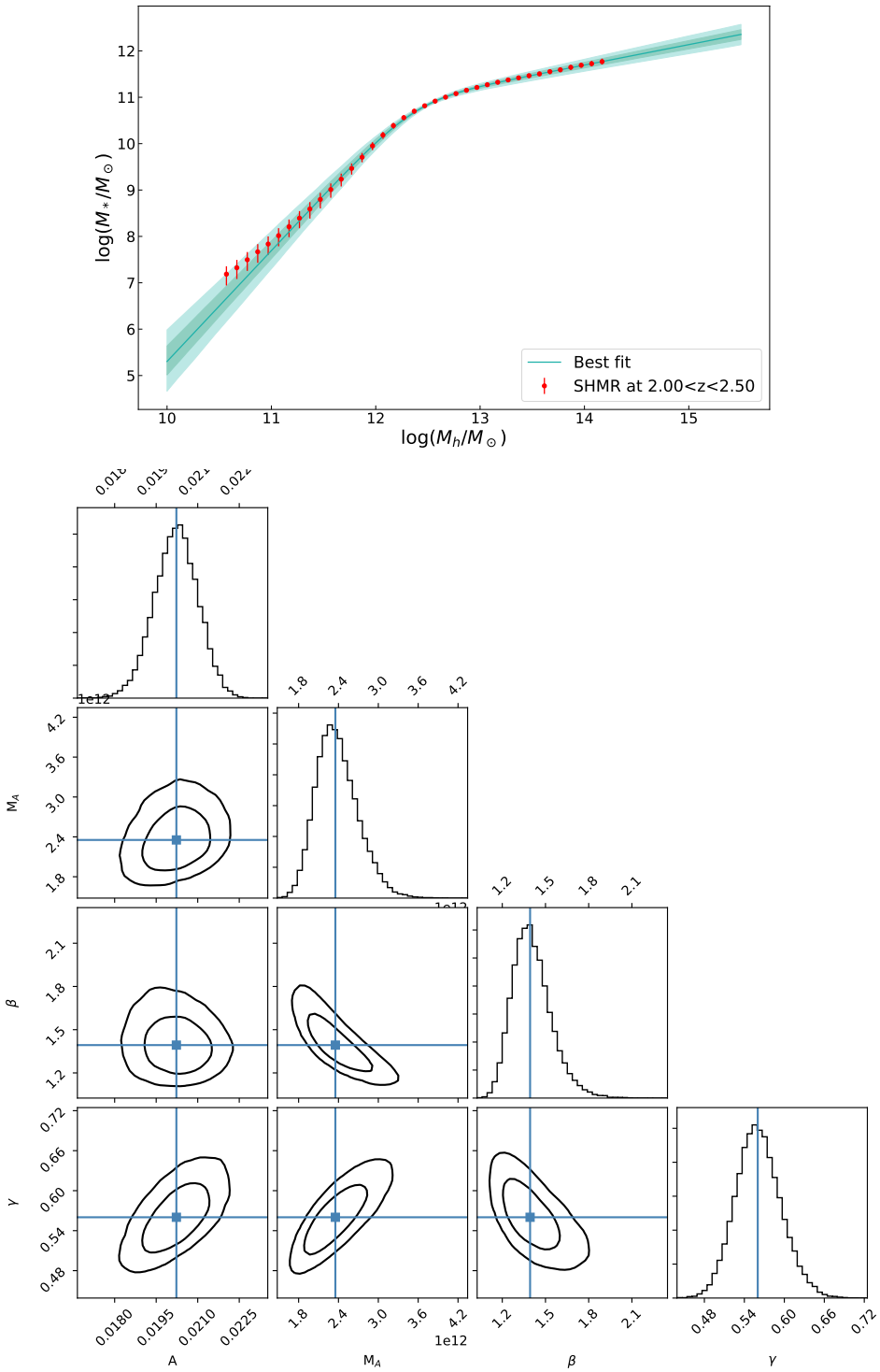

Fig. A.34 Best-fit and posterior probability distribution for the Millennium I+II with *relative* scatter at $2.0 < z < 2.5$. Points, lines and colors as in Fig. A.1.

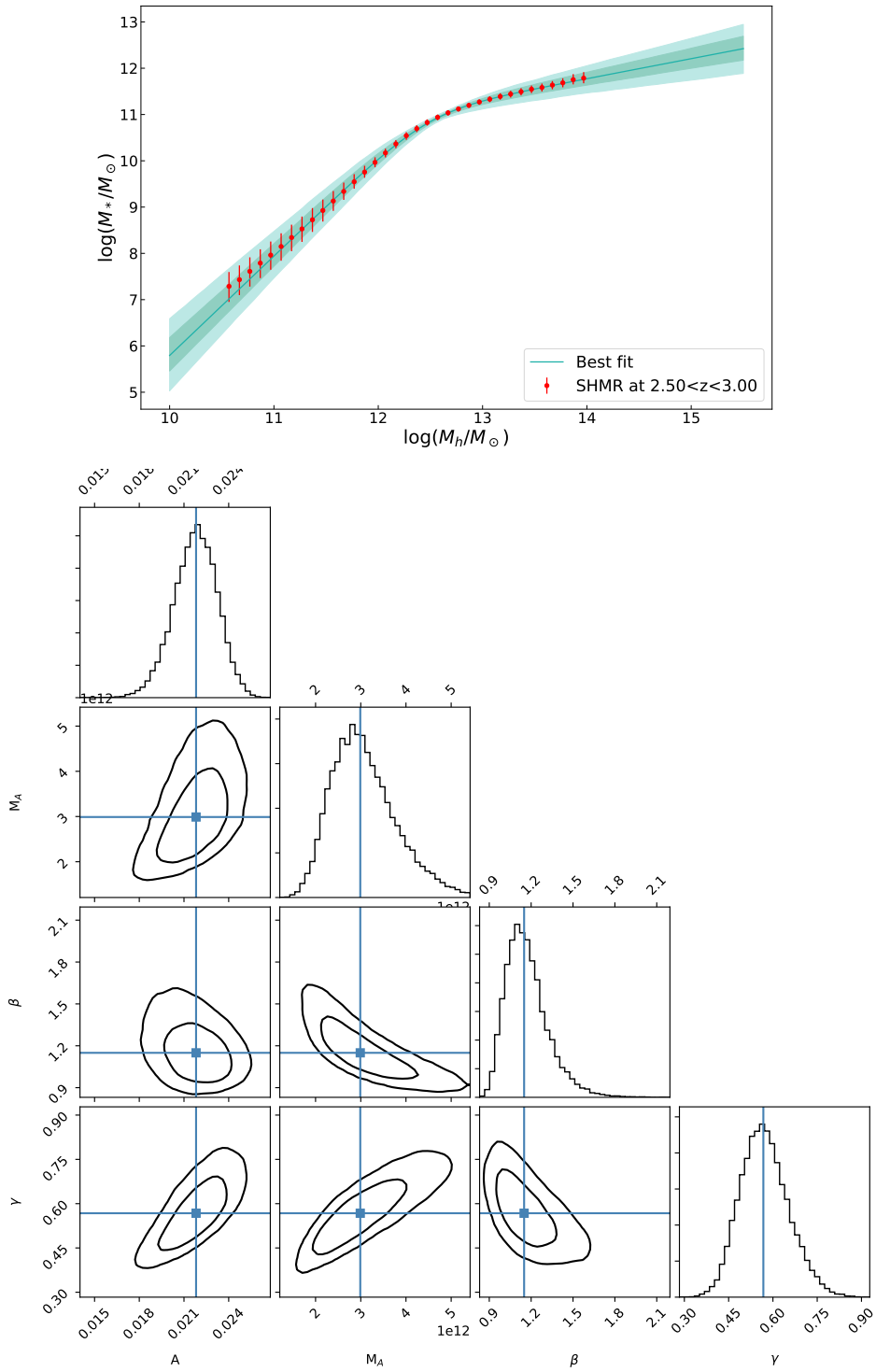

Fig. A.35 Best-fit and posterior probability distribution for the Millennium I+II with *relative* scatter at $2.5 < z < 3.0$. Points, lines and colors as in Fig. A.1.

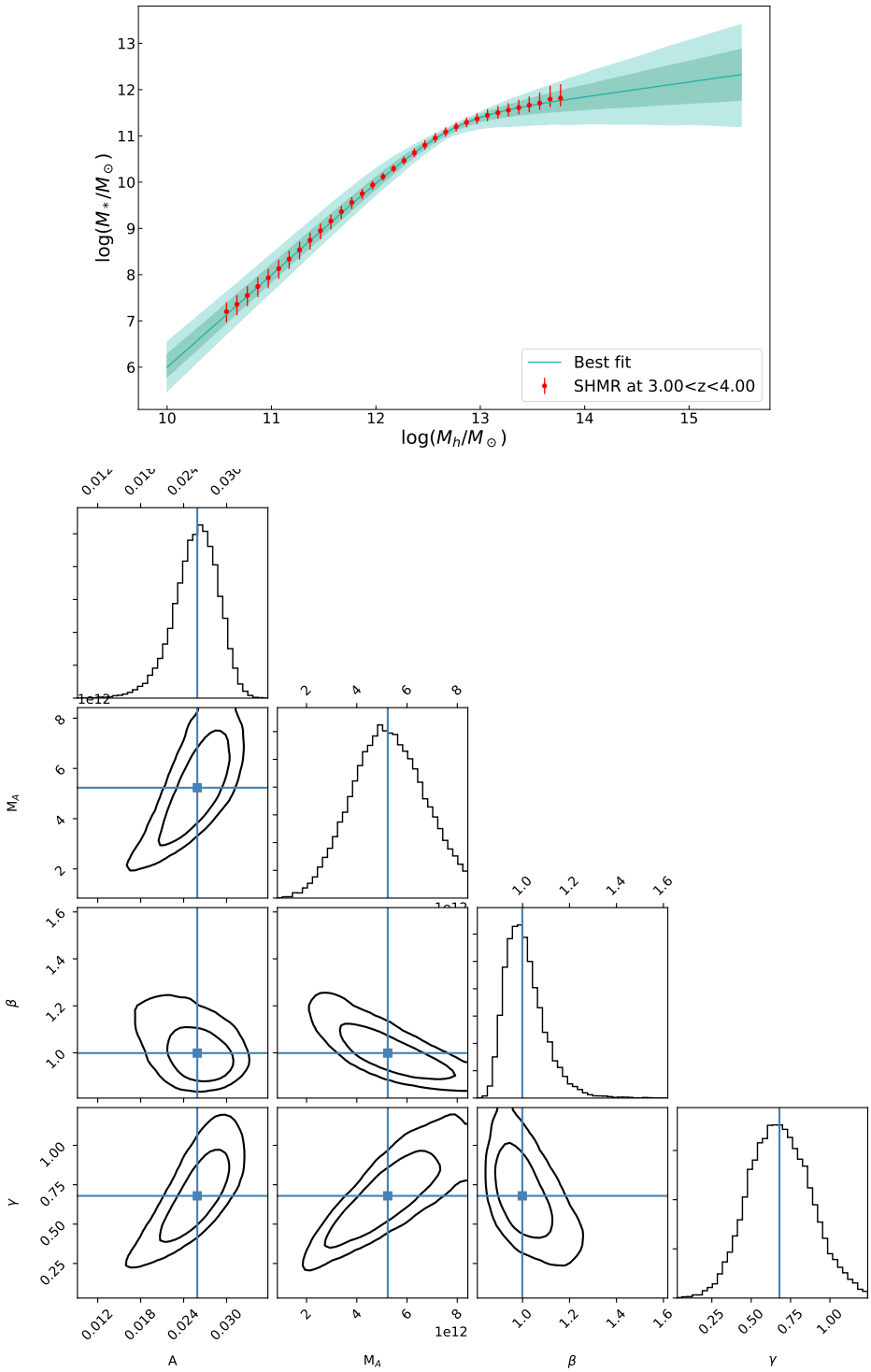

Fig. A.36 Best-fit and posterior probability distribution for the Millennium I+II with *relative* scatter at $3.0 < z < 4.0$. Points, lines and colors as in Fig. A.1.

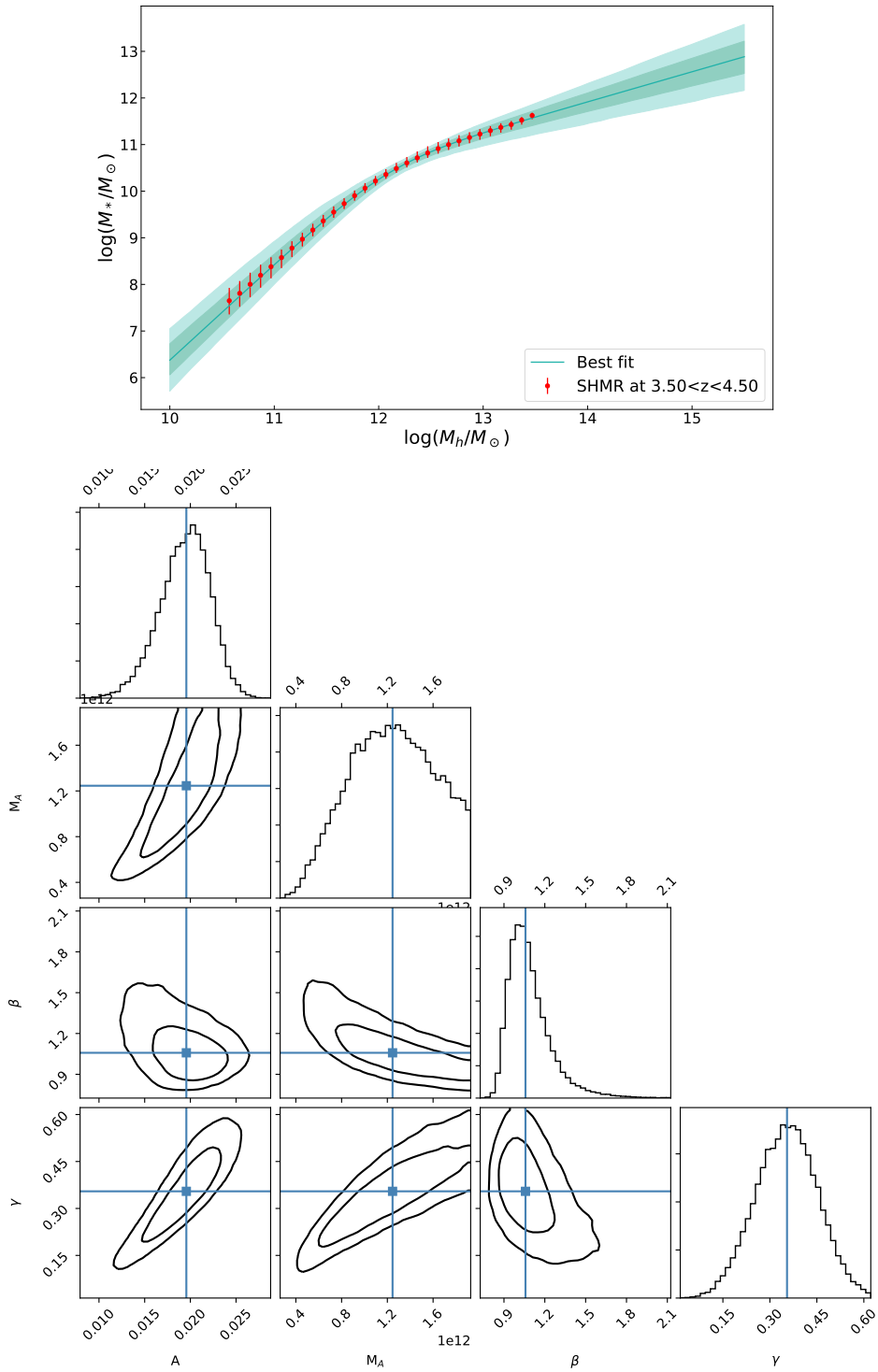

Fig. A.37 Best-fit and posterior probability distribution for the Millennium I+II with *relative* scatter at $3.5 < z < 4.5$. Points, lines and colors as in Fig. A.1.

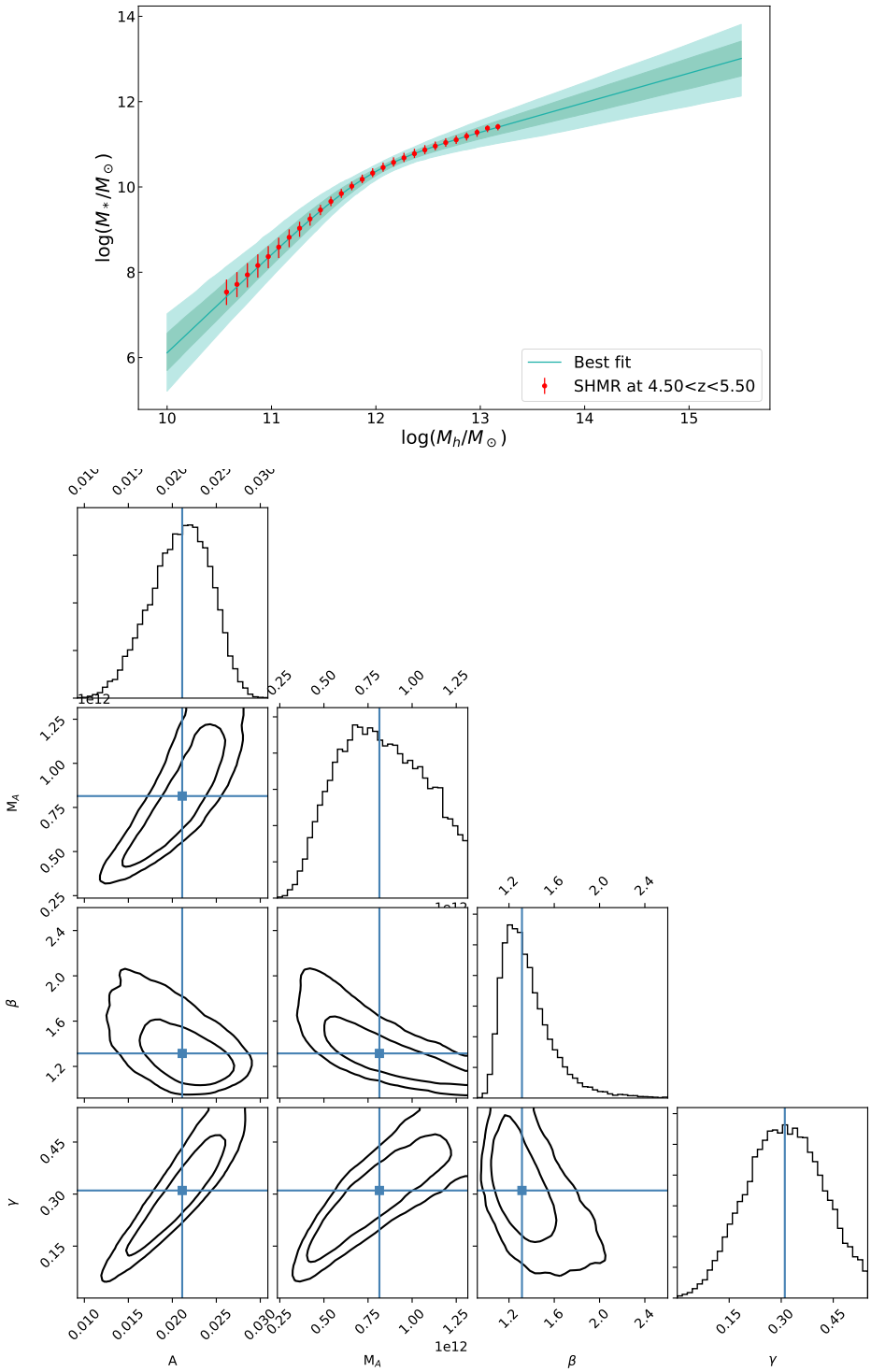

Fig. A.38 Best-fit and posterior probability distribution for the Millennium I+II with *relative* scatter at $4.5 < z < 5.5$. Points, lines and colors as in Fig. A.1.

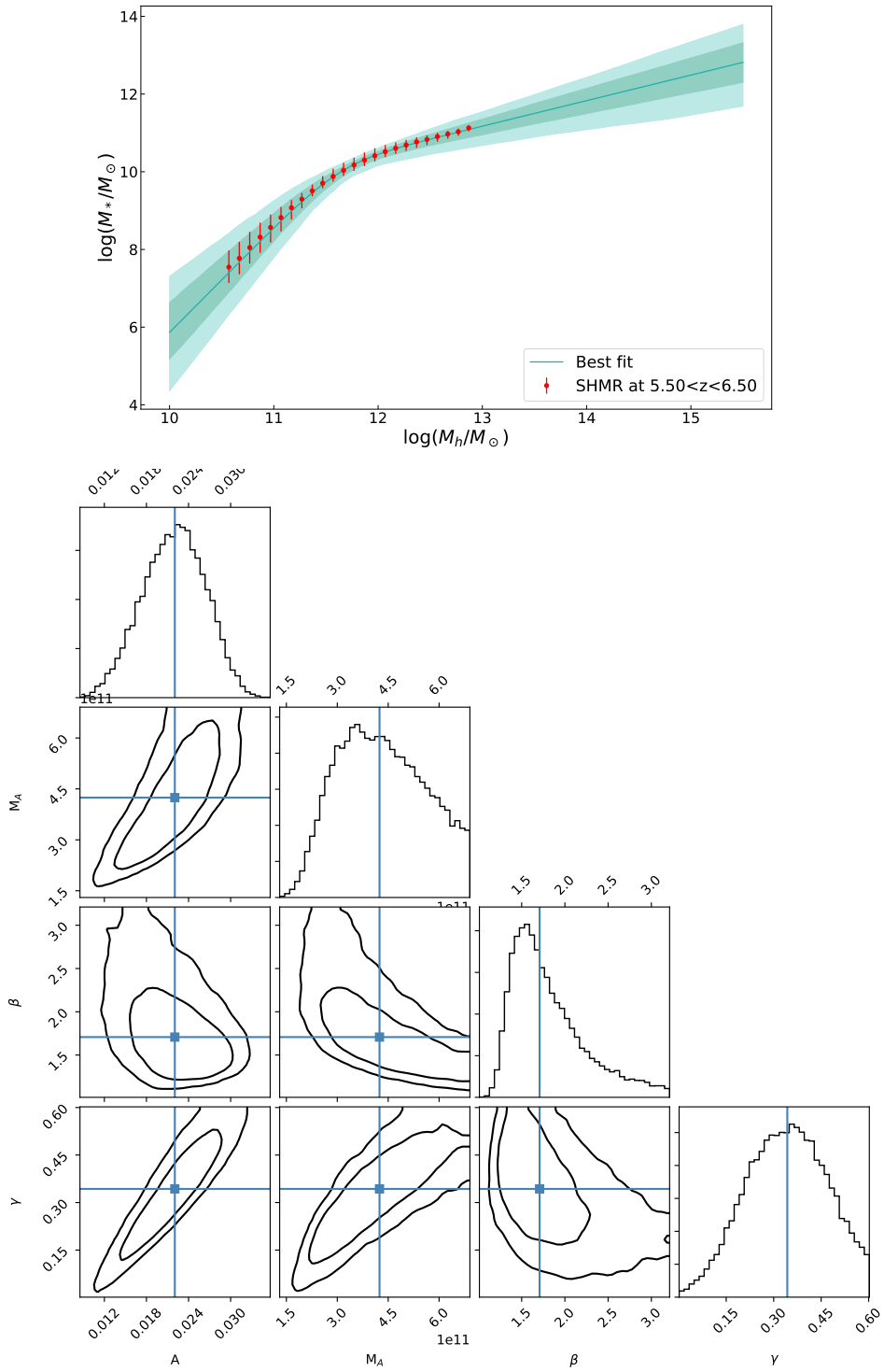

Fig. A.39 Best-fit and posterior probability distribution for the Millennium I+II with *relative* scatter at $5.5 < z < 6.5$. Points, lines and colors as in Fig. A.1.

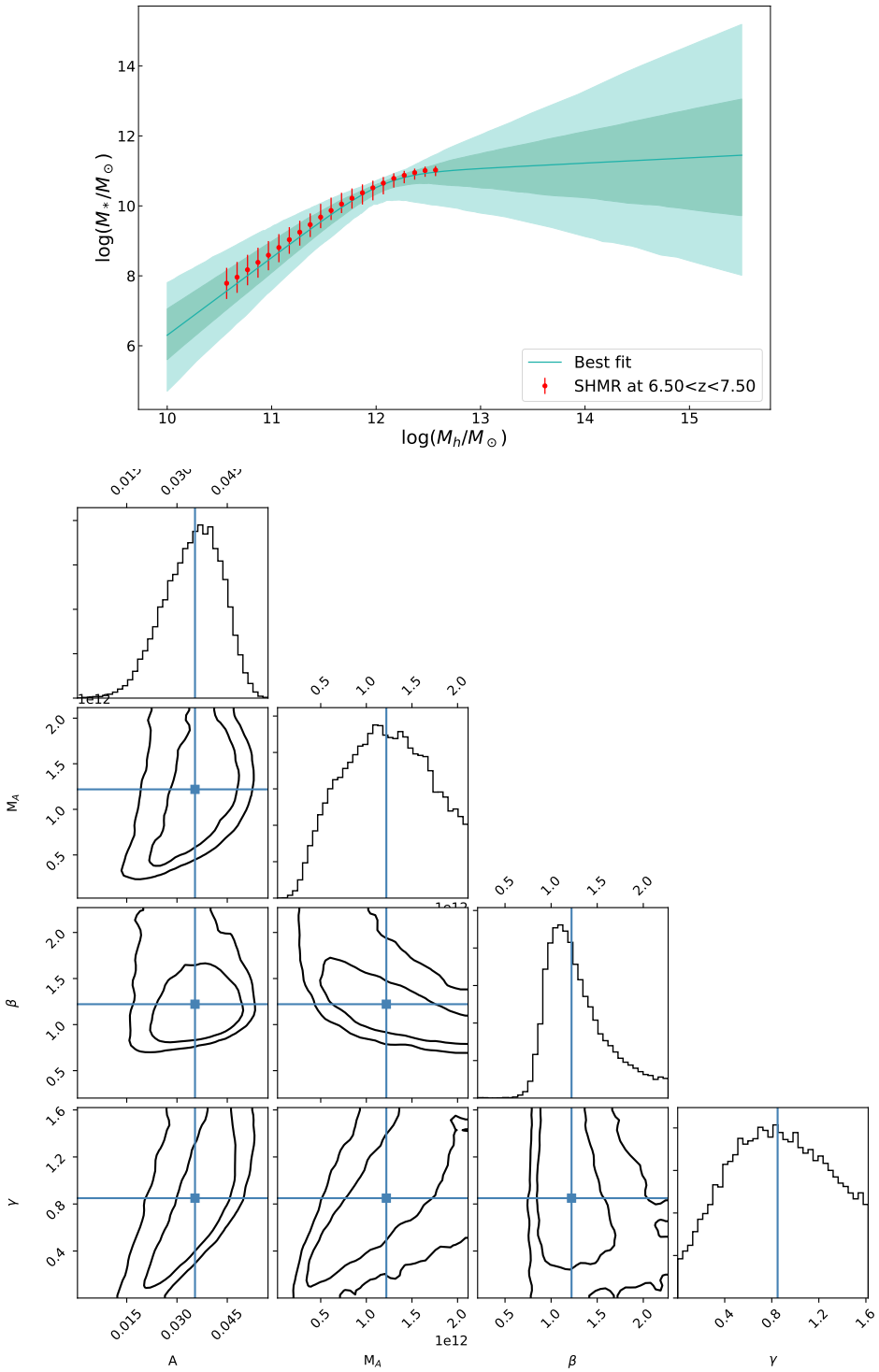

Fig. A.40 Best-fit and posterior probability distribution for the Millennium I+II with *relative* scatter at $6.5 < z < 7.5$. Points, lines and colors as in Fig. A.1.

B

POSTERIOR PROBABILITY DISTRIBUTIONS OF THE EMPIRICAL MODEL

In this Appendix, we report the plots of all the one and two dimensional projections of the posterior probability distributions of the free parameters of the fit of the empirical model, performed in Sect. 3.2.

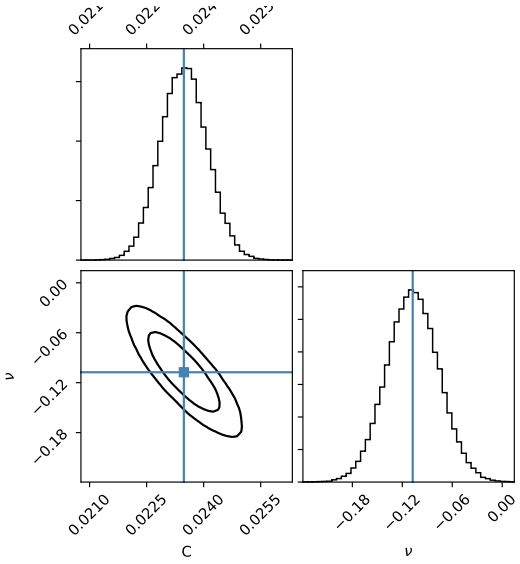

Fig. B.1 Posterior probability distribution for the parameter *A* of the empirical model.

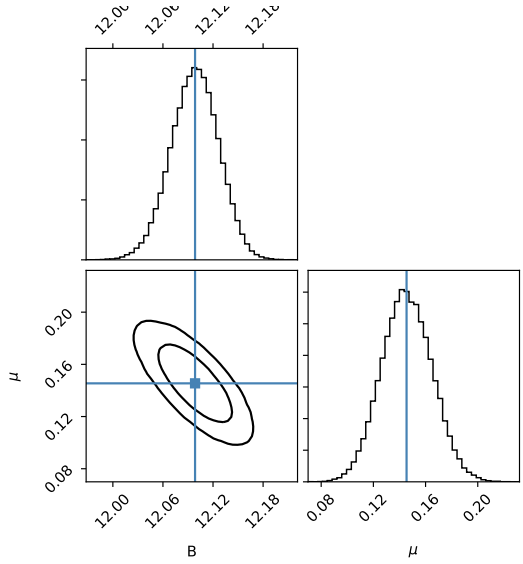

Fig. B.2 Posterior probability distribution for the parameter M_A of the empirical model.

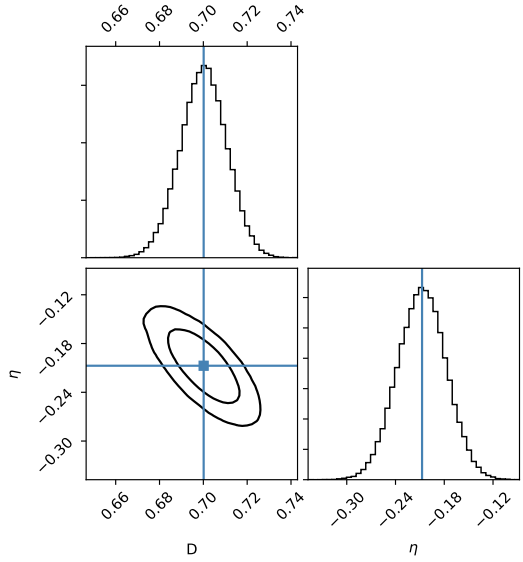

Fig. B.3 Posterior probability distribution for the parameter γ of the empirical model.

C

DETAILS ON LITERATURE RESULTS FOR THE SHMR

In this appendix we describe the literature works with which we compare our results on the Millennium I+II simulation in Figs. 3.12, 3.13 and 3.14.

C.1 Moster et al. (2013, 2010)

Moster et al. (2010) and Moster et al. (2013) used the same functional form as we adopted for the SHMR. Both Moster et al. (2010) and Moster et al. (2013) used a SHAM technique to match simulated halos from the Millennium simulation (Springel et al., 2005) to observed SMFs. However, they used different SMFs based on the results of Panter et al. (2007) at $z = 0$, and Fontana et al. (2006) at $z > 0$ in Moster et al. (2010), and Li & White (2009) at $z \sim 0$ and Pérez-González et al. (2008) at $z > 0$ in Moster et al. (2013). This choice is reflected in differences in the stellar mass at fixed halo mass.

At $z \sim 0$ our results are in good agreement with Moster et al. (2013) results down to $\log(M_h/M_\odot) \sim 12.5$. Below this threshold, our results predict lower stellar masses at fixed halo masses. At increasing redshift the agreement worsens. At $z \sim 1$ and $z \sim 3$ our results differ not only in the SHMR normalization, but also in the slopes at high and low masses (up to a factor of ~ 2.3 and ~ 4 at $\log(M_h/M_\odot) \sim 14.5$ at $z \sim 1$ and $z \sim 3$, respectively). The Moster et al. (2010) results differ from ours at any redshift in the values of the stellar mass at fixed halo masses (with a difference of a factor of ~ 1.7 in (M_*/M_h) at $\log(M_h/M_\odot) = 11.8$ at $z = 0$), but also in the low- and high-mass slopes of the SHMR.

C.2 Guo et al. (2010)

Guo et al. (2010) used an approach similar to that of Moster et al. (2010), based on stellar masses from Li & White (2009), but they did not account for scatter in stellar mass at fixed halo mass. Consequently, their results do not match Moster et al. (2010). As for Moster et al. (2013), at $z \sim 0$, our results agree well at high masses (i.e., $\log(M_*/M_h) \gtrsim 13.0$), but show differences at lower halo masses (e.g., a difference of a factor of ~ 2.5 in (M_*/M_h) is found at $\log(M_h/M_\odot) = 11.8$).

C.3 Zheng et al. (2007)

Zheng et al. (2007) used the galaxy clustering for luminosity-selected samples in the SDSS (at $z \sim 0$) and in the DEEP2 Galaxy Redshift Survey (Coil et al. 2006 at $z \sim 1$) to constrain the halo occupation distribution (HOD). This gives a direct constraint on the r-band luminosity of central galaxies as a function of halo mass. Stellar masses for this sample were then determined using the $g-r$ color and the r-band luminosity, assuming a WMAP1 cosmology. This method allows for scatter in the luminosity at fixed halo mass to be constrained as a parameter in the model. Results from Zheng et al. (2007) are not in good agreement with our results at $z \sim 0$ and differences grow larger (up to 0.4 dex) at $z \sim 1$.

C.4 Behroozi et al. (2010, 2013)

Behroozi et al. (2010, 2013) used an approach similar to what we used here, but with a much more complicated functional form to parameterize the SHMR (also accounting for a variable scatter in the relation for a total of 14 free parameters in the fit, compared to the 4 we used). Moreover, at $z \sim 0$ Behroozi et al. (2010) used Li & White (2009) SMFs, and Behroozi et al. (2013) used Moustakas et al. (2013) SMFs. At higher redshifts, Behroozi et al. (2010) and Behroozi et al. (2013) used several SMFs (see their papers for details). We find good agreement in the slope of the SHMR, especially with the Behroozi et al. (2010) results which are in excellent agreement with our findings at masses $\log(M_h/M_\odot) \gtrsim 12.5$.

At $z \sim 1$ and $z \sim 3$ there is not agreement on the slopes of the SHMR between Behroozi's results and ours. At $z \sim 1$ and $\log(M_h/M_\odot) = 11.8$, differences are of a factor of ~ 1.6 and ~ 2 for Behroozi et al. (2010) and Behroozi et al. (2013), respectively, while at $z \sim 3$ and $\log(M_h/M_\odot) = 13$ differences are up to a factor of ~ 1.3 and ~ 1.8 for Behroozi et al. (2010) and Behroozi et al. (2013), respectively.

C.5 Reddick et al. (2013)

Reddick et al. (2013) used additional input from the correlation function and conditional SMF as measured by SDSS. This result is in fair agreement with our result in the normalization of the SHMR. In particular, a difference of a factor of $\lesssim 1.1$ in (M_*/M_h) is found at $\log(M_h/M_\odot) = 11.8$.

C.6 Yang et al. (2012)

Yang et al. (2012) adopted an approach similar to the abundance matching, but with some differences. In particular, their approach assumes the subhalo abundance as a function of the mass at accretion and the accretion time, following the Yang et al. (2011) model. At $z \sim 0$ they used SMFs of SDSS DR7 (Abazajian et al., 2009), while for $z > 0$ they used SMFs from Pérez-González et al. (2008) and Drory et al. (2005). At $z \sim 0$, their results slightly overestimate our results down to halo masses of

$\log(M_h/M_\odot) \sim 12.5$. At lower masses, Yang et al. (2012) predict much higher stellar masses with respect to our result. At $z > 0$, the agreement worsens and the differences increase to a factor of ~ 2 at $\log(M_h/M_\odot) = 12.5$ in (M_*/M_h) at $z \sim 3$.

C.7 Rodríguez-Puebla et al. (2017)

Rodríguez-Puebla et al. (2017) estimated the SHMR as a function of redshift using a SHAM technique and several observed SMFs, based on different observational campaigns and techniques (see Rodríguez-Puebla et al. 2017 for details). Their results are not consistent with the results we obtain, with differences in the normalization of the SHMR and also in the slope of the relation at low and high masses. We find a difference of a factor of ~ 1.8 in (M_*/M_h) at $\log(M_h/M_\odot) = 11.8$ between their results and ours.

C.8 Carretero et al. (2015)

Carretero et al. (2015) combined a HOD model to a SHAM technique to link galaxy luminosities to dark matter halos. In particular, they used dark matter simulations from MICE (Fosalba et al., 2008) along with luminosity functions from the SDSS survey (Blanton et al., 2003). Even if the slope of the SHMR at high halo masses (i.e., $\log(M_h/M_\odot) \gtrsim 12.5$) is similar to the slope in our work, we find differences in the normalization of the SHMR, with a difference in (M_*/M_h) of a factor of ~ 1.3 at $\log(M_*/M_h) = 13.5$ with respect our results.

C.9 Behroozi et al. (2019)

Behroozi et al. (2019) presented a method for determining individual galaxy star formation rates from their host halos potential well depths, assembly histories, and redshifts. For each halo, the galaxy stellar mass is derived from the star formation histories along the halo assembly and merger history. The model is calibrated through several observations of the SMF and the cosmic star formation rate. However, their results disagree with ours at all redshifts, with differences in the slopes (at high and low halo masses) and in the normalization of the SHMR. As an example, at a halo mass of $\log(M_h/M_\odot) = 11.5$ at $z \sim 0$, a difference of a factor ~ 1.7 in (M_*/M_h) is found.

C.10 Moster et al. (2018)

Moster et al. (2018) also presented an empirical model of galaxy formation. They assigned a star formation rate to each dark matter halo based on its growth rate and computed the stellar masses by integrating it. Several observations of the cosmic star formation rate densities were used to calibrate the model (see Moster et al. (2018) for more details). At $z \sim 0$, and for $\log(M_h/M_\odot) \lesssim 12.5$, the Moster et al. (2018) results are inconsistent with our findings in the slope of the SHMR and in the

normalization (e.g., a difference of a factor of ~ 1.5 in (M_*/M_h) can be seen at $\log(M_h/M_\odot) = 11.5$ with respect to our results). Moving toward higher halo masses, the normalization of the SHMR is in fair agreement with our finding but the slope is still different. Moving to higher redshifts our results disagree with those of Moster et al. (2018) at $\log(M_h/M_\odot) \lesssim 12.5$, while for masses above this limit the agreement is good.

C.11 Yang et al. (2009)

At the high-mass end, Yang et al. (2009) have directly identified clusters and groups corresponding to dark matter halos, and measured the stellar masses of their central galaxies. They used a group catalog matched to halos to determine halo masses. Their results disagree with ours in the normalization of the SHMR at all halo masses (e.g., a difference of a factor of ~ 1.4 in (M_*/M_h) can be seen at $\log(M_h/M_\odot) = 13$ with respect to our results), but the slope at high halo masses is consistent with ours..

C.12 Wang & Jing (2010)

Wang & Jing (2010) applied the empirical method built for redshift $z = 0$ in their previous work (Wang et al., 2006) to a higher redshift to link galaxy stellar mass directly with its hosting dark matter halo mass at redshift of about 0.8. The SHMR is found by fitting the SMF and the correlation functions at different stellar mass intervals from VIMOS-VLT Deep Survey (VVDS) observation. Positions of galaxies are predicted by following the merging histories of halos and the trajectories of subhalos in the Millennium Simulation (Springel et al., 2005). Their results are not consistent with our findings at all halo masses nor in the slopes or in the normalization.

C.13 Legrand et al. (2019)

Legrand et al. (2019) used a parametric abundance matching technique to link observed SMFs on the COSMOS field (Davidzon et al., 2017) to halo mass functions. In particular, they used the method developed in Behroozi et al. (2010, 2013). In Legrand et al. (2019) work, the adopted SMFs are the ones more similar to ours, given that they have been calibrated on the COSMOS field. This similarity, is reflected in their results, which agree well with ours at $z \sim 0$. At higher redshifts the agreement is lost with differences that go up to a factor of ~ 2.2 at $z \sim 3$ and $\log(M_h/M_\odot) = 14$ in (M_*/M_h) scale.

C.14 Stefanon et al. (2017)

Stefanon et al. (2017) evaluated the luminosity function in the z band from $z \sim 4$ to $z \sim 7$ in the CANDELS and COSMOS fields. Then they abundance matched their luminosity functions to halo

mass functions to evaluate the SHMR. Their results differ from ours in (M_*/M_h) scale by a factor of ~ 1.5 and ~ 3 at $z \sim 5$ and $z \sim 7$, respectively.

C.15 Harikane et al. (2016, 2018)

Both Harikane et al. (2016) and Harikane et al. (2018) evaluate the SHMR from a clustering analysis, and consequent HOD modelling. Harikane et al. (2016) uses observations from the Hubble Legacy Imaging and an early SUBARU survey data. Harikane et al. (2018) instead uses the full Hyper Suprime-Cam (HSC) Subaru dataset from $z \sim 4$ to $z \sim 6$ over an area of ~ 100 deg^2. Comparing to our results, we find that Harikane et al. (2016) results are fully consistent with ours both at $z \sim 5$ and $z \sim 7$. We find that the Harikane et al. (2018) results are consistent with ours at $z \sim 7$ but differ by a factor of ~ 3 at $z \sim 5$ and $\log(M_h/M_\odot) = 12.5$ in (M_*/M_h) scale.

C.16 Tacchella et al. (2018)

Tacchella et al. (2018) presented an empirical model that connects the dark matter halo population to the stellar mass and star-formation content of galaxies at $z > 4$. Similarly to Moster et al. (2018) and Behroozi et al. (2019) they extract dark mater halo merger trees from an N-body simulation that are then populated with galaxies by assuming that the SFR of a halo is proportional to its accretion rate. In addition, Tacchella and collaborators introduced a scatter in the stellar-to-halo mass ratio with values that range from 0.14 dex to 0.18 dex from $z = 4$ to $z = 10$. At $z \sim 5$ their results differ from ours up to ~ 1 dex at $\log(M_h/M_\odot) = 10$ in (M_*/M_h), while differences at $z \sim 7$ are of the order of ~ 0.6 dex at the same halo mass.

D

MASSIVE AND OLD QUIESCENT GALAXIES AT HIGH REDSHIFTS

In this Appendix we report a study we conducted to identify and confirm the presence of massive and quiescent galaxies at high redshift. The content of this Appendix is reported in a recently published paper: Girelli, Bolzonella, & Cimatti (2019)

More in detail, questions of how massive quiescent galaxies rapidly assembled and how abundant they are at high redshift are increasingly important in the study of galaxy formation. Looking at these systems can shed light on the processes of galaxy mass assembly and quenching of the star formation at early epochs. In order to address these questions, we aim to identify and characterize massive quiescent galaxies from $z \sim 2.5$ out to the highest redshifts at which these systems can be found. The final purpose is to compare the results with the predictions of state-of-the-art semi-analytical models of galaxy formation and evolution.

We defined observer-frame color-color diagrams to optimally select quiescent galaxies at $z > 2.5$ and applied them to the COSMOS2015 catalog. We refined the spectral energy distribution (SED) fitting analysis for the selected candidates to confirm their quiescent nature, then derived their number density, mass density, and stellar mass functions. Finally, we compared the results with previous observations and some current semi-analytic models.

We selected candidates for quiescent galaxies in the redshift range $2.5 \lesssim z \lesssim 4.5$ from the COSMOS2015 catalog by means of two observed color-color diagrams. The additional SED fitting analysis allowed us to select 128 galaxies, consistent with being massive ($\log(M_*/M_\odot) \geq 10.6$), old (ages $\gtrsim 0.5$ Gyr), and quiescent ($\log(\mathrm{sSFR}\,[\mathrm{yr}^{-1}]) \leq -10.5$) objects at high redshift ($2.5 < z < 4.5$). Their number and mass densities are in fair agreement with previous observations and, if confirmed, show a discrepancy with current semi-analytical models of galaxy formation and evolution (Henriques et al., 2015), that underpredict the number of massive quiescent systems up to a factor of ~ 12 at $2.5 \leq z < 3.0$ and ~ 10 at $z \sim 4.0$. The evolution of the stellar mass functions (SMFs) of these systems is similar to previous estimates and indicates a disagreement with models, particularly with regard to the shape of the SMF.

The present results add further evidence to the possibility that massive and quiescent galaxies can exist out to at least $z \sim 4$. If future spectroscopic observations carried out with, for example, the James Webb Space Telecope (JWST), confirm the substantial presence of such a population, further work on modeling the stellar mass assembly, as well as supermassive black hole (BH) accretion and feedback processes at early cosmic epochs, is needed to understand how these systems formed, evolved, and quenched their star formation.

D.1 Introduction

The formation of galaxies and their properties are driven by the evolution of both dark matter and baryons. While dark matter halos assembled most of their mass through sequential merging, some fundamental questions remain still open (Naab & Ostriker, 2017), particularly those regarding the formation of massive galaxies and their transformation into quiescent systems.

Recent developments support a scenario where galaxies assembled most of their mass not only through sequential merging, but also through smooth accretion by cold gas streams that penetrate the shock-heated media of massive dark matter halos and grow dense, unstable, turbulent discs with bulges, and trigger rapid star formation (e.g., Dekel et al. 2009).

Different models of galaxy formation and evolution have been developed in order to explain the emergence of massive objects (e.g., Henriques et al. 2015; Sheth et al. 2001) and their transformation into quiescent systems (e.g., Guo et al. 2011, 2013a; Henriques et al. 2017; Naab et al. 2014). However, when these models are applied to simulations (e.g., the Munich Simulation: Croton 2006; Croton et al. 2016; De Lucia & Blaizot 2007; Henriques et al. 2015; Kauffmann et al. 1999; Springel et al. 2001), they predict results which are not fully consistent with the observed evolution of galaxy properties. In particular, the presence of a population of high-redshift massive (and sometimes quiescent) galaxies can create tension between models and observations (e.g., the impossibly early galaxy problem, as in Steinhardt et al. 2016, referring to the problem of such rapid assembly of massive systems). Therefore, a robust determination of the abundance of massive quiescent galaxies at high redshift is a powerful test bench for galaxy formation models that also have to reproduce the mechanisms for quenching star formation in order to produce quiescent galaxies.

Many recent studies (e.g., Caputi et al. 2012; Castro-Rodríguez & López-Corredoira 2012; Daddi et al. 2004; Deshmukh et al. 2018; Fontana et al. 2006; Ilbert et al. 2006; Mawatari et al. 2016; Merlin et al. 2018, 2019a; Muzzin et al. 2013; Nayyeri et al. 2014; Stefanon et al. 2013; Straatman et al. 2014; Wang et al. 2016; Wiklind et al. 2008) have identified a population of massive quiescent galaxies at high redshift ($z \gtrsim 2.5$). Due to the current observational limits, these objects are just photometric candidates based on spectral energy distribution (SED) fitting analysis of broad-band photometry with population synthesis models. There are few notable exceptions for which deep near-infrared (NIR) spectroscopy confirms the passive nature of the candidates and determines their redshifts (at $z = 3$ in Gobat et al. 2012, and $z = 3.7$ in Glazebrook et al. 2017). Moreover, in a recent work Schreiber et al. (2018) obtain Keck-MOSFIRE H and K-band spectra for 24 candidate quiescent galaxies at $3 < z < 4$

and confirm the redshift and passive nature for eight of them, adding further evidence to the existence of a significant population of quiescent galaxies at high-redshift. This is a strong evidence that star formation in these galaxies occurred very fast within the first billion years of the universe, followed by a passive evolution (Mancini et al., 2009; Oesch et al., 2013; Stefanon et al., 2013; Straatman et al., 2014). The common technique adopted to select and identify quiescent galaxies at $z > 3$ consists of two steps: the selection of likely candidates based on colors (observed or rest-frame) and the subsequent identification of the most likely old and high redshift galaxies among these candidates by means of a spectral energy distribution (SED) fitting analysis with population synthesis models (e.g., Nayyeri et al. 2014; Wang et al. 2016; Wiklind et al. 2008). This two-step process is required because, as it is discussed further in this paper, the colors of these high redshift quiescent galaxies are to some extent degenerate with regard to those of dusty star-forming galaxies at the same or lower redshift (as is also known for quiescent galaxies at lower redshift, e.g., Pozzetti & Mannucci 2000). A recent example is the work by Merlin et al. (2018) in which the authors search for passive galaxies at $z > 3$ in the GOODS-South field using photometric data and then select galaxies with star formation rate SFR $= 0$ with the aid of a SED fitting analysis adopting top-hat star formation histories. All these results demonstrate the increasing importance of the quest for identifying the population of passive and quiescent galaxies at high redshift.

The aim of this work is to devise observed color-selection diagrams that can efficiently identify the bulk of the population of $z \geq 2.5$ massive quiescent galaxies, including those that could be missed by other selection techniques. In Sect. D.2, we present new observed color selections to identify quiescent galaxies at $z \gtrsim 2.5$. We carefully studied the effects of all the parameters characterizing evolutionary tracks, which is presented in Appendix D.9. The data used to test the new criteria are given in Sect. D.3. In Sect. D.3.3, we present the selection of the quiescent candidates through color selections and in Sect. D.4, the SED fitting analysis needed to ascertain their passive nature. In Sect. D.5, we revise the number density of quiescent objects at high redshift and compare our results to recent galaxy formation models. Moreover, in Sect. D.6, we present our estimate of the mass functions for the quiescent population. A discussion on our results and a comparison with previous observations and current semi-analytic models is presented in Sect. D.7. A summary of the methods adopted and the results is presented in Sect. D.8. Throughout this work, a standard cold dark matter (ΛCDM) cosmology is adopted with Hubble constant $H_0 = 70\,\mathrm{km\,s^{-1}\,Mpc^{-1}}$, total matter density $\Omega_\mathrm{M} = 0.3$ and dark energy density $\Omega_\Lambda = 0.7$. All magnitudes are expressed in the AB system and log is base 10 logarithm, if not otherwise specified.

D.2 Color selections at $z > 2.5$

One of the most efficient ways of selecting quiescent galaxies is based on colors, a method which relies on the identification of spectral features via photometry.

Color-color selection can be performed using rest-frame or observed quantities. The approach with rest-frame colors, such as UVJ (Williams et al., 2009) and NUVRJ (see Laigle et al. 2016 or Ilbert

et al. 2013 for details), requires an estimate of the redshift, which for large and deep surveys is usually derived from photometry, with rest-frame colors evaluated using the observed SED. High-redshift quiescent galaxies are characterized by SEDs which make them often too faint to be detected at optical wavelengths, and therefore rest-frame colors are usually extrapolated (Ilbert et al., 2013). Instead, apparent colors (e.g., Nayyeri et al. 2014) have the advantage of relying only on observations, although the lack of redshift measurement can add a further level of degeneracy. In this paper we will follow this second approach, in order to pre-select quiescent candidates based only upon observed data, and then an ad-hoc SED fitting analysis is performed in order to confirm their nature.

To identify quiescent galaxies by means of observed colors we use the strength of the Balmer and D4000 breaks (e.g., Bica et al. 1994), redshifted to near-infrared (NIR) wavelengths for $2.5 \lesssim z \lesssim 4.5$. The Balmer break at $\lambda_{\rm rest} = 3646$ Å is due to the absorption by Balmer series down to the Balmer limit (strongest in A-type stars). The so-called D4000 break at 4000 Å is mostly produced by H and K absorption lines of calcium at $\lambda_{\rm rest} = 3968$ Å and $\lambda_{\rm rest} = 3933$ Å respectively, characteristic of solar-type stars, along with several metallic absorption lines. Both discontinuities can be used to select galaxies which ceased star formation (post-starburst, quiescent passive) since their breaks are much more prominent than in star forming galaxies.

D.2.1 Color predictions with evolutionary tracks

To identify the locus populated by high-z passive galaxies on a color-color diagram we used evolutionary tracks derived with stellar population synthesis (SPS) models. Some previous work on color selection determination (e.g., Mawatari et al. 2016; Nayyeri et al. 2014; Wang et al. 2016; Wiklind et al. 2008) adopts a fixed age for the stellar populations and follows their color evolution with redshift. In our work, we decided to follow a more physically-motivated approach, letting colors evolve also with age after having fixed a formation redshift in order to avoid ages larger than the age of the universe at the considered redshift. Therefore, in our approach we have to consider several values of formation redshift to explore the whole parameter space of the evolutionary tracks, as done in Appendix D.9.7.

To parametrize quiescent objects, we computed color tracks from BC03 (Bruzual & Charlot, 2003) models, adopting a Chabrier IMF (Chabrier, 2003), solar metallicity ($Z = Z_{\odot} = 0.02$), and exponentially declining star formation histories with different e-folding times τ. Star-forming galaxies are generally assumed to be reproduced by a constant star formation template: we built evolutionary tracks of this galaxy template using the code *fsps* (Conroy et al., 2009, 2010), including the contribution of nebular emission lines that are evaluated with the results of Byler et al. (2017) based on CLOUDY (Ferland et al., 2013). Among the free parameters available in the model, we chose to adopt the Chabrier IMF, Padova's stellar isochrones, and BaSeL libraries for better consistency with BC03 models. We considered the aging of both the star-forming and the quiescent templates. Therefore, a redshift of formation must be fixed when computing the color tracks as a function of redshift, and we

chose as our reference $z_{\rm form} = 6$. We also allowed for different values of dust extinction A_V applied through the Calzetti's attenuation law (Calzetti et al., 2000).

We tested the robustness of the selection criteria against different choices of parameters for extinction laws, initial mass functions (IMFs), star formation histories (SFHs), metallicities, stellar population synthesis (SPS) models (e.g., Maraston 2005, hereafter M05), redshift of formation, and also considering whether the inclusion (or not) of emission lines changes the selection criteria in Appendix D.9.

We systematically looked for optimal selections using near- and mid-infrared observed colors. It is indeed necessary to use red bands and/or near/mid-infrared bands for three main reasons: first, because quiescent galaxies are characterized by intrinsically red SEDs; second, because the effect of redshift and k-correction makes these objects almost undetected in optical blue bands due to their faint UV emission; and finally, because at $z > 3$, the radiation blue-ward the Lyman-limit is largely suppressed by the inter-galactic medium (IGM) absorption and, therefore, all the galaxies start to become suppressed in the u filter (Guhathakurta et al., 1990; Steidel et al., 1999, 1996). In particular, we used the photometry in the bands i, z, Y, J, H, $K_{\rm s}$, IRAC[3.6] and IRAC[4.5], with transmission curves of the instruments which have observed the COSMOS field[1], and whose characteristics are listed in Table D.1.

Based on the vast exploration of possible colors, we selected two criteria that perform well in selecting quiescent objects at $2.5 \lesssim z \lesssim 4.5$. We stress that the purpose of this work is to be as inclusive as possible: we decided to maximize the completeness of the quiescent galaxies selection by including objects that can be missed by other criteria. The consequence of this choice will be the lower purity of the sample; contamination from other types of objects will have to be removed with the aid of an SED fitting.

D.2.2 $JK_s[3.6][4.5]$ selection

We designed the color selection using the observed colors $J - K_{\rm s}$ and IRAC$[3.6]$ − IRAC$[4.5]$ (hereafter $[3.6] - [4.5]$) to select quiescent galaxies in the redshift range $z \approx 2 - 4$. At $z \approx 2$ the Balmer break is redshifted at $\lambda \approx 1.09\,\mu$m, while for $z \approx 4$ to $\lambda \approx 1.82\,\mu$m; the D4000 break is redshifted at $\lambda \approx 1.2\,\mu$m at $z \approx 2$ and at $\lambda \approx 2.0\,\mu$m at $z \approx 4$. The color $J - K_{\rm s}$ can therefore identify the breaks, while the color $[3.6] - [4.5]$ has been chosen since it best complements the other color to avoid overlaps between different tracks.

In the top panels of Fig. D.1, two SEDs of quiescent galaxies at fixed ages and redshifted to different z with no dust extinction are shown to illustrate the location of the D4000 and Balmer breaks for the objects of interest with respect to the used filters. The cyan line shows a SED of a quiescent galaxy of 0.5 Gyr redshifted to $z = 4$ while the magenta line shows a SED of a quiescent galaxy of 1

[1] Transmission curves, including filter, optics, mirror, atmosphere, and detector are taken from http://cosmos.astro.caltech.edu/page/filterset

Table D.1 List of filters used in this work and their main characteristics. The last two columns represent the median limiting magnitude with a $3''$ diameter aperture and a depth of 2σ, i.e., $S/N = 2$ and 3σ, i.e., $S/N = 3$, respectively.

Filter	$\lambda_{\rm eff}$ (Å)	$\Delta\lambda$ (Å)	$2\sigma(3'')$	$3\sigma(3'')$
$u_{\rm CFHT}$	3823.3	670	27.8	26.6
$B_{\rm Subaru}$	4458.3	946	27.8	27.0
$V_{\rm Subaru}$	5477.8	955	26.9	26.2
$r_{\rm Subaru}$	6288.7	1382	26.7	26.5
$i^{+}_{\rm Subaru}$	7683.9	1497	26.5	26.2
$z^{++}_{\rm Subaru}$	9105.7	1370	26.0	25.9
$Y_{\rm VISTA}$	10214.2	970	25.5	25.3
$J_{\rm VISTA}$	12534.6	1720	25.2	24.9
$H_{\rm VISTA}$	16453.4	2900	24.8	24.6
$K_{\rm s,VISTA}$	21539.9	3090	24.8	24.7
IRAC[3.6]	35634.3	7460	26.3	25.5
IRAC[4.5]	45110.1	10110	26.0	25.5

Gyr at $z = 3$. Filter transmission curves are also shown in order to indicate the location of the Balmer and D4000 breaks with respect to the chosen colors.

We identified the following criteria to select quiescent galaxies in the redshift range $z = 2-4$ and limit the contamination from star-forming galaxies:

$$\begin{cases} ([3.6]-[4.5]) \geq 0 \\ (J-K_{\rm s}) \geq 0.975([3.6]-[4.5])+1.92 \text{ for } [3.6]-[4.5] < 0.4 \\ (J-K_{\rm s}) \geq 9.0([3.6]-[4.5])-1.33 \text{ for } [3.6]-[4.5] \geq 0.4 \end{cases} \tag{D.1}$$

which correspond to the gray shaded area in the left panel of Fig. D.1. In the same panel, we show the color-color diagram and different evolutionary tracks built as described in the previous section. More precisely, we show three different tracks parametrizing quiescent galaxies with different extinction values. In particular, magenta tracks show a track with $A_V = 0$, orange a track with $A_V = 1$ and the red a track with $A_V = 2$. The choice of $A_V = 2$ is an extreme case: in fact, we do not expect to find any quiescent candidate with such high extinction value. However, in order to be as inclusive as possible, we do not exclude the region covered by this track. High-extinction star-forming galaxies can, in principle, contaminate the sample, but even though the black track in Fig. D.1, which reproduces the color evolution of a galaxy with constant star formation history and $A_V = 5$, falls within the selection region, these interlopers are at lower redshift ($z \lesssim 2$) and can be removed from the sample once SED fitting is performed.

D.2.3 $HK_s[3.6]$ selection

This color selection is designed to identify quiescent galaxies at slightly higher redshift with respect to the previous color selection, that is, in the range $z = 3-4.5$, using filters H, K_s and IRAC $3.6\,\mu$m. From $z \approx 3$ to $z \approx 4.5$, both the Balmer and the D4000 break are located in the wavelength range bracketed by H and K_s filters (from $\lambda = 1.64\,\mu$m to $\lambda = 2.15\,\mu$m). Since the D4000 and Balmer breaks develop on different timescales, the color $H - K_s$ can be used to select quiescent galaxies for broad ranges of age. In the top-right panel of Fig. D.1, two SEDs of quiescent galaxies at fixed ages and redshifted to different z are shown to illustrate the location of the breaks with respect to the filters used.

In the bottom-right panel of Fig. D.1, we show the color-color diagram and different evolutionary tracks built as described in the previous section. As for the previous color selection, the color $K_s - [3.6]$ has been chosen in order to best complement the information of the other color.

To select quiescent galaxies in the redshift range $z = 3-4.5$, and to exclude most star-forming galaxies, we designed the following selection criteria:

$$\begin{cases} K_s - [3.6] \geq 0.2 \\ H - K_s \geq 0.617(K_s - [3.6]) + 0.58 \end{cases} \tag{D.2}$$

which correspond to the gray shaded area in the right panel of Fig. D.1. Star-forming galaxies may enter the color selection region for extreme values of extinction ($A_V \gtrsim 5$) at lower redshift: the contamination by dusty and star-forming galaxies cannot be completely excluded, but they can be removed with the SED fitting analysis.

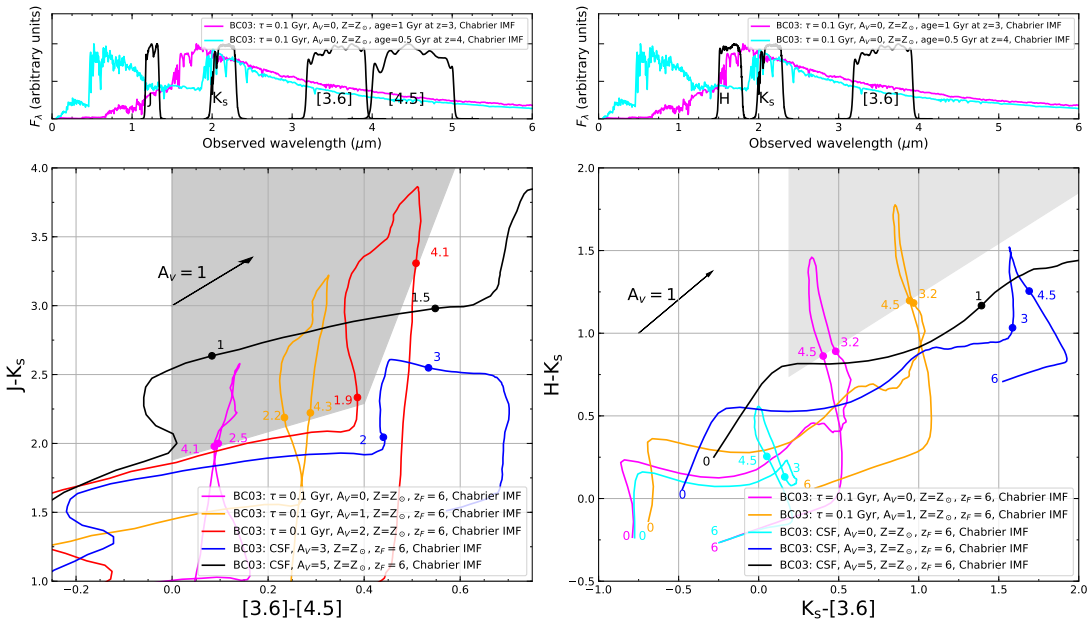

Fig. D.1 Top panels: two SEDs of quiescent galaxies. SED in magenta represents a population of 1 Gyr redshifted to $z = 3$ (i.e., $z_{\rm form} \approx 6$), while the cyan line shows the SED of a population of 0.5 Gyr redshifted to $z = 4$ (i.e., again $z_{\rm form} \approx 6$). Filters transmission curves used in COSMOS field and in the tracks evaluations are also shown. **Bottom panels:** the $JK_{\rm s}[3.6][4.5]$ and $HK_{\rm s}[3.6]$ color-color diagrams with different evolutionary tracks both for star-forming galaxies and passive galaxies. Tracks representing star-forming galaxies are shown in cyan, blue and black with $A_V = 0$, $A_V = 3$, and $A_V = 5$ respectively. Three tracks for quiescent galaxies (with exponentially declining star formation history $\tau = 0.1$ Gyr and solar metallicity) are shown in magenta, orange and red with different extinction values ($A_V = 0$, $A_V = 1$, and $A_V = 2$ respectively). Gray shaded areas represent the selection region for quiescent galaxies at $2.5 \lesssim z \lesssim 4$ in the left panel and at $3 \lesssim z \lesssim 4.5$ in the right panel. The numbers near the tracks of the same color represent the redshift. A vector corresponding to a magnitude extinction of $A_V = 1$ using Calzetti's law is also shown.

D.3 Application to real data

We applied the proposed color-color diagrams to real data. To this aim, we used the multi-waveband deep photometric observations available in the COSMOS field (Scoville et al., 2007).

D.3.1 The COSMOS2015 catalog and colors

We used the COSMOS2015 catalog (Laigle et al., 2016), which is the latest public release of data in the COSMOS field. This catalog provides the deepest optical and infrared observations of the field and the photometry has been obtained using a detection image evaluated by combining NIR images of UltraVISTA ($YJHK_{\rm s}$) with the optical z^{++}-band data from Subaru. Since deep optical and IR data are especially important for the purpose of this paper, the characteristics of the catalog are particularly suitable for our work. In COSMOS2015, optical and NIR photometric data are provided in different

apertures: $2''$, $3''$ (denoted APER2 and APER3 respectively), ISO (isophotal), and AUTO apertures. AUTO apertures are object to object variable apertures, automatically evaluated by SExtractor (Bertin & Arnouts, 1996) in order to approximately measure the total flux of the object. IRAC data are instead provided only as total magnitudes and fluxes.

In the color-color diagrams presented in Sects. D.2.3 and D.2.2, we combine NIR and IRAC data and, therefore, total magnitudes are needed for all the filters. Following Laigle et al. 2016, instead of using AUTO magnitudes in NIR filters, we rescaled APER3 magnitudes to reproduce the total flux normalization for each object since these aperture magnitudes provide better results in SED fitting for photometric redshifts. We computed total magnitudes in optical and NIR bands following the prescriptions in Eqs. 9 and 10 of Laigle et al. 2016. In particular, we applied to each object a photometric offset that normalizes the aperture magnitudes to the total ones, preserving the colors that have been better determined in aperture photometry. We also corrected magnitudes for foreground galactic extinction using the values given in the catalog, which are computed at each object position using the Schlegel et al. (1998) dust maps. Finally, we applied corrections to both NIR and IRAC magnitudes using the small systematic offsets given in the catalog, estimated by matching the predicted magnitudes and the observed ones using the spectroscopic sample.

A census of the photometric bands adopted in this paper and the depth of observations at 2σ and 3σ are presented in Table D.1. The 3σ values are provided in Laigle et al. (2016), while 2σ, that will be used in the following, have been evaluated as the magnitude of objects with photometric error $\Delta m \sim 0.54$ (corresponding to $S/N = 2$).

D.3.2 Parent sample

In this work we focus on massive galaxies and in order to build a mass-selected sample, we used as a proxy NIR apparent magnitudes in filter IRAC[4.5]. In fact, since stars with small masses ($M \lesssim 1$ $M_\odot$), which make up the bulk of the mass of a galaxy, mostly emit in the redder part of the spectrum, a selection in NIR magnitudes roughly corresponds to a selection in stellar mass. Moreover, as shown e.g., in Bell & de Jong (2001), the stellar mass-to-light ratios in the rest-frame NIR bands vary only by a factor of 2 or less over a wide range of star-forming histories, in contrast with a factor of 10 in blue bands. This means that the luminosity of a galaxy in the NIR is a good tracer of its stellar mass.

Using population synthesis models, we derived the relations between stellar mass and magnitudes in filter IRAC[4.5] as a function of redshift: at $z = 3$ the expected magnitude of a passive galaxy with mass $M = 10^{10.6} M_\odot$ is $m_{[4.5]} \simeq 22.3$, that is, passive galaxies brighter than this limit should be characterized by stellar masses larger than $10^{10.6} M_\odot$. The same type of object with the same stellar mass can be observed with a magnitude of $m_{[4.5]} \simeq 22.6$ at $z = 4$ and $m_{[4.5]} \simeq 22.3$ at $z = 5$. Assuming a different formation redshift $z_{\rm form} = 8$, the expected magnitude of a passive galaxy with $M = 10^{10.6} M_\odot$ at $z = 3$ is $m_{[4.5]} \simeq 22.4$, while considering models with low metallicity ($Z = 0.008$) or a longer timescale of star formation ($\tau = 0.3$ Gyr), the corresponding magnitude is $m_{[4.5]} \simeq 22.2$.

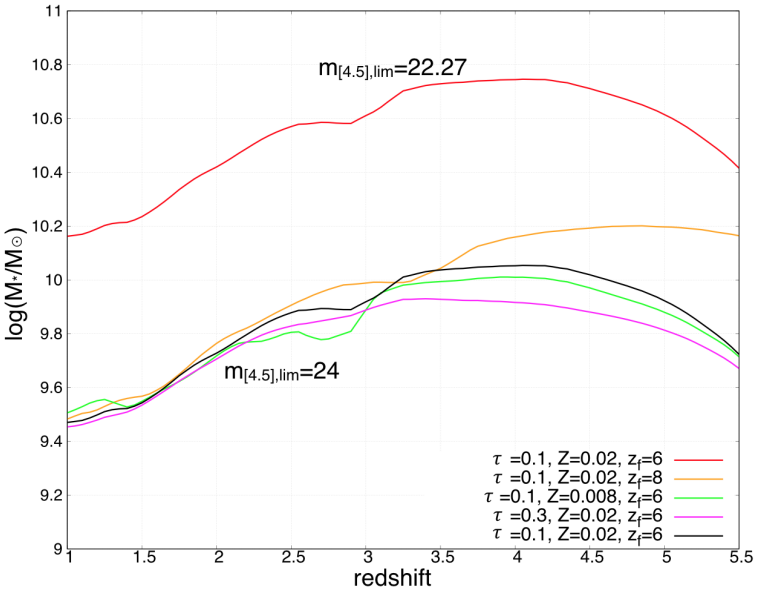

Fig. D.2 Stellar mass as a function of redshift for different theoretical parametrizations of quiescent galaxies: we adopted an exponentially declining star formation history with characteristic time $\tau = 0.1\,\mathrm{Gyr}$, $Z = Z_\odot = 0.02$, $A_V = 0$, $z_{\mathrm{form}} = 6$. Red and black lines correspond to magnitudes $m_{[4.5]} = 22.27$ and 24, respectively. Orange, green, and magenta lines represent different models of a quiescent galaxy differing in redshift of formation, metallicity, and e-folding time of the SFH, respectively.

Based on previous considerations, we first defined and selected a parent sample with a cut at $m_{[4.5]} \leq 24$ to guarantee both the sensitivity to stellar masses $\log(M/M_\odot) \gtrsim 10$ for quiescent galaxies and reliable photometry. In terms of the signal-to-noise ratio, this magnitude limit ensures that more than 99% of the considered data have an $S/N > 3$ (also see Table D.1). Moreover, we considered only sources with $S/N \geq 3$ (i.e., $\Delta m \leq 0.36$) at $4.5\,\mu$m. Spectroscopically confirmed stars and active galactic nuclei (AGN), for a total of 743 objects, have also been removed.

All the above selections were performed inside the region with the best quality photometry: FLAG_PETER, which defines good optical areas, that is, masking regions where bright stars may contaminate the photometry of nearby objects, while FLAG_COSMOS and FLAG_HJMCC define the area in COSMOS field covered by UltraVISTA. UltraVISTA data are primarily important in this work as they are the basis of our selections. The final sky area considered after applying the cited flags is $1.38\,\mathrm{deg}^2$.

The parent sample is then composed of 212 897 objects (out of the 1 182 108 entries in the original COSMOS2015 catalog). The whole parent sample is shown in gray in Fig. D.3 in our color-color diagrams.

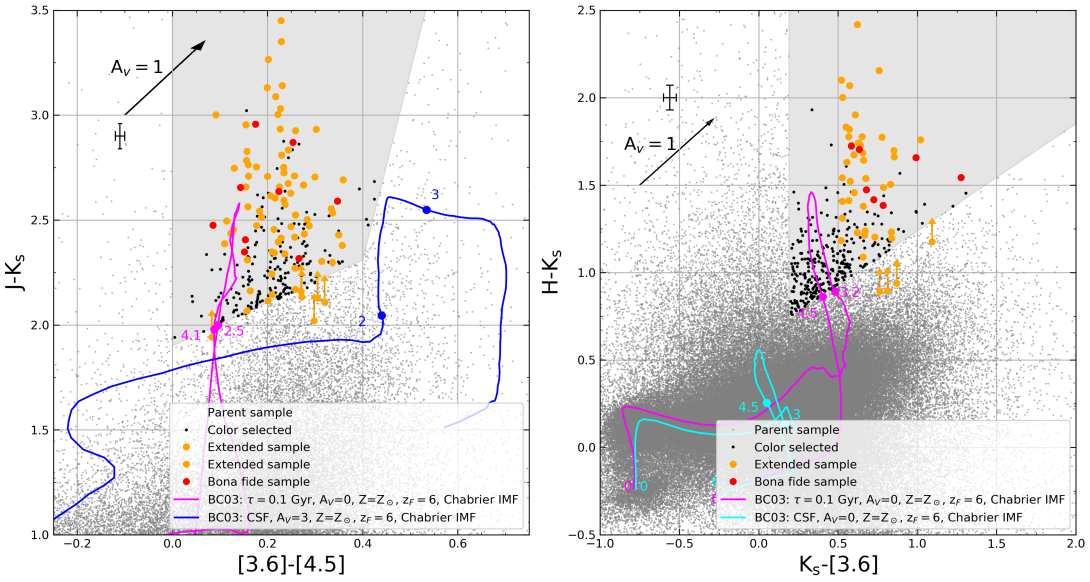

Fig. D.3 Observed color-color diagrams. Left: $JK_s[3.6][4.5]$. Right: $HK_s[3.6]$. Gray shaded areas represent the color selection regions defined in Sect.D.2 and the evolution of the colors of a quiescent and a star-forming galaxies are plotted as a reference. Gray points represent the whole parent sample selected as in Sect. D.3.2, black points show the color-selected-only quiescent candidate. Red points are "bona fide" objects, while orange points belong to the "extended" sample, both defined in Sect.D.4. The mean photometric errors of the color-selected candidates (black points) are also shown. Objects that are non-detected in one or more filters in the color-selected sample are not shown in order to improve clarity given their large number. Only undetected objects belonging to extended or bona fide samples are shown with arrows indicating the lower limits of the involved color. Non-detections correspond to $< 2\sigma$.

D.3.3 Photometric requirements

To select quiescent candidates through color-color diagrams, we impose the following photometric requirements:

1. We defined as the detection limit in each filter of interest a conservative value of $S/N = 2$, corresponding to a maximum photometric error of $\Delta m = 0.54$ magnitudes, in order to include in the color selection any possible quiescent candidate. In addition, we also considered galaxies non-detected (i.e., with $S/N < 2$) in some of the filters used in the diagrams; when a non-detection occured, the magnitude limit in that filter was considered from Table D.1 to derive a lower or upper limit of the color.

2. To minimize the fraction of lower redshift and star-forming objects, we removed from our sample those objects detected in the u band with $S/N > 2$; given our parent sample cut at $m_{[4.5]} \leq 24$, this choice corresponds to removing from the sample those objects with blue $u - m_{[4.5]}$ colors, which are characteristic only of star-forming galaxies or very-low-redshift quiescent galaxies.

3. We imposed a non-detection condition at $24\,\mu$m measured by MIPS (Multiband Imaging Photometer on Spitzer) to minimize the fraction of dusty star-forming galaxies that would significantly emit at $24\,\mu$m because of the dust re-emission; a detection limit of $S/N = 2$ was chosen.

D.3.4 Candidates identification through color selections

Candidates are identified from the parent sample using color-color diagrams defined in Sect. D.2. As mentioned above, we also include in the selection extremely faint quiescent objects that may not be detected in some of the filters involved in the diagram. Moreover, sources which satisfy the selection criteria but do not meet the u and/or the $24\,\mu$m non-detection conditions were removed from the sample (a total of 182743 objects in the parent sample were rejected due to these cuts).

A total of 1047 objects (0.49% of parent sample) were selected using at least one of the two criteria (183 objects were selected by both color selections simultaneously. See Table D.2 for details). In Fig. D.3, we show these candidates as black dots, together with two evolutionary tracks for comparison with previous plots. Objects that are non-detected in one or more filters in the color-selected sample are not shown for the purposes of clarity given their large number. We notice that a large number of objects is located just below the selection boxes: the color errors will therefore result in a larger number of objects scattered upwards into the selection box than downwards, producing an overestimate of the number of selected objects. This bias and the other possible sources of contamination are the object of the SED fitting refinement illustrated in Sect. D.4.

Figure D.4 illustrates the properties of the selected objects in gray: the redshift distribution of the selected sample peaks at $z_{\rm phot} \approx 3.5$ and appears to be bimodal, as a result of the combination of the two adopted color diagrams. A non-negligible fraction of objects exhibits photometric redshifts in the range $2 < z_{\rm phot} < 2.5$: a contamination by non-quiescent and/or $z < 2.5$ objects was expected. In fact, the chosen color selections (with generous selection boxes), the parent sample (with a deep cut at 24 magnitudes at $4.5\,\mu$m), and the photometric requirements (with an undetection requirement at 2σ in u and $24\,\mu$m bands) have been designed in order to include any possible quiescent candidate, given their rareness at $z \geq 2.5$. We also expect a certain degree of contamination by star-forming galaxies with prominent emission lines. With the aid of the full photometric data, the SED fitting procedure is expected to be able to identify the truly quiescent objects at the highest redshifts and remove the interlopers belonging to different redshift ranges or galaxy types.

D.4 SED fitting and physical properties

The SED fitting analysis of the selected objects allows us to select the most massive ($\log(M_*/M_\odot) > 10.6$) high redshift ($z \gtrsim 2.5-3$) quiescent galaxies, hereafter defined as galaxies characterized by $\log({\rm sSFR}\,[{\rm yr}^{-1}]) < -10.5$, where sSFR is the specific star formation rate (${\rm sSFR} = {\rm SFR}/M_*$). Since there are no spectroscopic redshifts measured for the candidates selected in the previous section, to

evaluate the physical properties of the candidates we assumed the photometric redshifts that have been carefully optimized by Laigle et al. (2016) in the COSMOS2015 catalog. We then carried out the SED fitting to estimate physical properties, such as the stellar mass, extinction, age, and specific star formation rate (sSFR). The exploration of the parameter space has not been designed to consider all the possible SEDs, but only to break the degeneracy between the two specific galaxy populations we expect from the color-color selection, that is, high-redshift quiescent objects and dusty star-forming contaminants.

We used the hyperzmass code (Bolzonella et al., 2010, 2000) to evaluate the best fit SED, corresponding to the minimum χ^2 derived from the comparison between observed and model photometry at fixed $z = z_{\rm phot}$ from COSMOS2015. From the best fit SED we derive the stellar mass, star formation rate, age, and extinction. In the following we describe the relevant parameters of the fitting procedure, which makes use of the input photometric catalog including the information of photometric redshift.

To avoid degeneracies between similarly probable solutions, we tailored the set of templates considering only the two populations we expected to be included in our selection. We used two evolving templates with solar metallicity and Chabrier IMF: an exponentially declining star formation history built with BC03 SPS, with timescale of 0.1 Gyr, representing a quiescent galaxy, and a template with constant star formation including emission lines, built with *fsps* (Conroy et al., 2009, 2010), appropriate for star-forming galaxies. Each template contains 221 spectra for evolving ages from $t = 0$ to $t = 20$ Gyr. No formation redshift was imposed but only ages smaller than the age of the universe at the photometric redshift were considered. Other population synthesis models are available from the literature (e.g., Maraston 2005, hereafter M05); different choices could lead to variation in the stellar masses of $0.10 - 0.15$ dex depending on the considered SPS model (e.g., Ilbert et al. 2013; Walcher et al. 2011). For consistency and continuity with previous works (e.g., Davidzon et al. 2017; Ilbert et al. 2013; Laigle et al. 2016; Muzzin et al. 2013), BC03+fsps models were adopted as reference templates here.

Moreover, we performed several SED-fitting runs using different extinction laws: in particular, those of Calzetti et al. (2000), which are characteristic of starburst galaxies, Fitzpatrick (1986) for the Large Magellanic Cloud, and Seaton (1979) for the Milky Way (see Sect. D.9.2 for the expected differences in the color selection). We chose as our reference the results obtained using the law of Calzetti et al. (2000). We set the range of extinction between $A_V = 0.0$ and $A_V = 5.0$ both for the τ model and for star forming galaxies. Although high values of extinction are not expected in quiescent galaxies, we let the parameter assume all the values in the range to avoid any bias on the age, and consequently, on the stellar mass because of the well-known degeneracy among these parameters (e.g., Papovich et al., 2001). As a result of making this choice, we expected to select galaxies that would be more consistent with being quiescent than dusty star-forming.

The filters used for the fit are u, B, V, r, i^+, z^{++},Y, J, H, $K_{\rm s}$, IRAC[3.6] and IRAC[4.5]. The fluxes in the IRAC[5.8] and IRAC[8.0] bands have not been included in the final fit because of the shallower depth and worse PSF (point spread function) of these bands, which makes them much less suitable for constraining the SED shape. The filters used in the fit sample the optical/NIR wavelengths

well enough even at the high redshifts considered in this work, so that the stellar mass can still be reliably determined (see e.g., Conroy, 2013; Mitchell et al., 2013; Pacifici et al., 2012; Taylor et al., 2011). To avoid the problem of dealing with non-detections that should require a statistical treatment as in Sawicki (2012), we directly used fluxes (corrected to total) with their face values and errors. In this way, the χ^2 can be estimated also for very small or negative values of the measured fluxes, as explained in Laigle et al. (2016), and the number of data points used to constrain the fit is always ≥ 9.

Moreover, the intergalactic medium average opacity of intervening systems along the line of sight of high redshift objects has been taken into account following Madau (1995).

D.4.1 Results of SED fitting procedure

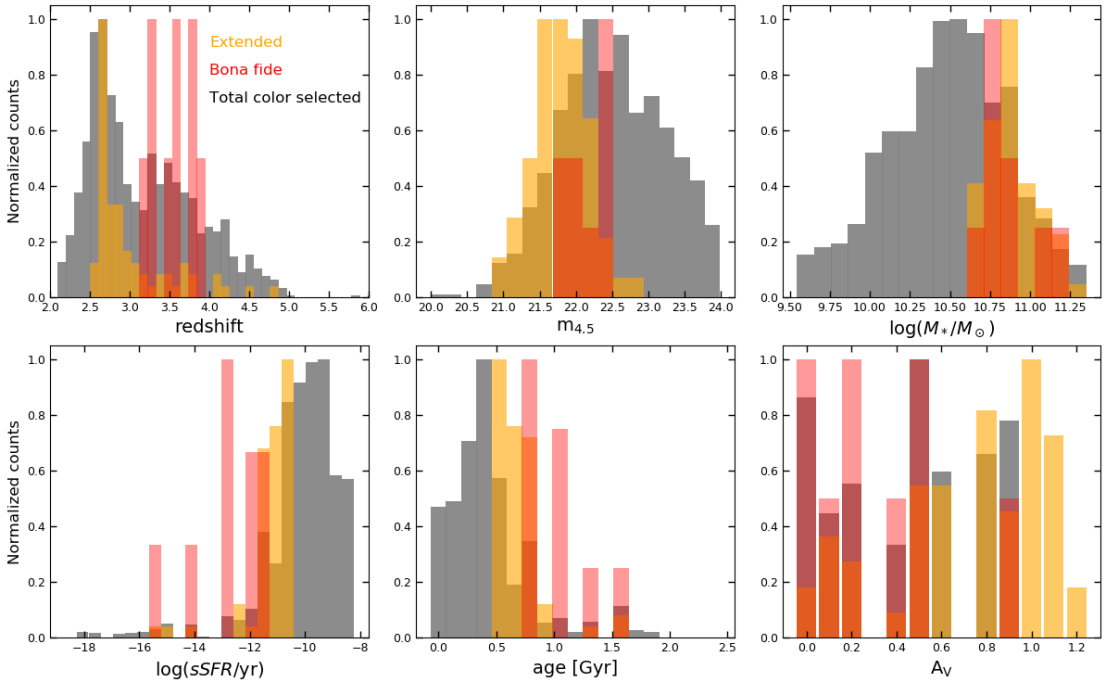

Fig. D.4 Distribution of physical properties of the color selected sample (gray) of the extended (orange) and bona fide (red) sub-samples.

We divided our color-selected sample in two classes (the extended and the bona fide samples), following the results of the SED fitting.

The extended sample is defined to have $z_{\rm phot} \geq 2.5$, $\log(M_*/M_\odot) \geq 10.6$, $\log({\rm sSFR}\,[{\rm yr}^{-1}]) \leq -10.5$ and the reduced χ^2 of the best fit with the model of quiescent galaxies smaller than the one using the model with constant star formation ($\chi^2_{\rm q} < \chi^2_{\rm sf}$).

The bona fide sample, characterized by more restrictive criteria, i.e., $z_{\rm phot} \geq 3.0$, $\log(M_*/M_\odot) \geq 10.6$, $\log({\rm sSFR}\,[{\rm yr}^{-1}]) \leq -11$, $\chi^2_{\rm sf} - \chi^2_{\rm q} > 2$, and $\chi^2_{\rm q} < 2$.

In particular, we choose the stellar mass cut at $\log(M_*/M_\odot) \geq 10.6$ in order to guarantee the completeness of our samples and facilitate the comparison with results and mass functions that have

previously been published in the literature. We present the results of all the selections in Table D.2. The total number of objects in the bona fide sample is nine. The extended sample is made up of 128 objects. By using the different extinction laws mentioned in the previous section (i.e., Fitzpatrick 1986; Seaton 1979), we obtain almost identical results. In further detail, we find that eight objects of the bona fide sample were selected independently from the extinction law adopted in the fit, while the object left out from our reference sample is the one with the largest amount of dust ($A_V = 0.9$) in Fig. D.4. This object is fitted with a value of $A_V = 1.0$ by Fitzpatrick and Seaton extinction laws, but is excluded from the bona fide sample due to the higher sSFR ($\log(\mathrm{sSFR}\,[\mathrm{yr}^{-1}]) \approx -10.9$ both for Fitzpatrck and Seaton laws). Also, the extended sample shows little variation compared to our reference results derived using Calzetti et al. (2000) extinction law: we select 131 objects assuming Fitzpatrick?s law, and 137 with Seaton?s law. In the color-color diagrams illustrated in Fig. D.3, together with the parent sample in gray and candidates selected in Sect. D.3.3 in black, we show the bona fide and extended samples with red and orange points, respectively. Red and orange points below the selection regions correspond to objects that are non-detected in one filter (H or J): they have been fully considered in the samples as their color is consistent with the selection criteria when considering it as a lower limit.

We present in Fig. D.5, the SED fitting results for all the galaxies in the *bona fide* sample, showing both the best-fit quiescent template, and the best-fit using only the star-forming template. The star-forming model at the same redshift is not able to reproduce the break strength located between the bands H and K_s, nor the faint fluxes at blue/near UV rest frame wavelengths. Similar results for the fit with the two classes of SEDs are valid for all the other objects: on one side, the inclusion of emission lines is not sufficient to mimic the D4000 break, while on the other, the fluxes blue-ward of the break are too high despite the large values allowed for dust extinction.

Figure D.4 summarizes the main physical properties of the extended and bona fide samples derived through the SED fitting analysis, taking as a reference fit the one using Calzetti's extinction law. In particular, the bona fide sample is shown in red while the extended sample is in orange. The properties shown are the photometric redshift and the observed magnitude at 4.5 μm from the COSMOS2015 catalog, the stellar mass, the sSFR, the age, and the dust extinction from the SED fitting analysis. Many of the extended sample objects are located at $2.5 \lesssim z \lesssim 3.0$, whereas for the bona fide sample, the median redshift is $z \approx 3.38$. Compared to the total sample selected in Sect. D.3.3 (shown in gray), the distributions of $m_{[4.5]}$ peak at brighter magnitudes. The other panels of the figure show how the *bona fide* and *extended* samples represent the most massive and quiescent galaxies chosen through color selections. We notice that three galaxies of the *bona fide* sample have best fit with $0.5 \leq A_V \leq 0.9$, which are extinction values approaching those of Lyman-break galaxies at the same redshifts (Shapley et al., 2005). However, recent works (Gobat et al., 2018; Martis et al., 2019) claim that quiescent galaxies at high redshifts ($1 < z < 4$) can contain at least two orders of magnitude more dust at a fixed stellar mass compared with local early-type galaxies (ETGs). They found that these dusty ($A_V \geq 1.0$) high-z quiescent galaxies can comprise up to $\sim 20-25\%$ of the population of quiescent galaxies, which is consistent with our findings. Moreover, we stress that the results we

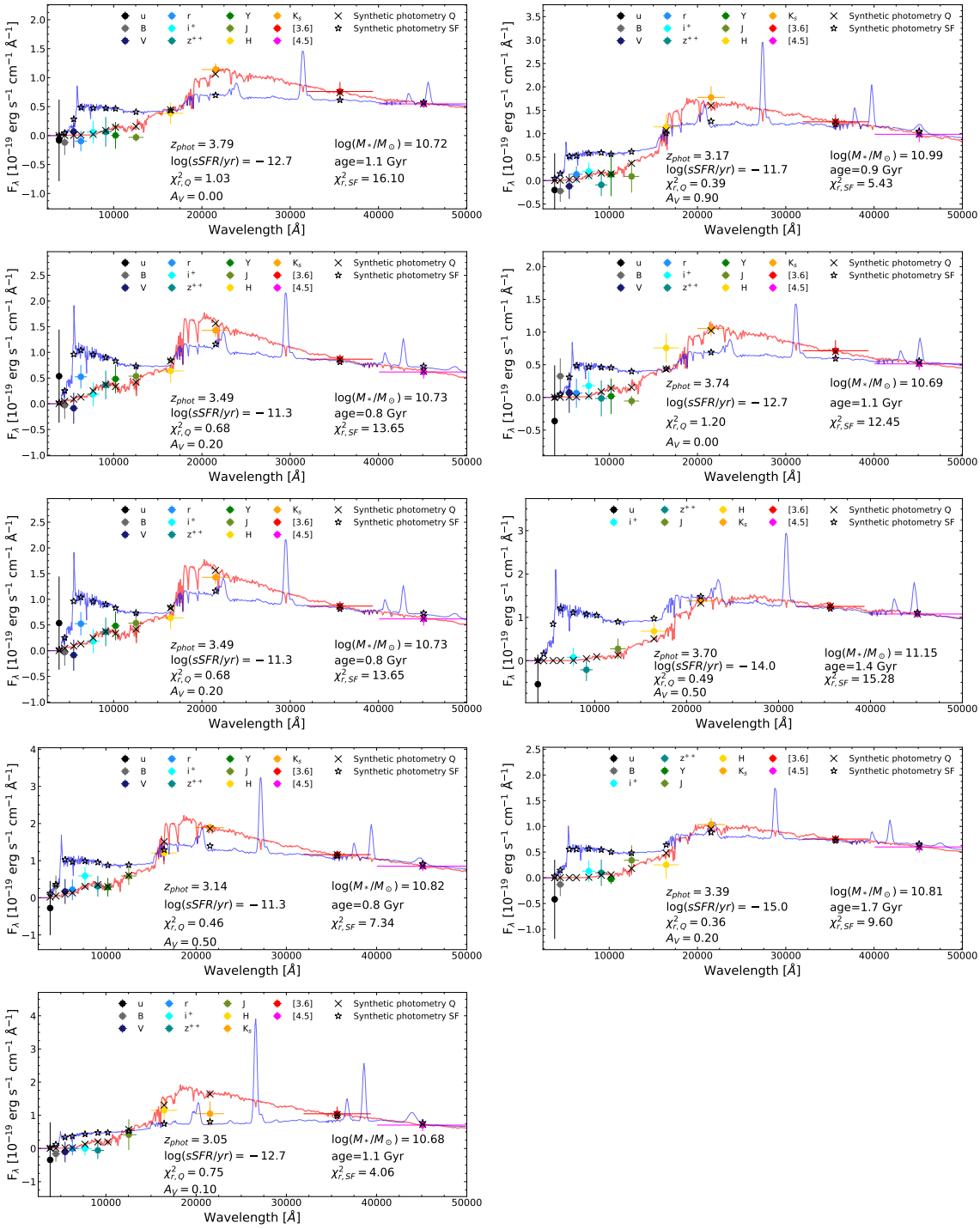

Fig. D.5 Best-fit models for all bona fide objects: colored points represent photometric points with error-bars, red lines are best-fit SEDs. The best fit using the star-forming template is shown with a blue line. Error bars in the wavelength scale refer to the width of the considered filter. Physical parameters evaluated through the SED fitting are shown in inserted labels. Black tilted crosses and stars show the synthetic photometry, evaluated by integrating the best-fit templates in the several bands, for the best-fit quiescent and star-forming templates respectively. All filters used in the fit are listed in inserted legends for each plot.

find are dependent on the population synthesis model we adopt. In fact, if we adopt a different SPS model (e.g., Maraston 2005), the best-fit A_V value may change, along with other physical parameters degenerate with dust extinction, such as the age of the galaxy. We explore this possibility, using the SPS model of Maraston 2005 in the following Section.

Out of our 128 quiescent candidates (extended sample) we find that 98 of them are also classified as quiescent in the COSMOS2015 catalog, where quiescent galaxies are identified using the locations of galaxies in the color?color plane NUV $-$ r/$r-J$ (Williams et al., 2009).

M05 vs BC03 models

We derive the best-fit physical parameters also using M05 models (Maraston, 2005) to evaluate the robustness of our selections. The two models (i.e., BC03 and M05) differ in the treatment of the thermally-pulsing asymptotic giant branch (TP-AGB) phase. The contribution of the TP-AGB stars to the integrated light of a synthetic stellar population critically depends on what is adopted for the stellar mass loss during this phase. The higher the mass loss, the sooner the star loses its envelope and the sooner the TP-AGB phase is terminated. In M05 the TP-AGB phase contribution is much higher than in BC03 models. The result is that the M05 models are brighter and redder than the BC03 models for ages between ~ 0.2 and ~ 2 Gyr at $\lambda > 2-2.5\,\mu$m (Maraston et al., 2006). This implies that the M05 models give, in general, younger ages and lower stellar masses compared to BC03 models. At older ages, this tendency is reversed.

In order to perform a fair comparison we apply the same criteria used to define the bona fide and extended samples described at the beginning of the section. While we adopt for BC03 models a Chabrier IMF for consistency and continuity with other works in the literature (e.g., Davidzon et al. 2017; Ilbert et al. 2013; Laigle et al. 2016; Muzzin et al. 2013), for M05 models, a Chabrier IMF is not available, so we adopt a Kroupa IMF (Kroupa, 2001) and apply a statistical offset to stellar masses, such as $\log M_{*,\mathrm{Chabrier}} = \log M_{*,\mathrm{Kroupa}} - 0.04$, to take into account the different IMF. All other parameters are consistent between the two models. Moreover, for the M05 SED fitting run we also adopted the star-forming template that includes emission lines built with *fsps*.

Using M05 models to fit the data, 20% fewer objects are included in the bona fide sample with respect to BC03 results (i.e., eight objects are selected in the M05 bona fide sample), while $\approx 33\%$ fewer objects are included in the extended sample. The case of having different numbers of objects is expected since M05 models predict for ages between ~ 0.2 and ~ 2 Gyr (i.e., the typical ages for galaxies at $z \gtrsim 3$) a higher flux per unit mass with respect to BC03 models (Maraston et al., 2006) at $\lambda \gtrsim 2\,\mu$m, due to a higher contribution from stars in the TP-AGB phase. This reflects in a lower normalization needed for the theoretical SED to fit the observed data, and ultimately to a lower mass estimate. As a consequence, fewer objects satisfy the $\log(M_*/M_\odot) \geq 10.6$ condition.

To have a fair comparison between the number of objects selected with BC03 and M05 models, we compute the median offset of the mass estimation between BC03 and M05 models of the bona fide and extended samples. We find that the median value of $\log(M_{*,\mathrm{BC03}}/M_{*,\mathrm{M05}})$ is ≈ 0.24 when

considering the extended sample, which is larger than the value of 0.14 used by Henriques et al. (2015). However, the value adopted by Henriques et al. (2015) was derived by Domínguez Sánchez et al. (2011) and Pozzetti et al. (2010) for a mix of different galaxy populations, while the difference is expected to be larger for objects that quenched their star formation. Assuming a lower mass cut of $\log(M_*/M_\odot) \geq 10.6 - 0.24 = 10.36$, the total number of objects in bona fide and extended samples is more in agreement with the results obtained using BC03 models, which are, respectively, 8% smaller and 33% bigger than the BC03 results.

We also investigated the dependence of the derived age on the adopted model. If we leave the dust extinction free to change in the process of SED-fitting, then similar ages are obtained either with M05 or BC03 models (both for the extended and bona fide samples). However, the BC03 model predicts a mean extinction value of 0.81 mag for the extended sample and $\langle A_V \rangle = 0.31$ for the bona fide, while M05 models predict a mean extinction of 0.17 and 0.09 mag for the extended and bona fide samples, respectively. If, instead, we do not allow for dust extinction (i.e., we fix $A_V = 0$), the mean values of the ages predicted by the two models differ, with M05 models predicting ≈ 0.4 Gyr younger ages with respect to BC03 models. These results are in agreement with the work presented in Maraston et al. (2006), where similar conclusions are found for a sample of seven passive galaxies at $z > 2$ when dust extinction is forced to assume only very small values.

There is no consensus, yet, in the literature about which of the two models better represents high redshift galaxies, in other words, about the relative importance of the TP-AGB phase in high redshift objects. In fact, while, for example, Maraston et al. (2006) finds a better fit of high-z galaxies using M05 models, other studies, such as that of Kriek et al. (2010), find better fits using BC03 models. In this paper, we do not find any strong evidence in favor or against any of the two considered SPS models. In the following of this paper, we will use BC03 results to ease the comparison with previous work (e.g., Davidzon et al. 2017, Ilbert et al. 2013, Muzzin et al. 2013).

Table D.2 All objects selected through color selections and results of BC03 SED fitting, that is, both objects detected in all bands of interest (i.e., J,H,K_s,[3.6],[4.5]) and also objects with one or more non-detections in bands of interest.

Number of objects in parent sample	Color selection	Number of objects color selected with $m_{4.5} \leq 24$	Number of objects color selected with $M_* > 10^{10.6}\,M_\odot$ $m_{4.5} \leq 24$ & $z_{\rm phot} \geq 2.5$	Number of objects in *extended* sample	Number of objects in *bona fide* sample
212897	HK_s[3.6]	768	160	43	7
	JK_s[3.6] [4.5]	462	263	95	9

D.5 Number and mass densities

Table D.3 Bona fide sample as selected by means of SED fitting with BC03 models: number and mass densities in different redshift bins. Errors include Poissonian errors, cosmic variance, and photometric redshift errors. Note: no objects in the bona fide sample are located at $z \geq 4$.

Δz	Number *bona fide*	z median	$\log(M_*/M_\odot)$ median	$\log(\rho_N)$ (Mpc^{-3})	$\log(\rho_*)$ ($M_\odot\,\mathrm{Mpc}^{-3}$)
$3.0 \leq z < 3.5$	5	3.17	10.81	$-6.044^{+0.173}_{-0.293}$	$4.614^{+0.172}_{-0.290}$
$3.5 \leq z < 4.0$	4	3.72	10.70	$-6.283^{+0.191}_{-0.351}$	$4.599^{+0.157}_{-0.249}$

Table D.4 Extended sample as selected by means of SED fitting with BC03 models: number and mass densities in different redshift bins. Errors include Poissonian errors, cosmic variance, and photometric redshift errors added in quadrature.

Δz	Number *extended*	z median	$\log(M_*/M_\odot)$ median	$\log(\rho_N)$ (Mpc^{-3})	$\log(\rho_*)$ ($M_\odot\,\mathrm{Mpc}^{-3}$)
$2.5 \leq z < 3.0$	98	2.60	10.81	$-4.924^{+0.080}_{-0.098}$	$5.949^{+0.077}_{-0.095}$
$3.0 \leq z < 3.5$	14	3.30	10.83	$-5.757^{+0.126}_{-0.178}$	$5.123^{+0.119}_{-0.164}$
$3.5 \leq z < 4.0$	9	3.62	10.76	$-5.930^{+0.148}_{-0.228}$	$4.843^{+0.147}_{-0.224}$
$z \geq 4.0$	7	4.03	10.82	$-6.018^{+0.164}_{-0.268}$	$4.912^{+0.144}_{-0.218}$

We use the results obtained in the previous section to estimate the number and stellar mass densities of quiescent galaxies at $z > 2.5$ and compare them to observations and state-of-the-art semi-analytical models. In Tables D.3 and D.4, the number and mass densities of the bona fide and extended samples are presented in redshift bins and shown in Fig. D.6. To evaluate the number and mass densities, we consider only massive galaxies with $M \geq 10^{10.6}\,M_\odot$, both for the extended sample (red diamonds) and for the bona fide sample (red squares).

The error bars we show in Fig. D.6 have been evaluated by adding in quadrature Gaussian errors for the object counting (we approximated Poissonian statistic with the Gaussian one given that for large counts, the two statistics match), cosmic variance, and the scatter between different redshift bins due to photometric redshift errors. To take into account cosmic variance, we follow the prescriptions of Moster et al. (2011). In particular, we choose the field size to be consistent with the COSMOS field we are considering, we impose the same mass cut we adopt (i.e., $\log(M_*/M_\odot) \geq 10.6$) and for each redshift bin we choose the median redshift of the objects grouped in that bin. We find that, for our mass range, the cosmic variance ranges from a value of $\sigma_{\mathrm{CV}} = 0.15$ at $2.5 \leq z < 3.0$ to $\sigma_{\mathrm{CV}} = 0.25$ from at $z \geq 4.0$. To take into account the scatter of objects between different redshift bins due to photometric errors, we checked how much the number of objects in the adopted bins can change by applying a noise of $\sigma_z \sim 0.03(1+z)$ to the redshift distribution of a sample selected with $m_{4.5} < 24$. We used the COSMOS catalog itself and a lightcone from H15 model to estimate the variation in the number of objects in high redshift bins, and we find that it is always less than $\sim 7\%$. We adopted

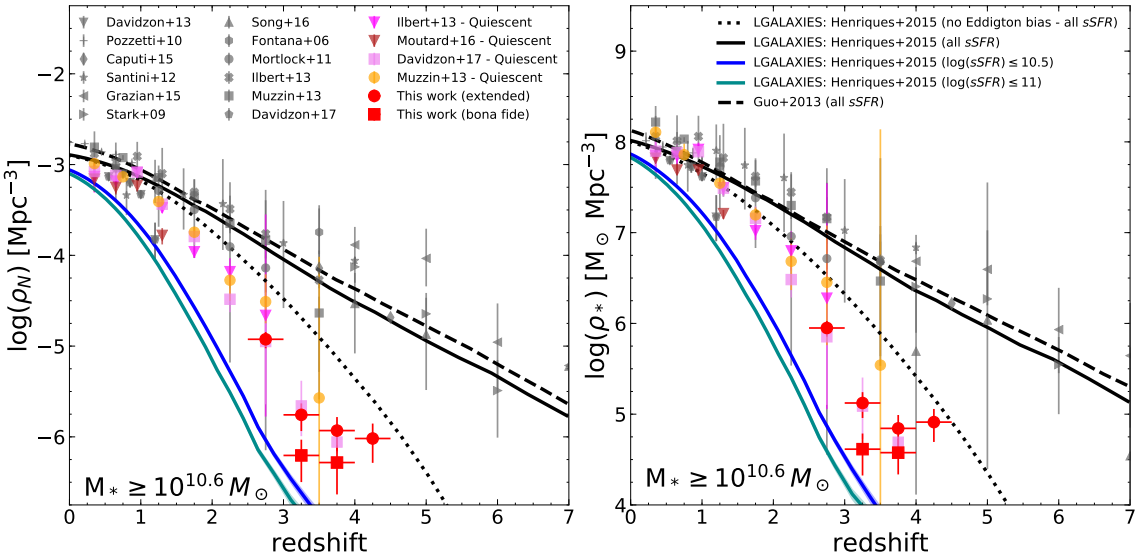

Fig. D.6 Number and stellar mass densities of galaxies with $M \geq 10^{10.6}\,M_{\odot}$ as function of redshift for total population of galaxies (in gray) or quiescent galaxies (colored points) in literature, compared to those obtained in this work. Our results are shown as red diamonds and squares for the BC03 extended and bona fide samples, respectively, with error bars representing the Poissonian errors, cosmic variance, and photometric redshift errors added in quadrature. The forecasts of two semi-analytic models are also shown: the black dashed and continuous lines represent the Guo et al. (2013a) and the H15 models, respectively, estimated for the entire population of galaxies and convolved for the Eddington bias. The black dotted line represents the H15 model for the entire population not convolved for the Eddington bias. Blue and cyan shaded regions represent the H15 model with Poissonian error for the selected quiescent populations characterized by $\log(\mathrm{sSFR}\,[\mathrm{yr}^{-1}]) \leq -10.5$ and ≤ -11, respectively.

an additional error of 10% on our measurements of number and mass densities. We notice that the assumption on the scatter can be optimistic given the lack of spectroscopic control samples for this class of objects, but even assuming a scatter as large as $\sigma_z \sim 0.10(1+z)$, we expect a contamination of 11% in the wide bin $3.0 \leq z < 4.5$ adopted in Sect. D.6, and a maximum contamination of $\sim 20\%$ at $3.5 \leq z < 4.0$ and $\lesssim 50\%$ at $4.0 \leq z < 4.5$.

We find the following results. For the extended sample: we find a decrease by a factor of $\sim 14^{+3}_{-7}$ in the number of quiescent object from the lowest redshift bin (i.e., $2.5 \leq z < 3.0$) to the highest one (i.e., $z \geq 4.0$), and the same decrease is found by considering the mass densities between the same redshift intervals. In addition, we find a decrease by a factor $\sim 66^{+28}_{-27}$ and $\sim 100 \pm^{+29}_{-35}$ in the number density and mass density, respectively, between Davidzon et al. (2017) data for the quiescent population at $0.2 < z < 0.5$ and our estimate in the redshift bin $2.5 \leq z < 3.0$. Between the same redshift bins, considering the results of Moutard et al. (2016b), which are evaluated on the VIPERS multi-lambda catalog (on 22 deg^2) and are, therefore, more statistically significant and less subject to cosmic variance with respect to results on COSMOS, we find a decrease by a factor $\sim 57^{+14}_{-19}$ and

$\sim 78 \pm^{+15}_{-19}$ in the number density and mass density, respectively. Concerning the bona fide sample: between the lowest redshift bin (i.e., $3.0 \leq z < 3.5$) to the highest (i.e., $3.5 \leq z < 4.0$) we find an evolution by a factor of ~ 1.7 in the number density and almost no evolution in the mass densities.

The errors on the estimated factors have been evaluated by propagating the errors of our measurements. When considering the Davidzon et al. (2017) data, the errors on their measurements have also been considered and propagated. Interestingly, the 10% uncertainty we add to our error budget in order to take photometric redshift errors into account, is similar to what Ilbert et al. (2013) quoted as error relative to the template fitting procedure, including photometric redshift error and stellar mass estimate uncertainties.

D.5.1 Comparison with previous results

In Fig. D.6, we compare the evolution of number and stellar mass densities with results from the literature, specifically, Caputi et al. (2015); Davidzon et al. (2013, 2017); Fontana et al. (2006); Grazian et al. (2015); Ilbert et al. (2013); Mortlock et al. (2011); Muzzin et al. (2013); Pozzetti et al. (2010); Santini et al. (2012); Song et al. (2016); Stark et al. (2009). The datapoints have been rescaled where necessary to the cosmology we adopted (see Sect. D.1) and to a Chabrier IMF. We consider only massive galaxies with $M \geq 10^{10.6} M_{\odot}$ both for the full sample of galaxies (gray points) and for the sub-sample of quiescent galaxies (colored points). The literature we used featured data which focused on quiescent galaxies (Davidzon et al. 2017; Ilbert et al. 2013; Moutard et al. 2016b; Muzzin et al. 2013). All of them, like the present work, collect a galaxy sample where photometric redshifts and stellar masses are derived via SED fitting. The classification of quiescent galaxies is based on the sSFR in the present work, whereas it is based on the NUVrJ diagram for Davidzon et al. (2017), Moutard et al. (2016b) and Ilbert et al. (2013), and on the UVJ diagram for Muzzin et al. (2013). We have been able to evaluate the number and mass densities of quiescent galaxies at the highest redshifts from the stellar mass functions that have been published. Data from Davidzon et al. (2017) are estimated by means of the integral of their stellar mass function for the quiescent population, obtained from COSMOS2015 catalog. The same recipe has been applied to the stellar mass function of quiescent galaxies of Muzzin et al. (2013) selected from a NIR-selected sample of galaxies out to $z \sim 4$, and to the mass functions of Moutard et al. (2016b) at $z \leq 1.5$ derived in a $22\,\mathrm{deg}^2$ field. The results of the present work are in broad agreement with the results obtained by Ilbert et al. (2013), Muzzin et al. (2013), and Davidzon et al. (2017).

D.5.2 Comparison with semi-analytic models

We compared our results with the number and stellar mass densities obtained using semi-analytic models by Guo et al. (2013a, hereafter G13) and Henriques et al. (2015, hereafter H15) for the total and the quiescent populations. Both models are based on the Munich galaxy formation model (Croton, 2006; Guo et al., 2011, 2013a; Henriques et al., 2015; Kauffmann et al., 1999; Springel et al., 2001; **?**) which has been implemented in the Millennium (Springel et al., 2005) simulation of dark matter

in a box with comoving side of $500\,\mathrm{Mpc}\,h^{-1}$, and with cosmological parameters adopted from the Wilkinson Microwave Anisotropy Probe (Komatsu, 2006) and from the Planck Collaboration et al. (2014) for G13 and H15, respectively. We used the data from the Millennium database[2], selecting galaxies directly from the snapshots of the simulation. Before applying the same selection criteria adopted for observed galaxies, we convolved stellar masses with a Gaussian in $\log(M_*/M_\odot)$, with width increasing with redshift $\sigma_{\log M_*} = 0.08(1+z)$, in order to account for the Eddington bias, as done in Henriques et al. (2015). We set the Hubble parameter as in our reference ΛCDM cosmology, and we selected galaxies with $\log(M_*/M_\odot) \geq 10.6$ at all sSFR for the total population shown in Fig. D.6. For quiescent galaxies, we selected massive galaxies (i.e., $\log(M_*/M_\odot) \geq 10.6$) with two different cuts in $\log(\mathrm{sSFR}\,[\mathrm{yr}^{-1}])$: one at -10.5 to match our extended sample definition and one at -11 to match the bona fide selection (shown in Fig. D.6 as blue and cyan lines respectively). It can be argued that the different star formation histories assumed in our SED fit and in the models may bias the comparison between the values. However, it has been shown by Laigle et al. (2019) that the instantaneous or short time-scale sSFR derived for a COSMOS-like photometric sample using exponentially declining SFHs reproduces the intrinsic values of a simulation with stochastic SFHs reasonably well.

In Fig. D.6, we also show the effect of the correction for the Eddington bias for the total population in the H15 model: the convolution with the Eddington bias tends to increase the number counts of galaxies especially at high redshift, since more galaxies with small masses (which are more numerous than galaxies at high masses) are scattered upwards of the mass threshold than high mass galaxies scattered downwards of the same limit. Since the observed values are naturally the result of the convolution of intrinsic properties and observational errors, it is fundamental to take this bias into account in order to make a fair comparison between models and observations. Figure D.6 shows that the amount of the convolved error is what is needed to match the densities of massive observed galaxies at high redshift.

While the total number and mass densities by H15 and G13 are in good agreement with the literature data, Fig. D.6 shows that the same quantities for passive galaxies derived by H15 are underestimated when compared with results from the present work and from the literature at high redshift: even considering a large scattering in photometric redshifts as mentioned above, the decrease in number and mass densities is not sufficient to fully reconcile the results with the models, at least for the extended sample, as we discuss in Sect. D.7.

D.6 Stellar mass functions

The stellar mass function (SMF) of galaxies has been studied extensively over the past years out to $z \sim 4-5$, for both star-forming and quiescent galaxies (e.g., Davidzon et al. 2017; Fontana et al. 2006; Grazian et al. 2015; Ilbert et al. 2013; Muzzin et al. 2013). In this section, we estimate the stellar mass function for quiescent galaxies at $z > 2.5$ and compare it to other observations and models.

[2]http://gavo.mpa-garching.mpg.de/MyMillennium/ Help/databases/henriques2015a/ database

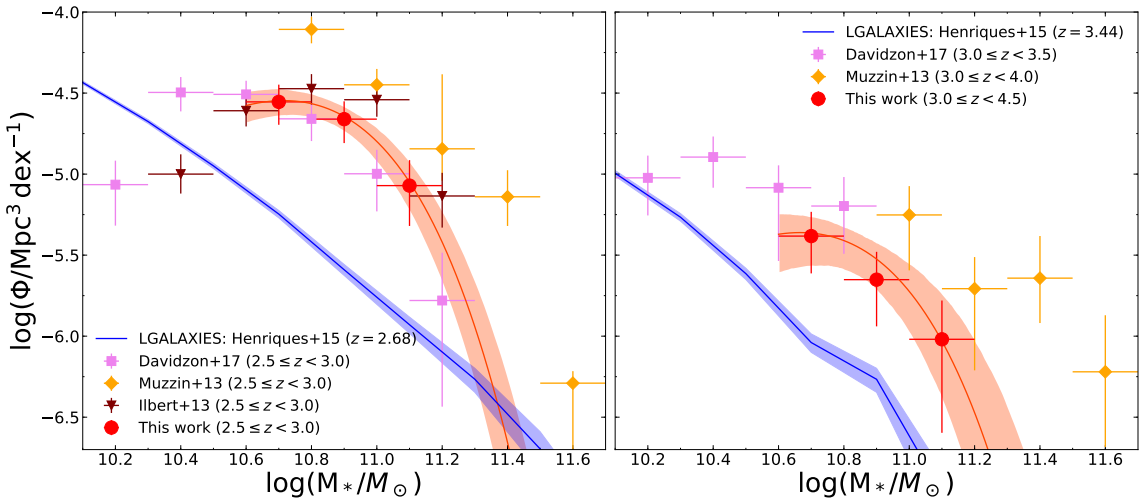

Fig. D.7 Stellar mass function of *extended* galaxies, in two redshift bins between $z = 2.5$ and 4.5. In each panel, the data points are shown as red circles in bins of $\Delta \log M/M_{\odot} = 0.1$. Error bars include Poisson noise, cosmic variance, and photometric redshift errors. The data points are fitted by a single Schechter function, shown by a red solid line, while the red shaded area is its 1σ uncertainty. Data points (with their error bars) from other works are also shown: violet squares are taken from Davidzon et al. (2017), in magenta triangles we plot the mass functions by Ilbert et al. (2013), and in orange circles the one by Muzzin et al. (2013). The blue lines shows the H15 model for quiescent galaxies at $z = 2.68$ (left) and $z = 3.44$ (right).

We estimate the stellar mass function of the *extended* sample into two redshift bins: $2.5 < z < 3$ and $3.0 < z < 4.5$ with the $1/V_{\rm max}$ method (considering, for all the galaxies, the $V_{\rm max}$ equal to the volume defined by the redshift bin since we assume it to be complete for masses above $\sim 10^{10} M_{\odot}$, as shown in Fig. D.2). We fit our data (3 mass bins for each redshift interval) with a Schechter function (Schechter, 1976):

$$\Phi(M)dM = \Phi^* \left(\frac{M}{M^*}\right)^{\alpha} \exp\left(-\frac{M}{M^*}\right) \frac{dM}{M^*} \tag{D.3}$$

using the software package *emcee* (Foreman-Mackey et al., 2013), an MIT-licensed pure-python implementation of affine invariant Markov chain Monte Carlo (MCMC) ensemble sampler (Goodman & Weare, 2010). Since we are probing only the massive end of the function, the slope of the power law part of the function is not constrained. We thus fix the parameter $\alpha = 1.15$, following Davidzon et al. (2017) and assuming the same slope they find at lower redshift. We report in Table D.5 the Schechter parameters fitting the data points in the two redshift bins along with the 1σ errors.

Table D.5 Schechter parameters of best-fit stellar mass functions.

redshift	$\log(M^*)$ $[M_{\odot}]$	α (fixed)	Φ^* $[10^{-5}\mathrm{Mpc}^{-3}]$
$2.5 < z < 3.0$	$10.38^{+0.05}_{-0.05}$	1.15	$10.21^{+1.80}_{-1.88}$
$3.0 \leq z < 4.5$	$10.33^{+0.09}_{-0.12}$	1.15	$1.56^{+0.46}_{-0.57}$

In Fig. D.7, the data points along with the best-fit Schechter functions are shown. Error bars include the contribution of Poissonian errors, cosmic variance, and photometric redshift errors added in quadrature, while in the abscissa, they represent the mass bin $\Delta \log M/M_{\odot} = 0.2$. For the cosmic variance, we once again used the prescriptions of Moster et al. (2011), deriving for each bin the cosmic variance on the COSMOS field, at the median redshift of the objects grouped in each bin and in the mass range covered by the bin. To account for photometric redshift errors, we considered a 10% error, as explained in Sect.D.5.

We compared our SMF with the literature data in the same redshift bins (rescaling masses to Chabrier IMF and ΛCDM cosmology when required). We selected previous works that focused on quiescent galaxies (Davidzon et al. 2017; Ilbert et al. 2013; Muzzin et al. 2013) and whose characteristics are explained in Sect. D.5.1. In Fig. D.7, we also show in blue the SMF for the H15 model (described in Sect. D.5.2) that is derived in the snapshot located at $z = 2.68$ for the redshift bin $2.5 \leq z < 3.0$ and at $z = 3.44$ for the redshift bin $3.0 \leq z < 4.5$. We chose the snapshots located at redshifts that were the nearest to the median redshift of our observed galaxies in the two bins, which are $z = 2.60$ and $z = 3.35$. We selected quiescent galaxies in the snapshots in the same way we selected the extended sample, that is, $\log(M_*/M_{\odot}) \geq 10.6$ and $\log(\mathrm{sSFR}\,[\mathrm{yr}^{-1}]) \leq -10.5$, after convolving the masses with a Gaussian of width $0.08(1+z)$ in $\log(M_*)$. In Sect. D.7, we present an extensive discussion of our results and a comparison with results in the literature and semi-analytic models.

D.7 Discussion

D.7.1 Comparison with previous observations

In Fig. D.6, we compare our estimates of the number and mass densities with several results presented in the literature. The observed densities of the quiescent population are characterized by a rather small scatter: our results are in good agreement with Davidzon et al. (2017) at all redshifts, while larger differences are visible with Muzzin et al. (2013) and Ilbert et al. (2013), especially at $z < 3$. This can be due to different input photometric datasets, SED fitting analysis performed on the data, and the different criteria adopted to define a quiescent galaxy (see Sect. D.5.1).

From the comparison of the observed SMFs in Fig. D.7, it is evident that at $z > 3.0$ Muzzin et al. (2013) estimate a greater number of very massive ($> 10^{11} M_{\odot}$) quiescent galaxies than all the other works. The estimate by Ilbert et al. (2013) is, instead, only slightly higher than ours at $2.5 < z < 3$, while we obtain the best agreement with Davidzon et al. (2017) in both redshift bins. Since all the SMFs are derived in the same field, differences cannot be simply ascribed to observations on different fields.

Based on Fig. D.7, there is a noticeable evolution between the two redshift bins. This effect can be due to the fast evolution of colors. We note once again that our classification is based on apparent color selections designed to identify the Balmer and D4000 breaks. A passively evolving stellar

population develops pronounced Balmer and D4000 breaks in $t \approx 0.3$ Gyr (Bica et al., 1994), while the redshift interval from $z = 4.5$ to $z = 2.5$ corresponds to 1.2 Gyr. This means that a galaxy that quenched its star formation at $z \approx 4-4.5$, and since then has been passively evolving, had enough time to develop the pronounced Balmer and D4000 breaks needed to be identified as quiescent at $z \approx 2.5-3$ through our color selections. Therefore, if the quenching of the star formation occurs at around $z \approx 4-4.5$ for a large number of objects, it is reasonable to expect such a fast evolution in the number of passive galaxies. Another possible explanation for the evolution between the two redshift bins is the evolution of the stellar mass: the rapid increase of objects with stellar masses $M_* > 10^{10.6} M_\odot$ may reflect the emergence of a high merging rate, assembling more and more massive quiescent galaxies as they move down with redshift, although the lack of evolution in M^* of the Schechter function can challenge this interpretation.

D.7.2 Comparison with models

According to our results and other results in the literature, the H15 model tends to underpredict quiescent galaxies at $z \gtrsim 2.5$, both in number and in the content of their stellar mass, as visible in Fig. D.6. In particular, when considering the bona fide sample, we find that the H15 model underpredicts the number of quiescent objects in the redshift bin $3.0 \leq z < 3.5$ by a factor of $\sim 4.9^{+2.3}_{-2.4}$ up to a value of $\sim 6.0^{+3.1}_{-3.5}$ at $z \sim 4$. By checking the differences in the mass densities, we find that the model underpredicts observed values at $3.0 \leq z < 3.5$ by a factor of $\sim 4.2^{+2.0}_{-2.4}$ and it shows a difference by a factor of $\sim 6.2^{+2.5}_{-2.7}$ at $z \sim 4$. The differences between H15 model and our results are all the more evident when considering the extended sample. In this case, in the redshift bin $2.5 \leq z < 3.0$ we find a difference by a factor of $\sim 11.9^{+2.7}_{-2.9}$ in the number densities, while the mass densities differ by a factor of $\sim 11.1^{+1.0}_{-1.2}$. Moreover, at $z \sim 4$ we find a difference by a factor of $\sim 10.1^{+5.8}_{-6.1}$ in the number densities and by a factor of $\sim 19.2^{+3.9}_{-4.1}$ when considering the mass densities (also in this case, we simply propagated the errors in our measurements).

Considering the SMFs in the left panel of Fig. D.7 (i.e., at $2.5 \leq z < 3.0$), the H15 model appears not to reproduce the shape of the observed SMFs. In particular, it emerges that the model overpredicts low-mass ($\log(M_*/M_\odot) \lesssim 10.4$) and high-mass ($\log(M_*/M_\odot) \gtrsim 11.4$) systems while objects in the intermediate mass range appear to be underpredicted (by a factor of ~ 8.7 at $\log(M_*/M_\odot) = 10.9$). Also, in the right panel of Fig. D.6 (i.e., at $3.0 \leq z < 4.5$), it is evident that the model seems to under-predict objects in the whole mass range (by a factor of ~ 4.4 at $\log(M_*/M_\odot) = 10.9$) with the exception of low-mass systems, i.e., $\log(M_*/M_\odot) \lesssim 10.2$. These discrepancies reflect the intrinsic difficulty in treating the processes involved in galaxy formation, and in particular, the processes related to the transformation of star-forming galaxies into quiescent objects and their mass assembly at $z \gtrsim 2.5$. In Cecchi et al. (2019) we compare high-redshift observed quiescent galaxies to different semi-analytic models (SAMs) and discuss the quenching mechanisms that led to their formation.

In the current scenario, such massive quiescent galaxies are the result of a strong active galactic nuclei (AGN) feedback from the central supermassive black holes (BHs) which significantly affects

galaxy formation processes. The AGN feedback can take place in two main ways: the jet (or radio) mode, and the radiative mode (sometimes called quasar mode or bright mode). The mechanism that is primarily, or entirely, responsible for quenching in the jet mode is connected with highly collimated jets of relativistic particles, in which star formation dies out because the hot gas halo is continually heated, and the supply of new cold gas is cut off (Bower et al., 2006; Croton, 2006; Kimm et al., 2009; Somerville et al., 2008). In the radiative mode, quenching is associated with mergers and rapid BH growth, followed by a quasar wind which expels gas from galaxy's center, explaining the growth of the quiescent population (Hopkins et al., 2008a,b). Cosmological zoom-in simulations, which include fast momentum-driven AGN winds, also appear to be able to quench star formation. Moreover, it appears that it can also maintain quiescence over long timescales without any explicit jet mode type feedback (Choi et al., 2014). Conversely, Gabor & Davé (2015) suggested that the presence of a gaseous halo kept hot by AGN feedback is sufficient to quench a galaxy without the need for additional radiative mode feedback. What the relative importance is of these AGN feedback mechanisms that are responsible for the early appearance of the population of quiescent galaxies at high redshift is still a matter of debate. However, a feedback mechanism is fundamental in order to quench star formation and form massive quiescent galaxies.

In the H15 model, massive galaxies can be quenched by AGN feedback depending on black-hole and hot-gas mass and, therefore, indirectly on stellar mass. In addition, galaxies of any mass can be quenched by ram-pressure or tidal stripping of gas and through the suppression of gaseous infall. It is argued by Henriques et al. (2017) that this combination of processes produces quenching efficiencies which depend on stellar mass, host halo mass, environment density, distance to group centre, and group central galaxy properties. In the case of massive galaxies, the quenching is likely due to AGN feedback. As explained in Henriques et al. (2017), both the quasar and the radio accretion modes on the black hole are considered in the model; while the quasar mode produces no feedback on the galaxy, the radio mode produces a strong feedback by avoiding further hot gas condensation and, therefore, star formation is suppressed once the cold gas is exhausted.

If our result (that is, the under-prediction of quiescent objects at $2.5 \lesssim z \lesssim 3$ in H15) is confirmed, it would imply that the considered model is not efficient enough in producing massive quiescent galaxies at high redshifts. Considering the ingredients of the model, this may be due to the parametrization of the radio mode AGN feedback on the galaxy, or the timescale of this feedback process is too long to produce massive quiescent objects at such redshifts or, in addition, a different accretion mechanism on the black hole should be considered.

On the observations side, the scatter between different observed samples of quiescent objects makes it evident that there is a need for deeper observations on different fields (all the data reported in the plot for quiescent galaxies belong to the COSMOS field) and spectroscopic confirmation to better constrain the population of massive quiescent galaxies at $z \gtrsim 2.5 - 3.0$, whose presence should be explained by models of galaxy formation but still aren't (see Naab & Ostriker 2017; Somerville & Davé 2015 for two extensive reviews on theoretical state-of-the-art models of galaxy formation).

D.8 Summary and Conclusions

The results of the present study can be summarized as follows:

1. We identified two new color selections using near-infrared bands to select quiescent galaxies at $2.5 \lesssim z \lesssim 4.5$. The color selections are based on the identification of strong spectral features characterizing these evolved objects, that is, the D4000 and Balmer breaks.

2. We studied the effectiveness of our color selections by exploring all the parameters characterizing evolutionary tracks, as well as the effects of emission lines.

3. We applied the color selection to the COSMOS2015 catalog, selecting a parent sample with a cut at $m_{[4.5]} \leq 24$. Through a SED fitting analysis we tightened the selection considering only the most massive ($\log(M_*/M_\odot) > 10.6$) high redshift ($z_{\rm phot} \gtrsim 2.5$) quiescent ($\log(\mathrm{sSFR}\,[\mathrm{yr}^{-1}]) < -10.5$) galaxies. The proposed color selections coupled with SED fitting analysis allowed us to build a reliable sample of quiescent candidates, aimed at maximizing its completeness.

4. The objects consistent with being the most quiescent massive galaxies (i.e., the bona fide sample) have observed number densities that decrease by a factor of ~ 1.7 from the redshift bin $3.0 \leq z < 3.5$ to the bin $z \geq 4$ while mass densities show almost no evolution with redshift. Considering the extended sample, we found a decrease by a factor of $\sim 12.4^{+3}_{-7}$ in the number of quiescent object and by a factor of $\sim 10.9^{+3}_{-6}$ in their mass densities from the lowest redshift bin (i.e., $2.5 \leq z < 3.0$) to the highest one (i.e., $z \geq 4.0$). In addition, we find a difference in the number density (mass density) by a factor of $\sim 66^{+28}_{-27}$ ($\sim 100^{+29}_{-35}$) between our lowest redshift bin (i.e., $2.5 \leq z < 3.0$) and Davidzon et al. (2017) data for the quiescent population in the redshift bin $0.2 < z < 0.5$.

5. We estimated the stellar mass functions for our sample of quiescent galaxies and their fit with a Schechter function.

6. According to our results, the semi-analytical model by Henriques et al. (2015) is not able to fully account for the number and mass densities and the stellar mass functions of candidate quiescent objects unless a severe effect of contamination is what is affecting our bona fide sample, in which case the significance of the disagreement with observed data can decrease. In particular, considering the bona fide sample, the model seems to underpredict the number of quiescent objects in the redshift bin $3.0 \leq z < 3.5$ by a factor of $\sim 4.9^{+2.4}_{-2.3}$ that grows to a value of $\sim 6.0^{+3.1}_{-3.5}$ at $z \geq 4.0$. In considering the mass densities, we find that the model underpredicts our estimates in the redshift bin $3.0 \leq z < 3.5$ by a factor of $\sim 4.2^{+2.4}_{-2.0}$ and it shows a difference by a factor of $\sim 6.2^{+2.7}_{-2.5}$ at $z \geq 4.0$. The differences between H15 model and our results is notably evident when considering the extended sample. In this case, the redshift bin $2.5 \leq z < 3.0$ demonstrates a difference by a factor of $\sim 11.9^{+2.7}_{-2.9}$ in the number densities, while the mass densities differ by a factor of $\sim 11.1^{+1.0}_{-1.2}$. Moreover, at $z \geq 4.0$ we

find a difference by a factor of $\sim 10.1^{+5.8}_{-6.1}$ in the number densities and by a factor of $\sim 19.2^{+3.9}_{-4.1}$ considering the mass densities. Moreover, the shape of the SMF is not fully reproduced by the model.

7. This method can be used to select targets for spectroscopic follow-up, especially with future facilities such as the James Webb Space Telescope. If future spectroscopic observations confirm the presence of a population of quiescent galaxies at high redshift, as proposed in the present work, some further internal mechanisms of quenching will be needed to explain the presence of such galaxies at high redshift that are becoming more and more numerous, given the many studies devoted to this topic. In semi-analytic models, the AGN-feedback needed to quench star-formation at high stellar masses could be an ingredient that still needs to be fully understood and parametrized differently.

D.9 Exploring evolutionary tracks's parameters space

In this final Section, we explored the effects of different evolutionary tracks on the choice of color criteria. We analyzed, in particular, the impact of considering star forming galaxies with emission lines, different extinction laws, IMFs, stellar population synthesis (SPS) models, metallicities, SFHs, and redshifts of formation. In all following plots: gray shaded areas represent the selection region for quiescent galaxies, colored numbers represent the redshift of the nearby point for the evolutionary track with the same color and a vector corresponding to a magnitude extinction of $A_V = 1$ using Calzetti's law is shown.

D.9.1 Emission lines

We built the evolution of a galaxy template of constant star formation with the contribution of nebular emission lines using the code *fsps* (Conroy et al., 2009, 2010). As shown in Fig. D.8, considering a template with emission lines in the $HK_s[3.6]$ diagram does not affect the selection criteria. Instead, considering the $JK_s[3.6][4.5]$ selection, some contamination by star forming galaxies with emission lines is expected at $2.2 \lesssim z \lesssim 3.0$ for extinction values around $A_V \sim 3$. In Fig. D.8, it can be seen that higher (or lower) values of A_V would not affect the selection box contaminating the candidates. Considering the SED fitting procedure for a star-forming template with emission lines, this contamination may be kept under control with the aid of optical bands where the emission-line galaxies should be characterized by a larger flux with respect to a quiescent object (see also the top panels of Fig. D.8).

D.9.2 Extinction laws

We also tested our color-color diagrams using three different extinction laws. In particular, as shown in Fig. D.9, we computed the evolutionary tracks using the Calzetti law (Calzetti et al., 2000), characteristic of starburst (SB) galaxies, the Fitzpatrick law (Fitzpatrick, 1986) derived for the Large Magellanic Cloud (LMC), and the Seaton law (Seaton, 1979) obtained for the Milky Way (MW). The main differences among them are the bump at 2200 Å, which is absent in starburst galaxies, and the slope in the UV, which is steeper for the LMC extinction law.

As shown in Fig. D.9, tracks built with MW and LMC laws are, in general, very similar and differ slightly from the SB law we used as a reference in the present paper. Adopting different extinction laws does not affect the selection criteria of quiescent galaxies. The tracks of color evolution for star-forming galaxies can cross our selection boxes in the $JK_s[3.6][4.5]$ diagram when adopting LMC and MW extinction laws, but only at $z \lesssim 3$.

D.9.3 IMF

We tested our selections with the IMFs of Chabrier (2003); Kroupa (2001); Salpeter (1955) and we found no appreciable differences in evolutionary tracks . This was expected because the SED of a

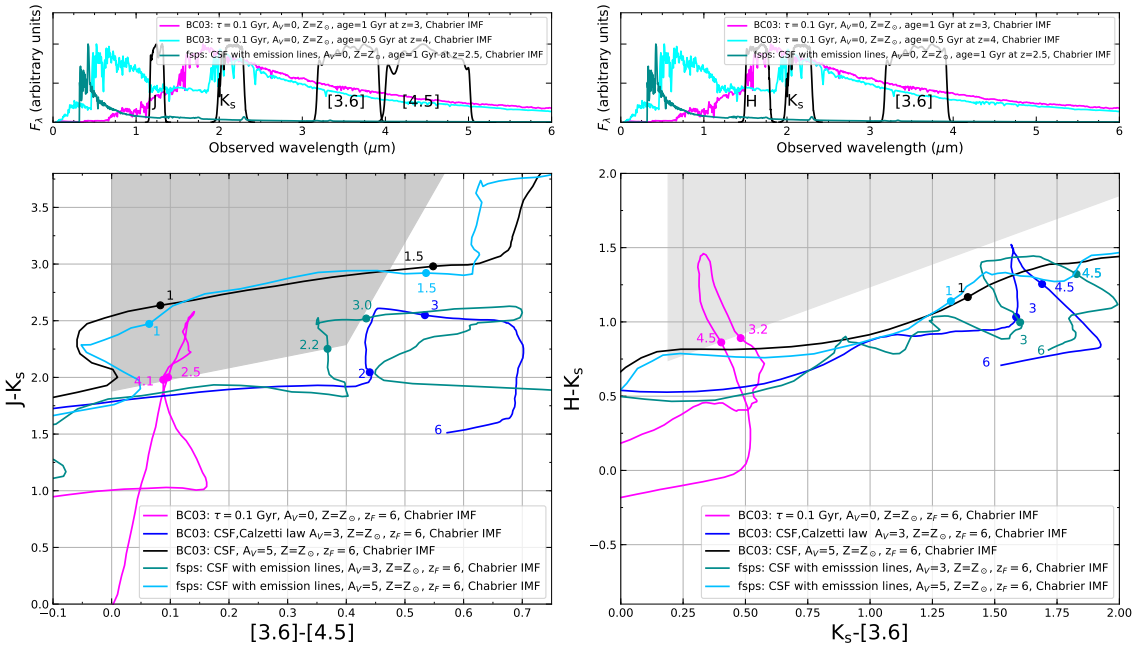

Fig. D.8 Effect of emission lines on $JK_s[3.6][4.5]$ and $HK_s[3.6]$ color-color diagrams. **Top panels:** two SEDs of quiescent galaxies (magenta and cyan lines), representing a population 1 Gyr old redshifted to $z = 3$ and a population 0.5 Gyr old redshifted to $z = 4$ (i.e., $z_{\rm form} \approx 6$) built with BC03 models. A star forming SED with emission lines built from *fsps*, 1 Gyr old and redshifted to $z = 2.5$ is shown in dark-cyan. Also the filters transmission curves, used in COSMOS field and in the tracks computation, are shown. **Bottom:** evolution in color-color plots for star-forming and passive galaxies. Tracks representing star-forming galaxies are shown in blue, black dark-cyan, and cyan, and their characteristics are shown in the legend inside the plot. A track for quiescent galaxies (with *e*-folding time of $\tau = 0.1$ Gyr and solar metallicity) is shown in magenta.

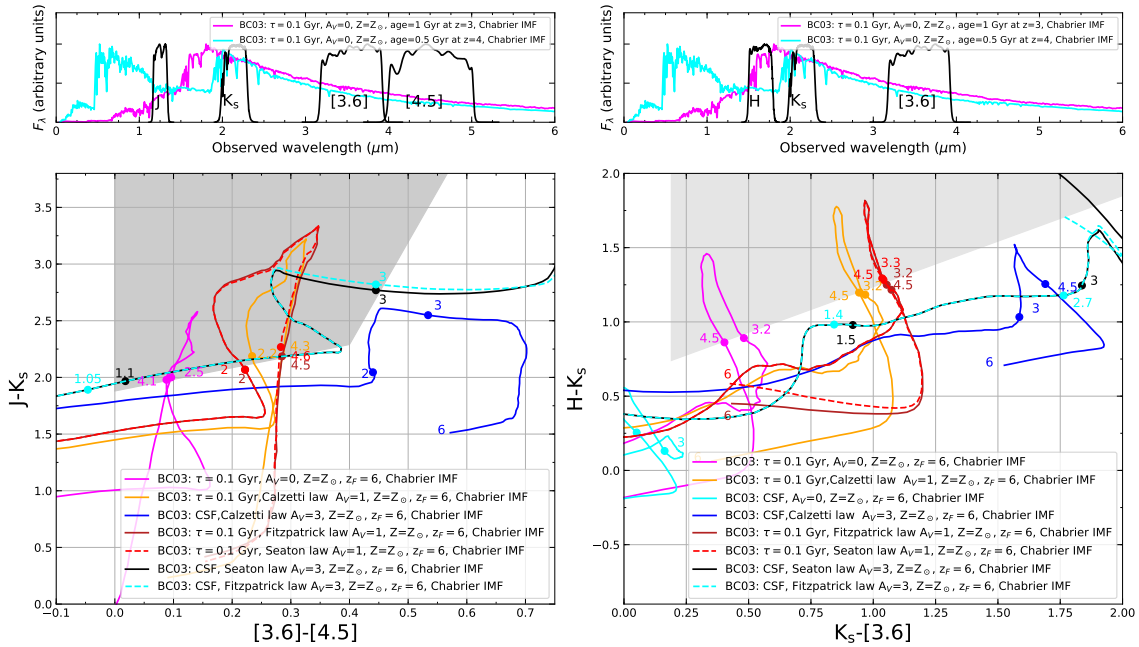

Fig. D.9 Effect of different extinction laws on $JK_s[3.6][4.5]$ and $HK_s[3.6]$ color-color diagrams. **Top panels:** two SEDs of quiescent galaxies (magenta and cyan lines), that is, a population 1 Gyr old redshifted to $z = 3$ and a population 0.5 Gyr old redshifted to $z = 4$ (i.e., $z_{\rm form} \approx 6$) built with BC03 models. **Bottom:** evolution in the color-color plots for star-forming and passive galaxies. Tracks representing star-forming galaxies are shown in solid blue, solid black and dashed cyan lines, for the Calzetti, Seaton and Fitzpatrick laws, respectively, and their characteristics are shown in the inserted legends. Tracks for quiescent galaxies (with e-folding time of $\tau = 0.1$ Gyr and solar metallicity) are shown in solid magenta, solid orange, dashed red and brown for the Calzetti ($A_V = 0$ and $A_V = 1$), Seaton and Fitzpatrick laws, respectively.

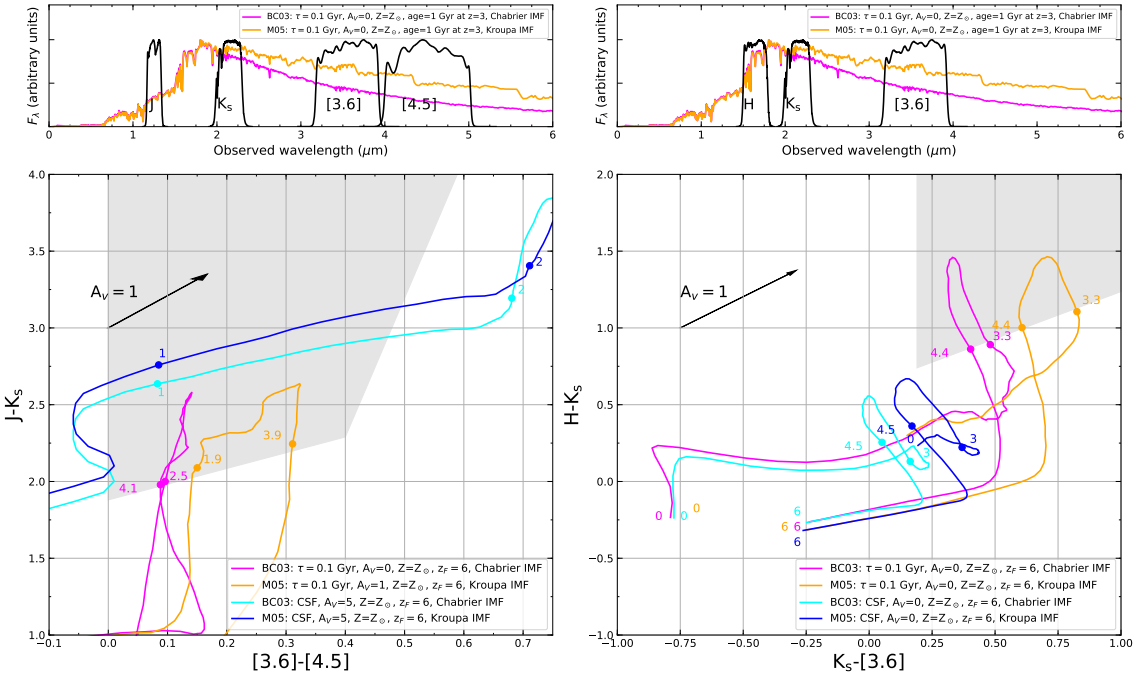

Fig. D.10 Effect of the choice of SPS models on $JK_s[3.6][4.5]$ and $HK_s[3.6]$ color-color diagrams. **Top panels:** two SEDs of quiescent galaxies, that is, a population 1 Gyr old redshifted to $z = 3$ (i.e. $z_{\rm form} \approx 6$) built with BC03 models (magenta line) and with M05 models (orange line). **Bottom:** evolution in color-color plots for star-forming and passive galaxies. Tracks representing star-forming galaxies are shown in blue and cyan, while their characteristics are shown in the inserted legends. Tracks for quiescent galaxies (with *e*-folding time of $\tau = 0.1$ Gyr and solar metallicity) are shown in magenta and orange for BC03 and M05, respectively.

passively evolving galaxy is mainly determined by the stars at the turnoff and considering the possible ages of a galaxy at $z3$, the stars dominating the emission, and, therefore, the colors, are in the portion of the IMF that is similar for all the mentioned IMFs.

D.9.4 SPS models

The difference between BC03 and M05 models (Bruzual & Charlot, 2003; Maraston, 2005) for the building of evolutionary tracks is explored in Fig. D.10. As explained in Sect D.4.1, for $\lambda > 2-2.5\,\mu$m and ages between ~ 0.2 and ~ 2 Gyr, a notable difference in flux between the two models is expected (Maraston et al., 2006) which means that a difference in $K_s - [3.6]$ color is also expected. However, both models generate evolutionary tracks for quiescent galaxies which fall in the selection region for approximately the same redshift range, and leave tracks for star-forming galaxies outside of it. Therefore, the choice of the model adopted does not affect the color selection criteria. The difference between BC03 and M05 results in SED fitting for observed galaxies is also explored in Sect. D.4.1, where no appreciable difference has been found.

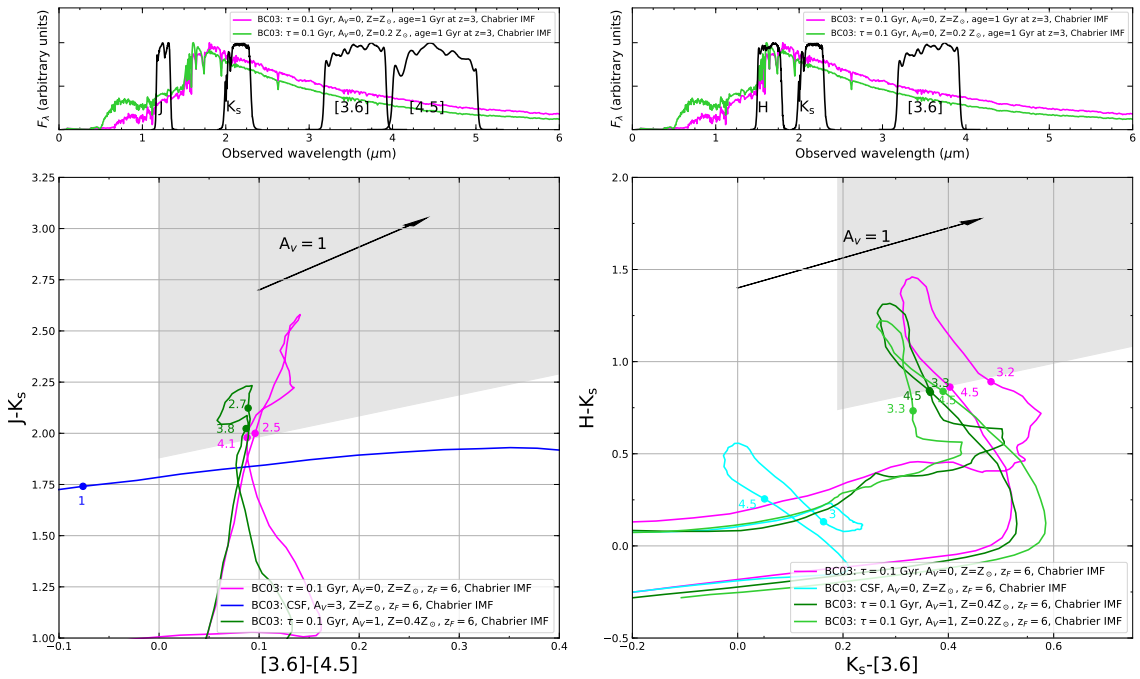

Fig. D.11 Effect of metallicity on $JK_s[3.6][4.5]$ and $HK_s[3.6]$ color-color diagrams. **Top panels:** two SEDs of quiescent galaxies are shown. In particular, the magenta SED represents a population 1 Gyr old redshifted to $z = 3$ (i.e. $z_{\rm form} \approx 6$) with $Z = Z_\odot$, while the green line shows the SED of a population of a 1 Gyr redshifted to $z = 3$ (i.e. again $z_{\rm form} \approx 6$) with $Z = 0.2 Z_\odot$. **Bottom:** color-color plots with evolutionary tracks for star-forming and passive galaxies. Tracks representing star-forming galaxies are shown in blue and cyan, while their characteristics are shown in the inserted legends. Three tracks for quiescent galaxies are shown in magenta, dark-green and light-green for different metallicities ($Z = Z_\odot$, $Z = 0.4 Z_\odot$, $Z = 0.2 Z_\odot$ respectively).

D.9.5 Metallicity

The effect of different metallicities is explored in Fig. D.11 (for $Z = 0.02\,, 0.008\,, 0.0004$): we found that all the derived tracks enter the color selection for $z \approx 3 - 3.5$ and exit for $z \approx 4 - 4.5$, suggesting that the color selection is valid for a wide range of metallicities . Assuming a metallicity in the range of $Z = Z_\odot$ to $0.2 Z_\odot$ is reasonable even for high redshift galaxies (e.g., Finkelstein 2016; Mannucci et al. 2010; Papovich et al. 2001; Sawicki & Yee 1998; Shapley et al. 2001). For instance, according to Glazebrook et al. (2017), a quiescent galaxy at $z = 3.7$ is consistent with having a solar metallicity.

D.9.6 Star formation histories

As already mentioned, star formation histories for quiescent galaxies have been parametrized with an exponentially declining star formation with short e-folding times in order to guarantee a negligible SFR after a few hundreds Myr. Star formation histories follow the formula $\mathrm{SFR}(t) \propto \tau^{-1} e^{-t/\tau}$ where τ is the e-folding time. High-redshift quiescent galaxies need to have formed their stellar mass

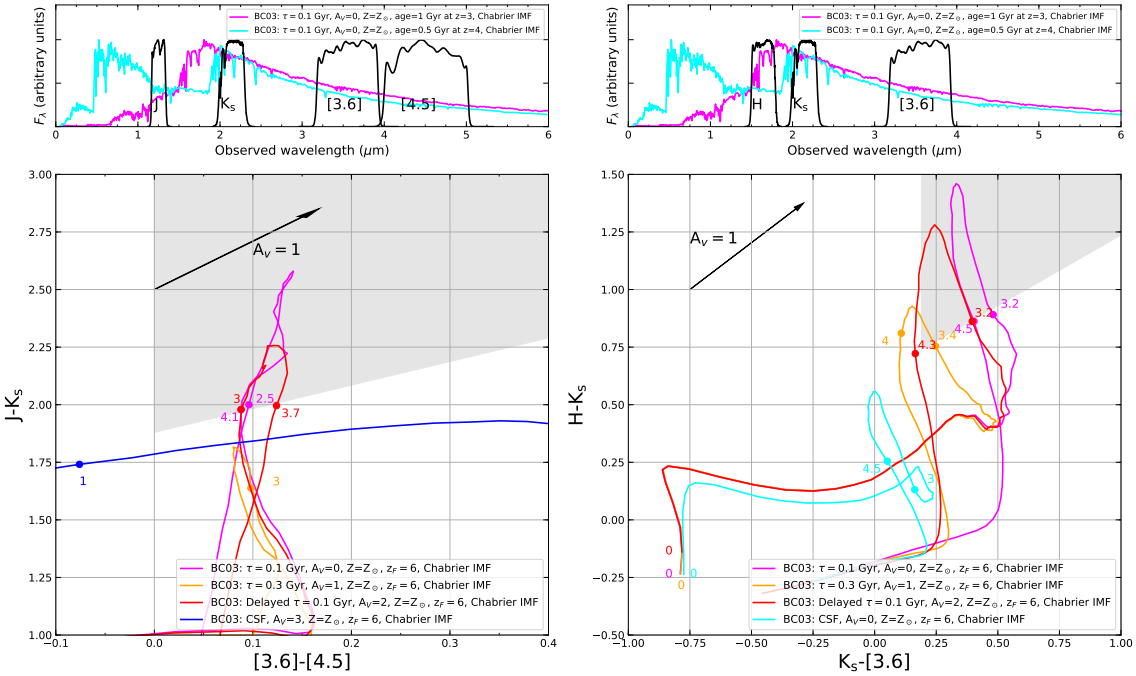

Fig. D.12 Effect of SFHs on $JK_s[3.6][4.5]$ and $HK_s[3.6]$ color-color diagrams. **Top panels:** two SEDs of quiescent galaxies are shown in magenta SED and cyan, representing a population of 1 Gyr redshifted to $z = 3$ (i.e. $z_{\rm form} \approx 6$), and a population of 0.5 Gyr redshifted to $z = 4$ (i.e., again $z_{\rm form} \approx 6$), respectively. **Bottom:** color-color plots with evolutionary tracks for star-forming and passive galaxies. Tracks representing star-forming galaxies are shown in blue and cyan and their characteristics are shown in the inserted legends. Three tracks for quiescent galaxies are shown in magenta, orange and red: the magenta track is parametrized with an exponentially declining star formation with $\tau = 0.1$ Gyr, orange track has $\tau = 0.3$ Gyr, and red track has been parametrized with a delayed star formation history where $\tau = 0.1$ Gyr.

quickly since they are observed at $z \geq 3$ when the universe was only 2 Gyr old; therefore, a timescale of $\tau = 0.1$ Gyr is often assumed. By considering different e-folding times and assuming the same redshift of formation $z_{\rm form} = 6$, models with a longer e-folding time will be characterised by bluer colors with respect to the model, with a shorter τ at the same redshift. The color selection is still valid assuming an e-folding time of 0.3 Gyr, even though at fixed ages (or redshift) tracks with longer e-folding times are bluer. Assuming even larger e-folding times will not allow for the selection of passive galaxies at high redshift since the stellar population do not have enough time to evolve and develop the D4000 and Balmer breaks.

Delayed star formation histories, parametrized as $\propto \tau^{-2} t\, e^{-t/\tau}$, have also been explored. In particular, choosing timescales of the SFH that are small compared to the time between $z_{\rm form}$ and $z_{\rm obs}$ (e.g., $\tau \approx 0.1$ Gyr), the color selections are still valid, although on a slightly narrower redshift interval. Longer e-folding times would instead represent star-forming galaxies in the redshift interval $z \approx 2.5 - 4$.

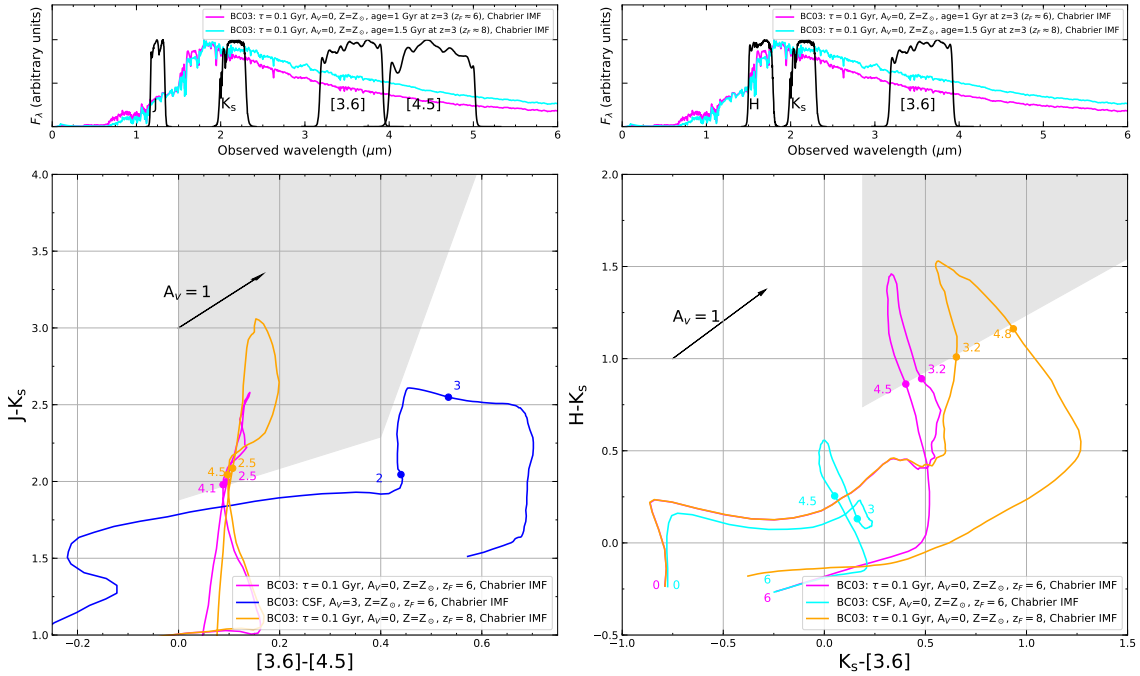

Fig. D.13 Effect of formation redshift on $JK_s[3.6][4.5]$ and $HK_s[3.6]$ color-color diagrams. **Top panels:** two SEDs of quiescent galaxies are shown. In particular, magenta SED represents a population of 1 Gyr redshifted to $z = 3$ (i.e. $z_{\rm form} \approx 6$), while cyan line shows SED for a population of 1.5 Gyr redshifted to $z = 3$ (i.e. $z_{\rm form} \approx 8$). **Bottom:** color-color plots with evolutionary tracks for star-forming and passive galaxies. Tracks representing star-forming galaxies are shown in blue and cyan and their characteristics are shown in the inserted legends. Two tracks for quiescent galaxies with redshift of formation $z_{\rm form} = 6$ and $z_{\rm form} = 8$ are shown in magenta and orange respectively. Their *e*-folding time is $\tau = 0.1$ Gyr and they have solar metallicity.

D.9.7 Redshift of formation

Models with higher $z_{\rm form}$ are, in general, characterized by redder colors at the same redshift since the galaxy which forms at a higher z will exhibit prominent breaks at earlier epochs. This leads to a slightly wider redshift interval for the selection (for $z_{\rm form} = 8$ we select quiescent galaxies in the range $3 \lesssim z \lesssim 4.8$ for $HK_s[3.6]$ and in the range $2.5 \lesssim z \lesssim 4.5$ for $JK_s[3.6][4.5]$) since galaxies enter the color selections at higher redshifts than they did with our adopted reference value of $z_{\rm form} = 6$.

REFERENCES

Abadi, M. G., Navarro, J. F., Fardal, M., Babul, A., & Steinmetz, M. 2010, MNRAS, 407, 435

Abazajian, K. N., Adelman-McCarthy, J. K., Agüeros, M. A., et al. 2009, ApJS, 182, 543

Abraham, R. G., van den Bergh, S., Glazebrook, K., et al. 1996, ApJS, 107, 1

Adami, C., Giles, P., Koulouridis, E., et al. 2018, A&A, 620, A5

Alabi, A. B., Forbes, D. A., Romanowsky, A. J., et al. 2017, MNRAS, 468, 3949

Andreon, S. 2010, MNRAS, 407, 263

Andreon, S. 2013, A&A, 554, A79

Andreon, S., Puddu, E., de Propris, R., & Cuillandre, J. C. 2008, MNRAS, 385, 979

Angulo, R. E. & Hilbert, S. 2015, MNRAS, 448, 364

Angulo, R. E. & White, S. D. M. 2010, MNRAS, 405, 143

Arnouts, S., Moscardini, L., Vanzella, E., et al. 2002, MNRAS, 329, 355

Ashby, M. L. N., Willner, S. P., Fazio, G. G., et al. 2015, ApJS, 218, 33

Ashby, M. L. N., Willner, S. P., Fazio, G. G., et al. 2013, ApJ, 769, 80

Asquith, R., Pearce, F. R., Almaini, O., et al. 2018, MNRAS, 480, 1197

Bagley, M. B., Scarlata, C., Mehta, V., et al. 2020, ApJ, 897, 98

Baldry, I. K., Driver, S. P., Loveday, J., et al. 2012, MNRAS, 421, 621

Baldry, I. K., Glazebrook, K., & Driver, S. P. 2008, MNRAS, 388, 945

Baldry, I. K., Robotham, A. S. G., Hill, D. T., et al. 2010, MNRAS, 404, 86

Baldwin, J. A., Phillips, M. M., & Terlevich, R. 1981, PASP, 93, 5

Barro, G., Faber, S. M., Koo, D. C., et al. 2017, ApJ, 840, 47

Beckwith, S. V. W., Stiavelli, M., Koekemoer, A. M., et al. 2006, AJ, 132, 1729

Behroozi, P., Knebe, A., Pearce, F. R., et al. 2015, MNRAS, 454, 3020

Behroozi, P., Wechsler, R. H., Hearin, A. P., & Conroy, C. 2019, MNRAS, 1134

Behroozi, P. S., Conroy, C., & Wechsler, R. H. 2010, ApJ, 717, 379

Behroozi, P. S., Wechsler, R. H., & Conroy, C. 2013, ApJ, 770, 57

Bell, E. F. & de Jong, R. S. 2001, ApJ, 550, 212

Bell, E. F., McIntosh, D. H., Katz, N., & Weinberg, M. D. 2003, ApJS, 149, 289

Bell, E. F., Wolf, C., Meisenheimer, K., et al. 2004, ApJ, 608, 752

Bellstedt, S., Robotham, A. S. G., Driver, S. P., et al. 2020, MNRAS[[arXiv]2005.11917]

Benson, A. J. 2010, Phys. Rep., 495, 33

Benson, A. J., Bower, R. G., Frenk, C. S., et al. 2003, ApJ, 599, 38

Bernardi, M., Meert, A., Sheth, R. K., et al. 2013, MNRAS, 436, 697

Bertin, E. 2009, Mem. Soc. Astron. Italiana, 80, 422

Bertin, E. & Arnouts, S. 1996, A&AS, 117, 393

Bertschinger, E. 1985, ApJS, 58, 1

Béthermin, M., Wu, H.-Y., Lagache, G., et al. 2017, A&A, 607, A89

Beutler, F., Blake, C., Colless, M., et al. 2011, MNRAS, 416, 3017

Bica, E., Alloin, D., & Schmitt, H. R. 1994, A&A, 283, 805

Bielby, R., Hudelot, P., McCracken, H. J., et al. 2012, A&A, 545, A23

Birrer, S., Lilly, S., Amara, A., Paranjape, A., & Refregier, A. 2014, ApJ, 793, 12

Blaizot, J., Wadadekar, Y., Guiderdoni, B., et al. 2005, MNRAS, 360, 159

Blanton, M. R., Hogg, D. W., Bahcall, N. A., et al. 2003, ApJ, 592, 819

Blanton, M. R., Schlegel, D. J., Strauss, M. A., et al. 2005, AJ, 129, 2562

Bolzonella, M., Kovač, K., Pozzetti, L., et al. 2010, A&A, 524, A76

Bolzonella, M., Miralles, J.-M., & Pelló, R. 2000, A&A, 363, 476

Boselli, A., Cortese, L., & Boquien, M. 2014, A&A, 564, A65

Bothwell, M. S., Kennicutt, R. C., Johnson, B. D., et al. 2011, MNRAS, 415, 1815

Bouwens, R. J., Illingworth, G. D., González, V., et al. 2010, ApJ, 725, 1587

Bouwens, R. J., Illingworth, G. D., Oesch, P. A., et al. 2015, ApJ, 803, 34

Bower, R. G., Benson, A. J., Malbon, R., et al. 2006, MNRAS, 370, 645

Bowler, R. A. A., Jarvis, M. J., Dunlop, J. S., et al. 2020, MNRAS, 493, 2059

Boylan-Kolchin, M., Springel, V., White, S. D. M., Jenkins, A., & Lemson, G. 2009, MNRAS, 398, 1150

Brammer, G. B., van Dokkum, P. G., & Coppi, P. 2008, ApJ, 686, 1503

Brinchmann, J., Charlot, S., Heckman, T. M., et al. 2004, arXiv e-prints, astro

Bruzual, G. & Charlot, S. 2003, MNRAS, 344, 1000

Bryan, G. L. & Norman, M. L. 1998, ApJ, 495, 80

Burgarella, D., Buat, V., Gruppioni, C., et al. 2013, A&A, 554, A70

Byler, N., Dalcanton, J. J., Conroy, C., & Johnson, B. D. 2017, ApJ, 840, 44

Calzetti, D., Armus, L., Bohlin, R. C., et al. 2000, ApJ, 533, 682

Calzetti, D., Wu, S. Y., Hong, S., et al. 2010, ApJ, 714, 1256

Caputi, K. I., Cirasuolo, M., Dunlop, J. S., et al. 2011, MNRAS, 413, 162

Caputi, K. I., Dunlop, J. S., McLure, R. J., et al. 2012, ApJ, 750, L20

Caputi, K. I., Ilbert, O., Laigle, C., et al. 2015, ApJ, 810, 73

Carretero, J., Castander, F. J., Gaztañaga, E., Crocce, M., & Fosalba, P. 2015, MNRAS, 447, 646

Cassata, P., Guzzo, L., Franceschini, A., et al. 2007, ApJS, 172, 270

Castro-Rodríguez, N. & López-Corredoira, M. 2012, A&A, 537, A31

Cecchi, R., Bolzonella, M., Cimatti, A., & Girelli, G. 2019, ApJ, 880, L14

Chabrier, G. 2003, PASP, 115, 763

Choi, E., Naab, T., Ostriker, J. P., Johansson, P. H., & Moster, B. P. 2014, MNRAS, 442, 440

Choi, J.-H., Weinberg, M. D., & Katz, N. 2007, MNRAS, 381, 987

Chua, K. T. E., Pillepich, A., Rodriguez-Gomez, V., et al. 2017, MNRAS, 472, 4343

Cibinel, A., Carollo, C. M., Lilly, S. J., et al. 2013, ApJ, 777, 116

Cimatti, A., Fraternali, F., & Nipoti, C. 2019, Introduction to Galaxy Formation and Evolution: From Primordial Gas to Present-Day Galaxies

Cirasuolo, M., Afonso, J., Carollo, M., et al. 2014, in Society of Photo-Optical Instrumentation Engineers (SPIE) Conference Series, Vol. 9147, Ground-based and Airborne Instrumentation for Astronomy V, 91470N

Citro, A., Pozzetti, L., Moresco, M., & Cimatti, A. 2016, A&A, 592, A19

Coil, A. L., Newman, J. A., Cooper, M. C., et al. 2006, ApJ, 644, 671

Conroy, C. 2013, Annual Review of Astronomy and Astrophysics, 51, 393

Conroy, C., Gunn, J. E., & White, M. 2009, ApJ, 699, 486

Conroy, C., Prada, F., Newman, J. A., et al. 2007, ApJ, 654, 153

Conroy, C., Wechsler, R. H., & Kravtsov, A. V. 2006, ApJ, 647, 201

Conroy, C., White, M., & Gunn, J. E. 2010, ApJ, 708, 58

Conselice, C. J., Bluck, A. F. L., Buitrago, F., et al. 2011, MNRAS, 413, 80

Cora, S. A., Hough, T., Vega-Martínez, C. A., & Orsi, Á. A. 2019, MNRAS, 483, 1686

Cora, S. A., Vega-Martínez, C. A., Hough, T., et al. 2018, MNRAS, 479, 2

Coupon, J., Arnouts, S., van Waerbeke, L., et al. 2015, MNRAS, 449, 1352

Cowie, L. L., Songaila, A., Hu, E. M., & Cohen, J. G. 1996, AJ, 112, 839

Cristóbal-Hornillos, D., Aguerri, J. A. L., Moles, M., et al. 2009, ApJ, 696, 1554

Croton, D. J. 2006, MNRAS, 369, 1808

Croton, D. J., Stevens, A. R. H., Tonini, C., et al. 2016, ApJS, 222, 22

Cucciati, O., Tresse, L., Ilbert, O., et al. 2012, A&A, 539, A31

Daddi, E., Cimatti, A., Renzini, A., et al. 2004, ApJ, 617, 746

Daddi, E., Dannerbauer, H., Elbaz, D., et al. 2008, ApJ, 673, L21

Daddi, E., Dickinson, M., Chary, R., et al. 2005, ApJ, 631, L13

Daddi, E., Dickinson, M., Morrison, G., et al. 2007, ApJ, 670, 156

Dahlen, T., Mobasher, B., Faber, S. M., et al. 2013, ApJ, 775, 93

Davé, R. 2009, in Astronomical Society of the Pacific Conference Series, Vol. 419, Galaxy Evolution: Emerging Insights and Future Challenges, ed. S. Jogee, I. Marinova, L. Hao, & G. A. Blanc, 347

Davé, R., Oppenheimer, B. D., Katz, N., Kollmeier, J. A., & Weinberg, D. H. 2010, MNRAS, 408, 2051

Davidzon, I., Bolzonella, M., Coupon, J., et al. 2013, A&A, 558, A23

Davidzon, I., Cucciati, O., Bolzonella, M., et al. 2016, A&A, 586, A23

Davidzon, I., Ilbert, O., Laigle, C., et al. 2017, A&A, 605, A70

Davies, L. J. M., Driver, S. P., Robotham, A. S. G., et al. 2016, MNRAS, 461, 458

Davis, M., Efstathiou, G., Frenk, C. S., & White, S. D. M. 1985, ApJ, 292, 371

Davis, M., Meiksin, A., Strauss, M. A., da Costa, L. N., & Yahil, A. 1988, ApJ, 333, L9

Davis, M. & Peebles, P. J. E. 1983, ApJ, 267, 465

Dayal, P. & Ferrara, A. 2018, Phys. Rep., 780, 1

de la Torre, S., Guzzo, L., Kovač, K., et al. 2010, MNRAS, 409, 867

de la Torre, S., Jullo, E., Giocoli, C., et al. 2017, A&A, 608, A44

de la Torre, S., Le Fèvre, O., Porciani, C., et al. 2011, MNRAS, 412, 825

de la Torre, S. & Peacock, J. A. 2013, MNRAS, 435, 743

De Lucia, G. & Blaizot, J. 2007, MNRAS, 375, 2

de Propris, R., Stanford, S. A., Eisenhardt, P. R., Dickinson, M., & Elston, R. 1999, AJ, 118, 719

Dekel, A., Birnboim, Y., Engel, G., et al. 2009, Nature, 457, 451

DeRose, J., Wechsler, R. H., Becker, M. R., et al. 2019, arXiv e-prints, arXiv:1901.02401

Deshmukh, S., Caputi, K. I., Ashby, M. L. N., et al. 2018, ApJ, 864, 166

Despali, G., Giocoli, C., Angulo, R. E., et al. 2016, MNRAS, 456, 2486

Despali, G. & Vegetti, S. 2017, MNRAS, 469, 1997

Dewdney, P. E., Hall, P. J., Schilizzi, R. T., & Lazio, T. J. L. W. 2009, IEEE Proceedings, 97, 1482

Dimauro, P., Huertas-Company, M., Daddi, E., et al. 2018, MNRAS, 478, 5410

Dolag, K., Borgani, S., Murante, G., & Springel, V. 2009, MNRAS, 399, 497

Domínguez Sánchez, H., Pozzi, F., Gruppioni, C., et al. 2011, MNRAS, 417, 900

Doré, O., Bock, J., Ashby, M., et al. 2014, arXiv e-prints, arXiv:1412.4872

Draine, B. T. 2003, ARA&A, 41, 241

Dressler, A. 1980, ApJ, 236, 351

Driver, S. P., Andrews, S. K., da Cunha, E., et al. 2018, MNRAS, 475, 2891

Driver, S. P., Hill, D. T., Kelvin, L. S., et al. 2011, MNRAS, 413, 971

Drory, N., Salvato, M., Gabasch, A., et al. 2005, ApJ, 619, L131

Dubois, Y., Pichon, C., Welker, C., et al. 2014, MNRAS, 444, 1453

Dunlop, J. S., McLure, R. J., Biggs, A. D., et al. 2017, MNRAS, 466, 861

Durkalec, A., Le Fèvre, O., Pollo, A., et al. 2015a, A&A, 583, A128

Durkalec, A., Le Fèvre, O., Pollo, A., et al. 2015b, A&A, 583, A128

Durkalec, A., Le Fèvre, O., Pollo, A., et al. 2018, A&A, 612, A42

Eckert, D., Ettori, S., Coupon, J., et al. 2016, A&A, 592, A12

Eddington, A. S. 1913, MNRAS, 73, 359

Elbaz, D., Daddi, E., Le Borgne, D., et al. 2007, A&A, 468, 33

Erfanianfar, G., Finoguenov, A., Furnell, K., et al. 2019, arXiv e-prints, arXiv:1908.01559

Erickson, L. K., Gottesman, S. T., & Hunter, Jr., J. H. 1987, Nature, 325, 779

Euclid Collaboration, Adam, R., Vannier, M., et al. 2019, A&A, 627, A23

Euclid Collaboration, Desprez, G., Paltani, S., et al. 2020, A&A, 644, A31

Faber, S. M., Willmer, C. N. A., Wolf, C., et al. 2007, ApJ, 665, 265

Fabian, A. C. 2012, ARA&A, 50, 455

Fassbender, R., Nastasi, A., Santos, J. S., et al. 2014, A&A, 568, A5

Faucher-Giguère, C.-A. & Kereš, D. 2011, MNRAS, 412, L118

Ferguson, H. C., Dickinson, M., Giavalisco, M., et al. 2004, ApJ, 600, L107

Ferland, G. J., Porter, R. L., van Hoof, P. A. M., et al. 2013, Rev. Mexicana Astron. Astrofis., 49, 137

Ferrara, A. 2008, Cosmological Feedbacks from the First Stars, ed. A. Loeb, A. Ferrara, & R. S. Ellis, 161–258

Finkelstein, S. L. 2016, PASA, 33, e037

Fioc, M. & Rocca-Volmerange, B. 1997, A&A, 500, 507

Fitzpatrick, E. L. 1986, AJ, 92, 1068

Fontana, A., Dunlop, J. S., Paris, D., et al. 2014, A&A, 570, A11

Fontana, A., Pozzetti, L., Donnarumma, I., et al. 2004, A&A, 424, 23

Fontana, A., Salimbeni, S., Grazian, A., et al. 2006, A&A, 459, 745

Fontanot, F., De Lucia, G., Hirschmann, M., et al. 2017, MNRAS, 464, 3812

Fontanot, F., De Lucia, G., Monaco, P., Somerville, R. S., & Santini, P. 2009, MNRAS, 397, 1776

Foreman-Mackey, D., Hogg, D. W., Lang, D., & Goodman, J. 2013, PASP, 125, 306

Fosalba, P., Gaztañaga, E., Castander, F. J., & Manera, M. 2008, MNRAS, 391, 435

Freedman, W. L., Madore, B. F., Gibson, B. K., et al. 2001, ApJ, 553, 47

Gabor, J. M. & Davé, R. 2015, MNRAS, 447, 374

Galametz, A., Grazian, A., Fontana, A., et al. 2013, ApJS, 206, 10

Gallazzi, A., Charlot, S., Brinchmann, J., White, S. D. M., & Tremonti, C. A. 2005, MNRAS, 362, 41

Gao, L., White, S. D. M., Jenkins, A., Stoehr, F., & Springel, V. 2004, MNRAS, 355, 819

Gelman, A. & Rubin, D. B. 1992, Statistical Science, 7, 457

Genzel, R., Burkert, A., Bouché, N., et al. 2008, ApJ, 687, 59

Giacconi, R., Zirm, A., Wang, J., et al. 2002, ApJS, 139, 369

Giocoli, C., Baldi, M., & Moscardini, L. 2018, MNRAS, 481, 2813

Giocoli, C., Meneghetti, M., Metcalf, R. B., Ettori, S., & Moscardini, L. 2014, MNRAS, 440, 1899

Giocoli, C., Tormen, G., Sheth, R. K., & van den Bosch, F. C. 2010, MNRAS, 404, 502

Giocoli, C., Tormen, G., & van den Bosch, F. C. 2008, MNRAS, 386, 2135

Giodini, S., Pierini, D., Finoguenov, A., et al. 2009, ApJ, 703, 982

Girelli, G., Bolzonella, M., & Cimatti, A. 2019, A&A, 632, A80

Girelli, G., Pozzetti, L., Bolzonella, M., et al. 2020, A&A, 634, A135

Gladders, M. D. & Yee, H. K. C. 2000, AJ, 120, 2148

Glazebrook, K., Schreiber, C., Labbé, I., et al. 2017, Nature, 544, 71

Gobat, R., Daddi, E., Magdis, G., et al. 2018, Nature Astronomy, 2, 239

Gobat, R., Strazzullo, V., Daddi, E., et al. 2012, ApJ, 759, L44

Goerdt, T., Dekel, A., Sternberg, A., Gnat, O., & Ceverino, D. 2012, MNRAS, 424, 2292

Gonzalez, A. H., Sivanandam, S., Zabludoff, A. I., & Zaritsky, D. 2013, ApJ, 778, 14

Gonzalez-Perez, V., Lacey, C. G., Baugh, C. M., et al. 2014, MNRAS, 439, 264

Goodman, J. & Weare, J. 2010, Communications in Applied Mathematics and Computational Science, Vol. 5, No. 1, p. 65-80, 2010, 5, 65

Gordon, K. D., Clayton, G. C., Misselt, K. A., Land olt, A. U., & Wolff, M. J. 2003, ApJ, 594, 279

Grazian, A., Fontana, A., Santini, P., et al. 2015, A&A, 575, A96

Grazian, A., Menci, N., Giallongo, E., et al. 2009, A&A, 505, 1041

Grogin, N. A., Kocevski, D. D., Faber, S. M., et al. 2011, ApJS, 197, 35

Gruppioni, C., Bethermin, M., Loiacono, F., et al. 2020, arXiv e-prints, arXiv:2006.04974

Gruppioni, C., Calura, F., Pozzi, F., et al. 2015, MNRAS, 451, 3419

Grylls, P. J., Shankar, F., Zanisi, L., & Bernardi, M. 2019, MNRAS, 483, 2506

Guhathakurta, P., Tyson, J. A., & Majewski, S. R. 1990, ApJ, 357, L9

Guo, Q., White, S., Boylan-Kolchin, M., et al. 2011, MNRAS, 413, 101

Guo, Q., White, S., Boylan-Kolchin, M., et al. 2013a, MNRAS, 435, 897

Guo, Q., White, S., Li, C., & Boylan-Kolchin, M. 2010, MNRAS, 404, 1111

Guo, Y., Ferguson, H. C., Giavalisco, M., et al. 2013b, ApJS, 207, 24

Guzzo, L., Scodeggio, M., Garilli, B., et al. 2014, A&A, 566, A108

Guzzo, L., Strauss, M. A., Fisher, K. B., Giovanelli, R., & Haynes, M. P. 1997, ApJ, 489, 37

Harikane, Y., Ouchi, M., Ono, Y., et al. 2016, ApJ, 821, 123

Harikane, Y., Ouchi, M., Ono, Y., et al. 2018, PASJ, 70, S11

Hayes, M., Östlin, G., Schaerer, D., et al. 2010, Nature, 464, 562

Heavens, A., Panter, B., Jimenez, R., & Dunlop, J. 2004, Nature, 428, 625

Henriques, B. M. B., White, S. D. M., Lemson, G., et al. 2012, MNRAS, 421, 2904

Henriques, B. M. B., White, S. D. M., Thomas, P. A., et al. 2015, MNRAS, 451, 2663

Henriques, B. M. B., White, S. D. M., Thomas, P. A., et al. 2013, MNRAS, 431, 3373

Henriques, B. M. B., White, S. D. M., Thomas, P. A., et al. 2017, MNRAS, 469, 2626

Hinshaw, G., Larson, D., Komatsu, E., et al. 2013, ApJS, 208, 19

Hopkins, P. F. 2015, MNRAS, 450, 53

Hopkins, P. F., Cox, T. J., Kereš, D., & Hernquist, L. 2008a, ApJS, 175, 390

Hopkins, P. F., Hernquist, L., Cox, T. J., & Kereš, D. 2008b, ApJS, 175, 356

Hoversten, E. A., Gronwall, C., Vanden Berk, D. E., et al. 2009, ApJ, 705, 1462

Hubble, E. P. 1927, The Observatory, 50, 276

Huertas-Company, M., Gravet, R., Cabrera-Vives, G., et al. 2015, ApJS, 221, 8

Ilbert, O., Arnouts, S., Le Floc'h, E., et al. 2015, A&A, 579, A2

Ilbert, O., Arnouts, S., McCracken, H. J., et al. 2006, A&A, 457, 841

Ilbert, O., McCracken, H. J., Le Fèvre, O., et al. 2013, A&A, 556, A55

Ilbert, O., Salvato, M., Le Floc'h, E., et al. 2010, ApJ, 709, 644

Inoue, A. K., Shimizu, I., Iwata, I., & Tanaka, M. 2014, MNRAS, 442, 1805

Iovino, A., Petropoulou, V., Scodeggio, M., et al. 2016, A&A, 592, A78

Jenkins, A., Frenk, C. S., White, S. D. M., et al. 2001, MNRAS, 321, 372

Juneau, S., Bournaud, F., Charlot, S., et al. 2014a, ApJ, 788, 88

Juneau, S., Bournaud, F., Charlot, S., et al. 2014b, ApJ, 788, 88

Juneau, S., Dickinson, M., Alexander, D. M., & Salim, S. 2011, ApJ, 736, 104

Kaiser, N. 1987, MNRAS, 227, 1

Kashino, D., Silverman, J. D., Sanders, D., et al. 2019, ApJS, 241, 10

Kauffmann, G., Colberg, J. M., Diaferio, A., & White, S. D. M. 1999, MNRAS, 303, 188

Kauffmann, G., Heckman, T. M., Tremonti, C., et al. 2003, MNRAS, 346, 1055

Kauffmann, G., White, S. D. M., & Guiderdoni, B. 1993, MNRAS, 264, 201

Keenan, F. P., Crockett, P. J., Aggarwal, K. M., Jess, D. B., & Mathioudakis, M. 2009, A&A, 495, 359

Keihänen, E., Kurki-Suonio, H., Lindholm, V., et al. 2019, arXiv e-prints [[arXiv]1905.01133]

Kennicutt, Robert C., J. 1998, ARA&A, 36, 189

Kewley, L. J., Dopita, M. A., Sutherland, R. S., Heisler, C. A., & Trevena, J. 2001, ApJ, 556, 121

Kewley, L. J., Maier, C., Yabe, K., et al. 2013, ApJ, 774, L10

Khusanova, Y., Béthermin, M., Le Fèvre, O., et al. 2020, arXiv e-prints, arXiv:2007.08384

Kim, J.-h., Agertz, O., Teyssier, R., et al. 2016, ApJ, 833, 202

Kimm, T., Somerville, R. S., Yi, S. K., et al. 2009, MNRAS, 394, 1131

Kimm, T., Yi, S. K., & Khochfar, S. 2011, ApJ, 729, 11

Kistler, M. D., Yüksel, H., Beacom, J. F., Hopkins, A. M., & Wyithe, J. S. B. 2009, ApJ, 705, L104

Kitzbichler, M. G. & White, S. D. M. 2007, MNRAS, 376, 2

Klypin, A. A., Trujillo-Gomez, S., & Primack, J. 2011, ApJ, 740, 102

Knebe, A., Knollmann, S. R., Muldrew, S. I., et al. 2011, MNRAS, 415, 2293

Knebe, A., Pearce, F. R., Gonzalez-Perez, V., et al. 2018, MNRAS, 475, 2936

Knebe, A., Pearce, F. R., Thomas, P. A., et al. 2015, MNRAS, 451, 4029

Kodama, T. & Arimoto, N. 1997, A&A, 320, 41

Kodama, T. & Bower, R. 2003, MNRAS, 346, 1

Koekemoer, A. M., Faber, S. M., Ferguson, H. C., et al. 2011, ApJS, 197, 36

Komatsu, E. 2006, Progress of Theoretical Physics Supplement, 163, 185

Kormendy, J. & Ho, L. C. 2013, ARA&A, 51, 511

Kravtsov, A. V. & Borgani, S. 2012, ARA&A, 50, 353

Kravtsov, A. V., Klypin, A. A., & Khokhlov, A. M. 1997, ApJS, 111, 73

Kravtsov, A. V., Vikhlinin, A. A., & Meshcheryakov, A. V. 2018, Astronomy Letters, 44, 8

Kriek, M., Labbé, I., Conroy, C., et al. 2010, ApJ, 722, L64

Kriek, M., van Dokkum, P. G., Labbé, I., et al. 2009, ApJ, 700, 221

Kroupa, P. 2001, MNRAS, 322, 231

Krumholz, M. R. 2015, arXiv e-prints, arXiv:1511.03457

Laigle, C., Davidzon, I., Ilbert, O., et al. 2019, Monthly Notices of the Royal Astronomical Society, 486, 5104

Laigle, C., McCracken, H. J., Ilbert, O., et al. 2016, ApJS, 224, 24

Landy, S. D. & Szalay, A. S. 1993, ApJ, 412, 64

Lang, P., Wuyts, S., Somerville, R. S., et al. 2014, ApJ, 788, 11

Laureijs, R., Amiaux, J., Arduini, S., et al. 2011, arXiv e-prints, arXiv:1110.3193

Lawrence, A., Warren, S. J., Almaini, O., et al. 2007, MNRAS, 379, 1599

Lee, J. & Yi, S. K. 2013, ApJ, 766, 38

Legrand, L., McCracken, H. J., Davidzon, I., et al. 2019, MNRAS, 486, 5468

Leroy, A. K., Walter, F., Brinks, E., et al. 2008, AJ, 136, 2782

Li, C., Jing, Y. P., Mao, S., et al. 2012, ApJ, 758, 50

Li, C. & White, S. D. M. 2009, MNRAS, 398, 2177

Lilly, S. J., Carollo, C. M., Pipino, A., Renzini, A., & Peng, Y. 2013, ApJ, 772, 119

Lilly, S. J., Le Fèvre, O., Renzini, A., et al. 2007, ApJS, 172, 70

Lin, Y.-T., Mohr, J. J., & Stanford, S. A. 2003, ApJ, 591, 749

Lin, Y.-T., Mohr, J. J., & Stanford, S. A. 2004, ApJ, 610, 745

Loiacono, F., Decarli, R., Gruppioni, C., et al. 2020, arXiv e-prints, arXiv:2006.04837

Lotz, J. M., Primack, J., & Madau, P. 2004, AJ, 128, 163

LSST Science Collaboration, Abell, P. A., Allison, J., et al. 2009, arXiv e-prints, arXiv:0912.0201

Lu, Y., Wechsler, R. H., Somerville, R. S., et al. 2014, ApJ, 795, 123

Madau, P. 1995, ApJ, 441, 18

Madau, P. & Dickinson, M. 2014, ARA&A, 52, 415

Madau, P. & Pozzetti, L. 2000, MNRAS, 312, L9

Madgwick, D. S., Hawkins, E., Lahav, O., et al. 2003, MNRAS, 344, 847

Mancini, C., Matute, I., Cimatti, A., et al. 2009, A&A, 500, 705

Mandelbaum, R., Seljak, U., Kauffmann, G., Hirata, C. M., & Brinkmann, J. 2006, MNRAS, 368, 715

Mandelbaum, R., Tasitsiomi, A., Seljak, U., Kravtsov, A. V., & Wechsler, R. H. 2005, MNRAS, 362, 1451

Mannucci, F., Cresci, G., Maiolino, R., Marconi, A., & Gnerucci, A. 2010, MNRAS, 408, 2115

Maraston, C. 2005, MNRAS, 362, 799

Maraston, C., Daddi, E., Renzini, A., et al. 2006, ApJ, 652, 85

Marrone, D. P., Spilker, J. S., Hayward, C. C., et al. 2018, Nature, 553, 51

Martin, C. L., Shapley, A. E., Coil, A. L., et al. 2012, ApJ, 760, 127

Martis, N. S., Marchesini, D. M., Muzzin, A., et al. 2019, arXiv e-prints, arXiv:1907.08152

Marulli, F., Bolzonella, M., Branchini, E., et al. 2013, A&A, 557, A17

Marulli, F., Veropalumbo, A., & Moresco, M. 2016, Astronomy and Computing, 14, 35

Mathis, J. S. 1990, ARA&A, 28, 37

Mathis, J. S. & Whiffen, G. 1989, ApJ, 341, 808

Matthee, J., Schaye, J., Crain, R. A., et al. 2017, MNRAS, 465, 2381

Maturi, M., Bellagamba, F., Radovich, M., et al. 2019, MNRAS, 485, 498

Mawatari, K., Yamada, T., Fazio, G. G., Huang, J.-S., & Ashby, M. L. N. 2016, PASJ, 68, 46

McAlpine, S., Helly, J. C., Schaller, M., et al. 2016, Astronomy and Computing, 15, 72

McConnell, N. J. & Ma, C.-P. 2013, ApJ, 764, 184

McCracken, H. J., Milvang-Jensen, B., Dunlop, J., et al. 2012, A&A, 544, A156

McCracken, H. J., Wolk, M., Colombi, S., et al. 2015, MNRAS, 449, 901

McKee, C. F. & Ostriker, E. C. 2007, ARA&A, 45, 565

Mehta, V., Scarlata, C., Capak, P., et al. 2018, ApJS, 235, 36

Mei, S., Holden, B. P., Blakeslee, J. P., et al. 2009, ApJ, 690, 42

Meneux, B., Guzzo, L., de la Torre, S., et al. 2009, A&A, 505, 463

Meneux, B., Guzzo, L., Garilli, B., et al. 2008, A&A, 478, 299

Merlin, E., Fontana, A., Castellano, M., et al. 2018, MNRAS, 473, 2098

Merlin, E., Fortuni, F., Torelli, M., et al. 2019a, MNRAS, 2241

Merlin, E., Fortuni, F., Torelli, M., et al. 2019b, MNRAS, 490, 3309

Merson, A. I., Baugh, C. M., Helly, J. C., et al. 2013, MNRAS, 429, 556

Meurer, G. R., Heckman, T. M., & Calzetti, D. 1999, ApJ, 521, 64

Mitchell, P. D., Lacey, C. G., Baugh, C. M., & Cole, S. 2013, Monthly Notices of the Royal Astronomical Society, 435, 87

Mitchell, P. D., Schaye, J., & Bower, R. G. 2020, MNRAS[[arXiv]2005.10262]

Mo, H., van den Bosch, F. C., & White, S. 2010, Galaxy Formation and Evolution

Monaco, P. 2016, Galaxies, 4, 53

Monaco, P., Fontanot, F., & Taffoni, G. 2007, MNRAS, 375, 1189

More, S., van den Bosch, F. C., & Cacciato, M. 2009a, MNRAS, 392, 917

More, S., van den Bosch, F. C., Cacciato, M., et al. 2009b, MNRAS, 392, 801

More, S., van den Bosch, F. C., Cacciato, M., et al. 2011, MNRAS, 410, 210

Moresco, M., Pozzetti, L., Cimatti, A., et al. 2013, A&A, 558, A61

Mortlock, A., Conselice, C. J., Bluck, A. F. L., et al. 2011, MNRAS, 413, 2845

Moster, B. P., Naab, T., & White, S. D. M. 2013, MNRAS, 428, 3121

Moster, B. P., Naab, T., & White, S. D. M. 2018, MNRAS, 477, 1822

Moster, B. P., Somerville, R. S., Maulbetsch, C., et al. 2010, ApJ, 710, 903

Moster, B. P., Somerville, R. S., Newman, J. A., & Rix, H.-W. 2011, ApJ, 731, 113

Moustakas, J., Coil, A. L., Aird, J., et al. 2013, ApJ, 767, 50

Moutard, T., Arnouts, S., Ilbert, O., et al. 2016a, A&A, 590, A103

Moutard, T., Arnouts, S., Ilbert, O., et al. 2016b, A&A, 590, A102

Muzzin, A., Marchesini, D., Stefanon, M., et al. 2013, ApJ, 777, 18

Naab, T., Oser, L., Emsellem, E., et al. 2014, MNRAS, 444, 3357

Naab, T. & Ostriker, J. P. 2017, ARA&A, 55, 59

Nadler, E. O., Oh, S. P., & Ji, S. 2017, MNRAS, 470, 500

Nagai, D. & Kravtsov, A. V. 2005, ApJ, 618, 557

Navarro, J. F., Frenk, C. S., & White, S. D. M. 1996, ApJ, 462, 563

Navarro, J. F., Frenk, C. S., & White, S. D. M. 1997, ApJ, 490, 493

Nayyeri, H., Mobasher, B., Hemmati, S., et al. 2014, ApJ, 794, 68

Nelson, D., Pillepich, A., Genel, S., et al. 2015, Astronomy and Computing, 13, 12

Nelson, D., Pillepich, A., Springel, V., et al. 2018, MNRAS, 475, 624

Nelson, D., Springel, V., Pillepich, A., et al. 2019, Computational Astrophysics and Cosmology, 6, 2

Niemiec, A., Jullo, E., Giocoli, C., Limousin, M., & Jauzac, M. 2019, MNRAS, 487, 653

Norberg, P., Baugh, C. M., Gaztañaga, E., & Croton, D. J. 2009, MNRAS, 396, 19

Novak, M., Smolčić, V., Delhaize, J., et al. 2017, A&A, 602, A5

Oesch, P. A., Bouwens, R. J., Illingworth, G. D., et al. 2013, ApJ, 773, 75

Oesch, P. A., Bouwens, R. J., Illingworth, G. D., Labbé, I., & Stefanon, M. 2018, ApJ, 855, 105

Oesch, P. A., Brammer, G., van Dokkum, P. G., et al. 2016, ApJ, 819, 129

Onions, J., Knebe, A., Pearce, F. R., et al. 2012, MNRAS, 423, 1200

Oppenheimer, B. D. & Davé, R. 2008, MNRAS, 387, 577

Ostriker, J. P. & McKee, C. F. 1988, Reviews of Modern Physics, 60, 1

Pacifici, C., Charlot, S., Blaizot, J., & Brinchmann, J. 2012, Monthly Notices of the Royal Astronomical Society, 421, 2002

Pan, Z., Peng, Y., Zheng, X., Wang, J., & Kong, X. 2019, ApJ, 876, 21

Pannella, M., Elbaz, D., Daddi, E., et al. 2015, ApJ, 807, 141

Pannella, M., Gabasch, A., Goranova, Y., et al. 2009, ApJ, 701, 787

Panter, B., Jimenez, R., Heavens, A. F., & Charlot, S. 2007, MNRAS, 378, 1550

Papovich, C., Dickinson, M., & Ferguson, H. C. 2001, ApJ, 559, 620

Pearson, W. J., Wang, L., Hurley, P. D., et al. 2018, A&A, 615, A146

Peebles, P. J. E. 1980, The large-scale structure of the universe

Pei, Y. C. 1992, ApJ, 395, 130

Pelló, R., Hudelot, P., Laporte, N., et al. 2018, A&A, 620, A51

Peng, Y.-j., Lilly, S. J., Kovač, K., et al. 2010, ApJ, 721, 193

Pérez-González, P. G., Rieke, G. H., Villar, V., et al. 2008, ApJ, 675, 234

Pezzotta, A., de la Torre, S., Bel, J., et al. 2017, A&A, 604, A33

Planck Collaboration, Adam, R., Ade, P. A. R., et al. 2016, A&A, 594, A1

Planck Collaboration, Ade, P. A. R., Aghanim, N., et al. 2014, A&A, 571, A1

Planck Collaboration, Aghanim, N., Akrami, Y., et al. 2018, arXiv e-prints, arXiv:1807.06209

Pollo, A., Meneux, B., Guzzo, L., et al. 2005, A&A, 439, 887

Posti, L., Fraternali, F., & Marasco, A. 2019, A&A, 626, A56

Potter, D., Stadel, J., & Teyssier, R. 2017, Computational Astrophysics and Cosmology, 4, 2

Pozzetti, L., Bolzonella, M., Lamareille, F., et al. 2007, A&A, 474, 443

Pozzetti, L., Bolzonella, M., Zucca, E., et al. 2010, A&A, 523, A13

Pozzetti, L., Hirata, C. M., Geach, J. E., et al. 2016, A&A, 590, A3

Pozzetti, L. & Mannucci, F. 2000, MNRAS, 317, L17

Prevot, M. L., Lequeux, J., Prevot, L., Maurice, E., & Rocca-Volmerange, B. 1984, A&A, 132, 389

Puchwein, E., Baldi, M., & Springel, V. 2013, MNRAS, 436, 348

Reddick, R. M., Wechsler, R. H., Tinker, J. L., & Behroozi, P. S. 2013, ApJ, 771, 30

Reed, D. S., Bower, R., Frenk, C. S., Jenkins, A., & Theuns, T. 2007, MNRAS, 374, 2

Renzini, A. 2006, ARA&A, 44, 141

Riess, A. G., Filippenko, A. V., Challis, P., et al. 1998, AJ, 116, 1009

Rodighiero, G., Cimatti, A., Gruppioni, C., et al. 2010, A&A, 518, L25

Rodighiero, G., Daddi, E., Baronchelli, I., et al. 2011, ApJ, 739, L40

Rodríguez-Puebla, A., Avila-Reese, V., Yang, X., et al. 2015, ApJ, 799, 130

Rodríguez-Puebla, A., Primack, J. R., Avila-Reese, V., & Faber, S. M. 2017, MNRAS, 470, 651

Rosdahl, J. & Blaizot, J. 2012, MNRAS, 423, 344

Rovilos, E., Burwitz, V., Szokoly, G., et al. 2009, A&A, 507, 195

Rowan-Robinson, M., Oliver, S., Wang, L., et al. 2016, MNRAS, 461, 1100

Rubin, K. H. R., Prochaska, J. X., Koo, D. C., & Phillips, A. C. 2012, ApJ, 747, L26

Saito, S., de la Torre, S., Ilbert, O., et al. 2020, MNRAS, 494, 199

Salmon, B., Papovich, C., Finkelstein, S. L., et al. 2015, ApJ, 799, 183

Salpeter, E. E. 1955, ApJ, 121, 161

Sánchez, S. F., Avila-Reese, V., Rodríguez-Puebla, A., et al. 2019, MNRAS, 482, 1557

Santini, P., Fontana, A., Castellano, M., et al. 2017, ApJ, 847, 76

Santini, P., Fontana, A., Grazian, A., et al. 2012, A&A, 538, A33

Sargent, M. T., Béthermin, M., Daddi, E., & Elbaz, D. 2012, ApJ, 747, L31

Sartoris, B., Biviano, A., Fedeli, C., et al. 2016, MNRAS, 459, 1764

Savage, B. D. & Mathis, J. S. 1979, ARA&A, 17, 73

Sawicki, M. 2012, PASP, 124, 1208

Sawicki, M., Arnouts, S., Huang, J., et al. 2019, MNRAS, 489, 5202

Sawicki, M. & Yee, H. K. C. 1998, AJ, 115, 1329

Schaye, J., Crain, R. A., Bower, R. G., et al. 2015, MNRAS, 446, 521

Schechter, P. 1976, ApJ, 203, 297

Schlafly, E. F. & Finkbeiner, D. P. 2011, ApJ, 737, 103

Schlegel, D. J., Finkbeiner, D. P., & Davis, M. 1998, ApJ, 500, 525

Schmidt, M. 1968, ApJ, 151, 393

Schreiber, C., Elbaz, D., Pannella, M., et al. 2017, A&A, 602, A96

Schreiber, C., Elbaz, D., Pannella, M., et al. 2018, EGG: Empirical Galaxy Generator

Schreiber, C., Pannella, M., Elbaz, D., et al. 2015, A&A, 575, A74

Scodeggio, M., Guzzo, L., Garilli, B., et al. 2018, A&A, 609, A84

Scoville, N., Aussel, H., Brusa, M., et al. 2007, ApJS, 172, 1

Seaton, M. J. 1979, MNRAS, 187, 73P

Shapley, A. E., Reddy, N. A., Kriek, M., et al. 2015, ApJ, 801, 88

Shapley, A. E., Steidel, C. C., Adelberger, K. L., et al. 2001, ApJ, 562, 95

Shapley, A. E., Steidel, C. C., Erb, D. K., et al. 2005, The Astrophysical Journal, 626, 698

Shen, S., Mo, H. J., White, S. D. M., et al. 2003, MNRAS, 343, 978

Sheth, R. K., Mo, H. J., & Tormen, G. 2001, MNRAS, 323, 1

Sijacki, D., Vogelsberger, M., Genel, S., et al. 2015, MNRAS, 452, 575

Silk, J. 1997, ApJ, 481, 703

Silk, J. & Mamon, G. A. 2012, Research in Astronomy and Astrophysics, 12, 917

Sobral, D., Matthee, J., Darvish, B., et al. 2018, MNRAS, 477, 2817

Somerville, R. S. & Davé, R. 2015, ARA&A, 53, 51

Somerville, R. S., Hopkins, P. F., Cox, T. J., Robertson, B. E., & Hernquist, L. 2008, MNRAS, 391, 481

Somerville, R. S., Moustakas, L. A., Mobasher, B., et al. 2004, ApJ, 600, L135

Song, M., Finkelstein, S. L., Ashby, M. L. N., et al. 2016, ApJ, 825, 5

Sparre, M., Hayward, C. C., Springel, V., et al. 2015, MNRAS, 447, 3548

Speagle, J. S., Steinhardt, C. L., Capak, P. L., & Silverman, J. D. 2014, ApJS, 214, 15

Spergel, D., Gehrels, N., Baltay, C., et al. 2015, arXiv e-prints, arXiv:1503.03757

Spergel, D. N., Verde, L., Peiris, H. V., et al. 2003, ApJS, 148, 175

Spitzer, L. 1978, Physical processes in the interstellar medium

Springel, V. 2010, MNRAS, 401, 791

Springel, V. & Hernquist, L. 2003, MNRAS, 339, 289

Springel, V., Wang, J., Vogelsberger, M., et al. 2008, MNRAS, 391, 1685

Springel, V., White, S. D. M., Jenkins, A., et al. 2005, Nature, 435, 629

Springel, V., White, S. D. M., Tormen, G., & Kauffmann, G. 2001, MNRAS, 328, 726

Stark, D. P., Ellis, R. S., Bunker, A., et al. 2009, ApJ, 697, 1493

Stefanon, M., Bouwens, R. J., Labbé, I., et al. 2017, ApJ, 843, 36

Stefanon, M., Labbé, I., Bouwens, R., & Oesch, P. 2020, in IAU Symposium, Vol. 352, IAU Symposium, ed. E. da Cunha, J. Hodge, J. Afonso, L. Pentericci, & D. Sobral, 115–118

Stefanon, M., Marchesini, D., Muzzin, A., et al. 2015, ApJ, 803, 11

Stefanon, M., Marchesini, D., Rudnick, G. H., Brammer, G. B., & Whitaker, K. E. 2013, ApJ, 768, 92

Steidel, C. C., Adelberger, K. L., Giavalisco, M., Dickinson, M., & Pettini, M. 1999, ApJ, 519, 1

Steidel, C. C., Giavalisco, M., Dickinson, M., & Adelberger, K. L. 1996, AJ, 112, 352

Steinhardt, C. L., Capak, P., Masters, D., & Speagle, J. S. 2016, ApJ, 824, 21

Stott, J. P., Swinbank, A. M., Johnson, H. L., et al. 2016, MNRAS, 457, 1888

Straatman, C. M. S., Labbé, I., Spitler, L. R., et al. 2014, ApJ, 783, L14

Straatman, C. M. S., Spitler, L. R., Quadri, R. F., et al. 2016, ApJ, 830, 51

Strazzullo, V., Rosati, P., Stanford, S. A., et al. 2006, A&A, 450, 909

Tacchella, S., Bose, S., Conroy, C., Eisenstein, D. J., & Johnson, B. D. 2018, ApJ, 868, 92

Tacconi, L. J., Neri, R., Genzel, R., et al. 2013, ApJ, 768, 74

Taylor, E. N., Hopkins, A. M., Baldry, I. K., et al. 2011, Monthly Notices of the Royal Astronomical Society, 418, 1587

Thomas, D., Maraston, C., Schawinski, K., Sarzi, M., & Silk, J. 2010, MNRAS, 404, 1775

Tomczak, A. R., Quadri, R. F., Tran, K.-V. H., et al. 2016, ApJ, 817, 118

Tomczak, A. R., Quadri, R. F., Tran, K.-V. H., et al. 2014, ApJ, 783, 85

Tremonti, C. A., Heckman, T. M., Kauffmann, G., et al. 2004, ApJ, 613, 898

Valentino, F., Tanaka, M., Davidzon, I., et al. 2020, ApJ, 889, 93

van den Bosch, F. C., Tormen, G., & Giocoli, C. 2005, MNRAS, 359, 1029

van den Bosch, F. C., Yang, X., & Mo, H. J. 2003, MNRAS, 340, 771

van der Wel, A., Bell, E. F., Häussler, B., et al. 2012, ApJS, 203, 24

van der Wel, A., Franx, M., van Dokkum, P. G., et al. 2014, ApJ, 788, 28

Veilleux, S. & Osterbrock, D. E. 1987, ApJS, 63, 295

Velander, M., van Uitert, E., Hoekstra, H., et al. 2014, MNRAS, 437, 2111

Vogelsberger, M., Genel, S., Springel, V., et al. 2014, Nature, 509, 177

Vogelsberger, M., Marinacci, F., Torrey, P., & Puchwein, E. 2020, Nature Reviews Physics, 2, 42

Walcher, J., Groves, B., Budavári, T., & Dale, D. 2011, Ap&SS, 331, 1

Wang, L., Dutton, A. A., Stinson, G. S., et al. 2015, MNRAS, 454, 83

Wang, L. & Jing, Y. P. 2010, MNRAS, 402, 1796

Wang, L., Li, C., Kauffmann, G., & De Lucia, G. 2006, MNRAS, 371, 537

Wang, T., Elbaz, D., Schreiber, C., et al. 2016, ApJ, 816, 84

Wechsler, R. H., Bullock, J. S., Primack, J. R., Kravtsov, A. V., & Dekel, A. 2002, ApJ, 568, 52

Wechsler, R. H. & Tinker, J. L. 2018, ARA&A, 56, 435

Weingartner, J. C. & Draine, B. T. 2001, ApJ, 548, 296

White, M. 2001, A&A, 367, 27

White, S. D. M. & Rees, M. J. 1978, MNRAS, 183, 341

Wiklind, T., Dickinson, M., Ferguson, H. C., et al. 2008, ApJ, 676, 781

Williams, R. J., Quadri, R. F., Franx, M., van Dokkum, P., & Labbé, I. 2009, ApJ, 691, 1879

Willick, J. A., Courteau, S., Faber, S. M., et al. 1997, ApJS, 109, 333

Yan, H., Dickinson, M., Stern, D., et al. 2005, ApJ, 634, 109

Yang, X., Mo, H. J., & van den Bosch, F. C. 2009, ApJ, 693, 830

Yang, X., Mo, H. J., van den Bosch, F. C., Zhang, Y., & Han, J. 2012, ApJ, 752, 41

Yang, X., Mo, H. J., Zhang, Y., & van den Bosch, F. C. 2011, ApJ, 741, 13

York, D. G., Adelman, J., Anderson, John E., J., et al. 2000, AJ, 120, 1579

Zahid, H. J., Dima, G. I., Kewley, L. J., Erb, D. K., & Davé, R. 2012, ApJ, 757, 54

Zehavi, I., Blanton, M. R., Frieman, J. A., et al. 2002, ApJ, 571, 172

Zehavi, I., Zheng, Z., Weinberg, D. H., et al. 2011, ApJ, 736, 59

Zhang, X., Feng, Y., Chen, H., & Yuan, Q. 2020, arXiv e-prints, arXiv:2010.13037

Zheng, Z., Coil, A. L., & Zehavi, I. 2007, ApJ, 667, 760